

Jiadong Zang · Vincent Cros
Axel Hoffmann *Editors*

Topology in Magnetism



Springer

Springer Series in Solid-State Sciences

Volume 192

Series editors

Bernhard Keimer, Stuttgart, Germany

Roberto Merlin, Ann Arbor, MI, USA

Hans-Joachim Queisser, Stuttgart, Germany

Klaus von Klitzing, Stuttgart, Germany

The Springer Series in Solid-State Sciences consists of fundamental scientific books prepared by leading researchers in the field. They strive to communicate, in a systematic and comprehensive way, the basic principles as well as new developments in theoretical and experimental solid-state physics.

More information about this series at <http://www.springer.com/series/682>

Jiadong Zang · Vincent Cros
Axel Hoffmann
Editors

Topology in Magnetism

Editors

Jiadong Zang
University of New Hampshire
Durham, NH, USA

Axel Hoffmann
Materials Science Division
Argonne National Laboratory
Lemont, IL, USA

Vincent Cros
Unité Mixte de Physique CNRS/Thales
Palaiseau, France

ISSN 0171-1873 ISSN 2197-4179 (electronic)

Springer Series in Solid-State Sciences

ISBN 978-3-319-97333-3 ISBN 978-3-319-97334-0 (eBook)
<https://doi.org/10.1007/978-3-319-97334-0>

Library of Congress Control Number: 2018949638

© Springer International Publishing AG, part of Springer Nature 2018

This work is subject to copyright. All rights are reserved by the Publisher, whether the whole or part of the material is concerned, specifically the rights of translation, reprinting, reuse of illustrations, recitation, broadcasting, reproduction on microfilms or in any other physical way, and transmission or information storage and retrieval, electronic adaptation, computer software, or by similar or dissimilar methodology now known or hereafter developed.

The use of general descriptive names, registered names, trademarks, service marks, etc. in this publication does not imply, even in the absence of a specific statement, that such names are exempt from the relevant protective laws and regulations and therefore free for general use.

The publisher, the authors and the editors are safe to assume that the advice and information in this book are believed to be true and accurate at the date of publication. Neither the publisher nor the authors or the editors give a warranty, express or implied, with respect to the material contained herein or for any errors or omissions that may have been made. The publisher remains neutral with regard to jurisdictional claims in published maps and institutional affiliations.

This Springer imprint is published by the registered company Springer Nature Switzerland AG
The registered company address is: Gewerbestrasse 11, 6330 Cham, Switzerland

Preface

The purpose of this collective book is to present selected topics of modern magnetism research, where the physical phenomena are directly related to topological properties. As was highlighted by the Nobel Prize in Physics in 2016 for the work of David J. Thouless, F. Duncan M. Haldane, and J. Michael Kosterlitz, concepts of topology have provided recently a powerful approach toward understanding a wide variety of contemporary condensed matter physics. Toward this end, combining topology with magnetism has given rise to numerous vibrant new topics, such as skyrmions and topological insulators. These are not only fundamentally interesting, but also are promising for a transformative revolution of information technology using topological charge as a new state variable.

We organized the book in roughly three parts. The first part focuses on phenomena that are governed by spin textures with non-trivial topology in real space. Chapter 1 (H.-B. Braun) provides a general overview of real space topological solitons in magnetic systems. Subsequently, Chap. 2 (A. Thiaville and J. Miltat) discusses to what extent magnetic domain walls are related to topology of spin textures and how this influences their dynamics. Related concepts are further explored in Chap. 3 (C. Behncke, C. F. Adolff, and G. Meier) for a specific type of topological solitons, namely magnetic vortices, that form in geometrically confined magnetic structures. Another type of topological soliton, magnetic skyrmions, is discussed in Chap. 4 (G. Chen), which focuses on skyrmions, a new magnetic state that can exist in magnetic multilayers where they have been considered as data carriers for information technologies, and in Chap. 5 (A. Bauer, A. Chacon, M. Halder, and C. Pfleiderer), which describes non-equilibrium behaviors of skyrmion lattices in bulk materials with lack of inversion symmetry.

The second part of the book is dedicated to physical phenomena, where the topology of the electronic band structure results in effective coupling between spin and charge transport. Toward this end, Chap. 6 (Y. Mokrousov) discusses the theoretical understanding of anomalous Hall effects, which despite their experimental discovery more than one hundred years ago, just very recently have been understood as fundamentally connected to the topology in momentum space and the related Berry phase physics. Chapter 7 (M. Althammer) discusses the closely

related spin Hall effect and focuses on how this effect can be experimentally explored via many different measurement approaches. This is followed by Chap. 8 (B. Wan, H.-Z. Lu, and X. Wan) by an introduction to Weyl semimetals, where the topology generates non-trivial surface and bulk electronic states. Lastly, Chap. 9 (L. Šmejkal and T. Jungwirth) discusses how the new field of antiferromagnetic spintronics provides interesting connections to topology in particular for Weyl and Dirac semimetals.

The last part of the book explores how topology may affect dynamics phenomena and excitations in magnetic systems. Chapter 10 (S. Demokritov) provides a detailed overview of spin waves, or magnons, and how their properties are influenced by geometric confinement of ferromagnets. This discussion is complemented by Chap. 11 (J. Åkerman), which focuses on localized magnetic excitations that are driven by spin transfer torques and how their dynamics relates to their topological properties. Finally, Chap. 12 (J. C. Y. Teo) describes how the antagonistic interplay between magnetism and superconductivity can give rise to novel quasiparticle excitations, Majorana fermions, whose unique topological properties are envisioned to be beneficial for robust quantum computation development.

Our hope is that the readers will find this a stimulating collection of concepts with intriguing connections between them. Our aim was to make the presentation of these concepts accessible to graduate students and researchers new to the field, while also providing a useful snapshot of the most recent developments that can serve as a reference for the expert. Through this effort, and together with the rapid pace of developments in many of the topics discussed in this book, we hope to contribute to the multitude of new exciting developments in the coming years resulting from exploiting topological concepts in the vast range of available magnetism-related materials systems.

Durham, NH, USA
Lemont, IL, USA
Paris, France

Jiadong Zang
Axel Hoffmann
Vincent Cros

Contents

1	Solitons in Real Space: Domain Walls, Vortices, Hedgehogs, and Skyrmions	1
Hans-Benjamin Braun		
1.1	Overview	2
1.2	Topological Defects—A Brief Synopsis	6
1.2.1	Homotopy	6
1.2.2	Winding Numbers	9
1.2.3	Singular Topological Defects	12
1.2.4	Smooth Defects—Skyrmions, Merons and Domain Walls	13
1.3	Energy and Magnetization Dynamics at the Nanoscale	17
1.3.1	Nanodots	18
1.3.2	Nanowires	20
1.3.3	Thin Films	21
1.4	Statics and Dynamics of Smooth Spin Textures	21
1.4.1	2π Bloch Walls and Breathers	22
1.4.2	Variational Ansatz for Static Skyrmions	28
1.4.3	Helicity Switching of Skyrmions	32
1.4.4	Dynamical Skyrmions	33
1.5	Conclusions	37
	References	38
2	Topology and Magnetic Domain Walls	41
André Thiaville and Jacques Miltat		
2.1	Introduction: Topology Applied to Magnetic Domain Walls	41
2.1.1	Domain Walls as Topological Defects	42
2.1.2	Domain Walls as Topologically Stable Textures	44
2.1.3	Lines as Topologically Stable Textures	47

2.2	Topology and the Theory of Magnetic Domain Walls	
	Dynamics	50
2.2.1	The Thiele Equation	51
2.2.2	The Canonical Momentum	54
2.3	Experiments with Bloch and Néel Lines	57
2.3.1	In-Plane Soft Magnetic Films	57
2.3.2	Perpendicular Magnetization Samples: Bubble Garnets	58
2.4	Experiments on Nanostrips of In-Plane Soft Materials	62
2.4.1	Topology of Domain Walls in Soft Nanostrips	63
2.4.2	Topological Dynamics of Domain Walls in Soft Nanostrips	65
2.4.3	Topology and the Spin Electromotive Force	68
2.4.4	Soft Nanowires, Nanotubes	69
2.5	Conclusion and Outlook	70
	References	71
3	Magnetic Vortices	75
	Carolin Behncke, Christian F. Adolff and Guido Meier	
3.1	Introduction and Motivation	76
3.1.1	Occurrence and Evidence	76
3.1.2	Applications	80
3.2	Static Properties	81
3.2.1	Stray-Fields	84
3.3	Dynamic Properties	87
3.3.1	Thiele Model for Magnetic Vortices	89
3.3.2	Strong Excitation and Switching	92
3.4	From Single Oscillators to Magnonic Vortex Crystals	96
3.4.1	Vortices as Coupled Harmonic Oscillators	96
3.4.2	Self-Organized State Formation	99
3.4.3	Benzene-Like Vortex Molecules	103
3.4.4	Band Structure Engineering of Magnonic Vortex Crystals	107
3.5	Summary and Outlook	110
	References	111
4	Magnetic Skyrmions in Thin Films	117
	Gong Chen	
4.1	Introduction	117
4.1.1	Magnetic Domain Structures in Thin Films	117
4.1.2	Spin Textures of Néel-Type Skyrmions	119
4.2	Experimental Realization of Skyrmions in Thin Films	120
4.2.1	Interfacial Dzyaloshinskii-Moriya Interaction	120
4.2.2	Experimental Observations of Magnetic Skyrmions	122

4.2.3	Quantifying the Interfacial DMI	126
4.2.4	Thin Films with Bulk DMI	129
4.2.5	Magnetic Imaging Techniques	130
4.3	Experimental Realization of Skyrmions in Artificial Structures	133
4.4	Creation and Manipulation of Skyrmions Towards to Application	136
4.4.1	Creations of Magnetic Skyrmions	136
4.4.2	Motion of Skyrmions in Patterned Films	138
4.5	Outlook	141
	References	143
5	Skyrmion Lattices Far from Equilibrium	151
	Andreas Bauer, Alfonso Chacon, Marco Halder and Christian Pfleiderer	
5.1	Introduction and Outline	151
5.2	Skyrmion Lattices in Cubic Chiral Magnets	152
5.2.1	Emergent Electrodynamics and Topological Protection	154
5.2.2	Metastable Skyrmion Lattices Under Field Cooling	156
5.3	Examples of Skyrmion Lattices Far from Equilibrium	160
5.3.1	Unwinding Processes Studied by MFM and LTEM	160
5.3.2	Topological Hall Effect in MnSi Under Pressure	162
5.3.3	Metastable Lattice in MnSi Under Rapid Cooling	164
5.3.4	Structural Phase Transition in Metastable Lattices	167
5.4	Conclusion and Outlook	168
	References	169
6	Anomalous Hall Effect	177
	Yuriy Mokrousov	
6.1	Introduction	177
6.2	Berry Phase and AHE	179
6.3	Intrinsic and Extrinsic AHE	183
6.4	Anisotropic AHE	186
6.5	Quantum Anomalous Hall Effect	189
6.6	AHE and Orbital Magnetism in Non-collinear Magnets	200
	References	205
7	Spin Hall Effect	209
	Matthias Althammer	
7.1	Introduction	209
7.2	Charge and Spin Currents	210

7.3	Spin Hall Effect	211
7.4	Experimental Determination of the Spin Hall Angle	213
7.4.1	Non-local Experiments	215
7.4.2	Spin Pumping	217
7.4.3	Spin-Transfer Torque Induced Ferromagnetic Resonance	222
7.4.4	Spin Hall Tunneling Spectroscopy	225
7.4.5	Spin Hall Magnetoresistance	226
7.5	Summary and Outlook	229
	References	230
8	Weyl Semimetals	239
	Bo Wan, Hai-Zhou Lu and Xiangang Wan	
8.1	Introduction	239
8.2	Topological Bulk States	240
8.3	Fermi Arc Surface States	244
8.4	Topological Anomalous Quantum Hall Effects	247
8.5	Magneto-Transport Phenomena in Weyl Semimetal	247
8.5.1	Effective Model	247
8.5.2	Topological Properties	248
8.5.3	Landau Bands	249
8.5.4	Magneto-Transport Phenomena	250
8.6	Materials Realization	255
8.7	Type-II Weyl Semimetals	258
8.8	Outlook	261
	References	262
9	Symmetry and Topology in Antiferromagnetic Spintronics	267
	Libor Šmejkal and Tomáš Jungwirth	
9.1	Introduction	268
9.2	Antiferromagnets: Symmetry and Topology	272
9.2.1	Magnetic Symmetry and Spintronics Effects	274
9.2.2	Electronic Structure and Band Touchings	277
9.3	Topological Antiferromagnetic Phases	278
9.3.1	Low Dimensional Dirac Antiferromagnets and Superconductors	278
9.3.2	3D Dirac Semimetal Antiferromagnets	280
9.3.3	Weyl Semimetal Antiferromagnets	282
9.4	Topological Antiferromagnetic Spintronics Effects	284
9.4.1	Large Magnetoresistance and Chiral Anomaly	284
9.4.2	Topological Phase Transitions and Anisotropic Magnetoresistance in Antiferromagnetic Systems	286
9.4.3	Anomalous Hall Effect in Noncollinear Antiferromagnets	288

9.4.4	Topological Hall Effects and Antiferromagnetic Skyrmions	290
9.5	Summary	291
	References	291
10	Magnons	299
	Sergej O. Demokritov	
10.1	Introduction	299
10.1.1	Spin Waves and Magnons	299
10.1.2	Magnons in Three and Two Dimensions	300
10.2	Brillouin Light Scattering—A Powerful Tool for Investigation of Magnons	303
10.3	Laterally Confined Magnons	305
10.3.1	Lateral Quantization of Magnons in Magnetic Stripes	305
10.3.2	Edge Magnons	305
10.3.3	Magnon Beams in Waveguides	307
10.3.4	Control and Manipulation with Magnon Beams	310
10.4	Magnons and the Spin Transfer Torque Effect	312
10.4.1	Spin Transfer Torque Effect and Damping Compensation	315
10.4.2	Spin-Torque- and Spin-Hall- Nanooscillators	316
10.4.3	STNO as Sources of Magnons	323
10.5	Bose-Einstein Condensation Magnons	325
10.6	Conclusion and Outlook	329
	References	330
11	Spin Transfer Torque Driven Magnetodynamical Solitons	335
	Johan Åkerman	
11.1	Introduction	335
11.2	Spin Transfer Torque Driven Spin Wave Auto-oscillations	336
11.2.1	Spin Currents and Spin Transfer Torque	337
11.2.2	The Spin Hall Effect	338
11.2.3	The Landau-Lifshitz-Gilbert-Slonczewski Equation	338
11.2.4	Non-linear Spin Wave Auto-oscillations	339
11.2.5	Spin Torque and Spin Hall Effect Nano-oscillators	339
11.3	Spin Wave Bullets	340
11.3.1	Macroscopic Spin Wave Bullets	341
11.3.2	Nanoscopic Spin Wave Bullets in STNOs	341
11.3.3	Direct Observation of Nanoscopic Spin Wave Bullets	341

11.4	Magnetic Droplets	342
11.4.1	Magnon Drops and Magnetic Droplets	342
11.4.2	Experimental Demonstrations of Magnetic Droplets	342
11.4.3	Drift Instability and Auto-modulation	343
11.4.4	Breathing and Droplet Perimeter Modes	345
11.4.5	Direct Microscopic Observation of Magnetic Droplets	347
11.4.6	Edge and 1-Dimensional Magnetic Droplets	348
11.4.7	Interacting and Merging Droplets	349
11.5	Topological Magnetodynamical Solitons	350
11.5.1	Adding Topology to Magnon Drops	350
11.5.2	Dynamically Stabilized Skyrmions	350
11.5.3	Possible Experimental Demonstrations of Dynamical Skyrmions	351
11.6	Conclusions and Outlook	352
	References	352
12	Majorana States	357
	Jeffrey C. Y. Teo	
12.1	Background and Motivation	358
12.2	Time Reversal Breaking Topological Superconductors	362
12.2.1	Topological Superconductors in One Dimension	363
12.2.2	Topological Superconductors in Two Dimensions	374
12.3	Superconducting Heterostructures and Topological Defects	389
12.3.1	Majorana Bound States at Topological Point Junctions	389
12.3.2	Majorana Channels Along Topological Line Junctions	398
12.4	Summary	405
	References	406
Index		413

Contributors

Christian F. Adolf Institut für Angewandte Physik und Zentrum für Mikrostrukturforschung, Hamburg, Germany

Johan Åkerman Department of Physics, University of Gothenburg, Gothenburg, Sweden; Materials and Nanophysics, KTH Royal Institute of Technology, Kista, Sweden

Matthias Althammer Walther-Meißner-Institut, Bayerische Akademie der Wissenschaften, Garching, Germany

Andreas Bauer Physik-Department, Technische Universität München, Garching, Germany

Carolin Behncke Institut für Angewandte Physik und Zentrum für Mikrostrukturforschung, Hamburg, Germany

Hans-Benjamin Braun School of Physics, University College Dublin, Dublin, Ireland; School of Theoretical Physics, Dublin Institute of Advanced Studies, Dublin, Ireland

Alfonso Chacon Physik-Department, Technische Universität München, Garching, Germany

Gong Chen Physics Department, University of California, Davis, CA, USA

Sergej O. Demokritov Institute for Applied Physics and Center for Nanotechnology, University of Münster, Münster, Germany

Marco Halder Physik-Department, Technische Universität München, Garching, Germany

Tomáš Jungwirth Institute of Physics, Academy of Sciences of the Czech Republic, Prague, Czech Republic; School of Physics and Astronomy, University of Nottingham, University Park, Nottingham, UK

Hai-Zhou Lu Department of Physics, Institute for Quantum Science and Engineering, South University of Science and Technology of China, Shenzhen, China; Shenzhen Key Laboratory of Quantum Science and Engineering, Shenzhen, China

Guido Meier Max-Planck Institute for the Structure and Dynamics of Matter, Hamburg, Germany

Jacques Miltat Laboratoire de Physique des Solides, Université Paris-Sud, Orsay, France

Yuriy Mokrousov Institute for Advanced Simulation, Forschungszentrum Jülich GmbH, Jülich, Germany; Institute of Physics, Johannes Gutenberg-University Mainz, Mainz, Germany

Christian Pfleiderer Physik-Department, Technische Universität München, Garching, Germany

Libor Šmejkal Institut für Physik, Johannes Gutenberg-Universität, Mainz, Germany; Institute of Physics, Academy of Sciences of the Czech Republic, Prague, Czech Republic; Faculty of Mathematics and Physics, Department of Condensed Matter Physics, Charles University, Prague, Czech Republic

Jeffrey C. Y. Teo Department of Physics, University of Virginia, Charlottesville, VA, USA

André Thiaville Laboratoire de Physique des Solides, Université Paris-Sud, Orsay, France

Bo Wan National Laboratory of Solid State Microstructures, School of Physics, Collaborative Innovation Center of Advanced Microstructures, Nanjing University, Nanjing, China; Department of Physics, Institute for Quantum Science and Engineering, South University of Science and Technology of China, Shenzhen, China

Xiangang Wan National Laboratory of Solid State Microstructures, School of Physics, Collaborative Innovation Center of Advanced Microstructures, Nanjing University, Nanjing, China

Chapter 1

Solitons in Real Space: Domain Walls, Vortices, Hedgehogs, and Skyrmions



Hans-Benjamin Braun

Abstract Recent years have seen tremendous progress in the understanding of topological phenomena in magnetism, in particular at the nanoscale. In this overview, we consider smooth topological textures such as smooth domain walls, meron or vortices, and most importantly skyrmions. These structures derive their topological stability from the fact that they cannot be undone without violating the continuity of the magnetization field, similar to a knot in a rope. Owing to their topological stability, domain walls and skyrmions are prominent candidates in racetrack-type memories introduced by Parkin and co-workers. These smooth textures should be contrasted with singular topological point defects where the magnetization field is forced to vanish in a submanifold. Such point defects include Ising domain walls, vortices of easy-plane spins, and 3D Bloch points, ‘hedgehogs’, or ‘monopoles’. As domain walls, vortices, and skyrmions including their dynamical versions will be discussed in detail in later chapters by Thiaville and Miltat, Behncke and Meier, Chen, Bauer et al., and Åkerman, we give analytical arguments how domain walls emerge in quasi 1D nanowires, how magnetization reverses via nucleation, and why skyrmions exist in thin films. A variational ansatz for skyrmions that is derived from an exact 2π domain wall profile provides an excellent approximation to numerical and experimental observations in films that include Dzyaloshinskii-Moriya interaction (DMI) and dipolar interactions. In systems of vanishing DMI, the two helical states of a skyrmion are degenerate, and switching between the two helicities occurs in a topologically allowed fashion. This mechanism is closely related to domain wall nucleation in nanowires. Finally we show that dynamical skyrmions may be regarded as 2D siblings of domain wall breathers, and can be described by the same variational ansatz inspired from 2π domain walls as static skyrmions in thin films.

H.-B. Braun (✉)

School of Physics, University College Dublin, Dublin, Ireland
e-mail: bbraun@stp.dias.ie

H.-B. Braun

School of Theoretical Physics, Dublin Institute of Advanced Studies, Dublin 4, Ireland

1.1 Overview

Topological objects in magnetism have attracted the attention of physicists since the early work on domain walls of Bloch and Landau-Lifshitz [1, 2]. With the friendly assistance of Heisenberg, Bloch gave the first analytical description of a domain wall in a ferromagnet before Landau and Lifshitz developed a more comprehensive phenomenological description of ferromagnets including their dynamics. A domain wall was thus the first example of a remarkable plethora of topological defects that may be hosted in magnets (cf. Fig. 1.1). They now include defects where the magnetization field is forced to vanish, such as vortices of easy-plane spins, hedgehogs or Bloch points, but also smooth objects that locally resemble domain walls such as

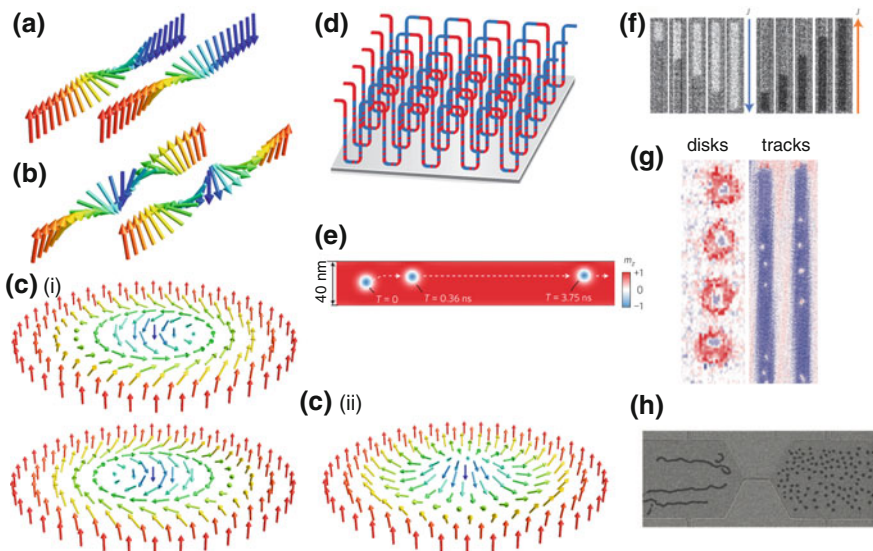


Fig. 1.1 Topologically nontrivial smooth textures in the magnetization field and their proposed use in racetrack-type magnetic memory. **a** Chiral left-handed and right-handed π Bloch-type domain walls. **b** 2π Bloch walls consisting of two π domain walls of equal chirality. **c** (i) Bloch-type skyrmions with either left or right-handed chirality. Skyrmions of one given chirality are favoured by $B20$ chiral materials such as MnSi [5, 10]. Skyrmions of either chirality exist for dipolar systems. (c) (ii) Hedgehog skyrmion of given chirality favoured by a surface induced Dzyaloshinskii-Moryia interaction (DMI). Note that in both (c) (i), (ii) the spin texture upon traversing the skyrmion corresponds to a 2π Bloch or Néel wall, respectively. Note that this similarity underlines the use of the analytical ansatz of a 2π domain wall [19] for a skyrmion profile [20]. **d** Design of a racetrack memory consisting of domain walls (cf. (a)) that are being pushed through effectively 1D wires as proposed by Parkin and co-workers [14]. **e** Racetrack memory based on skyrmions rather than domain walls as proposed by Sampaio et al. [21]. **f** Domain walls in racetrack nanowires as observed in [12]. **g** Skyrmions in dots (300 nm width) and tracks (200 nm width) observed at room temperature in a multilayer by Moreau-Luchaire et al. [13]. **h** Generation of skyrmions in a nanowire constriction [9]. Panel (d) adapted from [14], panels (e–h) are taken from [9, 12, 13, 21], respectively

merons (vortices) and skyrmions [3–6]. Initially proposed as nonlinear field configurations in baryonic field theories [3, 4], the interest in magnetic skyrmions surged as a consequence of the observation of a skyrmion lattice in the bulk magnet MnSi [5], a chiral magnet with a parity breaking Dzyaloshinskii-Moryia interaction (DMI) [7], a system that has been predicted to support vortex-type lattices [8].

Later chapters in this book include detailed discussion of the fascinating physics of topological spin textures including experiments on vortices (Chap. 3; Behncke, Adolf and Meier), domain walls including Bloch lines (Chap. 2; Thiaville and Miltat), skyrmions in bulk magnets (Chap. 5; Bauer et al.), DMI and skyrmions in thin films (Chap. 4; Chen), and their purely dynamically stabilized siblings (Chap. 11; Åkerman).

The absence or presence of domain walls has been found to be pivotal for a series of technological applications. In the design of hard magnets, the formation of domain walls is entirely undesired, and this includes the tiny nanoscale elements that store elementary bits on magnetic hard disk drives. In contrast, the presence of domain walls is crucial in soft magnets. Being localized objects, their position breaks translational symmetry which entails the existence of an energyless Goldstone-mode in the excitation spectrum. Correspondingly, domain walls may usually be easily moved at low fields in the Oe range or via spin torques which are required to overcome weak pinning due to imperfections.

This reinforces the observation that it is the existence of the topological defects per se and not the details about their stabilization that determines most of the physical behaviour. This translates also into the physics of skyrmions which—once they exist—display particle-like properties [9], irrespective of the underlying stabilizing energy terms [10, 11]. For example the emergent magnetic and electric fields arise entirely due to the topological properties of the skyrmion-like spin textures, cf. the chapter by Bauer et al. in this volume. In fact, the formation of skyrmions results from an interplay of the (usually larger) chiral DMI-type interaction and the (usually smaller) dipolar interaction, which in turn depends on the geometry and length scales of the nanostructures.

The experimental design of such nanostructures has seen a striking advance during the past decade. It includes subtle engineering of DMI at interfaces [12, 13], but also the geometric tailoring of the material into dots, pillars, wires and (ultra-) thin films with nanoscale dimensions enforcing magnetism in zero, one and two dimensions, respectively. For example, magnetism in one dimension is essential for concepts such as the racetrack memory [14]. Indeed, in hindsight it appears surprising that the theoretical proposal of the onset of effectively 1D behaviour [15] in nanowires and pillars was initially met with disbelief [16]. This is even more surprising given the fact that current hard disk media design [17] has evolved to pillar dimensions at the nanoscale that are just at the predicted dimensional cross-over predicted in [15].

The ability to produce samples of reduced dimensions allows judicious control and generation of topological defects. With the vision towards manipulating domain walls in effectively 1D nanowires, Slonczewski discovered the ability to move domain walls (cf. Fig. 1.1a, b), with the help of spin torque associated with spin polarized currents [18]. This enabled the influential proposal of the racetrack memory by Parkin and

co-workers [14], where the domain wall takes the role of an information carrier. This latter proposal generated significant activity in the manipulation of domain walls in nanowires including recent observation of record speeds of 750 m/s [12].

Due to their topological stability similar to 2π domain walls (cf. Fig. 1.1b), skyrmions are thus, alongside domain walls, attractive candidates to serve as information carriers in racetrack-type memories (cf. Fig. 1.1c–h). Analogous to domain walls, they can be transported through nanowires via spin polarized currents [21, 22] which are considerably smaller than those required to displace domain walls. In contrast to individual π domain walls, skyrmions have the appealing feature that they leave the magnetization field intact far away from their centre, something which is only satisfied for pairs of standard π domain walls or 2π domain walls (cf. Fig. 1.1b).

We are thus led to investigate the origin of the extraordinary stability of smooth textures such as domain walls and skyrmions as well as singular defects such as vortices and hedgehogs. A unified description of these textures roots in topology, or homotopy, and the concept of winding number will allow for a universal, yet simple classification of these textures. It provides an easy argument about stability of these textures and whether they can easily be transformed into each other. In order to relate topology with the formalism of micromagnetics it is useful to recall that the latter implies that the magnetic material is described by a continuous magnetization field $\mathbf{M}(\mathbf{r}, t)$ of constant magnitude M_0 which is defined in a continuous space parametrized by \mathbf{r} and depends on time t . These conditions are usually satisfied well below the critical temperature T_c and for magnetization configurations that vary slowly compared to the spacing of the underlying crystal lattice.

In the context of data storage applications we are interested in magnetization configurations that are particularly stable and hence are robust against transformations. However, for applications, it also needs to be ensured that information can be written onto the storage medium, and hence that such configurations can be created at manageable fields. It is thus important to know how magnetization configurations can be transformed into each other. In other words, we would like to have easy arguments which inform us about the stability and transformability of magnetization configurations under the above stated tenets of micromagnetics.¹

The question whether two magnetization configurations can be continuously deformed into each other leads us immediately to mathematical homotopy theory which investigates deformability of functions. Two magnetization configurations are said to be topologically (homotopically) equivalent to each other if it is possible to deform them continuously into each other without having to surpass an infinite energy barrier (or resort to the discreteness of the lattice). Two configurations are topologically inequivalent if such a continuous deformation is not possible without surpassing an infinite energy barrier (in the bulk of an infinite sample).

¹Here we refer to micromagnetics as a formalism based on a continuous magnetization field defined in continuous space. In recent years it has become common to use the term micromagnetics to exclusively describe numerical approaches. However, this is too narrow a terminology and potentially misleading as the formalism as originally set out by Brown [23] was an analytical continuum theory and did not refer to numerical methods. In contrast, numerical methods involve a discrete mesh whose scale is usually considerably larger than the physical lattice.

Mutually deformable configurations form equivalence classes ('homotopy classes') that are sometimes referred to as 'topological sectors'. Configurations exhibit 'topological stability' if they are topologically nontrivial and cannot be deformed into the uniform state. Such configurations then belong to a topological sector that is different from the 'topologically trivial' sector corresponding to uniform magnetization.

It is important to note that this classification refers to a highly idealized situation and in real magnets the topological energy barriers are never infinite for several reasons [11]: (i) The magnetization field may vanish in certain regions of measure zero ('singular defects'), or, what is closely related, the magnetization is actually defined on a discrete lattice. (ii) experimental systems are necessarily finite and topological defects may be injected or ejected from the edge of the sample. (iii) Anisotropies are always finite and hence the restriction of the spins to easy-axis, easy-plane behaviour is an approximation.

It is convenient to distinguish between *singular topological defects* where the magnetization is forced to vanish in a point or along a line or plane, and *smooth topological textures* where the magnetization is smooth at all points. Singular topological defects require that one steps outside the framework of continuous micromagnetics. Examples of such singular defects are Ising-type domain walls, vortices and vortex lines in easy-plane systems, and Bloch points or hedgehogs. In contrast, smooth topological defects involve an entirely smooth and continuous magnetization configuration. Examples are skyrmions, merons, and smooth π and 2π domain walls. In order to put these structures into common context, we now give a brief synopsis of homotopy which gives criteria for mutual deformability of magnetization configurations and we closely follow [11] in the next section.

After the introduction to topological concepts and their implication on the stability of topological spin textures in Sect. 1.2 we shall discuss in Sect. 1.3 the relevant energy terms in nanomagnets of reduced dimensions such as dots, pillars, wires and films. In Sect. 1.4 we show that exact analytical solutions for the spin-profile of topological textures such as 2π domain walls [19] can be obtained. This includes dynamical generalizations such as soliton-soliton breathers corresponding to a dynamically bound state of two repulsive domain walls of same chirality. It turns out that this analytical expression [19] is also an excellent approximation for skyrmions [19, 20], which allows to determine the field dependence of skyrmion profiles as shown in Sect. 1.4.2. The helicity switching of a skyrmion and its close relation to soliton-antisoliton nucleation in nanowires is addressed in Sect. 1.4.3. Finally, we shall discuss dynamical skyrmions in Sect. 1.4.4. Their existence provides an explicit example that the (dynamical or static) robustness of a skyrmion state is entirely induced by topology and not by energetic details. A topologically trivial droplet shows much less stability and tuneability and is thus less suitable for practical applications such as microwave generators. Interestingly, the dynamical stabilization of such dynamical skyrmion state is closely related to the stabilization of the dynamical soliton-soliton breather. As a consequence, a dynamical skyrmion may even exist when DMI is absent. It only requires the effectively dissipationless environment underneath a point contact injecting a spin polarized current.

1.2 Topological Defects—A Brief Synopsis

1.2.1 Homotopy

The experimental ubiquity of topologically nontrivial textures in the magnetization field is a direct consequence of their defining mathematical aspect: Similar to a knot in a rope, they cannot be ‘unwound’ easily into the uniform ferromagnetic state. The stability of these textures is thus directly a consequence of their ‘resistance’ against deformations. Indeed, the mathematical theory of homotopy is concerned with the mutual deformability of arbitrary functions which for us turn out to be the magnetization field. Mathematical methods thus help us to decide which magnetic structures can be continuously deformed into each other without violating the continuity of the magnetization field. Relaxing the constraint of continuous magnetization fields, this could happen in singularities, e.g., (Bloch-) points or lines where the magnetization vanishes.

The concept of homotopy is most easily understood by considering mappings f from a 1-sphere into the order parameter space X , $S^1 \rightarrow X$, which we assume to start and end at the ‘base point’ x_0 and which therefore constitute *loops*. Later we shall consider the specific cases where $X = \mathbb{S}^0, \mathbb{S}^1, \mathbb{S}^2$, which correspond to *easy-axis*, *easy-plane* and *isotropic spins*, respectively. As illustrated in Fig. 1.2a for $X = \mathbb{R}^2$, if a loop f can be shrunk to point, it is called ‘*null-homotopic*’,² or somewhat loosely, ‘*topologically trivial*’. As shown in Fig. 1.2b, this is not always possible if the space X is not simply connected, e.g. for $X = \mathbb{R}^2 \setminus \{0\}$. Two ‘loops’ f, g are ‘*homotopic*’ (or ‘*topologically equivalent*’), $f \sim g$, if they can be continuously deformed into

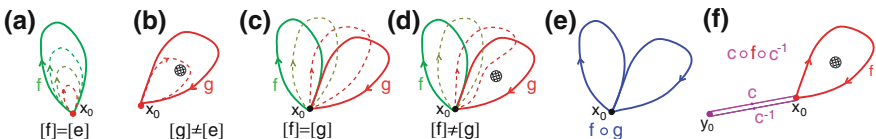


Fig. 1.2 Examples of homotopies. **a** A loop f is null-homotopic if it can be continuously deformed into a point as indicated by the sequence of dashed curves. The loop f is then homotopically equivalent to the identity e , hence the homotopy class of loop f equals that of the identity $[f] = [e]$, or equivalently, $f \sim 0$. **b** If the topological space X is not simply connected as indicated by the hashed area, e.g., as for $\mathbb{R}^2 \setminus \{0\}$, then there exist loops g which cannot be deformed into the identity, and thus $[g] \neq [e]$. **c** Two loops f and g are homotopic if they can be continuously deformed into each other as indicated by the dashed curves. Correspondingly the homotopy class of loop f equals that of loop g . **d** If the topological space X is not simply connected, then there exist loops f, g that are homotopically inequivalent. **e** Concatenation $f \circ g$ of two loops f, g is obtained by traversing first loop f , then loop g , with f, g as defined in the previous panels. **f** For an Abelian fundamental group, there is a trivial isomorphism connecting the fundamental groups with different base points, i.e. $\pi_1(X, x_0) \cong \pi_1(X, y_0)$. Taken with permission from [11]

²If every map from S^1 into a space X is null-homotopic, then X is called ‘simply connected’ (e.g., \mathbb{R}^2).

each other, as illustrated in Fig. 1.2c. Such a deformation is not always possible as is illustrated in Fig. 1.2d for the non-simply connected space $X = \mathbb{R}^2 \setminus \{0\}$.

Since homotopy is an equivalence relation (cf., e.g. [24]), the set of loops in space X can be divided into disjoint *homotopy classes*. The equivalence class of a loop f is usually denoted by $[f]$. In Fig. 1.2c, the loops f and g are homotopically equivalent to each other, i.e., $f \sim g$, and hence their homotopy classes are identical, $[f] = [g]$. A null-homotopic loop f is denoted by $[f] = [e]$, where e denotes the identity, and this is sometimes also denoted by $f \sim 0$. In the magnetic context this would correspond to a uniformly magnetized state. In Fig. 1.2d, X is not simply connected, and the two loops f, g are homotopically inequivalent and therefore $[f] \neq [g]$. Below we shall see that a homotopy class $[f]$ can be classified by a topological invariant, a so-called ‘winding number’, ‘degree’, or ‘index’ $w = \deg f$. In the simple case of $S^1 \rightarrow S^1$ the winding number states how many time a path wraps around the the unit circle (cf. Fig. 1.3a).

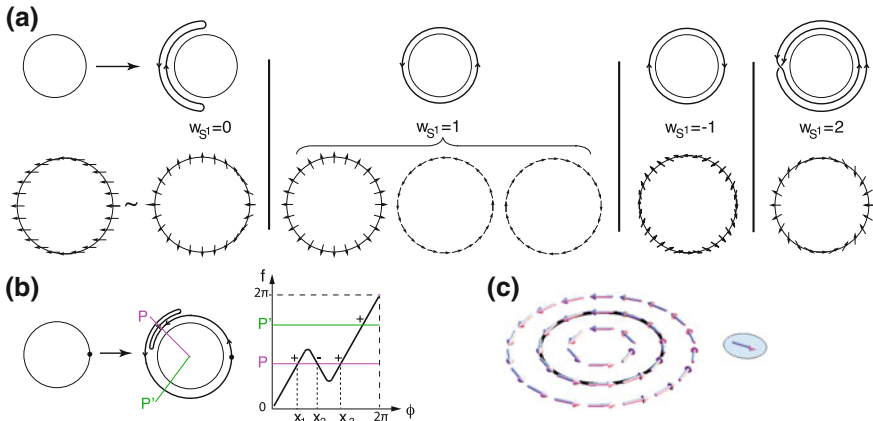


Fig. 1.3 Topologically distinct configurations and associated winding numbers of easy-plane configurations on a circle. Shown are examples of topologically distinct easy-plane spin configurations on a circle. These configurations correspond to mappings f from a circle S^1 onto a circle S^1 which can be classified by the winding number $w_{S^1} \equiv \deg f$, the number of times the circle is wrapped on itself. Configurations with different winding numbers are topologically inequivalent and cannot be deformed into each other without breaking the continuity of the magnetization field. **a** Configurations corresponding to winding numbers $w_{S^1} = 0, 1, -1, 2$ cannot be mutually deformed into each other as indicated by vertical lines. These configurations respectively correspond to a uniform, a vortex, an antivortex, and a double vortex state. **b** Generally, $w = \deg f$ is formally given as the number of preimages x_k of an (arbitrary) point P in the target manifold, weighted with the sign of the mapping. Here an example with $w_{S^1} = 1$ is shown. **c** Mappings with winding number $w_{S^1} = 1$ describe the (topological) stability of a simple vortex configuration of an easy-plane spin. Encircling the vortex core along the black solid path the spin direction always completes a full rotation by 2π , no matter how small the radius. This case corresponds to the situation shown in panel (a) for the case $w_{S^1} = 1$ and hence in an infinite sample the vortex cannot be transformed to the uniform ferromagnetic state with $w_{S^1} = 0$.

Two loops f, g with the same base point x_0 can be joined or ‘concatenated’ to form a new loop, $f \circ g$, which has the same base point and which is defined as the loop that is generated by first traversing loop f and subsequently loop g , a process that is illustrated in Fig. 1.2e. This operation can be used to define a concatenation operation on homotopy classes defined via $[f] \circ [g] \equiv [f \circ g]$. With this operation the set of homotopy classes gains a group structure and forms the *homotopy group* (e.g. [24]). For the mapping $S^1 \rightarrow X$, this group is called the the ‘*first homotopy group*’ or ‘*fundamental group*’ $\pi_1(X, x_0)$ of X at x_0 . Note that this fundamental group may either be Abelian or non-Abelian. Here we are mostly interested in Abelian fundamental groups. However, non-Abelian fundamental groups arise for situations as simple as for a plane with two points removed, $X = \mathbb{R}^2 \setminus \{x_1, x_2\}$, and they also play an important role for biaxial nematics [25].

So far we have considered loops starting and ending at a base point x_0 . However, in order to make contact with our main goal, namely the classification of magnetic topological defects, we are interested in freely sliding contours or unbased mappings, e.g. in freely movable circles or spheres whose diameter is continuously shrinking, cf. Figs. 1.3c and 1.4. This motivates considering the ‘*free*’ homotopy of unbased loops, i.e., loops without a fixed base point. Indeed, for Abelian $\pi_1(X, x_0)$, which includes all our cases of interest, one may construct a (path independent) isomorphism between fundamental groups defined at different base points x_0, y_0 , i.e., $\pi_1(X, x_0) \cong \pi_1(X, y_0)$, cf. Fig. 1.2f. Hence, in the Abelian case, all based fundamental groups are isomorphic to each other and hence isomorphic to an abstract fundamental group

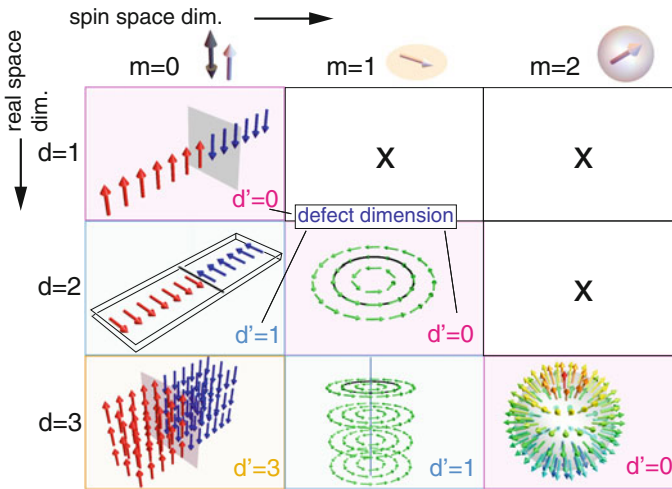


Fig. 1.4 Overview of singular point defects as a function of real space and spin dimensions. The dimension m of the spin configuration space (‘target space’) is increasing from left to right, while space dimensions d are increasing from top to bottom. The dimension d' of the singular defect is given by the Kléman-Toulouse [30] relation $d' = d - m - 1$, where d is the space dimension and S^m the spin configuration space. Crosses indicate absence of singular point defects

which is denoted by $\pi_1(X)$. More precisely, if $\pi_1(X)$ is Abelian then there is a one to one correspondence between elements of the fundamental group and classes of freely homotopic (i.e. unbased) loops.

Thus we arrived at one of the main conclusions: Topological defects (point defects in 2D, line defects in 3D) are topologically equivalent precisely when they are characterized by the same element of the fundamental group in order parameter space (in the Abelian case).

In order to classify point defects in 3D we need to consider spheres that surround the defects rather than loops (cf. Fig. 1.4). We are thus led to consider the mappings, $S^2 \rightarrow X$, from a 2-sphere into order parameter space. In close analogy to the case above, point defects will then be characterized by freely homotopic classes of maps of a sphere into the order parameter space. If the mapping on a sphere on the surrounding sphere cannot be shrunk to a point, the defect is said to be topologically nontrivial. Without going into details, a group structure can also be given to the homotopy classes of spheres into X , which yields the second homotopy group $\pi_2(X)$. Generally, the homotopy classes of mappings of $S^n \rightarrow X$ form a group $\pi_n(X)$, the so called n th homotopy group. All groups $\pi_n(X)$ with $n \geq 2$ are Abelian.

1.2.2 Winding Numbers

Now that we have seen that mutually deformable configurations form equivalence classes, it is useful to identify a quantity that serves as a fingerprint for a given equivalence class. Such an equivalence class would for example correspond to a simple translation of a domain wall or a skyrmion, but it may also be more involved and consist of the two helicity states of a skyrmion (cf. Sect. 1.4.3). Such a fingerprint is given by the so-called degree of a mapping f , $\deg f$, also known as the *winding number* w . Configurations with different winding numbers cannot be continuously deformed into each other without introducing point defects.

In magnetism, the aligned ferromagnetic state is characterized by a winding number 0 and is ‘*topologically trivial*’, while vortex or skyrmion-type configurations have nonvanishing winding number as we shall see below, and hence are referred to as being ‘*topologically nontrivial*’. Thus, the latter configurations cannot continuously be deformed into the uniform state, which renders them ‘*topologically stable*’. Of course, such topological stability implies the existence of smooth mappings, and thus magnetization configurations that vary slowly with respect to the lattice. In actual physical situations, these infinite topological energy barriers become finite [11] if (i) either the magnetization field is allowed to vary at the scale of the lattice, or if (ii) one takes into account the finiteness of actual easy-axis and easy-plane anisotropies, which contrasts with the underlying assumption of topological considerations that the (‘target’) spin configuration space be strictly an m -sphere S^m . For example, it is possible to unwind 2π domain walls in a 1D chain of easy-plane spins if the anisotropy is finite. The spin configuration (‘target’) space then changes from easy-plane S^1 to spherical S^2 , and in 1D no strict topological defects can exist since $\pi_1(S^2) = 0$.

This unwinding of 2π domain walls over the hard-axis is also known as ‘escape via the third dimension’ and lies at the heart of the instability of 2π domain walls in large external fields [19].

Formally, the winding numbers $\deg f$ provide a bijection of the homotopy classes into the integers \mathbb{Z} , as originally shown by Hopf. Two functions f, g are homotopically equivalent iff $\deg f = \deg g$, and the mapping is topologically trivial when $\deg f = 0$. In contrast to the previous section where we discussed homotopy at the example of planar curves, in magnetism we are concerned with the more general mapping that the magnetization field $= \mathbf{m}(\mathbf{x})$ provides. Generally, we consider a mapping $f : M \rightarrow N$, and we are mostly interested in mappings from an m -sphere to an n -sphere, i.e., $M = S^m$, and $N = S^n$. The latter constitutes the configuration space or ‘target manifold’ N of an individual spin. For example, an isotropic spin has S^2 , an easy-plane spin S^1 , and an Ising spin the 0-sphere as target manifold. The ‘base manifold’ M , is either an m -sphere enclosing a singular topological point defect, or in the case of a continuous texture such as a skyrmion or a smooth 2π domain wall, the base manifold is defined by real space \mathbb{R}^m with infinity compactified to a point, since magnetization configurations are assumed to take an identical value at infinity.

For equal dimension of the base and the target manifold, $n \geq 1$, the homotopy group is simply

$$\pi_n(S^n) \cong \mathbb{Z}, \quad (1.1)$$

and thus Abelian. Thus each homotopy class of deformable configurations can be characterized by an integer. This integer is indeed the degree or winding number of the mapping, and it counts how many times the target manifold is wrapped around the base manifold under the mapping. Topologically nontrivial configurations characterized by a nonzero winding number exist whenever the dimensions of the sphere constituting the base manifold and that of the target manifold agree. We note that the $n = 0$ case describing Ising spins is a slight exception since then $\pi_0(S^0) \cong \mathbb{Z}_2$, rather than the integers \mathbb{Z} .

Before we compute the winding number in the general case, we start with the simple example of easy-plane spins arranged on a circle as illustrated in Fig. 1.3a, b, where winding numbers w_{S^1} are those of the mapping $f : S^1 \rightarrow S^1$. Figure 1.3a shows configurations of different winding numbers, separated by vertical bars. From left are shown, deformed uniform states ($w_{S^1} = 0$), radial, right-handed (counter-clockwise, CCW), and left-handed (clockwise, CW) vortices ($w_{S^1} = 1$), antivortices ($w_{S^1} = -1$), and double-vortices ($w_{S^1} = 2$).

Note that magnetic vortices and antivortices have widely been studied in experiments. Recently, whole networks of vortices and antivortices have been created after quenching and their mutual interaction has been studied recently [26]. It should be noted that most of these textures exhibit cores [27, 28], and thus their order parameter space is not strictly S^1 , and therefore these textures should more adequately be regarded as merons (cf. Sect. 1.2.4).

How can we compute the winding number? We now go into some mathematical details of its derivation as it appears frequently without derivation in the remainder of this book, in particular as ‘skyrmion number’ for spherical spins. We continue with

our simple example of easy spins which define a mapping $f : S^1 \rightarrow S^1$. As shown in Fig. 1.3b, we now may consider an arbitrary point $P \in S^1$ in the image, that is a particular angle of the easy-plane spin with respect to predefined axis. The degree of the mapping f is then obtained by summing over all ‘preimages’ \mathbf{x}_k , defined via $f(\mathbf{x}_k) = P$, each weighted with the sign of the functional determinant, i.e.,

$$\deg f = \sum_{\mathbf{x}_k \in f^{-1}(P)} \operatorname{sgn} D(\mathbf{x}_k), \quad (1.2)$$

with the Jacobian, $D \equiv \det(\partial f^i / \partial x^j)$, which is assumed to be nonsingular in \mathbf{x}_k . It is clear from the example in Fig. 1.3b that the degree is independent of the choice of the point P , a fact that can also be shown generally (Brouwer fixed point theorem).

The expression (1.2) may readily be generalized to mappings $f : S^n \rightarrow S^n$ in higher dimensions where it is conveniently expressed as $\deg f = \int d^n x D(\mathbf{x}) \delta(f(\mathbf{x}) - P)$, with \mathbf{x} a point in compactified \mathbb{R}^n that is isomorphic to S^n . Using an unnormalized averaging function μ on the target manifold N , one may also express this as $\deg f = \int_M d^m x D(\mathbf{x}) \mu(f(\mathbf{x})) / \int_N d^n y \mu(\mathbf{y})$. The most general and useful expression for the degree of a mapping or ‘winding number’ is given by [11],

$$\deg f = \frac{\int_M f^* \Omega}{\int_N \Omega}, \quad (1.3)$$

where Ω is a differential n -form defined on the target manifold N and $f^* \Omega$ denotes its pullback onto the base manifold M . In magnetism, we are interested in $M = N = S^n$, and Ω is then conveniently chosen as a surface volume form with respect to the metric induced from \mathbb{R}^{n+1} , i.e., $\Omega = *rdr$.³ We now simplify the most general expression (1.3) for the common cases of easy-plane spins and spherical spins. The magnetization components are identified with those of the mapping f , i.e., $m^a = f^a$.

Easy plane spins—In this case the target space is given by S^1 , and we may introduce the azimuthal angle ϕ and write $\mathbf{m} = (\cos \phi(x), \sin \phi(x), 0)$. In this case (1.3) reduces to the S^1 -winding number,

$$w_{S^1} \equiv \deg f = \frac{1}{2\pi} \int dm^1 m^2 - dm^2 m^1 = \frac{1}{2\pi} \int_{-L/2}^{L/2} dx \partial_x \phi \quad (1.4)$$

where x is a parameter along the loop of length L in real space. This ‘loop’ may also include the case of linear interval provided that the magnetization at the ends of the interval takes the same value $\phi(-L/2) = \phi(L/2) = \phi_0$. As we further discuss below, a 2π domain wall confined to the easy-plane provides an example of a configuration

³Specifically, we have $\Omega = *rdr \equiv \frac{1}{n!} \varepsilon_{i_0 i_1 \dots i_n} x^{i_0} dx^{i_1} \wedge \dots \wedge dx^{i_n}$. This differential n -form satisfies $d\Omega = \omega$ where ω is the standard volume element on \mathbb{R}^{n+1} . Correspondingly, $\int_N \Omega = \int_{B^{n+1}} d\Omega = (n+1) \int_{B^{n+1}} \omega = (n+1) V_{n+1}$, where in the first step we made use of Stokes’ theorem and B^{n+1} denotes the unit ball in \mathbb{R}^{n+1} with $\partial B^{n+1} = S^n$ and V_{n+1} its volume.

with $\deg f = \pm 1$, with the sign referring to the total *chirality* of the 2π domain wall [19], which can be detected in experiment [29].

Spherical spins—In this case, the target space S^2 can, e.g., be parametrized as $\mathbf{m} = (m^1, m^2, m^3)$ with the constraint $|\mathbf{m}| = 1$. Here the base manifold M is two-dimensional and can be parametrized by x_1, x_2 which may, e.g., refer to spherical ($M = S^2$), polar or cartesian coordinates ($M = \mathbb{R}^2$). In this case, the general expression (1.3) for the degree or S^2 -winding number takes the following form [11],

$$\begin{aligned} w_{S^2} \equiv \deg f &= \frac{1}{8\pi} \int_N \varepsilon_{abc} m^a dm^b \wedge dm^c = \frac{1}{8\pi} \int_M \varepsilon_{abc} m^a \partial_i m^b \partial_j m^c dx^i \wedge dx^j \\ &= \frac{1}{4\pi} \int_M \mathbf{m} \cdot (\partial_1 \mathbf{m} \times \partial_2 \mathbf{m}) dx_1 dx_2. \end{aligned} \quad (1.5)$$

Here we used a double summation convention in the first two equations and the notation $\partial_i m^b \equiv \partial m^b / \partial x^i$. Note that with Cartesian coordinates the last expression is often referred to as ‘*skyrmion number*’, $w \equiv \deg f$. If we use the the usual spherical coordinates for the magnetization unit vector, $\mathbf{m} = (\sin \theta \cos \phi, \sin \theta \sin \phi, \cos \theta)$, in order to accommodate the constraint $|\mathbf{m}| = 1$, then the degree (1.5) may be expressed as

$$w_{S^2} \equiv \deg f = \frac{1}{4\pi} \int_M \sin \theta (\partial_1 \theta \partial_2 \phi - \partial_2 \theta \partial_1 \phi) dx_1 dx_2. \quad (1.6)$$

Note that in both (1.6) and the last expression in (1.5) the manifold M is usually understood to be either the compactified plane \mathbb{R}^2 , or a 2-sphere. Hence the coordinates x_1, x_2 are not necessarily Cartesian, but may be chosen to be arbitrary curvilinear coordinates in real space such as, e.g., real-space polar coordinates ϑ, φ .

In the following sections we now return to the general case of arbitrary dimensions and use the winding number to classify singular topological point defects and smooth textures. Singular point defects have a vanishing magnetization field at the centre, and are characterized by the fact that for a spin with configuration space S^n , the winding number evaluated on an n -sphere S^n wrapping around the defect will be nonzero. Explicitly, we consider a wrapping 2-sphere for an isotropic spin with $n = 2$, a wrapping 1-sphere or circle for an easy-plane spin with $n = 1$, and a 0-sphere consisting of two points for an Ising spin ($n = 0$). Smooth topological textures such as 2π domain walls and skyrmions have a magnetization field that is smooth everywhere, but are topologically nontrivial resembling ‘knots’ in the magnetization field that cannot continuously be transformed to the uniform magnetization state. We now consider these two cases in more detail.

1.2.3 Singular Topological Defects

Singular topological defects have a magnetization field that is forced to vanish in a d' -dimensional subspace within a d -dimensional sample. These two quantities are

different as can be seen from the familiar example of a 2D vortex shown in Fig. 1.3c which corresponds to $d' = 0$ and $d = 2$, as the vortex core represents a point in a 2D sample. Generally, we may consider wrapping a d' -dimensional defect with an r -sphere, S^r , and an overview of all relevant cases is shown in Fig. 1.4. The space dimension of the sample d , the dimension d' of the defect, and the dimension of the surrounding r -sphere are related as follows [30],

$$d = d' + r + 1. \quad (1.7)$$

The internal spin space is described by an m -sphere S^m , which includes all cases of major interest, namely easy-axis ($m = 0$), easy-plane ($m = 1$) and isotropic spins ($m = 2$). The statement (1.1) about homotopy groups implies that nontrivial mappings exist for a mapping of an m -sphere onto a sphere of the same dimension, i.e., $\pi_m(S^m) = \mathbb{Z}$, for $m \geq 1$. Topological defects may also exist for $m = 0$, a case that describes domain walls in easy-axis or Ising magnets, cf. Fig. 1.4 (i). However, this case is special as there is either a defect or no defect, as two domain walls can be annihilated. This is expressed by $\pi_0(S^0) = \mathbb{Z}_2$ [31].

Since we are mapping the r -sphere of the surrounding path onto the m -sphere of internal spin space, the relation (1.1) implies that topological defects may exist when $r = m$, or [30],

$$d = d' + m + 1, \quad (1.8)$$

where d is the space dimension of the sample, d' the dimension of the defect ($d' \leq d - 1$), and S^m the internal spin configuration space. If we consider n -dimensional (normalized) vector order parameters, then $m = n - 1$, and $d = d' + n$.

We now discuss the various examples as illustrated in Fig. 1.4: In the left column it is shown that for an easy-axis or Ising-type spin ($m = 0$), the defect in accordance with (1.8) will be a ‘domain wall’ and thus a 2D object in $d = 3$, a line in $d = 2$ and a point in $d = 1$. The middle column illustrates the case of easy-plane spins ($m = 1$) that may form a *vortex line* in $d = 3$ and the by now familiar example of a *planar vortex* in $d = 2$ with a zero dimensional ($d' = 0$) vortex core. Finally as illustrated in Fig. 1.4 (iii), spherical spins in $d = 3$ with $m = 2$ may form a ‘hedgehog’, ‘monopole’, or ‘Bloch-point’ point defect ($d' = 0$) in the magnetization field. Note that the remaining ‘entries’ in the table shown in Fig. 1.4 do not exist as $\pi_n(S^m) = 0$ for $n < m$ which excludes the existence of topologically nontrivial textures.

1.2.4 Smooth Defects—Skyrmions, Merons and Domain Walls

Apart from the singular point defects there is a second category of topologically nontrivial textures where the magnetization field is smooth and finite at all space points. A smooth defect is characterized by the fact that it cannot be deformed

continuously to the ferromagnetic state in a sample that extends to infinity. This resembles a knot tied into a rope that cannot be untied without using the ends or by cutting the rope.

We consider textures where the magnetization is assumed to tend asymptotically to a uniform value, i.e., $\mathbf{m}_\infty = \text{const.}$ as $|\mathbf{r}| \rightarrow \infty$. The direct space \mathbb{R}^d can then be stereographically projected onto the punctured sphere of dimensionality d with the missing point corresponding to $|\mathbf{r}| \rightarrow \infty$ (a so called one-point compactification). If the configuration space of the order parameter is an m -sphere, S^m , then topological defects may arise when $d = m$, due to the relation (1.1). Here we are interested in dimensions $d \leq 2$. In contrast to the singular defect configurations discussed above, such as Ising domain walls, vortices and hedgehogs, the present configurations are smooth and do not contain singular points where the order parameter \mathbf{m} is forced to vanish.

Domain walls—A simple example arises when $m = d = 1$, i.e. when easy-plane spins are arranged along a 1D chain. This is the situation described by a 1D sine-Gordon model [32, 33] involving a compact field variable $\phi(x, t)$. Due to $\pi_1(S^1) = \mathbb{Z}$, topologically distinct field configurations (for either periodic boundary conditions or ϕ fixed at infinity), are then characterized by how many times they wrap around the easy-plane circle S^1 as one proceeds along the sample. The degree or winding number $w_{S^1} = (1/2\pi) \int dx \partial_x \phi$ as given by (1.4) then counts the number of times (including the sign) the field wraps around the unit circle as one traverses the sample cf. Fig. 1.5. Wrapping around exactly once corresponds to one (topological) soliton in a *bona fide* sine-Gordon model [32–35], with w characterizing its winding number or total ‘chirality’. For example, a single 2π soliton in the sine-Gordon (sG) model is characterized by $w_{S^1} = \pm 1$ as illustrated in Fig. 1.4a, while sG soliton pairs may then correspond to total winding number $|w_{S^1}| = 2$ when the two solitons have the same chirality in which they are referred to as soliton-soliton pairs. In contrast, two solitons of opposite chirality have winding number zero as they can be continuously deformed into the uniform ‘vacuum’ state.

Note, however, that for magnetic systems with an easy-axis anisotropy the magnetization in a domain wall does not fully wind around the unit circle. In this case, easy-plane solitons rather connect two anisotropy minima that differ by an angle π , cf. Fig. 1.1a. A complete twist around the unit circle ($w_{S^1} = \pm 1$) would involve a *pair* of magnetic domain walls or π -solitons with the same chirality cf. Fig. 1.1b. Here chirality is defined as $C_x = (1/\pi) \int_{-\infty}^{\infty} dx \partial_x \theta$ with θ the (extended) polar angle within the easy plane. Therefore soliton pair configurations with two π -solitons of same chirality have winding number $|w_{S^1}| = 1$ and are topologically stable with respect to the easy-plane. Such configurations are therefore termed ‘soliton-soliton’ pairs. In contrast, two solitons of opposite chirality have winding number $w_{S^1} = 0$, are therefore homotopically equivalent to the ferromagnetic state and are termed ‘soliton-antisoliton’ pairs. These configurations will be discussed in Sects. 1.4.1.2 and 1.4.1.3. Soliton-antisoliton configurations play the role of energy barriers in nanopillars or nanowires as used in magnetic storage media, for details we refer to [11].

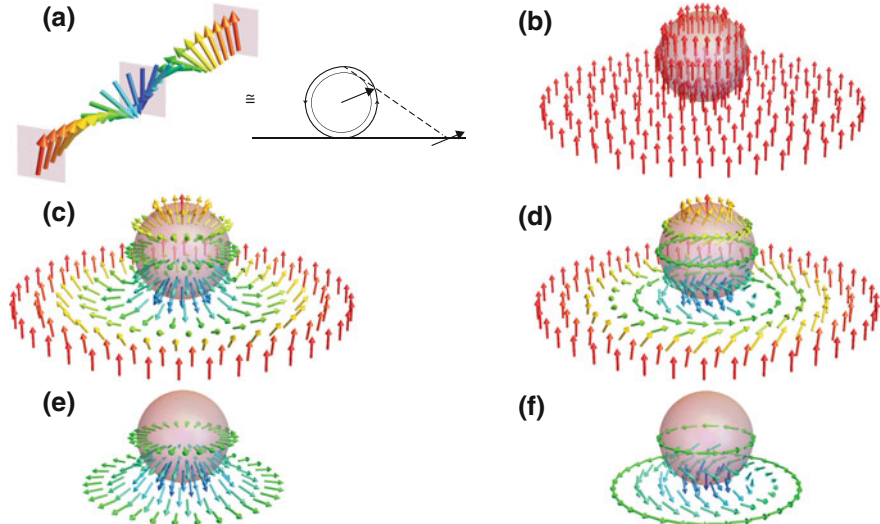


Fig. 1.5 2π domain walls, skyrmions and merons (or vortices) as smooth, nonsingular topological textures that owe their stability to the homotopy relations $\pi_n(S^n) = \mathbb{Z}$ as exemplified by stereographic projection. **a** A 2π -domain wall in an easy-plane system wraps once around the unit circle as one proceeds along the chain. **b** The uniform ferromagnetic state maps to a single point and hence represents a topologically trivial state. **c** A hedgehog skyrmion in a 2D sample. The topological stability is apparent when the 2D sample is projected to a sphere via stereographic projection while maintaining the spin direction. A hedgehog skyrmion leads to a hedgehog defect on the sphere. The topological stability of the skyrmion is a consequence of the relation $\pi_2(S^2) = \mathbb{Z}$. **d** Upon stereographical projection, a Bloch-type skyrmion results in a hedgehog defect that has been ‘combed’ along the equator. This results from a continuous deformation of the hedgehog structure shown in **(c)**. Configurations **(c)** and **(d)** cannot be deformed into the uniform state shown in **(b)** without violating continuity of the magnetization field on the sphere. This illustrates the topological stability of skyrmions. **e** A hedgehog-type meron, often also described as a vortex (albeit with nonvanishing core magnetization), corresponds to half a skyrmion which is evident upon stereographic projection. **f** A Bloch-type meron is topologically equivalent to the hedgehog-type meron shown in **(d)**

In this context it should also be noted that chirality itself is not caused by the DMI as is sometimes argued in the literature. Chirality may emerge completely spontaneously. In fact, it has been shown that already at the quantum level chirality emerges due to solitons undergoing quantum fluctuations in a spin chain, an effect that was observed via polarized neutron scattering [36]. Note that this emergence of chirality is *spontaneous* and related to the double valuedness of a spin-1/2 wavefunction. It is thus fundamentally different from a chirality that arises due to an explicit parity breaking DM-type interaction in the Hamiltonian which gives rise to spin spirals observed in thin films [37, 38] (Fig. 1.6).

Skyrmions—We are now in a position to explain the topological stability of skyrmions. For $d = m = 2$, i.e., isotropic spins on a 2D plane, (1.1) predicts $\pi_2(S^2) = \mathbb{Z}$, explaining the existence of (simple) skyrmions with winding number $|w_{S^2}| = 1$ (cf. Fig. 1.5). As shown in Fig. 1.5c, stereographic projection (here

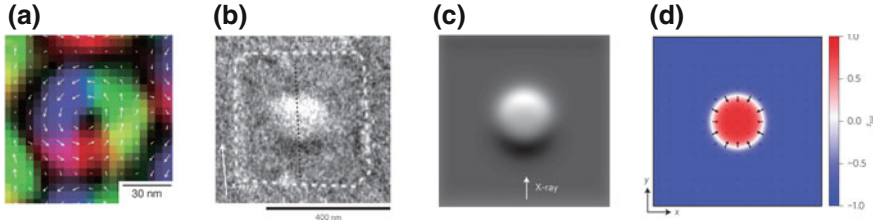


Fig. 1.6 Experimental detection and modelling of the in-plane components of a spin texture of a skyrmion. **a** Skyrmion as part of a skyrmion lattice in the chiral thin film magnet $\text{Fe}_{0.5}\text{Co}_{0.5}\text{Si}$ [39] as detected with Lorentz transmission electron microscopy (LTEM). **b** Skyrmion in a sputtered $\text{Pt}/\text{Co}/\text{MgO}$ nanostructure as observed with photoemission electron microscopy (PEEM) [40]. Here regions with magnetization components antiparallel to the x-ray beam orientation appear with dark contrast and regions with magnetization parallel to the beam appear in white as shown in the simulation **c**. **d** shows the corresponding spin texture with the color bar indicating m_z . Note that LTEM is not sensitive to the out of plane component while PEEM is only weakly sensitive to it for a beam incident under an oblique angle. Image in **(a)** and **(b)**–**(d)** are taken from [39] and [40], respectively

with respect to the south pole), yields a hedgehog spin texture on the sphere which is evidently topologically nontrivial according to our discussion in Sect. 1.2.3. It cannot be continuously transformed into the ferromagnetic state shown in Fig. 1.5b, i.e., the hedgehog “cannot be combed into the uniform ferromagnetic state” a statement ascribed to Polyakov. Note that the spin structure remains topologically nontrivial if the spins rotate tangentially and form a ‘Bloch skyrmion’ (cf. Fig. 1.5c). It is instructive to explicitly evaluate the winding number (1.6) for a skyrmion-type structure parametrized by spherical coordinates $\mathbf{m} = (\sin \theta \cos \phi, \sin \theta \sin \phi, \cos \theta)$, with the symmetric ansatz $\theta(\rho)$ and $\phi(\varphi)$, where ρ, φ denote polar coordinates in the plane. The winding number (1.6) then takes the simple form,

$$w_{S^2} = \frac{q}{2} [m_z(0) - m_z(\infty)], \quad (1.9)$$

where $m_z = \cos \theta$, and $q = w_{S^1} = (1/2\pi) \int_0^{2\pi} d\varphi \partial_\varphi \phi$ is the S^1 -winding number along the domain wall delimiting the skyrmion. With $\phi = \varphi + \chi$, we obtain for $\chi = \pm\pi/2$ a chiral Bloch-type skyrmion as shown in Fig. 1.1c (i), while $\chi = 0, \pi$ describes a Néel or hedgehog skyrmion (cf. Fig. 1.1c (i)). For all these cases we have $q = 1$ and thus for all textures shown in Fig. 1.1 we obtain $w_{S^2} = -1$. The reversed configuration obtained via the substitution $m_z \mapsto 1 - m_z$ yields $w_{S^2} = 1$. Of course any texture that arises via a *smooth* deformation from these symmetric textures will share their winding number.

Merons—A vortex with a ‘core’ of out-of-easy plane magnetization is also referred to as a ‘meron’, in order to distinguish it from its superconducting sibling where the order parameter vanishes at its centre. Such configurations are described in detail in the chapter by Behncke and Meier. In contrast to the skyrmion, the magnetization resembles that of a vortex for large ρ as shown in Fig. 1.3c and thus $m_z(\rho \rightarrow \infty) = 0$.

For a symmetric vortex, the azimuthal angle of the magnetization can be parametrized as $\phi = q\varphi + \chi$, where $q = \pm 1$ is often referred to as the (topological) vorticity, equalling w_{S^1} in Fig. 1.3a. For a meron the winding number (1.9) then becomes,

$$w_{S^2} = pq/2, \quad (1.10)$$

where $p \equiv m_z(0) = \pm 1$ is often referred to as the ‘polarity’ of the vortex. We thus see that for a meron $|w_{S^2}| = 1/2$, which is half that of a skyrmion. This can also be seen directly from a stereographic projection as shown in Fig. 1.5e, f.

Historically, after Skyrme’s initial work [3, 4], these defects acquired popularity in magnetism thanks to Belavin and Polyakov’s work where topologically nontrivial solution for isotropic magnets or nonlinear sigma models were explicitly constructed [41].

1.3 Energy and Magnetization Dynamics at the Nanoscale

We start with a few considerations that are shared by simple nanostructures, namely dots, nanowires, and thin films. Within the framework of micromagnetics, the magnetization dynamics is assumed to obey the so called Landau-Lifshitz-Gilbert (LLG) equations of motion for the magnetization unit vector \mathbf{m} ,

$$\partial_t \mathbf{m} = -\gamma \mu_0 \mathbf{m} \times \mathbf{H}_{\text{eff}} + \alpha \mathbf{m} \times \partial_t \mathbf{m}. \quad (1.11)$$

Here $\gamma \equiv ge/(2m_e) = g\mu_B/\hbar > 0$ denotes the gyromagnetic ratio, with $e > 0$ the electron charge, g the electron’s g -factor, μ_B the Bohr magneton, m_e the electron mass, and $\alpha > 0$ denotes a dimensionless damping constant. The first term on the right hand side describes precession in the effective magnetic field,

$$\mu_0 \mathbf{H}_{\text{eff}} = -\frac{1}{M_0} \frac{\delta E}{\delta \mathbf{m}}, \quad (1.12)$$

where E is the total magnetic energy to be given below. The second term on the r.h.s. of (1.11) is a damping term, proportional to the damping constant α . It is often more convenient to rewrite the LLG equations as follows,

$$\frac{1 + \alpha^2}{\gamma \mu_0} \partial_t \mathbf{m} = -\mathbf{m} \times \mathbf{H}_{\text{eff}} - \alpha \mathbf{m} \times (\mathbf{m} \times \mathbf{H}_{\text{eff}}), \quad (1.13)$$

which up to the damping dependent renormalization of the precession frequency resembles the form originally proposed by Landau and Lifshitz. In the absence of pinning, it is understood that the magnetization satisfies the above free boundary conditions at the sample surface at all times. Note that in contrast to the Bloch equations describing magnetic resonance, the LLG equations only lead to transverse

but not longitudinal relaxation of the magnetization, since all terms on the r.h.s. of (1.13) conserve the magnitude of the magnetization, i.e., $|\mathbf{m}| = 1$ at all times. This restriction is relieved by passing on to the so-called Landau-Lifshitz-Bloch equation [42]. Current induced torques can be added to the r.h.s. of (1.13) [18, 43] as discussed in the chapter by Thiaville and Miltat.

The total magnetic energy is given by

$$E = \int d^3x \left\{ A(\nabla \mathbf{m})^2 - K_{e,\text{cryst}} m_z^2 + K_{h,\text{cryst}} m_x^2 - \mu_0 H M_0 m_z \right\} + E_m, \quad (1.14)$$

where E_m denotes the magnetostatic energy. Note that for the moment we neglected the Dzyaloshinskii-Moriya interaction (DMI) which will be introduced in Sect. 1.3.3 below. Often it is convenient to parametrize the magnetization unit vector as $\mathbf{m} = (\sin \theta \cos \phi, \sin \theta \sin \phi, \cos \theta)$. The equations of motion (1.13) can then be expressed as (cf. appendix of [11]),

$$\begin{aligned} \frac{1 + \alpha^2}{\gamma \mu_0} \sin \theta \partial_t \phi &= -H_{\text{eff}}^\theta + \alpha \frac{H_{\text{eff}}^\phi}{\sin \theta}, \\ \frac{1 + \alpha^2}{\gamma \mu_0} \partial_t \theta &= \frac{H_{\text{eff}}^\phi}{\sin \theta} + \alpha H_{\text{eff}}^\theta, \end{aligned} \quad (1.15)$$

where $\mu_0 H_{\text{eff}}^\eta(\mathbf{x}) = -(1/M_0)(\delta E / \delta \eta(\mathbf{x}))$ with $\eta = \phi, \theta$ denoting the spherical components of the effective field, and $\delta/\delta\eta(\mathbf{x})$ being the functional derivative with respect to $\eta(\mathbf{x})$. For the reduced dimensions characteristic of the nanostructures discussed below, this functional derivative reduces as follows: In quasi 1D situations, it has to be replaced by $\delta(E/\mathcal{A})/\delta\eta(x)$ with \mathcal{A} the sample cross-section, and for a spatially uniform magnetization it reduces to the partial derivative $\partial(E/V)/\partial\eta$.

1.3.1 Nanodots

Even though zero-dimensional magnetic nanodots do not exhibit topological spin textures, we briefly note how the energy is reduced for such structures whose dimensions L are sufficiently small that they satisfy the inequality,

$$L < \pi \delta_m, \quad (1.16)$$

where $\delta_m = 2\sqrt{A/\mu_0 M_0^2}$ is also known as the ‘exchange length’. Except for dimensions $L \simeq \pi \delta_m$ where nonuniform demagnetizing fields will lead to noticeable nonuniform magnetization configurations including ‘configurational anisotropy’ [44, 45], the magnetization will be uniform to high accuracy in the absence of pinning effects at the sample surface, i.e., vanishing normal derivative. For $\mathbf{m} = \text{const.}$, the energy (1.14) can be expressed as,

$$E = V \left\{ -K_{e,\text{cryst}} m_z^2 + K_{h,\text{cryst}} m_x^2 - \mu_0 H M_0 m_z \right\} + E_m, \quad (1.17)$$

where V denotes the sample volume. For ellipsoidal samples and coordinates aligned with the principal axes, the demagnetizing energy is diagonal in the magnetization components,

$$E_m = \frac{\mu_0 V}{2} \sum_i N_i M_i^2, \quad N_i = -\frac{1}{4\pi} \frac{\partial^2}{\partial r_i^2} \int_V d^3 r' \frac{1}{|\mathbf{r} - \mathbf{r}'|}, \quad (1.18)$$

where the demagnetizing factors N_i are \mathbf{r} -independent for an ellipsoidal sample and satisfy $\sum_i N_i = 1$. For a sphere, all $N_i = 1/3$, whereas for a cylinder extending along x one has $N_y = N_z = 1/2$, $N_x = 0$, while for an infinite disk with normal along z one has $N_z = 1$.

The energy of a single domain particle of ellipsoidal shape can be expressed as (here the long-axis is chosen to be the x -axis),

$$E = V \left\{ -K_{e,\text{eff}} m_z^2 + K_{h,\text{eff}} m_x^2 - \mu_0 H M_0 m_z \right\}, \quad (1.19)$$

where the *effective anisotropy constants* contain both demagnetizing and crystalline effects [19],

$$\begin{aligned} K_{e,\text{eff}} &= K_{e,\text{cryst}} - (\mu_0/2) M_0^2 (N_z - N_y), \\ K_{h,\text{eff}} &= K_{h,\text{cryst}} + (\mu_0/2) M_0^2 (N_x - N_y). \end{aligned} \quad (1.20)$$

In particular we find that for a cylindrically shaped particle, the shape anisotropy effectively induces an easy-axis anisotropy along the particle axis even in the absence of crystalline anisotropies. Conversely, crystalline anisotropies may override the shape anisotropy and give rise to a remanent state where the magnetization is tilted away from the long-axis of a nanowire, an effect that has first been observed for ultrathin Co slabs [46] where the crystalline anisotropy is induced by strain due to the substrate.

However, there can be a subtle modification of this argument: If the transverse length scales are of the order of the exchange length and if the sample has non-ellipsoidal shape, e.g., a square platelet magnetized in plane, then a ‘configurational anisotropy’ [44, 45] may arise even though the above argument would predict an absence of anisotropies in the film plane. The origin of this shape induced anisotropy lies in the fact that for non-ellipsoidal samples, the demagnetizing field is nonuniform and induces small nonuniformities in the magnetization distribution.

1.3.2 Nanowires

Also extended samples with sufficiently small lateral dimensions may exhibit a reduced dimensionality. In fact, the tremendous progress in sample preparation techniques [46–50] now allows to tailor samples that exhibit zero, one or two-dimensional behavior respectively. Here we are interested in quasi-one dimensional (1D) structures, so called ‘nanowires’. Such wires are a fundamental component of prospective ‘racetrack’ memories [51] that exploit the stability of domain walls in nanowires to encode information. We have seen in the previous Sect. 1.3.1 that for diameters d such that,

$$d < 2\pi\delta_m, \quad (1.21)$$

the magnetization will be quasi 1D, depending only on the coordinate along the wire, i.e., $\mathbf{m} = \mathbf{m}(x)$. If there is an additional easy-axis anisotropy, δ_m should be replaced by $\delta_0 = \sqrt{A/K_e}$ with $K_e = K_{e,\text{eff}}$ given by (1.20). Such 1D behavior was first predicted theoretically [19] and is now regularly observed. Since such quasi-1D ferromagnets of nanoscale dimensions can now artificially be created and constitute essential components of proposed nanodevices [14, 51–54] we shall review the properties of 1D solutions of the Landau-Lifshitz equations in more detail. In particular, we shall see that such a micromagnetic description is in excellent agreement with magnetization profiles measured via scanning probe microscopy, demonstrating the success of micromagnetics framework even at nanoscale dimensions. Dynamical solutions of the Landau-Lifshitz equations include moving domain walls but also remarkable phenomena such as exotic breathers consisting of mutually repulsive domain walls of the same chirality [55] as discussed below.

In sufficiently narrow wires with the transverse dimensions satisfying the condition (1.21) and which we assume to be perpendicularly magnetized (e.g. [12]), the energy per unit cross-sectional area $\mathcal{E} = E/\mathcal{A}$ takes the following form [19],

$$\mathcal{E} = \int_{-L/2}^{L/2} dx \left\{ A(\partial_x \mathbf{m})^2 + K_{h,\text{eff}} m_x^2 - K_{e,\text{eff}} m_z^2 - \mu_0 H M_0 m_z \right\}, \quad (1.22)$$

while the magnetization dynamics is given by the Landau-Lifshitz equations (1.13) with the magnetization unit vector depending only on one space direction and time, i.e. $\mathbf{m} = \mathbf{m}(x, t)$. Here, A is the exchange constant, $K_{h,\text{eff}} > 0$ defines an easy-plane with $m_x = 0$, while $K_{e,\text{eff}} > 0$ favors an easy-axis within this plane, and finally, the last term describes the coupling to an external field H along the easy-axis. As in the case of a magnetic dot, the anisotropy constants will be effective ones and in general contain crystalline and shape contributions [15, 56] as defined in (1.20).⁴

⁴For a nanowire with effective easy-axis along the wire (x-axis), as is relevant for data storage in perpendicular hard disk media, the field is applied along wire and the effective anisotropies are given by $-K_{e,\text{eff}} m_x^2 + K_{h,\text{eff}} m_z^2$ with $K_{e,\text{eff}} = K_{e,\text{cryst}} + (\mu_0/2)M_0^2(N_x - N_y)$ and correspondingly for $K_{h,\text{eff}}$. The nucleus solution is then obtained via the replacement $\theta \rightarrow \phi$. For a discussion of effective anisotropies for different sample shapes, cf. [19].

This reduction of the nonlocal dipolar to local anisotropies is valid as long as the magnetization is varying slowly compared to the sample cross section [15, 56]. In the closely related context of nucleation in a thin ring this has been verified in [57] and on the basis of numerical computations it was concluded that the 1D approximation even applies to rather wide annuli. In the case of slowly varying magnetization configurations in a thin film this local approximation has been proven rigorously in [58]. Note that all these results explicitly disprove an objection originally raised by Aharoni [16], which has first been addressed in [59] and in more detail in [56].

1.3.3 Thin Films

Apart from bulk materials, skyrmions exist in perpendicularly magnetized ultrathin films with an interfacial DMI. The energy of a film with surface normal along the z -direction is then given by,

$$E = t \int d^2x \left\{ A(\nabla \mathbf{m})^2 - K_{e,\text{eff}} m_z^2 - \mu_0 H M_0 m_z \right\} + E_{\text{DMI}} + E_{m,\text{nonloc}} + E_{m,\text{Néel}} \quad (1.23)$$

where t denotes the film thickness. Here we assume an interfacial DMI term given by

$$E_{\text{DMI}} = D t \int d^2x (m_z \text{div } \mathbf{m} - (\mathbf{m} \cdot \nabla) m_z). \quad (1.24)$$

where $D > 0$ is the constant characterizing the strength of DMI, having dimensions of energy per area. $E_{m,\text{nonloc}}$ denotes the nonlocal part of the magnetostatic interaction which helps to stabilize a skyrmion in addition to the DMI term as we shall see in Sect. 1.4.2. We also assume that the wall curvature is small such that it remains straight over distances larger than the film thickness. In this case the magnetostatic energy of a Néel wall exceeds that of a Bloch wall by an energy $E_{m,\text{Néel}}$ and we have assumed that no crystalline hard-axis anisotropy is present. Local demagnetizing effects are captured by an effective anisotropy as above, where for a thin film geometry we have $K_{e,\text{eff}} \equiv K_{e,\text{cryst}} - (\mu_0/2)M_0^2$ and for a perpendicularly magnetized film it is required that the effective easy-axis anisotropy satisfies $K_{e,\text{eff}} > 0$, which implies a “quality factor” $\mathcal{Q} \equiv K_{e,\text{cryst}}/(\mu_0/2)M_0^2 > 1$ for perpendicular spin orientation.

1.4 Statics and Dynamics of Smooth Spin Textures

After having derived the relevant effective energy densities for nanowires and thin films, we shall now discuss how they entail topologically nontrivial smooth magnetization textures. Our discussion starts with smooth π domain walls emphasizing their topological character in the form of ‘chirality’ and ‘charge’, which are related to S^1 and S^0 winding numbers. We then show how twisted and untwisted pairs of such domain walls respectively describe 2π domain walls, and nonuniform nucleation of

magnetization reversal in applied magnetic fields. A dynamical generalization of a 2π domain wall yields a soliton-soliton breather where the repulsive domain walls are stabilized entirely due to dynamical effects. Generalizing the 2π domain wall profile to two spatial dimensions yields a remarkable variational ansatz for a static skyrmion which excellently describes the field dependence of the skyrmion radius in thin films [19, 20]. As an example of a transition between topologically equivalent states that are, however, separated by an energy barrier, we discuss the helicity switching of skyrmions in DMI-free thin films. In bulk samples we discuss how the end points of skyrmion lines or their bifurcation involves the existence of singular point defects such as hedgehogs. This illustrates the role of singular point defects in mediating changes in winding numbers. The existence of dynamical skyrmions originates in a precessional stabilization of a skyrmion that even exists in DMI free materials. This mechanism is closely related to the precessional stabilization of the soliton-soliton breather. For a discussion of experimental aspects of dynamical skyrmions we refer to the chapter by J. Åkerman.

1.4.1 2π Bloch Walls and Breathers

We first consider some examples of domain wall configurations in quasi 1D samples ('nanowires') that can be derived in analytically closed form, and demonstrate that such configurations indeed agree rather well with observed magnetization profiles in nanowires [60]. In order to find explicit solutions of the Landau-Lifshitz equations it is convenient to incorporate the constraint $|\mathbf{m}(x, t)| = 1$ by introducing angular fields via $\mathbf{m} = (\sin \theta \cos \phi, \sin \theta \sin \phi, \cos \theta)$. As we are interested in static configurations of minimal energy, we consider configurations that are restricted to the easy-plane, $m_x = 0$ and the energy per unit area (1.22) then can be expressed as follows,

$$\mathcal{E} = 2K_e \int_{-L/2}^{L/2} dx \left\{ \frac{1}{2} \delta_0^2 (\partial_x \theta)^2 + U_0(\theta) \right\}, \quad (1.25)$$

where

$$U_0(\theta) = (1/2) \sin^2 \theta - h \cos \theta, \quad (1.26)$$

the characteristic length scale is defined as $\delta_0 = \sqrt{A/K_e}$, and the reduced external field is given by

$$h = \mu_0 H M_0 / 2K_e. \quad (1.27)$$

Here we used for simplicity the notation $K_e \equiv K_{e,\text{eff}}$. The azimuthal angle has been fixed to the easy-plane value $\phi = \pm\pi/2$. In the following it is convenient to restrict to the case $\phi = \pi/2$ and instead let θ ($\text{mod } 2\pi$) vary on an extended range from 0 to 2π . This may be mapped back to the standard parametrization with $0 \leq \theta \leq \pi$, via $\theta \rightarrow 2\pi - \theta$, $\phi \rightarrow \phi + \pi$.

Static solutions are then obtained from an integration of the Euler-Lagrange equations $\delta\mathcal{E}/\delta\theta = 0$, or explicitly

$$-\delta_0^2 \partial_x^2 \theta + U_0'(\theta) = 0. \quad (1.28)$$

which has the first integral,

$$(1/2)\delta_0^2(\partial_x \theta)^2 - U_0(\theta) = c \quad (1.29)$$

where c is an integration constant larger than the minimum of $-U_0$. Here we are interested in spatially localized, ‘solitary’ objects such as domain walls or domain wall pairs and hence we choose boundary conditions such that $\partial_x \theta = 0$ at $x = \pm L/2$. In this chapter we take the limit $L \rightarrow \infty$ as we are interested in configurations that exist in arbitrarily long samples.

1.4.1.1 A Single π -Domain Wall

In the absence of an external field, the Euler-Lagrange equation (1.28) is solved by the the Bloch-wall,⁵ ‘domain-wall’, or ‘ π -soliton’,

$$\theta_0(x/\delta_0) = 2 \arctan e^{-x/\delta_0}, \quad (1.30)$$

which interpolates between the domains of ‘up’ and ‘down’ magnetization and is therefore also referred to as ‘kink’. The Bloch-wall has width $\delta_0 = \sqrt{A/K_e}$ and an energy per area, $\mathcal{E}_s = 4\sqrt{AK_e}$. As stated in the previous section, the azimuthal angle for all 1D situations is assumed to be fixed to easy-plane value $\phi = \pi/2$, and $\theta \pmod{2\pi}$ varies on an extended range. The symmetries of the original energy density (1.25) imply a fourfold degeneracy of this soliton solution. These soliton solutions can be written as

$$\theta_{QC}(x/\delta_0) = 2QC \arctan e^{Qx/\delta_0} \quad (1.31)$$

with soliton ‘chirality’ [61–63], $C = \pm 1$, and soliton ‘charge’, $Q = \pm 1$, as internal degrees of freedom.⁶ The chiral degree of freedom is related to the sense of rotation of the magnetization as one proceeds along the x -axis, cf. Fig. 1.1a. As evident from Fig. 1.4a, b, the ‘chirality’ and the ‘charge’ are descendants of the winding numbers discussed before: The chiral degree of freedom C is twice the easy-plane winding number of the homotopy group $\pi_1(S^1)$, while the charge Q is related to the easy-axis winding number of $\pi_0(S^0) \cong \mathbb{Z}_2$ where the two elements distinguish either the presence of a π domain wall (or an odd number of them), or the absence of a

⁵It is amusing to note that Bloch in his paper actually acknowledges Heisenberg for the solution of the corresponding differential equation, so perhaps it should be more appropriately named the ‘Heisenberg-Bloch’ wall. Also, note that in the sequel we usually do not distinguish between Bloch and Néel walls for the quasi 1D situation.

⁶With $\partial_x \theta_{QC} = C \operatorname{sech} x$ and $\cos \theta_{QC} = -\tanh(Qx)$ we immediately verify that $(1/\pi) \int_{-\infty}^{\infty} dx \partial_x \theta_{QC} = C$ and $[\cos \theta_{QC}(-\infty) - \cos \theta_{QC}(\infty)]/2 = Q$.

domain wall (or the presence of an even number). Obviously consecutive domain walls have opposite values of Q such that the first domain wall fixes the charge values of all others. Note that it is the domain wall position that is exploited in racetrack type memories. In contrast, the chiral degree of freedom may be used to carry information and thus could play an important additional role in ‘racetrack’-type domain wall memory devices [53, 54, 64], cf. Fig. 1.1. Note that the sign of the soliton ‘charge’ Q determines the response of a domain wall towards an applied magnetic field: If an external field is applied in the ‘up’ direction, i.e. along the positive z -axis, then the soliton of positive (negative) charge would move in positive (negative) x direction. Note that the chiral degree of freedom also exists in absence of a parity breaking Dzyaloshinskii-Moriya interaction, as the configuration θ_s then minimizes the energy (1.22) for both $\phi = \pm\pi/2$. However, note that this chiral degree of freedom does not exist in a strict Ising type system as discussed above, where static solitons involve sharp phase boundaries with no internal degree of freedom. Chirality may, however, emerge due to quantum effects [36].

Charge and (vector) chirality can, respectively, be generalized for arbitrary domain wall configurations,

$$Q = -\frac{1}{2} \int_{-\infty}^{\infty} dx \partial_x m_z, \quad \mathbf{C} = \frac{1}{\pi} \int_{-\infty}^{\infty} dx \mathbf{m} \times \partial_x \mathbf{m}. \quad (1.32)$$

This definition shall also be useful for the description of out-of easy-plane dynamic scattering solutions and breathers that will be discussed below. For a simple π domain wall (static or moving), we have as expected $Q = \pm 1$, while for arbitrary solutions whose azimuthal angle is x -independent, $\phi(x, t) = \phi(t)$, we have,

$$\mathbf{C} = \hat{\mathbf{c}} \frac{1}{\pi} \int_{-\infty}^{\infty} dx \partial_x \theta, \quad (1.33)$$

which points along the unit vector $\hat{\mathbf{c}} = (-\sin \phi, \cos \phi, 0)$. For an isolated static Bloch wall with $\phi = \pm\pi/2$ this reduces to the above definition, namely, $C \equiv C_x = (1/\pi) \int dx \partial_x \theta = \pm 1$. Solitons of fixed charge $Q = 1$, but opposite chiralities $C = \pm 1$ are shown in Fig. 1.1. For solutions such as a 2π Bloch wall which covers the singular point $\theta = \pi$, one should return to (1.32), or use the reparametrization $\theta \rightarrow 2\pi - \theta, \phi \rightarrow \phi + \pi$.

In DMI free systems domain walls of opposite chirality are energetically degenerate. This degeneracy may give rise to a so-called *Bloch line*. If the domain walls of opposite chirality are horizontally separated, a vertical Bloch line (VBL) results, if they are separated vertically, a horizontal Bloch line (HBL) occurs. We refer to Chap. 2 by Thiaville and Miltat for a discussion of many experimental examples of such structures. It should also be noted that with proper adaptation the charge Q and chirality C can be used to classify the spin twists inside a domain wall carrying a Bloch line [63].

An isolated Bloch wall is only stable for a vanishing field. For a nonvanishing external field, $H \neq 0$, and depending on damping, either oscillatory or steady domain

wall motion results as observed in isolated nanowires [12, 53] (cf. Fig. 1.1f). Static solutions will then consist of pairs of domain walls or solitons. Since the solitons carry a chiral degree of freedom, two solitons with same chirality can be combined to form a so-called soliton-soliton ('ss') pair, or the two solitons may be arranged with opposite chirality to form a soliton-antisoliton ('s̄s̄') pair. This terminology reflects the fact that the former configuration is stable and not easily annihilated, in contrast to wall pairs with opposite chirality which turn out to be relevant in the context of thermally induced magnetization reversal [11, 15]. We now discuss each of these cases separately as they both surprisingly will also turn out to be relevant for helicity switching and dynamical states of skyrmions, respectively.

1.4.1.2 Soliton-Antisoliton Pairs as Nuclei for Magnetization Reversal

In the presence of an applied magnetic field, the Euler-Lagrange equations (1.28) are solved by the following profile [15, 19],

$$\begin{aligned}\theta_{s\bar{s}}(x) &= 2 \arctan \left(\frac{\cosh(x/\delta_{s\bar{s}})}{\sinh R_{s\bar{s}}} \right), \\ &= \theta_0 \left(-\frac{x}{\delta_{s\bar{s}}} + R_{s\bar{s}} \right) + \theta_0 \left(\frac{x}{\delta_{s\bar{s}}} + R_{s\bar{s}} \right),\end{aligned}\quad (1.34)$$

for field values smaller than the anisotropy field, i.e., $h < 1$ and we restrict ourselves again to the case $\phi = \pi/2$. The second equation explicitly shows that this configuration consists of two coherently superimposed domain walls of *opposite* chirality placed at positions $x = \pm R_{s\bar{s}}\delta_{s\bar{s}}$, or in other words, that they describe a soliton-antisoliton pair with winding number zero [19]. Formally this follows immediately by computing $w_{S^1} = (1/2\pi) \int_{-\infty}^{\infty} \partial_x \theta_{s\bar{s}} = 0$ which in turn follows from the chirality of one soliton, $(1/\pi) \int_{-\infty}^{\infty} \partial_x \theta_0(x) = -1$ (cf. footnote 5).

The 'radius' $R_{s\bar{s}}$ and the characteristic width $\delta_{s\bar{s}}$ are both related to the external field h via the following relations,

$$h = \operatorname{sech}^2 R_{s\bar{s}}, \quad \delta_{s\bar{s}}/\delta_0 = \coth R_{s\bar{s}}, \quad (1.35)$$

where as above, the reduced field is defined by $h = \mu_0 H M_0 / 2K_e$. For fields approaching the anisotropy field, $h \rightarrow 1$, we have $R_{s\bar{s}} \rightarrow 0$, and thus the two superimposed solitons nearly annihilate each other while the length scale $\delta_{s\bar{s}}$ diverges. For small fields, the two solitons are far from each other and the structure $\theta_{s\bar{s}}(x)$ describes a reversed domain of size $\sim 2\delta_0 \ln(2/\sqrt{h})$, which is immersed in the initial state with the magnetization pointing antiparallel to the field. The energy per area of the the soliton-antisoliton pair with respect to the metastable state is given by,

$$\mathcal{E}_{s\bar{s}} = 2\mathcal{E}_s [\tanh R_{s\bar{s}} - R_{s\bar{s}} \operatorname{sech}^2 R_{s\bar{s}}], \quad (1.36)$$

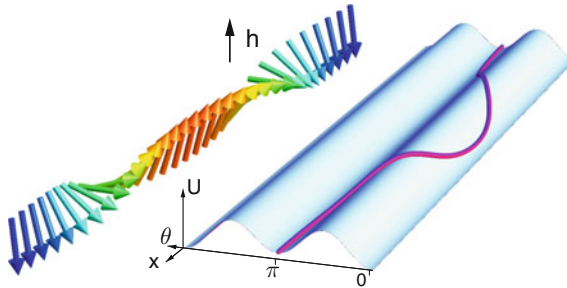


Fig. 1.7 Soliton-antisoliton configuration of an easy-plane magnet with vanishing total winding number $w_{S^1} = 0$. Left: Soliton-antisoliton configuration of domain walls of opposite chirality (1.34). Right: Corresponding energy landscape with spin configuration represented as an elastic rope (magenta) which illustrates the instability of the soliton-antisoliton thus characterizing it as a nucleus for magnetization reversal

which is the sum of deformation and Zeeman energy. Here $\mathcal{E}_s = 4\sqrt{AK_e}$ is the energy of a single π -domain wall. It is clear that for small $R_{s\bar{s}}$, the energy tends to zero since the two soliton annihilate each other, while for large soliton separation $R_{s\bar{s}}$ the energy approaches that of two independent domain walls. Figure 1.7 illustrates the magnetization configuration of the soliton-antisoliton pair for $R_{s\bar{s}} = 2.2$. The right panel shows a visualization where the magnetization configuration is interpreted as an elastic rope that is laid over the energy surface. From this interpretation it is clear that this magnetization configuration is unstable and represents the *critical nucleus* for magnetization reversal in nanowires. It describes the (spatially nonuniform) energy barrier for thermally activated switching between the metastable state with the magnetization aligned antiparallel to the field and the stable state with magnetization along the field (cf. see footnote 4).

More formally, it can be shown that the configuration constitutes a saddle point with exactly one unstable direction [19]. As a critical nucleus, it generalizes the famous *Néel-Brown* mechanism for thermally activated magnetization reversal for uniform nanoparticles to narrow nanowires where the magnetization varies along the length of the particle. The cross-over between the two mechanisms occurs at a critical length of $2L_{\text{crit}} = 2\pi\delta_0/\sqrt{1-h^2}$ if nucleation occurs in the interior of the particle or at L_{crit} if one domain wall is nucleated from the sample end. In the absence of pinning, reversal proceeds via the uniform Néel-Brown mechanism for sample lengths smaller than these critical values.

The size dependent cross-over of the switching mechanism has been observed in Co islands [65]. It is interesting to note that this cross-over is of tantamount importance for the design of perpendicularly magnetized media for magnetic harddisks [11, 17].

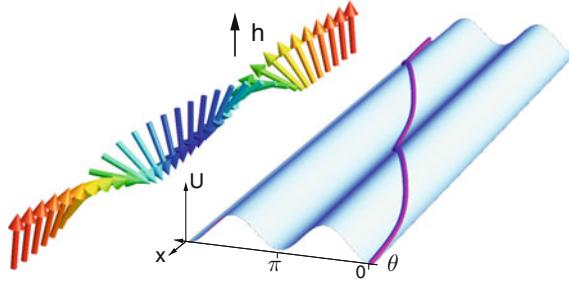


Fig. 1.8 Soliton-soliton configuration of an easy-plane magnet with total winding number $w_{S^1} = 1$. Left: Soliton-soliton configuration of two domain walls of same chirality (1.37). Right: Energy landscape with spin configuration represented as an elastic rope (magenta) illustrating the (topological) stability of the 2π domain wall if restricted to the easy-plane

1.4.1.3 2π Bloch Walls

The soliton-soliton pair that extremizes the Euler-Lagrange (1.28) equation in the presence of an applied field can be expressed as [19],

$$\begin{aligned}\theta_{ss}(x) &= 2 \arctan \left(\frac{\cosh R_{ss}}{\sinh(x/\delta_{ss})} \right), \\ &= \theta_0 \left(\frac{x}{\delta_{ss}} - R_{ss} \right) + \theta_0 \left(\frac{x}{\delta_{ss}} + R_{ss} \right),\end{aligned}\quad (1.37)$$

with the two possible values $\phi = \pm\pi/2$ that define the overall chirality of the domain wall pair, i.e. $w_{S^1} = (1/2\pi) \int_{-\infty}^{\infty} \partial_x \theta_{ss} = \pm 1$. One of these two chiral states can be favoured by, e.g., interfacial DMI and this effect can for example be observed by spin-polarized photoemission electron microscopy (SPLEEM) [29] for both Bloch-type and Néel-type domain walls (Fig. 1.8).

For convenience, the angle θ is assumed here to vary between 0 and 2π , but of course the configuration may be mapped back to the standard intervals via $(\theta, \phi) \mapsto (2\pi - \theta, \phi + \pi)$. The second equation in (1.37) explicitly demonstrates that the configuration consists of a superposition of two solitons with the *same* chirality located at $x = \pm R_{ss} \delta_{ss}$, respectively. The soliton separation R_{ss} and intrinsic width δ_{ss} of the soliton-soliton pair depend on the reduced external field via

$$h = \operatorname{csch}^2 R_{ss}, \quad \delta_{ss}/\delta_0 = \tanh R_{ss}, \quad (1.38)$$

where $\operatorname{csch} x \equiv 1/\sinh x$.

With increasing field, the two twisted solitons get pushed together as R_{ss} decreases. Since the field counteracts the mutual exchange repulsion the intrinsic width decreases with increasing field. The repulsive nature of the soliton-soliton pair is reflected by the energy,

$$\mathcal{E}_{ss} = 2\mathcal{E}_s [\coth R_{ss} + R_{ss} \operatorname{csch}^2 R_{ss}], \quad (1.39)$$

which diverges at short distances, while for large intersoliton separation it approaches the energy $2\mathcal{E}_s$ of two independent domain walls. The soliton-soliton pair $\theta_{ss}(x)$ is thus stabilized by the balance between exchange repulsion of the two twisted domain walls and the ‘pressure’ exerted by the external field.

Experimentally, such repulsive interaction between soliton-soliton pairs was indeed observed in nanowires as shown in Fig. 1.10 [60]. Even quantitatively, the measured profile agrees remarkably well with the predictions of [19], as given in (1.37), (1.38). In larger samples this effect is more difficult to observe as the dipolar interaction in general keeps the domain walls too far apart for the mutual exchange repulsion to become detectable. However, in sufficiently thin films or in nanowires, the dipolar interaction is sufficiently weak and such structures become observable, exact criteria are presented in [19].

1.4.1.4 Soliton-Soliton Breathers

With a view on the dynamical skyrmions to be discussed below, it appears convenient to point out that there is a class of remarkable analytical breather solutions of the dissipationless Landau-Lifshitz equations [54, 55] that is also described by the ansatz (1.37) but now with time dependent $R_{ss}(t)$ and $\phi_{ss}(t)$ without applied field. The solutions correspond to two solitons of same chirality, a soliton-soliton (*ss*) pair whose relative distance proportional to $R(t)$ periodically oscillates with time while the azimuthal angle $\phi_{ss}(t)$ undergoes precession with half the period of the breathing oscillation. These results are illustrated in Fig. 1.9 which shows the time dependence of the azimuthal angle $\phi_{ss}(t)$ describing nonuniform precession, the breathing oscillation of m_z as a function of time and the magnetization profiles at the moments of closest and farthest separation of the two solitons. For the explicit analytical expressions we refer to [54, 55]. It is interesting to note that this soliton-soliton breather is closely related to the dynamical skyrmion discussed below (cf. also the contribution by J. Åkerman in this volume), as it approximately describes the time-dependent variation of the magnetization profile across a dynamical skyrmion.

1.4.2 Variational Ansatz for Static Skyrmions

It is evident that the thin film energy (1.23) cannot be analytically minimized even under the assumption of cylindrically symmetric structures and it is therefore important to find a good variational ansatz. Such an ansatz is provided by the exact solution of a 2π domain wall in an external field as given by θ_{ss} as given in (1.37) and originally derived in [19]. The success of this profile in describing measured scanning tunneling microscopy (STM) data for 2π domain walls is shown in Fig. 1.10a, b (cf. [60]). We are thus motivated to use the following variational profile for a skyrmion,

$$\begin{aligned}\theta_{\text{sk}}(\rho) &= \theta_0 \left(\frac{\rho}{\delta} - R \right) + \theta_0 \left(\frac{\rho}{\delta} + R \right), \\ \phi_{\text{sk}}(\varphi) &= \varphi + \psi,\end{aligned}\quad (1.40)$$

where θ_0 describes the profile of a π domain wall as given by (1.30), with φ and $\rho > 0$ as polar coordinates in real space with $\mathbf{r} = (\rho \cos \varphi, \rho \sin \varphi, 0)$, and ψ is a constant. Here δ is a width and R a dimensionless parameter characterizing the “radius” of the skyrmion. The locus of $\theta = \pi/2$ occurs at a radius $a = \delta \text{arsinh}(\cosh(R))$.

This parametrization yields a skyrmion with ‘down’ magnetization at the centre, i.e., $\theta(\rho = 0) = \pi$, and inserting the ansatz into the expression for the winding number (1.9) reveals that $w_{S^2} = -1$ for *all* values of the variational parameters R, δ . A skyrmion with $w = 1$ results upon substituting $\theta_{\text{sk}} \mapsto \pi - \theta_{\text{sk}}$. Note that $\psi = 0, \pi$ describe hedgehog skyrmions favoured by surface DMI, while $\psi = \pi/2, 3\pi/2$ describe Bloch skyrmions favoured by either bulk DMI in B20 materials or by dipolar interactions. The variational parameters R, δ may, e.g., be used to fit experimental

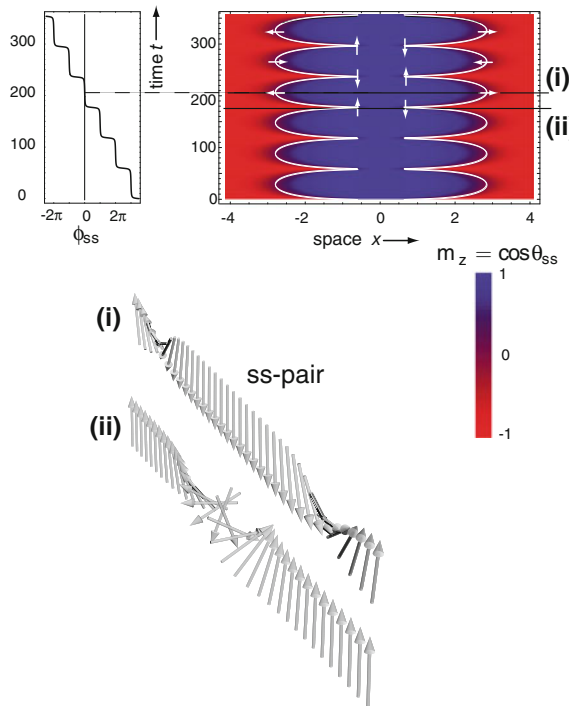


Fig. 1.9 Time evolution of a soliton-soliton (*ss*) breather in absence of an applied field. The left panel shows the time evolution of the azimuthal angle $\phi_{ss}(t)$ of the magnetization, while the right panel shows the evolution of $m_z(t)$. The solid white line indicates the soliton ‘world lines’ $\pm R_{ss}(t)$, and the arrows indicate the transverse magnetization at the instants of largest separation (i) and closest approach (ii). Note that the period of the azimuthal oscillation is twice as large as that of the oscillation of the m_z -component. Bottom panel shows magnetization profiles at instants (i), (ii). Adapted from [54]

data as shown in Fig. 1.10c, d. However, we may also theoretically determine the parameters δ , R variationally by inserting the ansatz (1.40) into the total energy (1.23). From subsequent minimization with respect to R and δ we obtain $\delta = \delta_0$ and in the narrow wall limit, we obtain the following physical skyrmion radius as a function of the applied magnetic field,

$$R = \left(\mathcal{D} + \frac{2}{3} \mathcal{D}^{-1} \tau - 1 \right) \frac{\delta_1}{h}. \quad (1.41)$$

Here the reduced DMI constant is given by $\mathcal{D} = \pi D / 4\sqrt{AK_e}$, the dimensionless dipolar field strength (or inverse ‘quality factor’) is $\mathcal{D}^{-1} = \mu_0 M_0^2 / 2K_e$, the reduced field is $h = \mu_0 M_0 H_{\text{ext}} / 2K_e$ and the reduced film thickness is given by $\tau = t / \delta_0$ with $\delta_0 = \sqrt{A/K_e}$ and $K_e = K_{e,\text{eff}}$. The result (1.41) has two important consequences:

- (i) It shows that the DMI and the dipolar interaction are in tandem responsible for the stabilization of a skyrmion in an entirely symmetric way. While the dipolar interaction is always present in ferromagnets, it is DMI that is usually dominant. Nonetheless it is important to note that the dipolar interaction can help stabilizing the skyrmion even for slightly subcritical values of the DMI, i.e., $\mathcal{D} < 1$.

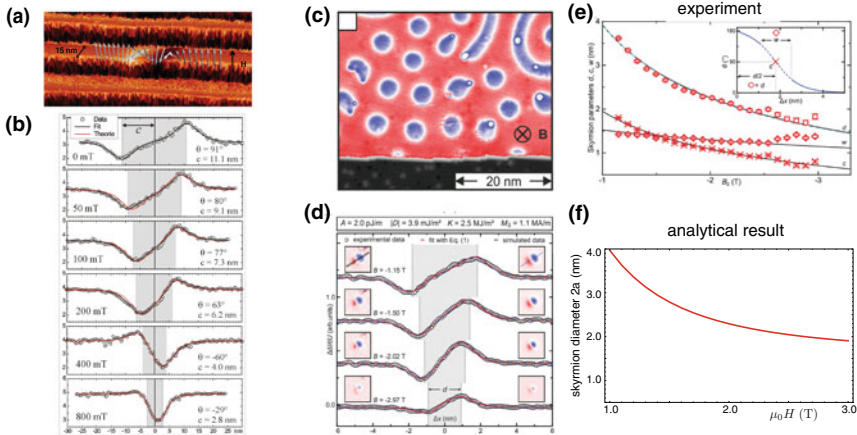


Fig. 1.10 Description of 2π domain wall and skyrmion profiles by the function θ_{ss} as given in (1.37) from [19]. **a** A Fe nanowire on a W substrate at fixed external field [60]. Superimposed is the soliton-soliton pair configuration from (1.37). **b** Observed magnetization profiles as a function of applied field. The theoretical fits are obtained from the expression (1.37) with the field dependence given by the analytical expression (1.38) (cf. [19]). **c** Scanning tunneling microscopy (STM) image of out of plane components of skyrmions. **d** Fits for 3D skyrmion profile using the ansatz (1.40) based on (1.37). **e** Observed field dependence of skyrmion radius [20]. **f** Analytical result for the field dependence of the skyrmion radius with parameters taken from the experiments in [20]. Panels (a), (b) are taken from [60], panels (c–e) from [20].

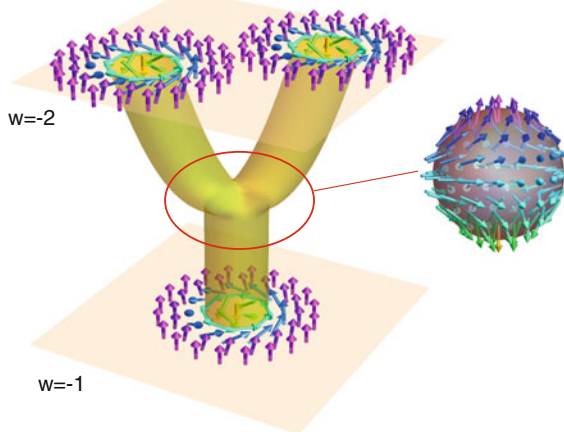


Fig. 1.11 Branching of a skyrmion line into two skyrmion lines. As this entails a discontinuous change of the winding number at slices for a given z coordinate (here from $w_{S^2} = -1$ to $w_{S^2} = -2$), such a process can only be accomplished at the expense of a (anti-)hedgehog singular point defect at the branching point (cf. Fig. 1.4). The hedgehog is characterized by a winding number $w_{S^2} = -1$, cf. text. After Milde et al. [66]

- (ii) It explains experimental data very well: For the parameters of [20], where $(2/3)\mathcal{Q}^{-1}\tau \simeq 0.2$, (1.41) yields the result shown in Fig. 1.10e, f, in excellent agreement with the observations.

1.4.2.1 Creation of Skyrmions via Hedgehogs

So far, we considered smooth topological magnetization textures such as domain walls and skyrmions per se and did not analyse their possible creation or destruction. In thin films, skyrmions may be created at sample edges, but also in the interior of samples in constrictions [9] or under point contacts [67]. In this latter case, this process involves the change of a winding number which cannot occur by any smooth deformation of the magnetization. This can only occur by processes that violate the continuity of the magnetization field and thus lie outside the ‘micromagnetics’ framework [23]. Topological point defects are obvious candidates for such processes that can change the winding number. At the same time this provides us with a link between the topological point defects considered in Sect. 1.2.3 and the smooth topological defects of Sect. 1.2.4. How well is then the skyrmion number conserved in a real system? In order to approach this issue, Milde et al. [66] analyzed MFM images and considered the occurrence of skyrmion lines or tubes in a thick film. Interpreting their MFM data they discovered situations such as the one depicted in Fig. 1.11. In this case, the winding number w_{S^2} changes abruptly as a function of the z -coordinate perpendicular to the film surface. This can only occur at the expense of the formation of a singular point defect, in this case an (anti-)hedgehog. It is defined via the polar angles of the magnetization, $\Theta = \vartheta$, $\Phi = -\varphi + \pi$, where $x_1 = \vartheta$ and

$x_2 = \varphi$ denote the polar angles in real space. With this parametrization, the degree or topological charge (1.6) of the hedgehog shown in Fig. 1.11 is readily evaluated to be $w_{S^2} = -1$. This singular point defect forces the (continuous) magnetization field to go to zero in a continuous description, or in a discrete lattice description, the defect will be located between grid points.

1.4.3 Helicity Switching of Skyrmions

In systems with parity breaking DMI, the helicity of the skyrmion is fixed by the sign of the DMI term. However, in centrosymmetric crystals, the two helicity states of a skyrmion are energetically degenerate. This is for example realised in thin films of $\text{La}_{0.5}\text{Ba}_{0.5}\text{MnO}_3$ [68] or $\text{BaFe}_{12-x-0.05}\text{Sc}_x\text{Mg}_{0.05}\text{O}_{19}$ ($x = 1.8$) as studied in [69]. As both helicity states have the same winding (skyrmion) number, they must be connected via a path of finite energy that involves configurations with the same winding number. In films of finite thickness larger than the domain wall width, the energies of Bloch and Néel skyrmions are not energetically degenerate [19]: The dipolar energy density of a Néel wall configuration exceeds that of a Bloch configuration by an energy density $(\mu_0/2)M_r^2$, where M_r is the nonvanishing radial magnetization component of the Néel skyrmion. For a skyrmion radius R that is larger than the wall width, $R \gg \delta_0$, the effective energy along the circumference of the skyrmion is given by [69],

$$E_{\text{eff}}[\phi] = 2tR\delta_0 \int_0^{2\pi} d\varphi \left\{ \frac{A}{R^2} \partial_\varphi \tilde{\phi} + \frac{\mu_0}{2} M_0^2 R \sin^2 \tilde{\phi} \right\} \quad (1.42)$$

which is analogous to the energy of a nanowire for $h = 0$ (cf. (1.25)). We defined $\tilde{\phi} = \phi - \varphi + \pi/2$ such that left-handed or right-handed Bloch skyrmions respectively correspond to $\tilde{\phi} = 0, \pi$, which both have vanishing wall demagnetizing energy. Here we assumed that the film thickness t is larger than the domain wall width δ_0 . The effective energy (1.42) is derived under the assumption that the described azimuthal variations $\tilde{\phi}(\varphi)$ have zero winding number, $\oint d\varphi \partial_\varphi \tilde{\phi} = 0$.

The problem is now formally analogous to that of domain wall nucleation in a nanowire in absence of an external field. We know that two states with right and left helicity, i.e., $\tilde{\phi}_{CCW} = 0$ and $\tilde{\phi}_{CW} = \pi$, minimize the magnetostatic energy (cf. Fig. 1.12). They are separated by a nonuniform energy barrier configuration that we may approximately express as,

$$\phi_b \approx -\phi_0 \left(\frac{1}{\lambda} \left(\varphi - \frac{\pi}{2} \right) \right) + \phi_0 \left(\frac{1}{\lambda} \left(\varphi - \frac{3\pi}{2} \right) \right), \quad (1.43)$$

where ϕ_0 is defined analogous to θ_0 , i.e. $\phi_0(s) = 2 \arctan e^{-s}$. Equation (1.43) describes the coherent superposition of two π -solitons of opposite chirality at two azimuthally diametrically opposed positions on the skyrmion (cf. Fig. 1.12), and the total winding number is vanishing as required (cf. footnote 5). Here the (dimen-

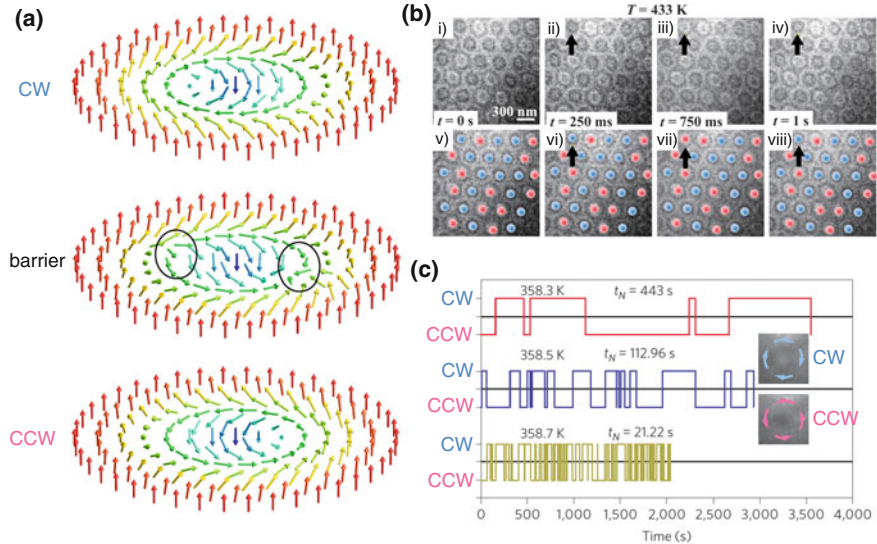


Fig. 1.12 Thermally activated switching across a barrier between the two helicity states with clockwise (CW) and counterclockwise (CCW) rotating magnetization within the skyrmion (cf. also Fig. 1.3). (a) In the absence of DMI, the CW and CCW state are energetically degenerate and separated by an energy barrier which involves the nucleation two Bloch lines of opposite chirality (highlighted by black circles) in analogy to the nucleation of soliton-antisoliton pairs in Sect. 1.4.1.2. (b) Real-space observations of zero-field room-temperature skyrmions and their dynamical helicity reversals in a (001) $\text{BaFe}_{12-x-0.05}\text{Sc}_x\text{Mg}_{0.05}\text{O}_{19}$ ($x = 1.8$) thin plate (sample thickness is below 100 nm). Panels (i)–(iv) are snapshots of *in situ* Lorentz TEM (LTEM) movies while panels (v)–(viii) are identical images but colour coded with the blue and red dots indicating skyrmions with CW and CCW helicities. The black arrow highlights the skyrmion whose helicity switches between the frames. Images are taken at a temperature $T = 433$ K. Taken from [69] (c) Temperature dependent telegraph noise due to helicity switching in a centrosymmetric thin film or $\text{La}_{0.5}\text{Ba}_{0.5}\text{MnO}_3$ at temperatures above the critical temperature $T_C \approx 300$ K of the thin film. Taken from [68]

sionless) width is given by $\tilde{\lambda} = \lambda/R$, where $\lambda \equiv \sqrt{A/(\mu_0/2)M^2}$ is the ‘Bloch line thickness’ that determines the width of the transition region between the states of right and left helicity. Consequently (1.43) requires that $\lambda/R \ll \pi$. Note that λ plays a role analogous to the domain wall thickness in the domain wall nucleation problem described above.

1.4.4 Dynamical Skyrmions

So far we emphasized the topological properties of static skyrmions. It is these topological properties that govern various physical properties such as for example the emergent fields as discussed in subsequent chapters in this book by Thiaville and Miltat (Chap. 2), and Bauer et al. (Chap. 5). The energetic details of skyrmion

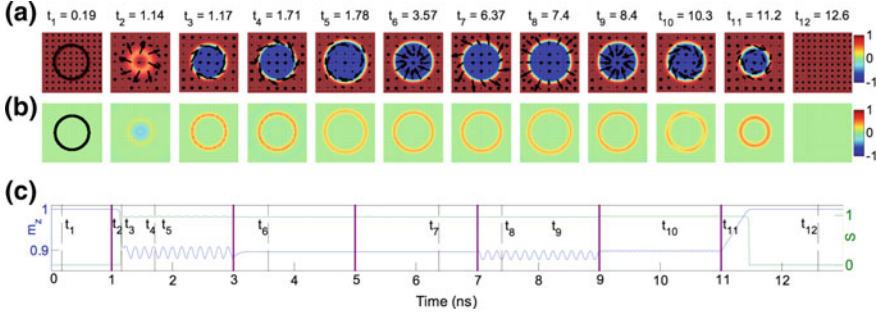


Fig. 1.13 Simulation of a nanocontact (NC) spin torque oscillator with radius 40 nm and a current $J = 6 \cdot 10^8 \text{ A/cm}^2$ showing the nucleation of dynamical skyrmion without DMI and dipolar interactions from an initial FM state, and its subsequent tuning by spin transfer torque, damping α , DMI, and dipolar interaction. **a** Top-view of the spin structure at different times; the black circle indicates the NC; color bar indicates m_z . **b** Top-view of the topological density at the same times as in (a); **c** Time-trace of the m_z -component averaged over the simulation area and time-trace of the skyrmion number; dashed vertical lines correspond to the snapshots above. For $0 < t < 1$ ns, the system undergoes an initial relaxation from FM state. For $1 \text{ ns} < t < 3 \text{ ns}$, a dynamical skyrmion is nucleated under a finite spin transfer torque assisted by the corresponding Oersted field without DMI. For $3 \text{ ns} < t < 5 \text{ ns}$, the Oe field is artificially turned off and breathing disappears. For $5 \text{ ns} < t < 7 \text{ ns}$, both current and damping are turned off. For $7 \text{ ns} < t < 9 \text{ ns}$, a moderate DMI is added and breathing resumes. For $9 \text{ ns} < t < 11 \text{ ns}$, we only turn on dipolar interactions (both Oe and DMI are off) and minor breathing is again observed. For $t > 11$ ns, the dynamical skyrmion will dissipate into a uniform ferromagnetic state. From [70]

formation are somewhat less relevant and in fact we have seen in Sect. 1.4.2 that not only DMI but also dipolar interactions may essentially contribute to the stabilization of a skyrmion in a thin film.

The notion that it is topology rather than energetics being the defining property of a skyrmion is emphasized by the remarkable fact that skyrmions can also be stabilized via a purely dynamical mechanism. This does not require the existence of DMI and/or dipolar interactions [70]. Such dynamical stabilization exists even when dipolar interaction and DMI are entirely absent. In this case, the z -component of the magnetization (along the easy-axis) is conserved, and as a consequence the precessing skyrmion retains a constant radius. For magnets with arbitrarily weak dipolar and/or DMI, the magnetization along z is no longer conserved, and the skyrmion shows breathing while the magnetization at its circumference is continuously precessing.

Such dynamical skyrmions can be created and tuned under a nanocontact as illustrated in Fig. 1.13. The various time intervals show the nucleation of a dynamical skyrmion, its sustenance, and its subsequent tuning by varying the spin transfer torque, damping, DMI and the dipolar interaction. The medium underneath a nanocontact is effectively dissipationless. Comparing the time intervals $3 \text{ ns} < t < 5 \text{ ns}$ and $5 \text{ ns} < t < 7 \text{ ns}$ in Fig. 1.13, with and without damping and spin torque respectively, it is seen that damping can be entirely compensated by the action of a spin torque.

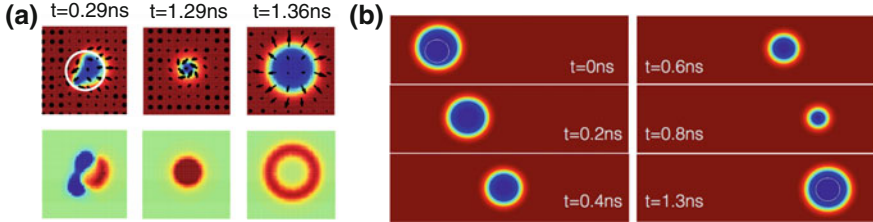


Fig. 1.14 Dynamical skyrmion creation in a point contact and transport of a dynamical skyrmion through a DMI-free material. **a** Nucleation of a dynamical skyrmion under a point contact (white circle) of diameter 30 nm [70]. Initially, a topologically trivial ‘droplet’ is created ($t = 0.29$) which exhibits significant distortion of its shape over time. After some delay, a new, topologically nontrivial dynamical skyrmion is nucleated whose shape remains remarkably circular but with varying radius over time. Top panel shows the magnetization component perpendicular to the film, while the bottom panels show the topological density $\rho_{\text{top}} \propto \mathbf{m} \cdot (\partial_x \mathbf{m} \times \partial_y \mathbf{m})$ with blue (red) indicating negative (positive) values. Note that between $t = 1.29$ ns and $t = 1.36$ ns the skyrmion shows appreciable breathing due to the presence of DMI while the magnetization shows complete precession. It should be emphasized, however, that the dynamical skyrmion also exists in materials with small or negligible DMI making it an attractive candidate for the design of robust spin torque oscillators in non DMI materials. **b** Current induced motion of a dynamical skyrmion in a nanowire without DMI. Illustrating the quasiparticle nature of the dynamical skyrmion, it is nucleated and transported coherently by an in-plane current to a second nanocontact at a distance of 150 nm, where it is trapped again and restored to its original size. (Images from [70])

Figure 1.14 illustrates the importance of the nontrivial topology onto the dynamical behaviour. Panel (a) demonstrates that the initial nontopological droplet ($w_{S^2} = 0$) exhibits significant deformation. In contrast, once the texture has transformed into a skyrmion with $|w_{S^2}| = 1$, it is remarkably stable. The created dynamical skyrmion can then be transported through a medium without DMI as shown in Fig. 1.14b.

From Fig. 1.13 it follows that the spin torque effectively generates a lossless medium under the nanocontact. This is confirmed by the analytical results that are shown in Fig. 1.15 and whose derivation we now sketch: We study the Landau-Lifshitz equations in the presence of a nanocontact,

$$\partial_t \mathbf{m} = -\gamma \mathbf{m} \times \mu_0 \mathbf{H}_{\text{eff}} + \alpha \mathbf{m} \times \partial_t \mathbf{m} + \gamma \sigma(I) \Theta(a_c - r) \mathbf{m} \times (\mathbf{m} \times \hat{\mathbf{z}}). \quad (1.44)$$

here $\gamma > 0$ is the gyromagnetic ratio, $\mu_0 \mathbf{H}_{\text{eff}} = -\delta E / \delta \mathbf{M}$, and $\sigma(I) = (\hbar I P / 2eV) \times (1/2K_e)$, where V is the magnetic volume under the nanocontact.

We may now use the 2π domain wall ansatz (1.37) for the skyrmion profile,

$$\begin{aligned} \theta(t) &= \theta_0(r/\delta - R(t)) + \theta_0(r/\delta + R(t)), \\ \phi(t) &= \psi + \varphi(t), \end{aligned} \quad (1.45)$$

where $R(t)$ is now the time dependent radius of the dynamical skyrmion texture, $(\theta(t), \phi(t))$, and $\mathbf{r} = r \mathbf{e}_r + \psi \mathbf{e}_\psi$ the position vector in polar coordinates, and $\varphi(t)$ the relative angle measured with respect to the radial direction. Inserting this into

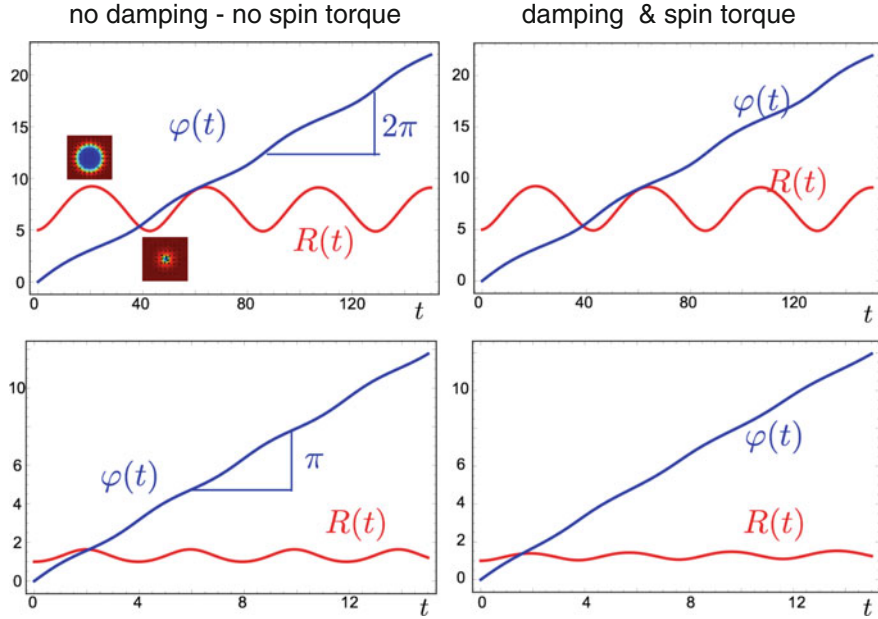


Fig. 1.15 Analytical description of a dynamical skyrmion and dissipationless character of a magnetic medium under a nanocontact. Time dependent radius $R(t)$ and azimuthal angle $\varphi(t)$ with either no damping and no spin torque (left), or damping and spin torque (right) are shown, with time in units of $M_0/2\gamma K_e$. The striking similarity illustrates the dissipationless character of the environment underneath a nanocontact. Top row: Oscillations in the presence of DMI. Bottom row: Dipolar interactions only

the equation of motion (1.44), assuming $R \gg \delta$, and after integration we obtain the following effective equation of motion [70],

$$\begin{aligned}\dot{R} &= F(\varphi, R) - \alpha\dot{\varphi} + \sigma(I)\tilde{\Theta}(a_c - R), \\ \dot{\varphi} &= (1/R) + \alpha\dot{R},\end{aligned}\quad (1.46)$$

where $\tilde{\Theta}$ denotes a smoothed-out step-function. All energy terms that violate conservation of m_z , i.e., the component perpendicular to the film plane, namely DMI, dipolar interaction distinguishing between Néel and Bloch walls, and the Oersted field contribute to

$$F(\varphi, R) = -\mathcal{D} \sin \varphi + \lambda \mathcal{D}^{-1} / 2 + (\pi h_{\text{Oe}}/R) \cos \varphi, \quad (1.47)$$

with the dimensionless parameters given by $\mathcal{D} = \pi D/4\sqrt{AK_e}$, $\mathcal{D}^{-1} = \mu_0 M_0^2/2K_e$, $h_{\text{Oe}} = (\mu_0 M_0/K_e)(I_{\text{tot}}/8\pi\delta_0)$ and $\lambda < 1$ a numerical parameter depending on film thickness and λ to 1 for $t/\delta_0 \gg 1$.

From (1.46) we may infer that a dynamical skyrmion can even exist in the undamped and undriven case in the absence of DMI when $F = 0$. We then have $R = \text{const.}$ and $\omega R = 1$ with $\omega = \dot{\phi}$ and thus the dynamical skyrmion shows uniform precession with frequency inversely proportional to constant R . If we include damping, spin torque and nonvanishing F , the results of integrating (1.46) are shown in Fig. 1.15. In the top row the results for only \mathcal{D} contributing to F is shown, while the bottom row shows F determined by the dipolar term prop to \mathcal{D}^{-1} . The results clearly illustrate that the radial oscillation or ‘breathing’ of the dynamical skyrmion results from the contributions to the function F . In both cases it is clear that the spin torque compensates the effect of damping such as to reproduce the dissipationless and undriven solutions with $\alpha = \sigma(I) = 0$.

Thus the existence of dynamical skyrmions provides striking evidence that it is the topological feature of spin textures and not energetic details that endow these textures with extraordinary stability that renders them useful for applications. In particular, the stability and the current tuneability of the dynamical skyrmion spin torque oscillators makes them suitable candidates for microwave applications [70].

1.5 Conclusions

In this introductory chapter we presented an overview of topological textures in magnetism that will be discussed in more detail later in this book. This will include Chap. 2 on domain walls and Bloch lines by Thiaville and Miltat, Chap. 3 on vortices (merons) by Behncke, Adolff and Meier, Chap. 5 on skyrmions in bulk magnets by Bauer et al., Chap. 4 on skyrmions in thin films and multilayers by Chen, and Chap. 11 on dynamical skyrmions generated by spin torque oscillator by Åkerman. Such textures have attracted much recent interest as their stability with respect to deformations renders them attractive candidates for prospective memory applications. Moreover, electrons moving in the background field of such textures experience exotic emergent electromagnetic fields. Here we emphasized a topological perspective, with the winding number as the essential parameter to characterize topologically nontrivial textures in the magnetization field. There are two main classes of such textures: On the one hand we considered topological point defects such as Ising domain walls in chains, planar vortices with easy-plane spins, and hedgehogs (Bloch points, or monopoles). On the other hand there are smooth topological textures such as chiral domain walls, 2π domain walls, merons, and most prominently, skyrmions. The latter are robust against continuous deformations, but may be destroyed or created either in time or in space via topological point defects such as Bloch points. Without doubt, skyrmions are the topological textures that have attracted most attention during the past few years. This includes the groundbreaking work which involved early theory [8], neutron scattering experiments in MnSi, a B20 bulk magnet [5], and thin films with interface DMI [71], and engineered DMI in multilayers stabilizing skyrmions at room temperature [13]. Due to their large mobility, skyrmions also have been proposed [21] and demonstrated [22] as alternatives to domain walls in racetrack memory devices [14]. Skyrmions can control the magnon excitations

[72, 73], thus paving the way for intrinsically magnetic dynamic magnonics [74] as alternative to magnonics controlled by static structural [75] or externally dynamic potentials [76]. The contributions in this volume are testament to the rapid progress of this field during the past few years, and the journey to harness topological defects for information storage and processing purposes has just begun.

Acknowledgements I gratefully acknowledge numerous helpful discussions with J. Åkerman, P. Böni, R.V. Hügli, B. Roessli, and Y. Zhou. This research has been supported by Science Foundation Ireland under 11/PI/1048.

References

1. F. Bloch, *Zeit. f. Phys.* **61**, 206–219 (1930)
2. D. Landau, E. Lifshitz, *Phys. Zeit. Sowj.* **61**, 153–169 (1935)
3. T.H.R. Skyrme, *Proc. R. Soc. Lond. Ser. A* **260**, 127–138 (1961)
4. T.H.R. Skyrme, *Nucl. Phys.* **31**, 556–569 (1962)
5. S. Mühlbauer, B. Binz, F. Jonietz, C. Pfleiderer, A. Rosch, A. Neubauer, R. Georgii, P. Böni, *Science* **323**, 915–919 (2009)
6. U.K. Rössler, A.N. Bogdanov, C. Pfleiderer, *Nature* **442**, 797–801 (2006)
7. B. Roessli, P. Böni, W.E. Fischer, Y. Endoh, *Phys. Rev. Lett.* **88**, 237204 (2002)
8. A.N. Bogdanov, D.A. Yablonsky, *Sov. Phys. JETP* **55**, 178–182 (1989)
9. W. Jiang, P. Upadhyaya, W. Zhang, G. Yu, M. Jungfleisch, F. Fradin, J. Pearson, Y. Tserkovnyak, K. Wang, O. Heinonen, S. te Velthuis, A. Hoffmann, *Science* **349**, 283–286 (2015)
10. N. Nagaosa, Y. Tokura, *Nat. Nanotechnol.* **8**, 899–911 (2013)
11. H.B. Braun, *Adv. Phys.* **61**, 1–116 (2012)
12. S.-H. Yang, K.-S. Ryu, S. Parkin, *Nat. Nanotechnol.* **10**, 221–226 (2015)
13. C. Moreau-Luchaire, C. Moutafis, N. Reyren, J. Sampaio, C.A.F. Vaz, N. Van Horne, K. Bouzehouane, K. Garcia, C. Deranlot, P. Wernicke, P. Wohlhuter, J.M. George, M. Weigand, J. Raabe, V. Cros, A. Fert, *Nat. Nanotechnol.* **11**, 444–449 (2016)
14. S.S.P. Parkin, M. Hayashi, L. Thomas, *Science* **320**, 190–194 (2008)
15. H.B. Braun, *Phys. Rev. Lett.* **71**, 3557–3560 (1993)
16. A. Aharoni, *J. Appl. Phys.* **80**, 3133–3134 (1996)
17. H.J. Richter, *J. Phys. D* **40**, R149–R177 (2007)
18. A. Malozemoff, J. Slonczewski, *Magnetic Domain Walls in Bubble Materials. Advances in Materials and Device Research* (Academic Press Inc, 1979)
19. H.B. Braun, *Phys. Rev. B* **50**, 16485 (1994)
20. N. Romming, A. Kubetzka, C. Hanneken, K. von Bergmann, R. Wiesendanger, *Phys. Rev. Lett.* **114**, 177203 (2015)
21. J. Sampaio, V. Cros, S. Rohart, A. Thiaville, A. Fert, *Nat. Nanotechnol.* **8**, 839–844 (2013)
22. S. Woo, K. Litzius, B. Krueger, M.-Y. Im, L. Caretta, K. Richter, M. Mann, A. Krone, R.M. Reeve, M. Weigand, P. Agrawal, I. Lemesh, M.-A. Mawass, P. Fischer, M. Kläui, G.R.S.D. Beach, *Nat. Mat.* **15**, 501–506 (2016)
23. W.F. Brown, *Micromagnetics* (Interscience, 1963)
24. M. Nakahara, *Geometry, Topology and Physics*. Graduate Student Series in Physics (Hilger, Bristol, 1990)
25. N. Mermin, *Rev. Mod. Phys.* **51**, 591–648 (1979)
26. T. Eggebrecht, M. Möller, J.G. Gatzmann, N. Rubiano da Silva, A. Feist, U. Martens, H. Ulrichs, M. Münenberg, C. Ropers, S. Schäfer, *Phys. Rev. Lett.* **118**, 097203 (2017)
27. A. Wachowiak, J. Wiebe, M. Bode, O. Pietzsch, M. Morgenstern, R. Wiesendanger, *Science* **298**, 577–580 (2002)

28. T. Kamionka, M. Martens, K.W. Chou, M. Curcic, A. Drews, G. Schütz, T. Tyliaszczak, H. Stoll, B. Van Waeyenberge, G. Meier, Phys. Rev. Lett. **105**, 137204 (2010)
29. G. Chen, A.T. N'Diaye, S.P. Kang, H.Y. Kwon, C. Won, Y. Wu, Z.Q. Qiu, A.K. Schmid, Nat. Commun. **6**, 6598 (2015)
30. G. Toulouse, M. Kleman, J. De Phys. Lett. **37**, L149–L151 (1976)
31. V.P. Mineev, Topologically stable defects and solitons in ordered media, in *Classic Reviews in Physics*, vol. 1 (Harwood Academic Publishers, 1998)
32. J. Rubinstein, J. Math. Phys. **11**, 258–267 (1970)
33. D. Finkelstein, C. Misner, Ann. Phys. **6**, 230–243 (1959)
34. U. Enz, Helv. Phys. Acta **37**, 245–253 (1964)
35. R. Rajaraman, *Solitons and Instantons an Introduction to Solitons and Instantons in Quantum Field Theory* (North-Holland, Amsterdam a.o., 1982)
36. H.B. Braun, J. Kulda, B. Roessli, D. Visser, K.W. Krämer, H.U. Güdel, P. Böni, Nat. Phys. **1**, 159–163 (2005)
37. M. Bode, M. Heide, K. von Bergmann, P. Ferriani, S. Heinze, G. Bihlmayer, A. Kubetzka, O. Pietzsch, S. Blügel, R. Wiesendanger, Nature **447**, 190–193 (2007)
38. N. Grisewood, J. Eves, T. Usher, H.B. Braun, J. Appl. Phys. **111**, 07c706 (2012)
39. X.Z. Yu, Y. Onose, N. Kanazawa, J.H. Park, J.H. Han, Y. Matsui, N. Nagaosa, Y. Tokura, Nature **465**, 901–904 (2010)
40. O. Boulle, J. Vogel, H.X. Yang, S. Pizzini, D.D. Chaves, A. Locatelli, T.O. Mentes, A. Sala, L.D. Buda-Prejbeanu, O. Klein, M. Belmeguenai, Y. Roussigne, A. Stashkevich, S.M. Cherif, L. Aballe, M. Foerster, M. Chshiev, S. Auffret, I.M. Miron, G. Gaudin, Nat. Nanotechnol. **11**, 449–455 (2016)
41. A.A. Belavin, A.M. Polyakov, JETP Lett. **22**, 245 (1975)
42. O. Chubykalo-Fesenko, U. Nowak, R.W. Chantrell, D. Garanin, Phys. Rev. B **74**, 094436 (2006)
43. A. Thiaville, Y. Nakatani, J. Miltat, Y. Suzuki, Europhys. Lett. **69**, 990 (2005)
44. M.E. Schabes, H.N. Bertram, J. Appl. Phys. **64**, 1347–1357 (1988)
45. R.P. Cowburn, A.O. Adeyeye, M.E. Welland, Phys. Rev. Lett. **81**, 5414–5417 (1998)
46. C. Stamm, F. Marty, A. Vaterlaus, V. Weich, S. Egger, U. Maier, U. Ramsperger, H. Fuhrmann, D. Pescia, Science **282**, 449–451 (1998)
47. M. Hehn, K. Ounadjela, J.P. Bucher, F. Rousseaux, D. Decanini, B. Bartenlian, C. Chappert, Science **272**, 1782–1785 (1996)
48. U. Ebels, A. Radulescu, Y. Henry, L. Piraux, K. Ounadjela, Phys. Rev. Lett. **84**, 983–986 (2000)
49. E.Y. Vedmedenko, A. Kubetzka, K. von Bergmann, O. Pietzsch, M. Bode, J. Kirschner, H.P. Oepen, R. Wiesendanger, Phys. Rev. Lett. **92**, 077207 (2004)
50. G. Woltersdorf, C.H. Back, Phys. Rev. Lett. **99**, 227207 (2007)
51. S. Parkin, U.S. Patents 6834005, 6898132, 6920062, 7031178
52. M. Hayashi, L. Thomas, R. Moriya, C. Rettner, S.S.P. Parkin, Science **320**, 209–211 (2008)
53. L. Thomas, M. Hayashi, X. Jiang, R. Moriya, C. Rettner, S.S.P. Parkin, Nature **443**, 197–200 (2006)
54. J.L. Eves, N. Grisewood, R.V. Hügli, H.B. Braun, J. Magn. Magn. Mater. **322**, 1381–1384 (2010)
55. H.B. Braun, O. Brodbeck, Phys. Rev. Lett. **70**, 3335–3338 (1993)
56. H.B. Braun, J. Appl. Phys. **85**, 6172–6174 (1999)
57. G.D. Chaves-O'Flynn, A.D. Kent, D.L. Stein, Phys. Rev. B **79**, 184421 (2009)
58. R. Kohn, V. Slastikov, Arch. Ration. Mech. Anal. **178** (2005)
59. H.B. Braun, J. Appl. Phys. **76**, 6310–6315 (1994)
60. A. Kubetzka, O. Pietzsch, M. Bode, R. Wiesendanger, Phys. Rev. B **67**, 020401 (2003)
61. H.B. Braun, D. Loss, Europhys. Lett. **31**, 555 (1995)
62. H.B. Braun, D. Loss, Phys. Rev. B **53**, 3237–3255 (1996)
63. Y. Yoshimura, K.-J. Kim, T. Taniguchi, T. Tono, K. Ueda, R. Hiramatsu, T. Moriyama, K. Yamada, Y. Nakatani, T. Ono, Nat. Phys. **12**, 157–161 (2016)
64. E.R. Lewis, D. Petit, A.V. Jausovec, L. O'Brien, D.E. Read, H.T. Zeng, R.P. Cowburn, Phys. Rev. Lett. **102**, 057209 (2009)

65. A. Cavallin, F.D. Natterer, S. Ouazi, G. Moulas, A. Lehnert, S. Rusponi, H. Brune, Phys. Rev. B **90**, 144427 (2014)
66. P. Milde, D. Koehler, J. Seidel, L.M. Eng, A. Bauer, A. Chacon, J. Kindervater, S. Mühlbauer, C. Pfleiderer, S. Buhrandt, C. Schuette, A. Rosch, Science **340**, 1076–1080 (2013)
67. S.M. Mohseni, S.R. Sani, J. Persson, T.N.A. Nguyen, S. Chung, Y. Pogoryelov, P.K. Muduli, E. Iacocca, A. Eklund, R.K. Dumas, S. Bonetti, A. Deac, M.A. Hoefer, J. Åkerman, Science **339**, 1295–1298 (2013)
68. M. Nagao, Y.-G. So, H. Yoshida, M. Isobe, T. Hara, K. Ishizuka, K. Kimoto, Nat. Nanotechnol. **8**, 325–328 (2013)
69. X.Z. Yu, K. Shibata, W. Koshibae, Y. Tokunaga, Y. Kaneko, T. Nagai, K. Kimoto, Y. Taguchi, N. Nagaosa, Y. Tokura, Phys. Rev. B **93**, 134417 (2016)
70. Y. Zhou, E. Iacocca, A.A. Awad, R.K. Dumas, F.C. Zhang, H.B. Braun, J. Åkerman, Nat. Commun. **6**, 8193 (2015)
71. N. Romming, C. Hanneken, M. Menzel, J.E. Bickel, B. Wolter, K. von Bergmann, A. Kubetzka, R. Wiesendanger, Science **341**, 636–639 (2013)
72. T. Schwarze, J. Waizner, M. Garst, A. Bauer, I. Stasinopoulos, H. Berger, C. Pfleiderer, D. Gründler, Nat. Mat. **14**, 478–483 (2015)
73. S.A. Montoya, S. Couture, J.J. Chess, J.C.T. Lee, N. Kent, M.-Y. Im, S.D. Kevan, P. Fischer, B.J. McMorran, S. Roy, V. Lomakin, E.E. Fullerton, Phys. Rev. B **95**, 224405 (2017)
74. F. Ma, Y. Zhou, H.B. Braun, W.S. Lew, Nano Lett. **15**, 4029–4036 (2015)
75. Z.K. Wang, V.L. Zhang, H.S. Lim, S.C. Ng, M.H. Kuok, S. Jain, A.O. Adeyeye, Appl. Phys. Lett. **94**, 083112 (2009)
76. A.D. Karenowska, J.F. Gregg, V.S. Tiberkevich, A.N. Slavin, A.V. Chumak, A.A. Serga, B. Hillebrands, Phys. Rev. Lett. **108**, 015505 (2012)

Chapter 2

Topology and Magnetic Domain Walls



André Thiaville and Jacques Miltat

Abstract This chapter presents the various connections between topology and magnetic domain walls. To begin with, we expose what topology tells us about magnetic domain walls, answering questions like: may domain walls be topological defects?, are there topologically different classes of domain walls? We then turn to dynamics, explaining the profound link between topology and the dynamics of magnetic textures, domain walls here. Experimental aspects are reviewed in the next sections, constructed according to material and sample types, with a special role played by bubble garnet films where a number of fundamental concepts were introduced. The authors try to provide a unified view of the vast literature on the subject, that spreads over four decades and different research thematics.

2.1 Introduction: Topology Applied to Magnetic Domain Walls

The topological theory of defects is a well-established field in condensed matter physics (see the introduction Chap. 1, by H.B. Braun). The basic inputs for this theory are the dimensionality and topology of both the order parameter space V and the physical space. For ferro-magnetism, well below the Curie temperature, the magnitude of the local magnetization may be assumed to be constant (vs. space and time). Hence $V = S^{n-1}$, the sphere with $n - 1$ degrees of freedom, n being the number of components of the magnetic moment vector (Table 2.1). The case $n = 1$ corresponds to the Ising model, and S^0 consists only of 2 points ('up' and 'down'); $n = 2$ corresponds to the XY-model, S^1 being the unit circle in that plane; finally $n = 3$ pertains to the Heisenberg model with 3-component spins, S^2 being

A. Thiaville (✉) · J. Miltat

Laboratoire de Physique des Solides, Université Paris-Sud,
CNRS UMR 8502, Bâtiment 510, Centre universitaire, 91405 Orsay, France
e-mail: andre.thiaville@u-psud.fr

J. Miltat
e-mail: jacques.miltat@u-psud.fr

Table 2.1 Symbols used in the topological theory of defects

Symbol	Meaning	Values
d	Physical space dimension	1, 2, 3
n	Number of magnetization components	1 (Ising), 2 (XY), 3 (Heisenberg)
d'	Defect dimensionality	0, 1, 2 ($d' < d$)
r	Contour dimensionality	0, 1, 2 ($r < d$)

the unit sphere in that space. The cases $n = 1, 2$ have to be taken as limiting cases: a perfect Ising or XY magnet is not known in nature, so that we should consider only the $n = 3$ case. However, when the magnetic anisotropy is very large (easy-axis or easy-plane), be it crystalline anisotropy or just a demagnetizing effect, then it makes sense to consider the lower n cases. By the process known as ‘escape in the higher dimensions’, the topological defects that may appear for $n < 3$ can be regularized, meaning that the order parameter is no longer singular at the defect core. What remains after this process is the topological stability of the regularized texture. This is the second aspect of the topological analysis of magnetic textures. We explain below how both aspects apply to magnetic domain walls.

With respect to the physical space, we restrict ourselves in this chapter to the topologically trivial euclidian spaces, of dimension d (Table 2.1).¹ This means that the samples are either the full \mathbb{R}^d , or parts of it when the sample is finite for some of its d dimensions. Again, we live in and cannot escape from the $d = 3$ space, but nevertheless can fabricate samples that are close, down to the atomic size for the finite dimension, to $d = 2$ (an atomic monolayer), $d = 1$ (an atomic chain), and $d = 0$ (an atom). In fact, one does not need to go down to the single atom size to reduce d by one unit, as the magnetic textures cannot vary over the characteristic lengths of micromagnetics, that are the domain wall width parameter Δ and the exchange length Λ [2], the latter of the order of a few nanometers for ferromagnets. Thus, all values of the physical space dimension d are experimentally relevant, and will be considered.

2.1.1 Domain Walls as Topological Defects

Topology is based on the assumption of continuity. The micromagnetic theory [2, 3] describes a magnetization orientation that, without leaving the order parameter space V , changes continuously with position in the physical space. It is therefore possible to apply topology to the description of magnetic textures. Within this mathematical picture, a defect is a part of the physical space across which the magnetization changes discontinuously. It is customary to call d' the dimension of the defect: $d' = 0$ is a point defect, $d' = 1$ is a line defect, and quite generally $d' = d - 1$ is a

¹ An example of a topologically non-trivial space is the Möbius strip [1].

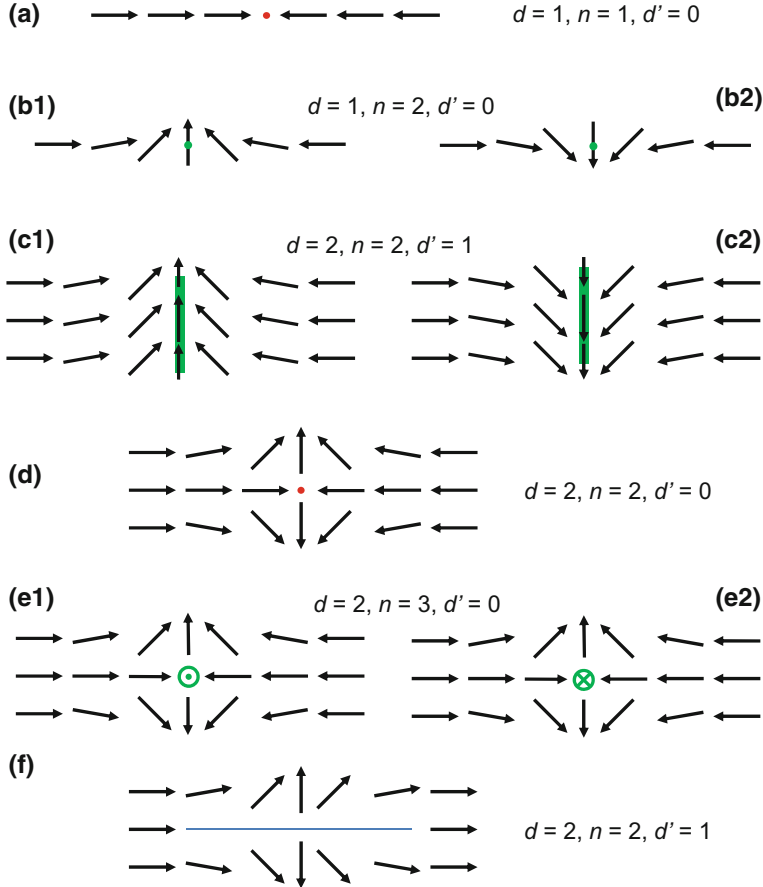


Fig. 2.1 Emblematic cases of topological defects and of their escape in the higher dimensions: in $d = 1$ space dimension, the topological defect for $n = 1$ (a) becomes regular by considering $n = 2$, in two topologically different walls (b1), (b2). In $d = 2$, the 2D analogue (c1) of (b1) can be converted to the analogue (c2) of (b2), by a punctual $n = 2$ topological defect (d). The topological defect (d) for $n = 2$ can be regularized in $n = 3$ into an antivortex with up (e1) or down-oriented (e2) core. Topological defects are drawn in red in this chapter, whereas a green symbol indicates a regular, but topologically stable texture. For pedagogy, a non-topological linear defect for $d = 2$ and $n = 2$, reminiscent of a domain wall in a soft magnetic microstructure, is shown in (f): it can be removed by continuous rotation of the magnetization

wall defect (Table 2.1). A defect is said to be topological when it cannot be removed by any continuous variation of the order parameter (see Fig. 2.1f for an example of a non-topological defect). By continuous variations are meant those variations that do not need to be the same for every position in physical space, but change continuously as a function of position (and respect the boundary conditions if they apply). Figure 2.1 illustrates several typical cases of topological defects, and Table 2.1 recalls the meaning of the various symbols used in this theory.

To test for the presence of a defect, one draws around it a contour, a generalization of the Burgers circuit of dislocation theory [4–6]. Let r be the dimensionality of this contour (Table 2.1). One then gets the obvious relation [4–6] $d = d' + r + 1$: in $d = 3$ dimensions, to test for a line defect ($d' = 1$) one draws a loop ($r = 1$) around it; to test for a domain wall in any space dimension d , one considers two points ($r = 0$). As explained in the introduction Chap. 1, by H. B. Braun, the topological classification of the defects of dimensionality d' in a d -dimensional space is given by the r -th homotopy group of the order parameter space V , denoted by $\Pi_r(V)$. Indeed, this group is the set of equivalence classes of r -dimensional contours drawn on V . Algebraic topology is the mathematical framework to ‘compute’ these homotopy groups. The unity element of this group describes the so-called topologically trivial textures, i.e. those that do not contain a topological defect. For the case of n -component spins ($V = S^{n-1}$), the relevant results of algebraic topology are expressed by $\Pi_p(S^p) = \mathbb{Z}$, $\Pi_{p' < p}(S^p) = 0$, with the special case $\Pi_0(S^0) = \mathbb{Z}_2$, where \mathbb{Z} is the set of signed integers, and $\mathbb{Z}_2 \equiv \mathbb{Z}/2 = \{0, 1\}$.² As the order parameter space of magnetism is simple, both in structure and number of dimensions, these results are intuitive: a loop is required to span a circle, and a ball for the sphere. From the previous expressions of r and n we obtain that, in magnetism, topological defects exist only for $d = d' + n$ [4].

For domain walls, we have per definition $d' = d - 1$, and thus obtain that walls are topological defects only for $n = 1$, i.e. Ising spins. This result is obvious: for Ising spins no moment can be assigned to a domain wall, but for a larger number of components this is possible (cf. e.g. Fig. 2.1(b) compared to Fig. 2.1(a)). On the other hand, if we stick to the physically reasonable case $n = 3$, we see from the above relation that topological defects can only be obtained at $d = 3$, in the form of singular points ($d' = 0$). This defect is the so-called Bloch point [8, 9], the only topological defect in $n = 3$ magnetism [5]. Note that, even if domain walls are not topological defects for $n = 3$, some domain wall structures inherently contain a Bloch point (see Sect. 2.4.4). Finally, if we also consider the limiting case of the XY-model ($n = 2$), then we have topological defects for $d' = d - 2$: coreless vortex lines for $d = 3$, and coreless vortices for $d = 2$ (e.g. Fig. 2.1(d)), the latter being discussed in more detail in Chap. 3 on vortices, by C. Behnke, Ch.F. Adolf and G. Meier. We shall see in the experimental sections below that these sub-structures do play a role in the statics and dynamics of magnetic domain walls.

2.1.2 Domain Walls as Topologically Stable Textures

Topology is not limited to defects, as this whole book shows, and we can apply topological arguments to other objects or subjects. Here we discuss the topological stability of continuous textures, more generally the possibility or not to transform continuously one texture into another. A texture will be termed topologically stable

²Other values of p and p' are given in mathematical textbooks, e.g. [7] Sect. 2.4.1.

if it cannot be continuously erased, i.e. transformed into the ground state texture that is taken as zero (it is the uniform state in many cases, but not always, consider a ring for example) [8, 10]. Such a texture is also called a topological soliton [11]: it can deform under continuous magnetization variations, but its topological character (equivalence class in the relevant homotopy group) does not change, by definition. Thus, a topological soliton is a soliton regarding topology, in comparison with solitons in fluid dynamics where the shape is preserved even if the soliton moves.

In the previous section, we showed mathematically that domain walls are topological defects only for Ising spins. Does it mean that for $n > 1$ domain walls are not stable? The answer is obviously no, and this can also be proved by topology. The important point now is to consider boundary conditions.³ If we fix magnetization at plus and minus infinity along some direction (call it x) to take different values (as we could do by a field gradient for example) that are denoted \mathbf{m}_- and \mathbf{m}_+ , we physically force a domain wall to exist. If we take any path in physical space from $x = -\infty$ to $x = +\infty$ and plot its image on the order parameter space V , it will have to start from \mathbf{m}_- and end at \mathbf{m}_+ (Fig. 2.2(a)). Such a pinned path cannot be contracted to a point. Thus, a domain wall has to exist when the magnetization is fixed to different values at infinity: a domain wall is topologically stable under such conditions. Note that this says nothing about e.g. the domain wall width, or center position, as such parameters can be modified by continuous variations of the magnetization texture.

Beyond this obvious remark, we now go one step further and ask the question: are all domain walls topologically equivalent? For $d = 1$ this means: keeping its endpoints mapped onto the order parameter space fixed at \mathbf{m}_- and \mathbf{m}_+ , can we continuously deform a path (call it p_1) into any other one (call it p_2)? By tracing first path p_1 from $x = -\infty$ to $+\infty$ and then back to $x = -\infty$ along p_2 , one draws a closed loop on the order parameter space. Thus we are again lead to consider the first homotopy group $\Pi_1(V)$. If this group is trivial, the closed loop can be continuously contracted to a point, so that p_1 can be continuously transformed to p_2 . Therefore all domain walls are topologically equivalent in this case. As stated above, the first homotopy group is not trivial for $n = 2$ only (Fig. 2.2(b-d)). We thus obtain that for XY spins in $d = 1$ there is an infinite (countable) number of topologically different domain walls (see Fig. 2.2(b-d) for three examples). Note that the argument is not limited to $d = 1$, as the drawings in Fig. 2.2 may let think: for $d = 2, 3$ there are an infinite number of physical space paths that go from $x = -\infty$ to $x = +\infty$, but in the absence of topological defect as assumed in this section they all have to go through the same side of S^1 .⁴

The transformation between two topologically inequivalent textures, which by definition cannot occur continuously, occurs discontinuously hence involves a topological defect. This link between these two aspects of topology applied to magnetic

³The mathematical objects adapted to this case are called relative homotopy groups. See e.g. [7] for a reference textbook. As the spaces that are considered are easily visualized, we can avoid the mathematical machinery here.

⁴If two paths existed that use the two sides of S^1 , they would form a loop that encloses S^1 once, so that a topological defect of $n = 2$ would exist, a vortex point in $d = 2$ or a vortex line in $d = 3$.

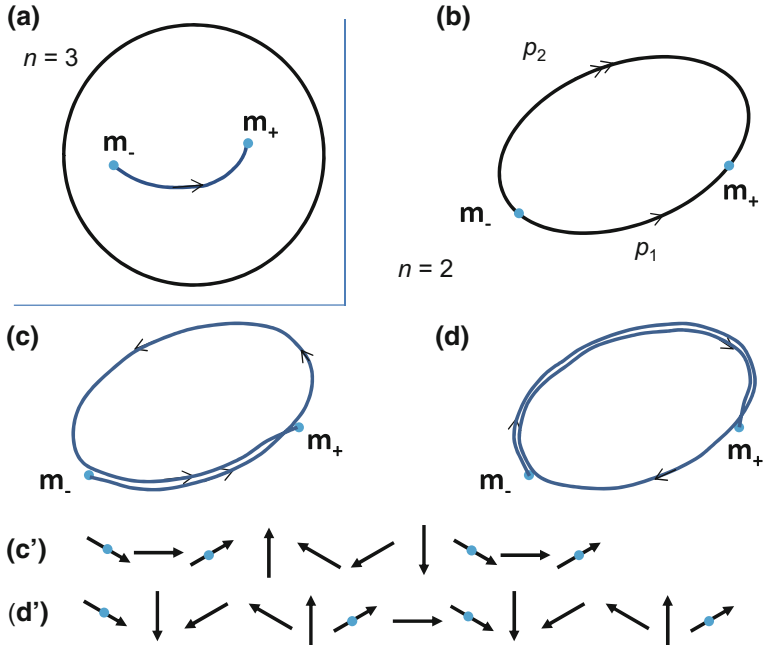


Fig. 2.2 Topological stability of domain walls is guaranteed when the magnetization is fixed to different values \mathbf{m}_- and \mathbf{m}_+ at infinity, as shown by the following plots that are drawn in order parameter space $V = S^{n-1}$. (a) For $n = 3$ all domain walls are topologically equivalent. (b) For $n = 2$ they are not, as path p_1 cannot be continuously transformed to path p_2 . Real-space pictures of paths p_1 and p_2 are shown in Fig. 2.1(b1, b2). Two other topologically different paths are shown in (c, d) for $n = 2$, that can be denoted $p_1 * (p_2)^{-1} * p_1$ and $p_2 * (p_1)^{-1} * p_2$, respectively (in these last two figures, for clarity, the path was drawn outside of $V = S^1$ and the drawing of V was removed). Corresponding real-space structures are shown in (c') and (d'); they can be seen as three domain walls of the same rotation sense (also called winding domain walls)

textures is generic [6, 12], as could be guessed by the fact that the same homotopy group is invoked to describe the classes of equivalent topological solitons and of topological defects. Thus, to jump (in space or in time) from one topological soliton to an inequivalent one (trivial or not), a topological defect equivalent to the difference of classes is required. Indeed, instead of discontinuously flipping all moments within the wall from one type to the other, it is energetically less costly to start this flipping at one edge of the sample, thus injecting a topological defect, which then by crossing the sample performs the domain wall switching (if the sample is infinite, a pair of opposite topological defects has to be injected, and they travel in opposite directions to perform the flipping). As an example, the intermediate state between Fig. 2.1(c1) and Fig. 2.1(c2) is drawn in Fig. 2.1(d): it is a topological defect (for $n = 2$) called antivortex.

Figure 2.1 starts with a topological defect (a), goes to topologically stable regular textures (b1, b2) by ‘escape in the second dimension’ ($n: 1 \rightarrow 2$) and finally arrives

at the topological defect involved in the switching between these topologically stable textures (d), as captured in its motion through an additional space dimension ($d: 1 \rightarrow 2$). It is instructive to perform this cycle once again, from Fig. 2.1(d). This antivortex wall, upon increasing n to 3 ('escape in the third dimension') becomes a regular texture. The obtained antivortex core can point out of or in the plane of the drawing (Fig. 2.1(e1, e2)). Are these two antivortex walls topologically different? As the map on $V = S^2$ shows, this is not the case: just rotate all the points by 180° around the domains magnetization axis. More generally, to get the topological stability of a (anti)vortex wall, or simply of a (anti) vortex in $d = 2$ and $n = 3$, we need additional boundary conditions. These are detailed in Sect. 2.4 for the vortex wall, and in Sect. 2.1.3 for wall substructures called lines.

2.1.3 *Lines as Topologically Stable Textures*

Up to now we have neither described nor explored the zoology of magnetic domain walls. We need to do so to some extent, now. In the simple case of a uniaxial material with no torque applied to the domains, a domain wall corresponds to a 180° rotation of the magnetic moments. At the center of the domain wall, the magnetic moment by definition resides in the plane normal to the easy axis. This leaves a large freedom for the magnetic structure of the domain walls, and the reader is referred to textbooks for an in-depth description of the various domain wall structures [2]. Historically, the first known domain wall structure is the Bloch wall, where the volumic magnetic charge density $-M_s \operatorname{div} \mathbf{m}$ is zero so as to avoid a magnetostatic energy cost (in an infinite medium). For thin films of soft materials (with a small in-plane anisotropy so as to define an easy axis), it was later shown by Néel that, as Bloch walls bear surface magnetic charges, a magnetization rotation in the other direction is favored, leading to a globally zero but locally non-zero volumic magnetic charge (see textbooks for drawings).

Bloch walls of alternating rotation sense were first observed in rings made of NiFeCo (perminvar, a soft magnetic material) [13], and the lines separating them shortly after called Bloch lines [14]. In parallel to this study of bulk samples (typical thickness $100 \mu\text{m}$), observations on deeply sub-micrometric permalloy films [15] revealed complex walls with a two-dimensional structure called cross-ties, interpreted as alternating Néel walls separated by 'circular' and 'cross' lines, also sometimes called Bloch lines and cross-ties, respectively.⁵

The study of lines developed markedly in the 70s, as part of the research on magnetic 'bubbles'. Bubble garnets are single crystalline plates or epitaxial films (defect density as low as 1 cm^{-2}) having a small magnetization (garnets are ferrimagnets)

⁵Whereas for domain walls a rich taxonomy has developed, with Bloch, Néel, asymmetric Bloch, asymmetric Néel, cross-tie walls, followed recently by transverse, vortex, asymmetric transverse, Bloch point walls etc., such is not the case of lines, that are nearly always called Bloch lines. Feldtkeller [8] proposed a denomination logics for lines, based on which type of wall they display in their core, but this has not been adopted by the whole community.

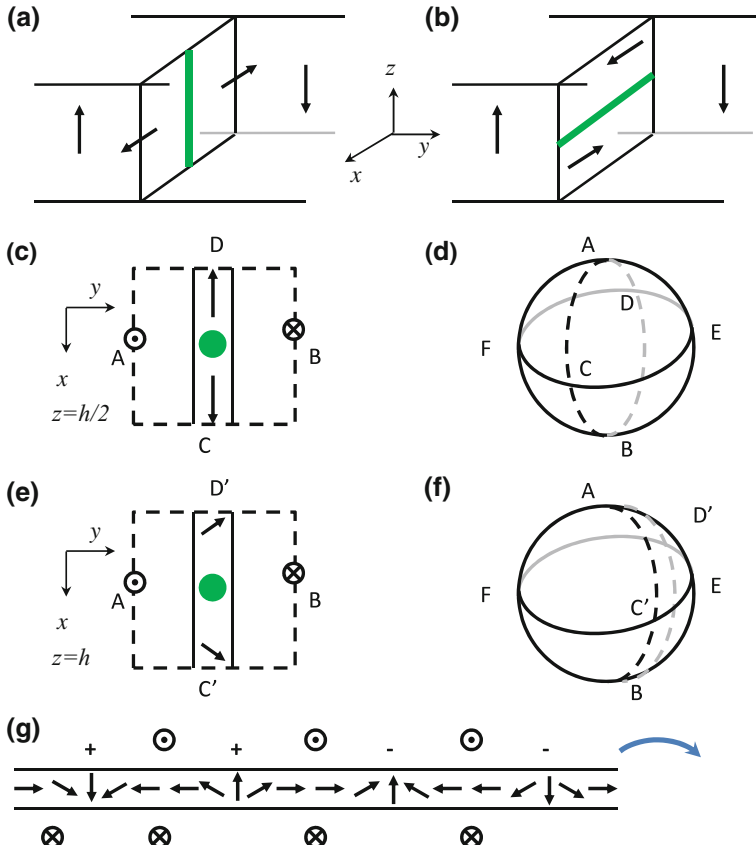


Fig. 2.3 The two types of lines in a film with perpendicular easy axis, vertical Bloch line (a) and horizontal Bloch line (b). For the VBL, the spins in the z plane at mid-thickness $z = h/2$ are shown in (c), the dashed contour indicating the spins fixed far away from the line. This contour is mapped in (d) on the unit sphere, showing that the simplest mappings must contain either point E or point F, corresponding to two topologically distinct VBL configurations with opposite topological numbers. Similar drawings are made in (e, f) for the plane $z = h$ at the top of the film, where the twisted structure of the Bloch walls due to the stray field from the domains is apparent. The conventional denomination of VBLs for bubbles is shown in (g), with the contour orientation drawn on the side by a blue curved arrow. VBLs with the same sign form winding pairs, with $\pm 2\pi$ magnetization rotation across the pair

with in case of films a perpendicular anisotropy due to the growth process, strong enough to stabilize a perpendicular magnetization [9]. Under a moderate field applied along the easy axis, called bias field, isolated reversed domains become stable. They are cylindrical with a circular base, and were hence called bubble domains or simply bubbles. The objective of this research was to develop solid-state ‘bubble memories’ that came to the market, in which a bit is represented by the presence or absence of a bubble.

The study of bubble dynamics revealed a large impact of the presence of lines within their walls. Two types of lines schematically exist, the horizontal Bloch lines (HBL) and the vertical Bloch lines (VBL), as shown in Fig. 2.3(a, b). Whereas VBLs are stable in the absence of fields, HBLs only appear in dynamics.

Similarly to domain walls, lines are topologically stable if the magnetization within the domain wall far away from the line is fixed, the magnetization in the domains far away from the wall being also fixed. As shown in Fig. 2.3, in such conditions lines are topologically stable, and exist in variants that are not continuously accessible from one to the other. For the VBL shown in Fig. 2.3(c, d), analyzed in the sample midplane, the simplest mappings cover an hemisphere once, and the topological or winding number (see the introduction chapter, by H. B. Braun, for its definition) is $+1/2$ if the mapping contains point E, whereas it is $-1/2$ if it contains point F.⁶ If the analysis plane is located at the film surface, the walls are no longer Bloch but partly or fully Néel, in response to the stray field from the adjacent domains [9], see Fig. 2.3(e, f). The two topological numbers then become $+1/2 - \tau$ resp. $-1/2 - \tau$ with $0 \leq \tau \leq 1/2$, and the same occurs at the bottom film surface with an opposite τ . The conventional denomination of VBL by the sign of the magnetization winding is shown in Fig. 2.3(g). The winding is computed with the convention that the down-magnetized region forms a closed domain so that, in the drawing, a clockwise motion means moving along the domain wall from left to right.

The stability of VBL pairs is a nice illustration of the topological approach. Assuming first that magnetization in the domains is fixed and that no changes occur within the sample thickness, a domain wall becomes a segment of \mathbb{R}^1 . If one moreover assumes that the domain wall magnetizations are the same, then \mathbb{R}^1 can be closed into the circle S^1 . On the other hand, the domain wall possible magnetizations, all orthogonal to the easy axis, also belong to S^1 . Thus, a wall segment with identical magnetizations at both ends corresponds to an element of $\Pi_1(S^1) = \mathbb{Z}$. The zero element is the uniform wall, or any domain wall structure that can be continuously transformed to that, like the segment containing the two central VBLs in Fig. 2.3(g), such a VBL pair being called unwinding. Non-zero elements are walls made of winding VBL pairs, like the two left or the two right VBLs in Fig. 2.3(g). Lifting the restriction to consider only the domain wall magnetization does not change the result, as one is lead to consider mappings of a 2D square to S^2 made of circuits that all start from point A and end at point B, the first and last circuits going through point C. This is described by the homotopy group $\Pi_2(S^2) = \mathbb{Z}$, so that the same result is obtained. Finally, if only continuous changes are considered when moving across the sample thickness, the restriction to $d = 2$ is allowed. Note that Fig. 2.3(e) versus Fig. 2.3(c), extended to the VBL pair case, shows the well-known but not so simple change across the thickness that takes place for a VBL pair in a sufficiently thick film.

⁶This can be figured out simply by remarking that, at the VBL core one has $\partial\mathbf{m}/\partial x$ along $+x$ and $\partial\mathbf{m}/\partial y$ along $-z$, so that $\partial\mathbf{m}/\partial x \times \partial\mathbf{m}/\partial y$ is along $+y$, parallel resp. antiparallel to the local magnetization for cases E resp. F.

2.2 Topology and the Theory of Magnetic Domain Walls Dynamics

We have surveyed the topological characterization of magnetic domain walls, with cases where domain walls are topological defects and cases where domain walls are topologically stable in different configurations. We now describe the role of topology in the dynamics of domain walls and their substructures. This opens the way to an experimental assessment of topology.

The basic equation for the dynamics of a magnetization texture is the Landau-Lifchitz-Gilbert (LLG) equation [2, 16, 17]. The local unit magnetization vector being $\mathbf{m}(\mathbf{r}, t)$, its time derivative obeys

$$\frac{\partial \mathbf{m}}{\partial t} = \gamma_0 \mathbf{H}_{\text{eff}} \times \mathbf{m} + \alpha \mathbf{m} \times \frac{\partial \mathbf{m}}{\partial t}, \quad (2.1)$$

where $\gamma_0 = \mu_0 g |\mu_B| / \hbar > 0$ is the gyromagnetic ratio with g the gyromagnetic factor ($g \approx 2$ for electron spins), α the adimensional Gilbert damping constant, and \mathbf{H}_{eff} is the effective field of micromagnetics. The dynamics implies two torques that are orthogonal. The first one describes the precession of magnetization around the effective field. The second leads to a progressive alignment of magnetization with the effective field (damping of the precessional motion). The effective field derives from the energy density \mathcal{E} of the system considered, according to the functional derivative⁷

$$\mathbf{H}_{\text{eff}} = -\frac{1}{\mu_0 M_s} \frac{\delta \mathcal{E}}{\delta \mathbf{m}}, \quad (2.2)$$

with M_s the spontaneous magnetization at the temperature considered. Beyond the basic LLG (2.1), where the effective field derives from an energy density so that the total energy is conserved for zero damping, other torque terms have been added on the right-hand side (r.h.s.), prominently the spin-transfer torque (STT) (for recent reviews see [18–21]) and its recent companion the spin-orbit torque (SOT) [22], so as to describe the direct interaction of magnetization with electrical currents. We take them into account by a torque \mathbf{T} added on the r.h.s. of (2.1). For example, STT for current within the magnetic film is described by [23] $\mathbf{T} = -(\mathbf{u} \cdot \nabla) \mathbf{m} + \beta \mathbf{m} \times (\mathbf{u} \cdot \nabla) \mathbf{m}$, where \mathbf{u} is a ‘spin-drift’ velocity parallel to the current density vector, and β is the so-called non-adiabaticity factor. This torque does indeed not derive from an energy density.

We now briefly recall the physics of domain wall dynamics. The basic model for the dynamics of magnetic domain walls is the one-dimensional analysis by Schryer and Walker [24] where two regimes were evidenced. At fields below the so-called

⁷The functional derivative differs from the partial derivative as soon as \mathcal{E} contains terms involving gradients of \mathbf{m} . In the energy differential, the terms involving the gradients of the variation of \mathbf{m} have to be integrated by parts to be transformed into terms involving only the variations of \mathbf{m} . This integration also produces surface terms, that contribute to the micromagnetic boundary conditions. See [2] for details.

Walker field, H_W , motion is stationary and the velocity V obeys the relation found long ago [16] that, in the most general form, reads $V = (\gamma_0 \Delta_T / \alpha) H$.⁸ In this expression, Δ_T is the wall width parameter as defined from Thiele's equation (see (2.9) below). At the Walker field, the velocity is maximum,⁹ this value being called maximum velocity or Walker velocity. Beyond this field, the domain wall structure is no longer stationary and the velocity generally drops. This phenomenon is known as Walker breakdown. The vast literature on domain wall dynamics since this seminal work has revealed, in realistic situations that are not one-dimensional, what form this breakdown exactly takes and at which field it occurs. The Walker breakdown marks the beginning of the precessional regime of domain wall motion. At fields much larger than the Walker field, magnetization precession in the wall results into a zero average drive of the domain wall, leading to the 'hard wall' velocity relation [25] $V = [\gamma_0 \Delta \alpha / (1 + \alpha^2)] H$ where Δ is an average domain wall width parameter. As usually $\alpha \ll 1$, velocity is significantly lower in the precessional regime in comparison to the stationary regime.

2.2.1 The Thiele Equation

The LLG equation, being integro-differential in space (because of the magnetostatic and exchange interactions, respectively) can be analytically solved in a very limited number of cases. Thus it is most often solved numerically, several open codes being available [26–28]. Nevertheless, under some assumptions, much simpler equations can be derived from it, a very useful one being the Thiele equation [29, 30]. It is rederived here in a generalized way.

The calculation starts, strangely enough but importantly so, by solving (2.1) in order to get the effective field. One obtains

$$\mathbf{H}_{\text{eff}} = \left[\mathbf{m} \times \frac{\partial \mathbf{m}}{\partial t} + \alpha \frac{\partial \mathbf{m}}{\partial t} - \mathbf{m} \times \mathbf{T} \right] / \gamma_0 + \lambda \mathbf{m} , \quad (2.3)$$

where λ is an arbitrary scalar function. Thiele's assumption consists in looking for magnetic configurations that are in rigid translation motion. Mathematically, this means that there exists a magnetization texture $\mathbf{m}_0(\mathbf{r})$ that depends only on space, and a position vector in physical space $\mathbf{R}(t)$ that depends only on time t , such that

$$\mathbf{m}(\mathbf{r}, t) = \mathbf{m}_0[\mathbf{r} - \mathbf{R}(t)] . \quad (2.4)$$

From this, the time derivative is immediately

⁸Note that, in general, velocity is not linear with field as the moving domain wall structure differs from the rest structure, so that the Thiele domain wall width is not a constant.

⁹This is not exactly so, though, when Δ_T varies much with field.

$$\frac{\partial \mathbf{m}}{\partial t} = - \sum_j V_j \frac{\partial \mathbf{m}_0}{\partial r_j}, \quad (2.5)$$

where we introduced the texture velocity $\mathbf{V} = d\mathbf{R}/dt$. The force on the rigid texture is, by the definitions of the force and of the effective field,

$$F_i = -\frac{dE}{dR_i} = \mu_0 M_s \int \mathbf{H}_{\text{eff}} \cdot \frac{\partial \mathbf{m}_0}{\partial R_i} = -\mu_0 M_s \int \mathbf{H}_{\text{eff}} \cdot \frac{\partial \mathbf{m}_0}{\partial r_i}, \quad (2.6)$$

where $E = \int \mathcal{E}$ is the total energy of the texture (note that all integrals written in this chapter are over the $d = 3$ physical space). Inserting in (2.6) the expression of the effective field (2.3) with all derivatives of magnetization expressed in the rigidly displacing structure approximation, one gets after some rearranging

$$0 = F_{\text{ext},i} + F_{\text{gyro},i} + F_{\text{dissip},i} = F_i - \frac{\mu_0 M_s}{\gamma_0} \int \left(\frac{\partial \mathbf{m}_0}{\partial r_i} \times \mathbf{m}_0 \right) \cdot \mathbf{T} + \frac{\mu_0 M_s}{\gamma_0} \sum_j V_j \int \left(\frac{\partial \mathbf{m}_0}{\partial r_i} \times \frac{\partial \mathbf{m}_0}{\partial r_j} \right) \cdot \mathbf{m}_0 - \alpha \frac{\mu_0 M_s}{\gamma_0} \sum_j V_j \int \left(\frac{\partial \mathbf{m}_0}{\partial r_i} \cdot \frac{\partial \mathbf{m}_0}{\partial r_j} \right). \quad (2.7)$$

This equation expresses the balance of three forces. The first force (first two terms of r.h.s.) expresses the external action on the texture. It generalizes Thiele's original expression [29] by including the force from torques \mathbf{T} that do not derive from an energy density.¹⁰ Then come the two forces introduced by Thiele, the so-called gyrotropic force (third term in (2.7); its name reminds one that it derives from the precession term in LLG), and the dissipative force (fourth term, deriving from the damping term in LLG).

Before discussing these two forces, we treat the important case of the spin-transfer torque. It proves very simple [23]: the velocity in the gyrotropic force expression becomes a relative velocity $\mathbf{V} - \mathbf{u}$ (a relation first proved by L. Berger [31]), and for the dissipation force $\alpha \mathbf{V}$ is replaced by $\alpha \mathbf{V} - \beta \mathbf{u}$. Thus we are led back to the standard case, just with relative velocities.

Let us now look more closely at the gyrotropic force. Its expression shows that the j velocity component contributes to components $i \neq j$ of the force, in an anti-symmetric way. Hence one can write quite generally $\mathbf{F}_{\text{gyro}} = \mathbf{G} \times \mathbf{V}$, \mathbf{G} being the so-called gyrovector, with components

$$G_i = -\frac{\mu_0 M_s}{\gamma_0} \frac{\varepsilon_{ijk}}{2} \int \left(\frac{\partial \mathbf{m}_0}{\partial r_j} \times \frac{\partial \mathbf{m}_0}{\partial r_k} \right) \cdot \mathbf{m}_0, \quad (2.8)$$

¹⁰It may prove more pedagogical to input all external actions in \mathbf{T} rather than in \mathbf{H}_{eff} ; then \mathbf{F} is zero as the self-energy of the texture \mathbf{m}_0 should be independent of position (assuming a uniform medium, infinitely extended). See Sect. 2.4 for the special case of an infinite extension in one dimension only.

ε_{ijk} being the fully antisymmetric tensor ($\varepsilon_{xyz} = 1$, $\varepsilon_{xzy} = -1$, $\varepsilon_{xxz} = 0$, etc.). This means that the gyrotropic force is always orthogonal to the texture velocity, like the Lorentz force acting on a charged particle in a magnetic field. In the case of a thin film, where only in-plane variations of \mathbf{m} occur, the gyrovector has only a perpendicular component. Apart from the factor $(\mu_0 M_s / \gamma_0) h$ (namely the surfacic density of angular momentum, h being the sample thickness), this is exactly \mathcal{Q} , 4π times the skyrmion number defined in the introduction Chap. 1, by H. B. Braun. Thus, we see that textures that cover a non-zero area on the unit sphere (i.e. have a non-zero vertical gyrovector component) get deflected sideways within the film plane. If the texture is topological, the value of this unit sphere area is fixed, so that the gyrovector is a vector that is constant in time. A direct connection between topology and dynamics of magnetic textures is thus established.

We also need to come back to the dissipative force. In the case of a nanowire (extended in the x direction, cross-section Σ), which is more general than assuming a strictly one-dimensional physics, the forces for steady-state dynamics can only be along x (thus, a gyrotropic force if it exists has to be balanced by a confinement force from the nanowire edges). It is then useful to express the dissipation force in terms of a domain wall width that has been called ¹¹ the Thiele domain wall width Δ_T , defined as

$$\frac{2}{\Delta_T} = \frac{1}{\Sigma} \int \left(\frac{\partial \mathbf{m}}{\partial x} \right)^2. \quad (2.9)$$

Indeed, under a field H collinear to the domains magnetization one finds from (2.7, 2.9) a domain wall steady-state velocity V obeying the famous relation of one-dimensional domain wall dynamics [2, 16, 33] $V = (\gamma_0 \Delta_T / \alpha) H$. For a discussion of the Thiele domain wall width, that comes from energy dissipation, compared to the more intuitive geometrical, and imaging domain wall widths, the reader should consult [34, 35].

The assumption underlying the derivation of the Thiele equation is a rigid displacement of the magnetic texture. A situation where this is physically legitimate is the case of stationary motion. In such a case, \mathbf{m}_0 is the moving texture, that may differ from the structure at rest, as well known for the dynamics of domain walls [16, 24, 25, 36]. In practice, the Thiele equation is employed in a much wider variety of situations, with the additional approximation that \mathbf{m}_0 is the texture at rest.

In order to describe non-steady state motion, where velocity changes, it has been proposed to account for the deformability of the texture by writing [37, 38] $\mathbf{m}(\mathbf{r}, t) = \mathbf{m}_0[\mathbf{r} - \mathbf{R}(t), \mathbf{V}(t)]$. This leads to an inertial force in the Thiele equation, with an expression for the mass that generalizes the early calculation [36] of the Bloch wall mass. The systematic incorporation of higher derivatives is discussed in [39].

Another generalization recently proposed in the context of magnetic skyrmions [40] considers local densities for both gyrovector and dissipation, thus allowing for

¹¹This domain wall width is implicitly defined in [30] (Sect. 2.4) when applying the Thiele equation to the dynamics of a simple domain wall. The explicit definition of the Thiele domain wall width occurred later [32].

texture deformation. This approach implements a bridge between the Thiele equation and the Slonczewski equations described below.

2.2.2 The Canonical Momentum

We start by considering the bubble material case, where this concept was introduced. A general framework to describe the dynamics of domain walls in films with perpendicular magnetization, allowing for arbitrary wall shape and magnetic moment orientation, is afforded by the Slonczewski equations [9, 25].

They generalize the Walker solution for the dynamics of a Bloch wall [33], and describe the domain wall dynamics by two variables, the local wall displacement q along its normal and the local domain wall magnetic moment angle ψ , in the plane orthogonal to the easy axis (Fig. 2.4). The two variables are function of time at least, and of position within the domain wall surface in the most general version. At the wall sub-structures (lines), ψ deviates strongly from the in-plane angle of the plane tangent to the domain wall, a situation specifically discussed in the next section. To describe the magnetization everywhere, the assumption is made that the magnetization polar angle θ [writing $\mathbf{m} = (\sin \theta \cos \phi, \sin \theta \sin \phi, \cos \theta)$, with $\phi = \psi$ at the wall position $\theta = \pi/2$, z being the normal to the film] varies with the coordinate normal to the wall according to the Bloch wall profile, namely $\theta = 2 \arctan \exp(x/\Delta)$ with a fixed domain wall width parameter Δ (as soon as the domain wall curvature radii are larger than a few domain wall widths, there is no conflict in assigning to each position a unique magnetization, practically even if not mathematically). The LLG equation

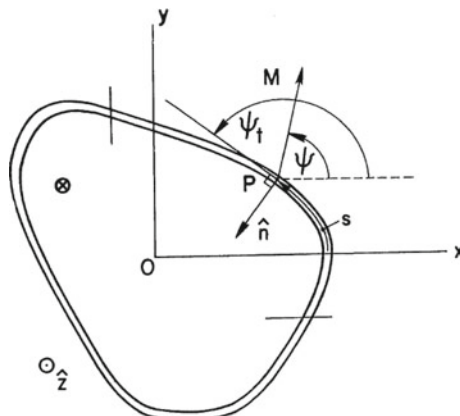


Fig. 2.4 Schematic of a general reversed domain. At point P along the domain wall (curvilinear abscissa s), the tangent to the domain wall is shown (angle ψ_t), as well as the orientation of the domain wall magnetic moment (angle ψ in the absolute frame). The oriented normal to the domain wall (vector \mathbf{n}) is the direction along which the domain wall displacement q is measured. Reproduced, with permission by Academic Press, from [9]

then transforms into two coupled (q, ψ) equations, the Slonczewski equations [25]:

$$\frac{\delta\sigma}{\delta q} = -\frac{2\mu_0 M_s}{\gamma_0} \left(\frac{\partial\psi}{\partial t} + \frac{\alpha}{\Delta} \frac{\partial q}{\partial t} \right), \quad (2.10)$$

$$\frac{\delta\sigma}{\delta\psi} = \frac{2\mu_0 M_s}{\gamma_0} \left(\frac{\partial q}{\partial t} - \alpha \Delta \frac{\partial\psi}{\partial t} \right). \quad (2.11)$$

The conservative dynamics (obtained by setting $\alpha = 0$) implies that q and ψ are conjugated in Hamilton's sense, the Hamiltonian being σ , the domain wall energy.¹² Thus

$$p = 2(\mu_0 M_s / \gamma_0) \psi \quad (2.12)$$

has been called the canonical momentum surface density. It is a linear momentum, oriented along the normal to the domain wall.

The linear momentum conservation equation (2.10) directly leads to what is called the automotion effect. For a free wall in a uniform medium, energy is independent of position thus $\delta\sigma/\delta q = 0$, so that the time variations of angle ψ and position q are linked. If the wall structure has changed, inducing a change of the domain wall angle denoted $[\psi]$, the dissipation of the associated momentum change leads to a domain wall displacement $[q]$ given by

$$[q] = -(\Delta/\alpha) [\psi], \quad (2.13)$$

called automotion. Remarkably, the sign of the automotion depends on the sign of the change of ψ .

The generalization to a global quantity, for example and obviously at that time for a bubble domain, led to the canonical momentum concept [41–43]. A vast literature exists on this subject, with papers entitled *Force, momentum and topology of a moving magnetic domain* [43] or, more recently, *Topology and dynamics in ferromagnetic media* [44]. The subject is also connected to the question of the spin electromotive force, discussed later (Sect. 2.4.3).

Going back to the derivation of the Thiele equation, we get from (2.3) and (2.6), without making the rigid translation assumption so as to allow for transformations of the texture (the profile of ψ over the domain wall surface, mainly),

$$F_i = \frac{\mu_0 M_s}{\gamma_0} \int \left(\mathbf{m} \times \frac{\partial \mathbf{m}}{\partial r_i} \right) \cdot \frac{\partial \mathbf{m}}{\partial t} - \alpha \frac{\mu_0 M_s}{\gamma_0} \int \frac{\partial \mathbf{m}}{\partial r_i} \cdot \frac{\partial \mathbf{m}}{\partial t} - \frac{\mu_0 M_s}{\gamma_0} \int \left(\mathbf{m} \times \frac{\partial \mathbf{m}}{\partial r_i} \right) \cdot \mathbf{T}. \quad (2.14)$$

The comparison of the above equation, in the conservative case, to Newton's second law leads to write that the global linear momentum P_i conjugated to the global position X_i of the texture satisfies

¹²We stick to the historical formulation that refers to the domain wall energy density σ , but in fact it is the total energy $E = \int \mathcal{E} d^3r = \int \mathcal{E} dq dS = \int \sigma dS$. Indeed, expressing the effect of an easy axis field by $\delta\sigma/\delta q = 2\mu_0 M_s H$, which means a position-dependent domain wall energy, is physically artificial.

$$\frac{dP_i}{dt} = \frac{\mu_0 M_s}{\gamma_0} \int \left(\mathbf{m} \times \frac{\partial \mathbf{m}}{\partial r_i} \right) \cdot \frac{\partial \mathbf{m}}{\partial t}. \quad (2.15)$$

It is a priori not mathematically guaranteed that this expression defines a momentum vector \mathbf{P} . In the case of bubble domains [41–43], the r.h.s. of (2.15) can be naturally split into two parts, by separating the time evolution into that due to the bubble displacement and that due to the evolution of the magnetic structure of the domain wall (the bubble being assumed to remain circular with constant radius). The first part exactly gives minus the gyrotropic force $-\mathbf{G} \times \mathbf{V}$ [43], a result that was to be expected. The second part is the momentum of the domain coming from the domain wall internal magnetization (ψ) dynamics. Neglecting the width of vertical Bloch lines and assuming vertical domain walls, this second part of the momentum was found to be simply $\Psi_x = \pi h \sum_j \varepsilon_j y'_j$ and $\Psi_y = -\pi h \sum_j \varepsilon_j x'_j$, using the reduced momentum $\Psi_i = P_i / (2\mu_0 M_s / \gamma_0)$ and with x'_j , y'_j and ε_j denoting, for the j -th VBL, its relative x, y position from the bubble center and its polarity (see drawing in Fig. 2.6(c)). The appealing character of this zero-width Bloch lines approximation is that they are shown to concentrate all the domain wall momentum. In addition, this analysis shows that a global domain momentum \mathbf{P} is indeed defined by (2.15), once the gyrotropic force contribution is extracted. The application of the domain momentum concept to the experiments on bubbles is described in another section (Sect. 2.3).

The second case where the canonical momentum of a texture was employed concerns soft nanostrips (see Sect. 2.4 for an introduction to the peculiarities of such samples). In a narrow strip, a domain wall can transform, but cannot move in the transverse (y) direction, so that only the longitudinal component P_x of the global momentum is relevant. Using the same proportionality relation as in (2.12), and dropping the x -subscripts, one is led to define for a nanostrip a generalized domain wall magnetic moment angle [45] through

$$\frac{d\Psi}{dt} = \frac{1}{2\Sigma} \int \left(\mathbf{m} \times \frac{\partial \mathbf{m}}{\partial x} \right) \cdot \frac{\partial \mathbf{m}}{\partial t}, \quad (2.16)$$

where Σ is the nanostrip cross-section area. For a 1D domain wall with the Bloch profile [$\theta(x) = 2 \arctan \exp((x - q)/\Delta)$, $\phi(x) = \psi$], one can check that the angle Ψ thus defined is identical to the angle ψ of the DW magnetic moment. For more realistic 2D DWs (TW, ATW, VW; see Sect. 2.4 for definition), it has been numerically checked [45] that this indeed defines an angle Ψ that behaves as expected, although no general mathematical proof could be given. A further generalization of the wall global position Q according to

$$\frac{dQ}{dt} = -\frac{\Delta_T}{2\Sigma} \int \frac{\partial \mathbf{m}}{\partial t} \cdot \frac{\partial \mathbf{m}}{\partial x} \quad (2.17)$$

leads to recover the linear momentum conservation Slonczewski equation (2.10), this time for the global domain wall position and angle [45].

2.3 Experiments with Bloch and Néel Lines

In the previous section, we have proved that topology for $n = 3$ should manifest itself by a deflection in the motion of a magnetic texture. But an infinite, straight domain wall cannot show such a motion. Moreover, a one-dimensional texture covers no surface on S^2 hence has a zero gyrovector. So we need to study cases more complex than infinitely long and straight one-dimensional domain walls. Finite domains (e.g. a bubble domain) are one such case, but the largest physical richness appears when investigating magnetic domain walls that are not one-dimensional, i.e. walls whose magnetization varies along the domain wall surface, so that they contain lines.

2.3.1 In-Plane Soft Magnetic Films

The quasi-static motion of Bloch lines was observed, under a field parallel to the domain wall magnetization,¹³ thereby proving that the domain wall is really subdivided into segments with opposite magnetizations. In one case [47], short field pulses were applied and a Bloch line mobility measured, the field directly favoring Bloch line motion. The first stroboscopic analysis of Bloch lines motion was performed [48] by means of Lorentz electron microscopy. In these experiments, the sole motion of ‘circular’ lines was observed, whereas the ‘cross’ lines and the wall supporting them remained immobile. These experiments could be performed only for a hard axis field so that, again, the field did exert a direct force on lines. Such is the case also of later studies performed on thin film heads (e.g. [49]). Thus, to the knowledge of the authors, no topological (gyrotropic) effect in domain wall dynamics could be evidenced at the time in soft metallic magnetic films with in-plane easy axis.

The resonant motion of a circular line (vortex) at the junction of four 90° Néel walls was first observed in garnet epilayer patterned microstructures with in-plane easy axes [50]. The vortex orbit necessarily implies the existence of a gyrotropic force. Soon after, several experiments performed on iron garnet crystal slabs with a single in-plane easy axis did allow for a direct observation of gyrotropic effects [46], the application of an easy axis field inducing both wall and line motion. The phase relation between wall and line motion was consistent with the action of a gyrotropic force on the line (Fig. 2.5). Joint line and wall motion was also achieved under the action of a field primarily favoring line motion. The phase relation between moving adjacent lines along a given wall was also consistent with the topological expectation. Finally, the opposite gyrotropic (topological) forces acting on line segments separated by a Bloch point did allow for the first detection of point singularities [51] and, upon application of suitable fields, their manipulation and, even, a first estimate of their mobility [52].

¹³Soft magnetic films often display a small in-plane uniaxial anisotropy.

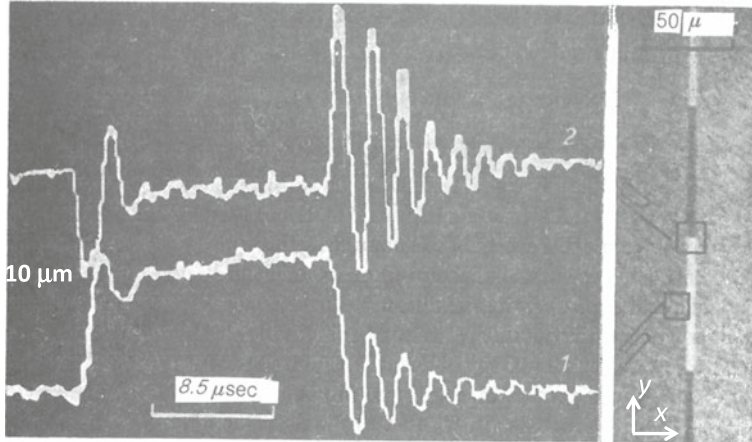


Fig. 2.5 Dynamics of one domain wall containing Bloch lines in a $50 \mu\text{m}$ thick single crystalline yttrium iron garnet plate, excited by an easy-axis field pulse and observed by magneto-optics. The photometric traces (left) show the domain wall motion (in the x direction, curve 1) and the Bloch line motion along the domain wall (in the y direction, curve 2). The right picture is a magneto-optical image of the sample, the domains magnetizations being along $\pm y$, the easy axis. In the domain wall, Bloch segments of alternate polarities ($\pm z$) are seen, with black and white contrasts. The gray boxes show the areas over which the optical intensity was integrated to produce the traces shown. Reproduced, with permission by AIP, from [46]

2.3.2 Perpendicular Magnetization Samples: Bubble Garnets

The two types of lines in the domain walls of such samples have been described in Sect. 2.1.3. Because of the twisted Néel-Bloch-Néel nature of the walls in finite thickness films, a VBL has a gyrovector density that varies along its length (see Fig. 2.3(c, e)). For an HBL, the gyrovector is constant along its length, but now changes according to the vertical position of the line, again because of the domains' inhomogeneous stray field. Note that the gyrovector of a line is always along the line.

2.3.2.1 Role of Horizontal Bloch Lines

Experimentally, HBLs were first invoked to explain the complex motion of simple walls, for example in a bubble without VBLs, under pulse bias fields (dynamic bubble collapse experiments). A first HBL model was built by Slonczewski [53] under the assumption of rigid vertical domain walls, that could be analytically solved. From the Thiele equation we see that for a domain wall moving in the y direction, an HBL which has a gyrovector oriented in the x direction experiences a gyrotropic force in the z direction (see Fig. 2.3(b) for axes), hence the prediction of the HBL model that such lines are nucleated at one sample surface and cross the film, reducing the

domain wall velocity. This model describes a realization of the Walker breakdown in a finite-thickness sample, with the inhomogeneous Néel-Bloch-Néel wall structure. Above the Walker breakdown, it leads to the phenomenon of HBL ‘punch-through’, where the 2π twist of the HBL is released by its expulsion.

It was then soon realized [54] that the rigid wall assumption was not justified, again invoking the Thiele equation argument that a moving HBL locally affects the domain wall dynamics. Time-resolved measurements (by local magneto-optics) of the dynamics of parallel domain walls submitted to a bias field pulse [55] required, to be correctly reproduced, the numerical solution of the full one-dimensional Slonczewski equations (unknowns $q(z)$ and $\psi(z)$). More elaborate measurements in which a single domain wall was investigated, and using an optical dark-field technique where light is scattered according to the wall orientation relative to the vertical, gave an even better agreement with the 1D Slonczewski equations [56]. A proof of the topological dynamics is that the HBL pushes the domain wall forward when it travels back to its original surface, as opposed to the initial part of the motion where the HBL slows down the domain wall, an effect that could also be accounted for by the increased energy dissipation at the HBL. This is another example of the automotion effect. The domain wall push by a relaxing HBL can also be rationalized by the canonical momentum concept: in a zero-width HBL model one gets, similarly to the calculation for VBLs in a bubble, a canonical momentum per unit wall length whose domain wall normal component reads $dP_n/dt = (2\mu_0 M_s/\gamma_0)\Delta\psi(z_L)dz_L/dt$, z_L being the HBL vertical position and $\Delta\psi(z_L)$ the jump of domain wall magnetization angle at this position.

2.3.2.2 Role of Vertical Bloch Lines

Experiments involving VBLs are much more numerous, as VBLs are statically stable. A first type of experiments investigates the effects of VBL on the statics and dynamics of bubbles. The best-known effect of the presence of VBLs is the lateral deflection of bubbles, first seen when applying a bias field gradient (Fig. 2.6(a)) [9, 57] (this effect has in fact been the motivation behind Thiele’s equation). A more elaborate measurement of the effect was later obtained by submitting bubbles to a bias field gradient whose in-plane direction rotates at MHz frequencies, applying a rotating radial force to the bubble. Figure 2.6(b) shows results obtained with this technique, where the slopes are determined by S , the bubble winding number.¹⁴ These experiments revealed another effect of the presence of VBLs, namely that the bubbles have an apparent mass that greatly exceeds what would be computed from the Döring formula [60]. The explanation of this fact was obtained [61] through the concept of the canonical momentum, as sketched in Fig. 2.6(c): due to the gyroscopic force the VBLs gather on opposite lateral sides of the moving bubble according to

¹⁴By convention for bubbles, the bias field is up so that the bubble core magnetization is down. Thus topological and winding numbers are in one-to-one correspondence (in fact, they are simply opposite, as the core is down-magnetized).

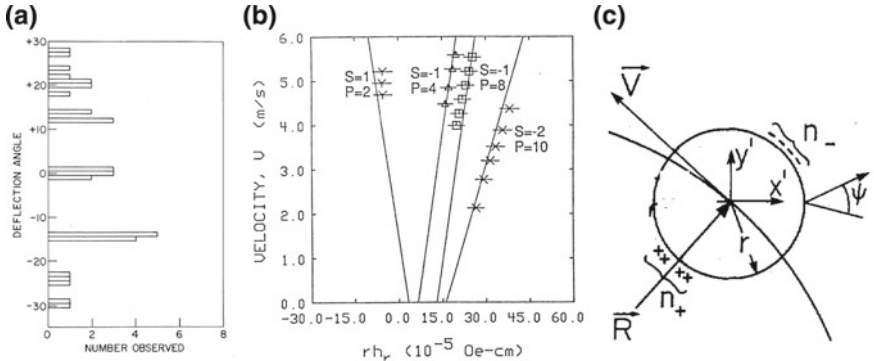


Fig. 2.6 Gyrotropic bubble deflection experiments. (a) Histogram, for randomly chosen bubbles, of deflection angles from the pulsed gradient field direction (from [57]). (b) Bubbles rotation velocity versus radial drive ($r \nabla H_z$ with r the bubble radius), as a function of bubble state given by the winding number S and the total VBL number P (from [58]). (c) Schematic of a rotating bubble (adapted from [59]) with \mathbf{R} the bubble position vector from the device center, and \mathbf{V} its velocity vector tangent to the bubble center trajectory (arc of circle). As the two VBLs created by a HBL loop punch-through have opposite polarities, they are deflected to opposite sides of the moving bubble (+ and - signs on both bubble sides) so that the second part of the bubble momentum is indeed given by the total VBL number (see Sect. 2.2.2), hence its denomination P in (b). Panel (a) is reproduced, with permission by AIP, from [53]. Panels (b,c) are reproduced, with permission by IEEE, from [58, 59], respectively

their sign, and are thus stable so (see Fig. 2.3(g)). The moving bubble therefore has a canonical momentum, tangent to its trajectory and proportional to the total VBL number (P in Fig. 2.6b). From the force equation (2.15), a radial force appears on a rotating bubble, proportional to the angular velocity and the VBLs number, that adds to the inertial force [61] and can be much larger.

Many other manifestations of the gyrotropic force on bubbles through Bloch lines exist (see [9] for a survey). These include, keeping the terminology introduced in each case, (i) the overshoot effect by which bubbles continue to move after the field gradient pulse has terminated [41, 62]; (ii) the bubble automotion due to a bias field pulse, with displacement in different directions for bubbles prepared in different states by an in-plane field [63], also called bias jump when the bubbles were prepared only by gradient propagation [64] and (iii) the bubble turnaround effect, a bubble lateral displacement when the sign of the pulsed field gradient is reversed [65]. All these effects could be explained by (i) the nucleation of VBL pairs of opposite topological numbers, either statically by an in-plane field or dynamically [66] through the nucleation and motion of an HBL that ‘punches-through’ at the other film surface, transforming into two VBLs,¹⁵ together with (ii) the gyrotropic

¹⁵The two VBLs indeed have same core magnetization, namely that of the HBL, same magnetization gradient normal to the domain wall and opposite magnetization gradients along the domain wall, hence opposite vertical gyrovector components.

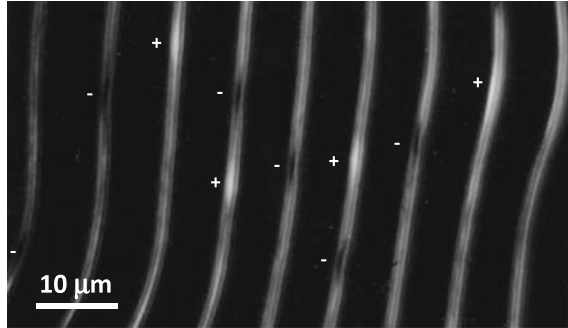


Fig. 2.7 Optical observation of Bloch lines in a bubble garnet film, by an anisotropic dark field technique [67, 68]. Only the domain walls scatter light, through the magneto-optical effect. Around the position of VBLs and according to their magnetostatic charge, the wall tilts, increasing or decreasing the scattering of light (+ or - signs on the left of walls; beware that these signs are unrelated to those of the gyrovectors of the VBLs)

motion of these VBLs, during the bubble preparation phase or during the subsequent bias field pulse.

A second type of experiments was performed later, within the research effort on the so-called Bloch line memory [69], a successor of the bubble memory that never reached the market [70]. In this memory, an information bit is represented by the presence or absence of a winding VBL pair, i.e. VBLs having the same topological number. The memory is organized in shift registers, each being the domain wall of an elongated stripe domain, around which the data are circulated so as to read or write them at gates. The VBL pair propagation is realized by asymmetric bias field pulses, in order to have motion only during the sharp leading edge of the pulse. As all VBLs have the same gyrovector, they all displace in the same direction, so that this memory relies on the dynamic consequences of topology in magnetism. The amplification factor from domain wall velocity to VBL (isolated, or in clusters) has been measured, evidencing a drop with the number of VBLs in the cluster due to the large domain wall deformations that occur at the cluster [71]. The expected progressive change of the global gyrovector of a single VBL by control of the vertical position of a Bloch point along the line, has also been experimentally observed [72, 73]. These experiments used the static VBL visualization technique based on light scattering by the domain wall, through the wall local inclination in the vicinity of the VBL (Fig. 2.7) [67, 68].

The Bloch-line memory is touching topology in another aspect. A winding VBL pair is indeed a topologically stable structure within a uniform Bloch wall, with a topological number of ± 1 . The topological protection is nice for data stability, but at the same time prevents the writing of data. From the general arguments of Sect. 2.1, we know that a Bloch point is necessary. Indeed, the simple and efficient scheme devised to write winding VBL pairs [74]—called Bloch point writing—rests on the

injection of a Bloch point at the top sample surface, by a local magnetic field created with a thin conductor placed on the sample top surface.

2.3.2.3 Manifestation of Topological Stability in Experiments

This part is directly inspired by the book on domain walls in bubble materials, by Malozemoff and Slonczewski [9], Sects. 8D, 9B and 9C.

From the topological analysis, a unichiral bubble is a topologically stable structure, that cannot disappear in a continuous way. However, it is well known experimentally that a maximum bias field exists—the so-called collapse field, a fraction of the sample magnetization—above which the bubble collapses by implosion. The radial force analysis taking into account magnetostatic stabilization and domain wall surface indeed predicts that, at this field, the structure energy steadily decreases as radius decreases [9], so at least down to a radius of the order of the domain wall width. In such a dynamic process, it is therefore conceivable that, the bubble reaching such a small size with a large energy, a Bloch point can be injected that breaks the topological constraint.

This interpretation is strengthened by the observation of ‘hard bubbles’ [75], that have significantly larger collapse fields (up to twice the value, typically). The measured diameter versus bias field curves of such bubbles have been well reproduced by a model [76] where the magnetization in the domain wall has large winding numbers S , i.e. a large number of winding VBLs is present, so that the domain wall specific energy increases as the inverse square of the diameter. In such conditions the implosion of the bubble is prevented, and the collapse occurs only when the VBLs are so tightly packed that Bloch points are injected, removing them pair by pair as the bubble diameter decreases.

The enhanced stability of hard bubbles can therefore be taken as a signature of the reality of the topological stability of winding VBL pairs. This experimental stability of VBL pairs is the founding principle of the Bloch line memory [77]. To the authors’ knowledge, no systematic study of the VBL pair stability has been conducted (for example, by applying in-plane compressing fields for various durations at various temperatures, to a single VBL pair located on a single straight domain wall). Indirect studies however exist in which hard bubbles were heated-up and their collapse field tested when going back to room temperature [78].

2.4 Experiments on Nanostrips of In-Plane Soft Materials

With the continuous development of micro- and nanofabrication techniques, following progress in the deposition or growth of thin and ultrathin films, patterned sub-micrometric magnetic structures came under focus in the 90s. An interesting structure in this family is the nanostrip of width w , patterned out of a thin film of thickness h with $h \ll w$ (keeping the term nanowire for the case $h \sim w$), the prefix

nano meaning that $w < 1 \mu\text{m}$ so that h is a few nanometers, whereas the strip length is extremely long, allowing domain wall propagation in that direction. The typical exchange length of the material being $\Lambda = 5 \text{ nm}$, such small thicknesses prevent magnetization variations across the sample thickness. The interest in such structures was greatly enhanced by the experimental study of the spin-transfer torque (STT), as very small sample cross-sections are required for allowing current densities of a few 10^{12} A/m^2 (note that the total current heats both sample and substrate [79]). A large majority of these studies was performed on films of the soft alloy (permalloy) $\text{Ni}_{80}\text{Fe}_{20}$ that has vanishing anisotropy and magnetostriction. The latter property is extremely important, as whatever the deposition conditions, the resulting stress state of the film will not affect its magnetic properties (for non-zero magnetostriction films, some surprising consequences on magnetic structures are explored in [80, 81]). Low anisotropy is also important for domain wall propagation, because of the empirical linear correlation between anisotropy field and coercive field [82].

In such samples, due to the small width, magnetostatics favors magnetization along the strip axis. This gives rise to an unusual type of domain wall, the charged wall, not considered in the old domain theory that predates micromagnetics [2]. The walls are labelled head-to-head (HH) when they bear a positive magnetic charge ($-\text{div}(\mathbf{m})$), and tail-to-tail (TT) when the charge is negative.¹⁶ The basic walls in nanostrips are thus called transverse (TW), vortex (VW) and, for nanowires, Bloch-point walls [32, 34, 83].

2.4.1 Topology of Domain Walls in Soft Nanostrips

In this section we expose, in the general context of this chapter and book, the work by O. Tchernyshyov and collaborators [86–88]. Owing to magnetostatics, magnetization is pulled towards the tangent to the strip edges, a phenomenon deeply exploited in the past to predict and classify the possible magnetic textures in small elements patterned from soft magnetic films [89]. If this is taken as a mathematical prescription one obtains that at the edges the magnetization is Ising ($n = 1$), either parallel or antiparallel to the local tangent. From the homotopy result $\Pi_0(S^0) = \mathbb{Z}_2$, quoted in Sect. 2.1.1, we get that topological defects exist at the edges whatever the wall type, HH or TT. In reality, the Ising character of edge magnetization is not absolute, especially for small sample thickness as the demagnetizing field from in-plane variations of magnetization vanishes at zero thickness. Thus, the next-order description of the edge magnetization is the same as the first-order description of magnetization in the sample, namely XY ($n = 2$). By this ‘escape in the second dimension’, the previous topological defects Fig. 2.1(a) are regularized into topologically stable domain-wall configurations, as shown in Fig. 2.1(b1, b2), that have winding numbers of $\pm 1/2$.

¹⁶It is thus meaningless to try to call these walls Bloch or Néel, as the latter have no volume charge resp. a dipolar volume charge.

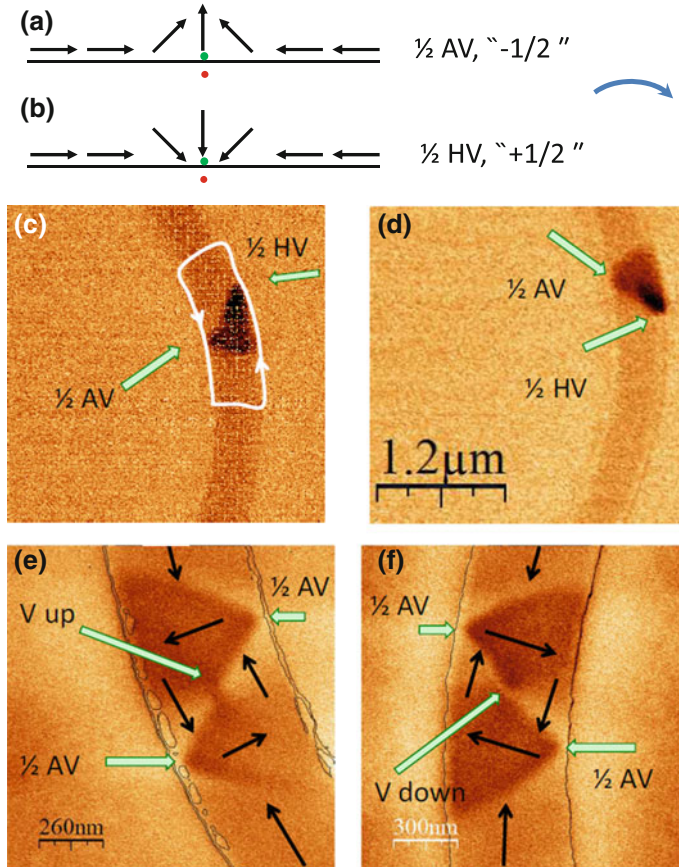


Fig. 2.8 Edge defects in a soft nanostrip for different domain walls. (a) schematic of a half-antivortex ($1/2$ AV) edge defect, with edge winding number $-1/2$, as found with the contour orientation drawn by the blue curved arrow on the side. (b) Same for a half hedgehog vortex ($1/2$ HV), with edge winding number $+1/2$. The virtual defect of the XY model is shown by the red dot, and the sample bottom edge is drawn by the line. (c–f) MFM images of domain walls in NiFe nanostrips, 17.5 nm thick [84]; the walls extend over the darker contrasts that correspond, in first approximation, to the magnetic charge density $-div\mathbf{m}$. (c–d) Asymmetric transverse walls with opposite asymmetries, bearing two edge defects of opposite winding number, indicated by large arrows. An oriented circuit around a domain wall, with two edge paths and two crossing paths, is drawn in (c). (e–f) Vortex walls, for which the two edge defects are half antivortices. The two vortex walls have opposite circulation and opposite core polarity. Magnetization in each region is sketched by black arrows. All MFM images taken from [85]

As shown by Tchernyshyov et al. [86], it is physically instructive to consider these edge configurations as ‘edge defects’, the manifestation of virtual defects located outside the sample, as sketched in Fig. 2.8(a, b). The virtual defects are characterized by a winding number (Fig. 2.8(a, b)), evaluated similarly to that of VBLs (see Fig. 2.3(g)) by replacing the reference down-magnetized domain by the medium outside the nanostrip, again in order to orient the travel along the domain wall. Note that in this escape in the second dimension there is no one-to-one correspondence between the $n = 1$ and the $n = 2$ defects, as drawn in Fig. 2.8(a, b) for the HH case.

To make connection with the general procedure outlined in Sect. 2.1.1, aimed at finding whether topological defects exist in the sample, we simply consider a circuit around the sample i.e. made of the two nanostrip edges connected by two crossing paths (Fig. 2.8(c)). Far enough from any structure, the crossing paths lead to no magnetization rotation, so that the magnetization rotation upon tracing one loop is just the sum of the rotations along each edge. As the sample as a whole is now investigated, the positive sense around the edges is the opposite of that used to identify the edge defects. We thus reach the conclusion [86] that the sum of the indices of the internal topological defects and of the edge defects is zero. For example, in Fig. 2.8(c, d) no topological defect is associated with the asymmetric transverse walls shown, whereas in Fig. 2.8(e, f) for vortex walls, a vortex with +1 topological index is present as two $-1/2$ edge defects exist.

2.4.2 *Topological Dynamics of Domain Walls in Soft Nanostrips*

The interest in such structures, initially just for field dynamics [90, 91], greatly increased with the study of the motion of domain walls by the spin-transfer torque, as such samples can withstand large current densities. These two means of action are considered separately below.

2.4.2.1 **Field Dynamics**

The nanostrips, that confine the domain wall degrees of freedom by both reducing the nanostrip width and thickness, hence both dimensions of the domain wall surface, offered a new playground for testing and refining the domain wall dynamics phenomenology. This concerns particularly the value of the Walker field, i.e. the process that fixes this threshold, and the domain wall dynamics little above the Walker field, where the differential mobility is predicted to be negative in the one-dimensional model, a feature anticipated to be removed by domain wall deformations in general [25].

As shown in Fig. 2.8, two basic types of domain walls exist in nanostrips, the transverse wall (TW) and the vortex wall (VW), with different stability regions in

the nanostrip thickness vs. width plane [83], the TW decaying into a lower symmetry asymmetric transverse wall (ATW) at large widths [34]. The edge defects analysis, performed in the frame of the XY model, shows that the (A)TW contains no topological defect, whereas the VW contains one vortex with topological index +1. To understand the dynamics of these walls, it is mandatory to consider the full structure of these walls in statics and in dynamics, hence to perform the ‘escape in the third dimension’ where the Heisenberg model now applies, with $n = 3$. In this model the vortex becomes a topologically stable structure (using similar boundary conditions as in Sect. 2.3.2) with a core oriented perpendicular to the sample plane, either up or down. The vortex covers half of the order parameter sphere, with a surface $\Omega = 2\pi p$ with p the core polarity (see the chapter on vortices, by C. Behnke, C. Adolf and G. Meier, for more details), so that it has a non-zero gyrovector.

From the Thiele expression, it is expected that the gyrotropic force pushes the vortex off the nanostrip center line—the equilibrium position owing to magnetostatics—when the VW moves, up to finally expelling it, the source of one Walker breakdown mechanism for a VW. This has been predicted by micromagnetic simulations [32, 45, 92], and experimentally observed through velocity fluctuations [93, 94], domain wall resistance oscillations [95], and time-resolved domain wall position measurements [96]. For a TW, even if there is no topological structure at rest (zero gyrovector), the Walker breakdown involves the injection of an antivortex at one edge, crossing the nanostrip width and reversing the TW transverse magnetic moment [97]. In all these cases, the direction of lateral motion of the vortex or antivortex is dictated by the gyrovector, hence by the polarity of the core of these structures times the winding number (+1 for the vortex, -1 for the antivortex). The richness of the post-breakdown dynamical behavior is beautifully illustrated in the systematic numerical study of 10-nm thick Ni-Fe nanostrips with different widths [92]. A simple physical understanding of these processes was developed, relying on the edge defects model [88] and including some magnetostatics-based energetics, the latter derived from the successful modeling of vortex dynamics in soft nanodisks (see the chapter on magnetic vortices, by Behnke, C. Adolf and G. Meier).

The comparison of the measured dynamics of vortex walls with the simple (Q, Ψ) model set up by Schryer and Walker revealed a very good agreement, once the effective anisotropy energy for the ‘DW moment angle’ Ψ was found [98]. This was very surprising at first sight, as the so-called 1D model of Schryer and Walker was clearly transferable to TWs in narrow nanostrips, but not a priori to the more complex VWs [32]. However, when considering the canonical momentum concept and its application to nanostrips, as exposed in Sect. 2.2.2, the surprise diminishes. The surprise completely disappears when, calculating the generalized Ψ in the composite singularity model of the VW [86], one finds the simple relation $d\Psi/dt = (\Omega/2)V_y/w$ [45, 88] with $\Omega = 2\pi p$ (p the vortex core polarity) being the surface covered on the sphere. This links the canonical momentum of the VW to the topological index of the core times the lateral core position, a result that resembles the evaluation of that momentum for bubble domains.

Another aspect of the topological domain wall dynamics is, similarly to the case of bubbles described in Sect. 2.3.2, the automotion of domain walls [84]. Starting

from an ATW nucleated by in-plane field in a bent nanostrip, it was observed that under transformation into the stable VW structure, the domain wall displaced by about $\pm 1 \mu\text{m}$. Observing by MFM the structures of both initial ATW and final VW, the injected vortex could be observed (as shown in Fig. 2.8(c–f), note especially the contrast corresponding to the vortex core polarity) as well as the path it took to reach the nanostrip center. These characteristics give access to the sign of the released canonical momentum. This momentum was observed to indeed match with the sign of the domain wall displacement along the nanostrip, according to (2.13) [84].

Coming back to the topological difference between TW and VW, discussed above and that would prevent such a transformation, the reader is reminded that this topological difference rests on the fact that the mappings of the edges on the unit sphere are fixed, like in Fig. 2.3(c–f). The expulsion of a vortex at one edge, or the fact that it enters at one edge, breaks this assumption. A more local source of automotion, in which a BP reverses the vortex core in a VW is also expected, but has not yet been observed.

2.4.2.2 Current-Induced Dynamics

Topology arguments also apply to the current-driven domain wall motion, here through the spin-transfer torque (STT). The modified Thiele equation that corresponds to this situation has been recalled in Sect. 2.2.1. In the case of the (A)TW, the gyrovector is zero.¹⁷ The generalized Thiele equation then tells that stationary domain wall motion under STT is only possible with a non-adiabatic (β) STT term, according to the relation $V = (\beta/\alpha) u$ [23, 99]. For a VW, on the other hand, the gyrovector is non-zero. Treating the VW as a vortex core that can move both along and across the nanostrip (a lateral restoring force should be added, restricting the latter motion), one obtains $V_x = u (G^2 + \alpha\beta D^2) / (\alpha^2 G^2 + D^2)$ and $V_y = u (\alpha - \beta) GD / (\alpha^2 G^2 + D^2)$. Thus, even in the absence of a non-adiabatic term, a VW moves along the carriers at velocity $V_x \approx u$ (for small damping α). The sideways motion of the core is proportional to the gyrovector and difference $\alpha - \beta$: it would be zero if $\beta = \alpha$ (as proposed in some models), and reverses with e.g. core polarity as observed by X-ray magnetic microscopy [100]. When the vortex core reaches the nanostrip edge and is not expelled, gyrotropic motion can no longer take place and the previous expression where motion is due to the non-adiabatic term is recovered. A behavior in good agreement with this model was observed in [101], where the DW structure was resolved by spin-polarized scanning electron microscopy, after each pulse, correlating the presence of the vortex with the domain wall displacement. Displacements of VWs accompanied with changes of structure are shown in Fig. 2.9. They were systematically recorded by the associated change of sample resistance, through the anisotropic magnetoresistance effect [102], but

¹⁷This is not exact, actually, as magnetization tilts slightly out-of-plane close to the half antivortex and half hedgehog vortex. The surface thus covered on the sphere is, however, not topologically protected.

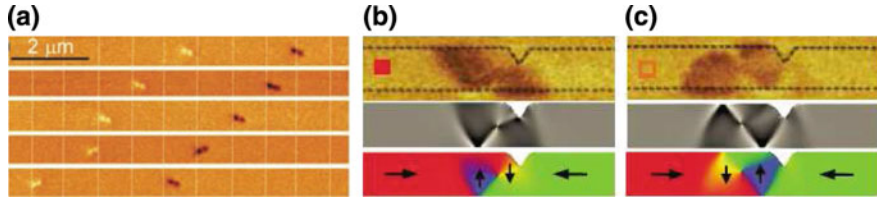


Fig. 2.9 Current-induced displacement of VVs in Ni-Fe nanowires, observed by MFM. (a) Successive displacements of two VVs in a $w = 100$ nm $h = 40$ nm nanowire with triangular notches 1 μ m apart (highlighted by vertical lines), under single 14 ns long, 26 mA current pulses, showing a few VW circulation reversals. Reproduced, with permission by AAAS, from [104]. (b) MFM image of a HH clockwise VW pinned by a triangular notch 100 nm deep, in a $w = 300$ nm $h = 10$ nm nanostrip, together with micromagnetic simulation of the structure, shown by a black and white image of divm and a color image of the in-plane magnetization. (c) Same for an anti-clockwise VW. Panels (b, c) are reproduced, with permission by APS, from [102]

the topological implications of such changes were not studied. As STT-induced DW motion was also observed for TWs in the same material [103], one has to assume that the non-adiabatic coefficient is not zero, so that DW motion by STT is not completely governed by topology.

Another topology-related effect of STT on domain walls is the observed oscillatory dependence of VW depinning by current pulses of varying duration, linked to the resonant excitation of the vortex core [98]. For an in-depth discussion of these matters, the reader is referred to the chapter by C. Behnke, C. Adolff and G. Meier, that is specifically devoted to vortices.

2.4.3 Topology and the Spin Electromotive Force

Early work by Luc Berger, the pioneer of the spin-transfer torque, led to the prediction that, in a metallic ferromagnet, a dc voltage develops across a domain wall with precessing magnetization [31]. This can be seen as an inverse effect of STT. At the local scale [105–108], an electro-motive force (same dimension as an electric field) is generated, expressed as

$$E_i = \mathcal{P} \frac{\hbar}{2e} \mathbf{m} \cdot \left(\frac{\partial \mathbf{m}}{\partial t} \times \frac{\partial \mathbf{m}}{\partial r_i} \right), \quad (2.18)$$

where $-e$ is the electron charge and \mathcal{P} is a spin polarization, the spin asymmetry of spin-flip scattering. This equation is very close to the definition of the generalized domain wall magnetic moment angle (2.16) in a nanostrip containing a domain wall. The evaluation of the average (over the nanostrip cross-section) voltage drop U_x across such a domain wall is indeed $U_x = \mathcal{P}(\hbar/e) d\Psi/dt$. This relation was obtained by Berger [31] and called ac ferro-Josephson effect.

In the above sections, we have seen that the change of the canonical momentum can be realized by the motion of topologically non-trivial substructures. Thus, the spin electromotive force can provide a detection of the motion (and hence the presence) of topological textures, see the chapter on bulk skyrmions, by A. Bauer et al., for another illustration of the effect. Note however that the spin electromotive force can exist even with topologically trivial textures: a TW with precessing domain wall magnetic moment has also a non-zero $d\Psi/dt$, even if it covers (nearly) no surface on the unit sphere.

For the specific case of domain walls, one experiment based on the creation and motion in the precessional regime of vortex walls has evidenced this effect, with measured dc voltages of the order of 1 μV , as expected [107].

2.4.4 *Soft Nanowires, Nanotubes*

Starting from a nanostrip where thickness h is much smaller than width w , and increasing the thickness or reducing the width, one moves smoothly to the nanowire case. The shape of the cross-section (rectangular with aspect ratio of order unity, or elliptical) appears to be unimportant, as practically the lateral dimensions are well above the micromagnetic characteristic lengths so that hypothetical sharp edges are magnetically rounded. A review of the domain wall structures in nanowires was recently published [109], comparing to nanostrips and trying to rationalize the description and denomination of domain walls.

A first finding of this analysis is that TW and VW cannot be distinguished when the thin film regime is left, as for example a TW seen from the sample side shows a outgoing magnetization that transforms into a vortex core as thickness grows. Topologically, this corresponds to the fact that for $n = 3$ all domain walls are topologically equivalent when there is no defect (Sect. 2.1.2). The apparent paradox with Sect. 2.4.1, where TWs with no gyrovector ($\Omega \approx 0$) were clearly separated from vortex/antivortex walls with non-zero gyrovector ($\Omega \approx \pm 2\pi p$) is easily explained. First, only the gyrovector component perpendicular to the film plane was referred to, as nothing can happen across the thickness of thin film of thickness smaller than the exchange length Λ . This restriction is lifted in a nanowire, where the other transverse component (y) of the gyrovector becomes relevant (corresponding to core motions across the sample thickness). Second, the quoted values of the surface covered on the sphere are no longer quantized as soon as the restriction of the edge spins to $n = 1$ or $n = 2$ is lifted when thickness increases. Thus, the general picture of the transverse-vortex wall—the denomination proposed in [109]—is that components G_z and G_y smoothly change as thickness increases.

The other notable feature of domain walls in nanowires, of sufficiently large transverse dimensions, is a stable domain wall that contains a Bloch point, that may be called Bloch point wall [32, 109] although other denominations were previously proposed [110, 111]. The Bloch point is enforced by the energy gain upon closing the flux of the domain wall, similarly to the case of VBLs in sufficiently thick garnet films

where a Bloch point allows closure of the domains stray field [112]. The Bloch point wall was recently observed by x-ray photoemission microscopy [113]. A specific dynamics was predicted for this wall by micromagnetic simulations [110, 114–116] in which topology plays no role as the integrated gyrovector components are zero, except at large drive [117].

Nanotubes are also starting to be experimentally investigated. Their domain wall structures are similar to those of nanowires, with the important change that the Bloch point disappears. The reader is referred to [117, 118] for additional information on this subject.

2.5 Conclusion and Outlook

In this chapter, we have first presented the topological approach to classify and describe the domain wall structures, in various samples and materials. The direct link between topology and the dynamics of magnetic textures, here domain walls and their substructures, has been described both theoretically and experimentally. The statics part did stress out the limits of the topological obstruction to some texture changes, as the topological defect of magnetism (the Bloch point) does occur in practice and can even be stable. The dynamics part, however, emphasized the direct and visible role of topology. Some relation between domain wall structure/topology and dynamics with transport properties was discussed. Part 2 of this book contains a more in-depth discussion of such effects, prominently the topological Hall effect.

In closing, we would like to mention that the topological classification does not describe all the physics of magnetic domain walls, be it statics or dynamics. Recent work on ultrathin films with structural inversion asymmetry has indeed revealed that chiral domain wall structures can be stabilized by the Dzyaloshinskii-Moriya interaction (DMI). Thus, although one can continuously transform a Bloch wall into a Néel wall and then into the opposite chirality Bloch wall (in a film with perpendicular magnetization, typically), the energy of all these structures differs because of DMI. The dynamics of these walls under the spin Hall effect is moreover directly impacted by the type (Bloch, Néel) and chirality (clockwise, anti-clockwise) of the domain walls (refer to the chapters on magnetic skyrmions for a discussion of this physics in that important case). It was not discussed here as topology, at least within the framework that we have used here, ignores chirality.

Acknowledgements The authors would like to acknowledge Maurice Kléman, formerly at LPS, for being an inspiration and, by his pioneering works, a source for the content of this chapter. They thank Jean-Yves Chauleau for providing MFM images of domain walls in Ni-Fe nanostrips, borrowed from his Ph.D. thesis [85]. The critical reading of the manuscript by O. Fruchart is gratefully acknowledged.

References

1. O.V. Pylypovskiy, V.P. Kravchuk, D.D. Sheka, D. Makarov, O.G. Schmidt, Y. Gaididei, Phys. Rev. Lett. **114**, 197204 (2015)
2. A. Hubert, R. Schäfer, *Magnetic Domains* (Springer, Berlin, 1998)
3. W.F. Brown Jr., *Micromagnetics* (Interscience Publishers, New York, 1963)
4. G. Toulouse, M. Kléman, J. Phys. Lett. **37**, L149 (1976)
5. M. Kléman, *Points, Lines and Walls* (Wiley, Chichester, 1983)
6. N.D. Mermin, Rev. Mod. Phys. **51**, 591 (1979)
7. A. Hatcher, *Algebraic Topology* (Cambridge University Press, Cambridge, 2002), <http://www.math.cornell.edu/~hatcher>
8. E. Feldtkeller, Z. angew. Phys. **19**, 530 (1965). English translation: IEEE. Trans. Magn. **53**, 0700308 (2017)
9. A.P. Malozemoff, J.C. Slonczewski, *Magnetic Domain Walls in Bubble Materials* (Academic Press, New York, 1979)
10. L. Michel, Rev. Mod. Phys. **52**, 617 (1980)
11. H.R. Trebin, Adv. Phys. **31**, 195 (1982)
12. V. Mineyev, G. Volovik, Phys. Rev. B **18**, 3197 (1978)
13. H.J. Williams, M. Goertz, J. Appl. Phys. **23**, 316 (1952)
14. R.W. DeBlois, C.D. Graham Jr., J. Appl. Phys. **29**, 931 (1958)
15. E.E. Huber Jr., D. Smith, J.B. Goodenough, J. Appl. Phys. **29**, 294 (1958)
16. L. Landau, E. Lifshitz, Phys. Z. Sowjetunion **8**, 153 (1935)
17. T.L. Gilbert, Phys. Rev. **100**, 1243 (1955). (abstract only)
18. M.D. Stiles, J. Miltat, *Spin Dynamics in Confined Magnetic Structures III* (Springer, Berlin, 2006), pp. 225–308
19. D.C. Ralph, M.D. Stiles, J. Magn. Magn. Mater. **320**, 1190 (2008)
20. D.C. Ralph, M.D. Stiles, J. Magn. Magn. Mater. **321**, 2508 (2009)
21. A. Brataas, A.D. Kent, H. Ohno, Nat. Mater. **11**, 372 (2012)
22. P. Gambardella, I.M. Miron, Phil. Trans. R. Soc. A **369**(13), 3175 (2011). <https://doi.org/10.1098/rsta.2010.0336>
23. A. Thiaville, Y. Nakatani, J. Miltat, Y. Suzuki, Europhys. Lett. **69**, 990 (2005)
24. N.L. Schryer, L.R. Walker, J. Appl. Phys. **45**, 5406 (1974)
25. J.C. Slonczewski, Int. J. Magn. **2**, 85 (1972)
26. M.J. Donahue, D.G. Porter, OOMMF user's guide, version 1.0, Interagency report NISTIR 6376 (1999)
27. T. Fischbacher, M. Franchin, G. Bordignon, H. Fangohr, IEEE Trans. Magn. **43**, 2896 (2007)
28. A. Vansteenkiste, J. Leliaert, M. Dvornik, M. Helsen, F. Garcia-Sanchez, B. Van Waeyenberge, AIP Adv. **4**, 107133 (2014)
29. A.A. Thiele, Phys. Rev. Lett. **30**, 230 (1973)
30. A.A. Thiele, J. Appl. Phys. **45**, 377 (1974)
31. L. Berger, Phys. Rev. B **33**, 1572 (1986)
32. A. Thiaville, Y. Nakatani, Domain wall dynamics in nanowires and nanostrips, in *Spin Dynamics in Confined Magnetic Structures III* (Springer, Berlin, 2006), pp. 161–206
33. J.F. Dillon Jr., *Magnetism*, vol. III (Academic Press, New York, 1963), pp. 415–464
34. Y. Nakatani, A. Thiaville, J. Miltat, J. Magn. Magn. Mater. **290–291**, 750 (2005)
35. E. Jué, A. Thiaville, S. Pizzini, J. Miltat, J. Sampaio, L.D. Buda-Prejbeanu, S. Rohart, J. Vogel, M. Bonfim, O. Boulle, S. Auffret, I.M. Miron, G. Gaudin, Phys. Rev. B **93**, 014403 (2016)
36. W. Döring, Z. Naturforsch. **3a**, 373 (1948)
37. G.M. Wysin, F.G. Mertens, Equations of motion for vortices in 2-D easy-plane magnets, in *Nonlinear Coherent Structures in Physics and Biology* (Springer, Berlin, 1991)
38. G.M. Wysin, F.G. Mertens, A.R. Völkel, A.R. Bishop, Mass and momentum for vortices in two-dimensional easy-plane magnets, in *Nonlinear Coherent Structures in Physics and Biology* (Plenum, New York, 1994)

39. F.G. Mertens, A.R. Bishop, Dynamics of vortices in two-dimensional magnets, in *Nonlinear Science at the Dawn of the 21st Century* (Springer, Berlin, 2000), pp. 137–170
40. W. Koshiba, N. Nagaosa, *New J. Phys.* **18**, 045007 (2016)
41. A.P. Malozemoff, J.C. DeLuca, *Appl. Phys. Lett.* **26**, 719 (1975)
42. A.A. Thiele, *J. Appl. Phys.* **47**, 2759 (1976)
43. J.C. Slonczewski, *J. Magn. Magn. Mater.* **12**, 108 (1979)
44. S. Komineas, N. Papanicolaou, *Phys. D* **99**, 81 (1996)
45. A. Thiaville, Y. Nakatani, F. Piéchon, J. Miltat, T. Ono, *Eur. Phys. J. B* **60**, 15 (2007)
46. V.S. Gornakov, L.M. Dedukh, V.I. Nikitenko, V.T. Synogach, *Sov. Phys. JETP* **63**, 1225 (1986)
47. L.J. Schewe, H.R. Irons, W.E. Anderson, in *AIP Conference Proceedings*, vol. 18, p. 1383 (1974)
48. O. Bostanjoglo, T. Rosin, *Phys. Stat. Sol. A* **57**, 561 (1980)
49. B.E. Argyle, B. Petek, M.E. Re, F. Suits, D.A. Herman, *J. Appl. Phys.* **64**, 6595 (1988)
50. B.E. Argyle, E. Terrenzio, J.C. Slonczewski, *Phys. Rev. Lett.* **53**, 190 (1984)
51. Y.P. Kabanov, L.M. Dedukh, V.I. Nikitenko, *JETP Lett.* **49**, 637 (1989)
52. V.S. Gornakov, V.I. Nikitenko, I.A. Prudnikov, *JETP Lett.* **50**, 513 (1990)
53. J.C. Slonczewski, *J. Appl. Phys.* **44**, 1759 (1973)
54. J.C. Slonczewski, *J. Appl. Phys.* **45**, 2705 (1974)
55. B.E. MacNeal, F.B. Humphrey, *IEEE Trans. Magn.* **15**, 1272 (1979)
56. K. Patek, A. Thiaville, J. Miltat, *Phys. Rev. B* **49**, 6678 (1994)
57. J.C. Slonczewski, A.P. Malozemoff, O. Voegeli, in *AIP Conference Proceedings* vol. 10, p. 458 (1973)
58. J.J. Fernandez de Castro, F.J. Friedlaender, D. Musselman, J.A. Nyenhuis, *IEEE Trans. Magn.* **23**, 3388 (1987)
59. J.A. Nyenhuis, F.J. Friedlaender, H. Sato, *IEEE Trans. Magn.* **19**, 1796 (1983)
60. C.A. Jones, M.V.C. Stroomer, O. Voegeli, F.J. Friedlaender, *IEEE Trans. Magn.* **15**, 926 (1979)
61. J.C. Slonczewski, *J. Appl. Phys.* **50**, 7850 (1979)
62. A.P. Malozemoff, J.C. Slonczewski, *IEEE Trans. Magn.* **11**, 1091 (1975)
63. B.E. Argyle, S. Maekawa, P. Dekker, J.C. Slonczewski, in *AIP Conference Proceedings*, vol. 34, p. 131 (1976)
64. A.P. Malozemoff, S. Maekawa, *J. Appl. Phys.* **47**, 3321 (1976)
65. S. Maekawa, P. Dekker, in *AIP Conference Proceedings*, vol. 34, p. 148 (1976)
66. F.B. Hagedorn, *J. Appl. Phys.* **45**, 3129 (1974)
67. A. Thiaville, L. Arnaud, F. Boileau, G. Sauron, J. Miltat, *IEEE Trans. Magn.* **24**, 1722 (1988)
68. A. Thiaville, J. Ben Youssef, Y. Nakatani, J. Miltat, *J. Appl. Phys.* **69**, 6090 (1991)
69. S. Konishi, K. Matsuyama, I. Chida, S. Kubota, H. Kawahara, M. Ohbo, *IEEE Trans. Magn.* **20**, 1129 (1984)
70. K. Mizuno, H. Matsutera, H. Kawahara, Y. Hidaka, *IEEE Trans. Magn.* **26**, 2520 (1990)
71. M.V. Chetkin, V.B. Smirnov, A.F. Novikov, I.V. Parygina, A.K. Zvezdin, S.V. Gomonov, *Sov. Phys. JETP* **67**, 2269 (1988)
72. A. Thiaville, J. Miltat, *J. Magn. Magn. Mater.* **104–107**, 335 (1992)
73. A. Thiaville, J. Miltat, *Europhys. Lett.* **26**, 1006 (1994)
74. Y. Maruyama, T. Ikeda, R. Suzuki, *IEEE Trans. J. Magn. Jpn.* **4**, 730 (1989)
75. W.J. Tabor, A.H. Bobeck, G.P. Vella-Coleiro, A. Rosencwaig, *Bell Syst. Tech. J.* **51**, 1427 (1972)
76. A. Rosencwaig, W.J. Tabor, T.J. Nelson, *Phys. Rev. Lett.* **29**, 946 (1972)
77. S. Konishi, *IEEE Trans. Magn.* **19**, 1838 (1983)
78. J. Haisma, K.L.L. van Mierloo, W.F. Druyvesteyn, U. Enz, *Appl. Phys. Lett.* **27**, 459 (1975)
79. C.Y. You, I.M. Sung, B.K. Joe, *Appl. Phys. Lett.* **89**, 222513 (2006)
80. D. Navas, C. Nam, D. Velazquez, C.A. Ross, *Phys. Rev. B* **81**, 224439 (2010)
81. J.Y. Chauleau, B.J. McMorran, R. Belkhou, N. Bergeard, T.O. Mentes, M.A. Niño, A. Locatelli, J. Unguris, S. Rohart, J. Miltat, A. Thiaville, *Phys. Rev. B* **84**, 094416 (2011)
82. H. Kronmüller, M. Fähnle, *Micromagnetization and the Microstructure of Ferromagnetic Solids* (Cambridge University Press, Cambridge, 2003)

83. R.D. McMichael, M.J. Donahue, IEEE Trans. Magn. **33**, 4167 (1997)
84. J.Y. Chauleau, R. Weil, A. Thiaville, J. Miltat, Phys. Rev. B **82**, 214414 (2010)
85. J.Y. Chauleau, Textures magnétiques et parois de domaines: les objets du transfert de spin. Ph.D. thesis, Université Paris-Sud, 2010
86. O. Tchernyshyov, G.W. Chern, Phys. Rev. Lett. **95**, 197204 (2005)
87. G.W. Chern, H. Youk, O. Tchernyshyov, J. Appl. Phys. **99**, 08Q505 (2006)
88. D.J. Clarke, O.A. Tretiakov, G.W. Chern, Y.B. Bazaliy, O. Tchernyshyov, Phys. Rev. B **78**, 134412 (2008)
89. H.A.M. van den Berg, IBM, J. Res. Develop. **33**, 540 (1989)
90. T. Ono, H. Miyajima, K. Shigeto, K. Mibu, N. Hosoito, T. Shinjo, Science **284**, 468 (1999)
91. D. Atkinson, D.A. Allwood, G. Xiong, M.D. Cooke, C.C. Faulkner, R.P. Cowburn, Nature Mater. **2**, 85 (2003)
92. J.Y. Lee, K.S. Lee, S. Choi, K.Y. Guslienko, S.K. Kim, Phys. Rev. B **76**, 184408 (2007)
93. G.D. Beach, C. Nistor, C. Knutson, M. Tsoi, J.L. Erskine, Nat. Mater. **4**, 741 (2005)
94. J. Yang, C. Nistor, G.S.D. Beach, J.L. Erskine, Phys. Rev. B **77**, 014413 (2008)
95. M. Hayashi, L. Thomas, C. Rettner, R. Moriya, S.S.P. Parkin, Nat. Phys. **3**, 21 (2007)
96. S. Glathe, R. Mattheis, D.V. Berkov, Appl. Phys. Lett. **93**, 072508 (2008)
97. Y. Nakatani, A. Thiaville, J. Miltat, Nat. Mater. **2**, 521 (2003)
98. L. Thomas, M. Hayashi, X. Jiang, R. Moriya, C. Rettner, S. Parkin, Nature **443**, 197 (2006)
99. S. Zhang, Z. Li, Phys. Rev. Lett. **93**, 127204 (2004)
100. L. Heyne, M. Kläui, D. Backes, T.A. Moore, S. Krzyk, U. Rüdiger, L.J. Heyderman, A.F. Rodríguez, F. Nolting, T.O. Mentes, M. Niño, A. Locatelli, K. Kirsch, R. Mattheis, Phys. Rev. Lett. **100**, 066603 (2008)
101. M. Kläui, P.O. Jubert, R. Allenspach, A. Bischof, J.A.C. Bland, G. Faini, U. Rüdiger, C.A.F. Vaz, L. Vila, C. Vouille, Phys. Rev. Lett. **95**, 026601 (2005)
102. M. Hayashi, L. Thomas, C. Rettner, R. Moriya, X. Jiang, S.S.P. Parkin, Phys. Rev. Lett. **97**, 207205 (2006)
103. N. Vernier, D.A. Allwood, D. Atkinson, M.D. Cooke, R.P. Cowburn, Europhys. Lett. **65**, 526 (2004)
104. S.S.P. Parkin, M. Hayashi, L. Thomas, Science **320**, 190 (2008)
105. G.E. Volovik, J. Phys. C Solid State Phys. **20**, L83 (1987)
106. S.E. Barnes, S. Maekawa, *Concepts in Spin Electronics* (Oxford University Press, Oxford, 2006)
107. S.A. Yang, G.S.D. Beach, C. Knutson, D. Xiao, Q. Niu, M. Tsoi, J.L. Erskine, Phys. Rev. Lett. **102**, 067201 (2009)
108. S.S.L. Zhang, S. Zhang, Phys. Rev. B **82**, 184423 (2010)
109. S. Jamet, N. Rougemaille, J.C. Toussaint, O. Fruchart, *Magnetic Nano- and Microwires*, chap. 25 (Elsevier, Amsterdam, 2015), pp. 783–811
110. H. Forster, T. Schrefl, W. Scholz, D. Suess, V. Tsiantos, J. Fidler, J. Magn. Magn. Mater. **249**, 181 (2002)
111. R. Hertel, J. Magn. Magn. Mater. **249**, 251 (2002)
112. A. Hubert, J. Magn. Magn. Mater. **2**, 25 (1976)
113. S. Da Col, S. Jamet, N. Rougemaille, A. Locatelli, T.O. Mentes, B. Santos Burgos, R. Afid, M. Darques, L. Cagnon, J.C. Toussaint, O. Fruchart, Phys. Rev. B **89**, 180405(R) (2014)
114. R. Hertel, J. Kirschner, Phys. B **343**, 206 (2004)
115. R. Hertel, J. Kirschner, J. Magn. Magn. Mater. **278**, L291 (2004)
116. C. Andreas, A. Kákay, R. Hertel, Phys. Rev. B **89**, 134403 (2014)
117. R. Hertel, J. Phys. Condens. Matter **28**, 483002 (2016)
118. P. Landeros, A.S. Núñez, J. Appl. Phys. **108**, 033917 (2010)

Chapter 3

Magnetic Vortices



Carolin Behncke, Christian F. Adolff and Guido Meier

Abstract Magnetic vortices are topological objects found in magnetic thin films and microstructures. The study of vortices has attracted much attention for their fundamental beauty and because vortices could be constituents of non-volatile storage and sensing devices as well as of radiofrequency and neuro-inspired devices. Many important experimental, theoretical, and simulational contributions have been made to understand the intricate details of the statics and dynamics of magnetic vortices. In this chapter we start from first experimental observations and proceed to the occurrence of vortices, their static properties as well as their topology. The polarization of vortex cores and the circularity of their in-plane magnetization are introduced. The minimization of micromagnetic energy contributions that lead to an out-of-plane core region and an in-plane circulation of magnetization are discussed, along with geometries for confinement and their response in static external magnetic fields. We analyze stray fields in the vicinity of a vortex, their hysteresis as well as their thermal stability before we address dynamic properties. The relation between handedness and sense of gyration are described and the harmonic oscillator model for small excitations is introduced. Then modifications of the oscillator model for strong excitations including nonlinearities are mentioned. We proceed to the core switching process that includes the creation, annihilation, and fusion of vortices and their topological counterpart the antivortex. Harmonic and pulsed excitations with fields and currents are discussed as well as the interaction of coupled vortices, where a vortex can be considered as a building block, for linear chains, vortex molecules and magnonic vortex crystals. The chapter concludes with current perspectives and challenges in the field of magnetic vortices.

C. Behncke (✉) · C. F. Adolff

Institut für Angewandte Physik und Zentrum für Mikrostrukturforschung,
Jungiusstr. 11, 20355 Hamburg, Germany
e-mail: cbehncke@physnet.uni-hamburg.de

C. F. Adolff

e-mail: cadolff@physnet.uni-hamburg.de

G. Meier

Max-Planck Institute for the Structure and Dynamics of Matter,
Luruper Chaussee 149, 22761 Hamburg, Germany
e-mail: gmeier@mpsd.mpg.de

3.1 Introduction and Motivation

3.1.1 Occurrence and Evidence

Vortices are fundamental topological objects found in many systems and within a large span of length scales. They form in stirred fluids and may be observed in phenomena such as smoke rings and air swirls in the wake of a starting aircraft. An example for vortices on the kilometer scale are low- or high-pressure areas that control the dynamics of the weather. Here, the vortex is called typhoon, hurricane or cyclone depending on the area of appearance and expresses as large scale flows of air mass around centers of low or high pressure. It is noteworthy that also the topological counterpart of the vortex, the so-called antivortex is important for the dynamics of the weather. The structure of these singularities results from the balance between the pressure-gradient [1] and the Coriolis force [2] and can be quantified by a vector field where the velocity of the air mass is described by a three-dimensional vector for every point in space. The air flow's sense of circulation depends on the orientation of the Coriolis force and the pressure-gradient force. While the circulation is counterclockwise for cyclones on the northern hemisphere, it is clockwise on the southern hemisphere due to the inversion of the direction of the Coriolis force. Thus, there are four possible combinations of high- and low-pressure areas with counterclockwise or clockwise circulation that depend on the hemisphere of the earth. Similar properties can be identified in magnetic vortices that emerge in ferromagnetic micro- and nanostructures. Rather than by the air flow, they are characterized by the orientation of the magnetic moments circulating in-plane around the center position of the ferromagnetic structure. In their center region the magnetic moments point out-of-plane, either up or down. This region is called vortex core and the corresponding state parameter is called polarization and can be compared to low or high pressures in the center of cyclones. In comparison to vortices in meteorology, magnetic vortices are twelve orders of magnitude smaller.

Figure 3.1 shows the magnetization configuration of a spiral skyrmion in comparison with a magnetic vortex. The word skyrmion is used to denote similar mathematical objects in different contexts, from elementary particles to liquid crystals, Bose-Einstein condensates and quantum Hall magnets [3, 4]. Magnetic skyrmions represent topologically stable chiral spin structures with particle-like properties [5]. Chapters 5 and 4 are dedicated to bulk and thin film skyrmions, respectively. The structure of skyrmions cannot be continuously deformed to a ferromagnetic or other magnetic state, thus skyrmions are topologically protected [6]. One important difference to vortices is that all combinations of circularity and polarity are possible for vortices because they lack symmetry breaking energy contributions, i.e. chiral interactions, known as Dzyaloshinskii-Moriya interactions [7, 8]. Having this difference in mind a vortex can be considered half a chiral skyrmion as it is sketched in Fig. 3.1. This notion can be described more specifically by the winding number that is introduced later in this chapter.

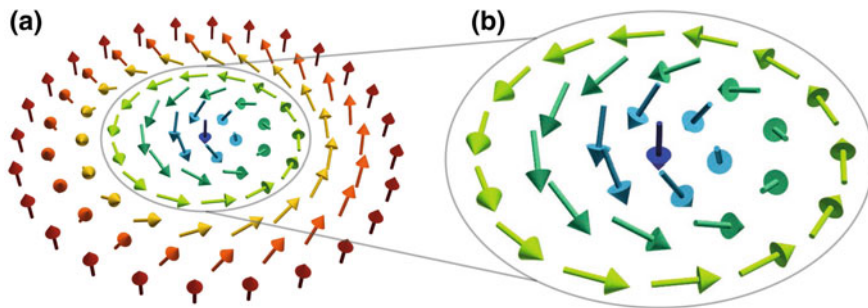


Fig. 3.1 Schematics of the magnetization configuration of **a** a spiral skyrmion and **b** a magnetic vortex

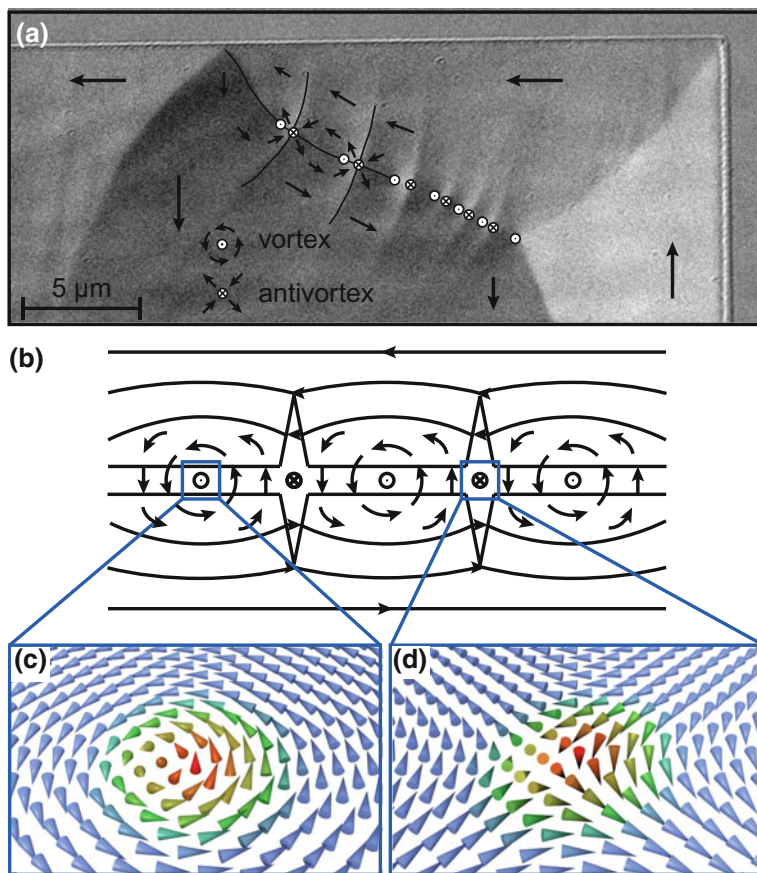


Fig. 3.2 **a** Edge of a large permalloy rectangle observed by Kerr microscopy. The domains align along the edges. The chain of vortices and antivortices forming a cross-tie wall in the middle is partially marked. **b** Schematic of a cross tie domain wall. **c** Magnetization distribution of a magnetic vortex core and **d** an antivortex core. **a** adapted from [14]. **c, d** by courtesy of Michael Martens

Magnetic vortices as singularities in domain walls in thin films have been known for many decades and have been studied in great detail [9–13]. Chapter 2 is dedicated to the topic of domain walls. Here we will focus on the aspects that are relevant for magnetic vortices. Different types of domain walls occur between magnetic domains. The wall types differ in their internal magnetization configuration. The most common wall is the Bloch wall where the magnetization turns in the plane of the wall. In thinner samples where the film thickness approaches the wall width, Néel walls begin to form. In Néel walls the magnetization turns perpendicular to the wall plane. The transition occurs to avoid surface charges that are generated by the Bloch wall. The reduction of energies in the wall can also lead to more complex wall structures. These so-called cross-tie walls contain magnetic singularities named vortices and antivortices. An example is shown in Fig. 3.2. This wall type contains Bloch lines at the positions of the vortices and antivortices and Néel lines in between and can thus be considered as a mixture of a Bloch and a Néel wall. In thin films the confinement is one-dimensional. A two-dimensional confinement of the magnetization as in nanowires forces the magnetic moments of different magnetic domains to point against each other, either head-to-head or tail-to-tail. The magnetization can rotate as in a Néel wall. These transverse walls as they are called in nanowires preferentially occur in narrow and thin wires. In wider nanowires vortex walls are observed. Figure 3.3a shows a vortex wall, where the magnetic moments curl around a singularity in the center. In even wider wires double vortex walls occur, as exemplarily shown in Fig. 3.3b.

The isolated magnetic vortex and antivortex have been studied intensively more recently [16–22]. The main strategy to isolate a vortex or an antivortex is to make use of the shape anisotropy in soft magnetic materials. Here, the demagnetization energy governs the magnetic state of the nano- or microstructure leading to a stabilization of a single vortex. Examples of microstructures isolating a vortex and an antivortex are shown in Fig. 3.4. It turns out that the stabilization of the vortex is rather straight

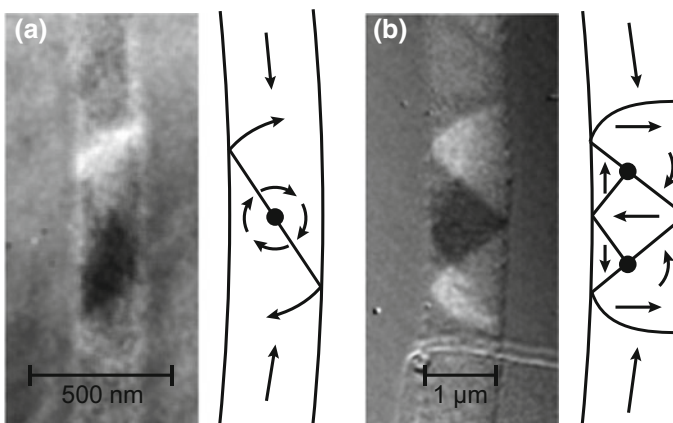


Fig. 3.3 X-ray magnetic circular dichroism (XMCD) signal (left) and schematic (right) of a vortex wall (a) and of a double vortex wall (b). Adapted from [15]

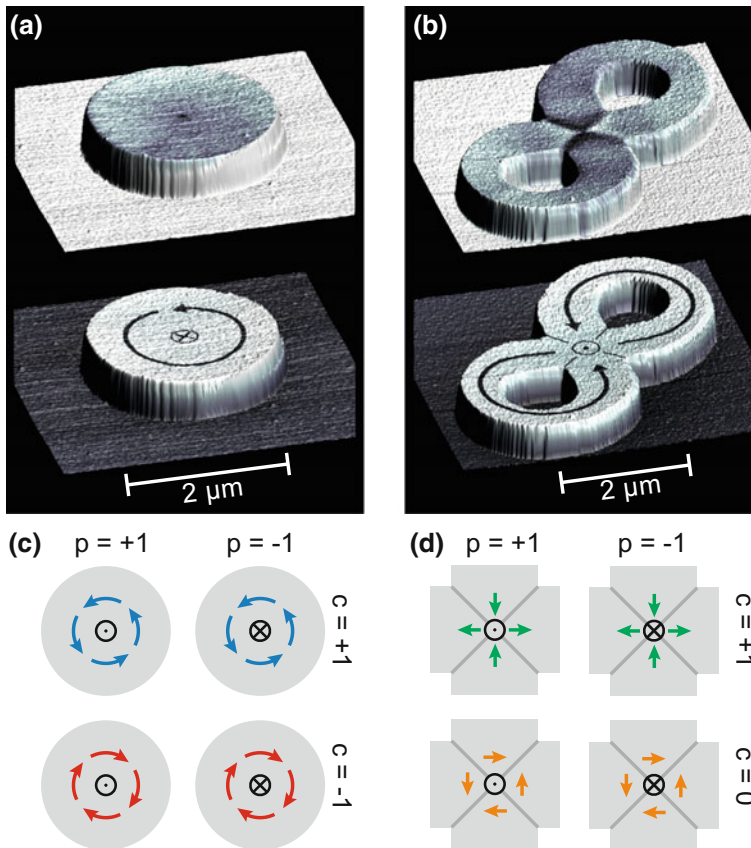


Fig. 3.4 **a** Microdisk in the vortex state and **b** microstructure in the antivortex state. The topology is overlaid with the corresponding magnetic-force micrograph (upper) and schematic of the magnetization state (lower). The microstructures consist of permalloy ($\text{Ni}_{80}\text{Fe}_{20}$) and have a thickness of 59 nm. **c** All four circularity and polarity states of the magnetic vortex. **d** Possible polarity states of a magnetic antivortex with the c -values $c = 1$ and $c = 0$. **a** and **b** are adapted from [29]

forward in thin microdisks with a diameter of a few micrometers [16], while the stabilization of an isolated antivortex is more elaborate [20, 21, 23, 24]. For vortices intentional symmetry breaking can be used to gain control over the circularity as well as the relation between circularity and polarity [25–28]. Figure 3.4a, b present atomic-force and magnetic-force micrographs of microstructures that contain these singularities. Figure 3.4c depicts all four possible states of the magnetic vortex while Fig. 3.4d shows the two possible polarity states of a magnetic antivortex for two experimentally interesting c values. We will come back to these important parameters,

namely circularity and polarization, in much more detail because they determine a wealth of static and dynamic properties of magnetic vortices and antivortices¹.

3.1.2 Applications

As a further motivation we list a number of possible applications as well as some current and future directions in the field of magnetic vortices. It has been shown, that vortices feature an oscillatory motion similar to the one of the classical harmonic oscillator [30, 31]. In combination with spin polarized currents that are available in ferromagnetic materials vortices can be applied as spin-torque oscillators [32, 33]. The latter are discussed in more detail in Chapters 10 and 11. The four possible combinations of the circulation and the polarization in vortices are energetically degenerate. In principle they can be attributed to two binary units of information (bit) making them promising candidates for potential storage devices. In the suggested device named vortex or antivortex random access memory (VRAM or AVRAM) the write and read processes are implemented by core switching and gyration [34, 35]. Thus, it is very important to obtain a full understanding of all excitation regimes starting from linear over nonlinear excitations to the switching process itself that occurs on the picosecond time scale [36]. Even more advanced excitation schemes of the core via interaction with spin waves and higher order modes have recently been studied [37]. The rather time consuming gyrotropic eigenmode at sub-GHz frequencies is avoided and a fast spin-wave mediated magnetic vortex core reversal in the deep sub-nanosecond regime can be achieved [38]. The interaction with spin waves also enables to use magnetic vortex cores as tunable spin-wave emitters [39]. In addition, magnetic vortices can interact via magnetostatic stray fields [40–42] leading to remarkable properties in tailored arrangements of magnetic vortices. Such properties can be linked to the field of magnonics [43, 44] that constitutes research on spin waves which is discussed in Chapter 10. Within this field, magnonic crystals are described as artificial wave-transmitting lattices that provide an alternating modulation of their magnetic properties. For magnetic vortices this alternating modulation can be obtained, which we will discuss in more detail. Magnetic vortices have been observed in structured ferromagnets of down to $100 \times 100 \text{ nm}^2$ [45]. Although this cell size is larger than the bit cells of state-of-the art memories, hard disk drives or solid state drives with NAND flash sizes of $22 \times 22 \text{ nm}^2$ [46], for the magnetic vortex these limits could be overcome by a volumetric strategy. Here, multiple layers would be fabricated onto a single substrate resulting in closely packed arrangements of vortices. This motivates

¹The word 'vortex' addresses the magnetization of the 'vortex core' with its out-of-plane component at the center pointing either up or down plus the surrounding magnetization curling in the plane either clockwise or counter-clockwise. We will try to be as precise as possible to distinguish the 'vortex core' from the 'vortex' as well as from the magnetization of a 'vortex state' within a microdisk or a microsquare, where the latter case even includes four domains and four domain walls. For the sake of readability we will nonetheless sometimes just write vortex to denote one of the three entities, which should then be clear from the context

to understand nearest neighbor interactions in the third dimension [47, 48]. An even more visionary application is investigated in [49], where biofunctionalized magnetic-vortex microdisks are studied for targeted cancer-cell destruction. In this approach an alternating magnetic field is applied to microdisks that contain vortices, creating an oscillation, which transmits a mechanical force to the cell. The vortex-mediated stimulus efficiently compromises the integrity of the cellular membrane and can initiate the programmed death of cancer cells. Recently the vortex attracted interest as a building block for a robust sensor application in the automotive industry, where, e.g., a modulated magnetic field determines the speed or the velocity of a component such as a wheel of a car [50]. This magneto-resistive device comprises a magnetic free layer with a spontaneously generated vortex and a magnetic reference layer having a non-closed flux magnetization pattern. Finally a very recent demonstration of neuro inspired vortex spin torque nano-oscillators comprising a magnetic tunnel junction caught much attention [51, 52]. Here vortices can be used to achieve spoken-digit recognition with an accuracy similar to that of state-of-the-art neural networks that open up a path to fast, parallel, on-chip computation based on networks of oscillators. These examples could go far beyond niche applications and could become mass products, which would benefit from the outstanding properties of these fundamental topological objects named magnetic vortices.

3.2 Static Properties

In vortices the winding of the magnetization around the center of the structure defines the so-called circularity c , while the magnetization direction of the center of the core is described by the polarization p . When ϕ is the angle of the local magnetization vector with respect to the x -axis as shown in Fig. 3.5 and β is the angle of the position vector \mathbf{r} with respect to the local magnetization, the circularity is defined as follows

$$\phi(\beta) = n\beta + \phi_0 \quad \text{and} \quad \phi_0 = \frac{c\pi}{2}, \quad (3.1)$$

where the curling of the magnetization is defined by the winding number n and the orientation of the magnetization pattern is given by the offset angle ϕ_0 . For vortices the winding number is $n = +1$, and the magnetization curls around the center in a closed loop, thus for $\phi = c\pi/2$ only two values are possible, i.e. $c = \pm 1$ and c is called circularity as it determines the rotation direction of the magnetization. For the topological counterparts, the antivortices with the winding number $n = -1$, the local magnetization curls in the opposite sense around the center, see Fig. 3.5b. The antivortex is not chiral, thus c can have any value in the interval $c \in [-2, 2[$ and represents the orientation of the antivortex.

From the mathematical definition of the static magnetization configuration we now turn to the realization of isolated confined vortices and antivortices in soft ferromagnetic thin film elements. Magnetic vortices emerge in ferromagnetic microstructures.

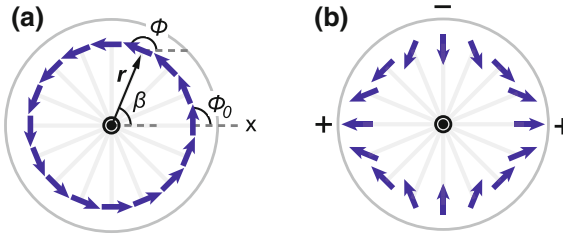


Fig. 3.5 Schematic magnetization pattern of **a** a vortex with $c = +1$ ($n = +1$) and **b** an antivortex with $c = +1$ ($n = -1$). Shown are the angle β of the position vector \mathbf{r} , the angle of the local magnetization vector ϕ , and the offset angle ϕ_0 . The magnetic flux is not closed for the antivortex, indicated by the magnetic charges representing magnetic poles. Adapted from [14]

As for all magnetic solids, the magnetic properties of such structures are characterized by the magnetic moment per volume, i.e., the magnetization \mathbf{M} . The magnetic induction \mathbf{B} of Maxwell's equations can be calculated from the magnetization and the external magnetic field \mathbf{H} according to

$$\mathbf{B} = \mu_0(\mathbf{H} + \mathbf{M}), \quad (3.2)$$

where $\mu_0 = 4\pi \times 10^7$ Vs/(Am) is the magnetic vacuum permeability. Unlike in diamagnetic or paramagnetic materials, the magnetic moments of the atoms in a ferromagnetic material are not independent, but spontaneously align parallel to each other inside of small regions, the so-called magnetic domains [19]. Ferromagnetic microstructures enclose a few or only a single domain. The absolute value of the magnetization inside such a domain $M_S = |\mathbf{M}|$, a material specific constant called saturation magnetization. Permalloy (Ni₈₀Fe₂₀), a widely used soft-magnetic material, which due to its low anisotropy simplifies the observation and investigation of the phenomena discussed in this chapter, has a value of $M_S = 8.6 \times 10^5$ A/m. Magnetic microstructures can be described in the micromagnetic model [53] that is based on the treatment of the magnetization as a continuous vector field $\mathbf{M}(\mathbf{r})$. Magnetic vortex states can be present in various magnetic microstructures, including disks, flat rectangular structures or wires [16, 54, 55]. Vortices are often enclosed in thin microdisks as depicted in Fig. 3.4a. Examples of microstructures that contain an isolated vortex or antivortex are depicted in Fig. 3.6. In the micromagnetic model the emergence of the vortex as the magnetic ground state can be motivated by the minimization of all micromagnetic energies. For soft magnetic microdisks two micromagnetic energies are dominant in the absence of external magnetic fields. The exchange energy models the parallel alignment of the magnetic moments in ferromagnetic materials. It is increased by local inhomogeneities of the magnetization. The demagnetization energy describes the interaction of the magnetization with the stray-field that is generated by the microstructure itself. The stray-field \mathbf{H}_d is a result of (3.2) and Maxwell's second equation. According to

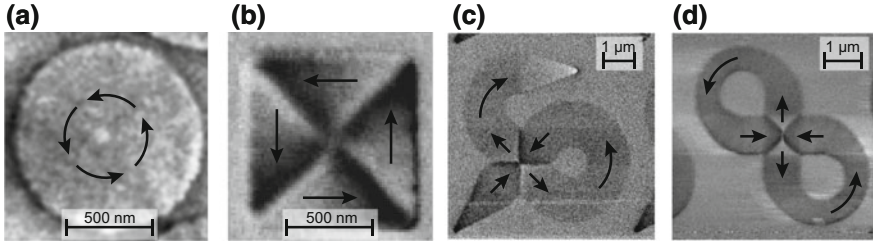


Fig. 3.6 Magnetic force micrographs that show microstructures in the magnetic vortex state (a, b) and in the magnetic antivortex state (c, d). **b** is adapted from [42] and **c** and **d** from [21]

$$\nabla \mathbf{B} = \mu_0 \nabla \cdot (\mathbf{H}_d + \mathbf{M}) = 0, \quad (3.3)$$

sources of the stray field \mathbf{H}_d are sinks of the magnetization \mathbf{M} . They are also called magnetic charges. The demagnetization energy is reduced when surface charges are avoided [56]. It follows that the magnetization aligns parallel to the surface of the microstructure. This effect is known as shape anisotropy and forces the magnetization to lie in the plane of the thin disk and align parallel to the border. In the core region the curling magnetization would lead to large angles between neighboring magnetic moments being unfavorable with regard to the exchange energy. Thus, the magnetization tilts out-of-plane in the core region and the magnetic vortex forms as the magnetic ground state in the disk. The diameter of the core has been determined by spin-polarized scanning tunneling microscopy to be only several nanometers [17]. Although the exact value depends on the exchange stiffness and the saturation magnetization, i.e. the exchange length as introduced by Kronmüller [56], core diameters are typically in the nanometer regime and are thus much smaller than the surrounding whirl of in-plane magnetization. Still, the core governs the dynamics of magnetic vortices as we will see in Sect. 3.3.

When an external magnetic field is applied, a third micromagnetic energy comes into play, the so-called Zeeman energy. It is minimized by a parallel alignment of the magnetization to the applied field. For very strong homogeneous and static magnetic fields the Zeeman energy becomes dominant over all other micromagnetic energies. Consequently, the magnetization of the whole disk aligns parallel to the field. The magnetic vortex state is destroyed. For smaller field strengths the vortex state is still present but the core region is deflected from the center of the disk in order to enlarge the number of magnetic moments that are aligned parallel to the field [57]. When the static magnetic field is rotated the deflection direction depends on the curling direction of the magnetization in the disk, i.e., the circularity c of the vortex. As depicted in Fig. 3.7 a static magnetic field \mathbf{H} that points initially in negative x -direction deflects a clockwise curling vortex ($c = -1$) in positive y -direction. By repetition of this consideration for static magnetic fields in three other directions in Fig. 3.7 we find that the vortex rotates with the rotation direction of the static external magnetic field. Figure 3.7b indicates the different reaction of an antivortex to the application of a static magnetic field. The antivortex rotates against the rotation

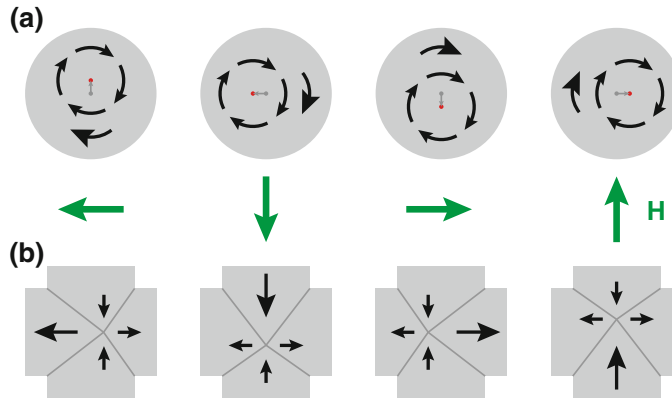


Fig. 3.7 Core deflection as a consequence of the application of a static magnetic field \mathbf{H} for **a** a magnetic vortex and **b** a magnetic antivortex

direction of the external field. This has strong implications on the statics and dynamics of antivortices [18, 20–24, 35, 58–60]. Research on antivortices is very interesting on its own, but goes beyond the scope of this chapter. Hence, in the remainder of the chapter we will focus on vortices. As mentioned before, the second state parameter of the magnetic vortex is the out-of-plane direction of the vortex core in the center of the disk labeled polarization p . For positive polarization $p = +1$, the magnetization of the core points in positive z -direction and for negative polarization $p = -1$ it points in negative z -direction. The polarization comes into play when the magnetic field that deflects the vortices in Fig. 3.7 is switched off instantaneously. We will discuss these dynamics in Sect. 3.3.

3.2.1 Stray-Fields

An important feature of the vortex state is that it almost perfectly closes the magnetic flux inside a sample. Thus, in the relaxed state without external fields almost no stray fields emerge from the structure. For microdisks only in the region of the core significant stray fields appear outside. This is the reason why in magnetic-force micrographs as in Fig. 3.6a only in the core region a magnetic contrast is observed. If an external field is applied the original flux closure is violated and a stray field outside of the structure appears. Figure 3.8 shows micromagnetic simulations of microdisks and -squares with a vortex in the center plus the stray fields that surround the structure. The stray fields outside of the microdisks almost perfectly resemble a dipolar field, see Fig. 3.8a, b. Microsquares on the other hand typically contain a Landau structure that comprises besides the vortex also four domains and four 90° domain walls. This leads to additional stray fields above the structure giving rise to the magnetic-force microscopy signal shown in Fig. 3.6b. In addition also the stray fields on the sides

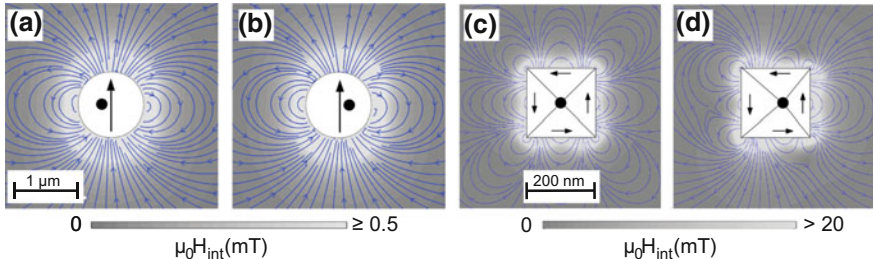
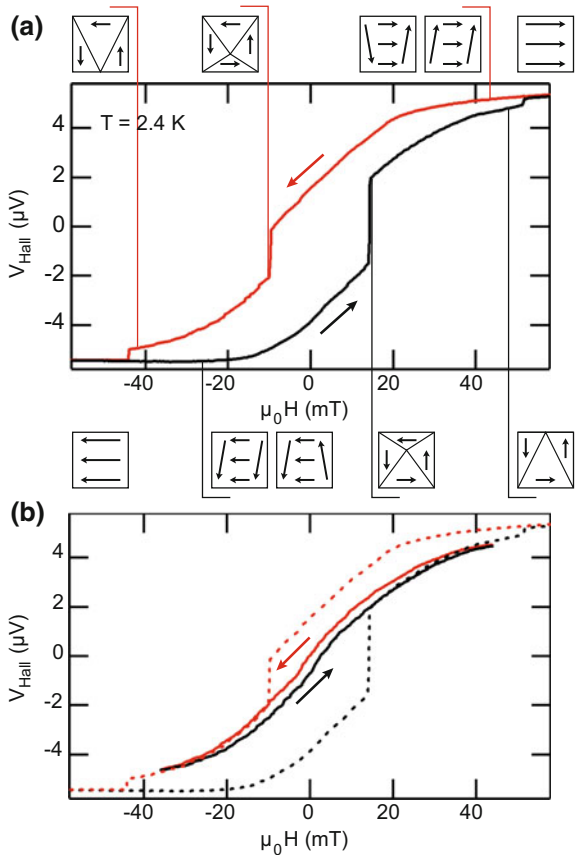


Fig. 3.8 Micromagnetic simulation of the stray field of **a** a disk with an off-centered vortex core with a circularity of $c = +1$, **b** a disk with an off-centered vortex core with $c = -1$, **c** a square in the Landau pattern with a vortex in the center, and **d** a square with an off-centered vortex core. Arrows outside the structure represent streamlines of the stray field. The black arrow in the disks in **a** and **b** show the direction of the in-plane average magnetization vector and the black points indicate the positions of the cores. Arrows inside the squares in **c** and **d** indicate the direction of the magnetization in the domains ($c = +1$). Figures **a** and **b** are adapted from [61] and **c** and **d** from [42]

of the microsquare show a more complicated symmetry as can be seen in Fig. 3.8c. However, if an external field moves the core in the square as calculated in Fig. 3.8d the overall shape of the stray field approximates again the field of a magnetic dipole. Only close to the microstructure, typically up to the distance of a side length, larger deviations from the dipole field occur. Consequently a microstructure that contains a magnetic vortex produces a rather small stray field in the relaxed state and an approximately dipolar field when the core is excited from its center position. This finding is important for the dynamics of interacting vortices that will be described in Sect. 3.4.

We now turn to Hall measurements that are capable of detecting the stray fields of single microstructures that contain a vortex. With this technique the hysteresis of an isolated magnetic vortex can be measured. Hall micromagnetometry measurements on permalloy squares are depicted in Fig. 3.9 [62]. It shows a typical Hall hysteresis curve of a $2 \times 2 \mu\text{m}^2$ square with a thickness of 20 nm. Coming from negative saturation, the Hall voltage, which corresponds to the stray-field of the microstructure increases continuously up to an external field of 17 mT, where a large steplike increase occurs. A further continuous increase of the Hall voltage is followed by a second, smaller steplike increase at 56 mT. In the opposite sweep direction, a similar magnetization reversal is observed with a large steplike reduction of the Hall voltage at -10 mT and a smaller reduction at -44 mT. The steps in the Hall hysteresis curve are identified as nucleation and annihilation of the vortex inside a Landau pattern. Repeated measurements show that the external fields required for vortex nucleation and annihilation are highly reproducible and well-defined within a full width at half maximum smaller than 0.5 mT. Figure 3.9b shows a minor loop between external fields of -38 mT and 44 mT. Prior to the measurement, the sample was first saturated in a strong negative field and then a field of 44 mT was applied. In both sweep directions of the minor loop, the Hall hysteresis curve is continuous and almost com-

Fig. 3.9 **a** Hall hysteresis of a Permalloy square at $T = 2.4$ K. The curve exhibits abrupt changes in the Hall voltage and thus in the average stray field underneath the microstructure. These steps correspond to irreversible changes in the magnetization as sketched. **b** Hall signal of the same microstructure for a minor loop between -38 mT and $+44$ mT for a Permalloy square. The dashed curves represent the full hysteresis. Reproduced from [62]



pletely reversible with only a small hysteretic contribution. Branches of the complete Hall hysteresis curve after the large steplike change of the Hall voltage are perfectly reproduced by the minor loop, and a continuous transition between the two branches including almost complete demagnetization of the sample in zero external field can be observed. Consequently, the minor loop is attributed to the distortion of a Landau pattern by increasing and reducing the size of the domain parallel to the external field of varying strength. Accordingly, the large steplike changes of the Hall voltage in the hysteresis curve represent the nucleation of the vortex and a Landau pattern. The annihilation of the vortex in external fields close to saturation is indicated by the small abrupt changes of the Hall voltage. The analysis shows that the magnetization reversal of the square is realized by nucleation, deflection, and annihilation of the vortex. The measurements shown in Fig. 3.9 are recorded at 2.4 K, which is the reason for the rather large nucleation and switching fields. It is interesting to investigate the nucleation process as a function of temperature, which has been done in similar approaches [63, 64]. Especially at elevated temperatures it was found by Östman et al. that the nucleation of the vortex can vanish and hysteresis free

remagnetization is observed. Details of this aspect of the magnetization process of vortices can be found in [64].

3.3 Dynamic Properties

We now describe the behavior of a magnetic vortex in case of time-dependent stimuli. Let us consider a constant magnetic field deflecting the vortex as in Fig. 3.7 that is switched off instantaneously. The micromagnetic energies change so that in the end the energetically most favorable configuration for the core is to be located in the center of the disk. This relaxed state is not reached directly but after a damped gyration of the vortex around the center of the disk [30], which is schematically depicted in Fig. 3.10. The gyration direction depends on the polarization of the vortex core. It is clockwise for negative polarization and counterclockwise for positive polarization. The circularity adds a phase to the gyration. All four possible cases are shown in Fig. 3.10. The gyration or gyrotropic mode is inherent to magnetic vortices and follows from the equation of motion, which will be discussed below. The frequency of the gyration depends on material parameters and the geometry of the disk [65]. For typical microstructures, e.g. permalloy disks with a radius of 1 μm and a thickness of 60 nm the resonance frequency of the gyrotropic mode is around 250 MHz. It is important to reduce the influence of pinning because otherwise the motion of the vortex core will be governed by local variations of the potential and not by the confinement of the microstructure [66, 67]. The gyrotropic mode can be excited in various ways using magnetic fields or electric currents [20, 36, 58, 68]. When excited at resonance the vortex core follows an approximately circular motion around the center of the disk.

The gyrotropic mode is described in the micromagnetic model by application of the equation of motion, i.e. the Landau-Lifshitz-Gilbert (LLG) equation, which is a differential equation for the magnetization $\mathbf{M}(\mathbf{r})$ [19, 69–71]

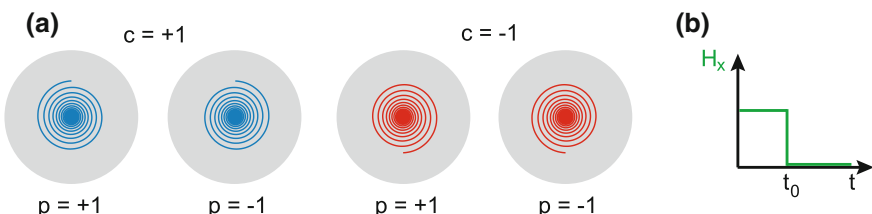


Fig. 3.10 Relaxation of a magnetic vortex subsequent to a deflection with a magnetic field in x -direction. **a** The vortex core performs a damped gyration to its equilibrium position at the center of the disk. The gyration direction depends on the polarization. A positive polarization $p = +1$ leads to a counterclockwise gyration. A negative polarization $p = -1$ leads to a clockwise gyration. The circularity determines the initial deflection of the vortex core. **b** Time dependence of the external magnetic field that initially deflects the vortex

$$\frac{d\mathbf{M}}{dt} = -\gamma [\mathbf{M} \times \mathbf{H}_{\text{eff}}] + \frac{\alpha}{M_S} \left[\mathbf{M} \times \frac{d\mathbf{M}}{dt} \right], \quad (3.4)$$

where $\gamma = \frac{\mu_0 g e}{2m_e}$ is the gyromagnetic ratio with the Landé factor $g \approx 2$ and the mass of the electron m_e , the Gilbert damping constant α , and the effective magnetic field H_{eff} .

Before we turn to the equation of motion in case of vortices we want to try to understand the dynamic reaction of a magnetic vortex to an instantaneously switched-on external magnetic field. Consider the vector-field representation of a vortex core in Fig. 3.11a for a vortex with $p = +1$ and $c = +1$ at time t_0 . In a gedankenexperiment we instantaneously switch on a homogeneous external magnetic field \mathbf{H} in y -direction, see Fig. 3.11. We assume a weakly damped system with $\alpha \ll 1$, which is often justified for soft magnetic materials. With that in mind we neglect the second term, i.e. the damping term in the LLG equation and examine the effect of the precession term. Application of $\frac{d\mathbf{M}}{dt} \propto \mathbf{H} \times \mathbf{M}$ on all vectors at time t_0 results in the next time step t_1 in the second vector field representation shown. We repeat this process recursively another two times yielding the four vector field representations

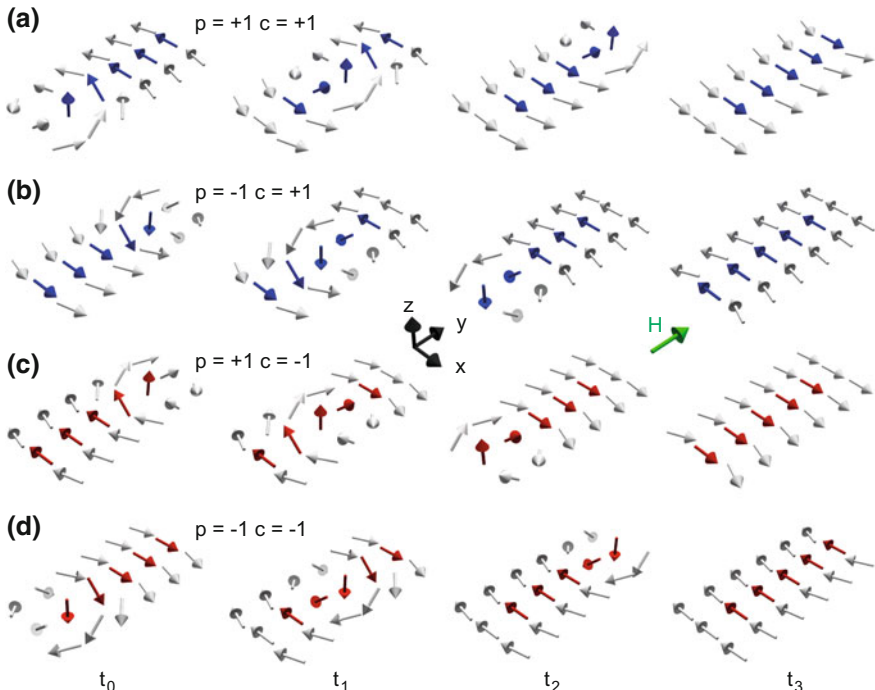


Fig. 3.11 Vector field representation of the reaction of a weakly damped magnetic vortex to switching on an external magnetic field in y -direction for the four possible polarity and circularity states. The initial movement of the magnetic vortex only depends on the handedness $c \cdot p$. Adapted from [29]

depicted in Fig. 3.11a. We observe that the core initially moves in the direction of the switched-on external magnetic field \mathbf{H} , i.e. in y -direction. We will see that this initial motion is in agreement with the full solution of the equation of motion. In Fig. 3.11b–d the other three cases for p and c are shown. The initial motion of the core is determined by the handedness $c \cdot p$. For $c \cdot p = -1$ as in Fig. 3.11b, the core initially moves in negative y -direction. In Fig. 3.11d the handedness $c \cdot p = 1$ again yields an initial motion in positive y -direction. The influence of the polarity alone sets in later when the gyrotropic mode evolves. These are important properties of vortex dynamics that we deduced here from rather simple considerations.

Using micromagnetic simulations that are based on the numerical solution of the LLG, the vortex dynamics can be predicted precisely. However, since the demagnetization energy leads to a mutual long-range coupling of all discretization cells, the numerical calculation is very time consuming. Even with the efficient implementation on graphics processing units [72] a simulation of the first 100 gyrations of a vortex contained in a standard-geometry disk can last for several days. Although the micromagnetic model with the LLG is very precise it is in most cases impracticable for the calculations of steady state motions of large arrangements of coupled magnetic vortices, which will be of importance. The Thiele model is a differential equation [73] that describes the vortex as a quasiparticle that is confined in a parabolic potential [31]. It can be deduced from the micromagnetic model and the LLG with the approximation that the magnetization is only translated but does not alter its overall form [74]. Thus, the deflection of the vortex core is synonymous with the deflection of the whole vortex. The task of calculating 100 gyrations of the vortex core in the Thiele model lasts only some milliseconds on a typical computer. Thus, the computing time can be reduced by several orders of magnitude with respect to the micromagnetic simulation. The Thiele model cannot explain polarization switching processes, which we will discuss in Sect. 3.3.2, because it assumes constant patterns of magnetization without internal excitation as a first principle. This is a major downside of the model when, e.g., collective polarization switching of magnetic vortices is investigated. In the experiments the switching is induced, when the vortex core reaches a velocity higher than 250 ms^{-1} [75]. This can only be understood in the micromagnetic model. Nevertheless, the Thiele model proved to be sufficient to explain many major findings in the field, which is the reason for us to recap some aspects of this model especially for the case of a magnetic vortex.

3.3.1 Thiele Model for Magnetic Vortices

²Originally the Thiele model was deduced from the LLG equation for the example of rigid magnetic bubbles in thin films [73] but it can also be adopted for magnetic vortices in thin-film elements [31]. The minimization of the sum E of the micromagnetic

²Figure 3.12 and parts of the text in this subchapter are reproduced from the Dissertation Thesis of C. F. Adolf [78].

energies is modeled by a force

$$\mathbf{F} = -\nabla E \quad (3.5)$$

that acts on the quasiparticle, i.e. the vortex at the position $\mathbf{x} = (x, y, z)^T$. This approach leads to the Thiele equation

$$(G_0^2 + \alpha^2 D_0^2) \dot{\mathbf{x}} = \mathbf{G} \times \mathbf{F} - \alpha D_0 \mathbf{F}. \quad (3.6)$$

Here, $\mathbf{G} = G_0 \mathbf{e}_z$ is the so-called gyrovector, and D_0 is the non-vanishing component of the diagonal dissipation tensor $D = \text{diag}(D_0, D_0, 0)$ [31]. Analytically G_0 and D_0 are given by [31, 61]:

$$D_0 = -\frac{2\pi\alpha\mu_0 M_S h \ln \frac{R}{a_{\text{core}}}}{\gamma}, \quad G_0 = -\frac{2\pi\mu_0 M_S h p}{\gamma}, \quad (3.7)$$

where γ is the gyromagnetic ratio and M_S is the material specific saturation magnetization. The radius and the height of the disk are denoted as R and h , respectively. The value of the parameter a_{core} is in the order of magnitude of the diameter of the vortex core. In the Thiele equation (3.6) two components add to the velocity $\dot{\mathbf{x}}$ of the vortex core. The first term on the right side describes the nature of the gyrotropic mode that moves the vortex perpendicular to the driving force \mathbf{F} . The second term depends on the dimensionless Gilbert damping parameter α and forces the vortex core back to its equilibrium position. It is a good approximation to assume that the magnetic vortex can only move in the x - y -plane. Thus only in-plane forces are considered and the z -component of the Thiele equation becomes zero. Then the equation can be represented in two dimensions:

$$(G_0^2 + \alpha^2 D_0^2) \dot{\mathbf{x}} = G_0 \tilde{r}_{90} \mathbf{F} - \alpha D_0 \mathbf{F}. \quad (3.8)$$

Here $\mathbf{x} = (x, y)^T$ is the deflection vector of the vortex core with respect to the center of the disk, \tilde{r}_{90} is a 90° rotation matrix in two dimensions, and $\mathbf{F} = (F_x, F_y)^T$ is the two-dimensional driving force. According to (3.5), the driving force \mathbf{F} follows from the total energy E that is deduced from the micromagnetic energies. For vortices the exchange and demagnetization energy are commonly modeled by a two-dimensional harmonic potential E_{harmonic} [31] and a Zeeman term E_{Zeeman} takes external magnetic fields into account [77]. The energy terms are given by

$$E_{\text{harmonic}} = \frac{1}{2} \kappa (x^2 + y^2), \quad E_{\text{Zeeman}} = \mu_0 M_S \pi R h c (H_y x - H_x y), \quad (3.9)$$

where the total energy E is the sum of the two. Calculations that show the two cases of vortex dynamics that were qualitatively discussed in the last section are shown in Fig. 3.12. In Fig. 3.12a the vortex is deflected by a static magnetic field that is switched off instantaneously, which makes the core freely gyrate back to its equilibrium position in the center of the disk. As expected for the positive polarization

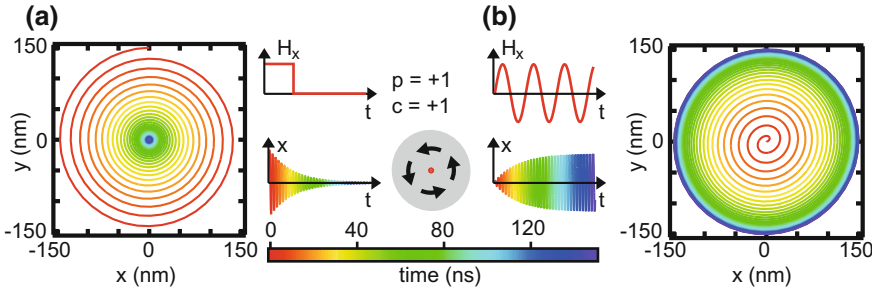


Fig. 3.12 Calculations for a single magnetic vortex in the Thiele model for two different magnetic field excitations. The temporal shape of the exciting magnetic field in x -direction H_x is depicted in the insets. The time t is color coded from red (0 ns) to blue (140 ns). Circularity and polarization are positive in this example. **a** Trajectory of the vortex core gyrating back to its equilibrium position with the eigenfrequency of the gyroscopic mode after it has been deflected with a magnetic field in x -direction that is then switched off instantaneously. **b** The vortex core is resonantly excited with an alternating magnetic field near the eigenfrequency of the gyroscopic mode. It performs a transient motion until it reaches circular trajectories in the stationary case. Adapted from [78]

in the example a counterclockwise gyration is obtained. The positive circularity causes the starting point of the gyration to be located in the upper part of the disk, in agreement with the considerations discussed in the context of Fig. 3.10. Figure 3.12b shows how the vortex reaches its stationary gyroscopic motion, when it is excited with a unidirectional alternating field near the eigenfrequency of the gyroscopic mode. At the very first instant we expect from the qualitative discussion of the vector-field representation of the core with positive circularity and polarity a motion along the direction of the exciting field. In the case calculated in Fig. 3.12b the field points along the positive x -direction at the beginning and indeed the core moves into this direction. However, as described in the discussion of the influence of static fields a force perpendicular to the field sets in that leads to a counterclockwise gyration as expected for positive polarization. For the comparison with experiments it is convenient to use the abbreviations

$$\omega_0 = -\frac{pG_0\kappa}{G_0^2 + D_0^2\alpha^2}, \quad \Gamma = -\frac{D_0\alpha\kappa}{G_0^2 + D_0^2\alpha} \quad (3.10)$$

that can both be directly measured. For small damping, the angular frequency of the gyroscopic motion equals the parameter ω_0 , while the parameter Γ describes the damping of the motion. Typical values are $\frac{\omega_0}{2\pi} = 250$ MHz and $\Gamma = 31 \cdot 10^6$ s $^{-1}$, which corresponds to a typical ratio $\frac{\Gamma}{\omega_0} \approx 2\alpha$ found in experiments [75].

3.3.2 Strong Excitation and Switching

So far the description remains within the linear regime, where the restoring forces are proportional to the deflection of the core. It is a harmonic oscillator model as the confining potential is parabolic, see (3.9). Such a description is applicable for small excitations [31]. If the excitation strength is increased the harmonic oscillator model has to be extended to a nonlinear oscillator model [79]. In this case the confining potential contains anharmonicities, i.e. deviations from the purely harmonic potential [79–81]. If vortex cores are excited to gyrate on rather large trajectories the local magnetization configuration shows deformations that are not present for small amplitudes of excitation. Although this puts the assumption of a rigid object into question it can be shown that the Thiele model is still applicable using a modified potential. Figure 3.13 shows results from micromagnetic simulations. At the beginning of the simulation the vortex core is located in the center of the sample at equilibrium, as illustrated in the lower part of Fig. 3.13a. An alternating excitation leads to a spiral trajectory until the steady state is reached. A snapshot of a strongly excited core moving in the steady state at its resonance frequency is depicted above the ground state in Fig. 3.13a, qualitatively underlining the validity of the assumption of a rigid particle model. The total energy of the gyration from the onset up to its steady state is depicted in Fig. 3.13b. At large core displacements the potential becomes steeper than a parabola and in the corners of the square the potential possesses tailing edges. Thus, the shape of the potential approaches the shape of the confining microstructure. It has been shown that this behavior can be modeled analytically with a nonparabolic isotropic plus a nonparabolic anisotropic contribution to the potential [79].

The influence of the nonparabolic potential on the resonances of vortices in squares of different sizes are summarized in Fig. 3.14, where micromagnetic simulations along with results from the nonparabolic Thiele model are depicted. Resonance

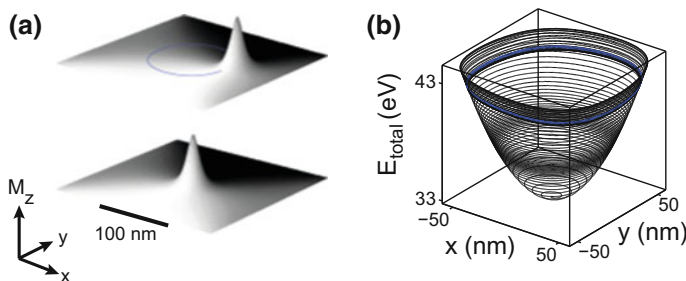


Fig. 3.13 Vortex in a square element with an edge length l of 200 nm and a thickness h of 10 nm. **a** The excited state with the core displaced by an alternating spin-polarized current of density $1 \times 10^{11} \text{ Am}^{-2}$ and frequency $2.7 \times 10^9 \text{ s}^{-1}$ is depicted above the equilibrium state with the core in the center. The magnetization component M_x is gray scaled; the component M_z is plotted on the z -axis. **b** Potential of vortex gyration. The blue line in **a** depicts the trajectory, the blue line in **b** the total energy of the steady-state motion. Reproduced from [79]

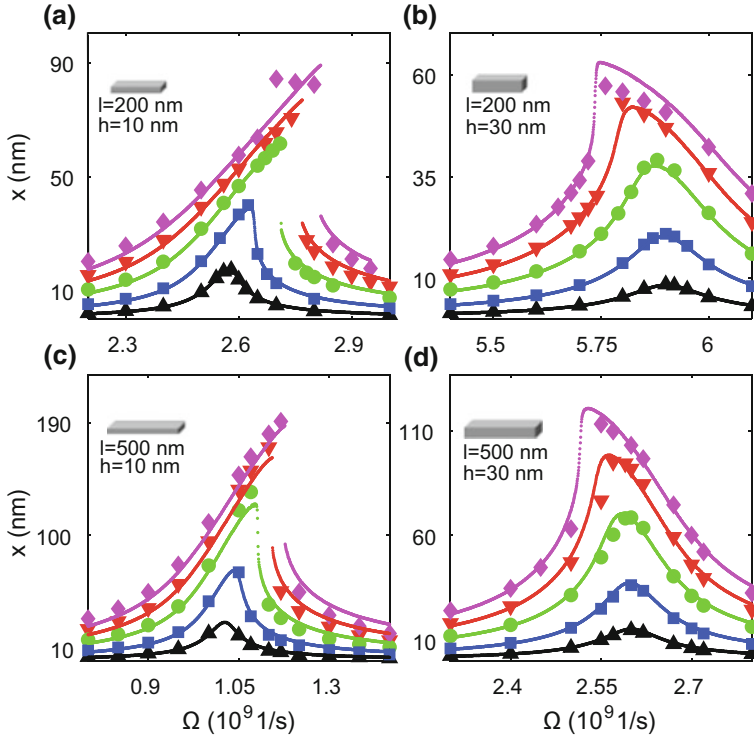


Fig. 3.14 Resonance curves of gyrating vortices driven by spin-polarized currents in square elements with four different geometries (length l and thickness h) as indicated in the insets of **a** to **d**. The maximum core displacement in x -direction versus excitation frequency Ω is shown. Reproduced from [79]

curves for five current amplitudes in four squares of different edge lengths and thicknesses are shown. When the excitation strength is increased, the higher order terms in the potential shift the resonance frequency. For thin samples ($h = 10$ nm) the resonance maximum experiences a blue shift, see Fig. 3.14a, c, whereas for thicker samples ($h = 30$ nm) the maximum shifts to the red, see Fig. 3.14b, d. For large excitation amplitudes the resonance curves exhibit gaps that are common features of nonlinear oscillators and are accompanied by jumps of the phase between gyration and excitation. The observed foldover, jump resonance phenomena, and frequency hysteresis behavior are typical for Duffing oscillators, describing the motion of a damped oscillator with a more complex potential than a harmonic motion, see e.g. [82].

If the excitation strength is increased even further the assumption of a nonparabolic potential will not be sufficient to describe the dynamics. If the vortex reaches high velocities it will switch its polarization. For this process the quasi-particle Thiele model will not be applicable any longer. Instead the reversal of the core polarization

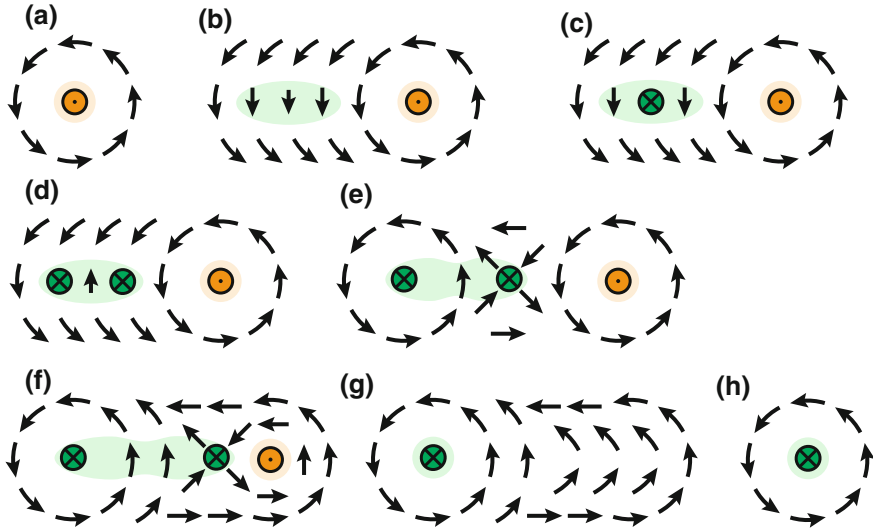


Fig. 3.15 Schematic representation of different steps in switching the vortex core polarization. The arrows represent the in-plane magnetization components, the color scale represents the out-of-plane component (orange, up; green, down). A description is given in the text. Modified from [36]

must be understood in terms of nucleation and subsequent annihilation of a vortex-antivortex pair [36, 83]. The origin of this process was found to be a gyrotropic field induced by the fast motion of the core [84]. This field tilts the magnetization next to the core in opposite direction that can be compared to a bow wave that forms at the bow of a ship when it moves through the water, see Fig. 3.15b. At this point the magnetic deformation has no topological charge but eventually develops a vortex-antivortex pair, see Fig. 3.15c–e. The antivortex annihilates with the original vortex (see Fig. 3.15f, g) under the emission of spin waves and leaves a new single vortex with reversed polarization, see Fig. 3.15h. The actual reversal process, disregarding the preceding excitation, takes place on short timescales <100 ps [83]. Dynamic vortex core switching was first discovered in the pioneering work of Van Waeyenberge and coworkers [36].

Switching of the vortex core by dynamical excitations has been investigated experimentally and theoretically [84–94], as has been the switching of an antivortex core [20, 68]. Dynamic vortex core switching has the disadvantage that there is no well-defined switching of the core into the desired polarization state. Once the excitation strength exceeds the critical amplitude for vortex core switching, the vortex will reverse its polarization repeatedly. This problem can be avoided by using rotating in-plane fields [37, 90, 91, 93] or rotating spinpolarized currents [20, 95] at low frequencies, which excite the gyrotropic vortex motion. Since the gyration sense of the vortex is determined only by the polarization p there is a high asymmetry in the gyrotropic resonance excited by rotating fields with different rotation senses [96]. Selective unidirectional switching only occurs when the rotation senses of the

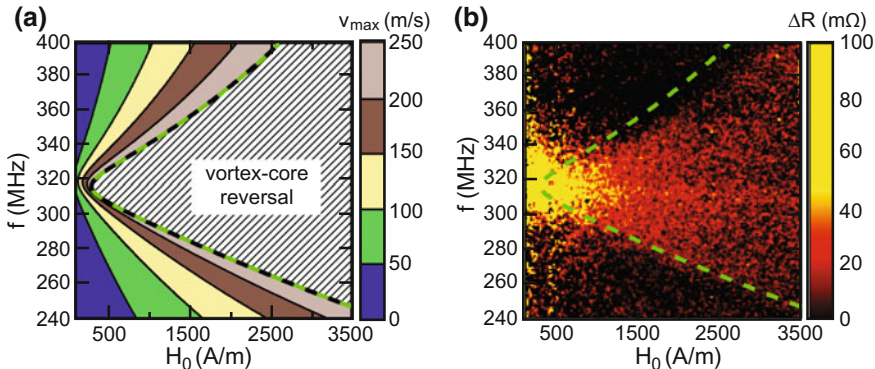


Fig. 3.16 **a** Calculated velocities v_{\max} of the vortex core in dependence of the amplitude H_0 and frequency f of the exciting field according to the Thiele model. The hatched region corresponds to trajectories with velocities above $v_c = 250$ m/s and implies core reversal. **b** Measured absorption spectra of the vortices in dependence of the exciting field amplitude. The dotted green line marks the calculated critical region from **a**. Reproduced from [75]

exciting field and of the freely gyrating vortex are the same [90, 91]. This type of switching leads to switching times larger than 1 ns. It has been shown that the vortex polarization can be selectively switched also by applying low rotating in-plane fields in the multi-GHz frequency range which excite azimuthal spin waves [37, 93]. More recently fast spin-wave mediated vortex core reversal has been found [38], where rotating spin waves in the GHz range with very short rotating magnetic-field bursts enable selective switching. Such fast concepts for switching are very attractive because they pave the way to competitive, i.e. picosecond time scale writing processes, e.g. in data storage devices. However, gyration switching alone provides a wealth of unexplored phenomena, especially in interacting systems. Therefore and because of space limitations we have to restrict ourselves to gyration switching for the remainder of this chapter.

When reconsidering the Thiele model a convenient criterion for the onset of gyration core switching is given as a critical velocity v_c of the core [96]. The value of the critical velocity only depends on the exchange stiffness A and the saturation magnetization M_S of the ferromagnet and not on the geometry of the sample. For permalloy a theoretical critical velocity of $v_c = 330$ m/s is given in agreement with micromagnetic simulations [96]. Experimentally a slightly lower critical velocity of $v_c \approx 250$ m/s was reported [75, 88, 94, 97]. The deformation of the core profile and the core switching cannot be modeled within the Thiele model because it assumes a constant magnetization pattern as a first principle. The model will especially fail when the velocity of the vortex core exceeds the critical value v_c and will predict unphysical trajectories. So these solutions are excluded from the calculations and identified as possible candidates for core switching. The solution of the equation of motion (3.8) is displayed as phase diagram in dependence of excitation strength and frequency in Fig. 3.16a. In the critical regime shown as hatched region the maximum

velocity exceeds the critical velocity ($v_{\max} > v_c = 250$ m/s) and core reversal occurs. Figure 3.16b shows experimental results from high frequency absorption measurements. The measured phase diagram shows the color coded resistance change, i.e., the absorbed power driving the magnetization dynamics, in dependence of the excitation frequency f and the excitation amplitude H_0 of the unidirectional magnetic field. For a field strength of $H_0 < 300$ A/m the absorption arises from the resonant excitation and gyration around 320 MHz. In this regime the absorbed power stabilizes stationary core trajectories against the damping of the gyration. The measured signal is proportional to the average of the squared core velocity v^2 [68]. For increasing field amplitudes above 300 A/m the frequency range of absorption gets broadened, spanning a characteristic cone-like region (red colored), that is clearly separated from the residual area. The marked isoline of Fig. 3.16a that denotes the exceeding of the critical velocity within the Thiele model can be identified in the measurement as a characteristic increase of the absorbed power. The reason for the particular power absorption in this region is the repeated reversal of the core polarization, which can be seen in direct comparison with Fig. 3.16a. Beside driving the vortex dynamics much of the systems micromagnetic energy is dissipated as highly damped spin waves resulting from the annihilation of the cores. Time- and spatially resolved measurements on the same and comparable samples confirm the conclusions [75]. The full experimental details are discussed in [68, 75].

3.4 From Single Oscillators to Magnonic Vortex Crystals

3.4.1 *Vortices as Coupled Harmonic Oscillators*

We now consider vortices as harmonic oscillators and apply the rigid vortex approach [74] as discussed in Sect. 3.3.1. For this chapter, the stray-field and thus the coupling of magnetic vortices is calculated from magnetic surface charges that arise from deflected vortices at the sides of the microstructure [40]. As mentioned before a dipolar field is often a good approximation for the field outside the microstructure, especially in the far field. The magnetization pattern of the deflected vortex itself remains constant. Volume charges are absent and top and bottom surface charges are neglected for now.

Coupled vortices have been investigated in physically separated magnetic microstructures [40, 42, 61, 99–103] and in physically connected microstructures [104–106]. In the first case magnetostatic interactions are of importance, whereas in the second case exchange coupling plays an important role. Additionally, the synchronization of vortex based spin torque nano-oscillators that are addressed in Chapters 10 and 11 in more detail, via dipolar or electrical coupling has attracted a lot of attention recently [107, 108]. A displaced vortex core and its motion in one disk generates dynamically rotating stray fields that affect the potential energy of the other disk, in which vortex gyration can be stimulated resonantly. The gyration

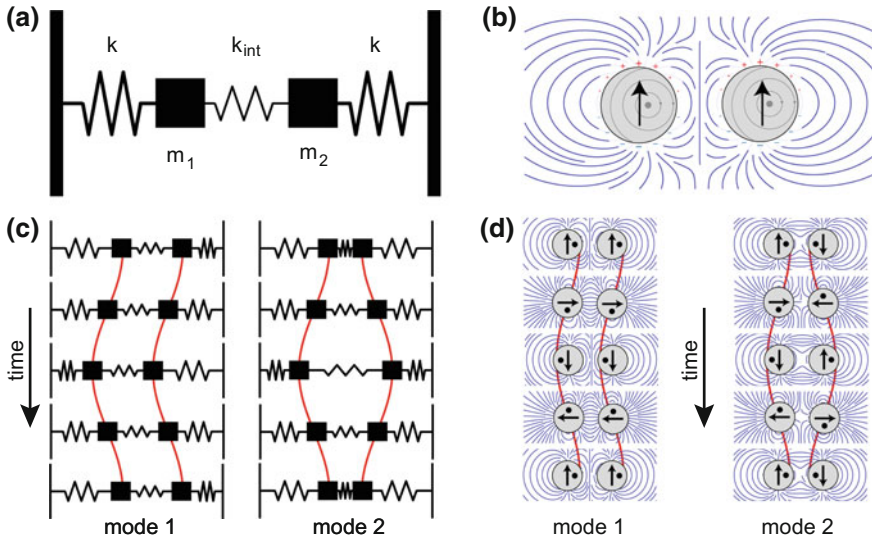


Fig. 3.17 Schematics of **a** two coupled harmonic oscillators and **b** two coupled magnetic vortices. The motions of the two systems can be described by a superposition of linearly independent modes. The two modes feature an in-phase and an out-of-phase motion of the quasiparticles as depicted in **c** for the coupled oscillators and in **d** for the coupled vortices. Reproduced from [98]

in the second structure will inversely affect the first structure and together a beating behavior is obtained. The relative vortex-core displacements in both disks as well as the disk-to-disk interdistance modify the interaction strength. These behaviors are analogous to those of coupled harmonic oscillators such as coupled pendulums or capacitively-coupled inductor-capacitor resonators [109]. We want to elucidate this analogy in more detail. It is known that the motions of coupled harmonic oscillators can be described by the superposition of linearly independent modes. The number of modes is identical to the number of coupled oscillators. Figure 3.17 depicts the two eigenmodes for a pair of classical oscillators and two coupled vortices. These modes have been calculated in the absence of damping [98]. In both cases one of the modes corresponds to an in-phase motion of the two particles and one corresponds to an out-of-phase motion. The frequency of the mode is determined by the energy of the interaction, i.e. the stiffness of the coupling spring, or the energy of the stray field throughout one oscillation period. The stray fields are depicted via dipoles that approximate the net magnetic moment of the deflected vortices. Here it becomes vivid that the interaction energy oscillates over time. The excitation of the gyrotrropic mode with external magnetic fields induces the indicated dipoles. These dipoles are independent of the circularity of the vortex. Thus, the dipole motions, and thereby the corresponding frequencies do not depend on the circularity. Note that the position of the vortex core still depends on the circularity. In other words, the inversion of the sign of the surface charges by changing the circularity of the vortex is canceled out

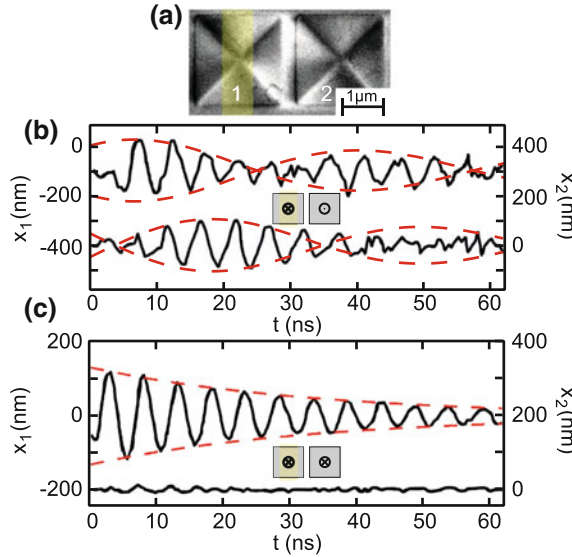


Fig. 3.18 **a** Magnetic force micrograph of a pair of permalloy squares with a center-to-center distance of $D = 2.5 \mu\text{m}$. A stripline (illustrated in yellow) is deposited on top of the left square (1). **b** and **c** Trajectories of vortex cores after pulse excitation with different polarization configurations (left core: upper trace, right core: lower trace). **b** Opposite core polarizations ($p_1 = -p_2$), **c** same core polarizations ($p_1 = p_2$). The dashed red lines are guides to the eye illustrating the beating (**b**) and the exponential decrease (**c**) of the vortex trajectories. Reproduced from [42]

by a phase shift of 180° of the excited vortex core motion. This behavior does not apply for a change of the relative polarities. Since the sense of gyration depends on the polarity of the vortex cores, the modes change for a coupled system of vortices with opposite polarities. This leads to different eigenfrequencies and modes. For the classical harmonic oscillator changing the relative polarities can be compared to a change of the stiffness constant k_{int} of the coupling spring. Changing the coupling between the individual oscillators then allows to modify collective modes also in larger systems, which we will cover in more detail in the next section.

Before that, we discuss measurements on two coupled vortices as shown in Fig. 3.18a. The magnetization dynamics of pairs of micron-sized permalloy squares coupled via their stray fields are investigated [42]. The trajectories of the vortex cores in the Landau-domain patterns of the squares are mapped in real space using time-resolved scanning transmission x-ray microscopy. After excitation of one of the vortex cores with a short magnetic-field pulse of 1.8 ns duration, the system propagates freely and behaves like coupled damped harmonic oscillators. Results are shown in Fig. 3.18 for opposite and equal core polarizations. When considering the excitation of the right vortex via a rotating in-plane magnetic field produced by the initially excited left vortex, it can be understood that only a very weak response of the second vortex core is observed for equal core polarizations as can be seen in Fig. 3.18c. However, in the case of opposite core polarizations as presented in

Fig. 3.18b the beating of the gyration amplitude is clearly observed and thus the coupling is strong. This behavior is fundamental and will play an important role as a building block for more complex arrangements of vortices, e.g. in one-dimensional chains or stacks [47, 99, 100, 110, 128], in two-dimensional arrays [28, 61, 111–113], and in three-dimensional stacked arrays [48].

3.4.2 *Self-Organized State Formation*

³The coupling in arrangements of magnetic vortices strongly depends on the relative polarizations of the vortex cores. A mechanism, we call self-organized state formation, allows to tune the polarization configuration in various kinds of vortex arrangements by the temporary application of high frequency magnetic fields. This allows for the manipulation of the properties of large regular arrangements of magnetic vortices that will be addressed as magnonic vortex crystals in the following. We will first introduce the phenomenon of self-organized state formation for rectangular crystals consisting of 3×3 vortices [114, 115]. Subsequently, different aspects of the self-organized state formation are examined on various types of magnetic vortex arrangements including large magnonic crystals with many more vortices. The self-organized state formation builds the basis for the manipulation of crystal properties, e.g., band-structure engineering or for experiments on benzene-like vortex molecules to be discussed later.

Figure 3.19 shows a schematic of the experiment. The vortices are excited by a harmonic field generated by a high frequency current applied to a stripline in coplanar waveguide geometry above the 3×3 disk array. The disks have a diameter of $2 \mu\text{m}$ and a height of 60 nm . The center-to-center distance is $2.25 \mu\text{m}$. These measurements have been performed at the MAXYMUS beamline at BESSY II in Berlin, Germany. At first the whole crystal is strongly excited by an alternating unidirectional magnetic field that causes all vortices to permanently switch their polarizations, see Sect. 3.3.2. The field amplitude is then reduced quasi statically (millisecond time scale) with respect to the periodicity of the vortex gyration (nanosecond time scale). As depicted in Fig. 3.19c, starting from above the switching threshold, the amplitude of the harmonic excitation is reduced until switching dies out. In a second step, the polarizations of the vortices are determined by evaluating the sense of gyration. For this, a harmonic field of decreased amplitude is applied to non-invasively detect the created polarization state. Vortices are found to be organized in preferred polarization states depending on the frequency of the primary excitation.

Complementing micromagnetic simulations help to understand the process of switching because it cannot be directly observed in the experiment [114]. Those simulations reveal that the vortex polarizations in an array of disks switch rather randomly at high amplitudes of a harmonic field that is applied to all magnetic

³Figures 3.19, 3.20 and 3.21 and parts of the text in this subchapter are reproduced from the Dissertation Thesis of C. F. Adolff [78].

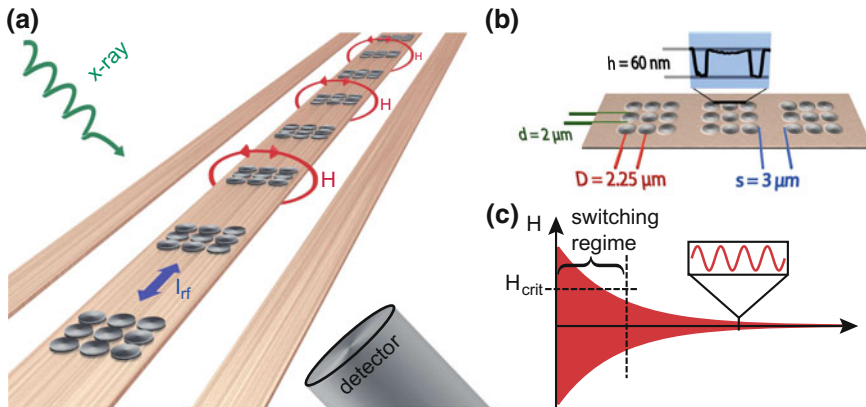


Fig. 3.19 **a** Vortex arrays investigated by scanning transmission x-ray microscopy. The magnetic field H is applied via an alternating current sent through a coplanar waveguide. **b** X-ray micrograph with in-plane contrast of three vortex arrays that comprise nine disks each. The magnetization curls in plane around the center of each disk (thickness 60 nm, diameter 2 μm , distance 2.25 μm). The inset shows a line scan of an atomic force micrograph and reveals the topography of the discs. **c** Timetrace of the magnetic field excitation used to tune the polarization states. The amplitude of the unidirectional harmonic excitation is reduced adiabatically until vortex core switching ceases. Adapted from [78]

vortices in the array. At intermediate field amplitudes the switching stops when certain stable polarization configurations are reached. The stability of such polarization states can be understood in terms of magnetic vortices as coupled harmonic oscillators as described above. The coupling strength depends on the distance between the magnetic nanodisks containing the vortex cores [40, 42, 100, 103]. When the center-to-center distance D between the disks exceeds twice the diameter $\frac{D}{d} > 2$, the coupling can be neglected [45, 61] and random polarization states should emerge independent of the excitation amplitude. Increased coupling can be obtained by reducing the center-to-center distance until it equals the disk diameter and the disks start to merge for $\frac{D}{d} \leq 1$). Smaller distances lead to exchange interaction at the intersection of the disks and will not be regarded here but has, e.g. been studied in [106].

Samples of spatially separated disks with different center-to-center distances are experimentally investigated [114]. Here we discuss the simpler case of weak coupling where neighbouring disks have a center-to-center distance of 3 μm ($\frac{D}{d} = 1.5$). For samples with a center-to-center distance of the disks of 2.25 μm ($\frac{D}{d} = 1.125$) stronger dipolar coupling is obtained, which creates a richer spectrum [42, 61]. Figure 3.20a summarizes the resulting polarization states that occur after the adiabatic field reduction with different frequencies. For an excitation frequency of 225 MHz during the adiabatic reduction of the excitation amplitude the resulting polarization configuration of the vortex cores is constant along the field direction and alternates in the perpendicular direction. Columns of the same polarization occur. In contrast, rows of constant polarization are observed at higher frequencies, i.e., 245

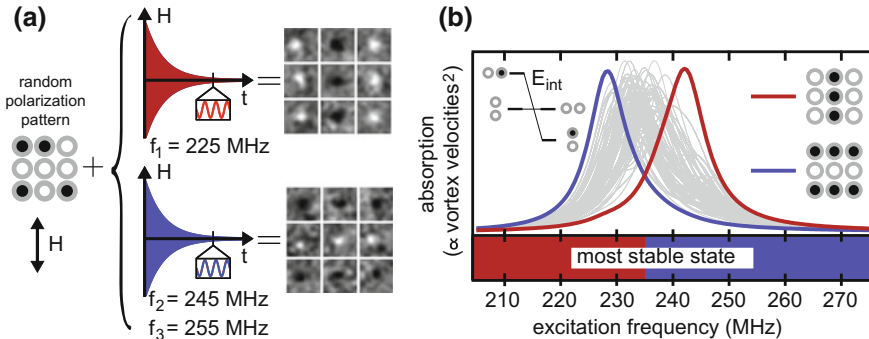


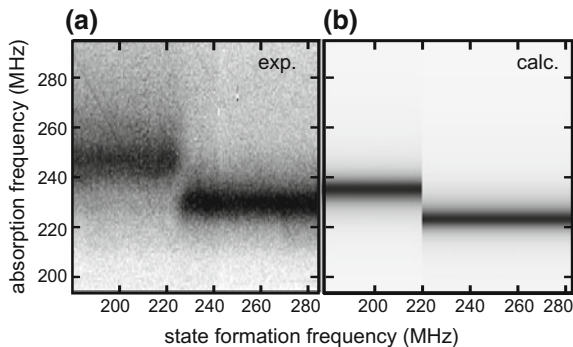
Fig. 3.20 Self-organized state formation in 3×3 crystals with a ratio of the center-to-center distance D to the disk diameter d of $D/d = 1.5$. **a** A variation of the frequency of the adiabatically reduced field excitation tunes differently ordered polarization states. For 225 MHz columns of constant polarization occur, and rows of constant polarization emerge at 245 and 255 MHz. No pattern could reproducibly be tuned at 235 MHz. **b** Absorption profiles of all $2^9 = 512$ possible polarization states numerically calculated in the extended Thiele model. The states of rows (blue) and columns (red) of constant polarization are highlighted. The bottom color scale depicts the most stable state, i.e., the state with the lowest absorption at a particular frequency. Those states are predicted to be tuned via self organized state formation. The inset in the upper-left corner schematically depicts (3.11). The interaction energy (absorption frequency) in a pair of disks varies for different alignments of the pair and the core polarizations. Adapted from [78]

and 255 MHz. When excited inbetween at 235 MHz no state could reproducibly be tuned for repeated measurements on the same crystal. This can be understood with the simplified dipolar stray-field coupling presented in Sect. 3.4.1. A 3×3 vortex crystal may be formed from pairs of horizontally and vertically coupled vortices as building blocks. In the experiments all disks in the crystal and thus all interacting pairs are excited with the unidirectional field in y -direction, regardless of the orientation of the pair (see Fig. 3.20a). This idealized model reveals that for a pair of vortices with alternating polarizations ($p_1 p_2 = -1$) the variation of the absorption peak $\omega_{p,\text{alt}}$, where the pair can be excited most efficiently, is proportional to the cosine of twice the angle ϑ between the x -axis and the connecting line of the two disks. Thus, in the alternating case, a pair that is placed perpendicular to the field direction ($\vartheta = 0$) can be excited most efficiently at a higher frequency than an identical pair that is aligned parallel ($\vartheta = \pi/2$). In the case of homogeneous polarizations ($p_1 p_2 = 1$), the frequency of the most efficient excitation $\omega_{p,\text{hom}}$ does not depend on the rotation angle ϑ and lies in between the above two frequencies. This leads to the relation

$$\omega_{p,\text{alt}}(\vartheta = 0) > \omega_{p,\text{hom}} > \omega_{p,\text{alt}}(\vartheta = \frac{\pi}{2}) \quad (3.11)$$

that is schematically depicted in the inset of Fig. 3.20b as energy term scheme. The absorptions for all $2^9 = 512$ polarization states have been calculated numerically using the Thiele model for interacting vortices [112, 114]. In Fig. 3.20b the emerging

Fig. 3.21 High-frequency absorption (FMR) measurements (a) and absorptions predicted via numerical calculations (b). Adapted from [78]



states are highlighted in red for the column state and in blue for the row state. As predicted from the analytical approach, the state with rows of constant polarization can be excited more efficiently at lower frequencies than the state with columns of constant polarization.

When a state is excited efficiently, the vortices in the crystal reach high velocities. At a critical velocity of about 250 ms^{-1} [75] the vortices switch their polarizations and thereby lead to another polarization state in the crystal. Thus, efficiently excitable states are less stable than states that cannot be excited efficiently at a particular frequency. One can see in Fig. 3.20b that the emerging states indeed are the least efficiently excitable states at the corresponding frequencies f_1 , f_2 , and f_3 of the adiabatically reduced field excitation. This can easily be motivated using the relations presented above. The adiabatic field reduction passes a critical field amplitude where only one polarization state will not switch. This least excitable state is eventually adjusted after several switching processes between instable polarization states. The two states of rows and columns of constant polarizations take turns in being the most stable states for frequencies below or above a transition frequency $f_{\text{trans}} \approx 235\text{ MHz}$ where they are equally excitable. This explains why no state could reproducibly be tuned at the frequency $f_4 = 235\text{ MHz}$ that is close to the transition frequency. In conclusion, the polarization states that emerge after a self-organized state formation with adiabatic field reduction can be predicted from the comparison of all possible absorptions in the crystal. Those have been numerically calculated for all 512 polarization states.⁴

Additional high-frequency absorption measurements are presented in Fig. 3.21. For these experiments additional samples with up to 60 identical 3×3 vortex arrays are prepared on silicon oxide wafers. The high-frequency absorption measurements allow to perform more measurements in a shorter time and give insight into the reproducibility of the state formation in the ensemble of crystals. In Fig. 3.21 the x -axes represent the state formation frequency f_{state} used to tune the polarization states as described above, and the y -axes account for the frequency of the absorption

⁴Note that only 136 polarization states are non-degenerate with respect to the frequency response (absorption) due to symmetry reasons.

spectrum f_{abs} of the emerging polarization patterns. The absorption is represented by the grey scale, where dark represents strong and light grey weak absorption. One can see that the absorption profiles vary for different state formation frequencies. It is straight forward to expect that the absorption signal measured after a specific state formation stems from crystals that are settled to the most stable polarization state. Thus, the absorption profile of the state that is least efficiently excitable at the state formation frequency f_{state} is expected. Consequently, the expected absorptions can be calculated in the Thiele model and are depicted along with the absorption measurements in Fig. 3.21b. Due to small variations in the preparation process, especially the change of substrate, the physical properties of the samples slightly differ from those determined for the samples used for X-ray microscopy. The theoretical prediction is calculated under the assumption that the ensemble completely settles in the state that is most stable at the state formation frequency. By comparing theoretically and experimentally obtained absorption spectra one can see that this approximation is valid, although the absorption profiles are broadened with respect to the calculations due to the variations in the ensemble mentioned above. The two absorption frequencies are attributed to the only two states, i.e., rows and columns of constant polarizations, that can be tuned for the weakly coupled sample type. The absorption intersect at around 226 MHz. At this frequency the most stable state should change according to the presented stability criterion, yielding the transition frequency $f_{\text{trans}} = 226$ MHz. When compared with the absorption measurement in Fig. 3.21a, indeed the form of the absorption changes at this frequency. The experiments and the calculation match in detail. This is a strong indication that the above model can also be used for the overall behavior of ensembles of vortices that exhibit small variations in the resonance frequency.

Self-organization in magnonic vortex crystals is a reproducible process and it is valid for larger ensembles of vortices as we will see. The absorption of the ensemble approximates the absorption of the least-exitable polarization state at the corresponding state formation frequency. This allows further studies to tailor the characteristic properties of magnonic vortex crystals by tuning the polarization state. It is predicted that the allowed energy bands in such a crystal can be adjusted via manipulation of the polarization pattern [116]. In the next section self-organized state formation is applied to adjust polarization states in benzene-like vortex molecules.

3.4.3 Benzene-Like Vortex Molecules

In a ring-like arrangement of six magnetic vortices the gyration motions feature normal modes that are similar to the vibrational modes of the actual benzene molecule [117]. In analogy to the description of a linear chain of harmonic oscillators with periodic boundary conditions these normal modes are plane waves with wavelengths that are fractions of the circumference of the ring. Different polarization patterns yield different dispersions of gyration waves. A convenient and powerful model to describe the motions of coupled vortices is the Thiele model introduced in

Sect. 3.3.1. This approach employs surface charges that emerge when the vortex is deflected from the center of the disk to approximate the coupling mediated by the stray field [40]. For a number of N coupled vortices the Thiele equation becomes a $2N$ -dimensional system of differential equations. This system can be reduced to an eigenvalue problem [112]. For a ring of vortices the eigenmodes can be determined by the exclusive use of symmetry considerations in analogy to the benzene molecule shown in [118]. Figure 3.22a depicts a vortex molecule consisting of six permalloy disks. The stripline on the lower disk excites the gyrotropic mode with the unidirectional high-frequency magnetic-field generated by an alternating current sent through the stripline. Assuming that the excitation will lead to approximately circular motions of the $N = 6$ vortices the vortex trajectories are given by

$$\mathbf{r}_i = a_i c_i \begin{pmatrix} \cos(\omega t + \varphi_i) \\ p_i \sin(\omega t + \varphi_i) \end{pmatrix}, i \in \{0, 1, \dots, N-1\}. \quad (3.12)$$

Due to the N -fold rotational symmetry and the linearity of the system, there is a basis of N normal modes, that fulfill this symmetry. For a ring of an even number of N disks the normal modes $\mathbf{r}_{i,\kappa}$ are given by

$$\mathbf{r}_{i,\kappa} \in \{\mathbf{r}_i \mid a_i = a_\kappa, \varphi_i = \varphi_{i,\kappa} = (\kappa + p_i)i\alpha + \phi_\kappa\}. \quad (3.13)$$

The integer number $\kappa \in [-N/2, \dots, N/2]$ indexes the normal mode and is analogous to the wave-number $k = 2\pi/\lambda$ in a linear chain of oscillators. The angle $\alpha = 2\pi/N$ corresponds to the lattice constant in a linear chain. Since a general vibration of the ring is given by a linear combination of the normal modes $\mathbf{r}_i = \sum_\kappa \mathbf{r}_{i,\kappa}$, the factor a_κ describes the contribution of the normal mode $\mathbf{r}_{i,\kappa}$ to the motion. The relative phases of the normal modes are given by ϕ_κ . Figure 3.22b depicts the form of the normal modes for equal circularities and polarizations ($c_i = 1, p_i = -1$) of all vortices. For each point in time the vortex cores are located on geometric roulettes, i.e., epitrochoids and hypotrochoids. For wave numbers κ with $|\kappa| > 0$ the form of the roulettes stays constant over time and they rotate around the center of the ring, whilst the vortex cores are always located on the curve. For positive wave numbers $\kappa > 0$ the roulettes rotate in the same direction as the vortices (clockwise). In contrast, for negative wave numbers the roulettes rotate anti-clockwise, i.e., against the gyration direction of the vortices. Thus, the sign of κ denotes the propagation direction of the waves. For $\kappa = 0$ the normal mode $\mathbf{r}_{i,0}$ is called the breathing mode since the vortices lie on a circle that changes its size over time. At the edge of the Brillouin zone $\kappa = \pm 3$ the waves can be understood as propagating in both directions. Figure 3.22c shows experimental results obtained by scanning transmission x-ray microscopy at the MAXYMUS beamline at BESSY II in Berlin, Germany, when the homogeneous polarization pattern $p_i = -1$ is present. The steady-state motions of the vortices are traced for different frequencies around the resonance frequency of an isolated disk. The gray line in each of the six graphs is a Lorentzian fit through the black data points that are proportional to the absolute gyration amplitude $|a_\kappa|$ of one normal mode $\mathbf{r}_{i,\kappa}$. These data points are obtained by applying a curve fit with

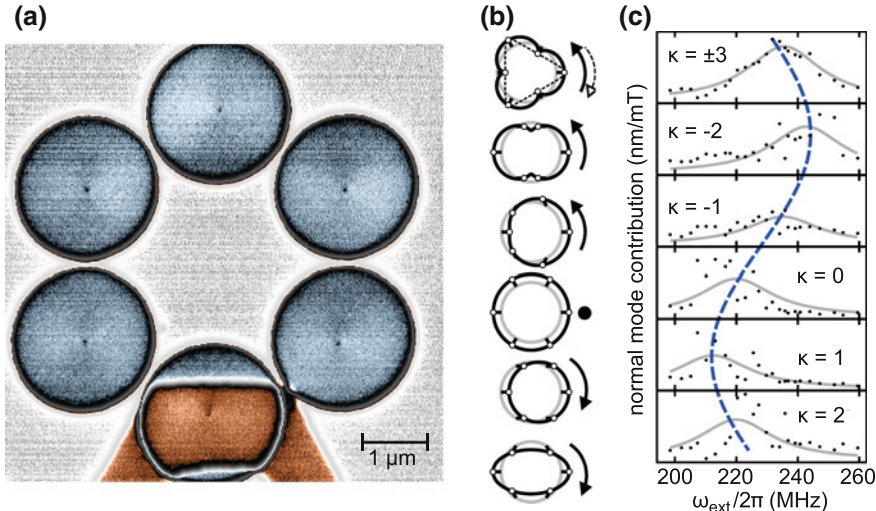


Fig. 3.22 Ring-like arrangement of six disks that contain a vortex each. The permalloy disks are 60 nm thick and have a 2 μ m diameter, the minimal distance between the disks is 50 nm. **a** X-ray micrograph of the vortex molecule with homogeneous core polarizations in all six disks. The magnetic contrast can be seen in the raw data of one time frame. The vortex cores appear as black dots. **b** Pictograms for the form and the propagation direction of the normal modes of the ring. **c** Experiments with a homogeneous core polarization pattern in the ring ($p_i = -1$). Each graph shows the contribution of a normal mode to the overall motions in the molecule for different excitation frequencies. The data points are obtained by a fit to the trajectories traced via scanning transmission x-ray microscopy. The solid lines are Lorentzian fit curves. The vertical scale of each graph ranges from 0 to 34 nm/mT. Adapted from [117]

the linear combination of normal modes given by (3.12) and (3.13) to the vortex trajectories of the six vortices. For each frequency one global curve fit is performed that comprises the complete motion of the six vortices and thus yields one data point in each of the six graphs. Each eigenmode has its maximum contribution at different frequencies that lie on a sinusoidal line (dashed blue). The alternating polarization pattern is shown in Fig. 3.23a. For this case, the symmetry of the ring changes due to the alternating polarizations. Here, two modes are degenerate and can be combined which results in standing waves. The combinations of such standing waves are depicted in Fig. 3.23b. The arrow-pictograms in Fig. 3.23b are identical to those used in [119] for the motions of the actual benzene molecule and underline the equivalence of the two systems. The standing waves are fitted to the trajectories and yield the results presented in Fig. 3.23c.

The dispersion relation of the vortex molecule can be obtained from the contribution of the eigenmodes to the motion of the vortices, see dashed blue and dashed green lines in Figs. 3.22c and 3.23c. Figure 3.24 summarizes the determined dispersion relations for the homogeneous and the alternating polarization configuration. The different bandwidths can be understood by a weaker coupling between vortices

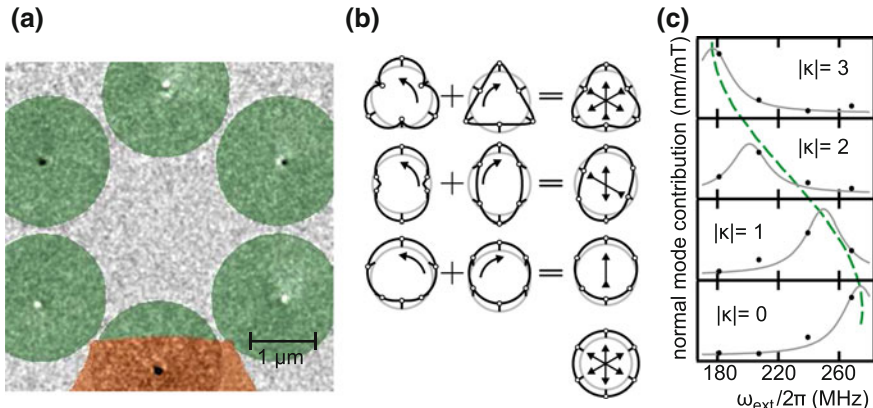


Fig. 3.23 **a** Vortex molecule with alternating polarizations. The static contrast is subtracted to emphasize the magnetic contrast even more prominently. Disks and stripline are colorized. In the captured movie black vortex cores gyrate clockwise ($p_i = -1$) and white cores counterclockwise ($p_i = 1$). **b** Pictograms of the composition of the normal modes to obtain standing waves. **c** Each graph shows the contribution of a standing wave to the overall motions in the molecule for different excitation frequencies. The data points are obtained by a fit to the trajectories traced via scanning transmission x-ray microscopy. The solid lines are fit curves. The vertical scale is identical to that in Fig. 3.22c. Adapted from [117]

of equal polarization in comparison to vortices with different polarizations, which has been discussed in Sect. 3.4.1. For negligible damping, there are sharp resonances when the eigenfrequency of a normal mode is met. In experiments the damping allows to excite the system in between those resonances. The normal modes mix in the way shown in Figs. 3.22c and 3.23c. The datapoints in Fig. 3.24 correspond to peaks of individual Lorentzian fits.

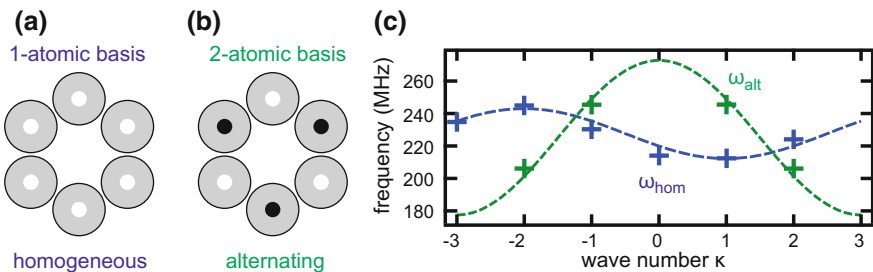


Fig. 3.24 Schematic representation of a ring with **a** equal and **b** alternating core polarities. **c** Experimentally determined dispersion relation for equal polarizations (blue) and alternating polarizations (green). The datapoints correspond to peaks of individual Lorentzian fits as presented in Figs. 3.22c and 3.23c. Adapted from [117]

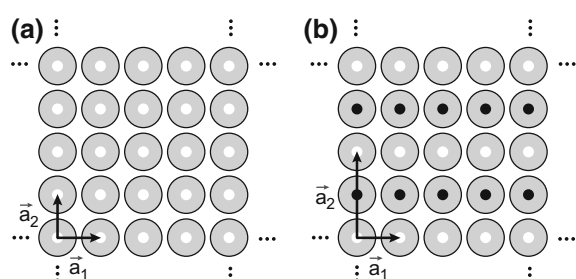
This experiment shows that there are strong similarities between the vibrational modes of benzene and the gyration modes of a six-fold ring of magnetic vortices. The symmetry of both systems determines the motions of the oscillators, i.e., the carbon atoms or the vortices. It allows to simplify the derivation of the fundamentally different dispersion relations of the vortex chain with periodic boundary conditions for the case of equal and alternating core polarizations. The example demonstrates the strength of self-organized state formation to adjust complex polarization patterns in interacting systems.

3.4.4 Band Structure Engineering of Magnonic Vortex Crystals

In the last section, the dispersion relation of a benzene-like vortex molecule was determined via the direct observation of the eigenmotions of the vortices. Larger periodic arrangements of vortices can be described as artificial crystals as the coupling between the vortices leads to a collective behavior. In analogy to photonic crystals, they are called magnonic crystals [43, 120] and feature a group velocity, a density of states, and a band structure [113, 116]. As for the benzene-like vortex molecule the band structure of two-dimensional vortex crystals is predicted to strongly depend on the polarization pattern [80, 116, 121]. Due to the different relative motions, the coupling between neighboring vortices differs for equal or different relative polarizations of the vortices (see Sect. 3.4.2). Therefore, different polarization patterns yield different crystal bases. Figure 3.25 depicts the patterns of homogeneous polarization and stripes of equal polarization for a two-dimensional rectangular arrangement of magnetic vortices. The resulting primitive vectors $\mathbf{a}_1, \mathbf{a}_2$ depend on the polarization configuration. This yields a single-vortex basis for the homogeneous polarization pattern depicted in Fig. 3.25a and a double-vortex basis for the striped polarization pattern depicted in Fig. 3.25b. As the Bravais lattice for the two polarization patterns are different, the crystal properties of the vortex crystal differ for the two polarization patterns.

Crystal properties can be determined experimentally by imprinting gyration waves into a vortex crystal. Neighboring vortices hereby gyrate with a phase-shift

Fig. 3.25 Primitive vectors for homogeneous polarization (a) and horizontally striped polarization (b). The white and black dots represent a vortex polarization of $p = 1$ and $p = -1$, respectively



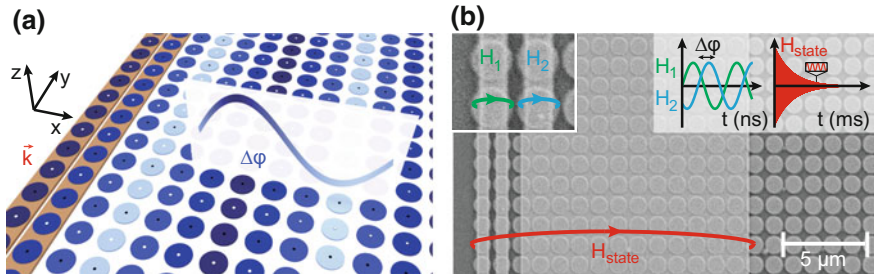


Fig. 3.26 **a** Schematic representation of gyration waves propagating through a two-dimensional vortex crystal imprinted by a phase-shifted excitation of the first two columns of vortices. **b** Scanning electron micrograph of a vortex crystal covered by copper striplines. All three striplines are used to tune the polarization pattern by self-organized state formation. The two thin striplines are used for band structure measurements. Adapted from [113]

forming waves with different wave lengths. In the sketch of Fig. 3.26a this phase-shifted gyration is represented by the color scale of the disks. Here, waves with a wavelengths of $\lambda = 6D$, where D is the center-to-center distance of the disks, that propagate in x -direction are depicted. These gyration waves are imprinted with the help of the two striplines on the left side of the array.

The polarization patterns can be tuned by self-organized state formation. A high frequency magnetic field is applied to a large area of magnetic vortices as shown in Fig. 3.26b and is then reduced adiabatically (see inset of Fig. 3.26b). Depending on the frequency of the high frequency magnetic field, different polarization patterns can be tuned in the crystal. Figure 3.27 shows the results for the polarization patterns as determined by scanning transmission x-ray microscopy. Therefore, the vortices are excited by a small alternating high frequency field that does not affect the polarization configuration. The size of the black or white dots in Fig. 3.27 represents the relative gyration amplitude during this non-invasive excitation. A horizontally striped polar-

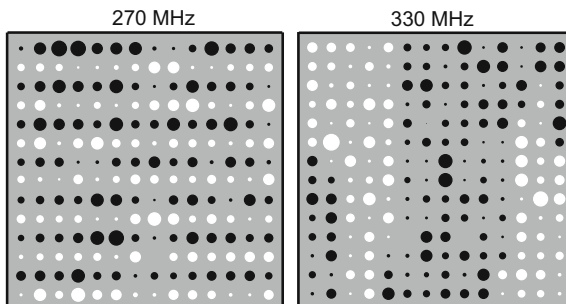
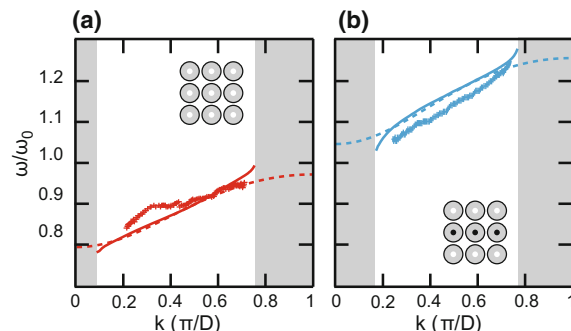


Fig. 3.27 Scanning transmission x-ray microscopy measurements after state formation with a frequency of 270 MHz and 330 MHz. The white and black dots correspond to $p = 1$ and $p = -1$, respectively. Their size depicts the relative gyration amplitude. Adapted from [113]

ization pattern is observed at $f_{\text{state}} = 270 \text{ MHz}$, while for state formation at 330 MHz large domains of homogeneous polarization emerge.

For the experimental determination of the dispersion relation of the vortex crystal gyration waves are imprinted into the crystal. Therefore, the collective motions of the vortices are excited and probed by the first two columns of vortices using the two thin striplines depicted in Fig. 3.26. Harmonic excitations $\mathbf{H}_1 = (H_0 \sin(\omega t), 0, 0)$ and $\mathbf{H}_2 = (H_0 \sin(\omega t + \Delta\varphi), 0, 0)$ are applied to the first and the second column of the crystal with different phase relations $\Delta\varphi$ creating waves with different wave lengths. Here, the boundary condition of the enforced phase relation of the first two columns allows excitation of collective motions with defined wave numbers. The resonance frequency of the crystal changes for different phase relations of the harmonic excitation and can be determined using ferromagnetic resonance spectroscopy. The power absorption due to the vortex gyration is hereby recorded in dependence of the excitation frequency. The band structure is obtained by translating each phase difference of the excitation $\Delta\varphi$ into a wave number k with the help of numerical calculations based on the Thiele model (Sect. 3.3.1). Figure 3.28 shows the dispersion relation of a vortex crystal with domains of homogeneous polarization (a) and horizontally striped polarization (b). The blue and red markers represent the maxima of the absorption spectra determined by ferromagnetic resonance spectroscopy. The two polarization patterns, i.e. horizontal stripes and large domains, feature different frequency offsets $\omega(k = 0)$ of their collective motions. By increasing the wave number k the resonance frequency increases. The variation of the absorption frequency of the striped pattern in Fig. 3.28b is stronger than for the homogeneous domain pattern shown in Fig. 3.28a. In other words, the bandwidth of the strongly interacting striped pattern is larger than the bandwidth of the weakly interacting homogeneous pattern. The band structure measurements are compared to calculations based on the Thiele model including damping (lines) and calculations for an infinite crystal without damping (dashed lines) obtained from [116]. Small differences between experiment and calculations are explained by slight geometrical irregularities of the microdisks that lead to a decrease in bandwidth of the resonances. Wave numbers above and below a value of about $0.2 \pi/D$ and $0.8 \pi/D$ (gray regions) cannot be excited experimentally in the crystal. This is presumably caused by waves that are

Fig. 3.28 Band structure measurements (markers), calculations based on the Thiele model including damping (lines), and calculations by Shibata et al. [116] without damping (dashed lines). **a** Homogeneous polarization pattern. **b** Horizontally striped polarization pattern. Adapted from [113]



absorbed before being transmitted into the crystal due to low group velocities in the gap regions. The partial wave number gaps vanish for zero damping. The experimentally determined dispersion relations for domains of homogeneous polarization and striped polarization show the theoretically expected behavior. The band structure can be reprogrammed by polarization pattern tuning, taking effect on the frequency offsets and the bandwidths of the dispersion relations.

3.5 Summary and Outlook

Magnetic vortices as fundamental topological objects possess properties that are governed by few parameters. For the single object the polarization and the circularity determine the static, the quasi-static and the dynamic behavior. The gyrotrropic mode is described in the micromagnetic model by application of the Landau-Lifshitz-Gilbert equation. For small excitations a harmonic oscillator model based on the Thiele equation describes the vortex dynamics precisely, where the handedness determines the sense of gyration and its phase. For strong excitations the oscillator model has to be modified by consideration of nonlinearities. For even stronger excitations core switching sets in, a process that includes the creation, annihilation, and fusion of vortices and their topological counterpart the antivortex. If excitations are applied to multiple vortices interactions play an important role. By application of magnetic field pulses and harmonic excitations in regular arrangements distinct eigenmodes with defined frequencies are identified. These eigenmodes crucially depend on the relative polarizations of the vortices in the arrangements. A polarization manipulation process based on a fundamental stability criterion has been found. When the absorption of the vortices reaches a certain threshold, the polarization pattern is destroyed and one remaining stable state is generated. This scheme is called self-organized state formation and it can be utilized as writing mechanism, although up to now such a writing process is not competitive with latest storage devices. Still it allows for restructuring large vortex crystals. Thereby, the dispersion relation of vortex arrays can be manipulated and determined experimentally for different polarization patterns. Very recently even a tunable geometrical frustration in a spin-ice like magnonic vortex crystals has been achieved by self-organized state formation [122]. For prospective applications the use of alternative materials as yttrium iron garnet might be an option [123]. Within the field of magnonic crystals, vortex arrangements provide an interesting model system that can be manipulated using self-organized state formation.

In future a volumetric approach by introducing multiple layers will allow for increased densities of three-dimensional vortex crystals [47, 48, 124]. It is also interesting to study higher order modes of excitation of interacting vortices with frequencies up to many GHz. The coupling in stacked magnetic thin films yields a non-reciprocal spin-wave dispersion with direction dependent group velocities. Thereby, propagating spin waves with wavelengths in the order of hundreds of nanometers have been imaged [39, 125]. Since the spin waves only occur in layers with oppo-

site vortex circularities, switching the circularity of one of the disks would tune the propagation of spin waves. In combination with switching processes based on the recently discovered spin-orbit torque [126], this effect would facilitate spin wave based logic devices and radiofrequency detection schemes based on magnetic vortices [127]. It can be stated that magnonic elements are promising candidates for the next generation of information processing devices. The oscillation of the magnetic vortex core can generate spin waves and can therefore serve as spin wave emitter [39]. Additionally it has been shown that it is possible to tune the relative polarization of vortex stacks with subnanosecond magnetic field bursts [125]. Such writing times are competitive with state-of-the-art random access memories and vortex stacks could provide non-volatile storage of information. Generation and control of spin-waves in stacks of vortices will create new possibilities for information processing devices.

Acknowledgements We are grateful to Ulrich Merkt for continuous support and fruitful discussions over many years. This chapter wouldn't have been possible without the contributions from Markus Bolte, André Drews, Max Häenze, Thomas Kamionka, Peter Lendecke, Michael Martens, Matthias Pues, Falk-Ulrich Stein, and Andreas Vogel. G.M. acknowledges support and new insights provided by Andrea Cavalleri. We acknowledge financial support from the Deutsche Forschungsgemeinschaft via SFB 668 ‘Magnetism from the Single Atom to the Nanostructure’, via Graduiertenkolleg 1286 ‘Functional Metal-Semiconductor Hybrid Systems’, and via excellence cluster ‘The Hamburg Centre for Ultrafast Imaging—Structure, Dynamics and Control of Matter on the Atomic Scale’.

References

1. I. Newton, *Philosophiae Naturalis Principia Mathematica* (Royal Society, London, 1687)
2. G.-G. Coriolis, J. de l'Ecole, R. Polytech. **15**, 144 (1835)
3. T.H.R. Skyrme, Nucl. Phys. **31**, 556 (1962)
4. A. Fert, V. Cros, J. Sampaio, Nat. Nanotechnol. **8**, 152 (2013)
5. S. Mühlbauer, B. Binz, F. Jonietz, C. Pfleiderer, A. Rosch, A. Neubauer, R. Georgii, P. Böni, Science **323**, 915 (2009)
6. O.A. Tretiakov, O. Tchernyshyov, Phys. Rev. B **75**, 012408 (2007)
7. I.E.J. Dzyaloshinskii, Phys. Chem. Sol. **4**, 241 (1958)
8. T. Moriya, Phys. Rev. **120**, 91 (1960)
9. E.E. Huber, D.O. Smith, J.B. Goodenough, J. Appl. Phys. **29**, 294 (1958)
10. S. Middelhoek, J. Appl. Phys. **34**, 1054 (1963)
11. W. Döring, J. Appl. Phys. **39**, 1006 (1968)
12. R. Feldtkeller, Z. Angew. Phys. **19**, 530 (1965)
13. A. Hubert, R. Schäfer, *Magnetic Domains—The Analysis of Magnetic Microstructures* (Springer, Berlin, Heidelberg, 1998)
14. M. Pues, Dissertation, University of Hamburg (2015)
15. G. Meier, M. Bolte, R. Eiselt, B. Krüger, D.-H. Kim, P. Fischer, Phys. Rev. Lett. **98**, 187202 (2007)
16. T. Shinjo, T. Okuno, R. Hassdorf, K. Shigeto, T. Ono, Science **289**, 930 (2000)
17. A. Wachowiak, J. Wiebe, M. Bode, O. Pietzsch, M. Morgenstern, R. Wiesendanger, Science **298**, 577 (2002)
18. M. Martens, T. Kamionka, A. Drews, B. Krüger, G. Meier, J. Appl. Phys. **112**, 013917 (2012)
19. J. Stöhr, H.C. Siegmann, *Magnetism: From Fundamentals to Nanoscale Dynamics* (Springer, Berlin, Heidelberg, 2006)

20. T. Kamionka, M. Martens, K.W. Chou, M. Curcic, A. Drews, G. Schütz, T. Tyliszczak, H. Stoll, B. Van Waeyenberge, G. Meier, *Phys. Rev. Lett.* **105**, 137204 (2010)
21. M. Pues, M. Martens, T. Kamionka, G. Meier, *Appl. Phys. Lett.* **100**, 162404 (2012)
22. A. Haldar, K.S. Buchanan, *Appl. Phys. Lett.* **102**, 112401 (2013)
23. K. Shigeto, T. Okuno, K. Mibu, T. Shinjo, T. Ono, *Appl. Phys. Lett.* **80**, 4190 (2002)
24. K. Kuepper, M. Buess, J. Raabe, C. Quitmann, J. Fassbender, *Phys. Rev. Lett.* **99**, 167202 (2007)
25. M.-Y. Im, P. Fischer, K. Yamada, T. Sato, S. Kasai, Y. Nakatani, T. Ono, *Nat. Commun.* **3**, 983 (2012)
26. M.-Y. Im, K.-S. Lee, A. Vogel, J.-I. Hong, G. Meier, P. Fischer, *Nat. Commun.* **5**, 5620 (2014)
27. V. Uhlíř, M. Urbánek, L. Hladík, J. Spousta, M.-Y. Im, P. Fischer, N. Eibagi, J.J. Kan, E.E. Fullerton, T. Šikola, *Nat. Nanotech.* **8**, 341 (2013)
28. M.-Y. Im, P. Fischer, H.-S. Han, A. Vogel, M.-S. Jung, W. Chao, Y.-S. Yu, G. Meier, J.-I. Hong, K.-S. Lee, *NPG Asia Mater.* **9**, e348 (2017)
29. T. Kamionka, Dissertation, University of Hamburg (2012)
30. S.-B. Choe, Y. Acremann, A. Scholl, A. Bauer, A. Doran, J. Stöhr, H.A. Padmore, *Science* **304**, 420 (2004)
31. B. Krüger, A. Drews, M. Bolte, U. Merkt, D. Pfannkuche, G. Meier, *Phys. Rev. B* **76**, 224426 (2007)
32. R. Lebrun, A. Jenkins, A. Dussaux, N. Locatelli, S. Tsunegi, E. Grimaldi, H. Kubota, P. Bortolotti, K. Yakushiji, J. Grollier, A. Fukushima, S. Yuasa, V. Cros, *Phys. Rev. Lett.* **115**, 017201 (2015)
33. S. Tsunegi, E. Grimaldi, R. Lebrun, H. Kubota, A.S. Jenkins, K. Yakushiji, A. Fukushima, P. Bortolotti, J. Grollier, S. Yuasa, V. Cros, *Sci. Rep.* **6**, 26849 (2016)
34. S. Bohlens, B. Krüger, A. Drews, M. Bolte, G. Meier, D. Pfannkuche, *Appl. Phys. Lett.* **93**, 142508 (2008)
35. A. Drews, B. Krüger, G. Meier, S. Bohlens, L. Bocklage, T. Matsuyama, M. Bolte, *Appl. Phys. Lett.* **94**, 062504 (2009)
36. B. Van Waeyenberge, A. Puzic, H. Stoll, K.W. Chou, T. Tyliszczak, R. Hertel, M. Fähnle, H. Brückl, K. Rott, G. Reiss, I. Neudecker, D. Weiss, C.H. Back, G. Schütz, *Nature* **444**, 461 (2006)
37. M. Kammerer, M. Weigand, M. Curcic, M. Noske, M. Sproll, A. Vansteenkiste, B. Van Waeyenberge, H. Stoll, G. Woltersdorf, C.H. Back, G. Schütz, *Nat. Commun.* **2**, 279 (2011)
38. M. Kammerer, H. Stoll, M. Noske, M. Sproll, M. Weigand, C. Illg, G. Woltersdorf, M. Fähnle, C. Back, G. Schütz, *Phys. Rev. B* **86**, 134426 (2012)
39. S. Wintz, V. Tiberkevich, M. Weigand, J. Raabe, J. Lindner, A. Erbe, A. Slavin, J. Fassbender, *Nat. Nanotechnol.* **11**, 948 (2016)
40. J. Shibata, K. Shigeto, Y. Otani, *Phys. Rev. B* **67**, 224404 (2003)
41. K.Y. Guslienko, K.S. Buchanan, S.D. Bader, V. Novosad, *Appl. Phys. Lett.* **86**, 223112 (2005)
42. A. Vogel, T. Kamionka, M. Martens, A. Drews, K.W. Chou, T. Tyliszczak, H. Stoll, B. Van Waeyenberge, G. Meier, *Phys. Rev. Lett.* **106**, 137201 (2011)
43. B. Lenk, H. Ulrichs, F. Garbs, M. Münzenberg, *Phys. Rep.* **507**, 107 (2011)
44. M. Krawczyk, D. Grundler, *J. Phys. Condens. Matter* **26**, 123202 (2014)
45. J. Mejía-López, D. Altbir, A.H. Romero, X. Batlle, I.V. Roshchin, C.-P. Li, I.K. Schuller, *J. Appl. Phys.* **100**, 104319 (2006)
46. R. Fontana, G. Decad, IBM Systems and Technology Group, Presentation (2014)
47. M. Hänze, C.F. Adolff, S. Velten, M. Weigand, G. Meier, *Phys. Rev. B* **93**, 054411 (2016)
48. M. Hänze, C.F. Adolff, B. Schulte, J. Möller, M. Weigand, G. Meier, *Sci. Rep.* **6**, 22402 (2016)
49. D.-H. Kim, E.A. Rozhkova, I.V. Ulasov, S.D. Bader, T. Rajh, M.S. Lesniak, V. Novosad, *Nat. Mater.* **9**, 165 (2009)
50. J. Zimmer, A. Satz, W. Raberg, H. Brueckl, D. Suess, United States Patent Application Publication, US 2015/0185297 A1 (2015)
51. J. Torrejon, M. Riou, F. Abreu Araujo, S. Tsunegi, G. Khalsa, D. Querlioz, P. Bortolotti, V. Cros, K. Yakushiji, A. Fukushima, H. Kubota, S. Yuasa, M.D. Stiles, J. Grollier, *Nature* **547**, 428 (2017)

52. M. Romera, P. Talatchian, S. Tsunegi, F. Abreu Araujo, V. Cros, P. Bortolotti, K. Yakushiji, A. Fukushima, H. Kubota, S. Yuasa, D. Vodenicarevic, N. Locatelli, D. Querlioz, J. Grollier (2017). [arXiv:1711.02704](https://arxiv.org/abs/1711.02704)
53. W.F. Brown, *J. Appl. Phys.* **30**, 62 (1959)
54. D. Goll, G. Schütz, H. Krommüller, *Phys. Rev. B* **67**, 094414 (2003)
55. Y. Nakatani, A. Thiaville, J. Miltat, *J. Magn. Magn. Mater.* **290**, 750 (2005)
56. H. Krommüller, *Z. Phys.* **168**, 478 (1962)
57. K.Y. Guslienko, V. Novosad, Y. Otani, H. Shima, K. Fukamichi, *Appl. Phys. Lett.* **78**, 3848 (2001)
58. T. Kamionka, M. Martens, K.W. Chou, A. Drews, T. Tyliszczak, H. Stoll, B. Van Waeyenberge, G. Meier, *Phys. Rev. B* **83**, 224422 (2011)
59. A. Drews, B. Krüger, M. Bolte, G. Meier, *Phys. Rev. B* **77**, 094413 (2008)
60. M. Pues, M. Martens, G. Meier, *J. Appl. Phys.* **116**, 153903 (2014)
61. A. Vogel, A. Drews, T. Kamionka, M. Bolte, G. Meier, *Phys. Rev. Lett.* **105**, 037201 (2010)
62. L. Breitenstein, P. Lendecke, S. Bohlens, G. Meier, U. Merkt, *J. Appl. Phys.* **104**, 083909 (2008)
63. G. Mihajlović, M.S. Patrick, J.E. Pearson, V. Novosad, S.D. Bader, M. Field, G.J. Sullivan, A. Hoffmann, *Appl. Phys. Lett.* **96**, 112501 (2010)
64. E. Östman, U.B. Arnalds, E. Melander, V. Kapaklis, G.K. Pálsson, A.Y. Saw, M.A. Verschueren, F. Kronast, E.T. Papaioannou, C.S. Fadley, B. Hjörvarsson, *New J. Phys.* **16**, 053002 (2014)
65. K.Y. Guslienko, B.A. Ivanov, V. Novosad, Y. Otani, H. Shima, K. Fukamichi, *J. Appl. Phys.* **91**, 8037 (2002)
66. R.L. Compton, P.A. Crowell, *Phys. Rev. Lett.* **97**, 137202 (2006)
67. R.L. Compton, T.Y. Chen, P.A. Crowell, *Phys. Rev. B* **81**, 144412 (2010)
68. T. Kamionka, M. Martens, A. Drews, B. Krüger, O. Albrecht, G. Meier, *Phys. Rev. B* **83**, 224424 (2011)
69. L.D. Landau, E. Lifshitz, *Phys. Z. Sowjetunion* **8**, 153 (1935)
70. T. L. Gilbert, Dissertation, Illinois Institute of Technology, 1956
71. T.L. Gilbert, I.E.E.E. Trans, *IEEE Trans. Magn.* **40**, 3443 (2004)
72. MICROMAGNUM, <http://micromagnum.informatik.uni-hamburg.de>
73. A.A. Thiele, *Phys. Rev. Lett.* **30**, 230 (1973)
74. K.Y. Guslienko, V. Novosad, Y. Otani, H. Shima, K. Fukamichi, *Phys. Rev. B* **65**, 024414 (2001)
75. M. Martens, T. Kamionka, M. Weigand, H. Stoll, T. Tyliszczak, G. Meier, *Phys. Rev. B* **87**, 054426 (2013)
76. C.F. Adolff, Dissertation, Verlag Dr. Hut (2016)
77. B. Krüger, A. Drews, M. Bolte, U. Merkt, D. Pfannkuche, G. Meier, *J. Appl. Phys.* **103**, 07A501 (2008)
78. C.F. Adolff, Dissertation, University of Hamburg (2015)
79. A. Drews, B. Krüger, G. Selke, T. Kamionka, A. Vogel, M. Martens, U. Merkt, D. Möller, G. Meier, *Phys. Rev. B* **85**, 144417 (2012)
80. O.V. Sukhostavets, B. Pigeau, S. Sangiao, G. de Loubens, V.V. Naletov, O. Klein, K. Mitsuzuka, S. Andrieu, F. Montaigne, K.Y. Guslienko, *Phys. Rev. Lett.* **111**, 247601 (2013)
81. H.H. Langner, T. Kamionka, M. Martens, M. Weigand, C.F. Adolff, U. Merkt, G. Meier, *Phys. Rev. B* **85**, 174436 (2012)
82. K.L. Liu, K. Young, *J. Math. Phys.* **27**, 502 (1986)
83. R. Hertel, C.M. Schneider, *Phys. Rev. Lett.* **97**, 177202 (2006)
84. K.Y. Guslienko, K.-S. Lee, S.-K. Kim, *Phys. Rev. Lett.* **100**, 027203 (2008)
85. Y.-S. Yu, K.-S. Lee, H. Jung, Y.-S. Choi, M.-W. Yoo, D.-S. Han, M.-Y. Im, P. Fischer, S.-K. Kim, *Phys. Rev. B* **83**, 174429 (2011)
86. Q.F. Xiao, J. Rudge, B.C. Choi, Y.K. Hong, G. Donohoe, *Appl. Phys. Lett.* **89**, 262507 (2006)
87. R. Hertel, S. Gliga, M. Fähnle, C.M. Schneider, *Phys. Rev. Lett.* **98**, 117201 (2007)

88. K. Yamada, S. Kasai, Y. Nakatani, K. Kobayashi, H. Kohno, A. Thiaville, T. Ono, *Nat. Mater.* **6**, 270 (2007)
89. K. Yamada, S. Kasai, Y. Nakatani, K. Kobayashi, T. Ono, *Appl. Phys. Lett.* **93**, 152502 (2008)
90. M. Curcic, B. Van Waeyenberge, A. Vansteenkiste, M. Weigand, V. Sackmann, H. Stoll, M. Fähnle, T. Tyliszczak, G. Woltersdorf, C.H. Back, G. Schütz, *Phys. Rev. Lett.* **101**, 197204 (2008)
91. M. Curcic, H. Stoll, M. Weigand, V. Sackmann, P. Jüllig, M. Kammerer, M. Noske, M. Sproll, B. Van Waeyenberge, A. Vansteenkiste, G. Woltersdorf, T. Tyliszczak, G. Schütz, *Phys. Status Solidi B* **248**, 2317 (2011)
92. M. Weigand, B. Van Waeyenberge, A. Vansteenkiste, M. Curcic, V. Sackmann, H. Stoll, T. Tyliszczak, K. Kaznatcheev, D. Bertwistle, G. Woltersdorf, C.H. Back, G. Schütz, *Phys. Rev. Lett.* **102**, 077201 (2009)
93. V.P. Kravchuk, D.D. Sheka, Y.B. Gaididei, F.G. Mertens, *J. Appl. Phys.* **102**, 043908 (2007)
94. A. Vansteenkiste, K.W. Chou, M. Weigand, M. Curcic, V. Sackmann, H. Stoll, T. Tyliszczak, G. Woltersdorf, C.H. Back, G. Schütz, B. Van Waeyenberge, *Nat. Phys.* **5**, 332 (2009)
95. S.-K. Kim, K.-S. Lee, Y.-S. Yu, Y.-S. Choi, *Appl. Phys. Lett.* **92**, 022509 (2008)
96. K.-S. Lee, S.-K. Kim, Y.-S. Yu, Y.-S. Choi, K.Y. Guslienko, H. Jung, P. Fischer, *Phys. Rev. Lett.* **101**, 267206 (2008)
97. K. Yamada, S. Kasai, Y. Nakatani, K. Kobayashi, T. Ono, *Appl. Phys. Lett.* **96**, 192508 (2010)
98. M. Hänze, Dissertation, University of Hamburg (2016)
99. A. Vogel, M. Martens, M. Weigand, G. Meier, *Appl. Phys. Lett.* **99**, 042506 (2011)
100. H. Jung, K.-S. Lee, D.-E. Jeong, Y.-S. Choi, Y.-S. Yu, D.-S. Han, A. Vogel, L. Bocklage, G. Meier, M.-Y. Im, P. Fischer, S.-K. Kim, *Sci. Rep.* **1**, 59 (2011)
101. S. Barman, A. Barman, Y. Otani, *I.E.E.E. Trans, IEEE Trans. Magn.* **46**, 1342 (2010)
102. A. Barman, S. Barman, T. Kimura, Y. Fukuma, Y. Otani, *J. Phys. D: Appl. Phys.* **43**, 422001 (2010)
103. S. Sugimoto, Y. Fukuma, S. Kasai, T. Kimura, A. Barman, Y. Otani, *Phys. Rev. Lett.* **106**, 197203 (2011)
104. K.S. Buchanan, P.E. Roy, M. Grimsditch, F.Y. Fradin, K.Y. Guslienko, S.D. Bader, V. Novosad, *Nat. Phys.* **1**, 172 (2005)
105. A. Ruotolo, V. Cros, B. Georges, A. Dussaux, J. Grollier, C. Deranlot, R. Guillemet, K. Bouzehouane, S. Fusil, A. Fert, *Nat. Nano.* **4**, 528 (2009)
106. S. Jain, V. Novosad, F.Y. Fradin, J.E. Pearson, V. Tiberkevich, A.N. Slavin, S.D. Bader, *Nat. Comm.* **3**, 1330 (2012)
107. N. Locatelli, A. Hamadeh, F. Abreu Araujo, A.D. Belanovsky, P.N. Skirdkov, R. Lebrun, V.V. Naletov, K.A. Zvezdin, M. Muñoz, J. Grollier, O. Klein, V. Cros, G. de Loubens, *Sci. Rep.* **5**, 17039 (2015)
108. R. Lebrun, S. Tsunegi, P. Bortolotti, H. Kubota, A.S. Jenkins, M. Romera, K. Yakushiji, A. Fukushima, J. Grollier, S. Yuasa, V. Cros, *Nat. Commun.* **8**, 15825 (2017)
109. S.T. Thornton, J.B. Marion, *Classical Dynamics of Particles and Systems*, 5th edn. (Thomson, 2004)
110. S. Wintz, C. Bunce, A. Neudert, M. Körner, T. Strache, M. Buhl, A. Erbe, S. Gemming, J. Raabe, C. Quitmann, J. Fassbender, *Phys. Rev. Lett.* **110**, 177201 (2013)
111. M. Hänze, C.F. Adolff, M. Weigand, G. Meier, *Phys. Rev. B* **91**, 104428 (2015)
112. M. Hänze, C.F. Adolff, M. Weigand, G. Meier, *Appl. Phys. Lett.* **104**, 182405 (2014)
113. C. Behncke, M. Hänze, C.F. Adolff, M. Weigand, G. Meier, *Phys. Rev. B* **91**, 224417 (2015)
114. C.F. Adolff, M. Hänze, A. Vogel, M. Weigand, M. Martens, G. Meier, *Phys. Rev. B* **88**, 224425 (2013)
115. H. Stoll, M. Noske, M. Weigand, K. Richter, B. Krüger, R.M. Reeve, M. Hänze, C.F. Adolff, F.-U. Stein, G. Meier, M. Kläui, G. Schütz, *Front. Phys.* **3**, 26 (2015)
116. J. Shibata, Y. Otani, *Phys. Rev. B* **70**, 012404 (2004)
117. C.F. Adolff, M. Hänze, M. Pues, M. Weigand, G. Meier, *Phys. Rev. B* **92**, 024426 (2015)
118. E. Wigner, *Math.-Phys.* **1**, 133 (1930)
119. E.B. Wilson, *Phys. Rev.* **45**, 706 (1934)

120. V.V. Kruglyak, S.O. Demokritov, D. Grundler, *J. Phys. D: Appl. Phys.* **43**, 264001 (2010)
121. A.Y. Galkin, B.A. Ivanov, C.E. Zaspel, *Phys. Rev. B* **74**, 144419 (2006)
122. C. Behncke, C. F. Adolff, S. Wintz, M. Hänze, B. Schulte, M. Weigand, S. Finizio, J. Raabe, G. Meier, *Sci. Rep.* **8**, 186 (2018)
123. A.A. Serga, A.V. Chumak, B. Hillebrands, *J. Phys. D: Appl. Phys.* **43**, 264002 (2010)
124. T. Tanigaki, Y. Takahashi, T. Shimakura, T. Akashi, R. Tsuneta, A. Sugawara, D. Shindo, *Nano Lett.* **15**, 1309 (2015)
125. M. Hänze, B. Schulte, C.F. Adolff, C. Behncke, M. Weigand, and G. Meier, in preparation
126. L. Liu, C.-F. Pai, Y. Li, H.W. Tseng, D.C. Ralph, R.A. Buhrman, *Science* **336**, 555 (2012)
127. A.S. Jenkins, R. Lebrun, E. Grimaldi, S. Tsunegi, P. Bortolotti, H. Kubota, K. Yakushiji, A. Fukushima, G. de Loubens, O. Klein, S. Yuasa, V. Cros, *Nat. Nano.* **11**, 360 (2016)
128. D.S. Han, A. Vogel, H. Jung, K.-S. Lee, M. Weigand, H. Stoll, G. Schütz, P. Fischer, G. Meier, S.-K. Kim, *Sci. Rep.* **3**, 2262 (2013)

Chapter 4

Magnetic Skyrmions in Thin Films



Gong Chen

Abstract The microstructure of magnetic materials such as magnetic domains and domain walls, linking to its basic physical properties, is generally considered as a result of the interplay between exchange interaction, anisotropy and magnetic dipolar interaction.

4.1 Introduction

4.1.1 Magnetic Domain Structures in Thin Films

The microstructure of magnetic materials such as magnetic domains and domain walls, linking to its basic physical properties, is generally considered as a result of the interplay between exchange interaction, anisotropy and magnetic dipolar interaction [1]. In 1970s, the development of molecular beam epitaxy technique benefited fundamental studies of semiconductor surfaces and thin films, as well as their practical applications in fabrications of conventional and novel devices [2]. A magnetic film is defined as thin, when the thickness of the film is comparable to the width of the magnetic domain wall. A consequence is that, spins along the direction normal to the film plane is usually aligned along same direction, in contrast to more complicated three dimensional spin structures in bulk materials, such as asymmetric Bloch wall or closure Domains [3]. Therefore spin textures in thin films are usually considered as two-dimensional spin lattices in this section.

We consider thin films with two basic geometries in the view of anisotropy, i.e. in-plane magnetized films and out-of-plane magnetized films. We note here, as magnetization within domains is generally parallel to the easy axes of magnetic anisotropy, the rotation of the spin structures within domain walls has richer degree of freedom, for instance, domain wall type could be Bloch-type or Néel type, and its rotation sense could be right-handedness or left-handedness.

G. Chen (✉)

Physics Department, University of California, Davis, CA 95616, USA

e-mail: gch@ucdavis.edu

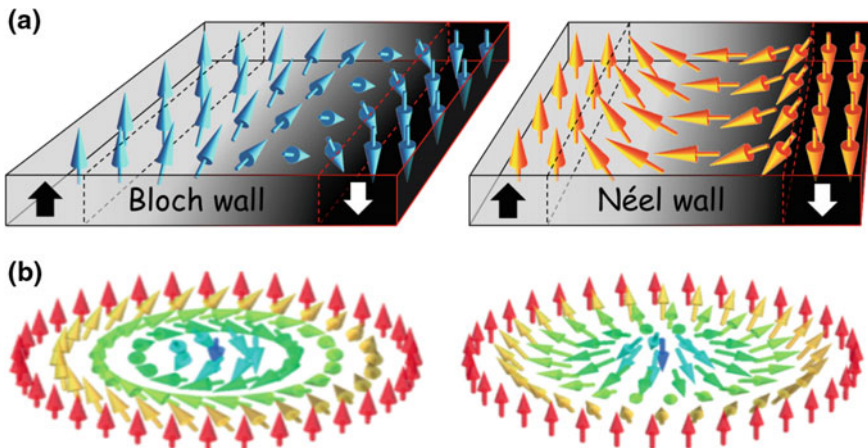


Fig. 4.1 **a** Sketches of Bloch wall and Néel wall in perpendicularly magnetized films, arrows indicate local magnetization direction. **b** Sketches of Bloch-type skyrmion (left) and Néel-type skyrmion (right), where the magnetization rotating from downward at the center of the skyrmion to upward of the external uniform magnetization at the edge of the skyrmion. Panels a is reproduced with permission from [14], © 2015 WILEY-VCH. Panels b is reproduced with permission from [15], courtesy of K. Everschor-Sitte, University of Cologne, Germany

In in-plane magnetized films, domain walls may rotate either towards to out-of-plane as Bloch wall in thicker films, or within film plane in thinner films depending on the stray field energy of the wall, which is related to the ratio of film thickness and the width of domain walls [1].

In perpendicularly magnetized films, domain walls have to rotate towards into the film plane, where the in-plane component could be parallel/perpendicular to the boundary direction, forming Bloch-type/Néel-type domain walls (see Fig. 4.1a). The formation of Bloch walls has been considered to cost less energy due to the stray field in the past [4]. More recently, chiral Néel domain walls (also called Dzyaloshinskii domain walls) have been predicted in ultrathin films [5] due to the presence of significant interfacial Dzyaloshinskii-Moriya interaction (DMI) [6, 7]. Chiral domain wall configuration was later directly imaged in Fe/Ni bilayer on Cu (where the dominant DMI likely locates at Fe/Ni interface), [8] and was confirmed in current-driven dynamics of domain walls [9, 10]. In terms of the domain formation, perpendicularly magnetized films exhibit fascinating domain patterns, which are known as stripe phase at zero external magnetic field or bubble phase in the presence of finite perpendicular magnetic field. The formation of those domain patterns have been attributed to the interplay between long range (dipolar) and short range (exchange) interactions [11]. In the past, the roles of domain wall spin structures in stripe phase or bubble phase have not been considered as important in magnetic field driven evolution of spin structures, in both theoretically [12] and experimentally [13].

In the chapter written by Thiaville and Miltat, topology and chirality of magnetic domain walls in thin films and multilayers are introduced in detail. In Sect. 4.2a of this chapter, we also briefly introduce how the presence of the DMI can greatly

enrich the possibilities of stabilizing domain wall configurations, extending common picture of achiral Bloch walls to chiral Néel walls or even mixed walls in between, where a combination of chiral Néel walls and bubble domains results in novel spin texture of the skyrmions. Here magnetic chirality is an additional degree of freedom in spin configurations that is opening up new directions in the field of spintronics.

4.1.2 Spin Textures of Néel-Type Skyrmions

The interfacial DMI stabilized skyrmions are commonly called hedgehog skyrmions or Néel-type skyrmions (see Fig. 4.1b), where all spins rotate from the center of magnetic skyrmion to its boundary as cycloidal (Néel-type) spin spirals with fixed chirality [16, 17]. This spin configuration dramatically differs from skyrmions observed in the presence of the bulk DMI [18], where spins within skyrmions rotate as helical spin spiral (Bloch-type). Such fundamental difference of Néel versus Bloch is associated with the orientation of the DMI vector in two cases, as discussed in the following.

The energy term of the interfacial DMI can be written as $E = -\mathbf{D}_{ij} \cdot (\mathbf{S}_i \times \mathbf{S}_j)$, where \mathbf{D}_{ij} is the vector of the DMI, \mathbf{S}_i and \mathbf{S}_j are spins at atomic sites i and j . The orientation of the DMI vector with respect to the distance vector \mathbf{r}_{ij} is determined by the fact that how the inversion symmetry of atoms breaks in the materials. In case of the DMI at interface, the broken inversion symmetry along the interface normal direction results in interfacial DMI [19], where the vector of the DMI usually aligns within the film plane and points to \mathbf{r}_{ij} normal direction [20]. Therefore the rotation between \mathbf{S}_i and \mathbf{S}_j as cycloidal (Néel-type) spin spirals has lowest DMI energy cost (see Fig. 4.2), and the sign of the DMI vector determines clockwise/counter-clockwise rotation sense. Moreover, $\mathbf{S}_i \times \mathbf{S}_j$ in helical (Bloch-type) spin spirals is always normal to \mathbf{r}_{ij} , resulting in zero interfacial DMI energy, as well as achiral Bloch-type configurations. In contrast, the vector of the DMI in bulk materials is usually parallel to \mathbf{r}_{ij} [21], which favors chiral Bloch-type configurations.

As introduced in the Chap. 2 written by Thiaville and Miltat, the spin configuration of a skyrmion gives rise to a topological charge, which can be characterized by a skyrmion winding number w . This number and can be expressed as $w = \frac{1}{4\pi} \iint \mathbf{m} \cdot (\partial_x \mathbf{m} \times \partial_y \mathbf{m}) dx dy$, which counts how many times the local magnetization vector \mathbf{m} is wrapped around a unit sphere [23]. A skyrmion with integer skyrmion winding number (1 or -1), is topologically inequivalent to other spin configurations with different skyrmion winding number such as uniform magnetization with zero skyrmion winding number. A physical manifestation of such topological quantization is that the skyrmion configurations are topologically protected from continuous deforming into other spin configurations with different skyrmion winding number. This protection associated energy barrier is considered as infinite from the point of view of topological classification, however, in real magnetic systems, the energy barrier is expected to be finite due to the approximation of the continuum description for discrete lattices in magnetic materials, the approximation of the restriction of magnetizations in systems with finite anisotropy, and possibilities of skyrmions annihilation at sample edges.

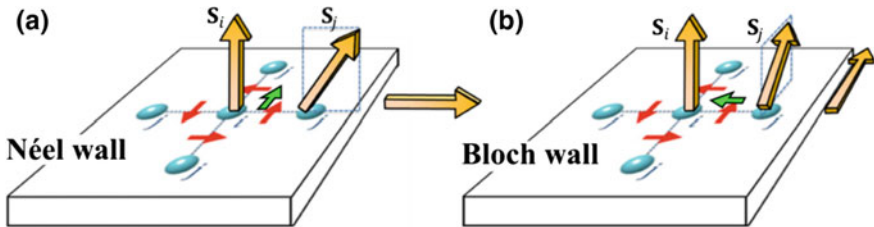


Fig. 4.2 Sketch of the interfacial DMI vector (red arrows) for an atom i (blue circle) surrounded by four atoms j . Yellow arrows indicate the orientation of local spins. Green arrows correspond to the direction of the cross-product $(\mathbf{S}_i \times \mathbf{S}_j)$. Panel **a** represents a case where the interfacial DMI energy can be influenced by Néel-type wall (green arrow is parallel to red arrow), Panel **b** represents a case where the interfacial DMI energy vanishes for Bloch-type wall (green arrow is perpendicular to red arrow). Figure is reproduced with permission from [22], © CRC press

4.2 Experimental Realization of Skyrmions in Thin Films

4.2.1 Interfacial Dzyaloshinskii-Moriya Interaction

The interfacial DMI is one of the most important and widely-used mechanisms to stabilize chiral spin textures in thin film systems. Historically Dzyaloshinskii proposed that the combination of spin-orbit coupling and low symmetry gives rise an antisymmetric exchange interaction written as $-\mathbf{D}_{ij} \cdot (\mathbf{S}_i \times \mathbf{S}_j)$, where \mathbf{D}_{ij} is the vector of the DMI, \mathbf{S}_i and \mathbf{S}_j are spins at atomic sites i and j [6]. Then Moriya introduced a microscopic model to calculate the antisymmetric exchange interaction in a localized magnetic system [7]. Dzyaloshinskii and Moriya also attributed the weak ferromagnetism in antiferromagnetic compounds, such as $\alpha\text{-Fe}_2\text{O}_3$, to this antisymmetric exchange interaction, which was later recognized as Dzyaloshinskii-Moriya interaction.

Beside possible influences of the DMI in low symmetry materials, Fert and Levy proposed another mechanism of the DMI that involves both magnetic and non-magnetic sites [24], where the vector of the DMI points normal to the plane defined by a triangle of two magnetic atoms and one non-magnetic atom, as shown in Fig. 4.3a. This picture was further extended to the surface/interface of thin films by Fert (see Fig. 4.3b) [19]. Later Crépieux and Lacroix discussed systematically the vector configurations of the DMI at surfaces of the simple cubic, body centered cubic and face-centered cubic structures (see Fig. 4.3c) [20]. For instance, considering a spin site \mathbf{S}_i and its four nearest neighbor spin sites \mathbf{S}_j on fcc(001) surface, four vectors of the DMI have same rotation sense as counterclockwise (black arrows in Fig. 4.3c) or clockwise (not shown), resulting in isotropic chirality in this in-plane symmetric surface sites. This picture is consistent with real-space observations of skyrmions with isotropic chirality in system with fcc(001) interface [25] and fcc(111) interface [26]. It is interesting to note that the vector of the interfacial DMI may also point to surface normal direction in cases of bcc(111) and fcc(110) surfaces (indicated as \mathbf{D}_4

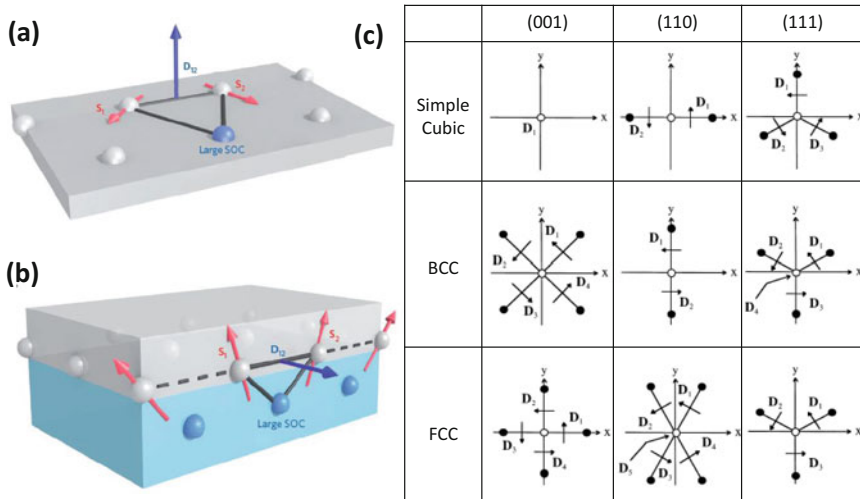


Fig. 4.3 **a** Sketch of a DMI generated in a triangle configuration composed of two atomic spins and one atom with strong spin-orbit coupling. **b** Sketch of a DMI at the interface between a ferromagnetic layer in gray and a metal in blue with strong spin-orbit coupling. The triangle configuration shown in panel a is highlighted by the black triangle. **c** The planer view of the DMI configurations for 9 basic atomic structures, where the orientations of the DMI vectors are indicated by black arrows when they are parallel to the surface plane. Two additional DMI vectors, \mathbf{D}_4 in bcc(111) and \mathbf{D}_5 fcc(110), are perpendicular to the film plane. Panel a and b are reproduced with permission from [27] © 2013 Macmillan Publishers Limited. Panel c is reproduced with permission from [20] © Elsevier

for bcc(111) and \mathbf{D}_5 for fcc(110) in Fig. 4.3c), which may extend the possibility of stabilizing non-collinear spin chirality in in-plane rotation geometry.

The presence of the interfacial DMI, was found to have significant influences on the formation of static spin structures, spin wave propagations as well as the dynamics of domain configuration, which will be introduced in the next section. These observations of diverse DMIs in different systems further trigger the investigation towards to the understanding of the sign and the magnitude of the DMI.

Using tight-binding model and ab initio calculations, Kashid et al. have investigated the $3d$ - $5d$ magnetic/non-magnetic atomic chains, including $3d$: Fe, Co and $5d$: Ir, Pt, Au [28], and they found that the hybridization, the bonding between d orbitals of the magnetic and nonmagnetic sites, the bandwidth and the energy difference between occupied and unoccupied states of different spin projection determine the sign and strength of the DMI.

Later Yang et al. have investigated Co/Pt bilayers using first-principles calculations [29], where the layer dependent DMI coefficient indicates the interfacial DMI at Co/Pt interface has a dominate contribution from Co spins of the interfacial Co layer, see Fig. 4.4a. They found that the large DMI from interfacial Co spins extend very weakly from the interface, and is mainly associated with the SOC energy of the adjacent Pt layer at the interface. They also found the lack of direct correlation

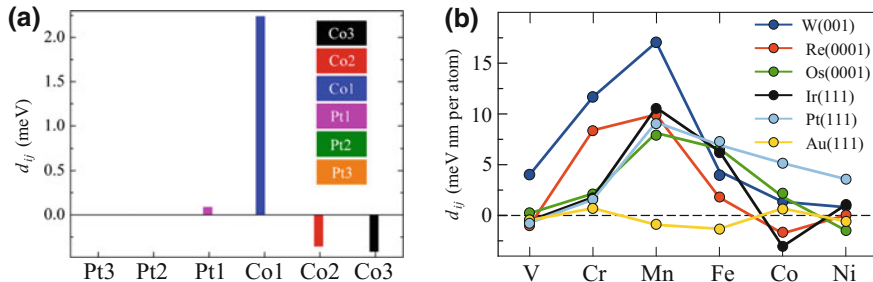


Fig. 4.4 **a** Layer-resolved DMI in three Co monolayers on three Pt monolayers, as obtained from ab initio calculation [29]. **b** Strength and sign of the DMI in 3d transition metal monolayers (x axis) on 5d substrates, as obtained from relativistic first-principles calculation [31]. A positive sign of d_{ij} indicates left-handed chirality. Panel a is reproduced with permission from [29], © 2015 American Physical Society. Panel b is reproduced with permission from [31], © 2016 American Physical Society

between DMI and proximity induced magnetism in Pt. Although induced magnetic moments within heavy metal layer at the interface due to the proximity effect were proposed as a dominating factor for the emergence of the interfacial DMI [30].

More recently, Belabbes et al. have systematically looked into 3d/5d interfaces using relativistic first-principles calculations [31], where 3d transition metals including V, Cr, Mn, Fe, Co, Ni, and 5d transition metals including W, Re, Os, Ir, Pt, Au are considered, see the calculated DMI in Fig. 4.4b. They revealed a tendency of the interfacial DMI that follows the Hund's first rule. In detail, they found that the ratio of DMI energy divided by the square of the spin magnetic moment increases monotonically from V to Mn, and decreases monotonically from Mn to Ni, which is similar to the dependence of magnetic moment per atom versus the 3d transition metals. This tendency is attributed to the 3d orbital occupations and their spin-flip mixing process with 5d states. For instance, according to Hund's first rule, Mn has five filled 3d orbitals with all spin up states, and the spin-up/spin-down channels are entirely occupied/unoccupied, therefore all possible transitions between these states contribute to the DMI. On the other hand, V and Ni have spin-up/spin-down channels that are largely unoccupied/occupied, and consequently the transition of 3d electrons does not contribute to the DMI.

Those theoretical efforts are highly desirable to further understand the mechanism of the interfacial DMI, which may also provide guide principles to optimize choices of materials towards to nanoscale chiral spin textures at room temperature.

4.2.2 Experimental Observations of Magnetic Skyrmions

In this section, experimental observations of chiral spin textures will be introduced. Experimentally, stabilizations of magnetic skyrmions generally require the assistant

of applied magnetic field. At the same time, chiral spin spirals/domain walls in the absence of the external field are highly relevant, and their observation will be briefly introduced as well.

The first experimental evidence of the interfacial DMI was reported in single atomic Mn layer grown on W(110) single crystal, where left-handed cycloidal spin spirals were observed at low temperature using a spin-polarized scanning tunneling microscopy (SP-STM), and the 12 nm period of the spin spiral was attributed to the interplay between the interfacial DMI and exchange interaction [32]. Such chiral spin spirals, including homogenous chiral spin spirals [33], inhomogeneous spin spirals [34], conical spin spirals [35], were later observed in other ultrathin films using SP-STM, where the rich types of the spin spirals were attributed to the delicate energy balance between the DMI and exchange interaction. For instance, homogenous (inhomogeneous) spin spiral states are favored when $D_{12}^2 > 4JK$ ($D_{12}^2 < 4JK$), where J is the exchange constant and K is the anisotropy constant, and conical spin spirals are favored when the higher-order exchange interaction is involved.

The atomic-scale skyrmion lattices were firstly identified in single atomic Fe grown on Ir(111) using SP-STM [36], as shown in Fig. 4.5a, where the four-spin interaction and the large interfacial DMI at Fe/Ir interface were dominating the spin structure. However, manipulation of individual skyrmion in such skyrmion lattice with 1 nm period is challenging, and later it was found that the presence of an additional monolayer Pd layer softens the exchange interaction in the system [37], resulting in spin spirals in zero field and skyrmions in 1.5T field with several nanometer diameter, see Fig. 4.5b [38], which allows the writing and deleting of single skyrmion by spin-polarized current (introduced in Sect. 4.4 of this chapter).

In systems mentioned above, the energy of the dipolar interaction was not considered. However, in thicker film the contribution of dipolar interaction become more significant and its energy competition against the interfacial DMI may result in two possible rotation modes, cycloidal spirals favored by the DMI or helical spirals favored by the dipolar interaction as introduced in Sect. 4.1a. In perpendicularly magnetized domains, these two rotation modes affect spin configuration within domain walls. For instance, in Fe/Ni bilayers grown on Cu(001) substrates, chiral Néel-type domain walls were observed in relatively thinner Fe/Ni region using spin-polarized low energy electron microscopy, and the domain wall transition from chiral Néel walls to achiral Bloch wall can be indeed triggered by tuning the thickness of the magnetic film [8]. Therefore, it is important to note that this picture also applies to skyrmions and bubble domains, where the entire spin configuration of the bubble-like domains could be either skyrmions or topological non-trivial bubble domains depending on whether the DMI dominates the system.

From the application point of view, realization of skyrmions in atomic thin magnetic layers usually requires low temperature or high magnetic field (Fe/Ir is an exception due to four-spin interaction). Moreover, skyrmions in bulk magnetic compounds with non-centrosymmetric structure are generally observed below or just around room temperature [18, 39, 40, 41, 42]. On the other hand, the magnetic multilayers with much higher Curie temperature have additional degree of freedom to

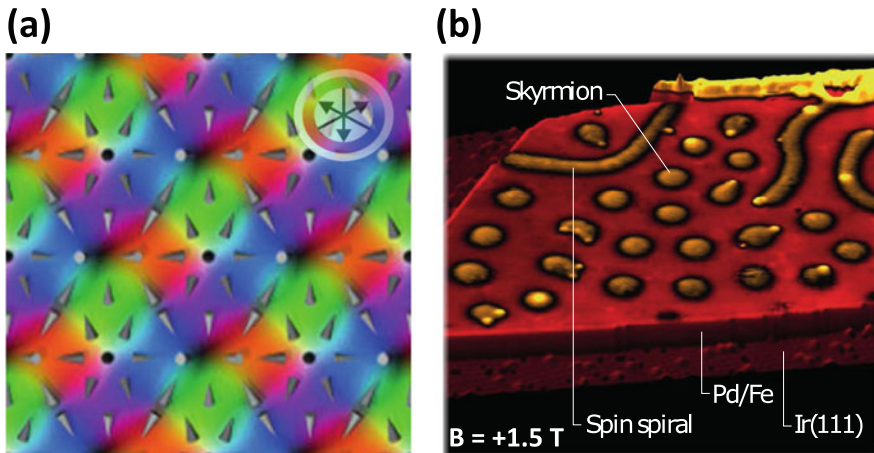


Fig. 4.5 **a** Observation of skyrmions lattice in single monolayer of Fe grown on Ir(111) by using spin-polarized scanning tunneling microscopy. The color wheel indicates the orientation of in-plane magnetization, and the square unit cell has a side length of 1 nm. **b** Individual skyrmions observed in a PdFe bilayer on Ir(111) using same technique as panel a. Panels a and b are reproduced with permission from [16], © 2016 Macmillan Publishers Limited

tailor magnetic properties of the film by choosing interfaces and stacking sequences. Recently, stabilizations of room temperature skyrmions in thin films are reported by several groups, which further trigger investigations of current-induced creation and manipulation of skyrmions in patterned thin films.

Room temperature skyrmions with size ranged from 700 nm to 2 μm were observed in asymmetric trilayer Ta(5 nm)/CoFeB(1.1 nm)/TaO_x(3 nm), see Fig. 4.6d, where the feature of chiral Néel-type spin configuration is identified by the current-driven skyrmion propagation [43]. It allows the creation of the skyrmions through spatially divergent in-plane electric currents in patterned films, which will be introduced in Sect. 4.3. Another example is the patterned Pt(3 nm)/Co(0.5–1 nm)/MgOx trilayer, where the feature of chiral Néel-wall is observed using photoemission electron microscopy [44] (Fig. 4.6h).

Experimental exams of spin structures in [Cu/Fe/Ni]_n [8] and [Ir/Co/Ni]_n [46] suggest that the asymmetric ternary multilayer stacking allows the enhancement of the total DMI. Due to the nature of interfacial DMI that flipping the interface reverses the sign of the DMI, further enhancement of the DMI has been proposed and demonstrated in [Ir(1 nm)/Co(0.6)/Pt(1)]₁₀ (Fig. 4.6a) [47], where the sign of the DMI at Co/Pt and Co/Ir are opposite, therefore flipping Co/Ir interface results in the same sign of the DMI at Ir/Co and Co/Pt, leading to the additive DMI stabilized skyrmions with small size ranged from 50 to 90 nm, see Fig. 4.6b–c. The other results show that [Pt(3)/Co(0.9)/Ta(4)]₁₅ and [Pt(4.5)/CoFeB(0.7)/MgO(1.4)]₁₅ multilayers where the combination of one strong interfacial DMI induced by Pt and one very weak interfacial DMI induced by Ta or MgO also results in accumulated total DMI [48],

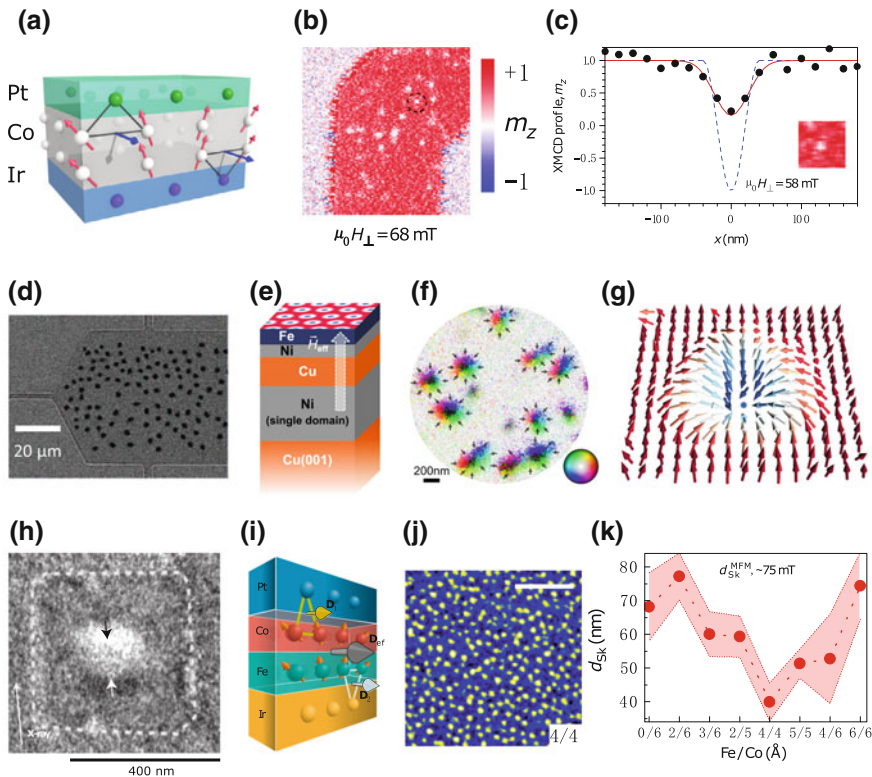


Fig. 4.6 Room temperature observation of skyrmions in thin films. **a** Schematic of Pt/Co/Ir trilayer where the vectors of the interfacial DMI are indicated by blue arrows and spins within Co layer are indicated by red arrows. **b** Scanning transmission X-ray microscopy image of an [Ir/Co/Pt]₁₀ multilayer obtained at room temperature in the presence of perpendicular magnetic fields of $B = 68$ mT. Color bar indicates the out-of-plane component of magnetizations. Field of view is 1.5 μm . **c** The profile of X-ray magnetic circular dichroism signal (black dots) across an individual skyrmion (insert) under 58 mT field. Red solid/blue dashed lines indicate ideal/experimental spin profile of the skyrmion. **d** Kerr microscopy image of Ta(5 nm)/CoFeB(1.1 nm)/TaO_x(3 nm), indicating the formation of skyrmion bubbles upon passing a current with inhomogeneity due to the geometrical constriction shown on the left. **e** Schematic of the zero-field stabilization of skyrmions. **f** Spin-polarized low-energy electron microscopy image highlighting three-dimensional spin structure of skyrmions. Color wheel indicates in-plane orientation of magnetization. **g** Arrows-array representation of the experimental data in same system, allowing the unambiguous determination of Néel-type skyrmions. **h** Photoemission electron microscopy image of a skyrmion in a square patterned Pt/Co/MgO trilayer, boundary is indicated by the white dashed line. Black/white arrows indicate the orientation of the in-plane component of spin structures within the skyrmion, highlight chiral Néel-feature. **i** Schematic of Pt/Co/Fe/Ir asymmetric multilayer. **j** Magnetic force microscopy images of skyrmions obtained in Pt/Co/Fe/Ir multilayers with thickness of Fe(4ML)/Co(4ML). **k** Variation of skyrmions size at $B \sim 75$ mT in [Pt/Co/Fe/Ir]₂₀ system. Panels a-c are reproduced with permission from [46], © Macmillan Publishers Limited. Panel d is reproduced with permission from [45], © 2016 Macmillan Publishers Limited. Panel e-g are reproduced with permission from [25], © AIP Publishing LLC. Panel h is reproduced with permission from [44], © Macmillan Publishers Limited. Panels i-k are reproduced with permission from [49], © Macmillan Publishers Limited

and this system allows investigations of the current-driven propagation of skyrmions in nanowires. More recently, efforts of systematic tailoring interfaces allow further enhancement of the DMI in Ir/Fe/Co/Pt systems, where the DMI at Ir/Fe was thought to be larger than Ir/Co but with same sign, resulting in sub-50 nm skyrmions at room temperature (Fig. 4.6i–k) [49], where the signature of skyrmions is supported by the observation of topological Hall effect within skyrmion phase.

Stabilization of skyrmions generally requires external magnetic field, however, multilayer stacking provides exciting opportunity for applying virtual magnetic field through interlayer exchange coupling [50, 51]. This has been demonstrated experimentally in a Fe/Ni bilayer which is exchange-coupled to a Ni layer through a Cu spacer layer (Fig. 4.6e). By tuning the thickness of the Cu spacer layer, spin structures in Fe/Ni bilayer evolve from stripe domain, bubble domain to single domain, where ~8.6 monolayer of Cu thickness provides just right amount of virtual magnetic field to stabilize bubble domains. Using spin-polarized low-energy electron microscopy, three orthogonal components of magnetization can be imaged with 20 nm lateral resolution, allowing the unambiguous identification of the bubble domains as chiral Néel-type skyrmions (Fig. 4.6f, g).

These strategies for stabilizing room temperature skyrmions towards sub-100 nm size as well as zero field ground state are highly promising for future skyrmion-based devices. Possible combinations of those strategies including tailoring the DMI, magnetic anisotropy, exchange interaction as well as interlayer coupling strength would be key ingredients to further optimizing the interfacial DMI stabilized skyrmions.

4.2.3 *Quantifying the Interfacial DMI*

It is fundamentally interesting to understand the DMI at interface. In this section, experimental techniques that allow the quantification of the interfacial DMI will be introduced. Briefly, the detection of the DMI can be done through measuring the spin structures, and spin wave propagations.

The pioneer work of detecting the cycloidal spin spirals using SP-STM [32–36], as introduced in Sect. 4.2a, allows the precise determination of the period of spin spirals. It gives rise opportunities to compare this period to theoretical mode based on density functional theory, therefore the strength of the DMI can be quantified indirectly through the comparison.

Experimental detections of the DMI were later achieved by measuring the spin wave propagations where the presence of the DMI breaks the degeneracy of spin waves. This asymmetric spin wave dispersion relation can be captured by both spin-polarized electron energy loss spectroscopy (SPEELS) and Brillouin light scattering (BLS). In SPEELS experiments, the spin waves were excited by a spin-flip scattering process, and the strength of the DMI vector \mathbf{D}_{ij} can be obtained by fitting the dependence of the energy asymmetry as a function of wave-vector transfer [52]. Because of the short life time (~10 fs) and short attenuation lengths (~1 nm), the measurement of the DMI using SPEELS is limited in the ultrathin films. On the other hand,

BLS measurements allow the detection of the buried interface in multilayers using a wave vector resolved BLS in a backscattering geometry [53–57], where microwaves excited spin waves with long-wavelength have longer lifetime (\sim ns) and coherence length (\sim μm). The picture of how the presence of the DMI shifts the spin-wave dispersion curves is given in Fig. 4.7c, where the strength of the DMI can be obtained by tracking slope of the frequency difference $\Delta f(k)$ plot for two counter-propagating spin waves at equal but opposite wave vectors: $\Delta f(k) = \frac{2\gamma}{\pi M_s} D_{DMI} k$, where γ is gyromagnetic ratio, M_s is the saturation magnetization, k is the spin wave propagation vector, and D_{DMI} is the interfacial DMI constant. An example of experimentally obtained $\Delta f(k)$ from the dispersion curves with opposite magnetization (red and black curves) is shown in Fig. 4.7c.

As introduced in Sect. 4.1, the interplay between the interfacial DMI and dipolar (stray field) energy may result in either Bloch wall that is dominated by stray field energy or Néel wall that is dominated by the DMI in perpendicularly magnetized systems. Tuning film thickness gives rise the access to tailor this interplay, and the film-thickness dependent domain wall transition from chiral Néel-type to non-chiral Bloch-type can be used to estimate the strength of the DMI by calculating stray field energy difference of Bloch and Néel near transition region, where the stray field energy difference and the DMI are comparable. Using spin-polarized low energy electron microscopy, one is able to obtain three orthogonal components of the spin textures so that the domain wall type can be unambiguously determined, see an example in Fig. 4.7a [8, 25, 46, 58], leading to the quantification of the total interfacial DMI of the systems.

In a weak perpendicular anisotropy system where domain pattern exhibits stripe domain, the perpendicular field dependent evolution of stripes has been studied in the past [59–63], where the contributions of exchange interaction, dipolar interaction, magnetic anisotropy and Zeeman energy were considered. This model later is extended to systems with significant DMI [48], where the field dependent periodicity of stripe domains was used to obtain domain wall surface energy density σ_{DW} . The strength of the DMI vector $|D|$ then can be derived from equation $\sigma_{DW} = 4\sqrt{AK_{u,eff}} - \pi|D|$, where A is the exchange stiffness, and $K_{u,eff}$ is the effective uniaxial anisotropy constant.

Another experimental effort of quantifying the DMI is based on perpendicularly magnetized bubble-like domain, where the presence of the DMI fixes the chirality within the domain boundary. The presence of an in-plane field competes with the DMI regarding to the spin configuration within the domain boundary, resulting in asymmetric bubble expansion, which can be used for quantification of the interfacial DMI [64–66]. In details, the orientation of the asymmetric propagation with respect to the applied in-plane field can be used to derive the sign of the DMI and the chirality within the boundary, for instance, the DMI-like field and the in-plane field could be parallel or antiparallel, which allows propagation with opposite directions. Moreover, systematic tests of the field-dependent bubble expansion allow one to locate the minimum velocity of the propagation, where the effective DMI field and the in-plane field balance each other. The DMI strength can be written as $D_{DM} = \mu_0 H_{in-plane} M_s \gamma_{dw}$, where μ_0 is the vacuum permeability and γ_{dw} is the domain

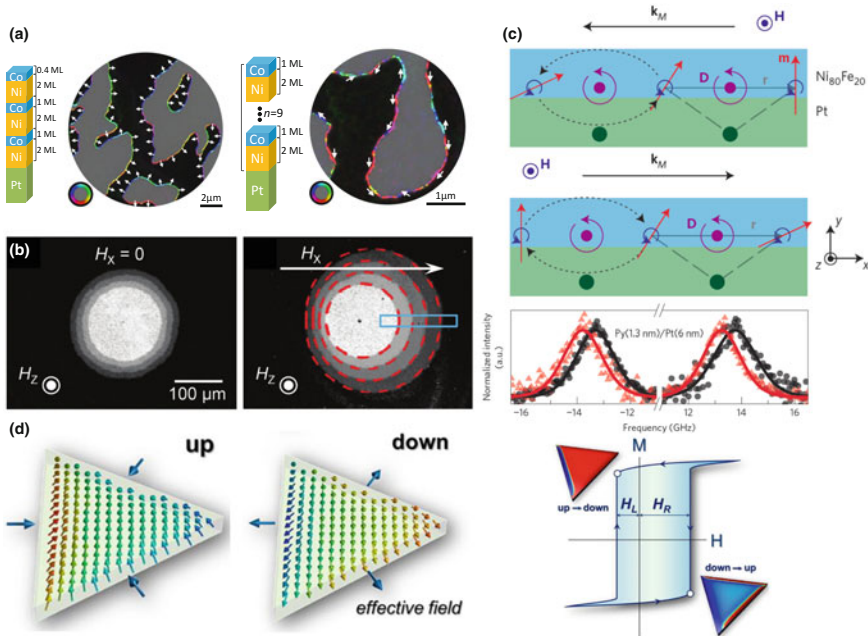


Fig. 4.7 **a** Quantifying the DMI based on a thickness-dependent transition of domain wall type. Spin-polarized low-energy electron microscopy image of $[\text{Co}/\text{Ni}]_3/\text{Pt}(111)$ (left) and $[\text{Co}/\text{Ni}]_9/\text{Pt}(111)$ (right). Out-of-plane component $+z/-z$ of magnetization is indicated by black/white, and in-plane component within domain walls is indicated by the color wheel as well as white arrows, highlighting magnetic domain walls as left-handed chiral Néel type and achiral Bloch type. **b** Quantifying the DMI based on asymmetric domain wall propagations. Kerr microscopy Images of $\text{Pt}/\text{Co}/\text{Pt}$ system show circular domain wall expansion driven by an out-of-plane magnetic field H_z (3 mT), without an in-plane magnetic field (left) and with an in-plane magnetic field H_x at 50 mT (right). Grey levels indicate four overlapped sequential images with a time step of 0.4 s. **c** Quantifying the DMI based on asymmetric spin wave propagation. (upper) Sketch of a Damon–Eshbach spin wave propagating at the $\text{Ni}_{80}\text{Fe}_{20}/\text{Pt}$ interface with wave vector $\mathbf{k}_M \parallel -x$. All individual moments precess in the external field \mathbf{H} in counterclockwise manner (the blue arrows). The dashed arrows indicate the spatial chirality of the spin wave along x . The preferred chirality of the DMI indicated by the purple arrow is identical to the spatial spin wave chirality. (middle) For $\mathbf{k}_M \parallel +x$, the spatial chirality of the spin wave is opposite to that favored by the DMI. The individual moments precess counterclockwise around the external magnetic field \mathbf{H} as above, but now \mathbf{k}_M points in the opposite direction. (lower) Spin-wave spectra measured by BLS in 1.3 nm $\text{Ni}_{80}\text{Fe}_{20}$ film with a 6 nm Pt underlayer with $\mu_0 H = \pm 295$ mT. Black circles and red triangles correspond to measurements carried out for the two opposite magnetizations. **d** Left, Schematic illustrations of spin configurations within triangle with magnetization up and down. Right, the preferential nucleation of domains at the edge induce a shift of magnetic hysteresis loops that is linked to the DMI. Panel a is reproduced with permission from [58], © 2013 Macmillan Publishers Limited. Panel b is reproduced with permission from [64], © 2013 American Physical Society. Panel c is reproduced with permission from [53], © 2015 Macmillan Publishers Limited. Panel d is reproduced with permission from [76], © 2016 American Chemical Society

wall width which equals to $\pi \sqrt{\mathcal{A}/K_{\text{eff}}}$, K_{eff} is the effective perpendicular magnetic anisotropy, \mathcal{A} is the spin-wave exchange stiffness constant. This approach of tuning the interplay between effective DMI field and external in-plane magnetic field was also applied to understand the dynamics of chiral spin textures [9, 10, 67–72].

The presence of the DMI may also influence the chirality of tiled spins at the edge of a film or patterned structure [73–75], which may induce an asymmetric domain nucleation [64, 65]. This asymmetric property could be lifted by preparing planar asymmetric triangle microstructure with a constant in-plane field, where a significant shift of the out-of-plane magnetic hysteresis loop is captured by Magneto-optic Kerr effect [76], see spin structures within triangle and the sketch of quantifying the DMI from the hysteresis loop in Fig. 4.7d. The shift of the loop is attributed to the preferential nucleation of domain walls due to the DMI induced magnetization titling at the edge, from where both sign and strength of the DMI vector can be quantified with help of the half-droplet model [65, 77]. Moreover, this approach is validated in symmetric square microstructures with the absence of the loop shift. These shape-dependent tests of the DMI, can also be employed by other magnetometry measurements such as vibration sample magnetometer (VSM) or superconducting quantum interference device (SQUID) magnetometer, providing a convenient way for rapid material screening.

4.2.4 Thin Films with Bulk DMI

Epitaxial growth of noncentrosymmetric compound thin films, chiefly B20 structures, has been desirable for both fundamental research and application, due to the well-controlled thickness, possibilities of precisely measuring transport properties and easy implementing patterns for the device fabrication. Intensive efforts have been made into fabricating and optimizing epitaxial B20 thin films [78–87], where Si(111) has been chosen as an excellent substrate for the epitaxial growth. The epitaxial quality of B20 thin films can be examined by X-ray diffraction [85–87], as well as transmission electron microscopy [86, 87], see an example of a MnSi thin film on Si(111), Fig. 4.8a. In contrast to the B20 bulk materials where the stabilization of skyrmions phase requires the external magnetic field [21, 39–41, 88], geometric constraints along the direction normal to the film plane in B20 thin films have been proposed as a possible driving force to suppress the helical phase [40, 86, 87, 89], which is usually the ground state in bulk B20 materials in the absence of the field [90].

Looking for features of the topological Hall effect in transport measurements [91, 92], has been considered as a strong evidence as the existence of skyrmions [93–96]. Huang et al. [85] and Gallagher et al. [87] indeed observed significant topological Hall effect not only in similar regions within temperature-magnetic field phase diagram where the skyrmions have been reported in bulk materials, but also in regions within the phase diagram near zero-field, indicating the extension of the skyrmions phase down to zero-field region in MnSi and FeGe, respectively. Figure 4.8c shows

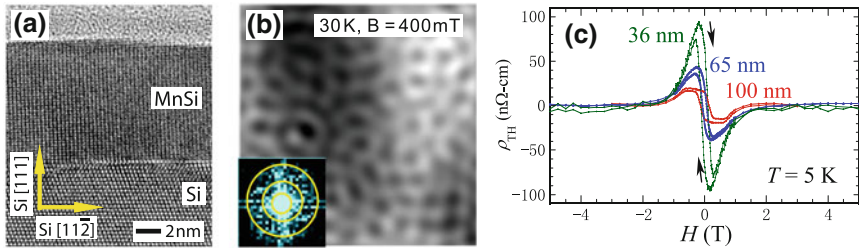


Fig. 4.8 **a** Cross-section transmission electron microscopy image of 10 nm MnSi thin film grown on Si(111) substrate. Scale bar is 2 nm. **b** Over-focused transmission electron microscopy image of 10 nm MnSi taken at 30 K and 400 mT. The image is filtered by shadowing the background noise as well as selecting magnetic reflection (highlighted by yellow lines in the inserted FFTs). **c** The topological Hall resistivity hysteresis loops for the 36, 65, and 100 nm FeGe films at 5 K. Panels a and b are reproduced with permission from [86], © 2013 American Physical Society. Panels c is reproduced with permission from [87], © 2017 American Physical Society

the topological Hall resistivity hysteresis loops for FeGe thin films with different thicknesses at 5 K [87], where substantial remanent values at zero field demonstrate robust Skyrmion formation in the absence of magnetic field.

Efforts of using Lorentz transmission electron microscopy have been also made to directly observe spin textures of MnSi thin films [86], in which the feature of topological Hall effect was also identified. With increasing magnetic field, the evolution from helical phase at zero field to skyrmion phase at 400 mT was observed in MnSi, see Fig. 4.8b. The skyrmion phases tested in 10 and 50 nm thick films are extended in a much wider temperature-magnetic field.

4.2.5 Magnetic Imaging Techniques

In this section, magnetic imaging techniques that allow the observation of skyrmions and their advantage/limitation will be briefly introduced. The techniques include, but are not limited to, spin-polarized low-energy electron microscopy (SPLEEM), photoemission electron microscopy (PEEM), scanning electron microscopy with polarization analysis (SEMPA), Kerr Microscopy, magnetic transmission X-ray microscopy (TXM), Lorentz transmission electron microscopy (LTEM), Spin polarized scanning tunneling microscopy (SP-STM), magnetic force microscopy (MFM) and magnetometry with nitrogen-vacancy defects in diamond.

SPLEEM is capable of capturing three dimensional spin structures on the surface of magnets [14, 97], allowing one to distinguish magnetic chirality for Bloch- or Néel-type [98, 99]. In SPLEEM measurements, spin-polarized electron beam with typically a few eV lands normal on the sample surface, and elastic back-scattering is detected. Magnetic contrast is obtained by comparing the difference between two images with spin-up and spin down (here the flip between spin-up and spin

down is triggered by changing the circular polarization of the incident laser onto the GaAs cathode). The magnetic contrast is proportional to $\mathbf{P} \cdot \mathbf{M}$, where \mathbf{P} is the spin-polarization direction of the incident electrons and \mathbf{M} is the magnetization direction. The orientation of the spin-polarization direction \mathbf{P} can be controlled into arbitrary direction by the combination of magnetic field and electric field, allowing the detection of three-dimensional spin structures by imaging three orthogonal directions independently. The energy of the incident electrons is typically ranged from zero to 30 eV, which is extremely surface sensitive with only a few monolayers probing depth. Strength of SPLEEM is the capability of imaging magnetic component along arbitrary direction. Lateral resolution of SPLEEM is typically 10–20 nm, which can be potentially upgraded down to a few nm with aberration corrector. Samples for SPLEEM are usually limited to *in situ* prepared single-crystalline thin films, because the energy of incident electrons is typically around several eV so that SPLEEM is extremely surface sensitive. The nature of the imaging mechanism with electrons also blocks imaging during the presence of external in-plane magnetic field due to the Lorentz force.

PEEM is powerful tool for imaging magnetic materials with element-sensitivity [100]. In PEEM measurements, X-ray lands on the surface with 30° grazing angle, and secondary electrons emitted from the sample surface (dashed black arrows) are accelerated by a strong electric field between sample and the objective lens of the microscope. Magnetic image is obtained by taking the difference between two images with opposite polarization of the X-ray. The mechanism of the magnetic contrast is based on X-ray magnetic dichroism, where X-ray magnetic circular/linear dichroism has been applied to study ferromagnetic/antiferromagnetic materials [101, 102]. Magnetic contrast is proportional to the component of magnetization projected onto the X-ray incident direction, for instance, with 30° grazing angle, X-ray is more sensitive to the in-plane magnetized component vs out-of-plane, however, in a system with well-defined anisotropy, one could control the fraction of the contrast from in-plane magnetized domain by rotating the film within the plane. Strength of PEEM is element-dependent sensitivity and opportunity to image antiferromagnetic domains based on X-ray magnetic linear dichroism. Functionality of a PEEM beam line is related to the availability of circularly/linearly polarized X-ray and energy range of the incident X-ray (soft X-ray or hard X-ray) at synchrotron. As same as SPLEEM, imaging samples in the presence of in-plane magnetic field is technically challenging, where the Lorentz force might be balanced by deflectors of the objective lens in PEEM.

SEMPA is capable of capturing three-dimensional spin structures [103]. In SEMPA experiments, electron beam with medium energy (10–50 keV) lands on the sample surface, and secondary electrons probed with high spatial resolution retain their spin-polarization orientation as they leave the sample surface. The spin polarization of the emitted secondary electrons carries the information of the local magnetization orientation can be analyzed by a spin-polarization analyzer, then the spin structure at the sample surface can be mapped as the electron beam is scanned point by point through the sample surface. This technique allows one to unambigu-

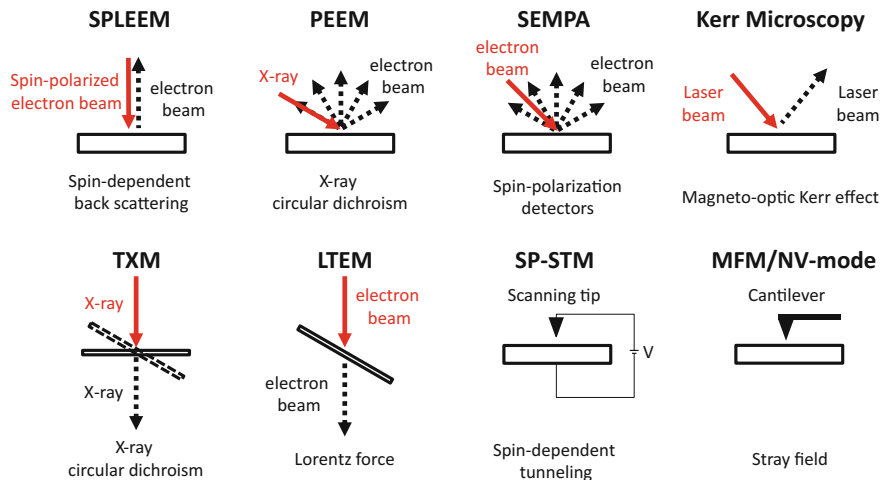


Fig. 4.9 Sketch of the imaging mode for variation of magnetic imaging techniques. Red solid arrows indicate the incident electron beam or X-ray, and dashed black arrows indicate the beam/X-ray that carries magnetic information. The mechanism of obtaining magnetic contrast is labelled below each technique

ously magnetic chirality within domain walls [104]. Samples that SEMPA can image also include three-dimensional objects.

Kerr Microscopy probes magnetic structures without electrons, providing opportunities to study real-time evolution of domain structures in the presence of magnetic field [105]. In Kerr Microscopy measurements, a light with linear polarization lands on the surface, and the plane of the polarization rotates upon reflection from a magnetic surface due to magneto-optic Kerr effect [106]. The magnetic contrast is directly sensitive to the magnitude and direction of magnetization. The sensitivity axis is parallel to the plane of incidence, which can be optically adjusted. Arbitrary magnetic fields can be applied during an observation so that domain nucleation and magnetization processes can be possibly captured [43]. A Kerr Microscope is essentially a polarization microscope, where its lateral resolution is limited around 300 nm.

TXM probes magnetic thin films with X-ray in transmission mode without electrons involved [107], giving opportunities for measurements with element-sensitivity in the presence of magnetic field. Magnetic contrast is given by x-ray magnetic dichroism and proportional to the projection of the magnetization onto the photon propagation direction. Contrast for in-plane component can be obtained by tilting the sample surface (see dashed lines in Fig. 4.9). The transmission mode is a relatively more flexible imaging condition, providing opportunities to study magnetic materials grown on 3D structures [108]. Magnetic field can be applied during the measurement, allowing one to explore field-dependent domain dynamics. Samples that TXM can probe need to be thin enough so that X-ray beam can partially go through, therefore samples are usually prepared on membranes such as silicon nitride.

LTEM probes magnetic thin films with high energy electron beam with transmission mode [109], which has been applied to study Bloch-type chirality in non-centrosymmetric compounds [18]. The magnetic contrast is given by the Lorentz force when electrons pass through a sample with magnetization normal to the beam orientation. Lateral resolution of LTEM is typically several nm, which is worse than conventional TEM as the objective lens is largely turned down. Note that LTEM mode does not provide contrast for Néel-type domain walls due to the fact that the deflected electron beam is shifted along the domain boundary without generating difference of the beam intensity. Tilting sample ranged with $\pm 30^\circ$ provides contrast to capture the domain shape from both Néel-type domain walls [110] and skyrmions [111], but not for chirality within the domain boundary.

SP-STM has been used as a powerful tool to reveal chiral spin textures at atomic scale in ultrathin films [112]. The magnetic contrast is given by the spin-dependent tunneling between sample surface and magnetic tip. The spin signal dependents on the orientation of magnetization on sample surfaces with respect to the orientation of magnetization on the tip, and three dimensional spin structures can be obtained using tips with different magnetization directions [34]. The detection using scanning tip also provides great opportunities to study the current-driven or voltage direction evolution of spin structures locally. SP-STM requires ultra-clean surface therefore samples usually need to be prepared in ultra-high vacuum environment.

Scanning nanomagnetometries using magnetic tip (MFM) [49] or nitrogen-vacancy [113] probe magnetic structure based on stray field from the sample surface. These techniques provide great opportunities to study domain structures in a very flexible experimental environment such as ex situ measurements without high-vacuum and in the presence of magnetic field. The magnetic domain wall structure such as Néel or Bloch-wall can be distinguished by modeling the experimental data obtained by nitrogen-vacancy tip with decent resolution.

4.3 Experimental Realization of Skyrmions in Artificial Structures

Magnetic skyrmions in thin films can also be realized in artificial structures. The idea of fabricating nanodots with a magnetic vortex state on perpendicularly magnetized films was proposed and tested by simulation [114]. Magnetic vortices have been intensively studied in nanostructures, and demonstrated as a robust state with a suitable aspect ratio, i.e. dot thickness versus diameter [115, 116]. The formation of skyrmions in these artificial structures is a result of imprinted vortex structure from nanodots onto the perpendicular magnetized underlayer, through an exchange coupling at the interface (Fig. 4.10a). Note the spin structures within each vortex can be viewed as Bloch-type, therefore the Bloch-type skyrmions stabilized by this strategy is different from the DMI stabilized Néel-type skyrmions in asymmetric multilayers.

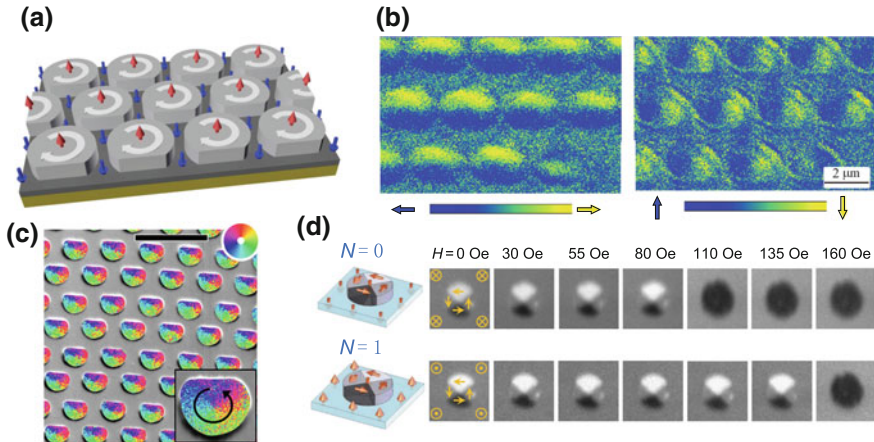


Fig. 4.10 **a** Schematic of an artificial skyrmion lattice. Ordered arrays of asymmetric magnetic nanodots are fabricated on top of a perpendicularly magnetized film. The arrows represent the orientation of magnetization. **b** Kerr Microscopy images of $\text{Co}/[\text{Co}/\text{Pt}]_n$ multilayer systems with horizontal (left) and vertical (right) magnetic sensitivity, respectively. The orientation of magnetization is indicated by the color bar. **c** SEMPA image of Bloch-type skyrmions at remanence state. The in-plane magnetization direction is highlighted by color, see color wheel at top right. Inset highlights the magnetization curling direction. The scale bar is $2 \mu\text{m}$. **d** PEEM images of the topological-trivial vortex state in upper row and skyrmion state in lower row) at remanence state, after applying variable external in-plane fields, indicating that the skyrmion state ($N=1$) has a stronger annihilation field. Panel a is reproduced with permission from [114], © 2013 American Physical Society. Panel b is reproduced with permission from [120], © 2014 American Physical Society. Panel d is reproduced with permission from [119], © 2014 Macmillan Publishers Limited

In contrast to the homo-chirality favored by the interfacial DMI, the in-plane curling spin configuration within a vortex could be either clockwise or counter-clockwise (circularity), and the core of a vortex could point either up or down along out of the plane (polarity) [114]. Four possible ground states with combination of two possible circularities and two possible polarities are expected to be energetically degenerate in a perfect circular shaped vortex. Experimental effects of achieving homo-chiral spin configuration of artificial skyrmions will be introduced in the following, i.e., same polarity and circularity over arrays of nanomagnets with asymmetric shape [117, 118].

Experimental realization of artificial skyrmions has been demonstrated in several systems, including Co dots on perpendicularly magnetized Ni film grown on Cu(001) [119], Co dots on $[\text{Co}/\text{Pt}]_n$ multilayers [120], as well as Co dots on ion-irradiated $[\text{Co}/\text{Pd}]_n$ multilayers [121]. The Bloch-type skyrmions are stable with the size of dots ranged from several hundred nanometers to a few microns. To set homo-chirality of the skyrmions, in-plane demagnetizing samples to define circularity and out-of-plane magnetizing samples to define the polarity are applied. For instance, in Co (dots)/ $[\text{Co}/\text{Pt}]_n$ multilayer system [120], the asymmetric Co dots were saturated into an in-plane magnetized single domain state by a magnetic field (≈ 20

mT) along the edge-cut (see Fig. 4.10a), and evolved to vortex states without change of the circularity upon the removal of field. Then the vortex core and surrounding underlayer area were magnetized along same direction by applying a perpendicular magnetic field ($\sim +1$ T) smaller than the saturation field (~ 1.3 T). The surrounding underlayer area was finally aligned antiparallel to the direction of vortex core with a smaller negative field (-150 mT). The circularity of the final state was imaged by Kerr microscopy, where the same circularity was observed cross the sample (see Fig. 4.10b).

In another system of Co dots on $[\text{Co}/\text{Pd}]_n$ multilayers [121], the Co/Pd underlayer was ion-irradiated to suppress the perpendicular magnetic anisotropy in regions underneath the Co dots. Then the Co/Pd underlayer was saturated along the positive out-of-plane direction. Subsequently the Co dots were saturated by an in-plane field (100 mT) along the edge-cut, and the nucleation of magnetic vortices with controlled polarity and circularity was triggered by removing the in-plane field followed by applying an additional negative out-of-plane field (-100 mT) for setting the polarity opposite to the surrounding underlayer area. Spin structures of the Co dots array were taken by SEMPA. Figure 4.10c shows that all asymmetric Co dots in the array form typical vortex spin structures with a uniform counter-clockwise circularity, where the orientation of in-plane magnetization is highlighted by the color wheel, indicating a successful control of the circularity.

For both cases introduced above, direct observation of the vortex core in the buried layer is technically challenging due to its small size and buried surface. Indirect detection was demonstrated in $\text{Co}(\text{dots})/[\text{Co}/\text{Pd}]_n$ system [121], where three possible states including skyrmion state, vortex state and mixed state can be controlled by the polarity-setting procedure introduced above. The difference of perpendicular remanent magnetization can be measured in magnetic hysteresis loop, where skyrmion/vortex configuration has the smallest/largest magnetization, and mixed lattice configuration with randomly aligned skyrmion or vortex configuration gives a curve in between skyrmion and vortex states [121].

The possibility to control the polarity of the vortex core offers an opportunity to study topological properties of skyrmions. For instance, the skyrmion number N can be calculated by the core polarity direction with respect to the magnetization direction of surrounding underlayer. In case of the skyrmion state with the core polarity opposite to the underlayer magnetization, skyrmion number is $N = 1$, whereas vortex state with the core parallel to the underlayer has $N = 0$ [119, 121]. A physical manifestation of this topological quantization is that a skyrmion state with $N = 1$, is topologically protected from transforming continuously into another state with different N , such as a single domain. This topological effect has been observed in Co dots on perpendicularly magnetized Ni film [119], during the annihilation of stable skyrmion and vortex states into a single domain state in the presence of an in-plane field. It was found that the in-plane annihilation field of the skyrmion state is significantly greater than that of the vortex state (see Fig. 4.10d), indicating a topological effect of the magnetic skyrmions during the core annihilation process.

These artificial Bloch-type skyrmions in thin-film nanostructures are stable at room temperature in the absence of external magnetic field, providing an interesting

platform to explore topological characters of such skyrmion systems. Indeed, very active research efforts in this direction have been demonstrated in the stabilization of skyrmion state [119–121], dynamic properties [122–125], topological characteristics [119, 125–127], as well as design of skyrmion based spin-ice system [128]. In most of the early studies of this field, the top nanodots, while playing a key role in stabilizing the skyrmion state, also hinders the propagation of skyrmions once they are created. Active efforts are underway, for instance, to achieve planar skyrmions without the protruding dots [121, 129], towards mobilizing artificial skyrmions. On the other hand, the vortex state in the nanodots is strongly determined by the aspect ratio of the dot, therefore further scaling down of the artificial skyrmion size is also possible.

4.4 Creation and Manipulation of Skyrmions Towards to Application

4.4.1 *Creations of Magnetic Skyrmions*

As a promising candidate for the memory and logic device, possibilities of manipulating skyrmions such as writing/deleting and driving skyrmions are desired. Several different strategies of effectively creating skyrmions have been proposed, aiming for reliable creation of skyrmions in a controlled way. For instance, vertical injection of spin-polarized current onto a Co/Pt disk allows the creation of single skyrmion by spin torques in the disk (Fig. 4.11a), where the current threshold of creating skyrmions is related to the current density, and the magnitude of the DMI [130].

The experimental demonstration of writing/deleting skyrmions was done using SP-STM in Pd/Fe/Ir(111) system [38], where the presence of the top Pd layer softens the exchange interaction in Fe/Ir(111) [36], leading to spin spirals and skyrmions with larger period instead of skyrmions at atomic-scale. This change of skyrmions size opens up a possibility of manipulating single skyrmion without being trapped in the skyrmion lattice. Then out-of-plane magnetic field is applied to fine tune the energy landscape of the system so that creating and deleting skyrmions have similar energy barrier height. Figure 4.11b shows the demonstration of local writing (upper row) and deleting (lower row) of single skyrmion, where the change of spin textures is triggered by injecting spin-polarized current through a STM tip.

More recently, an electric field generated between Fe(trilayer)/Ir(111) sample and non-magnetic STM tip has been used for generating and removing skyrmions as well (Fig. 4.11e) [131], where the polarity of the applied bias field determines the write/deleting process. Moreover, this approach is technically compatible to all electric read of skyrmion states using non-magnetic STM tip [132]. The latter is achieved by detecting novel magnetoresistance effect related with non-collinear spin textures such as skyrmions, where mixing between spin channels for non-collinear spin textures locally changes their electronic structure, which was theoretically explained by DFT calculation [133] or tight-binding model [132]. The combination of all electric-

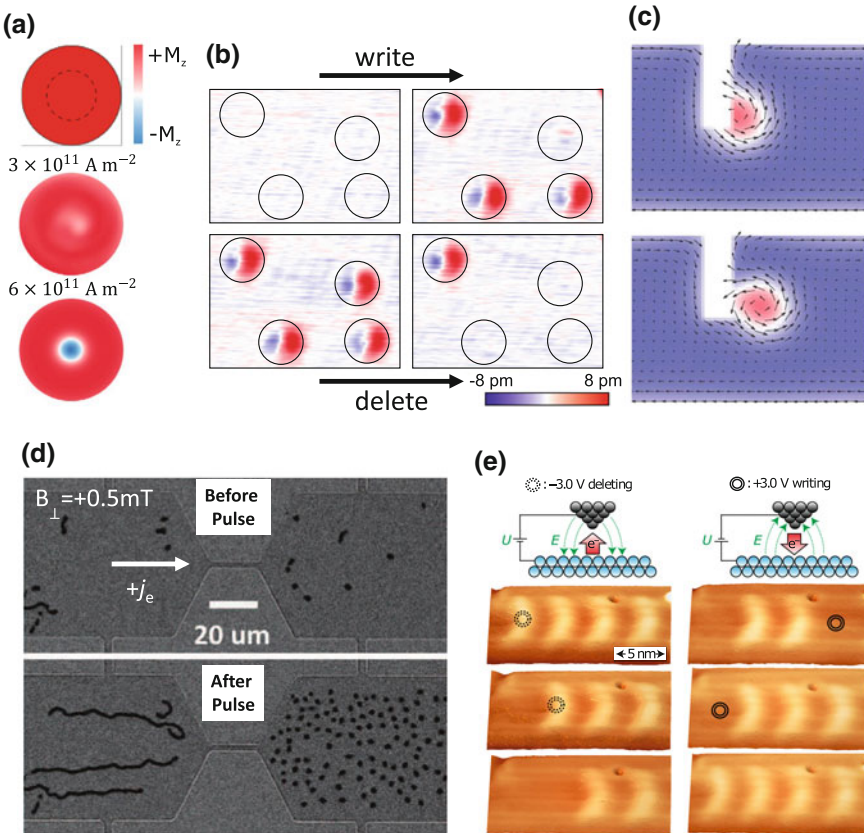


Fig. 4.11 **a** Top view of Co/Pt disk (top figure) where the area of the vertical spin injection is highlighted by dashed black circle. Lower figures show micromagnetic simulations of spin structure in Co/Pt disk with different current density. **b** Manipulation of individual skyrmion highlighted by red/blue (diameter 8 nm) in chosen area (black circles), upper/lower row demonstrates write/delete individual skyrmion in Pd/Fe/Ir(111) at a field of 3.25T. **c** Snapshots of dynamical spin configurations at selected times in creating a skyrmion with applied current $j = 3.6 \times 10^{11} \text{ A m}^{-2}$. In-plane/out-of-plane components of the magnetic moments are represented by arrows/color. Corresponding time for upper/lower figure is $18.89 \times 10^{-11} \text{ s}/28.60 \times 10^{-11} \text{ s}$. **d** Kerr microscopy images of Ta/CoFeB/TaO_x structure before and after applying a current pulse through structure constriction (darker gray), indicating creation and propagation of skyrmions (black dots). **e** Deleting/writing (left/right column) skyrmions by electric field in trilayer Fe on Ir(111). Circles highlight targeted area for manipulating skyrmions using spin-polarized STM. Brighter area indicates magnetic skyrmion where the distorted shape is induced by the strain. Panel a is reproduced with permission from [130], © 2013 Macmillan Publishers Limited. Panels b and d are reproduced with permission from [45], © 2016 Macmillan Publishers Limited. Panel c is reproduced with permission from [134], © 2013 Macmillan Publishers Limited. Panel e is reproduced with permission from [131], © 2017 Macmillan Publishers Limited

cal read and write/delete skyrmions provides way to realize skyrmion-based memory and logic devices.

The creation of skyrmions can also be realized without vertical injection [134]. Figure 4.11c shows a typical notch structure that has been used for domain wall pinning [27, 135–137]. In those structures, spins near the boundary have large in-plane tilted components due to DM interaction, which can be viewed as part of a spin spiral. The spin structure at the notch swells out in the presence of electric flow due to the spin transfer torque. As the in-plane component pushed further away from the boundary, spins point opposite direction is formed because of the DMI, which can be viewed as the core of a skyrmion (Fig. 4.11c, upper panel). This DMI favored spin twist eventually leads to the formation of a skyrmion (Fig. 4.11c lower panel). Note that the in-plane component near the boundary is essential for the skyrmion formation. For instance, skyrmions are no longer created in case where spins aligned along z-direction near boundary in the presence of a strong perpendicular magnetic field.

Another approach of creating skyrmions is based on planar constriction in Ta(5 nm)/CoFeB(1.1 nm)/TaO_x(3 nm) trilayers [43], where inhomogeneous electric current at the exit of a structure constriction gives rise a multidirectional spin torque [138], that acts differently on different part of the domain wall and results in the formation of skyrmion bubbles with micrometer size (Fig. 4.11d). In this case, an additional magnetic field along out-of-plane is applied to assist the formation of skyrmions due to the lower energy barrier between skyrmions and regular domain. Such approach of efficient creation of skyrmions can be easily integrated into a planar device [139]. The dynamical creation of sub-100 nm skyrmions has also been experimental realized in Si substrate/Ta/Co/[Pt/Ir/Co]₁₀/Pt based micrometer-size track under homogeneous current injection. Those skyrmions can be driven by spin-orbit torques arising from the adjacent heavy metal layer such as Ta, providing opportunities to explore the propagation of skyrmions that will be introduced later.

4.4.2 Motion of Skyrmions in Patterned Films

Concept of storing data by magnetic skyrmions in nanostructures replies on possibilities of moving skyrmions so that data saved in different area can be written and read without mechanical movement. Several skyrmion-based memory and logic devices have been proposed in the last few years [27, 140, 141]. Here binary bits can be encoded by the presence or absence of magnetic skyrmions, and data chains consisted of skyrmions and uniformed domain share similar concept that has been proposed in racetrack memory where data chains contain magnetic domains with opposite magnetization direction.

Applying electric current is one of major approaches to manipulate magnetization in nanostructure, where spin torques can be exerted either by spin-polarized current flowing within a ferromagnetic layer, or by spin current injected vertically through an adjacent heavy metal (spin Hall effect). Current-induced skyrmions motion has been explored by micromagnetic simulation for both cases [130], where the spin

Hall effect-spin torque drives skyrmions at faster velocity with same current density. Moreover, the skyrmion propagation trajectory contains not only a longitudinal motion that is parallel to the applied current direction, but also a transverse motion that is triggered by topology associated gyrotropic force [18, 27, 142–147]. The direction of longitudinal motion of skyrmions depends on the magnetic chirality of skyrmions (determined by the sign of the interfacial DM interaction) as well as the sign of the spin Hall angle in the adjacent heavy metal layer, whereas the direction of transverse motion of skyrmions depends on the sign of the topological charge carried by the skyrmions, which is determined by the magnetization direction within the skyrmion core. In a confined structure such as nanowire, skyrmions propagate towards the edge of the nanostructure, where skyrmions may keep moving along the edge by an additional repulsive force.

The Thiele equation [148], describing the dynamics of magnetic solitons, has been modified to analytically understand the current-induced motions of rigid skyrmions [18, 143, 144, 149–151]

$$\mathbf{G} \times \mathbf{v} - \alpha \mathbf{D} \cdot \mathbf{v} - 4\pi \mathbf{B} \cdot \mathbf{j} = 0$$

where $\mathbf{G} = (0, 0, -4\pi Q)$ is the gyromagnetic coupling vector, $\mathbf{v} = (v_x, v_y)$ is the skyrmion velocity along the x and y axis, α is the Gilbert damping coefficient, \mathbf{D} is the dissipative force tensor, the tensor \mathbf{B} represents the efficiency of the spin Hall torque over skyrmions, and \mathbf{j} is the electric current density flowing in the heavy metal. Here the first term is the topological Magnus force [143, 144, 152], which induces the transverse motion of skyrmions. The second term is the dissipative force related to the magnetic damping of a moving magnetic skyrmion, and the third term corresponds to the driving force from the spin Hall torque. The Thiele equation yields skyrmion longitudinal velocity $v_x = \frac{-j\alpha \mathbf{D} \mathbf{B}_{xx}}{(\alpha \mathbf{D})^2 + Q^2}$ and transverse velocity $v_y = \frac{j Q \mathbf{B}_{xx}}{(\alpha \mathbf{D})^2 + Q^2}$, from where the skyrmion Hall angle can be derived as $\arctan(-\frac{Q}{\alpha \mathbf{D}})$.

On the other hand, current-driven dynamics of skyrmions have been experimentally investigated in several systems, providing opportunities to explore the role of defeats which may pin skyrmions in thin film and multilayer systems [153–155]. Figure 4.12a shows experimental observation of skyrmion motion in Pt/Co/Ta and Pt/CoFeB/MgO nanowire tracks using short current pulses [48]. Strong pinning effects were found in Pt/Co/Ta nanowire tracks with polycrystalline Co layer due to local variation of the DMI strength, resulting in reduced skyrmions velocity and possible annihilation of skyrmions. In contrast, replacing polycrystalline Co layer to amorphous CoFeB layer leads to significantly reduced pinning effect due to the absence of grain boundaries in amorphous film. The influence of grains with variation of the DMI on the current-driven skyrmion motion was further investigated using micromagnetic simulations (Fig. 4.12b) [156], highlighting a grain-size dependent pinning effect. Simulation shows that the depinning current reaches maximum value and the cancellation of the skyrmion Hall effect at low current when sizes of grains are comparable to sizes of skyrmions.

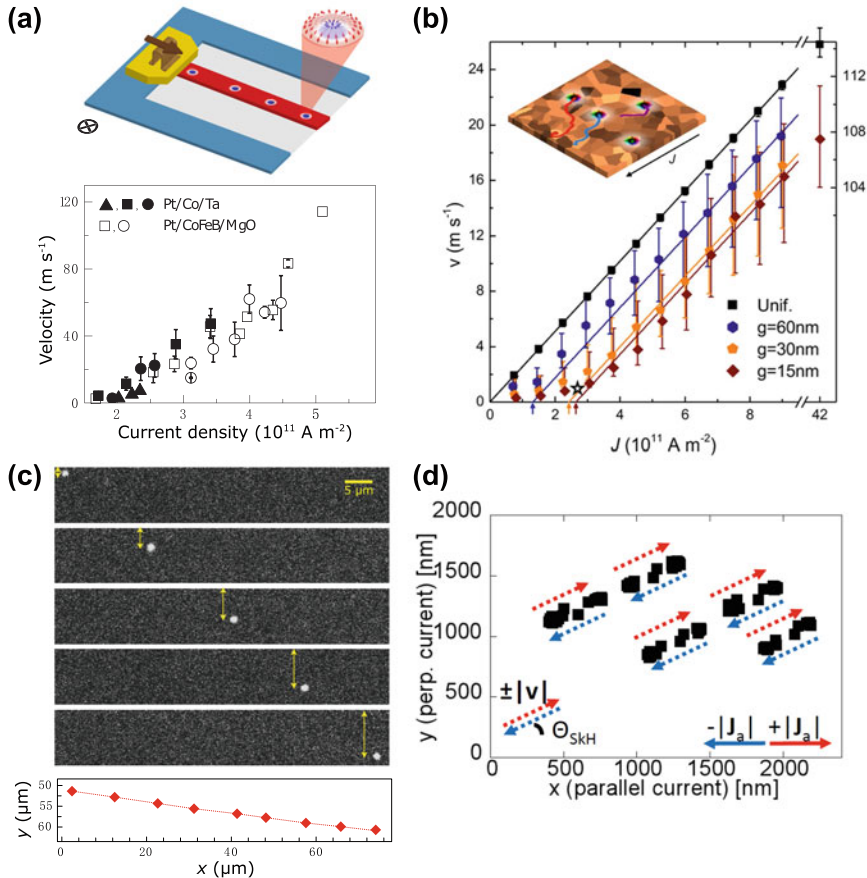


Fig. 4.12 **a** Upper panel: sketch of a magnetic track (in red) on a Si_3N_4 membrane (in grey) with current contacts (in gold) and skyrmions stabilized by an applied magnetic field. Lower panel: Average skyrmion velocity of Pt/Co/Ta and Pt/CoFeB/MgO versus current density. Different shaped symbols correspond to different devices. **b** Simulated grain size dependent mean velocity of the skyrmions as a function of current density, different grain sizes are indicated by uniform case (black square), $g=60\text{ nm}$ (blue hexagons), 30 nm (gold pentagons), and 15 nm (red diamonds). The stars indicate the experimental current density. **c** Kerr microscopy images of pulse current-driven skyrmion motion at $J = 2.8 \times 10^6 \text{ Am}^{-2}$ along $+x$ direction and magnetic field $H = 5.2 \text{ Oe}$ along $-z$ direction. Lower panel: summary of the skyrmion trajectory in Kerr microscopy images. **d** Skyrmion trajectories for one experimental current density $4.2 \times 10^{11} \text{ Am}^{-2}$. All skyrmions move in parallel and synchronously. These skyrmions move reproducibly with identical displacements for positive and negative pulses. The vertical range of $2 \mu\text{m}$ corresponds to the width of the wire. Panel a is reproduced with permission from [48], © 2016 Macmillan Publishers Limited. Panel b is reproduced with permission from [156], © 2017 American Chemical Society. Panel c is reproduced with permission from [150], © 2017 Macmillan Publishers Limited. Panel d is reproduced with permission from [157], © 2017 Macmillan Publishers Limited

Recently, the transverse motion of current-driven skyrmions, namely skyrmion Hall effect, has been directly observed using Kerr microscopy [150] as well as time-resolved X-ray microscopy [157]. The former result shows that the skyrmion trajectory deviates from the applied current direction about 30° in Ta(5 nm)/Co₂₀Fe₆₀B₂₀(CoFeB)(1.1 nm)/TaO_x(3 nm) trilayer (Fig. 4.12c), and the skyrmion Hall angle depends on both skyrmions size and velocity. This observation is attributed to a combination of the topological Magnus force and random pinning potentials in their materials. Then the competition between skyrmion driving force and pinning potentials leads to a current/velocity dependence of the skyrmion Hall angle. For example, the motion of skyrmions at very low current density shows a hopping-like behavior with a zero skyrmion Hall angle. Skyrmions are able to overcome pinning potentials gradually at higher current densities due to stronger driving forces. This tendency of the skyrmions Hall angle eventually saturates at a value that agrees well with the theoretical prediction in the absence of imperfections. The latter result shows the skyrmions Hall angle exceed 30° in [Pt(3.2 nm)/CoFeB(0.7 nm)/MgO(1.4 nm)]₁₅ multilayers with excellent homogeneity and a very low pinning energy landscape that is ideally for pump-probe dynamic measurements (Fig. 4.12d). The observation is attributed to a combination of internal excitation of the skyrmions and the field-like spin-orbit torque. Note that fully rigid skyrmions are expected to have no influence on the skyrmion trajectory by the field-like torque. However, once the skyrmion is allowed to slightly deform or breathe, skyrmion Hall effect can be affected more significantly at higher current densities by field-like torques, which scale linearly with current density.

The skyrmion Hall effect may hold potential for creating novel functionalities in devices such as topological sorting, because skyrmions with opposite topological charge follow trajectory with opposite transverse motion. In a nanowire track, the skyrmion Hall effect may push skyrmions propagate towards the edge of nanowires, where skyrmions may either bounce back or are annihilated. Several proposals of suppressing skyrmion Hall effect have been made to balance the topological Magnus force in two coupled skyrmions with opposite topological charge, where the net topological charge is zero. This can be realized in antiferromagnetically-coupled trilayers with skyrmions on two sides [158], or in skyrmions in antiferromagnetic materials [159]. More recently, zero skyrmion Hall angle has been found in antiskyrmions (where magnetic chirality is opposite along two in-plane orthogonal directions) at specific angle of the applied current with respect to the antiskyrmion spin textures [151], due to anisotropic chiral spin textures within antiskyrmions.

4.5 Outlook

Analog to the approach of controlling domain position by mechanically spinning magnetic disks in hard disk drives, the position of the domain in race-track memory is manipulated by means of the electrically-driven domain wall propagation in magnetic nanowires [160], which is expected to enable mechanical motion free

non-volatile memory device with higher density and better read/write performance. The key of the data manipulation is the electric-current driven domain wall propagation, which is a result of spin transfer torque (STT) or spin-orbit torque (SOT) (see details in the Chap. 7 written by M. Althammer). The STT is attributed to the transfer of spin angular momentum between spins of conduction electrons and local spin structures [161, 162]. The threshold current of the STT induced domain wall motion is significantly high ($\sim 10^6 \text{ A/cm}^2$) due to intrinsic pinning effects in real magnetic systems, and this threshold current can be reduced by four orders of magnitude in case of skyrmions [87], because of the zero-dimensional nature of skyrmion that has much less pinning effects influenced by local defects [163]. On the other hand, the SOT occurs when the spin Hall effect triggers the accumulation of spins at ferromagnetic layer/heavy metal interfaces [164], and those spins transfer their spin angular momentum to the adjacent ferromagnetic layer. Together with the chiral nature of chiral domain walls and skyrmions, the SOT also leads to high efficient electrical manipulation of chiral domain walls [165] and skyrmions [166].

Owing to the nanoscales spin texture, efficient electrical manipulation, and the topological properties, skyrmions are considered as a promising candidate for next-generation non-volatile magnetic memory devices with low-energy consumption and high-density [27]. Recently, Tremendous progress in the field of thin film based chiral spin textures has been made [167], since the theoretical proposal of the interfacial DMI [19, 20] as well as the experimental observation of the interfacial DMI stabilized cycloidal spin spirals [32]. In particular, skyrmions at room temperature have been achieved in multilayer structures [17], which further trigger the research interests for exploring the design strategies towards to nanometer size skyrmions with high stability. On the other hand, materials engineered DMI at interfaces beyond choices of metal/metal interfaces, such as ferromagnet/antiferromagnet interfaces [168], or ferromagnet/graphene interfaces have been demonstrated [169]. So far, most of the studies have been focusing on isotropic chirality systems, either in single-crystalline interfaces with relatively higher symmetries such as fcc(111), or polycrystalline or amorphous systems. Exploring the configuration of the interfacial DMI vectors at interfaces with lower symmetry such as bcc(110) and fcc(110) [20] might bring opportunities for finding novel chiral spin textures such as antiskyrmions in thin film systems [151, 170], that has been recently observed in bulk DMI system [171].

Current-driven skyrmions motion at velocity exceeding 100 m s^{-1} [48, 172] demonstrates potentials for skyrmions based racetrack-type memory applications [173, 174]. The demand for higher density of data storages, determined by the size of skyrmions, encourages researchers to tailor magnetic parameters in multilayer stacking for further minimizing sizes of skyrmions after the observation of sub-100 nm skyrmions [47] and sub-50 nm skyrmions [49]. Exciting opportunities remain in the field of thin film skyrmions for exploring unusual spin configurations, improving stabilities as well as dynamics towards to novel physics and potential applications.

Acknowledgements Gong Chen was supported by the NSF (DMR-1610060) and the UC Office of the President Multicampus Research Programs and Initiatives (MRP-17-454963).

References

1. A. Hubert, R. Schäfer, *Magnetic Domains* (Springer, Berlin, 1998)
2. B.A. Joyce, Molecular beam epitaxy. Rep. Prog. Phys. **48**, 1637 (1985)
3. A. Hubert, Stray-field-free magnetization configurations. Phys. Status Solidi **32**, 519–534 (1969)
4. Y.Z. Wu, C. Won, A. Scholl, A. Doran, H.W. Zhao, X.F. Jin, Z.Q. Qiu, Magnetic stripe domains in coupled magnetic sandwiches. Phys. Rev. Lett. **93**, 117205 (2004)
5. A. Thiaville, S. Rohart, É. Jué, V. Cros, A. Fert, Europhys. Lett. **100**, 57002 (2012)
6. I.E. Dzyaloshinskii, Thermodynamic theory of “weak” ferromagnetism in antiferromagnetic substances. Sov. Phys. JETP **5**, 1259–1272 (1957)
7. T. Moriya, Anisotropic superexchange interaction and weak ferromagnetism. Phys. Rev. **120**, 91–98 (1960)
8. G. Chen, J. Zhu, A. Quesada, J. Li, A.T. N’Diaye, Y. Huo, T.P. Ma, Y. Chen, H.Y. Kwon, C. Won, Z.Q. Qiu, A.K. Schmid, Y.Z. Wu, Novel chiral magnetic domain wall structure in Fe/Ni/Cu (001) films. Phys. Rev. Lett. **110**, 177204 (2013)
9. S. Emori, U. Bauer, S.M. Ahn, E. Martinez, G.S. Beach, Current-driven dynamics of chiral ferromagnetic domain walls. Nat. Mater. **12**, 611–616 (2013)
10. K.S. Ryu, L. Thomas, S.H. Yang, S. Parkin, Chiral spin torque at magnetic domain walls. Nat. Nanotech. **8**, 527–533 (2013)
11. K.-O. Ng, D. Vanderbilt, Stability of periodic domain structures in a two-dimensional dipolar model. Phys. Rev. B **52**, 2177 (1995)
12. A.B. Kashuba, V.L. Pokrovsky, Stripe domain structures in a thin ferromagnetic film. Phys. Rev. B **48**, 10335 (1993)
13. N. Saratz, A. Lichtenberger, O. Portmann, U. Ramsperger, A. Vindigni, D. Pescia, Experimental phase diagram of perpendicularly magnetized ultrathin ferromagnetic films. Phys. Rev. Lett. **104**, 077203 (2010)
14. G. Chen, A.K. Schmid, Imaging and tailoring the chirality of domain walls in magnetic films. Adv. Mater. **27**, 5738–5743 (2015)
15. K. Everschor, *Current-Induced Dynamics of Chiral Magnetic Structures: Skyrmions, Emergent Electrodynamics and Spin-Transfer Torques* (Univ. zu Köln, Thesis, 2012)
16. R. Wiesendanger, Nanoscale magnetic skyrmions in metallic films and multilayers: a new twist for spintronics. Nat. Rev. Mater. **1**, 16044 (2016)
17. A. Fert, N. Reyren, V. Cros, Magnetic skyrmions: advances in physics and potential applications. Nat. Rev. Mater. **2**, 17031 (2017)
18. N. Nagaosa, Y. Tokura, Topological properties and dynamics of magnetic skyrmions. Nat. Nanotech. **8**, 899–911 (2013)
19. A. Fert, Magnetic and transport properties of metallic multilayers. Metallic Multilayers. **59–60**, 439–480 (1990)
20. A. Crépieux, C. Lacroix, Dzyaloshinskii-Moriya interactions induced by symmetry breaking at a surface. J. Magn. Magn. Mater. **182**, 341–349 (1998)
21. X.Z. Yu, Y. Onose, N. Kanazawa, J.H. Park, J.H. Han, Y. Matsui, N. Nagaosa, Y. Tokura, Real-space observation of a two-dimensional skyrmion crystal. Nature **465**, 901–904 (2010)
22. G. Chen, A.K. Schmid, Y. Wu, Imaging and tailoring chiral spin textures using spin-polarized electron microscopy, in *Skyrmions: Topological Structures, Properties, and Applications. Chapter 5* (CRC Press, 2016)
23. H.-B. Braun, Topological effects in nanomagnetism: from superparamagnetism to chiral quantum solitons. Adv. Phys. **61**, 1–116 (2012)
24. A. Fert, P.M. Levy, Role of anisotropic exchange interactions in determining the properties of spin-glasses. Phys. Rev. Lett. **44**, 1538 (1980)
25. G. Chen, A. Mascaraque, A.T. N’Diaye, A.K. Schmid, Room temperature skyrmion ground state stabilized through interlayer exchange coupling. Appl. Phys. Lett. **106**, 242404 (2015)
26. N. Romming, A. Kubetzka, C. Hanneken, K. von Bergmann, R. Wiesendanger, Field-dependent size and shape of single magnetic skyrmions. Phys. Rev. Lett. **114**, 177203 (2015)

27. A. Fert, V. Cros, J. Sampaio, Skyrmions on the track. *Nat. Nanotech.* **8**, 152–156 (2013)
28. V. Kashid, T. Schena, B. Zimmermann, Y. Mokrousov, S. Blügel, V. Shah, H.G. Salunke, Dzyaloshinskii-Moriya interaction and chiral magnetism in 3d-5d zigzag chains: tight-binding model and ab initio calculations. *Phys. Rev. B* **90**, 054412 (2014)
29. H. Yang, A. Thiaville, S. Rohart, A. Fert, M. Chshiev, Anatomy of Dzyaloshinskii-Moriya interaction at Co/Pt interfaces. *Phys. Rev. Lett.* **115**, 267210 (2015)
30. K.S. Ryu, S.H. Yang, L. Thomas, S.S. Parkin, Chiral spin torque arising from proximity-induced magnetization. *Nat. Commun.* **5**, 3910 (2014)
31. A. Belabbes, G. Bihlmayer, F. Bechstedt, S. Blügel, A. Manchon, Hund's rule-Driven Dzyaloshinskii-Moriya interaction at 3d-5d interfaces. *Phys. Rev. Lett.* **117**, 247202 (2016)
32. M. Bode, M. Heide, K. von Bergmann, P. Ferriani, S. Heinze, G. Bihlmayer, A. Kubetzka, O. Pietzsch, S. Blügel, R. Wiesendanger, Chiral magnetic order at surfaces driven by inversion asymmetry. *Nature* **447**, 190–193 (2007)
33. P. Ferriani, K. von Bergmann, E.Y. Vedmedenko, S. Heinze, M. Bode, M. Heide, G. Bihlmayer, S. Blügel, R. Wiesendanger, Atomic-scale spin spiral with a unique rotational sense: Mn monolayer on W(001). *Phys. Rev. Lett.* **101**, 027201 (2008)
34. S. Meckler, N. Mikuszeit, A. Pressler, E.Y. Vedmedenko, O. Pietzsch, R. Wiesendanger, Real-space observation of a right-rotating inhomogeneous cycloidal spin spiral by spin-polarized scanning tunneling microscopy in a triple axes vector magnet. *Phys. Rev. Lett.* **103**, 157201 (2009)
35. Y. Yoshida, S. Schröder, P. Ferriani, D. Serrate, A. Kubetzka, K. von Bergmann, S. Heinze, R. Wiesendanger, Conical spin-spiral state in an ultrathin film driven by higher-order spin interactions. *Phys. Rev. Lett.* **108**, 087205 (2012)
36. S. Heinze, K. von Bergmann, M. Menzel, J. Brede, A. Kubetzka, R. Wiesendanger, G. Bihlmayer, S. Blügel, Spontaneous atomic-scale magnetic skyrmion lattice in two dimensions. *Nat. Phys.* **7**, 713–718 (2011)
37. B. Dupe, M. Hoffmann, C. Paillard, S. Heinze, Tailoring magnetic skyrmions in ultra-thin transition metal films. *Nat. Commun.* **5**, 4030 (2014)
38. N. Romming, C. Hanneken, M. Menzel, J.E. Bickel, B. Wolter, K. von Bergmann, A. Kubetzka, R. Wiesendanger, Writing and deleting single magnetic skyrmions. *Science* **341**, 636–639 (2013)
39. S. Mühlbauer, B. Binz, F. Jonietz, C. Pfleiderer, A. Rosch, A. Neubauer, R. Georgii, P. Böni, Skyrmion Lattice in a Chiral Magnet. *Science* **323**, 915–919 (2009)
40. X.Z. Yu, N. Kanazawa, Y. Onose, K. Kimoto, W.Z. Zhang, S. Ishiwata, Y. Matsui, Y. Tokura, Near room-temperature formation of a skyrmion crystal in thin-films of the helimagnet FeGe. *Nat. Mater.* **10**, 106–109 (2011)
41. Y. Tokunaga, X.Z. Yu, J.S. White, H.M. Rønnow, D. Morikawa, Y. Taguchi, Y. Tokura, A new class of chiral materials hosting magnetic skyrmions beyond room temperature. *Nat. Commun.* **6**, 7638 (2015)
42. N. Kanazawa, S. Seki, Y. Tokura, Noncentrosymmetric magnets hosting magnetic skyrmions. *Adv. Mater.* 1603227 (2017). <https://doi.org/10.1002/adma.201603227>
43. W. Jiang, P. Upadhyaya, W. Zhang, G. Yu, M.B. Jungfleisch, F.Y. Fradin, J.E. Pearson, Y. Tserkovnyak, K.L. Wang, O. Heinonen, S.G.E. te Velthuis, A. Hoffmann, Blowing magnetic skyrmion bubbles. *Science* **349**, 283–286 (2015)
44. O. Boulle, J. Vogel, H. Yang, S. Pizzini, D. de Souza Chaves, A. Locatelli, T.O. Mentes, A. Sala, L.D. Buda-Prejbeanu, O. Klein, M. Belmeguenai, Y. Roussigne, A. Stashkevich, S.M. Cherif, L. Aballe, M. Foerster, M. Chshiev, S. Auffret, I.M. Miron, G. Gaudin, Room-temperature chiral magnetic skyrmions in ultrathin magnetic nanostructures. *Nat. Nanotech.* **11**, 449–454 (2016)
45. A. Soumyanarayanan, N. Reyren, A. Fert, C. Panagopoulos, Emergent phenomena induced by spin-orbit coupling at surfaces and interfaces. *Nature* **539**, 509–517 (2016)
46. G. Chen, A.T. N'Diaye, Y.Z. Wu, A.K. Schmid, Ternary superlattice boosting interface-stabilized magnetic chirality. *Appl. Phys. Lett.* **106**, 062402 (2015)
47. C. Moreau-Luchaire, S.C. Mouta, N. Reyren, J. Sampaio, C.A. Vaz, N. Van Horne, K. Bouzehouane, K. Garcia, C. Deranlot, P. Wohlfhuter, J.M. George, M. Weigand, J.

Raabe, V. Cros, A. Fert, Additive interfacial chiral interaction in multilayers for stabilization of small individual skyrmions at room temperature. *Nat. Nanotech.* **11**, 444–448 (2016)

48. S. Woo, K. Litzius, B. Kruger, M.Y. Im, L. Caretta, K. Richter, M. Mann, A. Krone, R.M. Reeve, M. Weigand, P. Agrawal, I. Lemesh, M.A. Mawass, P. Fischer, M. Kläui, G.S. Beach, Observation of room-temperature magnetic skyrmions and their current-driven dynamics in ultrathin metallic ferromagnets. *Nat. Mater.* **15**, 501–506 (2016)

49. A. Soumyanarayanan, M. Raju, A.L. Oyarce, A.K.C. Tan, M.-Y. Im, A.P. Petrovic, P. Ho, K.H. Khoo, M. Tran, C.K. Gan, F. Ernult, C. Panagopoulos, Tunable room temperature magnetic skyrmions in Ir/Fe/Co/Pt Multilayers. *Nat. Mater.* **16**, 898–904 (2017)

50. Y.Z. Wu, C. Won, A. Scholl, A. Doran, H.W. Zhao, X.F. Jin, Z.Q. Qiu, Magnetic stripe domains in coupled magnetic sandwiches. *Phys. Rev. Lett.* **93**, 117205 (2004)

51. J. Wu, J. Choi, C. Won, Y.Z. Wu, A. Scholl, A. Doran, C. Hwang, Z.Q. Qiu, Stripe-to-bubble transition of magnetic domains at the spin reorientation of (Fe/Ni)/Cu/Ni/Cu(001). *Phys. Rev. B* **79**, 014429 (2009)

52. K. Zakeri, Y. Zhang, J. Prokop, T.H. Chuang, N. Sakr, W.X. Tang, J. Kirschner, Asymmetric spin-wave dispersion on Fe(110): direct evidence of the Dzyaloshinskii-Moriya interaction. *Phys. Rev. Lett.* **104**, 137203 (2010)

53. H.T. Nembach, J.M. Shaw, M. Weiler, E. Jué, T.J. Silva, Linear relation between Heisenberg exchange and interfacial Dzyaloshinskii–Moriya interaction in metal films. *Nat. Phys.* **11**, 825–829 (2015)

54. K. Di, V.L. Zhang, H.S. Lim, S.C. Ng, M.H. Kuok, J. Yu, J. Yoon, X. Qiu, H. Yang, Direct observation of the Dzyaloshinskii–Moriya interaction in a Pt/Co/Ni film. *Phys. Rev. Lett.* **114**, 047201 (2015)

55. K. Di, V.L. Zhang, H.S. Lim, S.C. Ng, M.H. Kuok, X. Qiu, H. Yang, Asymmetric spin-wave dispersion due to Dzyaloshinskii–Moriya interaction in an ultrathin Pt/CoFeB film. *Appl. Phys. Lett.* **106**, 052403 (2015)

56. M. Belmeguenai, J.-P. Adam, Y. Roussigné, S. Eimer, T. Devolder, J.-V. Kim, S.M. Cherif, A. Stashkevich, A. Thiaville, Interfacial Dzyaloshinskii–Moriya interaction in perpendicularly magnetized Pt/Co/AlO_x ultrathin films measured by Brillouin light spectroscopy. *Phys. Rev. B* **91**, 180405(R) (2015)

57. A.A. Stashkevich, M. Belmeguenai, Y. Roussigné, S.M. Cherif, M. Kostylev, M. Gabor, D. Lacour, C. Tiusan, M. Hehn, Experimental study of spin-wave dispersion in Py/Pt film structures in the presence of an interface Dzyaloshinskii–Moriya interaction. *Phys. Rev. B* **91**, 214409 (2015)

58. G. Chen, T.P. Ma, A.T. N'Diaye, H. Kwon, C. Won, Y.Z. Wu, A.K. Schmid, Tailoring the chirality of magnetic domain walls by interface engineering. *Nat. Commun.* **4**, 3671 (2013)

59. Y. Yafet, E.M. Gyorgy, Ferromagnetic strip domains in an atomic monolayer. *Phys. Rev. B* **38**, 9145 (1988)

60. A.B. Kashuba, V.L. Pokrovsky, Stripe domain structures in a thin ferromagnetic film. *Phys. Rev. B* **48**, 10335 (1993)

61. K.-O. Ng, D. Vanderbilt, Stability of periodic domain structures in a two-dimensional dipolar model. *Phys. Rev. B* **52**, 2177 (1995)

62. Y.Z. Wu, C. Won, A. Scholl, A. Doran, H.W. Zhao, X.F. Jin, Z.Q. Qiu, Magnetic stripe domains in coupled magnetic sandwiches. *Phys. Rev. Lett.* **93**, 117205 (2004)

63. N. Saratz, A. Lichtenberger, O. Portmann, U. Ramsperger, A. Vindigni, D. Pescia, Experimental phase diagram of perpendicularly magnetized ultrathin ferromagnetic films. *Phys. Rev. Lett.* **104**, 077203 (2010)

64. S.-G. Je, D.-H. Kim, S.-C. Yoo, B.-C. Min, K.-J. Lee, S.-B. Choe, Asymmetric magnetic domain-wall motion by the Dzyaloshinskii–Moriya interaction. *Phys. Rev. B* **88**, 214401 (2013)

65. A. Hrabec, N.A. Porter, A. Wells, M.J. Benitez, G. Burnell, S. McVitie, D. McGrouther, T.A. Moore, C.H. Marrows, Measuring and tailoring the Dzyaloshinskii–Moriya interaction in perpendicularly magnetized thin films. *Phys. Rev. B* **90**, 0204402(R) (2014)

66. S. Pizzini, J. Vogel, S. Rohart, L.D. Buda-Prejbeanu, E. Jué, O. Boulle, I.M. Miron, C.K. Safeer, S. Auffret, G. Gaudin, A. Thiaville, Chirality-Induced asymmetric magnetic nucleation in Pt/Co/AlOx ultrathin microstructures. *Phys. Rev. Lett.* **113**, 047203 (2014)
67. S. Emori, E. Martinez, K.-J. Lee, H.-W. Lee, U. Bauer, S.-M. Ahn, P. Agrawal, D.C. Bono, G.S.D. Beach, Spin Hall torque magnetometry of Dzyaloshinskii domain walls. *Phys. Rev. B* **90**, 184427 (2014)
68. J.H. Franken, M. Herps, H.J.M. Swagten, B. Koopmans, Tunable chiral spin texture in magnetic domain-walls. *Sci Rep.* **4**, 5248 (2014)
69. J. Torrejon, J. Kim, J. Sinha, S. Mitani, M. Hayashi, M. Yamanouchi, H. Ohno, Interface control of the magnetic chirality in CoFeB/MgO heterostructures with heavy-metal underlayers. *Nat. Commun.* **5**, 4655 (2014)
70. R. Lavrijsen, D.M.F. Hartmann, A. van den Brink, Y. Yin, B. Barcones, R.A. Duine, M.A. Verheijen, H.J.M. Swagten, B. Koopmans, Asymmetric magnetic bubble expansion under in-plane field in Pt/Co/Pt: effect of interface engineering. *Phys. Rev. B* **91**, 104414 (2015)
71. K.-W. Moon, D.-H. Kim, S.-C. Yoo, S.-G. Je, B.S. Chun, W. Kim, B.-C. Min, C. Hwang, S.-B. Choe, Magnetic bubblecade memory based on chiral domain walls. *Sci Rep.* **5**, 9166 (2015)
72. E. Jué, C.K. Safeer, M. Drouard, A. Lopez, P. Balint, L. Buda-Prejbeanu, O. Boulle, S. Auffret, A. Schuhl, A. Manchon, I.M. Miron, G. Gaudin. Chiral damping of magnetic domain walls. *Nat. Mater.* **15**, 272–277 (2016)
73. O. Boulle, S. Rohart, L.D. Buda-Prejbeanu, E. Jué, I.M. Miron, S. Pizzini, J. Vogel, G. Gaudin, A. Thiaville, Domain wall tilting in the presence of the Dzyaloshinskii-Moriya Interaction in out-of-plane magnetized magnetic nanotacks. *Phys. Rev. Lett.* **111**, 217203 (2013)
74. S.A. Meynell, M.N. Wilson, H. Fritzsche, A.N. Bogdanov, T.L. Monchesky, Surface twist instabilities and skyrmion states in chiral ferromagnets. *Phys. Rev. B* **90**, 014406 (2014)
75. M. Cubukcu, J. Sampaio, K. Bouzehouane, D. Apalkov, A.V. Khvalkovskiy, V. Cros, N. Reyren, Dzyaloshinskii-Moriya anisotropy in nanomagnets with in-plane magnetization. *Phys. Rev. B* **93**, 020401(R) (2016)
76. D.S. Han, N.H. Kim, J.S. Kim, Y. Yin, J.W. Koo, J. Cho, S. Lee, M. Kläui, H.J. Swagten, B. Koopmans, C.Y. You, Asymmetric hysteresis for probing Dzyaloshinskii-Moriya interaction. *Nano Lett.* **16**, 4438–4446 (2016)
77. J. Vogel, J. Moritz, O. Fruchart, Nucleation of magnetisation reversal, from nanoparticles to bulk materials. *C R Phys.* **7**, 977–987 (2006)
78. E. Magnano, E. Carleschi, A. Nicolaou, T. Pardini, M. Zangrandi, F. Parmigiani, Growth of manganese silicide films by co-deposition of Mn and Si on Si(111): A spectroscopic and morphological investigation. *Surf. Sci.* **600**, 3932–3937 (2006)
79. S. Higashi, P. Kocán, H. Tochihara, Reactive epitaxial growth of MnSi ultrathin films on Si(111) by Mn deposition. *Phys. Rev. B* **79**, 205312 (2009)
80. S. Azatyan, O. Utas, N. Denisov, A. Zотов, A. Saranin, Variable termination of MnSi/Si(111) $\sqrt{3} \times \sqrt{3}$ films and its effect on surface properties. *Surf. Sci.* **605**, 289–295 (2011)
81. E. Magnano, F. Bondino, C. Cepek, F. Parmigiani, M.C. Mozzati, Ferromagnetic and ordered MnSi(111) epitaxial layers. *Appl. Phys. Lett.* **96**, 152503 (2010)
82. E.A. Karhu, S. Kawhaji, T.L. Monchesky, C. Parsons, M.D. Robertson, C. Maunders, Structure and magnetic properties of MnSi epitaxial thin films. *Phys. Rev. B* **82**, 184417 (2010)
83. E.A. Karhu, U.K. Rößler, A.N. Bogdanov, S. Kawhaji, B.J. Kirby, H. Fritzsche, M.D. Robertson, C.F. Majkrzak, T.L. Monchesky, Chiral modulations and reorientation effects in MnSi thin films. *Phys. Rev. B* **85**, 094429 (2012)
84. M.N. Wilson, E.A. Karhu, A.S. Quigley, U.K. Rößler, A.B. Butenko, A.N. Bogdanov, M.D. Robertson, T.L. Monchesky, Extended elliptic skyrmion gratings in epitaxial MnSi thin films. *Phys. Rev. B* **86**, 144420 (2012)
85. S.X. Huang, C.L. Chien, Extended skyrmion phase in epitaxial FeGe (111) thin films. *Phys. Rev. Lett.* **108**, 267201 (2012)
86. Y.F. Li, N. Kanazawa, X.Z. Yu, A. Tsukazaki, M. Kawasaki, M. Ichikawa, X.F. Jin, F. Kagawa, Y. Tokura, Robust formation of skyrmions and topological Hall effect anomaly in epitaxial thin films of MnSi. *Phys. Rev. Lett.* **110**, 117202 (2013)

87. J.C. Gallagher, K.Y. Meng, J.T. Brangham, H.L. Wang, B.D. Esser, D.W. McComb, F.Y. Yang, Robust zero-field skyrmion formation in FeGe epitaxial thin films. *Phys. Rev. Lett.* **118**, 027201 (2017)
88. F. Jonietz, S. Mühlbauer, C. Pfleiderer, A. Neubauer, W. Münzer, A. Bauer, T. Adams, R. Georgii, P. Böni, R.A. Duine, K. Everschor, M. Garst, A. Rosch, Spin transfer torques in MnSi at ultralow current densities. *Science* **330**, 1648–1651 (2010)
89. N. Kanazawa, M. Kubota, A. Tsukazaki, Y. Kozuka, K.S. Takahashi, M. Kawasaki, M. Ichikawa, F. Kagawa, Y. Tokura, Discretized topological Hall effect emerging from skyrmions in constricted geometry. *Phys. Rev. B* **91**, 041122 (2015)
90. M. Uchida, Y. Onose, Y. Matsui, Y. Tokura, Real-space observation of helical spin order. *Science* **311**, 359–361 (2006)
91. J. Ye, Y.B. Kim, A.J. Millis, B.I. Shraiman, P. Majumdar, Z. Tešanović, Berry phase theory of the anomalous Hall effect: application to colossal magnetoresistance manganites. *Phys. Rev. Lett.* **83**, 3737 (1999)
92. P. Bruno, V.K. Dugaev, M. Taillefumier, Topological Hall effect and Berry phase in magnetic nanostructures. *Phys. Rev. Lett.* **93**, 096806 (2004)
93. A. Neubauer, C. Pfleiderer, B. Binz, A. Rosch, R. Ritz, P.G. Niklowitz, P. Böni, *Phys. Rev. Lett.* **102**, 186602 (2009)
94. M. Lee, W. Kang, Y. Onose, Y. Tokura, N.P. Ong, Unusual Hall effect anomaly in MnSi under pressure. *Phys. Rev. Lett.* **102**, 186601 (2009)
95. N. Kanazawa, Y. Onose, T. Arima, D. Okuyama, K. Ohoyama, S. Wakimoto, K. Kakurai, S. Ishiwata, Y. Tokura, Large topological Hall effect in a short-period helimagnet MnGe. *Phys. Rev. Lett.* **106**, 156603 (2011)
96. T. Schulz, R. Ritz, A. Bauer, M. Halder, M. Wagner, C. Franz, C. Pfleiderer, K. Everschor, M. Garst, A. Rosch, Emergent electrodynamics of skyrmions in a chiral magnet. *Nat. Phys.* **8**, 301–304 (2012)
97. N. Rougemaille, A.K. Schmid, Magnetic imaging with spin-polarized low-energy electron microscopy. *Eur. Phys. J. Appl. Phys.* **50**, 20101 (2010)
98. G. Chen, A.T. N'Diaye, S.P. Kang, H.Y. Kwon, C. Won, Y. Wu, Z.Q. Qiu, A.K. Schmid, Unlocking bloch-type chirality in ultrathin magnets through uniaxial strain. *Nat. Commun.* **6**, 6598 (2015)
99. G. Chen, S.P. Kang, C. Ophus, A.T. N'Diaye, H.Y. Kwon, R.T. Qiu, C. Won, K. Liu, Y. Wu, A.K. Schmid, Out-of-plane chiral domain wall spin-structures in ultrathin in-plane magnets. *Nat. Commun.* **8**, 15302 (2017)
100. A. Scholl, H. Ohldag, F. Nolting, J. Stöhr, H.A. Padmore, X-ray photoemission electron microscopy, a tool for the investigation of complex magnetic structures. *Rev. Sci. Instrum.* **73**, 1362 (2002)
101. C.T. Chen, Y.U. Idzerda, H.-J. Lin, N.V. Smith, G. Meigs, E. Chaban, G.H. Ho, E. Pellegrin, F. Sette, Experimental confirmation of the x-ray magnetic circular dichroism sum rules for iron and cobalt. *Phys. Rev. Lett.* **75**, 152 (1995)
102. J. Stöhr, A. Scholl, T.J. Regan, S. Anders, J. Lüning, M.R. Scheinfein, H.A. Padmore, R.L. White, Images of the antiferromagnetic structure of a NiO(100) surface by means of x-ray magnetic linear dichroism spectromicroscopy. *Phys. Rev. Lett.* **83**, 1862 (1999)
103. M.R. Scheinfein, J. Unguris, M.H. Kelley, D.T. Pierce, R.J. Celotta, Scanning electron microscopy with polarization analysis (SEMPA). *Rev. Sci. Instrum.* **61**, 2501 (1990)
104. E.C. Corredor, S. Kuhrau, F. Klootdt-Twesteren, R. Frömter, H.P. Oepen, SEMPA investigation of the Dzyaloshinskii-Moriya interaction in the single, ideally grown Co/Pt(111) interface. *Phys. Rev. B* **96**, 060410(R) (2017)
105. A. Neudert, J. McCord, D. Chumakov, R. Schäfer, L. Schultz, Small-amplitude magnetization dynamics in permalloy elements investigated by time-resolved wide-field Kerr microscopy. *Phys. Rev. B* **71**, 134405 (2005)
106. Z.Q. Qiu, S.D. Bader, Surface magneto-optic Kerr effect. *Rev. Sci. Instrum.* **71**, 1243 (2000)
107. D.-H. Kim, P. Fischer, W. Chao, E. Anderson, M.-Y. Im, S.-C. Shin, S.-B. Choe, Magnetic soft x-ray microscopy at 15 nm resolution probing nanoscale local magnetic hysteresis. *J. Appl. Phys.* **99**, 08H303 (2006)

108. R. Streubel, F. Kronast, P. Fischer, D. Parkinson, O.G. Schmidt, D. Makarov, Retrieving spin textures on curved magnetic thin films with full-field soft X-ray microscopies. *Nat. Commun.* **6**, 7612 (2015)
109. L. Reimer, H. Kohl, *Transmission Electron Microscopy* (Springer, 2008)
110. M.J. Benitez et al., Magnetic microscopy and topological stability of homochiral Néel domain walls in a Pt/Co/AlOx trilayer. *Nat. Commun.* **6**, 8957 (2015)
111. S.D. Pollard, J.A. Garlow, Yu. Jiawei, Z. Wang, Y. Zhu, H. Yangb, *Nat Commun.* **8**, 14761 (2017)
112. R. Wiesendanger, Spin mapping at the nanoscale and atomic scale. *Rev. Mod. Phys.* **81**, 1495 (2009)
113. J.-P. Tetienne, T. Hingant, L.J. Martínez, S. Rohart, A. Thiaville, L. Herrera Diez, K. Garcia, J.-P. Adam, J.-V. Kim, J.-F. Roch, I.M. Miron, G. Gaudin, L. Vila, B. Ocker, D. Ravelosona, V. Jacques, The nature of domain walls in ultrathin ferromagnets revealed by scanning nanomagnetometry. *Nat. Commun.* **6**, 6733 (2015)
114. L. Sun, R.X. Cao, B.F. Miao, Z. Feng, B. You, D. Wu, W. Zhang, A. Hu, H.F. Ding, Creating an artificial two-dimensional skyrmion crystal by nanopatterning. *Phys. Rev. Lett.* **110**, 167201 (2013)
115. R.P. Cowburn, D.K. Koltsov, A.O. Adeyeye, M.E. Welland, D.M. Tricker, Single-domain circular nanomagnets. *Phys. Rev. Lett.* **83**, 1042 (1999)
116. H.F. Ding, A.K. Schmid, D.Q. Li, K.Y. Guslienko, S.D. Bader, Magnetic bistability of Co nanodots. *Phys. Rev. Lett.* **94**, 157202 (2005)
117. R.K. Dumas, T. Gredig, C.P. Li, I.K. Schuller, K. Liu, Angular dependence of vortex-annihilation fields in asymmetric cobalt dots. *Phys. Rev. B* **80**, 014416 (2009)
118. R.K. Dumas, D.A. Gilbert, N. Eibagi, K. Liu, Chirality control via double vortices in asymmetric Co dots. *Phys. Rev. B* **83**, 060415 (2011)
119. J. Li, A. Tan, K.W. Moon, A. Doran, M.A. Marcus, A.T. Young, E. Arenholz, S. Ma, R.F. Yang, C. Hwang, Z.Q. Qiu, Tailoring the topology of an artificial magnetic skyrmion. *Nat. Commun.* **5**, 4704 (2014)
120. B.F. Miao, L. Sun, Y.W. Wu, X.D. Tao, X. Xiong, Y. Wen, R.X. Cao, P. Wang, D. Wu, Q.F. Zhan, B. You, J. Du, R.W. Li, H.F. Ding, Experimental realization of two-dimensional artificial skyrmion crystals at room temperature. *Phys. Rev. B* **90**, 174411 (2014)
121. D.A. Gilbert, B.B. Maranville, A.L. Balk, B.J. Kirby, P. Fischer, D.T. Pierce, J. Unguris, J.A. Borchers, K. Liu, Realization of ground-state artificial skyrmion lattices at room temperature. *Nat. Commun.* **6**, 8462 (2015)
122. B.F. Miao, Y. Wen, M. Yan, L. Sun, R.X. Cao, D. Wu, B. You, Z.S. Jiang, H.F. Ding, Micromagnetic study of excitation modes of an artificial skyrmion crystal. *Appl. Phys. Lett.* **107**, 222402 (2015)
123. K.Y. Guslienko, Z.V. Gareeva, Gyrotropic skyrmion modes in ultrathin magnetic circular dots. *IEEE Magn. Lett.* **8**, 2616333 (2017)
124. M. Charilaou, J.F. Loffler, Skyrmion oscillations in magnetic nanorods with chiral interactions. *Phys. Rev. B* **95**, 024409 (20170029)
125. M.Y. Im, P. Fischer, H.S. Han, A. Vogel, M.S. Jung, W. Chao, Y.S. Yu, G. Meier, J.I. Hong, K.S. Lee, Simultaneous control of magnetic topologies for reconfigurable vortex arrays. *Npg Asia Mater.* **9**, 199 (2017)
126. S. Zhang, A.K. Petford-Long, C. Phatak, Creation of artificial skyrmions and antiskyrmions by anisotropy engineering. *Sci. Rep.* **6**, 31248 (2016)
127. A. Tan, J. Li, A. Scholl, E. Arenholz, A.T. Young, Q. Li, C. Hwang, Z.Q. Qiu, Topology of spin meron pairs in coupled Ni/Fe/Co/Cu(001) disks. *Phys. Rev. B* **94**, 014433 (2016)
128. F.S. Ma, C. Reichhardt, W.L. Gan, C.J.O. Reichhardt, W.S. Lew, Emergent geometric frustration of artificial magnetic skyrmion crystals. *Phys. Rev. B* **94**, 144405 (2016)
129. D.A. Gilbert, T. Stückler, K. Lenz, I. Gilbert, J. Unguris, B.B. Maranville, J. Fassbender, H.M. Yu, K. Liu, J.A. Borchers, Room temperature planar artificial skyrmion lattices, in *MMM Conference*, (2016), pp. BC-07

130. J. Sampaio, V. Cros, S. Rohart, A. Thiaville, A. Fert, Nucleation, stability and current-induced motion of isolated magnetic skyrmions in nanostructures. *Nat. Nanotech.* **8**, 839–844 (2013)
131. P.J. Hsu, A. Kubetzka, A. Finco, N. Romming, K. von Bergmann, R. Wiesendanger, Electric-field-driven switching of individual magnetic skyrmions. *Nat. Nanotech.* **12**, 123–126 (2017)
132. C. Hanneken, F. Otte, A. Kubetzka, B. Dupe, N. Romming, K. von Bergmann, R. Wiesendanger, S. Heinze, Electrical detection of magnetic skyrmions by tunnelling non-collinear magnetoresistance. *Nat. Nanotech.* **10**, 1039–1042 (2015)
133. D.M. Crum et al., Perpendicular reading of single confined magnetic skyrmions. *Nat. Commun.* **6**, 8541 (2015)
134. J. Iwasaki, M. Mochizuki, N. Nagaosa, Current-induced skyrmion dynamics in constricted geometries. *Nat. Nanotech.* **8**, 742–747 (2013)
135. M. Kläui et al., Direct observation of domain-wall pinning at nanoscale constrictions. *Appl. Phys. Lett.* **87**, 102509 (2005)
136. E. Martinez et al., Thermal effects on domain wall depinning from a single notch. *Phys. Rev. Lett.* **98**, 267202 (2007)
137. Y. Jang et al., Current-induced domain wall nucleation and its pinning characteristics at a notch in a spin-valve nanowire. *Nanotechnology* **20**, 125401 (2009)
138. O. Heinonen, W. Jiang, H. Somaily, S.G.E. te Velthuis, A. Hoffmann, Generation of magnetic skyrmion bubbles by inhomogeneous spin Hall currents. *Phys. Rev. B* **93**, 094407 (2016)
139. K. von Bergmann, Magnetic bubbles with a twist. *Science* **349**, 234–235 (2015)
140. X. Zhang et al., Skyrmion–skyrmion and skyrmion–edge repulsions in skyrmion-based racetrack memory. *Sci. Rep.* **5**, 7643 (2015)
141. X. Zhang, M. Ezawa, Y. Zhou, Magnetic skyrmion logic gates: conversion, duplication and merging of skyrmions. *Sci. Rep.* **5**, 9400 (2015)
142. J. Zang, M. Mostovoy, J.H. Han, N. Nagaosa, *Phys. Rev. Lett.* **107**, 136804 (2011)
143. J. Iwasaki, M. Mochizuki, N. Nagaosa, Universal current–velocity relation of skyrmion motion in chiral magnets. *Nat. Commun.* **4**, 1463 (2013)
144. K. Everschor-Sitte, M. Sitte, Real-space Berry phases: skyrmion soccer. *J. Appl. Phys.* **115**, 172602 (2014)
145. C. Reichhardt, D. Ray, C.J.O. Reichhardt, Collective transport properties of driven skyrmions with random disorder. *Phys. Rev. Lett.* **114**, 217202 (2015)
146. C. Reichhardt, C.J.O. Reichhardt, Noise fluctuations and drive dependence of the skyrmion Hall effect in disordered systems. *New J. Phys.* **18**, 095005 (2016)
147. C. Reichhardt, C.J.O. Reichhardt, Magnus-induced dynamics of driven skyrmions on a quasi-one-dimensional periodic substrate. *Phys. Rev. B* **94**, 094413 (2016)
148. A. Thiele, Steady-state motion of magnetic domains. *Phys. Rev. Lett.* **30**, 230–233 (1973)
149. R. Tomasello, E. Martinez, R. Zivieri, L. Torres, M. Carpentieri, G. Finocchio, A strategy for the design of skyrmion racetrack memories. *Sci. Rep.* **4**, 6784 (2014)
150. W. Jiang, Z. Xichao, G. Yu, W. Zhang, X. Wang, M.B. Jungfleisch, J.E. Pearson, X. Cheng, O. Heinonen, K.L. Wang, Y. Zhou, A. Hoffmann, S.G.E. te Velthuis, Direct observation of the skyrmion Hall effect. *Nat. Phys.* **13**, 162–169 (2017)
151. S. Huang, C. Zhou, G. Chen, H. Shen, A.K. Schmid, K. Liu, W. Yizheng, Stabilization and current-induced motion of antiskyrmion in the presence of anisotropic Dzyaloshinskii–Moriya interaction. *Phys. Rev. B* **96**, 144412 (2017)
152. J. Muller, A. Rosch, Capturing of a magnetic skyrmion with a hole. *Phys. Rev. B* **91**, 054410 (2015)
153. Y.-H. Liu, Y.-Q. Li, A mechanism to pin skyrmions in chiral magnets. *J. Phys.: Condens. Matter* **25**, 076005 (2013)
154. R.L. Silva, L.D. Secchin, W.A. Moura-Melo, A.R. Pereira, R.L. Stamps, Emergence of skyrmion lattices and bimerons in chiral magnetic thin films with nonmagnetic impurities. *Phys. Rev. B* **89**, 054434 (2014)
155. J. Muller, A. Rosch, Capturing of a magnetic skyrmion with a hole. *Phys. Rev. B* **91**, 054410 (2015)

156. W. Legrand, D. Maccariello, N. Reyren, K. Garcia, C. Moutafis, C. Moreau-Luchaire, S. Collin, K. Bouzehouane, V. Cros, A. Fert, Room-temperature current-induced generation and motion of sub-100 nm skyrmions. *Nano Lett.* **17**, 2703–2712 (2017)
157. K. Litzius, I. Lemesh, B. Krüger, P. Bassirian, L. Caretta, K. Richter, F. Büttner, K. Sato, O.A. Tretiakov, J. Förster, R.M. Reeve, M. Weigand, I. Bykova, H. Stoll, G. Schütz, G.S.D. Beach, M. Kläui, Skyrmion Hall effect revealed by direct time-resolved X-ray microscopy. *Nat. Phys.* **13**, 170–175 (2017)
158. X. Zhang, Y. Zhou, M. Ezawa, Magnetic bilayer-skyrmions without skyrmion Hall effect. *Nat. Commun.* **7**, 10293 (2016)
159. J. Barker, O.A. Tretiakov, Static and dynamical properties of antiferromagnetic skyrmions in the presence of applied current and temperature. *Phys. Rev. Lett.* **116**, 147203 (2016)
160. S.S. Parkin, M. Hayashi, L. Thomas, Magnetic domain-wall racetrack memory. *Science* **320**, 190–194 (2008)
161. L. Berger, Emission of spin waves by a magnetic multilayer traversed by a current. *Phys. Rev. B* **54**, 9353–9358 (1996)
162. G. Tatara, H. Kohno, Theory of current-driven domain wall motion: Spin transfer versus momentum transfer. *Phys. Rev. Lett.* **92**, 08660 (2004)
163. S.Z. Lin, C. Reichhardt, C.D. Batista, A. Saxena, Particle model for skyrmions in metallic chiral magnets: Dynamics, pinning, and creep. *Phys. Rev. B* **87**, 214419 (2013)
164. J.E. Hirsch, Spin Hall effect. *Phys. Rev. Lett.* **83**, 1834–1837 (1999)
165. S. Emori, U. Bauer, S.M. Ahn, E. Martinez, G.S. Beach, Current-driven dynamics of chiral ferromagnetic domain walls. *Nat. Mater.* **12**, 611–616 (2013)
166. G.Q. Yu, P. Upadhyaya, X. Li, W.Y. Li, S.K. Kim, Y.B. Fan, K.L. Wong, Y. Tserkovnyak, P.K. Amiri, K.L. Wang, Room-temperature creation and spin orbit torque manipulation of skyrmions in thin films with engineered asymmetry. *Nano Lett.* **16**, 1981–1988 (2016)
167. W. Jiang, G. Chen, K. Liu, J. Zang, Suzanne G.E. te Velthuis, Axel Hoffmann, Skyrmions in magnetic multilayers. *Phys. Rep.* **704**, 1–49 (2017)
168. X. Ma, Yu. Guoqiang, S.A. Razavi, S.S. Sasaki, X. Li, K. Hao, S.H. Tolbert, K.L. Wang, X. Li, Dzyaloshinskii-Moriya Interaction across an Antiferromagnet-Ferromagnet Interface. *Phys. Rev. Lett.* **119**, 027202 (2017)
169. H. Yang, G. Chen, A.A.C. Cotta, A.T. N'Diaye, S.A. Nikolaev, E.A. Soares, W.A.A. Macedo, K. Liu, A.K. Schmid, A.Fert, M. Chshiev, Significant Dzyaloshinskii-Moriya Interaction at Graphene-Ferromagnet Interfaces due to Rashba-effect. *Nat. Mater.* **17**, 605–609 (2018)
170. M. Hoffmann, B. Zimmermann, G.P. Müller, D. Schürhoff, N.S. Kiselev, C. Melcher, S. Blügel, Antiskyrmions stabilized at interfaces by anisotropic Dzyaloshinskii-Moriya interactions. *Nat. Commun.* **8**, 308 (2017)
171. A.K. Nayak, V. Kumar, T. Ma, P. Werner, E. Pippel, R. Sahoo, F. Damay, U.K. Rößler, C. Felser, S.S.P. Parkin, Magnetic antiskyrmions above room temperature in tetragonal Heusler materials. *Nature* **548**, 561 (2017)
172. A. Hrabec, J. Sampaio, M. Belmeguenai, I. Gross, R. Weil, S.M. Chérif, A. Stachkevitch, V. Jacques, A. Thiaville, S. Rohart, Current-induced skyrmion generation and dynamics in symmetric bilayers. *Nat. Commun.* **8**, 15765 (2017)
173. G. Yu, P. Upadhyaya, Q. Shao, H. Wu, G. Yin, X. Li, C. He, W. Jiang, X. Han, P.K. Amiri, K.L. Wang, Room-temperature skyrmion shift device for memory application. *Nano Lett.* **17**, 261–268 (2017)
174. W. Jiang, W. Zhang, G.Q. Yu, M.B. Jungfleisch, P. Upadhyaya, H. Somaily, J.E. Pearson, Y. Tserkovnyak, K.L. Wang, O. Heinonen, S.G.E. te Velthuis, A. Hoffmann, Mobile Néel skyrmions at room temperature: status and future. *AIP Adv.* **6**, 055602 (2016)

Chapter 5

Skyrmion Lattices Far from Equilibrium



Andreas Bauer, Alfonso Chacon, Marco Halder and Christian Pfleiderer

Abstract Magnetic *skyrmions* are spin whirls with non-trivial topology that are remarkably robust. We review current research on *skyrmion* lattices far from equilibrium in cubic chiral magnets obtained under field cooling, providing access to generic properties of *skyrmions* in the non-thermal limit as well as concepts of spintronics applications.

5.1 Introduction and Outline

Proposed in the 1960s as a theoretical model for the description of nucleons as excitations of pion fields [1, 2], the theoretical suggestions of Tony Skyrme have been adopted in completely different areas of physics [3–7]. In the context of solid-state magnetism, the expression *skyrmion* refers to magnetic whirls with non-trivial topology as well as a non-linear (solitonic) character [8–19]. Thus, skyrmions may not be continuously transformed into topologically trivial states, such as a ferromagnetic or antiferromagnetic spin order, and the creation and destruction of skyrmions requires a topological winding or unwinding, respectively [20–22]. As a consequence, once a skyrmion has formed, it turns out to be rather robust—a phenomenon that is also referred to as topological protection. Regardless whether skyrmions are studied in magnetic bulk materials, thin-film heterostructures, or monolayers, it is in particular their non-trivial topology that leads to a set of unique properties attracting great interest.

A. Bauer · A. Chacon · M. Halder · C. Pfleiderer (✉)

Physik-Department, Technische Universität München, James-Franck-Straße, 85748 Garching, Germany

e-mail: Christian.Pfleiderer@frm2.tum.de

A. Bauer

e-mail: Andreas.Bauer@frm2.tum.de

In this article we consider putative similarities of skyrmions with rapidly cooled liquids, when the liquid state may persist well below the equilibrium freezing temperature. The resulting super-cooled configuration is metastable and the formation of a crystalline or glassy solid is triggered by tiny perturbations, such as impurities or mechanical shock. In a similar manner, due to their topological protection, skyrmion lattices in bulk materials may be super-cooled to temperatures well below the parameter regime of their equilibrium state. In contrast to super-cooled liquids, however, metastable skyrmion lattice configurations turn out to become increasingly robust with decreasing temperature. In turn, they survive in large parts of the magnetic phase diagram and, for instance, may be exploited in studies of the generic properties in the non-thermal limit. Likewise, super-cooled skyrmion phases may foster concepts for potential application in the context of data storage, spintronics, or microwave technologies [23–37].

In this chapter, we present a review of current research on skyrmions and skyrmion lattices far from equilibrium in cubic chiral magnets. We begin in Sect. 5.2 with a brief summary of the magnetic properties of this class of compounds with a particular focus on the skyrmion lattice state, followed by an account on consequences of the non-trivial topology in Sect. 5.2.1. The dependence of the magnetic phase diagram on the field and temperature history is discussed in Sect. 5.2.2 for the case of $\text{Fe}_{1-x}\text{Co}_x\text{Si}$. In Sect. 5.3, we present four examples from the recent literature investigating or exploiting metastable skyrmion lattices in chiral magnets. Namely, we describe studies on the unwinding processes of the skyrmion lattices by means of magnetic force microscopy and Lorentz force transmission electron microscopy on $\text{Fe}_{1-x}\text{Co}_x\text{Si}$ (Sect. 5.3.1), the topological Hall effect in MnSi under pressure (Sect. 5.3.2), the quenching of the skyrmion lattice in MnSi by means of current pulses (Sect. 5.3.3), and structural phase transitions in the metastable skyrmion lattice of MnSi and $\text{Co}_8\text{Zn}_8\text{Mn}_4$ (Sect. 5.3.4). The chapter closes with a short summary in Sect. 5.4.

5.2 Skyrmion Lattices in Cubic Chiral Magnets

Representing the most extensively studied class of materials hosting skyrmions, the cubic chiral magnets crystallize either in the space group $P2_13$, such as MnSi , $\text{Fe}_{1-x}\text{Co}_x\text{Si}$, FeGe , and Cu_2OSeO_3 , or in space groups $P4_132$ and $P4_332$, such as $\text{Co}_8\text{Zn}_8\text{Mn}_4$. Featuring a lack of inversion symmetry as key characteristic, the magnetic properties of these materials are generically governed by a hierarchy of energy scales that comprises in decreasing strength (i) exchange interactions, (ii) Dzyaloshinsky–Moriya interactions as leading-order spin–orbit coupling, and (iii) higher-order spin–orbit coupling terms also referred to as magnetocrystalline or cubic anisotropies. As a result, cubic chiral magnets share a generic magnetic phase diagram as depicted in Fig. 5.1a. Starting from a paramagnetic state at high temperatures, the helical state forms below the ordering temperature T_c in zero field. This state is characterized by long-wavelength helices that propagate along one of the equivalent directions favored by the cubic anisotropies, typically either $\langle 100 \rangle$

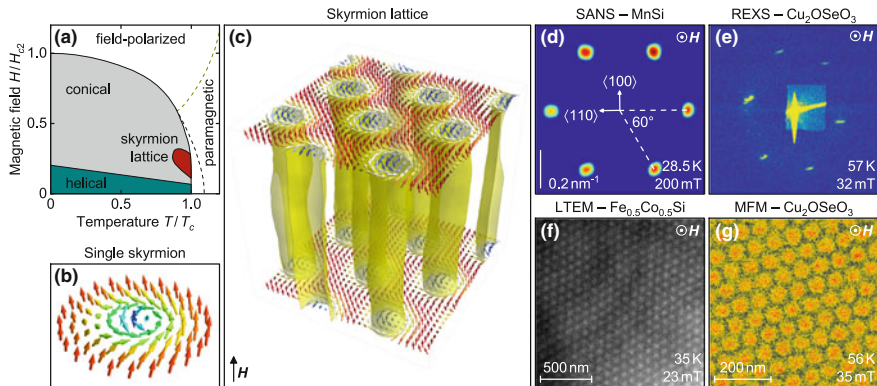


Fig. 5.1 Skyrmiон lattices in the cubic chiral magnets. **a** Typical magnetic phase diagram of the cubic chiral magnets comprising a paramagnetic and a field-polarized regime as well as the helical, the conical, and the skyrmion lattice state. **b** Schematic depiction of a single chiral skyrmion. **c** Schematic depiction of the trigonal skyrmion lattice state as it forms in the phase pocket in finite magnetic fields just below the helimagnetic ordering temperature, T_c . **d–g** Skyrmiон lattice state as observed in reciprocal and real space by means of small-angle neutron scattering (SANS), resonant elastic x-ray scattering (REXS), Lorentz force transmission electron microscopy (LTEM), and magnetic force microscopy (MFM) on different materials. See text for details Data and illustrations taken from [20, 22, 38–40]

or $\langle 111 \rangle$. With increasing field, the propagation direction of the helical modulation reorients into the field direction and the spins tilt towards the field, giving rise to the conical state that resembles the spin-flop phase of conventional antiferromagnets. Above a critical field H_{c2} , the system becomes field-polarized.

Perhaps most interesting in the phase diagram, a single pocket of a skyrmion lattice state is observed at intermediate fields just below T_c . In the following, we summarize the key characteristics of this spin state, while we refer to review articles such as [25, 41] or the supplement material of [8] for pedagogical introductions.

The spin configuration of a single chiral magnetic skyrmion is shown in Fig. 5.1b. In the skyrmion lattice state, these spin whirls form a regular trigonal (also often referred to as hexagonal) arrangement in the plane perpendicular to the applied field that may be described in terms of a phase-locked superposition of three helices and a ferromagnetic magnetization component. Along the field direction, the magnetic structure extends in the form of skyrmion tubes, as illustrated in Fig. 5.1c. The skyrmion lattice was first identified in MnSi by means of small-angle neutron scattering (SANS) [8], where a sixfold scattering pattern was observed for magnetic field parallel to the incident neutron beam, cf. Fig. 5.1d. Measurements for different field orientations, including arbitrary non-symmetry directions, revealed that the skyrmion lattice forms rather isotropically and is nearly independent from the underlying crystal lattice. Consistently, calculations taking into account thermal Gaussian fluctuations around the mean-field spin configurations established that the magnetic structure is stabilized by thermal fluctuations rather than by uniax-

ial anisotropies as predicted earlier [42, 43]. Note, however, that uniaxial pressure may increase the temperature range of the skyrmion lattice phase pocket [44, 45].

In recent years, neutron scattering studies [38, 46–51] were complemented by resonant elastic x-ray scattering (REXS) [39, 52, 53]. As shown in Fig. 5.1e, typical REXS patterns of the skyrmion lattice are highly reminiscent of the SANS data, offering new insights such as element specificity or high lateral resolution. In addition, the length scale of the skyrmion lattice in chiral magnets makes them ideally suited for real-space observations using techniques such as Lorentz force transmission electron microscopy (LTEM) [9, 54–57], magnetic force microscopy (MFM) [20, 40], or electron holography [58]. Typical pictures of the skyrmion lattice as recorded by means of LTEM and MFM are shown in Fig. 5.1f and 5.1g, respectively. Both techniques complement each other as the contrast in LTEM arises from the distribution of the in-plane magnetic moments, while MFM is sensitive to the stray field created by the out-of-plane components of the magnetization.

For the different materials known to date the characteristic temperature, magnetic field, and magnetic length scales vary by about two orders of magnitude, ranging from a few Kelvin to more than room temperature, from a few millitesla to about a Tesla, and from a few nanometer to several hundred nanometer, respectively [25, 41]. This wide parameter range allows to select compounds for specific fundamental experiments as well as putative applications such as tailored microwave devices, offering in addition the possibility to combine metallic, semiconducting, and insulating materials [59–62].

As an odd one out, MnGe, though also crystallizing with space group $P2_13$ and hosting Dzyaloshinsky–Moriya interactions, exhibits a distinctly different magnetic phase diagram dominated by a three-dimensional arrangement of short-wavelength spin whirls. The origin is presumably rather strong spin–orbit coupling outside the above-mentioned hierarchy of energy scales [63–66]. Moreover, recently the class of lacunar spinels generated great scientific interest when a triangular lattice of skyrmions based on spin cycloids was observed in the multiferroic compound GaV_4S_8 [16, 67]. In this material, the formation of the skyrmions is made possible by a Jahn–Teller distortion, resulting in strong anisotropies and confining the magnetic textures along certain high-symmetry directions. Very recently skyrmion lattice order based on spin cycloids was also reported for the tetragonal polar magnet VOSe_2O_5 [68]. In addition, thin film systems hosting skyrmions and other forms of topologically non-trivial spin order are vividly investigated, as elaborated on in Chap. 4 of this book. Instead of bulk Dzyaloshinsky–Moriya interactions dominating in volume materials, typically in these systems the non-trivial topology is associated with interfacial Dzyaloshinsky–Moriya interactions.

5.2.1 Emergent Electrodynamics and Topological Protection

The interplay of skyrmions in chiral magnets with spin currents, causing real-space Berry phases, may be elegantly described in terms of fictitious magnetic and electric fields of an emergent electrodynamics. As a simple experimental consequence in

metallic materials, this explains an additional contribution to the Hall effect in the skyrmion lattice state, referred to as the topological Hall effect. In fact, the observation of the topological Hall effect in MnSi provided first experimental evidence of the topologically non-trivial character of the skyrmion lattice state [69]. This was followed-up more recently by combined experimental studies and ab initio calculations, connecting the anomalous and the topological Hall contributions under substitutional doping in $\text{Mn}_{1-x}\text{Fe}_x\text{Si}$ quantitatively with reciprocal-space and real-space Berry phases, respectively [70]. Here measurements of the topological Hall effect on the metastable skyrmion lattice in MnSi under pressure, reviewed in Sect. 5.3.2, provided information on the intrinsic size of the Hall contribution when eliminating finite-temperature effects. Moreover, as discussed in Sect. 5.3.3, the topological Hall effect in the skyrmion lattice may also be exploited in order to detect the magnetic state of the sample in potential spintronics applications. Note that introductions on the anomalous Hall effect may be found in [71] or Chap. 6 of this book.

On a different note, the non-trivial topological character of the skyrmion lattice in bulk samples of MnSi was also confirmed in terms of the anomalous temperature and magnetic field dependence of higher-order SANS intensities [38]. However, while these studies revealed a very weak solitonic (particle-like) character of the skyrmion lattice in MnSi of order 10^{-4} , LTEM measurements of the dynamical properties at the fringes of skyrmion lattice domains in Cu_2OSeO_3 revealed particle-like characteristics akin those of hard spheres [57].

Further, connected with the momentum transfer exerted by the spin structure on the spin currents carried by the conduction electrons is a balancing momentum transfer on the skyrmions. In turn, for current densities exceeding defect-related pinning, the magnetic texture may start to drift due to the effects of spin transfer torques. Corresponding effects have been studied extensively in nano-scaled materials hosting ferromagnetic domain walls [72–78]. However, compared to these systems, the critical threshold current densities in skyrmion lattices are several orders of magnitude smaller, notably of the order $\sim 10^6 \text{ A/m}^2$ [79–82]. These ultra-low threshold current densities may be attributed to the combination of very efficient gyromagnetic coupling with the effects of weak collective pinning, reflecting the rather stiff long-range order of the skyrmion lattice [38]. As a result of the current induced drift, the emergent magnetic flux associated with the skyrmions induces an emergent electric field that may be detected in the form of the putative suppression of the topological Hall signal [83].

Considering insulating materials, the interplay of the skyrmions with spin currents due to magnons may play a dominant role leading, for instance, to a rotational motion of skyrmion lattice domains [57, 84]. Taken together, the emergent electrodynamics captures a remarkable variety of how skyrmion lattices may be manipulated by means of external control parameters. This includes, in particular, materials exhibiting strong magnetoelectric coupling, such as Cu_2OSeO_3 [85–88].

Finally, the emergent magnetic flux associated with each skyrmion is also expected to be reflected in the mechanisms underlying the creation and destruction of skyrmions, notably points of vanishing local magnetization referred to as Bloch points representing emergent magnetic monopoles [20]. However, while these pro-

cesses have been detected microscopically, the observation of the associated emergent electrodynamics is the subject of ongoing work awaiting clarification. Further, as a consequence of its non-trivial topological character, an enhanced stability of skyrmion lattices as compared to conventional thermodynamic forms of order may naively be expected. Indeed, the characteristic time scales associated with the unwinding processes, as explored by experiments in different chiral magnets and summarized in this chapter, depend sensitively on temperature and may drastically vary when compared between stoichiometric (clean) and doped (disordered) systems. In these studies, metastable skyrmion lattices, generated under field-cooling, prove to be particularly valuable as the topological unwinding slows down such that the underlying mechanisms may be studied in detail as reviewed in Sect. 5.3.1.

5.2.2 *Metastable Skyrmion Lattices Under Field Cooling*

Small-angle neutron scattering studies in $\text{Fe}_{1-x}\text{Co}_x\text{Si}$ revealed early on that field cooling this compound through the skyrmion lattice state may result in a metastable skyrmion lattice at low temperatures, i.e., well below the equilibrium phase pocket [46]. The thermodynamic ground state at these low temperature and field values is either the helical or conical state, which, however, is not recovered on time scale relevant for the experiments of several hours. For the detailed account presented below, it is instructive to distinguish the following temperature and field histories, where typical cooling rates are of the order ~ 10 K/min. Magnetic field sweeps are carried out in step mode, while data as a function of temperature are measured while sweeping the temperature at a rate of typically 0.5 K/min. Wherever possible, we combine measurements as a function of temperature and field.

- Zero-field cooling (ZFC): The measurements begin at a temperature well above T_c in zero field. For field sweeps, the sample is cooled to the desired temperature before data are recorded while increasing the magnetic field to $H > H_{c2}$. For temperature sweeps, the sample is cooled to 2 K before the desired magnetic field value is applied. Subsequently, data are recorded while increasing the sample temperature.
- High-field cooling (HFC): The measurements start in a high field, $H > H_{c2}$, at a temperature well above T_c . For field sweeps, the sample is cooled to the desired temperature before data are recorded while decreasing the magnetic field from $H > H_{c2}$ to $H < -H_{c2}$. For temperature sweeps, the sample is cooled to 2 K before the magnetic field is reduced to the desired value. Subsequently, data are recorded while increasing the sample temperature.
- Field cooling (FC): The measurements start at a temperature well above T_c with the desired field value applied. Subsequently, data are recorded while decreasing the sample temperature.
- Field cooling through the skyrmion lattice followed by a change of the field at a fixed temperature (FC $^\pm$): The measurements start at a temperature well above T_c

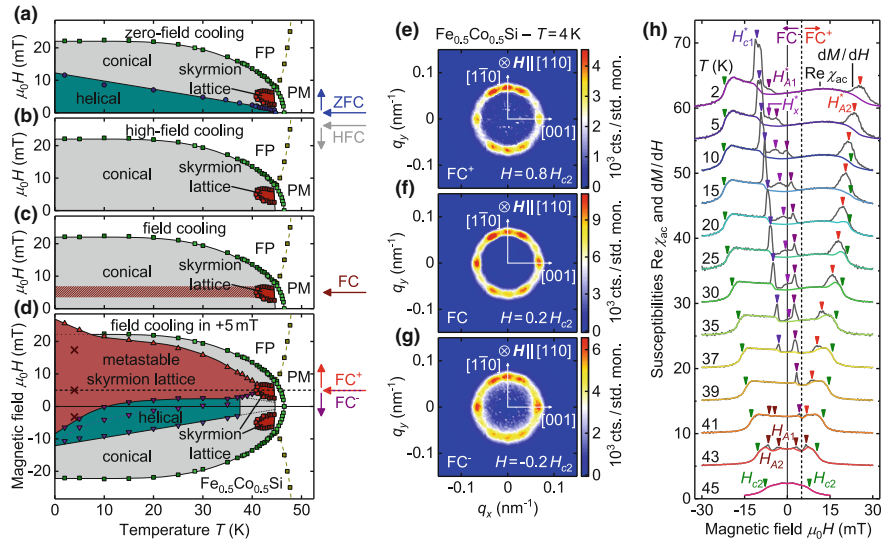


Fig. 5.2 Metastable skyrmion lattice under field cooling in $\text{Fe}_{1-x}\text{Co}_x\text{Si}$ ($x = 0.5$). **a–d** Magnetic phase diagram for different cooling histories. We distinguish zero-field cooling (ZFC), high-field cooling (HFC), field cooling (FC), and field cooling through the skyrmion lattice state followed by an increase or decrease of the magnetic field (FC $^+$ and FC $-$). **e–g** Small-angle neutron scattering data after FC $^+$, FC, and FC $-$ showing the pattern characteristic of the skyrmion lattice. **(h)** Susceptibility calculated from the measured magnetization, dM/dH , and real part of the ac susceptibility, $\text{Re } \chi_{\text{ac}}$, as a function of field for different temperatures after field cooling through the skyrmion lattice state (FC $^+$ and FC $-$). Colored triangles mark the transitions as shown in the magnetic phase diagram in panel **(d)**. Data have been offset by 5 for clarity. Data taken from [89, 90]

with an applied field value that allows to cross the phase pocket of the skyrmion lattice. Next, the sample is field-cooled to desired temperature before data are recorded while increasing the magnetic field to $H > H_{c2}$ (FC $^+$). Now, the sample is heated well above T_c , field-cooled a second time, and data are recorded while decreasing the field to $H < -H_{c2}$ (FC $-$).

In Fig. 5.2a–d the corresponding magnetic phase diagrams as inferred from susceptibility data are shown [90]. The cooling histories are sketched by the arrows on the right-hand side. After zero-field cooling, the situation corresponds to the generic magnetic phase diagram as observed in the cubic chiral magnets. After high-field cooling, the phase diagram is identical with one exception; no helical state with multiple macroscopic domains of helices propagating along the easy axes implied by the cubic anisotropies is recovered, at least on the time scales relevant for the experiments [89, 91]. This behavior is consistent with other doped compounds, such as $\text{Mn}_{1-x}\text{Fe}_x\text{Si}$ [92, 93]. It may be attributed to very weak cubic anisotropies in conjecture with pronounced defect pinning introduced by the substitutional doping.

After field cooling also no helical state is recovered. More importantly, however, when field cooling through the skyrmion lattice phase pocket, signatures character-

istic of the skyrmion lattice state can be traced down to lowest temperature in both SANS [46, 94] and AC susceptibility [89], cf. hatched area in Fig. 5.2c. Presumably due to the large amount of disorder, the characteristic time scales associated with the unwinding of the skyrmions are particularly slow in strongly doped systems such as $\text{Fe}_{1-x}\text{Co}_x\text{Si}$. Consequently, already very moderate cooling rates of the order K/min allow to pass through the low-temperature boundary of the reversible skyrmion lattice phase pocket fast enough to prevent the unwinding of the skyrmions into the conical state. At lower temperatures, thermal fluctuation are no longer sufficient to initiate the unwinding on time scale relevant for typical experiments and the system retains the skyrmion lattice order, although it is not the thermodynamic ground state.

When using the field-cooled metastable skyrmion lattice as a starting point and subsequently changing the applied field value (FC^+ and FC^-), the phase diagram shown in Fig. 5.2d is obtained. Here, the metastable skyrmion lattice state is observed across large parts of the phase diagram. At the borders of this regime, the change of the magnetic field has altered the energy landscape in a way that the characteristic time scales of the unwinding processes become fast compared to the typical time scales of the measurements (of the order of seconds).

It is interesting to note that for low temperatures magnetic fields in excess of H_{c2} or an inversion of the field direction are necessary to unwind the skyrmion lattice. This underscores the remarkable robustness of this state as a result of its topological protection. In fact, this behavior somehow contrasts the super-cooled liquids; while the latter become increasingly sensitive with decreasing temperature to tiny perturbations ultimately triggering solidification, the unwinding of the skyrmion lattice requires increasingly large changes of the magnetic field when cooled further below its reversible phase pocket.

Typical small-angle neutron scattering patterns recorded at temperature and field values that are marked by dark crosses in Fig. 5.2d are shown in Fig. 5.2e–g. For magnetic field applied along the neutron beam, the characteristic sixfold scattering pattern of the skyrmion lattice state is observed after field cooling (center). Increasing or decreasing the magnetic field within the regime of the metastable skyrmion lattice keeps the scattering pattern qualitatively unchanged. Note that data presented here represent sums over rocking scans around the vertical axis only, making spots closer to the vertical axis appear more intense. The twelvefold scattering pattern is due to two independent skyrmion lattice domains aligning along [001] and [110], respectively [95]. Multiple domains of skyrmion lattice with differing orientation were also reported in Cu_2OSeO_3 and MnSi [49, 96, 97].

The magnetic phase diagrams may, in fact, most accurately be inferred from susceptibility measurements. Typical data as a function of field after field cooling through the skyrmion lattice are shown in Fig. 5.2h for several temperatures. Here, the susceptibility calculated from the measured magnetization, dM/dH (gray curves), and the real part of the AC susceptibility, $\text{Re } \chi_{\text{ac}}$ (colored curves), are compared. The dashed vertical line marks the cooling field of +5 mT. Colored triangles indicate the data points as marked in the magnetic phase diagram in Fig. 5.2d.

At high temperatures just below T_c , at $T = 43$ K, the susceptibility exhibits the behavior typical of cubic chiral magnets. In particular, plateaus of reduced suscep-

tibility symmetrically emerging for positive and negative fields are characteristic of the reversible pocket of the skyrmion lattice state. Both susceptibilities, dM/dH and $\text{Re } \chi_{\text{ac}}$, track each other with the exception of the border between the conical and the skyrmion lattice state ($\pm H_{A1}$ and $\pm H_{A2}$, brown symbols). In these areas of phase coexistence slow dynamics and finite dissipation may be attributed to the complex winding and unwinding processes associated with the formation of the topologically non-trivial skyrmion lattice state [89, 91, 98–101], cf. Sect. 5.3.1.

Upon field cooling, the minimum associated with the skyrmion lattice persists around the cooling field, with the susceptibility curve becoming clearly asymmetric with respect to zero field. When increasing the field after field cooling (FC^+), a maximum in dM/dH may be attributed to the unwinding of the metastable skyrmion lattice into the conical state (H_{A2}^* , red symbols). Below ~ 8 K, H_{A2}^* exceeds the transition field of the conical-to-field-polarized transition as determined under different cooling histories (H_{c2} , green symbols). Consequently, at low temperatures the skyrmion lattice may unwind directly into a field-polarized spin configuration instead of into the conical state.

When decreasing the field after field cooling (FC^-), at rather high temperatures a maximum in dM/dH is also attributed to the unwinding of the skyrmion lattice into the conical state (H_{A1}^* , purple symbols). Once the helical state is the ground state at the field value triggering the unwinding, i.e., below 37 K, a plateau characteristic of the helical state is observed that again is bordered by a maximum in dM/dH in negative fields (H_{c1}^* , blueish symbols) that resembles the signature of the helical-to-conical transition. This contrasts the behavior after high-field cooling where no helical state is recovered in $\text{Fe}_{1-x}\text{Co}_x\text{Si}$. With decreasing temperature, an additional maximum labeled H_x^* of yet unknown origin appears between H_{A1}^* and H_{c1}^* . At low temperatures, below 5 K, no signatures associated with the unwinding processes are observed well into the regime of negative fields, i.e., once the metastable skyrmion lattice has formed it may even remain robust under field inversion.

Metastable skyrmion lattices were reported not only in disordered systems, such as $\text{Fe}_{1-x}\text{Co}_x\text{Si}$ or $\text{Co}_x\text{Zn}_y\text{Mn}_z$ [102, 103], but also in stoichiometric materials, such as MnSi [104] or Cu_2OSeO_3 [87]. The characteristic time scales, and therefore the required cooling rates for the observation of metastable skyrmion lattices, are strongly material dependent. While in disordered systems already moderate cooling rates of a few Kelvin per minute are sufficient, typically achieved in commercial cryostats, clean materials either require bespoke experimental setups allowing for rapid cooling or the application of additional tuning parameters such as pressure or electrical field. Nevertheless, as highlighted in the next section, metastable skyrmion lattices arising due to the topological protection of this spin state are a rather general phenomenon in cubic chiral magnets, providing, on the one hand, insights in fundamental aspects of this unconventional magnetic state and, on the other hand, progress towards novel applications.

5.3 Examples of Skyrmion Lattices Far from Equilibrium

In this section, four sets of studies are reviewed making use of metastable skyrmion lattices in chiral magnets, all prepared by means of field cooling through the reversible phase pocket.

5.3.1 *Unwinding Processes Studied by MFM and LTEM*

When skyrmion lattices transform into topologically trivial states, such as helical or conical order, complex unwinding mechanisms are involved. The first direct investigation of such processes in the cubic chiral magnets was carried out on the skyrmion lattice in $\text{Fe}_{1-x}\text{Co}_x\text{Si}$ ($x = 0.5$) under field cooling using magnetic force microscopy (MFM) on the surface of a bulk sample [20]. This study showed that for decreasing field skyrmions vanish by virtue of a coalescence, forming elongated structures reminiscent of the helical state. Combining the experimental observations with numerical simulations, this process was interpreted in terms of singular magnetic point defects, also referred to as Bloch points, zipping together neighboring skyrmion lines. Each defect provides a source or sink of exactly one emergent flux quantum and may hence be viewed as an emergent magnetic monopole. The investigation of metastable skyrmion lattice order offered two important experimental advantages. First, the magnetic contrast is enhanced due to the increase of the magnetic moment with decreasing temperatures. Second, experiments at low temperatures exclude the weakening of the topological stability due to thermal fluctuations locally suppressing the modulus of the local magnetization and, in turn, allow to reveal the generic mechanism of the topological unwinding.

Recently, Lorentz force transmission electron microscopy (LTEM) on a small bulk specimen of $\text{Fe}_{1-x}\text{Co}_x\text{Si}$ ($10 \times 10 \times 0.24 \mu\text{m}^3$, $x = 0.5$) [22] revealed that two rather different mechanisms occur under decreasing and increasing magnetic fields. For decreasing field, as schematically depicted in Fig. 5.3a, the well-established merging of neighboring skyrmion lines by means of a Bloch point moving towards the surface of the sample is observed. Shown in Fig. 5.3b–e are typical LTEM pictures and the time dependence of the contrast across the region marked by the white box, recorded as a function of time at fixed lateral position after field cooling the skyrmion lattice and subsequently reducing the magnetic field. Note, for instance, the two merging processes in the time dependence at $t \approx 4$ s and $t \approx 7$ s.

In contrast, as schematically depicted in Fig. 5.3f, for increasing field single skyrmion lines pinch off when the skyrmion lattice transforms into a field-polarized state. Here, lines split up by the formation of a pair of Bloch points, located at the end of the two resulting skyrmion strings, that subsequently travel towards the opposing surfaces of the sample. Corresponding LTEM data recorded after field cooling and subsequently increasing the magnetic field are presented in Fig. 5.3g–j. Note that due to a lack of in-plane modulation the conical and the field-polarized spin state are

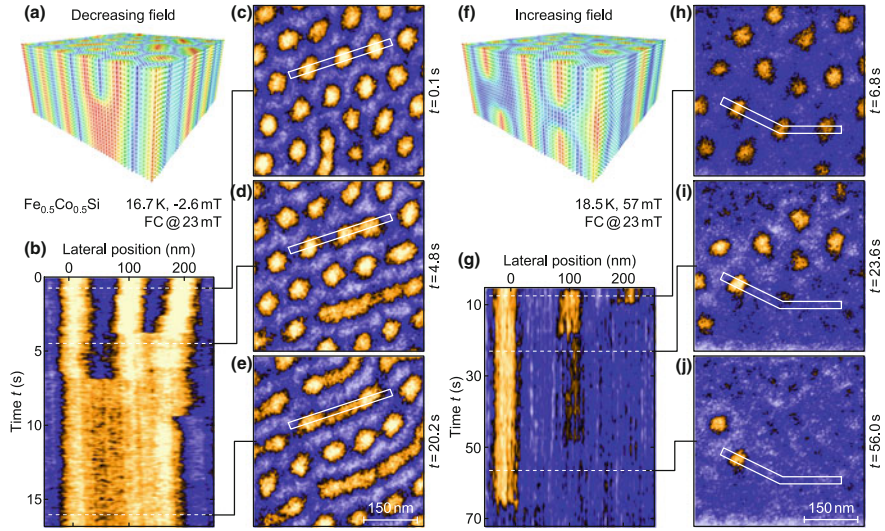


Fig. 5.3 Unwinding of the skyrmion lattice detected by means of Lorentz force transmission electron microscopy (LTEM) on $\text{Fe}_{1-x}\text{Co}_x\text{Si}$ ($x = 0.5$). **a** Schematic depiction of the merging of neighboring skyrmion lines for decreasing field. **b** Time evolution of the intensity across three skyrmions after field cooling the skyrmion lattice and subsequently decreasing the magnetic field to -2.6 mT. **c–e** Typical LTEM pictures at fixed times. The white box indicates the area for which the intensity is shown in panel (b). **f** Schematic depiction of the pinching off of single skyrmion lines for increasing field. **g** Temporal evolution of the intensity across three skyrmions after field cooling the skyrmion lattice and subsequently increasing the magnetic field to 57 mT. **h–j** Typical LTEM pictures at fixed times. The white box indicates the area for which the intensity is shown in panel (g) Data and illustrations taken from [22]

essentially indistinguishable in LTEM. As a function of time one skyrmion after the other vanishes. For instance, shown in Fig. 5.3g is the time dependence of the contrast across the white box marked in the LTEM pictures, the signature of the skyrmion on the right side suddenly disappears at $t \approx 10$ s.

For less than 10% of the decays an intermediate level of intensity is observed half-way during the decay. An example of such a two-step process is shown at a lateral position of about 100 nm with the intermediate intensity level persisting between $t \approx 20$ s and $t \approx 50$ s. This finding suggests that part of the skyrmion line survives with a length shorter than the thickness of the sample of 240 nm. Most likely, this metastable state is composed of a Bloch point trapped at a local defect and a skyrmion string that connects the Bloch point with either the surface or a second Bloch point inside the sample. An alternative scenario is provided by so-called chiral bobbers [105]. These objects are predicted to arise when the surface energy of the sample provides a repulsive potential for the Bloch point, hence slowing down the motion of the Bloch point just below the surface of the sample. Since the available data currently do not allow for a definite statement as to the possible existence of chiral bobbers, further studies will be required in the future.

Most notably, however, in [22] the metastability of the skyrmion lattice was used to tune the characteristic time scale of its decay into the time domain accessible by LTEM, in turn permitting to track the number of skyrmions as a function of time. It turned out that the time scale depends exponentially on temperature with the prefactor of this Arrhenius law being adjustable by more than 30 orders of magnitude by small changes of the magnetic field. The associated reduction of the lifetime of skyrmions with field corresponds to an extreme case of enthalpy–entropy compensation, drastically affecting topological unwinding processes and the topological protection of the skyrmions.

5.3.2 Topological Hall Effect in MnSi Under Pressure

As introduced in Sect. 5.2.1, a topological Hall effect was first identified in the reversible skyrmion lattice state of MnSi at ambient pressure, where an additional contribution of the order of $4 \text{ n}\Omega \text{ cm}$ was detected [69]. Assuming the absence of spin-flip scattering, the intrinsic size of the topological Hall contribution may be estimated by $\rho_{xy}^{\text{top}} = PR_0B_{\text{eff}}$. Here, P is the charge carrier spin polarization, the normal Hall constant R_0 captures non-spin-flip scattering, and the effective emergent magnetic field B_{eff} is given by the product of the emergent flux quantum that each skyrmion carries, h/e , and the skyrmion density. For MnSi, one obtains $B_{\text{eff}} = -13 \text{ T}$ implying contributions of the order of $50 \text{ n}\Omega \text{ cm}$ [106].

Finite-temperature effects such as spin-flip scattering result, however, in a considerably reduced topological Hall signal in the reversible skyrmion lattice phase pocket at elevated temperatures just below T_c . Therefore, in order to determine the intrinsic size of the topological Hall contribution, it proves instrumental to switch off these finite-temperature effects by generating a metastable skyrmion lattice state at low temperatures under field cooling. In MnSi, as a very clean system, however, no metastable skyrmion lattice state is observed when applying typical cooling rates of the order of K/min accessible with commercial cryostats. Remarkably, the characteristic time scales of the unwinding may be drastically increased when enhancing tiny inhomogeneities in the sample, as accomplished in an elegant way by the application of hydrostatic pressure by means of a clamp cell. In order to keep the inhomogeneities sufficiently small, the pressure medium typically consists of a liquid at ambient that gradually freezes with decreasing temperature, for instance mixtures of methanol and ethanol or fluorocarbons such as perfluorohexane and perfluoroheptane. Shown in Fig. 5.4a–c is the Hall resistivity of MnSi as a function of temperature for moderate hydrostatic pressures and applied fields for which the skyrmion lattice phase is crossed.

After zero-field cooling (ZFC), the Hall resistivity is dominated by a broad maximum around the helimagnetic transition temperature T_c . With increasing pressure, the transition temperature is suppressed while the characteristics of the curves remain unchanged. For low pressures, the topological Hall effect arising from the reversible skyrmion lattice phase pocket is visible as a weak shoulder on the low-temperature

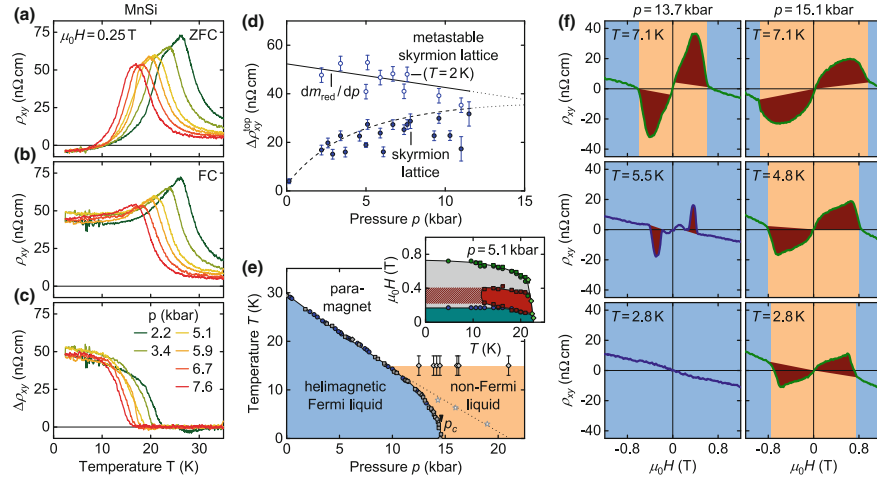


Fig. 5.4 Metastable skyrmi lattice and topological Hall effect in MnSi under pressure. **a, b** Temperature dependence of the Hall resistivity ρ_{xy} in an applied field crossing the skyrmi lattice state for different pressures after zero-field cooling (ZFC) and field cooling (FC), respectively. **c** Difference of the Hall resistivities after FC and ZFC attributed to the topological Hall effect. **d** Topological Hall contribution as determined in field sweeps in the reversible phase pocket (solid symbols) and after field cooling the skyrmi lattice (open symbols). **e** Pressure–temperature phase diagram in zero magnetic field. The helimagnetic regime exhibiting a Fermi-liquid resistivity (blue) and the extended regime of non-Fermi-liquid (orange) may be distinguished. Inset: Magnetic phase diagram at intermediate pressure [106]. **f** Typical field dependence of the Hall resistivity for different temperatures below (left column) and above (right column) the critical pressure p_c . Data taken from [106–108]

side of the broad maximum. Compared to zero-field cooling, after field cooling through the skyrmi lattice (FC) the Hall resistivity takes a distinctly higher and almost constant value at low temperatures. This discrepancy, illustrated in Fig. 5.4c, is attributed to the topological Hall contribution arising from the metastable skyrmi lattice as field-cooled to low temperatures.

As summarized in Fig. 5.4d, for the limit of ambient pressure, a contribution of about 50 nΩ cm is observed in the metastable skyrmi lattice at low temperatures (open symbols), in excellent agreement with the theoretical estimate. With increasing pressure the contribution decreases slightly (open symbols), tracking the evolution of the charge carrier spin polarization, which in turn follows the reduced magnetic moment $m_{\text{red}} = m(p)/m(p=0)$. With increasing pressure and hence decreasing transition temperature, the topological Hall contribution observed in the reversible phase pocket of skyrmi lattice order (solid symbols) approaches the low-temperature limit as finite-temperature effects are suppressed. The excellent agreement paved the way to a study quantitatively describing the anomalous and the topological Hall contributions in MnSi, $\text{Mn}_{1-x}\text{Fe}_x\text{Si}$, and $\text{Mn}_{1-x}\text{Co}_x\text{Si}$ in terms of reciprocal-space and real-space Berry phases, respectively [70].

As indicated in Fig. 5.4e, the magnetic phase diagram in MnSi remains qualitatively unchanged for intermediate pressures when the transition temperature is suppressed under the application of hydrostatic pressures. In addition, complex behavior emerges when static helimagnetic order is fully suppressed at $p_c = 14.6$ kbar [107, 109, 110]. The standard description of the metallic state, notably Fermi liquid (FL) theory, breaks down, giving rise to a so-called non-Fermi liquid (NFL) regime that extends over a remarkably large regime in pressure, temperature, and magnetic field [111, 112]. In this regime, the electrical resistivity exhibits an extended $T^{3/2}$ temperature dependence instead of the conventional T^2 dependence. In addition, so-called partial magnetic order in neutron scattering [113] and a lack of detectable spin relaxation in muon data [114] suggested the presence of dynamic spin correlations on a timescale between 10^{-10} s and 10^{-11} s. Tracking the topological Hall signal all the way between ambient pressures to above p_c , where it is observed across the entire parameter range of the NFL regime, cf. Fig. 5.4f, empirically established that spin correlations of non-trivial topological character drive the breakdown of Fermi liquid theory [108].

5.3.3 *Metastable Lattice in MnSi Under Rapid Cooling*

As mentioned above for MnSi, representing a pure material, typically no metastable skyrmion lattice state is observed under field cooling for the cooling rates accessible in standard commercial cryostats, i.e., at rates of several Kelvin per minute. To create a metastable state under these conditions two possibilities exist. First, the characteristic time scales of the skyrmion decay may be slowed down by introducing inhomogeneities, as discussed above. Second, the sample may be cooled at a very high rate using a bespoke experimental setup. The later approach, also referred to as violent quenching, was implemented by Oike and coworkers as follows [104]. A sample of MnSi with electrical contacts attached is cooled to low temperature, in this case 10 K, in a standard cryostat. By applying a short but intense current pulse, a current density of 3.1×10^6 A/m² for 100 ms, the sample is heated due to Joule heating, reaching a quasi-steady state several Kelvin above T_c . After the pulse ends, the sample is rapidly cooled by the thermal bath provided by the cryostat. Cooling rates up to 700 K/min are achieved when a rectangular current pulse shape is used, i.e., at a current ramp rate of $3.1 \cdot 10^8$ A/(m²s). Smaller cooling rates are realized by ramping down the current at slower rates. The electrical resistivity of the sample is used as an in-situ thermometer, similar to [83]. Note that the current densities used in these experiments are also sufficient to induce spin transfer torques in MnSi [79].

If the quench is carried out in an applied magnetic field for which the reversible pocket of the skyrmion lattice is crossed, the field and temperature history of the sample corresponds to the situation under field cooling in $\text{Fe}_{1-x}\text{Co}_x\text{Si}$. When the quench through the skyrmion lattice is followed by an increase or decrease of the field, the situation corresponds to the protocols FC^+ and FC^- , respectively. Shown in Fig. 5.5a is the magnetic phase diagram of MnSi under quenching, inferred from

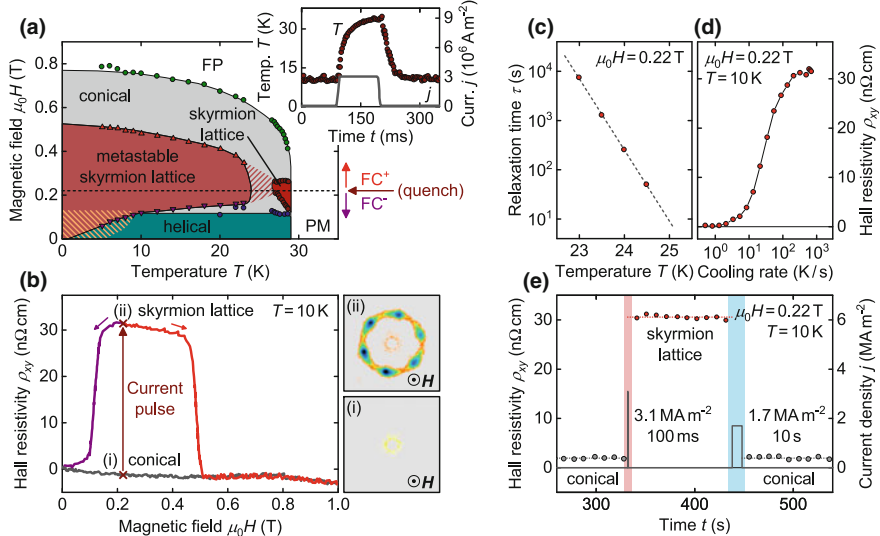


Fig. 5.5 Metastable skyrmion lattice in MnSi observed under rapid cooling (quenching). **a** Magnetic phase diagrams obtained after rapidly cooling through the reversible skyrmion lattice in an applied field of ~ 0.2 T and subsequently increasing or decreasing the magnetic field. Inset: Electrical current pulse used to achieve high cooling rates. **b** Hall resistivity at low temperatures as a function of field for the thermodynamic ground state (gray curve) and after the skyrmion lattice is metastably cooled down using a current pulse (purple and red curves). Insets (i) and (ii) show typical small-angle neutron scattering patterns. **c** Relaxation time associated with the decay of the skyrmion lattice as a function of temperature. **d** Dependence of the Hall resistivity on the cooling rate. Rates in excess of 100 K/s are necessary to observe the full value. **e** Hall resistivity at low temperatures and finite fields as a function of time when repeatedly switching between the conical state and the metastable skyrmion lattice state by means of appropriate current pulses. Data taken from [104, 115]

measurements of the electrical resistivity and Hall effect after FC^+ and FC^- . The inset shows a typical current pulse and the corresponding estimated sample temperature.

In general, the phase diagram of MnSi under quenching in field is highly reminiscent of that observed in $Fe_{1-x}Co_xSi$ under field cooling through the skyrmion lattice. The phase boundaries of the metastable (or quenched) skyrmion lattice state are thereby determined from measurements of the Hall effect as illustrated in Fig. 5.5b. If not field-cooled through the skyrmion lattice, i.e., under regular conditions, the Hall resistivity remains mostly featureless while the system undergoes transitions from the helical to the conical and finally into the field-polarized state as a function of increasing field. Using the conical state at 0.22 T as a starting point and applying a current pulse as described above, a drastic increase of the Hall resistivity is observed that is attributed to the topological Hall effect in the quenched skyrmion lattice state. When the magnetic field is subsequently increased (red curve) or decreased (purple curve), the Hall signal remains essentially constant until the change of the field finally triggers the unwinding of the skyrmion lattice state, cf. Sect. 5.3.1. Note that

the size of the signal is slightly smaller but consistent with the intrinsic topological Hall contribution discussed in the previous section.

The change of the magnetic state induced by the current pulse is also highlighted by typical small-angle neutron scattering patterns depicted in the insets (i) and (ii) [115]. For magnetic field parallel to the neutron beam, no intensity is observed prior to the application of the current pulse, consistent with the conical state. Following the current pulse, a sixfold scattering pattern appears, characteristic of the skyrmion lattice state.

Compared to the corresponding phase diagram of $\text{Fe}_{1-x}\text{Co}_x\text{Si}$ under FC^\pm , three minor differences may be noticed in MnSi. First, the metastable skyrmion lattice state covers a distinctly smaller portion of the magnetic phase diagram, for instance not reaching into the field-polarized regime at low temperatures and high field. Second, a gap is reported between the reversible and the metastable pocket of skyrmion lattice state (red hatching). Third, in a regime at low temperatures and fields (orange hatching) a structural transition of the skyrmion lattice was reported as observed in neutron scattering, cf. Sect. 5.3.4.

The putative gap just below the reversible phase pocket in MnSi originates in relatively fast characteristic time scales, i.e., at these temperatures the unwinding occurs on time scales that are fast compared to the time required to carry out the measurements. As shown in Fig. 5.5c, the relaxation time inferred from exponential fits to Hall resistivity data as a function of time becomes faster by several orders of magnitude with increasing temperature. Values of the order of seconds, readily accessible in the experiments from which the magnetic phase diagram are determined, are undercut at temperatures well below the reversible phase pocket. In turn, observing the full topological Hall signal at low temperatures, i.e., that a large volume fraction of the sample remains in the skyrmion lattice state, requires to pass the regime of fast unwinding at a sufficiently high rate. As shown in Fig. 5.5d, in the given sample of MnSi cooling rates in excess of several hundred Kelvin per second were necessary.

The high sensitivity of the characteristic time scales on the sample temperature permits to switch the magnetic state observed at low temperatures reproducibly by means of a carefully chosen combination of current pulses. Such a process is illustrated in Fig. 5.5e, using the (topological) Hall effect for discriminating between the metastable skyrmion lattice and the conical state. At low temperature and finite magnetic field, the sequence starts in the conical state as identified by a low Hall resistivity. A short and intense current pulse (red shading) heats the sample to temperatures well above T_c , followed by violent field cooling through the reversible pocket of skyrmion lattice state. As a result of this quench, a high Hall resistivity is observed, indicating the presence of the metastable skyrmion lattice state. Applying a longer but less intense current pulse (blue shading), heats the sample to temperatures just below the reversible phase pocket (red hatching in the phase diagram) thereby speeding up the characteristic time scale of the skyrmion decay. After the sample has cooled down, the system is again in the low-Hall-resistivity conical state. It was also demonstrated that this process may be carried out repeatedly, suggesting feasibility of data storage concepts that exploit metastable skyrmions, thermally assisted write mechanisms, and read-out via the topological Hall effect [116].

5.3.4 Structural Phase Transition in Metastable Lattices

The skyrmion lattices investigated in the reversible part of the phase diagram of cubic chiral magnets stabilize in a trigonal structure. In principle, further configurations may also be stabilized, such as square lattices, distorted lattices, or even glassy textures. As mentioned in the previous section, shown in Fig. 5.6a–c are small-angle neutron scattering data obtained in MnSi after violently quenching the skyrmion lattice to low temperatures [115]. Directly after quenching in an applied field of 0.2 T, the typical sixfold scattering pattern is observed in the plane perpendicular to the field, characteristic of the (metastable) trigonal skyrmion lattice state. When subsequently decreasing the magnetic field at low temperatures, the sixfold symmetry becomes less pronounced until a fourfold symmetric pattern with maxima along the $\langle 110 \rangle$ directions emerges. The regime for which such a fourfold pattern is observed coincides with a tail at the low-field end of the plateau associated with the topological Hall effect in the field dependence of the Hall resistivity after quenching, cf. below ~ 0.1 T in Fig. 5.5b. Note that intensity along the field direction after the quench indicates the presence of a coexisting conical state. With decreasing field, the latter transforms into a helical state characterized by intensity maxima along the $\langle 111 \rangle$ axes (not shown).

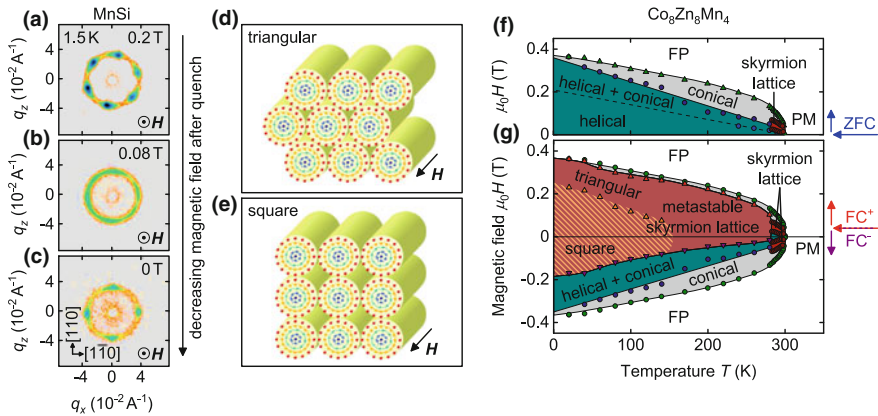


Fig. 5.6 Transition of the structure of the metastable skyrmion lattices in MnSi and $\text{Co}_8\text{Zn}_8\text{Mn}_4$. **a–c** Typical small-angle neutron scattering pattern for applied field along the neutron beam after quenching the skyrmion lattice. With decreasing field the sixfold pattern transforms into a fourfold pattern. **d, e** Schematic depiction of skyrmion lattices with trigonal and square arrangement, respectively. **f** Magnetic phase diagram of $\text{Co}_8\text{Zn}_8\text{Mn}_4$ following a field cooling from the reversible pocket of skyrmion lattice state. **g** Magnetic phase diagram of $\text{Co}_8\text{Zn}_8\text{Mn}_4$ after zero-field cooling. Data and illustrations taken from [102, 115]

Similar behavior was also reported in $\text{Co}_8\text{Zn}_8\text{Mn}_4$. The $\text{Co}_x\text{Zn}_y\text{Mn}_z$ series were the first materials not crystallizing in space group $P2_13$ in which the well-known chiral skyrmion lattice state was observed [51]. Instead, these compounds are based on $\text{Co}_{10}\text{Zn}_{10}$, belong to the space group $P4_132$ or $P4_332$, and offer transition temperatures exceeding room temperature. Akin to $\text{Fe}_{1-x}\text{Co}_x\text{Si}$, members of the $\text{Co}_x\text{Zn}_y\text{Mn}_z$ series appear to be notoriously prone to structural disorder and, as a result, exhibit a metastable skyrmion lattice state already at moderate cooling rates [102, 103]. The corresponding phase diagrams are shown in Fig. 5.6f, g. After zero-field cooling, the situation is highly reminiscent of other cubic chiral magnets. A pronounced regime of phase coexistence between the helical and conical state hints at the importance of disorder in this system. After cooling through the reversible pocket of skyrmion lattice order, a metastable skyrmion lattice is observed across large parts of the magnetic phase diagram. In contrast to $\text{Fe}_{1-x}\text{Co}_x\text{Si}$, however, from small-angle neutron scattering data a structural transition within the metastable skyrmion lattice state was reported [102]. Here, at low temperatures and low fields (orange hatching) a fourfold scattering pattern with maxima along the $\langle 100 \rangle$ directions was interpreted as evidence of a square arrangement of skyrmions. Note, however, that the $\langle 100 \rangle$ axes are also the easy axes for the helical pitch. Thus, intensity maxima arising from helical and square lattice skyrmion order may be superimposed and hard to distinguish.

Regardless of any ambiguities, these results suggest that topologically non-trivial spin textures may form in configurations other than the well-established trigonal skyrmion lattice, even in the cubic chiral magnets. For instance non-trigonal lattice morphologies or glassy states may be stable, metastable, or fluctuating spin configurations, leading to yet unexpected physical properties and novel possibilities of manipulating magnetic states. Further, note that also in the helical state of the cubic chiral magnets topologically non-trivial defects may emerge, in particular at the boundary to the conical state, providing another rich playground for both fundamental and application-oriented research [117–119].

5.4 Conclusion and Outlook

In summary, a review of the properties of metastable skyrmion lattice states in cubic chiral magnets as observed under field-cooling through the reversible phase pocket at high temperatures has been presented. Although not being the thermodynamic ground state at the given temperature and field value, metastable skyrmions display a remarkable robustness due to their topological properties. As a consequence, these metastable states do not only allow to study fundamental aspects associated with the creation and destruction of skyrmions or their interplay with electrons. They promise also novel concepts for spintronic devices that exploit topologically protected metastable states rather than requiring their formation as a spontaneous ground state.

We are deeply indebted to our co-workers, in particular: T. Adams, W. Anwand, C. H. Back, R. Bamler, G. Benka, H. Berger, S. Blügel, S. J. Blundell, P. Böni,

G. Brandl, S. Buhrandt, D. M. Burn, M. Butterling, A. Chacon, C. Duvinage, H.-M. Eiter, L. M. Eng, K. Everschor, A. I. Figueroa, C. Franz, F. Freimuth, M. Gangl, M. Garst, R. Georgii, T. Gigl, D. Grundler, R. Hackl, M. Halder, F. Haslbeck, W. Häußler, L. Heinen, T. Hesjedal, J. P. Hinton, C. Hugenschmidt, M. Janoschek, F. Jarzembeck, P. Jaschke, F. Jonietz, U. Keiderling, J. Kindervater, D. Köhler, J. D. Koralek, P. Krautscheid, M. Kronseder, P. Kudejova, M. Kugler, A. Kusmartseva, G. van der Laan, T. Lancaster, M. Leitner, P. Lemmens, S. Maendl, N. Martin, S. Mayr, D. Meier, T. N. G. Meier, M. Meven, P. Milde, Y. Mokrousov, S. Mühlbauer, E. Neuber, J. Orenstein, S. A. Parameswaran, B. Pedersen, F. L. Pratt, T. Prokscha, S. Pöllath, R. Ramesh, T. Reimann, M. Reiner, R. Ritz, A. Rosch, A. Rosenauer, F. Rucker, Z. Salman, S. Säubert, C. Schnarr, R. W. Schoenlein, M. Schowalter, T. Schröder, S. Schulte, T. Schulz, C. Schütte, T. Schwarze, K. Seemann, J. Seidel, A. Senyshyn, I. Stasinopoulos, A. Suter, L. Tutsch, A. Vishwanath, A. Wagner, M. Wagner, J. Waizner, T. Weber, S. Weichselbäumer, B. Wiedemann, J. Wild, F. Xiao, S. L. Zhang, J. Zweck, and the team of FRM II. Financial support through DFG FOR960, DFG TRR80, and ERC AdG 291079 (TOPFIT) is gratefully acknowledged.

References

1. T.H.R. Skyrme, A non-linear field theory. *Proc. R. Soc. Lond. A* **260**, 127 (1961). <https://doi.org/10.1098/rspa.1961.0018>
2. T.H.R. Skyrme, A unified field theory of mesons and baryons. *Nucl. Phys.* **31**, 556 (1962). [https://doi.org/10.1016/0029-5582\(62\)90775-7](https://doi.org/10.1016/0029-5582(62)90775-7)
3. G.S. Adkins, C.R. Nappi, E. Witten, Static properties of nucleons in the Skyrme model. *Nucl. Phys. B* **228**, 552 (1983). [https://doi.org/10.1016/0550-3213\(83\)90559-X](https://doi.org/10.1016/0550-3213(83)90559-X)
4. S.L. Sondhi, A. Karlhede, S.A. Kivelson, E.H. Rezayi, Skyrmions and the crossover from the integer to fractional quantum Hall effect at small Zeeman energies. *Phys. Rev. B* **47**, 16419 (1993). <https://doi.org/10.1103/PhysRevB.47.16419>
5. T.-L. Ho, Spinor Bose condensates in optical traps. *Phys. Rev. Lett.* **81**, 742 (1998). <https://doi.org/10.1103/PhysRevLett.81.742>
6. U.A. Khawaja, H. Stoof, Skyrmions in a ferromagnetic Bose–Einstein condensate. *Nature* **411**, 918 (2001). <https://doi.org/10.1038/35082010>
7. J. Fukuda, S. Žumer, Quasi-two-dimensional Skyrmion lattices in a chiral nematic liquid crystal. *Nat. Commun.* **2**, 246 (2011). <https://doi.org/10.1038/ncomms1250>
8. S. Mühlbauer, B. Binz, F. Jonietz, C. Pfleiderer, A. Rosch, A. Neubauer, R. Georgii, P. Böni, Skyrmion lattice in a chiral magnet. *Science* **323**, 915 (2009). <https://doi.org/10.1126/science.1166767>
9. X.Z. Yu, Y. Onose, N. Kanazawa, J.H. Park, J.H. Han, Y. Matsui, N. Nagaosa, Y. Tokura, Real-space observation of a two-dimensional skyrmion crystal. *Nature* **465**, 901 (2010). <https://doi.org/10.1038/nature09124>
10. S. Heinze, K.V. Bergmann, M. Menzel, J. Brede, A. Kubetzka, R. Wiesendanger, G. Bihlmayer, S. Blügel, Spontaneous atomic-scale magnetic skyrmion lattice in two dimensions. *Nat. Phys.* **7**, 713 (2011). <https://doi.org/10.1038/nphys2045>
11. M. Finazzi, M. Savoini, A.R. Khorsand, A. Tsukamoto, A. Itoh, L. Duò, A. Kirilyuk, T. Rasing, M. Ezawa, Laser-induced magnetic nanostructures with tunable topological properties. *Phys. Rev. Lett.* **110**, 177205 (2013). <https://doi.org/10.1103/PhysRevLett.110.177205>

12. N. Romming, C. Hanneken, M. Menzel, J.E. Bickel, B. Wolter, K.V. Bergmann, A. Kubetzka, R. Wiesendanger, Writing and deleting single magnetic skyrmions. *Science* **341**, 636 (2013). <https://doi.org/10.1126/science.1240573>
13. J. Sampaio, V. Cros, S. Rohart, A. Thiaville, A. Fert, Nucleation, stability and current-induced motion of isolated magnetic skyrmions in nanostructures. *Nat. Nano.* **8**, 839 (2013). <https://doi.org/10.1038/nnano.2013.210>
14. F. Büttner, C. Moutafis, M. Schneider, B. Krüger, C.M. Günther, J. Geilhufe, C.V. Korff Schmising, J. Mohanty, B. Pfau, S. Schaffert, A. Bisig, M. Foerster, T. Schulz, C.A.F. Vaz, J.H. Franken, H.J.M. Swagten, M. Kläui, S. Eisebitt, Dynamics and inertia of skyrmionic spin structures. *Nat. Phys.* **11**, 225 (2015). <https://doi.org/10.1038/nphys3234>
15. W. Jiang, P. Upadhyaya, W. Zhang, G. Yu, M.B. Jungfleisch, F.Y. Fradin, J.E. Pearson, Y. Tserkovnyak, K.L. Wang, O. Heinonen, S.G.E. te Velthuis, A. Hoffmann, Blowing magnetic skyrmion bubbles. *Science* **349**, 283 (2015). <https://doi.org/10.1126/science.aaa1442>
16. I. Kézsmárki, S. Bordács, P. Milde, E. Neuber, L.M. Eng, J.S. White, H.M. Rønnow, C.D. Dewhurst, M. Mochizuki, K. Yanai, H. Nakamura, D. Ehlers, V. Tsurkan, A. Loidl, Néel-type skyrmion lattice with confined orientation in the polar magnetic semiconductor GaV₄S₈. *Nat. Mater.* **14**, 1116 (2015). <https://doi.org/10.1038/nmat4402>
17. Y. Zhou, E. Iacocca, A.A. Awad, R.K. Dumas, F.C. Zhang, H.B. Braun, J. Åkerman, Dynamically stabilized magnetic skyrmions. *Nat. Commun.* **6**, 8193 (2015). <https://doi.org/10.1038/ncomms9193>
18. O. Boulle, J. Vogel, H. Yang, S. Pizzini, D. de Souza Chaves, A. Locatelli, T.O. Menteş, L.D. B.-P. A. Sala, O. Klein, M. Belmeguenai, Y. Roussign, A. Stashkevich, S.M. Chérif, L. Aballe, M. Foerster, M. Chshiev, S. Auffret, I.M. Miron, G. Gaudin, Room-temperature chiral magnetic skyrmions in ultrathin magnetic nanostructures. *Nat. Nano.* **11**, 449 (2016). <https://doi.org/10.1038/nnano.2015.315>
19. C. Moreau-Luchaire, C. Moutas, N. Reyren, J. Sampaio, C.A.F. Vaz, N.V. Horne, K. Bouzehouane, K. Garcia, C. Deranlot, P. Wohlhüter, J.-M. George, M. Weigand, J. Raabe, V. Cros, A. Fert, Additive interfacial chiral interaction in multilayers for stabilization of small individual skyrmions at room temperature. *Nat. Nano.* **11**, 444 (2016). <https://doi.org/10.1038/nnano.2015.313>
20. P. Milde, D. Köhler, J. Seidel, L.M. Eng, A. Bauer, A. Chacon, J. Kindervater, S. Mühlbauer, C. Pfleiderer, S. Buhrandt, C. Schütte, A. Rosch, Unwinding of a skyrmion lattice by magnetic monopoles. *Science* **340**, 1076 (2013). <https://doi.org/10.1126/science.1234657>
21. J. Li, A. Tan, K.W. Moon, A. Doran, M.A. Marcus, A.T. Young, E. Arenholz, S. Ma, R.F. Yang, C. Hwang, Z.Q. Qiu, Tailoring the topology of an artificial magnetic skyrmion. *Nat. Commun.* **5**, 4704 (2014). <https://doi.org/10.1038/ncomms5704>
22. J. Wild, T.N.G. Meier, S. Pöllath, M. Kronseder, A. Bauer, A. Chacon, M. Halder, M. Schowalter, A. Rosenauer, J. Zweck, J. Müller, A. Rosch, C. Pfleiderer, C. H. Back, Entropy-limited topological protection of skyrmions. *Sci. Adv.* **3**, e1701704 (2017). <https://doi.org/10.1126/sciadv.1701704>
23. A. Fert, V. Cros, J. Sampaio, Skyrmions on the track. *Nat. Nano.* **8**, 152 (2013). <https://doi.org/10.1038/nnano.2013.29>
24. J. Iwasaki, M. Mochizuki, N. Nagaosa, Current-induced skyrmion dynamics in constricted geometries. *Nat. Nano.* **8**, 742 (2013). <https://doi.org/10.1038/nnano.2013.176>
25. N. Nagaosa, Y. Tokura, Topological properties and dynamics of magnetic skyrmions. *Nat. Nano.* **8**, 899 (2013). <https://doi.org/10.1038/nnano.2013.243>
26. Y. Okamura, F. Kagawa, M. Mochizuki, M. Kubota, S. Seki, S. Ishiwata, M. Kawasaki, Y. Onose, Y. Tokura, Microwave magnetoelectric effect via skyrmion resonance modes in a helimagnetic multiferroic. *Nat. Commun.* **4**, 2391 (2013). <https://doi.org/10.1038/ncomms3391>
27. L. Sun, R.X. Cao, B.F. Miao, Z. Feng, B. You, D. Wu, W. Zhang, A. Hu, H.F. Ding, Creating an artificial two-dimensional skyrmion crystal by nanopatterning. *Phys. Rev. Lett.* **110**, 167201 (2013). <https://doi.org/10.1103/PhysRevLett.110.167201>
28. X. Yu, J.P. DeGrave, Y. Hara, T. Hara, S. Jin, Y. Tokura, Observation of the magnetic skyrmion lattice in a MnSi nanowire by Lorentz TEM. *Nano Lett.* **13**, 3755 (2013). <https://doi.org/10.1021/nl401687d>

29. J. Hagemeyer, N. Romming, K. von Bergmann, E.Y. Vedmedenko, R. Wiesendanger, Tailoring the topology of an artificial magnetic skyrmion. *Nat. Commun.* **6**, 8455 (2015). <https://doi.org/10.1038/ncomms9455>
30. S.-Z. Lin, C.D. Batista, C. Reichhardt, A. Saxena, AC current generation in chiral magnetic insulators and skyrmion motion induced by the spin seebeck effect. *Phys. Rev. Lett.* **112**, 187203 (2014). <https://doi.org/10.1103/PhysRevLett.112.187203>
31. X Zhang, G.P. Zhao, H. Fangohr, J.P. Liu, W.X. Xia, J. Xia, F.J. Morvan, Skyrmion-skyrmion and skyrmion-edge repulsions in skyrmion-based racetrack memory. *Sci. Rep.* **5**, 7643 (2015). <https://doi.org/10.1038/srep07643>
32. P.-J. Hsu, A. Kubetzka, A. Finco, N. Romming, K. von Bergmann, R. Wiesendanger, Electric-field-driven switching of individual magnetic skyrmions. *Nat. Nano.* **12**, 123 (2016). <https://doi.org/10.1038/nnano.2016.234>
33. W. Jiang, X. Zhang, G. Yu, W. Zhang, X. Wang, M.B. Jungfleisch, J.E. Pearson, X. Cheng, O. Heinonen, K.L. Wang, Y. Zhou, A. Hoffmann, S.G.E. te Velthuis, Direct observation of the skyrmion Hall effect. *Nat. Phys.* **13**, 162 (2016). <https://doi.org/10.1038/nphys3883>
34. R. Wiesendanger, Nanoscale magnetic skyrmions in metallic films and multilayers: a new twist for spintronics. *Nat. Rev. Mater.* **1**, 16044 (2016). <https://doi.org/10.1038/natrevmats.2016.44>
35. S. Woo, K. Litzius, B. Krüger, M.-Y. Im, L. Caretta, K. Richter, M. Mann, A. Krone, R.M. Reeve, M. Weigand, P. Agrawal, I. Lemesh, M.-A. Mawass, P. Fischer, M. Kläui, and G.S.D. Beach, Observation of room-temperature magnetic skyrmions and their current-driven dynamics in ultrathin metallic ferromagnets. *Nat. Mater.* **15**, 501 (2016). <https://doi.org/10.1038/nmat4593>
36. J. Müller, Magnetic skyrmions on a two-lane racetrack. *New J. Phys.* **19**, 025002 (2017). <https://doi.org/10.1088/1367-2630/aa5b55>
37. P. Huang, M. Cantoni, A. Kruchkov, R. Jayaraman, A. Magrez, F. Carbone, H.M. Rønnow, In situ electric field skyrmion creation in magnetoelectric Cu₂OSeO₃ (2017). [arXiv:1710.09200](https://arxiv.org/abs/1710.09200)
38. T. Adams, S. Mühlbauer, C. Pfleiderer, F. Jonietz, A. Bauer, A. Neubauer, R. Georgii, P. Böni, U. Keiderling, K. Everschor, M. Garst, A. Rosch, Long-range crystalline nature of the skyrmion lattice in MnSi. *Phys. Rev. Lett.* **107**, 217206 (2011). <https://doi.org/10.1103/PhysRevLett.107.217206>
39. S.L. Zhang, A. Bauer, D.M. Burn, P. Milde, E. Neuber, L.M. Eng, H. Berger, C. Pfleiderer, G. van der Laan, T. Hesjedal, Multidomain skyrmion lattice state in Cu₂OSeO₃. *Nano Lett.* **16**, 3285 (2016). <https://doi.org/10.1021/acs.nanolett.6b00845>
40. P. Milde, E. Neuber, A. Bauer, C. Pfleiderer, H. Berger, L.M. Eng, Heuristic description of magnetoelectricity of Cu₂OSeO₃. *Nano Lett.* **16**, 5612 (2016). <https://doi.org/10.1021/acs.nanolett.6b02167>
41. A. Bauer, C. Pfleiderer, Generic aspects of skyrmion lattices in chiral magnets, in *Topological Structures in Ferroic Materials: Domain Walls, Vortices and Skyrmions* (Springer International Publishing, 2016) p. 1. https://doi.org/10.1007/978-3-319-25301-5_1
42. A.N. Bogdanov, D.A. Yablonskii, Thermodynamically stable "vortices" in magnetically ordered crystals. The mixed state of magnets. *Sov. Phys. JETP* **95**, 178 (1989), http://jetp.ac.ru/cgi-bin/dn/e_068_01_0101.pdf
43. A. Bogdanov, A. Hubert, Thermodynamically stable magnetic vortex states in magnetic crystals, *J. Magn. Magn. Mater.* **138**, 255 (1994). [https://doi.org/10.1016/0304-8853\(94\)90046-9](https://doi.org/10.1016/0304-8853(94)90046-9)
44. A. Chacon, A. Bauer, T. Adams, F. Rucker, G. Brandl, R. Georgii, M. Garst, C. Pfleiderer, Uniaxial pressure dependence of magnetic order in MnSi. *Phys. Rev. Lett.* **115**, 267202 (2015). <https://doi.org/10.1103/PhysRevLett.115.267202>
45. Y. Nii, T. Nakajima, A. Kikkawa, Y. Yamasaki, K. Ohishi, J. Suzuki, Y. Taguchi, T. Arima, Y. Tokura, Y. Iwasa, Uniaxial stress control of skyrmion phase. *Nat. Commun.* **6**, 8539 (2015). <https://doi.org/10.1038/ncomms9539>
46. W. Münzer, A. Neubauer, T. Adams, S. Mühlbauer, C. Franz, F. Jonietz, R. Georgii, P. Böni, B. Pedersen, M. Schmidt, A. Rosch, C. Pfleiderer, Skyrmion lattice in the doped semiconductor

Fe_{1-x}Co_xSi. Phys. Rev. B **81**, 041203 (R) (2010). <https://doi.org/10.1103/PhysRevB.81.041203>

47. C. Pfleiderer, T. Adams, A. Bauer, W. Biberacher, B. Binz, F. Birkelbach, P. Böni, C. Franz, R. Georgii, M. Janoschek, F. Jonietz, T. Keller, R. Ritz, S. Mühlbauer, W. Münzer, A. Neubauer, B. Pedersen, A. Rosch, Skyrmion lattices in metallic and semiconducting B20 transition metal compounds. J. Phys.: Condens. Matter **22**, 164207 (2010). <https://doi.org/10.1088/0953-8984/22/16/164207>

48. T. Adams, A. Chacon, M. Wagner, A. Bauer, G. Brandl, B. Pedersen, H. Berger, P. Lemmens, C. Pfleiderer, Long-wavelength helimagnetic order and skyrmion lattice phase in Cu₂OSeO₃. Phys. Rev. Lett. **108**, 237204 (2012). <https://doi.org/10.1103/PhysRevLett.108.237204>

49. S. Seki, J.-H. Kim, D.S. Inosov, R. Georgii, B. Keimer, S. Ishiwata, Y. Tokura, Formation and rotation of skyrmion crystal in the chiral-lattice insulator Cu₂OSeO₃. Phys. Rev. B **85**, 220406 (R) (2012). <https://doi.org/10.1103/PhysRevB.85.220406>

50. E. Moskvin, S. Grigoriev, V. Dyadkin, H. Eckerlebe, M. Baenitz, M. Schmidt, H. Wilhelm, Complex chiral modulations in FeGe close to magnetic ordering. Phys. Rev. Lett. **110**, 077207 (2013). <https://doi.org/10.1103/PhysRevLett.110.077207>

51. Y. Tokunaga, X.Z. Yu, J.S. White, H.M. Rønnow, D. Morikawa, Y. Taguchi, Y. Tokura, A new class of chiral materials hosting magnetic skyrmions beyond room temperature. Nat. Commun. **6**, 7638 (2015). <https://doi.org/10.1038/ncomms8638>

52. M.C. Langner, S. Roy, S.K. Mishra, J.C.T. Lee, X.W. Shi, M.A. Hossain, Y.-D. Chuang, S. Seki, Y. Tokura, S.D. Kevan, R.W. Schoenlein, Coupled skyrmion sublattices in Cu₂OSeO₃. Phys. Rev. Lett. **112**, 167202 (2014). <https://doi.org/10.1103/PhysRevLett.112.167202>

53. S.L. Zhang, A. Bauer, H. Berger, C. Pfleiderer, G. van der Laan, T. Hesjedal, Multidomain skyrmion lattice state in Cu₂OSeO₃. Appl. Phys. Lett. **109**, 192406 (2016). <https://doi.org/10.1063/1.4967499>

54. X.Z. Yu, N. Kanazawa, Y. Onose, K. Kimoto, W.Z. Zhang, S. Ishiwata, Y. Matsui, Y. Tokura, Near room-temperature formation of a skyrmion crystal in thin-films of the helimagnet FeGe. Nat. Mater. **10**, 106 (2011). <https://doi.org/10.1038/nmat2916>

55. S. Seki, X.Z. Yu, S. Ishiwata, Y. Tokura, Observation of skyrmions in a multiferroic material. Science **336**, 198 (2012). <https://doi.org/10.1126/science.1214143>

56. J. Rajeswari, P. Huang, G.F. Mancini, Y. Murooka, T. Latychevskaia, D. McGrouther, M. Cantoni, E. Baldini, J.S. White, A. Magrez, T. Giamarchi, H.M. Rønnow, F. Carbone, Filming the formation and fluctuation of skyrmion domains by cryo-Lorentz transmission electron microscopy. Proc. Natl. Acad. Sci. USA **112**, 14212 (2015). <https://doi.org/10.1073/pnas.1513343112>

57. S. Pöllath, J. Wild, L. Heinen, T.N.G. Meier, M. Kronseder, L. Tutsch, A. Bauer, H. Berger, C. Pfleiderer, J Zweck, A. Rosch, C.H. Back, Dynamical defects in rotating magnetic skyrmion lattices. Phys. Rev. Lett. **118**, 207205 (2017). <https://doi.org/10.1103/PhysRevLett.118.207205>

58. H.S. Park, X. Yu, S. Aizawa, T. Tanigaki, T. Akashi, Y. Takahashi, T. Matsuda, N. Kanazawa, Y. Onose, D. Shindo, A. Tonomura, Y. Tokura, Observation of the magnetic flux and three-dimensional structure of skyrmion lattices by electron holography. Nat. Nano. **9**, 337 (2014). <https://doi.org/10.1038/nnano.2014.52>

59. M. Mochizuki, Spin-wave modes and their intense excitation effects in skyrmion crystals. Phys. Rev. Lett. **108**, 017601 (2012). <https://doi.org/10.1103/PhysRevLett.108.017601>

60. Y. Onose, Y. Okamura, S. Seki, S. Ishiwata, Y. Tokura, Observation of magnetic excitations of skyrmion crystal in a helimagnetic insulator Cu₂OSeO₃. Phys. Rev. Lett. **109**, 037603 (2012). <https://doi.org/10.1103/PhysRevLett.109.037603>

61. T. Schwarze, J. Waizner, M. Garst, A. Bauer, I. Stasinopoulos, H. Berger, A. Rosch, C. Pfleiderer, D. Grundler, Universal helimagnon and skyrmion excitations in metallic, semiconducting and insulating chiral magnets. Nat. Mater. **14**, 478 (2015). <https://doi.org/10.1038/nmat4223>

62. I. Stasinopoulos, S. Weichselbaumer, A. Bauer, J. Waizner, H. Berger, M. Garst, C. Pfleiderer, D. Grundler, Linearly polarized GHz magnetization dynamics of spin helix modes in the

ferrimagnetic insulator Cu₂OSeO₃. *Sci. Rep.* **7**, 7037 (2017). <https://doi.org/10.1038/s41598-017-07020-2>

- 63. N. Kanazawa, Y. Onose, T. Arima, D. Okuyama, K. Ohoyama, S. Wakimoto, K. Kakurai, S. Ishiwata, Y. Tokura, Large topological Hall effect in a short-period helimagnet MnGe. *Phys. Rev. Lett.* **106**, 156603 (2011). <https://doi.org/10.1103/PhysRevLett.106.156603>
- 64. Y. Shioi, N. Kanazawa, K. Shibata, Y. Onose, Y. Tokura, Topological Nernst effect in a three-dimensional skyrmion-lattice phase. *Phys. Rev. B* **88**, 064409 (2013). <https://doi.org/10.1103/PhysRevB.88.064409>
- 65. T. Tanigaki, K. Shibata, N. Kanazawa, X.Z. Yu, S. Aizawa, Y. Onose, H.S. Park, D. Shindo, Y. Tokura, Real-space observation of short-period cubic lattice of skyrmions in MnGe. *Nano Lett.* **15**, 5438 (2015). <https://doi.org/10.1021/acs.nanolett.5b02653>
- 66. N. Kanazawa, Y. Nii, X.-X. Zhang, A.S. Mishchenko, G.D. Filippis, F. Kagawa, Y. Iwasa, N. Nagaosa, and Y. Tokura, Critical phenomena of emergent magnetic monopoles in a chiral magnet. *Nat. Commun.* **7**, 11622 (2016). <https://doi.org/10.1038/ncomms11622>
- 67. E. Ruff, S. Widmann, P. Lunkenheimer, V. Tsurkan, S. Bordács, I. Kézsmárki, A. Loidl, Multiferroicity and skyrmions carrying electric polarization in GaV₄S₈. *Sci. Adv.* **1**, e1500916 (2015). <https://doi.org/10.1126/sciadv.1500916>
- 68. T. Kurumaji, T. Nakajima, V. Ukleev, A. Feoktystov, T. h. Arima, K. Kakurai, Y. Tokura, Néel-type skyrmion lattice in tetragonal polar magnet VOSe₂O₅. *Phys. Rev. Lett.* **119**, 237201 (2017)
- 69. A. Neubauer, C. Pfleiderer, B. Binz, A. Rosch, R. Ritz, P.G. Niklowitz, P. Böni, Topological Hall effect in the A phase of MnSi. *Phys. Rev. Lett.* **102**, 186602 (2009). <https://doi.org/10.1103/PhysRevLett.102.186602>
- 70. C. Franz, F. Freimuth, A. Bauer, R. Ritz, C. Schnarr, C. Duvinage, T. Adams, S. Blügel, A. Rosch, Y. Mokrousov, C. Pfleiderer, Real-space and reciprocal-space Berry phases in the Hall effect of Mn_{1-x}Fe_xSi. *Phys. Rev. Lett.* **112**, 186601 (2014). <https://doi.org/10.1103/PhysRevLett.112.186601>
- 71. N. Nagaosa, J. Sinova, S. Onoda, A.H. MacDonald, N.P. Ong, Anomalous Hall effect. *Rev. Mod. Phys.* **82**, 1539 (2010). <https://doi.org/10.1103/RevModPhys.82.1539>
- 72. J.C. Slonczewski, Current-driven excitation of magnetic multilayers. *J. Magn. Magn. Mater.* **159**, L1 (1996). [https://doi.org/10.1016/0304-8853\(96\)00062-5](https://doi.org/10.1016/0304-8853(96)00062-5)
- 73. L. Berger, Emission of spin waves by a magnetic multilayer traversed by a current. *Phys. Rev. B* **54**, 9353 (1996). <https://doi.org/10.1103/PhysRevB.54.9353>
- 74. M. Tsoi, A.G.M. Jansen, J. Bass, W.-C. Chiang, M. Seck, V. Tsoi, P. Wyder, Excitation of a magnetic multilayer by an electric current. *Phys. Rev. Lett.* **80**, 4281 (1998). <https://doi.org/10.1103/PhysRevLett.80.4281>
- 75. E.B. Myers, D.C. Ralph, J.A. Katine, R.N. Louie, R.A. Buhrman, Current-induced switching of domains in magnetic multilayer devices. *Science* **285**, 867 (1999). <https://doi.org/10.1126/science.285.5429.867>
- 76. J. Grollier, P. Boulenc, V. Cros, A. Hamzić, A. Vaurès, A. Fert, G. Faini, Switching a spin valve back and forth by current-induced domain wall motion. *Appl. Phys. Lett.* **83**, 509 (2003). <https://doi.org/10.1063/1.1594841>
- 77. S.S.P. Parkin, M. Hayashi, L. Thomas, Magnetic domain-wall racetrack memory. *Science* **320**, 190 (2008). <https://doi.org/10.1126/science.1145799>
- 78. S.S.P. Parkin, S.-H. Yang, Memory on the racetrack. *Nat. Nano.* **10**, 221 (2015). <https://doi.org/10.1038/nnano.2015.41>
- 79. F. Jonietz, S. Mühlbauer, C. Pfleiderer, A. Neubauer, W. Münzer, A. Bauer, T. Adams, R. Georgii, P. Böni, R.A. Duine, K. Everschor, M. Garst, A. Rosch, Spin transfer torques in MnSi at ultralow current densities. *Science* **330**, 1648 (2010). <https://doi.org/10.1126/science.1195709>
- 80. K. Everschor, M. Garst, R.A. Duine, A. Rosch, Current-induced rotational torques in the skyrmion lattice phase of chiral magnets. *Phys. Rev. B* **84**, 064401 (2011). <https://doi.org/10.1103/PhysRevB.84.064401>

81. X.Z. Yu, N. Kanazawa, W.Z. Zhang, T. Nagai, T. Hara, K. Kimoto, Y. Matsui, Y. Onose, Y. Tokura, Skyrmion flow near room temperature in an ultralow current density. *Nat. Commun.* **3**, 988 (2012). <https://doi.org/10.1038/ncomms1990>
82. J. Iwasaki, M. Mochizuki, N. Nagaosa, Universal current-velocity relation of skyrmion motion in chiral magnets. *Nat. Commun.* **4**, 1463 (2013). <https://doi.org/10.1038/ncomms2442>
83. T. Schulz, R. Ritz, A. Bauer, M. Halder, M. Wagner, C. Franz, C. Pfleiderer, K. Everschor, M. Garst, A. Rosch, Emergent electrodynamics of skyrmions in a chiral magnet. *Nat. Phys.* **8**, 301 (2012). <https://doi.org/10.1038/nphys2231>
84. M. Mochizuki, X.Z. Yu, S. Seki, N. Kanazawa, W. Koshiba, J. Zang, M. Mostovoy, Y. Tokura, N. Nagaosa, Thermally driven ratchet motion of a skyrmion microcrystal and topological magnon Hall effect. *Nat. Mater.* **13**, 241 (2014). <https://doi.org/10.1038/nmat3862>
85. S. Seki, S. Ishiwata, Y. Tokura, Magnetoelectric nature of skyrmions in a chiral magnetic insulator Cu_2OSeO_3 . *Phys. Rev. B* **86**, 060403 (2012). <https://doi.org/10.1103/PhysRevB.86.060403>
86. J.S. White, K. Prša, P. Huang, A.A. Omrani, I. Živković, M. Bartkowiak, H. Berger, A. Magrez, J.L. Gavilano, G. Nagy, J. Zang, H.M. Rønnow, Electric-field-induced skyrmion distortion and giant lattice rotation in the magnetoelectric insulator Cu_2OSeO_3 . *Phys. Rev. Lett.* **113**, 107203 (2014). <https://doi.org/10.1103/PhysRevLett.113.107203>
87. Y. Okamura, F. Kagawa, S. Seki, Y. Tokura, Transition to and from the skyrmion lattice phase by electric fields in a magnetoelectric compound. *Nat. Commun.* **7**, 12669 (2016). <https://doi.org/10.1038/ncomms12669>
88. A.J. Kruchkov, J.S. White, M. Bartkowiak, I. Zivcovic, A. Magrez, H.M. Rønnow, Direct control of the skyrmion phase stability by electric field in a magnetoelectric insulator (2017). [arXiv:1703.06081](https://arxiv.org/abs/1703.06081)
89. A. Bauer, M. Garst, C. Pfleiderer, History dependence of the magnetic properties of single-crystal $\text{Fe}_{1-x}\text{Co}_x\text{Si}$. *Phys. Rev. B* **93**, 235144 (2016). <https://doi.org/10.1103/PhysRevB.93.235144>
90. A. Bauer, A. Chacon, M. Halder, J. Kindervater, S. Mühlbauer, A. Heinemann, C. Pfleiderer, Topological protection of super-cooled skyrmion lattice order in $\text{Fe}_{1-x}\text{Co}_x\text{Si}$ (2018)
91. L.J. Bannenberg, A.J.E. Lefering, K. Kakurai, Y. Onose, Y. Endoh, Y. Tokura, C. Pappas, Magnetic relaxation phenomena in the chiral magnet $\text{Fe}_{1-x}\text{Co}_x\text{Si}$: An ac susceptibility study. *Phys. Rev. B* **94**, 134433 (2016). <https://doi.org/10.1103/PhysRevB.94.134433>
92. A. Bauer, A. Neubauer, C. Franz, W. Münzer, M. Garst, C. Pfleiderer, Quantum phase transitions in single-crystal $\text{Mn}_{1-x}\text{Fe}_x\text{Si}$ and $\text{Mn}_{1-x}\text{Co}_x\text{Si}$: Crystal growth, magnetization, ac susceptibility, and specific heat. *Phys. Rev. B* **82**, 064404 (2010). <https://doi.org/10.1103/PhysRevB.82.064404>
93. J. Kindervater, T. Adams, A. Bauer, F. Haslbeck, A. Chacon, S. Mühlbauer, F. Jonietz, A. Neubauer, U. Gasser, G. Nagy, N. Martin, W. Häußler, R. Georgii, M. Garst, C. Pfleiderer, Helical and skyrmion lattice order in $\text{Mn}_{1-x}\text{Fe}_x\text{Si}$ and $\text{Mn}_{1-x}\text{Co}_x\text{Si}$ (2018)
94. L.J. Bannenberg, K. Kakurai, F. Qian, E. Lelièvre-Berna, C.D. Dewhurst, Y. Onose, Y. Endoh, Y. Tokura, C. Pappas, Extended skyrmion lattice scattering and long-time memory in the chiral magnet $\text{Fe}_{1-x}\text{Co}_x\text{Si}$. *Phys. Rev. B* **94**, 104406 (2016). <https://doi.org/10.1103/PhysRevB.94.104406>
95. T. Adams, S. Mühlbauer, A. Neubauer, W. Münzer, F. Jonietz, R. Georgii, B. Pedersen, P. Böni, A. Rosch, C. Pfleiderer, Skyrmion lattice domains in $\text{Fe}_{1-x}\text{Co}_x\text{Si}$. *J. Phys.: Conf. Ser.* **200**, 032001 (2010). <https://doi.org/10.1088/1742-6596/200/3/032001>
96. K. Makino, J.D. Reim, D. Higashi, D. Okuyama, T.J. Sato, Y. Nambu, E.P. Gilbert, N. Booth, S. Seki, Y. Tokura, Thermal stability and irreversibility of skyrmion-lattice phases in Cu_2OSeO_3 . *Phys. Rev. B* **95**, 134412 (2017). <https://doi.org/10.1103/PhysRevB.95.134412>
97. L.J. Bannenberg, F. Qian, R.M. Dalglish, N. Martin, G. Chaboussant, M. Schmidt, D.L. Schlagel, T.A. Lograsso, H. Wilhelm, C. Pappas, Reorientations, relaxations, metastabilities and domains of skyrmion lattices. *Phys. Rev. B* **96**, 184416 (2017). <https://doi.org/10.1103/PhysRevB.96.184416>

98. A. Bauer, C. Pfleiderer, Magnetic phase diagram of MnSi inferred from magnetization and ac susceptibility. *Phys. Rev. B* **85**, 214418 (2012). <https://doi.org/10.1103/PhysRevB.85.214418>
99. A. Bauer, M. Garst, C. Pfleiderer, Specific heat of the skyrmion lattice phase and field-induced tricritical point in MnSi. *Phys. Rev. Lett.* **110**, 177207 (2013). <https://doi.org/10.1103/PhysRevLett.110.177207>
100. I. Levatić, V. Šurića, H. Berger, I. Živković, Dissipation processes in the insulating skyrmion compound Cu₂OSeO₃. *Phys. Rev. B* **90**, 224412 (2014). <https://doi.org/10.1103/PhysRevB.90.224412>
101. F. Qian, H. Wilhelm, A. Aqeel, T.T.M. Palstra, A.J.E. Lefering, E.H. Brück, C. Pappas, Phase diagram and magnetic relaxation phenomena in Cu₂OSeO₃. *Phys. Rev. B* **94**, 064418 (2016). <https://doi.org/10.1103/PhysRevB.94.064418>
102. K. Karube, J.S. White, N. Reynolds, J.L. Gavilano, H. Oike, A. Kikkawa, F. Kagawa, Y. Tokunaga, H.M. Rønnow, Y. Tokura, and Y. Taguchi, Robust metastable skyrmions and their triangular-square lattice structural transition in a high-temperature chiral magnet. *Nat. Mater.* **15**, 1237 (2015). <https://doi.org/10.1038/nmat4752>
103. K. Karube, J.S. White, D. Morikawa, M. Bartkowiak, A. Kikkawa, Y. Tokunaga, T. Arima, H.M. Rønnow, Y. Tokura, Y. Taguchi, Skyrmion formation in a bulk chiral magnet at zero magnetic field and above room temperature. *Phys. Rev. Mater.* **1**, 074405 (2017). <https://doi.org/10.1103/PhysRevMaterials.1.074405>
104. H. Oike, A. Kikkawa, N. Kanazawa, Y. Taguchi, M. Kawasaki, Y. Tokura, F. Kagawa, Interplay between topological and thermodynamic stability in a metastable magnetic skyrmion lattice. *Nat. Phys.* **12**, 62 (2016). <https://doi.org/10.1038/nphys3506>
105. F.N. Rybakov, A.B. Borisov, S. Blügel, N.S. Kiselev, New type of stable particlelike states in chiral magnets. *Phys. Rev. Lett.* **115**, 117201 (2015). <https://doi.org/10.1103/PhysRevLett.115.117201>
106. R. Ritz, M. Halder, C. Franz, A. Bauer, M. Wagner, R. Bamler, A. Rosch, C. Pfleiderer, Giant generic topological Hall resistivity of MnSi under pressure. *Phys. Rev. B* **87**, 134424 (2013). <https://doi.org/10.1103/PhysRevB.87.134424>
107. C. Pfleiderer, P. Böni, T. Keller, U.K. Rößler, A. Rosch, Non-fermi liquid metal without quantum criticality. *Science* **316**, 1871 (2007). <https://doi.org/10.1126/science.1142644>
108. R. Ritz, M. Halder, M. Wagner, C. Franz, A. Bauer, C. Pfleiderer, Formation of a topological non-Fermi liquid in MnSi. *Nature* **497**, 231 (2013). <https://doi.org/10.1038/nature12023>
109. C. Pfleiderer, G.J. McMullan, S.R. Julian, G.G. Lonzarich, Magnetic quantum phase transition in MnSi under hydrostatic pressure. *Phys. Rev. B* **55**, 8330 (1997). <https://doi.org/10.1103/PhysRevB.55.8330>
110. C. Thessieu, C. Pfleiderer, A.N. Stepanov, J. Flouquet, Field dependence of the magnetic quantum phase transition in MnSi. *J. Phys.: Condens. Matter* **9**, 6677 (1997). <https://doi.org/10.1088/0953-8984/9/31/019>
111. C. Pfleiderer, S.R. Julian, G.G. Lonzarich, Non-Fermi-liquid nature of the normal state of itinerant-electron ferromagnets. *Nature* **414**, 427 (2001). <https://doi.org/10.1038/35106527>
112. N. Doiron-Leyraud, J.R. Walker, L. Taillefer, M.J. Steiner, S.R. Julian, G.G. Lonzarich, Fermi-liquid breakdown in the paramagnetic phase of a pure metal. *Nature* **425**, 595 (2003). <https://doi.org/10.1038/nature01968>
113. C. Pfleiderer, D. Reznik, L. Pintschovius, H.V. Löhneysen, M. Garst, A. Rosch, Partial order in the non-Fermi-liquid phase of MnSi. *Nature* **427**, 227 (2004). <https://doi.org/10.1038/nature02232>
114. Y.J. Uemura, T. Goko, I.M. Gat-Malureanu, J.P. Carlo, P.L. Russo, A.T. Savici, A. Aczel, G.J. MacDougall, J.A. Rodriguez, G.M. Luke, S.R. Dunsiger, A. McCollam, J. Arai, C. Pfleiderer, P. Böni, K. Yoshimura, E. Baggio-Saitovitch, M.B. Fontes, J. Larrea, Y.V. Sushko, J. Sereni, Phase separation and suppression of critical dynamics at quantum phase transitions of MnSi and (Sr_{1-x}Ca_x)RuO₃. *Nat. Phys.* **3**, 29 (2007). <https://doi.org/10.1038/nphys488>
115. T. Nakajima, H. Oike, A. Kikkawa, E.P. Gilbert, N. Booth, K. Kakurai, Y. Taguchi, Y. Tokura, F. Kagawa, T.-H. Arima, Skyrmion lattice structural transition in MnSi. *Sci. Adv.* **3**, e1602562 (2017). <https://doi.org/10.1126/sciadv.1602562>

116. N. Kanazawa, M. Kubota, A. Tsukazaki, Y. Kozuka, K.S. Takahashi, M. Kawasaki, M. Ichikawa, F. Kagawa, Y. Tokura, Discretized topological Hall effect emerging from skyrmions in constricted geometry. *Phys. Rev. B* **91**, 041122 (2015). <https://doi.org/10.1103/PhysRevB.91.041122>
117. A. Dussaux, P. Schoenherr, K. Koumpouras, J. Chico, K. Chang, L. Lorenzelli, N. Kanazawa, Y. Tokura, M. Garst, A. Bergman, C.L. Degen, D. Meier, Local dynamics of topological magnetic defects in the itinerant helimagnet FeGe. *Nat. Commun.* **7**, 12430 (2016). <https://doi.org/10.1038/ncomms12430>
118. A. Bauer, A. Chacon, M. Wagner, M. Halder, R. Georgii, A. Rosch, C. Pfleiderer, M. Garst, Symmetry breaking, slow relaxation dynamics, and topological defects at the field-induced helix reorientation in MnSi. *Phys. Rev. B* **95**, 024429 (2017). <https://doi.org/10.1103/PhysRevB.95.024429>
119. J. Müller, J. Rajeswari, P. Huang, Y. Murooka, H.M. Rønnow, F. Carbone, A. Rosch, magnetic skyrmions and skyrmion clusters in the Helical phase of Cu₂OSeO₃. *Phys. Rev. Lett.* **119**, 137201 (2017). <https://doi.org/10.1103/PhysRevLett.119.137201>

Chapter 6

Anomalous Hall Effect



Yuriy Mokrousov

Abstract The anomalous Hall effect (AHE) is one of the most fundamental, practically important and for a long time most enigmatic phenomena exhibited by magnetic materials. Here, we briefly outline the relation of the anomalous Hall effect to the geometric properties of the electronic states as given by the Berry phase. The Berry phase origins of the AHE lead to its topological manifestations in insulators, which we review in detail based on key examples. In addition to the intrinsic AHE and its anisotropy in solids, we draw a deep correlation of this effect with orbital magnetism and magnetoelectric response, and discuss its emergence in non-collinear magnets.

6.1 Introduction

The anomalous Hall effect (AHE) is one of the oldest and most famous transport phenomena in magnetic materials. As was discovered long ago [1, 2], in ferromagnets the resistivity of the sample in the direction perpendicular to external electric \mathbf{E} and magnetic \mathbf{H} field acquires an additional contribution due to the magnetization of the sample [3, 4]:

$$\rho_{xy} = \rho_{OH} + \rho_{AH} = R_0 H + 4\pi R_S M, \quad (6.1)$$

where R_0 is the usual Hall coefficient, R_S is the anomalous (spontaneous) Hall coefficient, ρ_{OH} is the ordinary Hall resistivity and ρ_{AH} (or ρ_{xy}) is the anomalous Hall resistivity. The revival of interest in the anomalous Hall effect during past ten-twenty

Y. Mokrousov (✉)

Institute for Advanced Simulation, Forschungszentrum Jülich GmbH, Jülich, Germany
e-mail: y.mokrousov@fz-juelich.de

Y. Mokrousov

Institute of Physics, Johannes Gutenberg-University Mainz, Mainz, Germany
e-mail: ymokrous@uni-mainz.de

years can be attributed to several reasons. From practical point of view, utilizing the AHE for the purposes of modern spintronics enables us with a unique tool for generating and controlling spin-polarized currents in complex magnetic nanoscale systems. Besides, nowadays, the AHE is one of the main transport effects which is used to detect and characterize the magnetic properties in various situations. On the other hand, deeper understanding of the mechanisms behind the AHE was absolutely crucial for the advances in the much younger field of spin currents, spin Hall effect and related phenomena (see also Chap. 7). Moreover, recent progress in understanding the AHE from the point of view of Berry phases, geometrical and topological structure of the electronic states in infinite crystals eventually led to the fact that many abstract quantities and objects in this part of quantum physics became an important part in day-to-day life of a solid state physicist.

The finite anomalous Hall resistivity which roots in spin-orbit coupling (SOC), or, spin-orbit interaction (SOI), can be observed only in materials with broken time reversal symmetry, of which the most renowned class constitute ferromagnets. In ferromagnets, the time reversal symmetry is broken due to the presence of a finite effective exchange field, which causes an exchange splitting between the bands. Upon moving in the longitudinal electric field E_x electrons experience scattering which is responsible for “anomalous” contribution to the transverse velocity. In a simple picture, due to the spin-orbit coupling, this scattering depends on the spin of an incoming electron which results in the anomalous velocity of opposite sign for electrons of opposite spin, see Fig. 6.1. In a non-magnetic material, for which the number of spin-up and spin-down electrons is the same, this results in a zero transverse anomalous (charge) conductivity, but leads to the so-called spin Hall effect and can result in non-zero spin accumulation at the opposite sides of the sample [5, 6]. In a ferromagnet, due to a finite spin splitting of the electronic bands the numbers of spin-up and spin-down electrons differ, and the overall transverse AHE current is not zero.

The first attempts to explain the AHE were made a long time ago. And while the history of theoretical understanding of the AHE is particularly messy, the consistent picture of the AHE emerged quite slowly with years. In this manuscript we will consider the AHE in terms of a very appealing language of semiclassical dynamics and geometric phases. Semiclassical philosophy and formalism for the anomalous transport in solids has recently reached a degree of self-consistency and consistency with other more rigorous quantum mechanically approaches which makes it possible to use it as a common foundation for various effects, anomalous Hall effect included. In this chapter, we assume the geometric picture of the AHE, supported by considerations of the electronic structure in transition-metals, and discuss some selected aspects of this complex phenomenon. In Sect. 6.2 we introduce basic definitions related to the Berry curvature of Bloch electrons, and show the emergence of the AHE in a very simple yet appealing way. Section 6.3 is dedicated to the description of general features of the intrinsic AHE in real materials, and contains also some comments on the extrinsic origins of this effect. Section 6.4 is devoted to the discussion of the magneto-crystalline anisotropy of the AHE, while in Sect. 6.5 we present a very brief overview of the topological features of the AHE in insulators, i.e.

Chern numbers, emergence of the quantization of the AHE, its relation to various topologically non-trivial phases of matter, and relation to other “topological” phenomena such as spin-orbit torque. The final Sect. 6.6 is dedicated to the relation of the AHE to orbital magnetism, and the relation of the AHE to the real-space features of the spin distribution in non-collinear magnets. More details about the derivations and discussions of many of the aspects of the AHE can be found in three beautiful reviews [7–9].

6.2 Berry Phase and AHE

Within the setup of the Berry phase problem, given that our Hamiltonian smoothly depends on a general parameter λ , formally, we seek for the solution of the Schrödinger equation, $i\frac{\partial\psi(t)}{\partial t} = H(\lambda(t))\psi(t)$. Under the assumption of the adiabatic evolution, (i.e. assuming that if $\psi(t=0) = |n\lambda(t=0)\rangle$, where $|n\lambda\rangle$ is a set of non-degenerate eigenstates of $H(\lambda)$ with an eigenvalue $\varepsilon_n(\lambda)$, then during the evolution $|\psi(t)\rangle\langle\psi(t)| = |n\lambda(t)\rangle\langle n\lambda(t)|$), one can find that for a periodic evolution $\lambda(t=0) = \lambda(t=T)$, the solution of the Schrödinger equation at time T can be simply written as: $\psi(T) = e^{-i\alpha_{\text{dyn}}(T)} e^{i\gamma_n} |n\lambda(T)\rangle$. In this expression, besides the well-known dynamical phase $\alpha_{\text{dyn}}(T) = \int_0^T \varepsilon_n(\tau) d\tau$, the so-called Berry phase $\gamma_n = \int_0^T i \langle n\lambda(\tau) | \partial_\tau | n\lambda(\tau) \rangle d\tau \pmod{2\pi}$ appears [10, 11]. This gauge-invariant quantity has played a crucial role in various branches of physics related

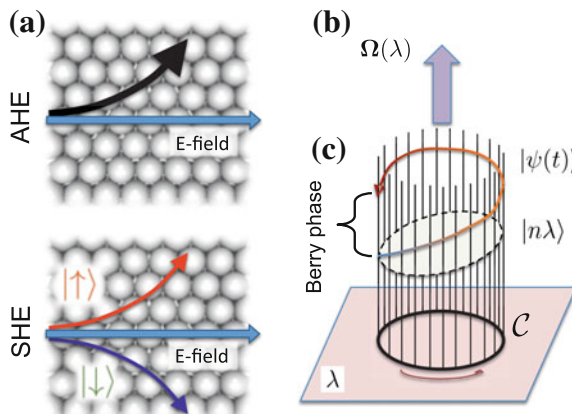


Fig. 6.1 **a** In solids the non-trivial geometry of Bloch electrons as manifested in Berry curvature results in a geometric contribution to the transverse velocity of electrons exposed to an electric field, which allows for understanding of the intrinsic anomalous Hall effect (AHE) and spin Hall effect (SHE) in solids in geometric terms. The figure is made by Bernd Zimmermann. **b** During the periodic adiabatic evolution in a λ -parameter space along a closed path \mathcal{C} , the wavefunction $\psi(t)$ makes a trajectory in the space of $\lambda \times \mathbb{U}(1)$, and acquires a phase at the end of this evolution. Under the assumption of zero eigen energy on \mathcal{C} , the acquired phase is known as the geometric, or, Berry phase

to geometrical and topological concepts. The Berry phase can be envisaged as an Aharonov-Bohm phase that a wavefunction acquires as it propagates along a closed loop exposed to an effective magnetic field as given by the Berry curvature Ω^n : $\gamma_n(\mathcal{C}) = \int_S \Omega^n$, where S is the surface of our λ -space which the propagation path \mathcal{C} encloses, see Fig. 6.1. The components of the Berry curvature tensor read:

$$\Omega_{ij}^n(\lambda) = -2\text{Im}\langle \partial_{\lambda_i} n(\lambda) | \partial_{\lambda_j} n(\lambda) \rangle = -2\text{Im} \sum_{m \neq n} \frac{\langle m\lambda | \partial_{\lambda_i} H(\lambda) | n\lambda \rangle \langle n\lambda | \partial_{\lambda_j} H(\lambda) | m\lambda \rangle}{[\varepsilon_n(\lambda) - \varepsilon_m(\lambda)]^2}, \quad (6.2)$$

from which it becomes apparent that the large contributions to this quantity come from the points of near degeneracies in the electronic structure.

In the following we show the close relation of the Berry phase to the AHE. For electrons in a periodic solid the eigenstates $\psi_{n\mathbf{k}}$ of the Hamiltonian can be classified by quantum numbers (\mathbf{k}, n) , where \mathbf{k} lies in the Brillouin zone (BZ), and n is a discrete index numbering the bands. The eigenfunctions can be written in the form $\psi_{n\mathbf{k}}(\mathbf{r}) = e^{i\mathbf{k}\cdot\mathbf{r}} u_{n\mathbf{k}}(\mathbf{r})$, where $u_{n\mathbf{k}}$ has the periodicity of the lattice. In terms of the lattice-periodic eigenstates and \mathbf{k} -dependent Hamiltonian $H(\mathbf{k}) \equiv H_{\mathbf{k}} \equiv e^{-i\mathbf{k}\cdot\mathbf{r}} \cdot H \cdot e^{i\mathbf{k}\cdot\mathbf{r}}$, also referred to as the Hamiltonian in crystal momentum representation, we are able to set up everything in terms of an eigenvalue problem of a \mathbf{k} -dependent Hamiltonian, acting on the same Hilbert space of periodic functions for every \mathbf{k} . This is exactly the setup suitable for studies of the Berry phase effects, if we identify the parameter λ from general mathematical theory with the Bloch vector \mathbf{k} . The corresponding components of the Berry curvature tensor of band n are given by $\Omega_{ij}^n(\mathbf{k}) = -2\text{Im}\langle \partial_{k_i} u_{n\mathbf{k}} | \partial_{k_j} u_{n\mathbf{k}} \rangle$. The components of the Berry curvature itself are sometimes written as a vector $\Omega_i^n(\mathbf{k}) := \Omega_i^n(\mathbf{k}) = (1/2)\epsilon_{lmi}\Omega_{lm}^n(\mathbf{k}) = -\text{Im}\langle \partial_{\mathbf{k}} u_{n\mathbf{k}} | \times | \partial_{\mathbf{k}} u_{n\mathbf{k}} \rangle$. The driving force behind the dynamics of an electron residing at a certain \mathbf{k} -point and band n could be an external electric or magnetic field as well as dependence of the Hamiltonian on another parameter, which cause the motion of an electron along certain orbits in \mathbf{k} -space and \mathbf{r} -space. The perturbation theory expression for the \mathbf{k} -space Berry curvature, looking at (6.2), can be written as:

$$\Omega_{ij}^n(\mathbf{k}) = -2\text{Im} \sum_{m \neq n} \frac{\langle u_{n\mathbf{k}} | \partial_{k_i} H_{\mathbf{k}} | u_{m\mathbf{k}} \rangle \langle u_{m\mathbf{k}} | \partial_{k_j} H_{\mathbf{k}} | u_{n\mathbf{k}} \rangle}{(\varepsilon_{n\mathbf{k}} - \varepsilon_{m\mathbf{k}})^2}. \quad (6.3)$$

We will also consider a situation, in which, besides the dependence on \mathbf{k} , the Hamiltonian of the system depends at the same time on another (multi-dimensional) parameter λ , that is, $H = H(\mathbf{k}, \lambda)$. Generally speaking, the Berry curvature form in this extended (λ, \mathbf{k}) space has components, which we call $\Omega_{\mathbf{k}\lambda}^n \equiv \Omega_{\mathbf{k}}^n$ and $\Omega_{\lambda\lambda}^n \equiv \Omega_{\lambda}^n$ and which are expressed in terms of derivatives of $u_{n\mathbf{k}}^{\lambda}$ with respect to only \mathbf{k} or λ , respectively. There is also the component of the Berry curvature, which involves both λ - and \mathbf{k} -derivatives: $\Omega_{\lambda\mathbf{k}}^n = -2\text{Im}\langle \partial_{\mathbf{k}} u_{n\mathbf{k}}^{\lambda} | \partial_{\lambda} u_{n\mathbf{k}}^{\lambda} \rangle$, and which can be written down in analogy to (6.3), with the derivative with respect to k_j replaced by a derivative by λ . We call this part of the Berry curvature the *mixed Berry curvature*. Based on general symmetry arguments, it is straightforward to show that the Berry curvature in \mathbf{k} -space

obeys the following symmetry properties: (i) in the presence of time-reversal symmetry, $\Omega^n(-\mathbf{k}) = -\Omega^n(\mathbf{k})$, while (ii) in the presence of the space inversion symmetry, $\Omega^n(-\mathbf{k}) = \Omega^n(\mathbf{k})$. This means that when both space and time inversion symmetry are present in a solid, the Berry curvature at each \mathbf{k} is identically zero. In materials which exhibit spontaneous magnetization, such as ferromagnets and antiferromagnets, the non-trivial Berry curvature is due to breaking of time-inversion symmetry.

When analyzing the velocity of electronic states in a solid, one has to go beyond the adiabatic approximation for the evolved wavefunction in order to show that up to first order in transition frequencies the velocity of an evolved in time via $\lambda(t)$ state reads:

$$\mathbf{v}_{n\mathbf{k}}^\lambda = \partial_{\mathbf{k}} \varepsilon_{n\mathbf{k}}^\lambda - \Omega_{n\mathbf{k}}^n \dot{\lambda}. \quad (6.4)$$

In this expression the first term on the right hand side is the *group velocity*. The change in λ gives, on the other hand, rise to the so-called *anomalous velocity*, which is expressed in terms of the mixed Berry curvature $\Omega_{n\mathbf{k}}^n$. Clearly, the anomalous velocity of a state depends on how fast the parameter λ is changed in time. And while in order to arrive at it, the consideration of the wavefunction dynamics which goes beyond the adiabatic approximation was necessary, the end result is manifestly *geometric*, giving rise to a magnitude of geometrical and topological effects in condensed matter.

Our understanding and corresponding acquired ability to describe the intrinsic anomalous Hall effect (AHE) in solids from the geometrical viewpoint is, perhaps, one of the most convincing achievements of the topological solid state physics over the past 50 years [8]. Having realized that the λ -dynamics of Bloch electrons results in a geometrical contribution to the velocity (6.4), it takes now a couple of lines to show that the electric field present in a solid can give rise to the Hall current [8]. Assume that without the field the unperturbed Hamiltonian of the system looks like $H(t=0) = \frac{\mathbf{p}^2}{2} + V(\mathbf{r})$, with corresponding Bloch vectors \mathbf{q} and the crystal momentum representation $H_{\mathbf{q}}$ of the Hamiltonian. To model the effect of the uniform electric field, we apply a constant in space, but varying in time vector potential $\mathbf{A}(t)$ such that $-\frac{\partial \mathbf{A}(t)}{\partial t} = \mathbf{E}$. This modifies the corresponding lattice Hamiltonian as follows: $H(t > 0) = \frac{1}{2}(\mathbf{p} + \mathbf{A}(t))^2 + V(\mathbf{r})$. Since the constant in space vector potential does not break the periodicity of the crystal, it cannot couple the unperturbed wavefunctions with different values of \mathbf{q} and it changes the energy of the states with an overall constant, which can be ignored. Therefore, once we are looking at a state labeled with a certain value of \mathbf{q} , during the evolution of this state $\dot{\mathbf{q}} = 0$. Nevertheless, we can also number our state in terms of the \mathbf{k} vector, which is the “proper” Bloch vector of the Hamiltonian $H_{\mathbf{k}}(t > 0)$: $\mathbf{k} = \mathbf{q} + \mathbf{A}(t) = \mathbf{k}(t)$, that is, the wavefunction at $\mathbf{k}(t)$ which solves the Schrödinger equation for $H(t)$, is identical to the wavefunction which solves the Schrödinger equation for $H(t=0)$ but at a wavevector $\mathbf{q} = \mathbf{k} - \mathbf{A}(t)$. From the latter equation, it follows that $\dot{\mathbf{k}} = -\mathbf{E}$. In order to employ the expression for the velocity of a certain state, we write the time-dependence of the Hamiltonian as follows: $H_{\mathbf{k}}^t = H_{\mathbf{k}(t)}$, which leads to $\partial_t H_{\mathbf{k}}^t = \partial_{\mathbf{k}} H_{\mathbf{k}} \cdot \partial_t \mathbf{k}(t) = -\mathbf{E} \cdot \partial_{\mathbf{k}} H_{\mathbf{k}}$. Substituting the latter into the expression for the velocity (6.4) with t playing the role of λ , and using (6.3) and (6.2), we get:

$$\dot{\mathbf{r}} := v_{n\mathbf{k}} = \partial_{\mathbf{k}} \varepsilon_{n\mathbf{k}} - \mathbf{E} \times \boldsymbol{\Omega}_n(\mathbf{k}). \quad (6.5)$$

This means that the non-zero Berry curvature of Bloch states in reciprocal space results in a transverse charge current as an electric field is applied to the solid. Generally, writing down the resulting current as $\mathbf{J} = \sigma \mathbf{E}$, the Berry curvature driven components of the conductivity tensor can be written as:

$$\sigma_{ij} = \frac{1}{(2\pi)^3} \sum_n \int_{BZ} \Omega_{ij}^n(\mathbf{k}) d\mathbf{k}, \quad (6.6)$$

where the sum over n runs over all occupied states at a given \mathbf{k} -point. For two dimensional insulators, as we shall discuss later, the value of the anomalous Hall conductivity is quantized. In metals such quantization does not occur—nevertheless, the integral of the Berry curvature over all occupied states gives the value of the *intrinsic* anomalous Hall conductivity. Owing to the presence of degeneracies and near degeneracies (which serve as the sources of the Berry curvature “field”) in the vicinity of the Fermi level in metals, the behaviour of the Berry curvature especially in transition-metals can be very non-trivial, singular and extremely sensitive to various parameters which determine the electronic structure (for a typical example see Fig. 6.2). In contrast to insulators, the presence of Fermi surface in metals also leads to promotion of the Hall current which comes from impurity scattering—this is the so-called *extrinsic* AHE. The relation between the magnitudes of the intrinsic

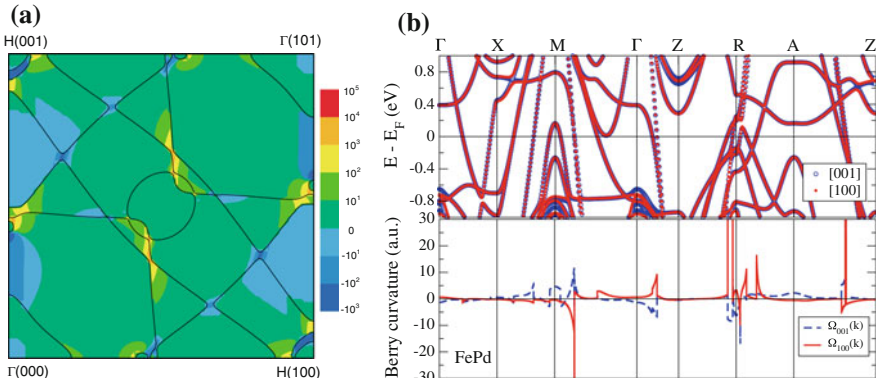


Fig. 6.2 **a** Fermi surface of bcc Fe in (010) plane (solid black lines) and the color map of the Berry curvature of all occupied states $-\Omega_{xy}(\mathbf{k})$ in that plane in atomic units. Taken from [12]. **b** Band structures and distribution of the Berry curvature along high-symmetry directions in the Brillouine zone for the magnetization along the [001] and [100] crystallographic axes in uniaxial L_1 ordered FePd alloy. Here [001] and [100] marks the only non-vanishing component of the Berry curvature vector along the direction of the magnetization. The spiky irregular structure of the Berry curvature, very sensitive to the electronic structure around the Fermi energy as modified i.e. by the choice of the magnetization direction, is prominent in this plot. Taken from [13]

and extrinsic currents strongly depends on the details of the electronic structure and disorder [9].

In a situation when the part of the spin-orbit interaction which mixes the spin character of the Bloch states can be neglected (which is often the case for light transition-metals), we can decompose the anomalous Hall conductivity into a sum of contributions coming from spin-up and spin-down bands. The difference between the two is proportional to the value of the spin Hall conductivity, that is, it is related to the magnitude of the transverse spin current caused by an electric field. This spin current manifests, for example, in the accumulation of spin at the boundaries of the sample, or in a finite torque that the spin current exerts on the magnetization of a magnet brought in contact with the material in which the spin current is generated. The non-zero value of such defined spin Hall conductivity in magnetic and non-magnetic materials of various nature constitutes the essence of the *spin Hall effect*, experimentally observed some years ago. The spin Hall effect is discussed in detail in Chap. 7 of this book.

6.3 Intrinsic and Extrinsic AHE

Owing to the fact that real impurity potentials in considered materials are normally unknown, attempts to estimate the magnitude of the extrinsic anomalous Hall conductivity at least qualitatively fail quite often when compared to the data obtained on real samples, and the computed conductivity values can differ by orders of magnitude depending on the impurity potential taken for the calculation. One of the first successful estimates for the AHE in a realistic situation was provided by Jungwirth and co-workers [14, 15], who applied Sundaram-Niu derived expression for the intrinsic AHC, (6.6), to arrive at the values of the AHC in (III, Mn)V ferromagnetic semiconductors which were found to be in a very good agreement with experiments.

A remarkably successful ab initio prediction of an intrinsic AHE was made by Yao et al. for elemental bcc Fe [12]. In this work, the AHC was found to exhibit a very slow convergence with the number of \mathbf{k} -points, which was found to originate in the appearance of large contributions of both signs to $\Omega_z(\mathbf{k})$ occurring over very small regions in \mathbf{k} -space. In Fe, the effect of SOI on the band structure is very small, except for the case of nearly degenerate states coupled by spin-orbit. Such pairs of states provide a very large contribution to the Berry curvature when the Fermi energy lies in the middle of a SOI-driven gap, since the small energy gap between occupied and unoccupied states gives rise to a small energy denominator in (6.2). For example, this mechanism explains the large spike in the Berry curvature prominent near $H(1,0,0)$ point in the direction of $P(\frac{1}{2}, \frac{1}{2}, \frac{1}{2})$, see Fig. 6.2. The largest contributions to the Berry curvature are, however, positioned away from the high-symmetry lines in the reciprocal space. For instance, as visible in Fig. 6.2 for the (010)-plane in Fe, the Berry curvature exhibits large peaks appearing on the background of large parts of the k -space with very small values.

Another example which we consider is the case of $L1_0$ FePd, for which the distribution of the Berry curvature along the high-symmetry lines in the Brillouin zone is shown in Fig. 6.2b. In this figure the singular contributions to the Berry curvature arising from the band degeneracies in the vicinity of the Fermi level are prominent. From the distribution of the Berry curvature presented in Fig. 6.2 for Fe and FePd we make a generally valid conclusion that a large part of the AHC in complex transition-metals is driven by the interband transitions between the states which are well-separated in energy. And although such transitions provide a seemingly insignificant contribution to the Berry curvature, as compared to the monopole-like contributions at special k -points, they occur over wide regions of the reciprocal space.

In another example, Fang et al. considered the influence of the spin-orbit induced band degeneracies on the anomalous Hall conductivity in detail on an example of $SrRuO_3$ [16]. This material exhibits a near degeneracy of the bands along the lines $k_x = k_y = 0$ and $k_x = \pm k_y$ due to symmetry [16]. According to first-principles calculations, this results in a large peak of the Berry curvature $\Omega_z(\mathbf{k})$ at the Γ point and its enhancement along the $k_x = \pm k_y$ lines in the Brillouin zone. Experimental measurements as well as ab initio calculations of Fang et al. show that in $SrRuO_3$ the anomalous Hall resistivity changes non-monotonously with temperature and even includes a sign change. Such behavior is far beyond the expectation based on the conventional expression in (6.1). The results of the calculations by Fang et al. revealed another aspect which became a hallmark of the intrinsic AHE: the AHC in this compound changed drastically as a function of the Fermi energy, exhibiting several changes in sign on the scale of 300 meV. The sharp and spiky structure of this distribution is a natural consequence of the singular behavior of the magnetic monopoles in reciprocal space.

The great popularity that the calculations and analysis of various intrinsic transverse transport phenomena in metals gained over the past decade is largely based on the observation that very often the estimates of e.g. intrinsic AHC performed in analogy to what was discussed above, do not only correctly reproduce the sign of the AHE as observed experimentally, but also often come close to the magnitude of the measured effect. For example, reported by Yao calculated value of σ_{xy} of 751 S/cm was only 25% off the experimental value of 1032 S/cm, extracted from data on iron whiskers at room temperature [20], while for the case of $SrRuO_3$ the calculated value of AHC of -60 S/cm is very close to that obtained in experiment of -100 S/cm. Experimentally, however, distinguishing different contributions from their scaling behavior with the impurity concentration and temperature does not present a trivial task [20–23]. In this context ab initio calculations of the AHE are important since they allow us to access different contributions separately and explicitly investigate the effect of disorder, which is pivotal for our ability to understand and engineer the behavior of the AHE in real materials. However, methods which rely on the exact knowledge of the disorder potential, which has to be explicitly included in the ab initio calculation, have a drawback that the calculations of the disorder driven contributions are much more complex than the calculations of the intrinsic part.

With vanishing disorder, a part of the AHE known as the *scattering-independent* AHE reaches a constant value, which is disorder-independent in nature [7, 9, 17].

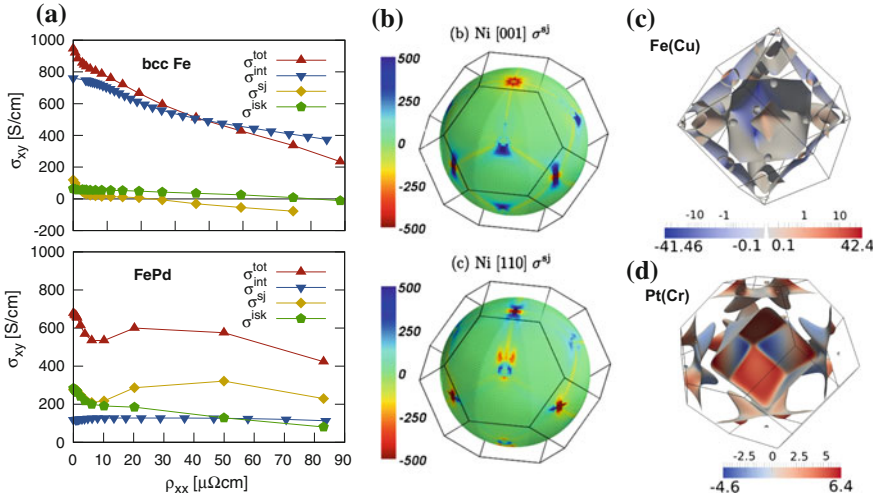


Fig. 6.3 **a** Additive decomposition of the total AHC (σ^{tot}), into intrinsic (σ^{int}), side jump (σ^{sj}), and intrinsic skew scattering (σ^{isk}) contributions, presented as a function of longitudinal resistivity in bcc Fe and L1₀ FePd, [17]. **b** Angle-resolved side-jump AHC in units of S/cm obtained as a sum of the contributions from all occupied states to the side-jump AHC as a function of \mathbf{k} -ray originating at the Γ -point in the 3D BZ for fcc Ni [001] and fcc Ni [110], [18]. **c** Fermi-surface distribution of the symmetrized skew-scattering AHC (in units of Bohr radius) in dilute alloys of bcc Fe with Cu impurities and fcc Pt with ferromagnetic Cr impurities [19]

In the clean limit of short-ranged Gaussian disorder this scattering-independent contribution to AHE can be explicitly identified [9, 17]. It was shown that the scattering-independent AHE in many cases provides the dominant source of the AHE in transition-metal ferromagnets which are moderately disordered [18], while it is also possible to conveniently compute the latter part of the AHE from the electronic structure of the pure crystals even for multi-band metals [17, 18]. In some sense, the clean limit scattering-independent AHE is the robust value, around which the disorder-sensitive contributions arise. Generally, a very attractive alternative approach to treating the effect of disorder on the AHE and related phenomena on the ab initio level lies in a combination of the short-ranged Gaussian disorder model with realistic electronic structure calculations. For example, it can be used to estimate the role of the intrinsic Berry curvature contribution to the overall scattering-independent Hall current. Among the discussed above materials the first-principles calculations show that the AHC in bcc Fe is mainly dominated by the Berry curvature contribution over a vast range of the disorder strength, while FePd presents a distinguished example for which the overall value of the AHC is largely determined by scattering-independent “side-jump” and “intrinsic skew-scattering” contributions, see Fig. 6.3a. The transparent expressions for the scattering-independent contributions in the clean limit allow also to investigate the largely unexplored behavior of the extrinsic AHE with respect to the band topology and electronic structure details, see for exam-

ple the behavior of the side-jump AHC on the “Fermi sphere” in fcc Ni, shown in Fig. 6.3b [18].

On the other side, in the limit of vanishing disorder the comparison of the experimental data to the intrinsic and generally scattering-independent values has to be done with caution owing to the divergence of the so-called *skew-scattering* contribution to the AHC with decreasing the concentration of e.g. impurities in the sample [9]. In contrast to the intrinsic, or, generally, scattering-independent contributions to the anomalous Hall resistivity which scale as ρ_{xx}^2 with diagonal resistivity of the sample, the resistivity due to the skew-scattering exhibits a linear dependence on ρ_{xx} . Since the skew-scattering contribution to the AHC can be attributed to the asymmetry in $\mathbf{k} \rightarrow \mathbf{k}'$ and $\mathbf{k}' \rightarrow \mathbf{k}$ scattering at the Fermi surface driven by SOI, it can be readily captured for example within the first principles Boltzmann formalism [19]. What we learn from the ab-initio analysis of the skew-scattering AHC in bcc Fe doped with Cu impurities and fcc Pt doped with magnetic Cr impurities, shown in Fig. 6.3, is that the skew-scattering in transition-metals exhibits an extremely non-trivial behavior, and can be determined both by isolated “hot spots” at the Fermi surfaces giving singularly large contributions (as e.g. is the case for Fe doped with Cu impurities), as well as by large parts of the Fermi surface providing much more modest values (as is the case for Pt doped with Cr impurities). Generally, more advanced techniques based for example on the coherent-potential approximation (CPA) are able to estimate the specific influence of different types of disorder due to intermixing, substitutional disorder, phonons and magnons on the AHE on equal footing, referring to the more general Kubo framework for response properties [24, 25], from which all the contributions to the AHE (including the intrinsic part) follow naturally [9, 17].

To summarize, since recently the estimations of the anomalous Hall conductivity based on (6.6) became a common approach to study the AHE in electronic structure theory [26]. The simplicity of the formulation based on the intrinsic mechanism gives a valuable opportunity to compute the AHE directly from the electronic structure of pristine materials, accessible from a variety of sophisticated electronic structure methods, rendering thus direct comparison to experiments. These days, an entire spectrum of methods commonly applied by the electronic structure community is used to investigate the AHE without the need for specific details concerning the disorder in, e.g., antiferromagnets, non-collinear magnets, oxide, or strongly correlated materials in bulk, thin films, and heterostructures. In other words, the credibility of (6.6) heralds the beginning of the ab-initio era in the practical applications of the AHE, and, generally, intrinsic “transverse” transport phenomena such as spin Hall effect, spin and anomalous Nernst effects, spin-orbit torque, etc.

6.4 Anisotropic AHE

The crystal field in a solid is anisotropic, which in combination with SOC results in a strong dependence of the orbital and spin character of the states in a crystal on the direction of the magnetization or choice of the spin quantization axis (SQA), since the

matrix elements of the orbital angular momentum operator are themselves strongly anisotropic. In ferromagnets, the anisotropy of the orbital angular momentum operator combined with the crystal field splitting leads to a dependence of the band energy on the magnetization direction which results in the magneto-crystalline anisotropy energy (MAE)—one of the most fundamental characteristics of magnetic materials. As far as the transport properties of metals are concerned, the aforementioned magnetocrystalline anisotropy of the electronic structure leads to such fundamental effects as tunneling anisotropic magnetoresistance [27, 28], anisotropic magnetoresistance [29], or ballistic anisotropic magnetoresistance [30]. As in the case of MAE, these effects can be often readily captured by only considering the modification in the topology of the bands in the reciprocal space, when the magnetization orientation is varied [27, 30–32]. This is in contrast to the SHE and AHE, which are very sensitive to band degeneracies at the Fermi energy [9]. In this case the dependence of the electronic bands on the magnetization direction (for AHE) or the SQA (for SHE) is either absent or can often be neglected, and it is the anisotropy of the orbital and spin resolution of the Bloch states which becomes of major importance, possibly resulting in a very pronounced anisotropy of the Hall effects [33].

The pronounced anisotropy of the Hall effects and spin-relaxation is an important tool for tuning the transport characteristics of devices in spintronics. The intrinsic magnetocrystalline anisotropy of solids should be properly taken care of when dealing with polycrystalline samples and especially when treating the effect of magnetization dynamics and temperature on the measured transverse current or spin-polarization [35]. The anisotropy of the AHE in metals is an experimentally relatively

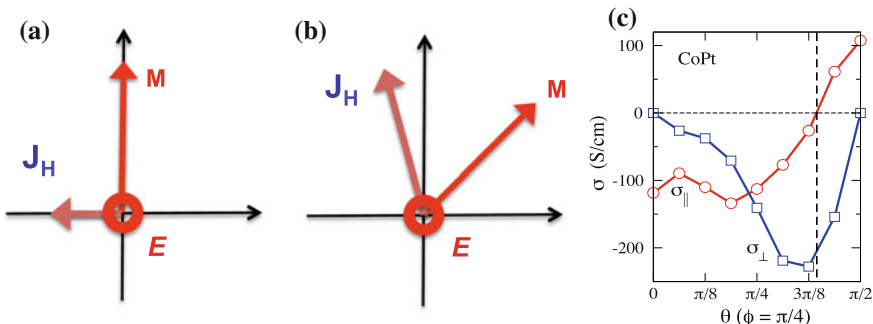


Fig. 6.4 **a** Even if for some high-symmetry directions of the magnetization \mathbf{M} in the crystal the anomalous Hall current \mathbf{J}_H can be perpendicular both to the applied electric field \mathbf{E} (pointing outside of the plane of the page) and \mathbf{M} (i.e. $\sigma_{\perp} = 0$), when the orientation of the magnetization is changed to lie along a general direction, not only the magnitude of \mathbf{J}_H can be changed significantly, but even its direction can deviate strongly from that determined by $\mathbf{M} \times \mathbf{E}$ (i.e. $\sigma_{\perp} \neq 0$), **b** The anisotropy of the AHE can be so pronounced that at some angle of \mathbf{M} with crystallographic axes the Hall current can be aligned with \mathbf{M} (i.e. $\sigma_{\perp} \neq 0$ and $\sigma_{\parallel} = 0$), as it is for example the case for L1₀ CoPt, for which the angular dependence of the AHC is shown in **c** (θ is counted with respect to the [001]-axis). Taken from [34]

well-studied effect, see for example the published data for bcc Fe [36], fcc Ni [37, 38], hcp Gd [39], as well as FeCr_2S_4 [40], $\text{Yb}_{14}\text{MnSb}_{11}$ [41], $\text{Y}_2\text{Fe}_{17-x}\text{Co}_x$ [42] and $R_2\text{Fe}_{17}$ ($R = \text{Y, Tb, Gd}$) [43]. Since the AHC tensor is 2-rank antisymmetric, it can be also seen as the AHC vector σ , with the components related to the corresponding components of the anomalous Hall conductivity tensor via $\sigma_i = \frac{1}{2} \sum_{jk} \epsilon_{ijk} \sigma_{jk}$ (with Levi-Civita tensor ϵ_{ijk}):

$$\mathbf{J}_H = \mathbf{E} \times \sigma. \quad (6.7)$$

The concept of the AHE anisotropy with respect to the direction of the magnetization \mathbf{M} in the crystal can be outlined as follows (see Fig. 6.4 for an illustration): not only the absolute magnitude of σ is dependent on the direction of magnetization, but also the orientation of σ exhibits a non-trivial dependence on \mathbf{M} . When \mathbf{M} points along a high symmetry direction, the anomalous Hall conductivity vector aligns with \mathbf{M} and the Hall current flows orthogonally to it. When \mathbf{M} is pointing along a general direction in the crystal the AHC vector can misalign with the magnetization direction, in which case [35, 38]:

$$\sigma(\mathbf{M}) = \sigma_{\parallel}(\mathbf{M}) + \sigma_{\perp}(\mathbf{M}), \quad (6.8)$$

where $\sigma_{\parallel}(\mathbf{M})$ and $\sigma_{\perp}(\mathbf{M})$ are the parallel and perpendicular to \mathbf{M} components of the AHC vector, respectively [35] (see also Fig. 6.4). Microscopically, the origin of the anisotropy of the AHE is apparent from the Berry curvature expression (6.2), which is dependent on the magnetization direction via the corresponding dependence of eigenenergies as well as wavefunctions. It is important to note that while in paramagnets with inversion symmetry the eigenspectrum does not depend on the SQA, the wavefunctions in a ferromagnet exhibit a far more complex dependence on \mathbf{M} , owing to the fact of broken time-reversal symmetry. Additionally, in uniaxial crystals, the velocity matrix elements are also anisotropic and this has to be taken into account.

Phenomenologically, the behavior of the anomalous Hall conductivity tensor $\sigma(\mathbf{M})$ with respect to orientation of \mathbf{M} can be described based on an expansion in powers of the direction cosines $\{\alpha_i\}$ of \mathbf{M} [3]:

$$\sigma_{ij}(\hat{\mathbf{M}}) = \sum_p a_{ijp} \alpha_p + \sum_{pqr} a_{ijpqr} \alpha_p \alpha_q \alpha_r + \dots, \quad (6.9)$$

where $\hat{\mathbf{M}}$ is the unit vector along \mathbf{M} . Only odd powers are participating in the expansion above owing to the fact that the AHC is odd under time reversal, $\sigma(-\mathbf{M}) = -\sigma(\mathbf{M})$. Additional constraints on the allowed terms in (6.9) are enforced by the crystal symmetry. Consistently with a small but non-vanishing AHC anisotropy measured in cubic ferromagnets [36–38], the expansion starts only with the 3rd-order term in cubic crystals. On the other hand, in uniaxial ferromagnets already the 1st-order term in (6.9) is allowed, and the corresponding anisotropy of the anomalous Hall effect can be very large [35, 39].

Theoretically, the microscopic explanation for a strongly anisotropic AHE in transition metals was given by Roman et al. [35]. The later work showed that the

main reason for the observed in agreement to experiment factor-of-four anisotropy of the intrinsic AHC in uniaxial hcp Co lies in the spiky and irregular behavior of the Berry curvature in the k -space. If we look at the distribution of the Berry curvature along the high symmetry lines for a typical uniaxial ferromagnet, such as $L1_0$ FePd (shown in Fig. 6.2), we observe the characteristic peaks in the vicinity of points of near-degeneracy across the Fermi level (around the M -point or in the middle of the ΓZ -path). The anisotropy of the wavefunctions and energies in the vicinity of these points results in the remarkable anisotropy of the Berry curvature in Fig. 6.2, both in magnitude (e.g. in the middle of the ΓZ -path) and sign (e.g. close to M -point). When integrated over the whole BZ, the anisotropy of the Berry curvature leads to a factor-of-two reduction in the AHC in FePd as the magnetization is changed from out-of-plane to in-plane. Overall, in accordance to experiments, the theoretically predicted small anisotropy of intrinsic AHC in bcc Fe (767 S/cm for [001]-direction of $\hat{\mathbf{M}}$ versus 810 S/cm for [110]-direction) is significantly enhanced in uniaxial hcp Co (477 vs. 100 S/cm for [001] and [100] directions, respectively), $L1_0$ FePt (818 vs. 409 S/cm for [001] and [110] directions, respectively), $L1_0$ FePd (135 vs. 276 S/cm for [001] and [110] directions respectively), and $L1_0$ CoPt (−119 vs. 107 S/cm for [001] and [110] directions respectively) [13]. The latter case of CoPt presents an example of the so-called anti-ordinary AHE, for which a certain angle of the magnetization with the crystallographic axes can be found so that the anomalous Hall current in aligned *along* the magnetization, in analogy to the planar Hall effect [31]. In CoPt this is the consequence of the fact that the $\sigma_{\parallel}(\mathbf{M})$ changes sign as \mathbf{M} is rotated from out-of-the-plane into the plane and eventually turns to zero for a certain angle, see Fig. 6.4c. This implies also the rotation of the Hall current in the opposite sense to that we would naively assume given an assumption that \mathbf{J}_H is always perpendicular to \mathbf{M} . On the side of the extrinsic AHE, recently, its pronounced anisotropy has been also found, both among the scattering-independent contributions [18] (see for example the anisotropy of the scattering-independent side-jump conductivity in fcc Ni as the magnetization direction is changed from [001] into [110] axis in Fig. 6.3b), as well as for the skew-scattering angle [44].

6.5 Quantum Anomalous Hall Effect

What is commonly referred to as the *Chern insulator* in solid state physics is a two-dimensional (2D) insulating solid with Hamiltonian $H(\mathbf{k})$ whose first Chern number, determined as an integral of the \mathbf{k} -space Berry curvature over the Brillouin zone, is a *non-zero* integer. The condition that the Chern number is non-zero means that the topological properties of our system are non-trivial, and that the wavefunction $u_{n\mathbf{k}}$ acquires a “twist” as we cross at least one of the equators of the 2D torus which represents the Brillouin zone. Chern insulator presents an example of a system for which the so-called periodic gauge in both k -directions cannot be found simultaneously. One of the most remarkable properties of Chern insulators is the quantization of their transverse Hall conductance according to (6.6):

$$\sigma_{xy} = \sum_n \frac{1}{2\pi} \int_{\text{BZ}} d\mathbf{k} \Omega_z^n(\mathbf{k}) = \sum_n C_n, \quad (6.10)$$

where C_n is the first Chern number of the occupied band n . From the point of view of adiabatic pumping, the quantization of the Hall conductance is due to the quantized charge which is pumped through the one-dimensional system along x described by Hamiltonian $H(k_x, k_y)$ as the parameter k_y is varied from one side of the BZ to the other.

Let us take a look at the mechanisms which can lead to appearance of Chern insulators. For this purpose we consider first the case of only two bands in \mathbf{k} -space. Neglecting the constant term, which does not change the topological properties and just shifts the energy, a generic 2D Hamiltonian reads:

$$H(\mathbf{k}) = \mathbf{d}(\mathbf{k}) \cdot \boldsymbol{\sigma}, \quad (6.11)$$

where $\boldsymbol{\sigma}$ is the vector of Pauli matrices. At each point in \mathbf{k} the energetic spectrum is given by two eigenvalues ε_+ and ε_- which are given by $\pm |\mathbf{d}(\mathbf{k})| = \pm d(\mathbf{k})$. Since the Berry curvature summed over both bands is always zero, we will consider only the lowest of the bands, ε_- . We also suppose that both bands are separated from each other by a gap. By comparing the Hamiltonian (6.11) to that of spin- $\frac{1}{2}$ in magnetic field, it can be shown that the physics of the problem is governed by the Dirac monopole problem [11]. Indeed, the Berry phase which is accumulated when going

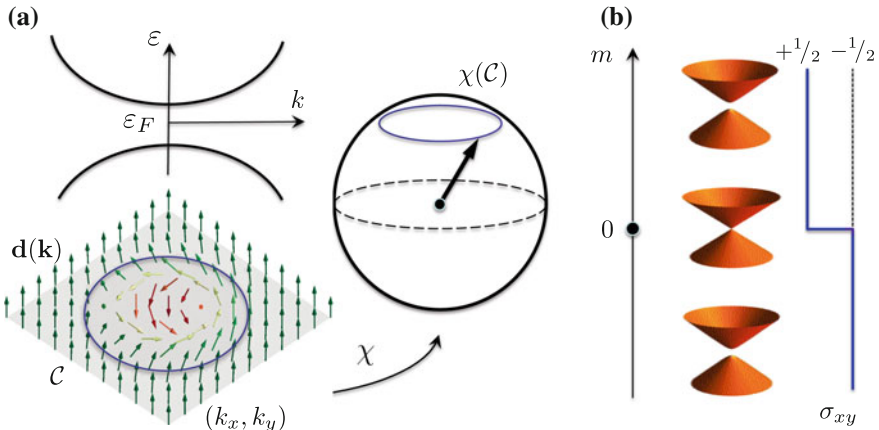


Fig. 6.5 **a** For a two-dimensional two-band insulator with the Hamiltonian $H(\mathbf{k}) = \mathbf{d}(\mathbf{k}) \cdot \boldsymbol{\sigma}$ the problem of finding the Berry curvature in k -space can be rewritten in terms of finding the winding number density of the vector field $\mathbf{d}(\mathbf{k})$. The whole problem can be mapped via transformation χ onto that of the spin- $\frac{1}{2}$ Dirac monopole. **b** A system described by two-dimensional massive Dirac Hamiltonian as given by (6.13) experiences a topological phase transition as a function of m , i.e. upon changing the sign of m across the metallic transition point at $m = 0$, the quantum Hall conductivity of the system as given by the Chern number changes by +1

along a closed loop \mathcal{C} in \mathbf{k} -space can be easily related to that picked up when going along a loop $\chi(\mathcal{C})$ on a unit sphere S^2 , where χ maps \mathbf{k} to the point \mathbf{d}/d on S^2 , see Fig. 6.5:

$$\chi : \mathbf{k} \longrightarrow \mathbf{n} = \mathbf{d}/d, \quad \mathbf{n} \in S^2. \quad (6.12)$$

The Berry curvature of the problem on S^2 is given by a field of the Dirac monopole with quantized charge at the origin, where the two bands touch each other and $\varepsilon_+ = \varepsilon_-$ [11]. The Berry curvature in the \mathbf{k} -space is readily obtained as $\Omega_{xy}(\mathbf{k}) = -\mathbf{n} \cdot (\partial_{k_x} \mathbf{n} \times \partial_{k_y} \mathbf{n})/2$, which in the physics of skyrmions is referred to as the density of topological charge. The physics of skyrmions emerging in real-space is discussed in detail in the first five chapters of this book. The first Chern number obtained as an integral of the Berry curvature over a *compact* manifold such as a 2D BZ, has to be an integer, and in the physics of skyrmions it is referred to the *winding number* and topological charge, since it stands for the number of times that the field $\mathbf{d}(\mathbf{k})$ winds around the S^2 as \mathbf{k} is varied.

The so-called massive Dirac Hamiltonian, which is of great importance for studying topological properties of solids, is given by ($d_x = k_x$, $d_y = k_y$ and $d_z = m$):

$$H(\mathbf{k}) = k_x \sigma_x + k_y \sigma_y + m \sigma_z. \quad (6.13)$$

The Berry curvature here can be evaluated analytically in \mathbb{R}^2 , and it is given by $\Omega_{xy}(\mathbf{k}) = m/[2(m^2 + k^2)^{3/2}]$, which leads to a half-integer Hall conductance $\sigma_{xy} = \text{sgn}(m)/2$ owing to the infinite size of the BZ over which the Berry curvature is integrated. At the point $m = 0$ in the Hamiltonian (6.13) there is a point of degeneracy in the spectrum at $k_x = k_y = 0$ and the transition between two Chern insulator phases for $m < 0$ and $m > 0$ occurs, see Fig. 6.5. Such situation is rather typical and can be generalized to the case of a 2D+1 Hamiltonian $H(k_x, k_y, \lambda) = H(\varkappa)$, where $\varkappa = (k_x, k_y, \lambda)$ and λ is a certain parameter, such as m in the Dirac model, values of hoppings in the lattice Hamiltonian, value of the spin-orbit strength, exchange field, magnetization direction, etc. According to the theorem by Bellisard [46], the change of the (k_x, k_y) Chern number when going through a point of degeneracy at a certain value of \varkappa^* (such as $(0, 0, 0)$ in the Dirac model) is given by the so-called *Berry index*:

$$\text{Indx}_B = \frac{1}{2\pi} \int_{S^2} \Omega_k(\varkappa) d\varkappa, \quad (6.14)$$

where S^2 is an infinitesimally small sphere which encloses \varkappa^* . Interestingly, the integer Berry index determines the change in the 2D Hall conductance irrespective of the compactness of the \mathbf{k} -space. E.g. for the massive Dirac Hamiltonian (6.13) the Berry index can be evaluated to be $+1$ at the point $(k_x = 0, k_y = 0, m = 0)$. It is worthy to note here that when the role of the parameter λ is played by the k_z Bloch vector of a 3D Hamiltonian $H(k_x, k_y, k_z)$, such points of degeneracy $\varkappa^* = \mathbf{k}^*$ are called here *Weyl points*. If such points happen to be present at the Fermi energy of a material with no other bands crossing it, such material is called a *topological metal*, or *Weyl semimetal*. The physics of topological metals is an exciting emerging field of

topological solid state physics. Chapter 8 of this book is dedicated to the fascinating properties of Weyl semimetals.

Historically, Thouless and co-workers [47] were the first to demonstrate that Chern insulators can arise for periodic 2D solids exposed to an external magnetic field, whose presence breaks the time-reversal symmetry and induces non-trivial geometry in the reciprocal space. Obtained in such a way Chern insulator can be named *quantum Hall insulator*, since the quantization of Hall conductance in such Chern insulators was observed in measurements of the integer quantum Hall effect. The quantum Hall insulators are to be distinguished from *spontaneous* Chern insulators, for which the Chern insulator state is realized without external fields, and the breaking of time-reversal symmetry is the intrinsic property of the material due to e.g. formation of local spin moments. We will refer to spontaneous Chern insulators as *quantum anomalous Hall insulators* (QAH insulators), since the quantization of conductance in QAH insulators is observed by measuring the anomalous Hall effect (AHE) for which external magnetic field plays a secondary role [9]. The corresponding effect is called the *quantum anomalous Hall effect* (QAHE), and its experimental observation has been recently presented [48].

Although the non-zero Chern number is due to non-trivial distribution of the Berry curvature in \mathbf{k} -space, a fruitful analysis of QAH phases can be achieved in real space by considering various mechanisms of electron hopping and interactions on a lattice, and corresponding tight-binding Hamiltonians. The first lattice model for a QAH insulator was given by Haldane [49]. The Hamiltonian on the honeycomb lattice within the spinless *Haldane model* looks very simple:

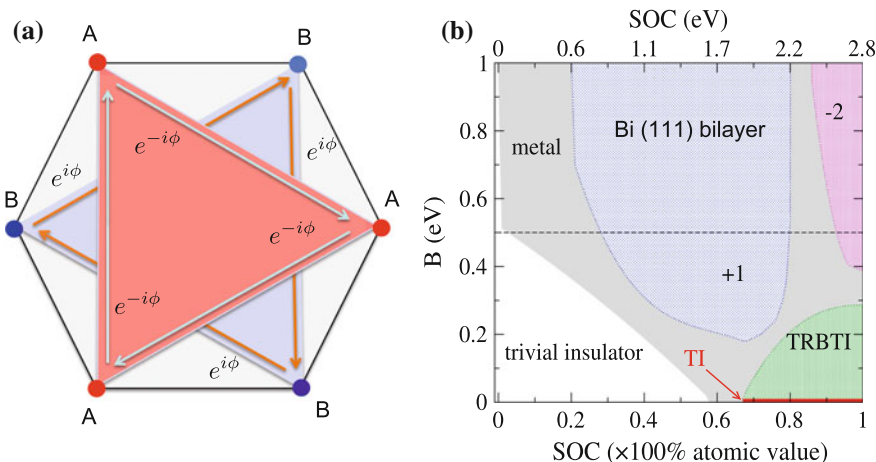


Fig. 6.6 **a** Real-space schematic representation of the Haldane model. **b** Right: The phase diagram of the Bi(111) bilayer with respect to the strength of atomic SOC and magnitude of exchange field B . Numbers denote the Chern number in the quantum anomalous Hall phase, “TI” stands for the topological insulator phase, while “TRBTI” stands for the time-reversal broken topological insulator phase. For more details see text and [45]

$$H = t_1 \sum_{\langle i, j \rangle} c_i^\dagger c_j + t_2 \sum_{\langle\langle i, j \rangle\rangle} e^{-i\sigma\phi} c_i^\dagger c_j, \quad (6.15)$$

where the first term corresponds to the hopping between the nearest neighbors, while the second term corresponds to the hopping between the next-nearest neighbors. The key feature of the Haldane model is that the next-nearest neighbor hopping t_2 acquires a complex phase $e^{-i\sigma\phi}$, where $\sigma = +1$ for the hopping on the A-sublattice, while $\sigma = -1$ for the hopping within the B-sublattice. The effect of acquiring a complex phase during electron hopping can be seen as a result of a fictitious magnetic field with the vector potential $\mathbf{A}(\mathbf{r})$: $e^{-i\phi} = e^{-i \int d\mathbf{r} \mathbf{A}(\mathbf{r})}$, where the integral is taken along the shortest path which connects the next-nearest neighbor sites. As the electron completes a closed path when hopping on the corresponding sublattice (see triangles in Fig. 6.6), it accumulates a phase which is proportional to the flux of the magnetic field through the corresponding triangle, in analogy to the Aharonov-Bohm effect. Since this phase is opposite for electrons of two sublattices, the total field acting on electrons averages to zero within the unit cell (the Haldane model is often called a model for a quantum Hall effect with zero magnetic field). Haldane showed by Fourier transforming the lattice Hamiltonian to the \mathbf{k} -space that the Chern number of this model equals $+1$ for $-\pi < \phi < 0$, and -1 for $0 < \phi < \pi$, see Fig. 6.6. The point $\phi = 0$ thus gives rise to Weyl points in (\mathbf{k}, ϕ) -space. Conceptually, the suggestion of his model by Haldane in 1988 stands at the origin of the tremendous advances in topological condensed matter physics which followed. One of the reasons for this is that the mechanism which gives non-zero Chern number within the Haldane model can be realized in actual materials, with intrinsic spin-orbit interaction (SOI) playing the role of the source of “fictitious” magnetic field which provides non-trivial band topology. To briefly demonstrate how this comes about we focus here on one of the many possible examples considered by now in the literature [50]. Namely, we consider the p_z orbitals on a strongly buckled honeycomb lattice of space-inversion symmetric (111) bilayer of Bismuth, see Fig. 6.7. The nearest-neighbor tight-binding multi-orbital lattice Hamiltonian of this system reads:

$$H = \sum_{ij} t_{ij} c_i^\dagger c_j + \sum_i c_i^\dagger (\varepsilon_i \mathbb{I} + B \sigma_z) c_i + H_{\text{SOC}}, \quad (6.16)$$

where the first term is the kinetic nearest-neighbor hopping between generally different multiple s and p (and d or f in transition and rare-earth metals) orbitals. The second term stands for an orbital on-site energy ε_i and the interaction with the Zeeman exchange field B directed along the z -axis, with \mathbb{I} (σ_z) as the identity (Pauli) matrix. The third term in Hamiltonian (6.16) is the on-site SOI Hamiltonian. Without the presence of B the system has time-reversal symmetry and its bands are degenerate in spin throughout the whole BZ. We use the exchange field to break the time-reversal symmetry and induce a non-zero QAH effect. To identify different origins of the Chern insulator phase, the spin-orbit interaction is further decomposed into spin-conserving and spin-flip parts:

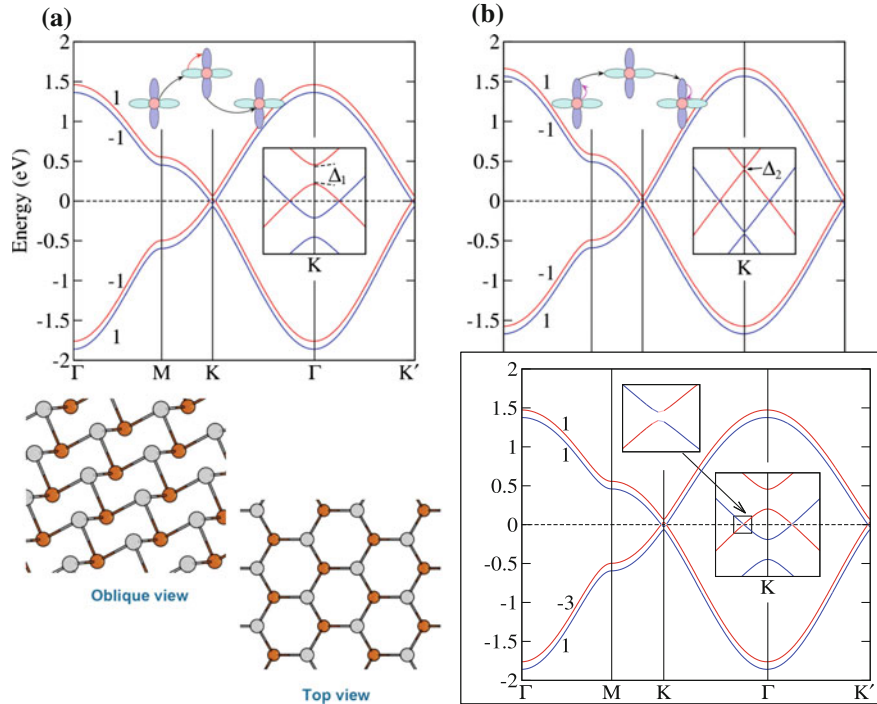


Fig. 6.7 Topological analysis of p_z bands in a buckled honeycomb bilayer. A small exchange field has been applied in all cases, yielding a QAH state in lower right figure. Without an exchange field, systems in **a** and **b** would be in a topological insulator state. Left up and right up figures correspond to the case with only spin-conserving SOC, and only spin-flip SOC included, while the full SOC is considered in the lower right figure. Red (blue) stands for the spin-down (spin-up) states. Dashed horizontal lines indicate the Fermi energy. In the case of isolated bands, numbers denote the Chern number for each individual band, while for overlapping bands, numbers stand for the Chern numbers of nonhybridizing spin-up (red) and spin-down (blue) bands. Insets display the electronic structure of the Dirac point at the Fermi energy, and sketches illustrate different channels for complex nearest-neighbor hopping [red circles denote p_z orbitals, while $p_{x,y}$ orbitals are indicated by blue ellipsoids; black (red) arrows depict the nearest-neighbor hoppings (SOC hybridization), respectively]. Lower left: top and side view of the Bi(111) bilayer. For more details see text and [45]

$$H_{\text{SOI}} = \xi \mathbf{l} \cdot \mathbf{s} = \xi l_z s_z + \xi (l^+ s^- + l^- s^+)/2, \quad (6.17)$$

where $\mathbf{l}(\mathbf{s})$ is the orbital (spin) angular momentum operator, and ξ is the atomic SOI strength. Since here we choose the direction of the spin-polarization to be aligned along z direction, the spin conserving part of the SOI, $\xi l_z s_z$, couples $\{p_x, p_y\}$ orbitals, while the spin-flip part of (6.17), $\xi (l^+ s^- + l^- s^+)/2$, couples p_z and $\{p_x, p_y\}$ orbitals via a flip of spin and a ± 1 change in the orbital quantum number.

We concentrate here only on the case of the p_z orbitals present around the Fermi energy, with other states being pushed away much higher in energy. This case is

particularly relevant for graphene physics. For the values of the spin-orbit strength and hopping parameters we choose those of Bi from [45]. First, consider the case when only spin-conserving SOI is present. On a buckled honeycomb lattice, such as Bi bilayer or silicene, p_z orbitals can hybridize directly with the $\{p_x, p_y\}$ orbitals on the neighboring site, and complex hoppings within the sublattice can be induced via the spin-conserving part of SOC which acts between p_x and p_y states. As illustrated with a sketch in Fig. 6.7, in this mechanism the corresponding virtual transitions read: $|p_z^A \uparrow\rangle \xrightarrow{t_{NN}} |p_{x,y}^B \uparrow\rangle \xrightarrow{\xi l_z s_z} |p_{x,y}^B \uparrow\rangle \xrightarrow{t_{NN}} |p_z^A \uparrow\rangle$, where t_{NN} indicates the direct hopping between p_z and $p_{x,y}$ orbitals on the neighboring sites, while superscripts A and B denote the nearest neighbor atomic sites in sublattice A and B. The SOI here acts as a magnetic field which is responsible for the generation of phase ϕ within the Haldane model. If we consider only one spin, we can indeed show that effective SOI induced next-nearest-neighbor (NNN) hopping leads to the opening of the gap at the Fermi energy (of the size Δ_1 in Fig. 6.7a) and the Chern number of the spin-up bands acquires a value of +1. Since the SOI coefficients are complex conjugate for spin-up and spin-down electrons, the ϕ of the complex hoppings for spin-down electrons is opposite in sign to spin-up electrons and same holds for the Chern numbers. Since the bands are spin-degenerate with $B = 0$ (we apply a small exchange field in Fig. 6.7 to artificially separate bands of opposite spin for visibility), this results in a zero total Chern number, and the system resides in a *topological insulator phase*.

On-site spin-flip SOI can give rise to complex next nearest neighbor hopping too, even if there is no direct hybridization between p_z and $\{p_x, p_y\}$ orbitals,

Fig. 6.7b. In this case, the corresponding virtual transitions are: $|p_z^A \uparrow\rangle \xrightarrow{\xi_{\text{flip}}} |p_{x,y}^A \downarrow\rangle \xrightarrow{t_{NN}} |p_{x,y}^B \downarrow\rangle \xrightarrow{t_{NN}} |p_{x,y}^A \downarrow\rangle \xrightarrow{\xi_{\text{flip}}} |p_z^A \uparrow\rangle$ where $\xi_{\text{flip}} = \xi(l^+s^- + l^-s^+)/2$, and t_{NN} stands for the direct hybridization between $p_{x,y}$ orbitals on neighboring A and B sites. The corresponding NNN hopping is again between electrons of the same spin, owing to two spin-flip processes which take place in between. In analogy to the case with spin-conserving SOI considered previously, the effective hoppings within A and B sublattices for fixed spin are of opposite sign and the resulting gap Δ_2 which opens due to latter virtual transitions is again topologically nontrivial. The resulting non-zero Chern numbers of the degenerate without B spin-up and spin-down bands are exactly the same as previously. As in the previous case, the coupling between the spin-up and spin-down p_z bands does not occur, and without an exchange field, Fig. 6.7b corresponds exactly to the topological insulator phase in graphene [51].

How do we make Chern insulators out of systems above? In principle, if we could apply a very strong exchange field which would shift the bands of a certain spin very high up in energy, we would readily obtain a QAH insulator. In real materials this is however seldomly achievable, since the magnitudes of typical exchange fields are normally smaller than the typical band width. Thus, the only way would be in breaking the time-reversal symmetry with a finite B , and ensuring that a topologically non-trivial band gap opens at the Fermi energy where bands of opposite spin meet. For example, we could start with a situation depicted in Fig. 6.7a with a small B , and add an admixture of the spin-flip SOI to the Hamiltonian. This will open a gap

at the points where the spin-up and spin-down bands were degenerate, see Fig. 6.7. In the vicinity of such a point the distribution of spin becomes non-trivial, as we can see in Fig. 6.7, namely, e.g. at the K-point the spin-distribution of the occupied band has a skyrmion structure. At this point, we can relate the distribution of spin to the distribution of vector $\mathbf{d}(\mathbf{k})$ and, according to the two-band analysis presented above, we can explain the fact that the Chern number of the occupied band changes. The spin distribution of the corresponding conduction band is also a skyrmion, but with an opposite winding number, which results in the opposite change of the Chern number of this band. What we have just achieved is the QAH state driven the exchange of the Chern number between the bands of opposite spin at the points at the Fermi energy where bands of opposite spin hybridize. Such points are called *spin-mixing points*.

We remark here, that Hamiltonians of real materials can be very complicated with many states present at the Fermi energy and various structural, spin-orbit and magnetic effects taking place. The phase diagrams of such materials as a function of parameters in the Hamiltonian can be studied from first principles methods. See for example the phase diagram of Bi(111) bilayer as a function of an exchange field and SOI strength calculated from ab initio in Fig. 6.6. So far, experimentally, the emergence of the QAHE has been demonstrated notably in Cr- and V-doped (Sb,Bi)₂Te₃ thin films at very low sub-100 mK temperatures [48, 52]. On the other hand the area of theoretical proposals for systems which would potentially exhibit the QAHE even at room temperatures, exploiting the complexity of the electronic structure that we discussed above, is blossoming, and here we can only mention a few. Historically one of the first suggestions employed the topologically non-trivial electronic structure of HgTe quantum wells, which were suggested to turn into the QAH insulator by magnetic doping [53], and a similar proposal has been made for InAs/GaSb quantum wells [54]. A whole promising class of systems is associated with graphene and other honeycomb-lattice materials (such as silicene) exposed to an exchange field and Rashba spin-orbit interaction as in the case of graphene decorated with transition-metal adatoms [55–57], or graphene magnetized by proximity with e.g. BiFeO₃ [58]. An alternative mechanism for magnetizing the topologically non-trivial materials is associated with functionalization: e.g. half-I-passivated stanene [59] or half-H-passivated Bi(111) bilayer [60] establish ferromagnetism due to dangling bonds, and can lead to the quantized AHC, see Fig. 6.8. While it was shown that systems which combine strong spin-orbit interaction and strong exchange in heavy transition-metal insulators such as EuS, CdO/EuO quantum wells, GdN/EuO bilayers, or 5d transition-metal trichlorides such as OsCl₃, can give rise to QAHE [61–64], the physics of transition-metal oxides is also promising for the realization of this effect in, e.g., SrIr/TiO₃ [65] or La₂MnIrO₆ [66].

While we have been discussing the quantized transverse charge conductance in Chern insulators, more generally, it can be shown that although in case of 2D insulators with time-reversal symmetry the transverse charge conductance has to vanish identically, the carriers of each spin separately, however, can possess a quantized Hall conductance of opposite sign. In an applied electric field the carriers of opposite spin will move in opposite directions, which will lead to the generation of the transverse *spin current*. Thus obtained spin conductance is quantized since the conductance

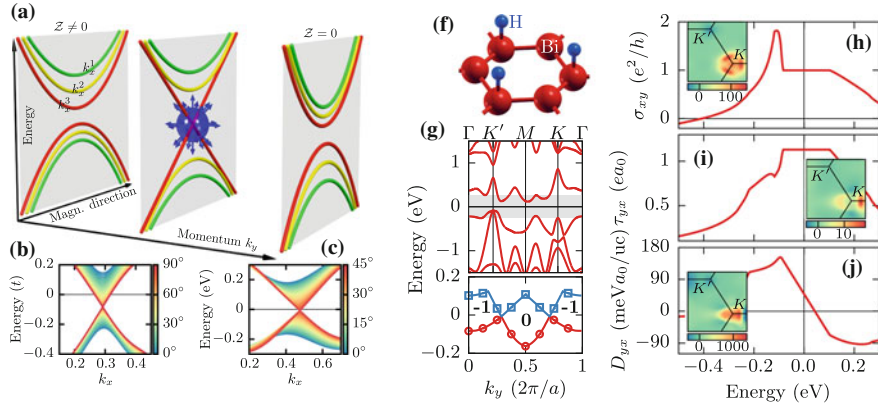


Fig. 6.8 **a** Schematic evolution of two energy bands in the complex phase space of crystal momentum and magnetization direction, where the colors of the bands indicate different k_x . If k_y is tuned, the electronic structure displays a monopole, which is correlated with a change in the mixed Chern number \mathcal{Z} . Such crossing points are observed in **(b)** the model of magnetically doped graphene with hopping t , and **(c)** the functionalized bismuth film. **f** Crystal structure of the semihydrogenated Bi(111) bilayer. **g** Top: First-principles band structure of the system for an out-of-plane magnetization, where the region of the topologically non-trivial band gap is highlighted. Bottom: Evolution of top of valence band (red circles) and bottom of conduction band (blue squares) in the (k_x, θ) -space. Bold integers denote the mixed Chern number \mathcal{Z} , and a is the in-plane lattice constant. **h–j** Energy dependence of AHC, torkance τ_{yx} , and DM spiralization D_{yx} , respectively, for an out-of-plane magnetization. For more details see text and [67]

for each spin is quantized, and it is proportional to the difference between the Chern numbers for each spin. This number is called the *spin Chern number*, and it is defined modulo 2. The system which exhibits a spin Chern number of $+1 \pmod{2}$ is called a *quantum spin Hall* (QSH) insulator, or, equivalently, a 2D *topological insulator*. In the definition above we required a clear separation of electronic states into spin-up and spin-down manifolds, which is naturally present if the spin-mixing part of the spin-orbit interaction is not considered. And while with full spin-orbit interaction present in the system the spin is not a good quantum number anymore, the concept of the spin Chern number can be generalized to this case as well. For 2D insulators with time-inversion the spin Chern number can be used alternatively to the \mathbb{Z}_2 index in order to classify topological phases [68].

The emergence of monopoles in the electronic structure which give rise to large values of the Berry curvature and quantization of Hall conductance in \mathbf{k} -space, can also have a strong impact on the mixed Berry curvature with respect to a parameter which is responsible for generation of such points. This closely relates the physics of the AHE and QAHE to the physics of “topologically-associated” effects. One of the most prominent examples of a typical parameter which can be used to change the topology and generate monopoles in the extended space is the magnetization direction $\hat{\mathbf{M}}$ in a 2D ferromagnet, which we characterize here with a single angle θ with respect to e.g. the z -axis. The “topological partner” of the AHE in this case

which is driven by the mixed component of the Berry curvature tensor $\Omega_{\mathbf{k}\theta}$, is the anti-damping spin-orbit torque (SOT). The effect of SOT provides an efficient means of magnetization control by electrical currents in systems that combine broken spatial inversion symmetry and spin-orbit interaction [69–71]. These current-induced torques are believed to play a key role in the practical implementation of various spintronics concepts, since they were demonstrated to mediate the switching of single ferromagnetic layers [72, 73] and antiferromagnets [74] via the exchange of spin angular momentum between the crystal lattice and the (staggered) collinear magnetization. Among the two different contributions to SOTs, the so-called (intrinsic) anti-damping SOTs are of utter importance owing to the robustness of their properties with respect to details of disorder [75], in analogy to the intrinsic AHE. The SOT in relation to topological properties of antiferromagnets is discussed in Chap. 9 of this book.

In a clean sample, the anti-damping SOT \mathbf{T} acting on the magnetization in linear response to the electric field \mathbf{E} is mediated by the so-called torkance tensor τ , i.e., $\mathbf{T} = \tau \mathbf{E}$ [75]. The Berry phase nature of the anti-damping SOT manifests in the fact that the tensor elements τ_{ij} are proportional to the mixed Berry curvature of all occupied states in the following way:

$$\tau_{ij} = \frac{2e}{N_{\mathbf{k}}} \hat{\mathbf{e}}_i \cdot \sum_{\mathbf{k}n}^{\text{occ}} \left[\hat{\mathbf{M}} \times \text{Im} \langle \partial_{\hat{\mathbf{M}}} u_{\mathbf{k}n} | \partial_{k_j} u_{\mathbf{k}n} \rangle \right], \quad (6.18)$$

where $N_{\mathbf{k}}$ is the number of \mathbf{k} -points, $e > 0$ denotes the elementary positive charge, and $\hat{\mathbf{e}}_i$ denotes the i th Cartesian unit vector. Intimately related to the anti-damping SOT is the Dzyaloshinskii-Moriya interaction (DMI) [76, 77], crucial for the emergence of chiral domain walls and chiral skyrmions [78–81], which can be quantified by the so-called spiralization tensor D reflecting the change of the free energy F due to chiral perturbations $\partial_j \hat{\mathbf{M}}$ according to $F = \sum_{ij} D_{ij} \hat{\mathbf{e}}_i \cdot (\hat{\mathbf{M}} \times \partial_j \hat{\mathbf{M}})$ [82]. The spiralization [82] is obtained as

$$D_{ij} = \frac{\hat{\mathbf{e}}_i}{N_{\mathbf{k}} V} \cdot \sum_{\mathbf{k}n}^{\text{occ}} \left[\hat{\mathbf{M}} \times \text{Im} \langle \partial_{\hat{\mathbf{M}}} u_{\mathbf{k}n} | h_{\mathbf{k}n} | \partial_{k_j} u_{\mathbf{k}n} \rangle \right], \quad (6.19)$$

where $h_{\mathbf{k}n} = H_{\mathbf{k}} + \varepsilon_{\mathbf{k}n} - 2\varepsilon_F$ and V is the unit cell volume. The SOT and DMI are thus related similarly to the way that the AHC and the orbital magnetization are connected to each other (see next section). For more details on the role and properties of the DMI see also chapters one to five.

As discussed previously, the presence of Weyl points, or, as we shall refer to them to distinguish the considered case, *mixed* Weyl points, in the electronic structure of the system in (k_x, k_y, θ) -space generates a flux of the Berry curvature around them which is determined by the Berry index, and leads not only to enhanced values of $\Omega_{\mathbf{k}}$ in their proximity, but also results in large values of $\Omega_{\mathbf{k}\theta}$, as should be manifested in large values of SOT and DMI. We refer to a system which exhibits only isolated mixed Weyl points at the Fermi energy in its electronic structure in

(k_x, k_y, θ) -space as a *mixed* Weyl semimetal (MWS) [67]. The Berry index of a mixed Weyl point can be probed by the change in the *mixed* Chern number, defined by $\mathcal{Z} = 1/(2\pi) \int \Omega_{k_x \theta} d\theta dk_x$, as k_y is varied (see Fig. 6.8), and/or by the change in the (k_x, k_y) -Chern number as the angle θ is varied. The latter observation is an indication that the mixed Weyl state is closely associated with a topological phase transition between a QAH and trivial insulator state. While the MWS nature of a graphene-based models has been demonstrated, see also Fig. 6.8, one of the more prominent MWS examples is semihydrogenated Bi(111) bilayer, which is a Chern insulator for an out-of-plane magnetization [67]. Analyzing the evolution of the mixed Chern number \mathcal{Z} as a function of k_y in Fig. 6.8g for the latter system, we detect two magnetic monopoles of opposite charge that emerge at the transition points between the topologically distinct phases with $\mathcal{Z} = -1$ and $\mathcal{Z} = 0$. Alternatively, these crossing points and the monopole charges in the composite phase space could be identified by monitoring the variation of the momentum-space Chern number with magnetization direction. These monopoles, acting as sources of the general curvature, occur at generic points near the valley K for $\theta = 43^\circ$ (see Fig. 6.8c) and in the vicinity of the K' -point for $\theta = 137^\circ$, respectively. For an out-of-plane magnetization, the complex nature of the electronic structure in momentum space manifests in the quantization of \mathcal{C} to $+1$, Fig. 6.8h, which is primarily due to the pronounced positive contributions near K . Calculations of the energy dependence of the torkance and spiralization in the system, shown in Fig. 6.8i and j, reveal the extraordinary magnitudes of these phenomena of the order of $1.1 \text{ } ea_0$ for τ_{yx} and $50 \text{ meV}a_0/\text{uc}$ for D_{yx} , exceeding the typical magnitudes of these effects in magnetic metallic materials.

Clearly, the magnetization switching via anti-damping SOTs in mixed Weyl semimetals can be utilized to induce topological phase transitions from a CI to a trivial magnetic insulator mediated by the complex interplay between magnetization direction and momentum-space topology in these systems. In the case of the functionalized Bi film, for instance, the material is a trivial magnetic insulator if $\hat{\mathbf{M}}$ is oriented parallel to the film plane. Overall, combining an exceptional electric-field response with a large band gap, the H-functionalized bismuth film serves as a distinct representative of a class of MWS materials, which lay out extremely promising vistas in room-temperature applications of magnetoelectric coupling phenomena for low-dissipation magnetization control (see e.g. [85, 86]). In the example considered here, the DMI changes over a wide range of values throughout the bulk band gap, implying that proper electronic-structure engineering enables us to tailor both strength and sign of the DMI in a given system, for example, by doping or applying strain. Such versatility could be particularly valuable for the stabilization of chiral magnetic structures such as skyrmions in insulating ferromagnets. In the latter case, very large values of the anti-damping SOT arising in these systems would open exciting perspectives in manipulation and dynamical properties of chiral objects associated with minimal energy consumption by magnetoelectric coupling effects. At the end, we would like to remark that magnetic monopoles in the composite phase space, which we discuss here, do not only govern the electric-field response in insulating magnets but are also relevant in metals, where they appear on the background of metallic bands.

6.6 AHE and Orbital Magnetism in Non-collinear Magnets

One of the most remarkable features of the AHE is that it emerges even in antiferromagnetic materials, i.e., antiferromagnets (AFMs), for which the overall spin magnetization, when integrated over the magnetic unit cell, vanishes. In contrast to the spin Hall effect [87], in collinear AFMs consisting of two identical “ferromagnetic” spin sublattices which point in opposite directions and are related to each other by a combined action of the time reversal symmetry and lattice translation, the AHE has to vanish by symmetry. However, generally speaking, in chiral non-collinear AFMs, the symmetry does not forbid the emergence of the AHE, and two distinct cases of its emergence can be distinguished. The first scenario relies on the observation that although in coplanar non-collinear AFMs the net moment is zero, the lowering of the symmetries due to non-collinearity in combination with SOC gives rise to a non-zero Berry curvature distribution in the Brillouin zone [83, 88] (see Fig. 6.9 for an illustration), with a net non-vanishing value of the AHC, which can be measured experimentally, as e.g. for Mn_3Sn and Mn_3Ge [89, 90]. The latter effect can be also seen as a consequence of the orbital Aharonov-Bohm effect of conduction electrons which acquire a non-zero Berry phase as they are hopping within an intricate wavefunction of d -electrons in a non-collinear host [91, 92]. The AHE and its pronounced anisotropy has been recently for example analyzed from ab-initio calculations in Mn_3X ($\text{X} = \text{Ga, Ge, Sn, Rh, Ir, Pt}$) coplanar antiferromagnets [93].

Within the second scenario for the emergence of the AHE in AFMs the role of the spin-orbit interaction in giving rise to the Hall current is taken over by the so-called scalar spin-chirality ξ , which, given three neighboring spins on a lattice (\mathbf{S}_1 , \mathbf{S}_2 and \mathbf{S}_3), can be defined according to $\xi = \mathbf{S}_1 \cdot (\mathbf{S}_1 \times \mathbf{S}_2)$, and which does not vanish if the three spins are non-coplanar. Effectively, in a system with non-zero ξ , an electron hopping on a lattice of non-collinear spins acquires a non-vanishing spin Berry phase, which can be understood as a consequence of an Aharonov-Bohm effect of electron spins in a “fictitious” magnetic field originated in ξ rather than in SOC [94, 95]. In fact, assuming that the angle between the three neighboring spins is infinitesimally small, we realize that ξ is nothing else but an infinitesimal solid angle between them, and can thus directly relate the scalar spin chirality to the magnitude of an “emergent” magnetic field (or, equivalently, density of topological charge) proportional to $\hat{\mathbf{M}} \cdot (\partial_x \hat{\mathbf{M}} \times \partial_y \hat{\mathbf{M}})$ generated by a two-dimensional xy -texture of the magnetization, such as for example a skyrmion. Since the emergent magnetic field in skyrmion lattices gives rise to the spin-dependent Lorentz force and the so-called *topological Hall effect* (THE) [79, 80, 95], the AHE in non-collinear magnets with non-vanishing ξ is often referred to by the same name, although one has to remember that while for skyrmions the topological Hall effect is the consequence of the Berry curvature in real space, the AHE in non-collinear magnets is driven by the Berry curvature in \mathbf{k} -space, and the difference between the two effects should be prominent e.g. in the different scaling with respect to the scattering rates in the presence of disorder [78]. It seems plausible that in non-collinear non-coplanar magnets both contributions which originate in the

emergent field rather than SOC (one stemming from the Lorentz force, i.e. THE, and the other in the anomalous velocity, i.e. AHE) should co-exist and contribute to the overall Hall signal (see corresponding discussion of the emergence of transverse pure *spin* currents in non-collinear magnets in [96, 97]).

The fingerprints of the scalar chirality-driven origin of the AHE have been demonstrated experimentally already for the pyrochlore oxide compounds such as $\text{Pr}_2\text{Ir}_2\text{O}_7$ or $\text{Nd}_2\text{Mo}_2\text{O}_7$, e.g. [98–100], where relatively small values of the AHC are typical. Recent theoretical and experimental proposal suggest a much larger magnitude of the chirality-driven AHE in antiferromagnetic Mn-based metallic compounds [83, 101, 102], see e.g. Fig. 6.10d, or non-collinear structures at surfaces such as nanoskyrmions [103] or frustrated spin lattices [84, 104]. As was shown theoretically for a frustrated 3×3 spin lattice emerging in an Fe monolayer deposited on Ir(001) [84], the lowering of symmetry at a surface makes it difficult to disentangle unambiguously the contributions to the AHE coming from scalar chirality and spin-orbit interaction, while both conceptually different channels can together give rise to gigantic values of the surface topological Hall effect, see Fig. 6.9. The scalar chirality mechanism alone can also lead to the emergence of the quantum anomalous Hall effect, e.g. it was predicted theoretically that non-collinearity in a layered oxide $\text{K}_{0.5}\text{RhO}_2$ leads to the formation of a Chern insulator gap of the size of 0.22 eV, for

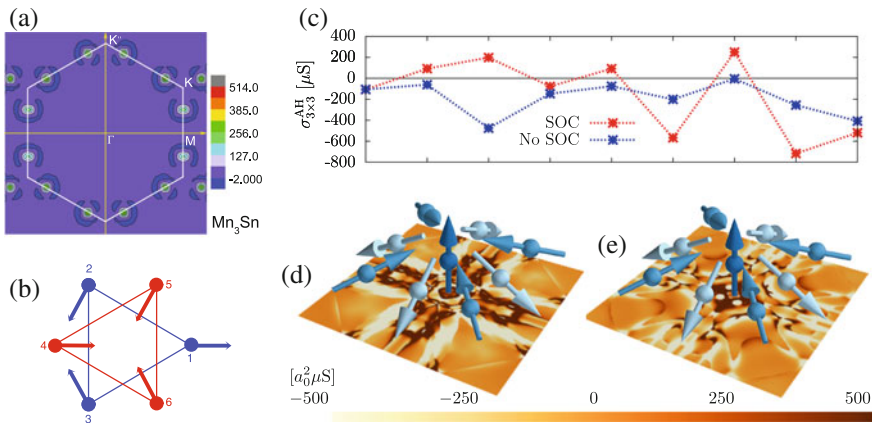


Fig. 6.9 The breaking of symmetry in coplanar non-collinear antiferromagnets in combination with SOC gives rise to the non-vanishing AHE and distribution of the Berry curvature in the reciprocal space, exemplified in (a) for a spin configuration of Mn_3Sn (b) considered in [83]. For chiral non-coplanar AFMs arising also at surfaces, the non-zero scalar spin chirality gives rise to the AHE prominent even without SOC: compare e.g. the values of the AHC for a 3×3 spin lattice of an Fe monolayer on Ir(001) surface (the real-space distribution of Fe moments is shown on top of the Brillouin zone in (e)) for the case with and without SOC and as functions of thickness in (c) [84]. The breaking of symmetry necessary for emergence of the Berry curvature in \mathbf{k} -space even without SOC is visible in (d) for the latter system, while adding SOC can influence the details of the Berry curvature distribution significantly (e)

which the effect of SOC is not crucial [105]. The rigorous relation between the AHE and symmetries in antiferromagnets is discussed in detail in chap. 9 of this book.

A deep relation between the anomalous Hall effect and the orbital magnetism has been discovered recently, after it was realized that our understanding of orbital magnetism in solids has been poor so far, and an ability to describe it reliably has been missing. Both spin and orbital magnetization (OM) are accessible separately, e.g., by means of magneto-mechanical or magnetic circular dichroism measurements, but the orbital contribution to the magnetization of solids is usually overshadowed by the spin counterpart, owing to the orbital moment quenching. However, in certain systems the OM yields an equally important contribution, which can even result in a spin-orbital compensation of magnetization. Its influence on spin-dependent transport magnetic susceptibility, orbital magnetoelectric response, magnetic anisotropy, and Dzyaloshinskii-Moriya interaction renders the OM crucial for understanding basic properties of magnets. A spontaneous OM in ferromagnets is a key manifestation of the spin-orbit interaction, lifting in part the quenching mechanism. Addressing the OM in solids is a subtle point as the position operator \mathbf{r} is ill-defined in the basis of extended Bloch states. Rather recently, a rigorous viewpoint at the OM was established within the so-called *modern theory* [8, 107], whose main result is that the OM at zero temperature is expressed as a genuine bulk property evaluated from the ground-state wave functions:

$$\mathbf{M} = \frac{e}{2\hbar} \int [dk] \left[\mathbf{m}_n(\mathbf{k}) + (\varepsilon_{n\mathbf{k}} - \varepsilon_F) \boldsymbol{\Omega}_{\mathbf{k}}^n \right], \quad (6.20)$$

where $[dk]$ stands for $\sum_n^{\text{occ}} d\mathbf{k}/(2\pi)^3$, and $\mathbf{m}(\mathbf{k}) = \text{Im} \langle \partial_{\mathbf{k}} u_{n\mathbf{k}} | \times [\varepsilon_{n\mathbf{k}} - H_{\mathbf{k}}] | \partial_{\mathbf{k}} u_{n\mathbf{k}} \rangle$ is the local wavepacket orbital moment. In a simple picture the contribution of the AHE to the OM, apparent in the equation above, comes from the circulating anomalous Hall currents which arise at the boundaries of a finite sample in response to the gradient of the crystal potential which builds up there, and which translates into the Berry curvature contribution when the thermodynamic limit of increasing the sample size is taken [8]. The modern theory expression has been applied in practise only a few times so far, but it seems that the large discrepancy between the OM evaluated according to (6.20) as compared to more simplistic approaches calls for our re-evaluation of the orbital physics in structurally, chemically and magnetically complex magnets [104]. One of the deep consequences of the geometrical nature of the OM is that, in contrast to the spin, the magnitude of the OM in the vicinity of band crossings can reach gigantic values, in analogy to the \mathbf{k} -space Berry curvature [108], see for example Fig. 6.10f. This observation has very far-reaching consequences for the magnitude of effects which are directly associated with the orbital magnetization at the Fermi surface, which concerns for example the orbital magnetoelectric effect, as recently discussed in the context of orbital Edelstein effect [109] and gyrotropic magnetic effect [110].

As far as non-collinear magnets are concerned, (6.20), which quantifies the relation between the AHE and the OM, hints at a possibility of observing non-vanishing orbital magnetization in chiral AFMs with vanishing spin magnetization, with OM

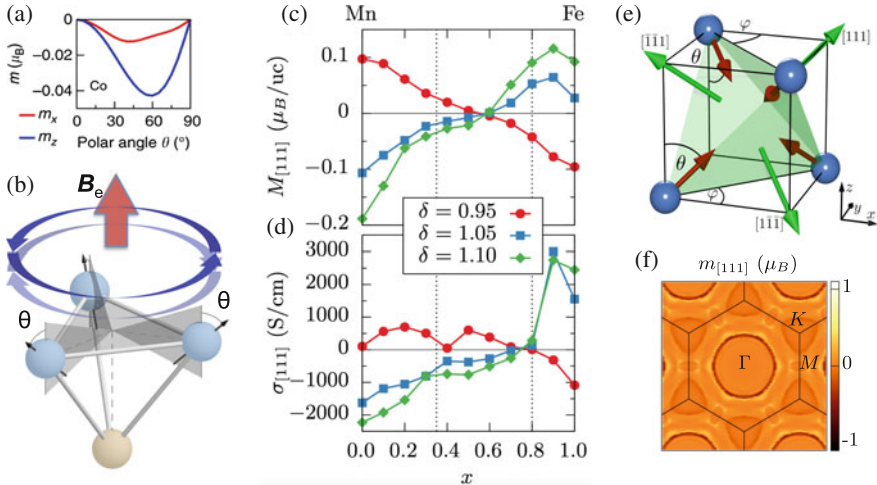


Fig. 6.10 In a situation of three spins on a surface with non-vanishing scalar spin chirality, the emergent magnetic field \mathbf{B}_e breaks the degeneracy between electronic states which realize left-propagating and right-propagating currents (b), resulting thus in a finite value of the out-of-plane (z) orbital moment even without SOC, as exemplified e.g. by ab-initio calculations for the m_z component of the orbital moment of a Co atom in a non-collinear Co trimer on Cu(111) (a). a is taken from [106]. In $\gamma\text{-Fe}_x\text{Mn}_{1-x}$ alloys which exhibit a $3Q$ -state (Fig. 6.10e) in a wide range of concentration x the topological orbital magnetization $M_{[111]}$ emerges upon a distortion along [111]-axis (quantified by parameter δ), c, accompanied by pronounced AHC, $\sigma_{[111]}$. Taken from [102], (d). The characteristic distribution of the topological orbital magnetization in the reciprocal space is shown in (f)

being rooted in the scalar spin chirality rather than SOC, in analogy to the topological Hall effect discussed above [94]. The origin of this remarkable phenomenon can be attributed to the effect of the emergent magnetic field in systems with scalar spin chirality, which couples to the orbital degree of freedom and breaks the degeneracy between the states in the electronic structure which carry right and left propagating currents, thus giving rise to the orbital moment, see Fig. 6.10b. As in the case of the AHE, the role of the emergent field in giving rise to the OM is undertaken by SOI in ferromagnets and co-planar antiferromagnets. While the relevance of this effect for finite non-collinear clusters has been recently confirmed theoretically [106], see Fig. 6.10a, the OM of infinite solids which originates in the scalar chirality is known as the *topological orbital magnetization* (TOM) [84], and its emergence has been studied in several works.

For prototypical antiferromagnetic $\gamma\text{-Fe}_x\text{Mn}_{1-x}$ alloys with the so-called $3Q$ spin structure, depicted in Fig. 6.10e, the emergence of the orbital magnetization of the order of $0.1\mu_B$ per unit cell and large AHE of the order of 1000 S/cm , shown in Fig. 6.10c, d, arising upon introducing a distortion along the [111]-axis (quantified by a parameter $\delta = d'/d$ where d and d' refer to the distance between adjacent (111) planes in the undistorted and distorted case, respectively) and tuning

the concentration x , has been shown in [102]. The values of the OM and AHC in this family of alloys were solely attributed to the spin-chirality mechanism, while the effect of SOC was found to be negligible. Since the spin magnetization in the $3Q$ -state is vanishing, the system thus presents an example of a *topological orbital ferromagnet* (TOF), i.e. a compensated AFM, whose macroscopic orbital magnetization is completely determined by the spin topology in real space without reference to SOI. Theoretical calculations also clearly indicate that both magnitude and sign of the TOM in TOFs can be controlled efficiently by means of proper electronic-structure engineering through application of strain and variation of the concentration in alloys, see Fig. 6.10. The magnitude of the OM in γ -FeMn can be enhanced even further by considering thin films with noncollinear spin textures. For example, in another TOF—a Mn monolayer deposited on Cu(111) which exhibits an in-plane $3Q$ -state in its ground state—the magnitude of TOM reaches as much as $1.5 \mu_B$, being very strongly correlated with the AHE in this system [104]. Another theoretical study performed for an Fe monolayer on Ir(001) surface indicates that in general, both SOC and scalar spin chirality can compete for the final value of the OM in low-dimensional antiferromagnets [84]. On the side of large-scale non-collinear structures, topological orbital magnetism emerges naturally in chiral skyrmions of various size [106, 111].

In a wider context, as compared to the spin of electrons, the orbital degrees of freedom offer higher flexibility regarding their internal structure and the size of orbital moments, rendering them versatile operational building blocks in the field of *orbitronics*. In this respect, TOFs as a new class of materials occupy a special place since their nontrivial orbital magnetism is a direct consequence of complex spin arrangement. This means that the properties of TOFs can be directly tuned by altering the latter spin distribution, e.g., via electric-field-induced spin torques [74] or by modifying the strength of the spin-spin interactions. The emergence of sizeable TOM zero-spin-magnetization TOFs opens a path to intriguing physics as orbital moments couple to external magnetic fields, optical perturbations, and orbital currents. For example, it is known that the chiral correlation between the spins on a lattice can display high stability with respect to fluctuations (see e.g. [112]), and one can expect that the long-range ferromagnetism of TOFs can survive the ordering temperature of the spin state. In addition, effective spin Hamiltonians used to describe the phase diagrams of TOFs in an external magnetic field require an amendment by the orbital Zeeman energy. The latter interaction of TOM with external magnetic fields can be also utilized to control the chirality of the spin texture owing to the close correlation between the spin structure and TOM.

Acknowledgements I would like to thank Frank Freimuth, Hongbin Zhang, Jürgen Weischenberg, Jan-Philipp Hanke, Patrick Buhl, Chengwang Niu, Gustav Bihlmayer, Klaus Seemann, Christopher Marrows, Martin Gradhand, Diemo Ködderitzsch, Hubert Ebert, Jairo Sinova, Stefan Blügel, Jakub Železný, Bernd Zimmermann and Ivo Souza for numerous discussions on the anomalous Hall effect.

References

1. E.H. Hall, Am. J. Math. **2**, 287 (1879)
2. E.H. Hall, Philos. Mag. **10**, 301 (1880)
3. C.M. Hurd, (Plenum, New York, 1972)
4. C.L. Chien, C.R. Westgate, (Plenum, New York, 1980)
5. J.E. Hirsch, Phys. Rev. Lett. **83**, 1834 (1999)
6. J. Sinova et al., Phys. Rev. Lett. **92**, 126603 (2004)
7. N.A. Sinitsyn, J. Phys.: Condens. Matter **20**, 023201 (2008)
8. D. Xiao, M.-C. Chang, Q. Niu, Rev. Mod. Phys. **82**, 1959 (2010)
9. N. Nagaosa, J. Sinova, S. Onoda, A.H. MacDonald, N.P. Ong, Rev. Mod. Phys. **82**, 1539 (2010)
10. M.V. Berry, Proc. R. Soc. Lond. A **392**, 45 (1984)
11. A. Bohm, A. Mostafazadeh, H. Koizumi, Q. Niu, J. Zwanziger, *The Geometric Phase in Quantum Systems* (Springer, Berlin, 2003)
12. Y. Yao et al., Phys. Rev. Lett. **92**, 037204 (2004)
13. Y. Mokrousov et al., J. Phys.: Cond. Mat. **25**, 163201 (2013)
14. T. Jungwirth, Q. Niu, A.H. MacDonald, Phys. Rev. Lett. **88**, 207208 (2002)
15. T. Jungwirth et al., Appl. Phys. Lett. **83**, 320 (2003)
16. Z. Fang et al., Science **302**, 92 (2003)
17. P. Czaja et al., Phys. Rev. B **89**, 014411 (2014)
18. J. Weischenberg et al., Phys. Rev. Lett. **89**, 014411 (2014)
19. B. Zimmermann et al., Phys. Rev. B **90**, 220403 (2014)
20. P.N. Dheer, Phys. Rev. **156**, 637 (1967)
21. J. Kötzler, W. Gil, Phys. Rev. B **72**, 060412 (2005)
22. J. Smit, Physica **21**, 877 (1955)
23. Y. Tian et al., Phys. Rev. Lett. **103**, 087206 (2009)
24. S. Lowitzer et al., Phys. Rev. Lett. **105**, 266604 (2010)
25. H. Ebert et al., Phys. Rev. B **91**, 165132 (2015)
26. X. Wang, D. Vanderbilt, J.R. Yates, I. Souza, Phys. Rev. B **76**, 195109 (2007)
27. M. Bode et al., Phys. Rev. Lett. **89**, 237205 (2002)
28. C. Gould et al., Phys. Rev. Lett. **93**, 117203 (2004)
29. T. McGuire, R. Potter, IEEE Trans. Magn. **11**, 1018 (1975)
30. J. Velev et al., Phys. Rev. Lett. **94**, 127203 (2005)
31. K.M. Seemann et al., Phys. Rev. Lett. **107**, 086603 (2011)
32. B.G. Park et al., Phys. Rev. Lett. **100**, 087204 (2008)
33. R.C. Fivaz, Phys. Rev. **183**, 586 (1969)
34. H. Zhang, S. Blügel, Y. Mokrousov, Phys. Rev. B **84**, 024401 (2011)
35. E. Roman et al., Phys. Rev. Lett. **103**, 097203 (2009)
36. A. Hirsch, Y. Weissman, Phys. Lett. A **44**, 239 (1973)
37. N. Volkenstein et al., Fiz. Metal. Metalloved. **11**, 152 (1961)
38. T. Hiraoka, J. Sci. Hiroshima Univ., Ser. A-2 **32**, 153 (1968)
39. R.S. Lee, S. Legvold, Phys. Rev. **162**, 431 (1967)
40. K. Ohgushi et al., J. Phys. Soc. Jpn. **75**, 013710 (2006)
41. B.C. Sales et al., Phys. Rev. B **77**, 024409 (2008)
42. J. Stankiewicz, K.P. Skokov, Phys. Rev. B **78**, 214435 (2008)
43. J. Stankiewicz et al., Phys. Rev. B **83**, 014419 (2011)
44. N.H. Long et al., Phys. Rev. B **90**, 064406 (2014)
45. H. Zhang et al., Phys. Rev. B **87**, 205132 (2013)
46. J. Bellissard, [arXiv:cond-mat/9504030](https://arxiv.org/abs/cond-mat/9504030)
47. D.J. Thouless, M. Kohmoto, M.P. Nightingale, M. den Nijs, Phys. Rev. Lett. **49**, 405 (1982)
48. C. Chang et al., Science **340**, 167 (2013)
49. F.D.M. Haldane, Phys. Rev. Lett. **61**, 2015 (1988)
50. Y. Ren et al., Rep. Prog. Phys. **79**, 066501 (2016)

51. C.L. Kane, E.J. Mele, Phys. Rev. Lett. **95**, 226801 (2005)
52. C. Chang et al., Nat. Mater. **14**, 473 (2015)
53. C. Liu et al., Phys. Rev. Lett. **101**, 146802 (2008)
54. Q. Wang et al., Phys. Rev. Lett. **113**, 147201 (2014)
55. Z. Qiao et al., Phys. Rev. B **82**, 161414 (2010)
56. J. Ding et al., Phys. Rev. B **84**, 195444 (2011)
57. H. Zhang et al., Phys. Rev. Lett. **108**, 056802 (2012)
58. Z. Qiao et al., Phys. Rev. Lett. **112**, 116404 (2014)
59. S. Wu et al., Phys. Rev. Lett. **113**, 256401 (2014)
60. C. Niu et al., Phys. Rev. B **91**, 041303 (2015)
61. K. Garrity et al., Phys. Rev. Lett. **110**, 116802 (2013)
62. K. Garrity et al., Phys. Rev. B **90**, 041109 (2014)
63. H. Zhang et al., Phys. Rev. Lett. **112**, 096804 (2014)
64. X. Sheng, B. Nikolić, Phys. Rev. B **95**, 201402 (2017)
65. Y. Chen et al., Phys. Rev. B **90**, 195145 (2014)
66. H. Zhang et al., Phys. Rev. B **90**, 156143 (2014)
67. J.-P. Hanke et al., Nat. Comm. **8**, 1479 (2017)
68. B.A. Bernevig, T.L. Hughes, *Topological Insulators and Topological Superconductors* (Princeton University Press, 2013)
69. A. Chernyshov et al., Nat. Phys. **5**, 656 (2009)
70. I.M. Miron et al., Nat. Mater. **9**, 230 (2010)
71. K. Garello et al., Nat. Nanotech. **8**, 587 (2013)
72. I.M. Miron et al., Nature **476**, 189 (2011)
73. L. Liu et al., Phys. Rev. Lett. **109**, 096602 (2012)
74. P. Wadley et al., Science **351**, 6273 (2016)
75. F. Freimuth et al., Phys. Rev. B **90**, 174423 (2014)
76. I. Dzyaloshinskii, J. Phys. Chem. Sol. **4**, 241 (1958)
77. T. Moriya, Phys. Rev. **120**, 91 (1960)
78. N. Kanazawa et al., Phys. Rev. Lett. **106**, 156603 (2011)
79. A. Neubauer et al., Phys. Rev. Lett. **102**, 186602 (2009)
80. C. Franz et al., Phys. Rev. Lett. **112**, 186601 (2014)
81. J. Gayles et al., Phys. Rev. Lett. **115**, 036602 (2015)
82. F. Freimuth et al., J. Phys.: Cond. Mat. **26**, 104202 (2014)
83. J. Kübler, C. Felser, Europ. Phys. Lett. **108**, 67001 (2014)
84. M. Hoffmann et al., Phys. Rev. B **92**, 020401(R) (2015)
85. C.O. Avcı et al., Nat. Mater. **16**, 309 (2017)
86. Y.-H. Chu et al., Nat. Mater. **6**, 478 (2008)
87. W. Zhang et al., Phys. Rev. Lett. **113**, 196602 (2014)
88. H. Chen et al., Phys. Rev. Lett. **112**, 017205 (2014)
89. S. Nakatsuji et al., Nature **527**, 212 (2015)
90. A.K. Nayak et al., Sci. Adv. **2**, 150187 (2016)
91. T. Tomizawa, H. Kontani, Phys. Rev. B **80**, 100401(R) (2009)
92. T. Tomizawa, H. Kontani, Phys. Rev. B **82**, 104412 (2010)
93. Y. Zhang et al., Phys. Rev. B **95**, 075128 (2017)
94. R. Shindou, N. Nagaosa, Phys. Rev. Lett. **87**, 116801 (2001)
95. P. Bruno et al., Phys. Rev. Lett. **93**, 096806 (2004)
96. P.M. Buhl et al., Phys. Status Solidi RRL **11**, 1700007 (2017)
97. J. Železný et al., Phys. Rev. Lett. **119**, 187204 (2017)
98. Y. Machida et al., Phys. Rev. Lett. **98**, 057203 (2007)
99. Y. Taguchi et al., Science **291**, 2573 (2001)
100. Y. Machida et al., Nat. (Lond.) **463**, 210 (2010)
101. C. Sürgers et al., Nat. Comm. **5**, 3400 (2014)
102. J.-P. Hanke et al., Sci. Rep. **7**, 41078 (2017)
103. S. Heinze et al., Nat. Phys. **7**, 713 (2011)

104. J.-P. Hanke et al., *Phys. Rev. B* **94**, 121114(R) (2016)
105. J. Zhou et al., *Phys. Rev. Lett.* **116**, 256601 (2016)
106. M.d. Santos Dias et al., *Nat. Comm.* **7**, 13613 (2016)
107. T. Thonhauser, *Int. J. Mod. Phys. B* **25**, 1429 (2011)
108. D. Go et al., *Sci. Rep.* **7**, 46742 (2017)
109. T. Yoda et al., *Sci. Rep.* **5**, 12024 (2015)
110. S. Zhong et al., *Phys. Rev. Lett.* **116**, 077201 (2016)
111. F. Lux et al., [arXiv:1807.05040](https://arxiv.org/abs/1807.05040) (2018)
112. M. Menzel et al., *Phys. Rev. Lett.* **108**, 197204 (2012)

Chapter 7

Spin Hall Effect



Matthias Althammer

Abstract The spin Hall effect is of current interest from a fundamental and a device application point of view. Most importantly, the spin Hall effect allows to transfer an electrical charge current into a pure spin current, i.e. a current carrying only (spin) angular momentum without an accompanying charge current. This property enables us to gain access to novel spin current related effects by using electrical generation and/or detection schemes. Within this chapter, we will give an overview of the multitude of phenomena associated with it, focussing on means to quantify the spin Hall effect.

7.1 Introduction

While the phenomena of the anomalous Hall effect has been experimentally discovered by Hall [45] in 1881, it took over a century to understand the microscopic mechanisms leading to this effect [83]. During this time it was found that the anomalous Hall effect is only a special case of a more general effect, that depends on the spin-orbit interaction in a material. This general effect is called now the spin Hall effect [34, 50, 51, 105]. The work on the spin Hall effect has lead to the discovery of many new phenomena, that could not have been imagined previously. Despite the fact that the spin Hall effect is now known for over a decade, the interest into it has not decayed, but rather increased in the last years. In the following we will discuss the most important recent findings in the field of the spin Hall effect.

This chapter is organized in the following way. First, the concept of pure charge and spin currents is established in Sect. 7.2. As a next step we introduce the spin Hall effect and the inverse spin Hall effect and discuss how these effects allow to transform a pure charge current into a pure spin current and vice versa. In Sect. 7.4 various experimental methods to quantify the spin Hall effect are summarized. This chapter is concluded in Sect. 7.5 with a short summary and an outlook.

M. Althammer (✉)

Walther-Meißner-Institut, Bayerische Akademie der Wissenschaften, Garching, Germany
e-mail: matthias.althammer@wmi.badw.de

7.2 Charge and Spin Currents

In a conventional electrical conductor charge currents and spin currents originate from the flow of mobile charge carriers, that posses a charge as well as a spin degree of freedom. Within the framework of Mott's two spin channel model, a pure, spin-unpolarized charge current \mathbf{J}_q is represented as the parallel flow of an equal number of spin-up and spin-down electrons as illustrated in Fig. 7.1a. In contrast, for a pure spin current spin-up and spin-down electrons flow in opposite directions as illustrated in Fig. 7.1c, such that the net charge current vanishes, while a finite spin current density \mathbf{J}_s is maintained. The combination of \mathbf{J}_q and \mathbf{J}_s is called a spin-polarized charge current and is realized as the parallel flow of an unequal number of spin-up and spin-down electrons as illustrated in Fig. 7.1b. Such a situation is most easily obtained by passing a charge current through a ferromagnetic conductor. It is important to note that while charge currents can only flow in electrical conductors via mobile charge carriers, pure spin currents can also be transported in electrical insulators with magnetic order, where the angular momentum of \mathbf{J}_s is then carried by excitation quanta of the magnetic order parameter (magnons).

In general, a current is the directed flow of a transport quantity. For a charge current the transport quantity is a scalar, which is the electron charge $-e$ ($e > 0$), such that one can write the charge current density as $\mathbf{j}_q = -en < \mathbf{v} >$, where n is the density of the electrons, \mathbf{v} is the velocity operator, and $< \dots >$ denotes the thermodynamic expectation value for a non-equilibrium state. A spin current density \mathbf{j}_s in an electrical conductor represents the flow of spin (angular) momentum, which is an axial vector. This fact is illustrated in Fig. 7.2. For all three cases in Fig. 7.2a, b, c the flow direction of \mathbf{j}_s is the same, while the orientation of the spin polarization \mathbf{s} changes. Thus, $\mathbf{j}_s = \hbar/4n < \mathbf{v} \times \boldsymbol{\sigma} + \boldsymbol{\sigma} \times \mathbf{v} >$ is represented in the weakly relativistic limit as a second-rank tensor [9, 19, 20], where $\boldsymbol{\sigma}$ is the vector of Pauli spin matrices and \hbar is the reduced Planck constant. Throughout the literature two different definitions for the transport quantity of the spin current can be found, it is either in units of angular

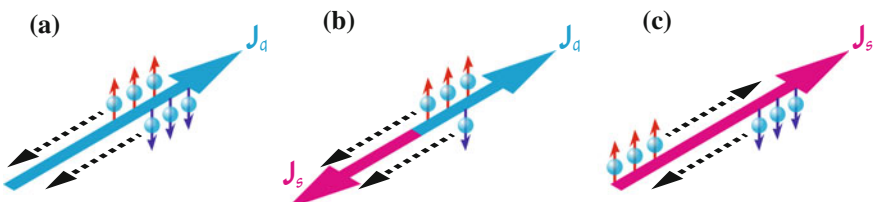


Fig. 7.1 Illustration of a pure charge, spin-polarized charge and pure spin currents. **a** For an identical number of spin-up and spin-down electrons moving in the same direction, we obtain a net spin-unpolarized charge current \mathbf{J}_q . **b** If the number of spin-up and spin-down electrons flowing in the same directions is unequal, this results in a spin-polarized current, i.e. a flow of a charge current \mathbf{J}_q and spin current \mathbf{J}_s at the same time. **c** If there is an identical number of spin-up and spin-down electrons moving in opposite directions, the net charge current vanishes, while the spin current \mathbf{J}_s remains finite

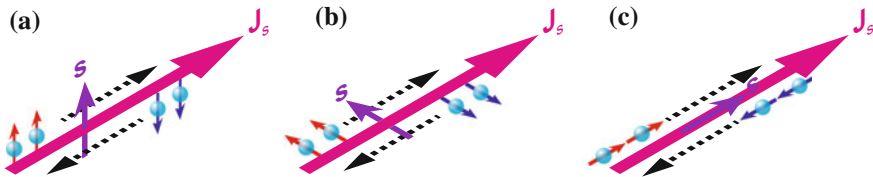


Fig. 7.2 Three different orientations ((a), (b), (c)) of the spin polarization vector \mathbf{s} for a fixed flow direction of the spin current

momentum or magnetic moment. Due to the fact that the angular momentum and magnetic moment of an electron are antiparallel, this introduces a factor of -1 between these two definitions of pure spin currents. Last but not least, it is important to realize that while charge is a conserved transport quantity, the spin polarization will be randomized on the length scale of the so-called spin flip length λ_{sf} . In this regard, charge and spin currents are dramatically different. In the following sections, we limit ourselves to the case of a spin current \mathbf{j}_s flowing in one direction with a perpendicular spin polarization \mathbf{s} , neglecting the second-rank tensor properties of the pure spin current.

7.3 Spin Hall Effect

The spin Hall effect (SHE) originates from the spin-dependent transverse velocity, which mobile charge carriers acquire while moving through a material with finite spin-orbit coupling due to extrinsic scattering effects and intrinsic bandstructure effects. These spin-dependent transverse velocities have already been discussed in Chap. 6 as the cause for the anomalous Hall effect (AHE). The very same extrinsic and intrinsic mechanisms that are responsible for the AHE also lead to the SHE. The SHE thus can be thought of as a more general version of the AHE, which is present in non-magnetic (i.e. materials without magnetic order) conductors. It is important to note that within this chapter we interpret the SHE as an effect arising in the bulk of a material, in contrast to interface effects like Bychkov-Rashba spin-orbit coupling [70].

The SHE manifests itself in an electrical conductive, non-magnetic material (NM) with finite spin-orbit coupling, by the transformation of a pure charge current into a pure spin current in the transverse direction of the charge current, caused by the spin-dependent transverse velocity acquired by the electrons. This process is illustrated in Fig. 7.3a. Due to the spin-dependent nature of these effects, the transverse velocity and the spin-polarization \mathbf{s} of the electrons are always perpendicular to each other, such that spin-up and spin-down electrons are deflected in opposite directions. As the same number of spin-up and spin-down electrons are moving in opposite directions, the net transverse charge current is 0, while a finite spin current \mathbf{j}_s flows in the

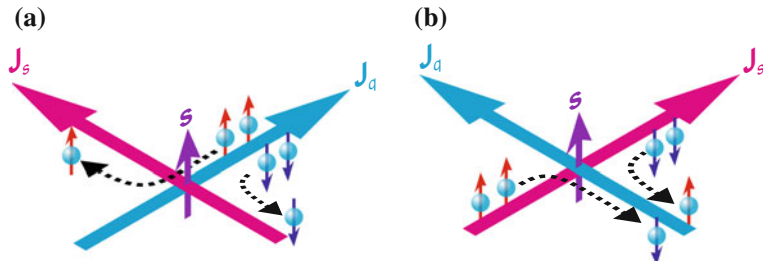


Fig. 7.3 Schematic of the spin Hall and inverse spin Hall effect. **a** The spin Hall effect is caused by spin-dependent scattering effects and transforms a charge current \mathbf{J}_q into a transverse spin current \mathbf{J}_s with a spin polarization \mathbf{s} . **b** In the inverse spin Hall effect a spin current \mathbf{J}_s with spin polarization \mathbf{s} is transformed into a transverse charge current \mathbf{J}_q

transverse direction. We can describe this spin current generation from a charge current by:

$$\mathbf{j}_s = \alpha_{\text{SH}} \left(-\frac{\hbar}{2e} \right) \mathbf{j}_q \times \mathbf{s}. \quad (7.1)$$

The spin Hall angle α_{SH} is a material dependent parameter that reflects the magnitude of the spin-dependent scattering effects. The SHE thus allows to generate a pure spin current in a material without magnetic order, but finite spin-orbit coupling.

Due to Onsager reciprocity the inverse process, a transformation of a pure spin current into a charge current due to spin-orbit coupling is also possible and then called the inverse spin Hall effect (ISHE), as illustrated in Fig. 7.3b. We first consider a pure spin current, with spin-up and spin-down electrons flowing in opposite directions. As both the spin direction and direction of movement are opposite, the spin-up and spin-down electrons are deflected in the same direction, due to the spin-dependent transverse velocity effects, and create a charge current \mathbf{j}_q given by:

$$\mathbf{j}_q = \alpha_{\text{SH}} \left(-\frac{2e}{\hbar} \right) \mathbf{j}_s \times \mathbf{s}. \quad (7.2)$$

Due to the vector product in (7.2) a charge current can only be generated via the ISHE if \mathbf{j}_s and \mathbf{s} are non-collinear. However, the ISHE enables the all-electrical detection of a pure spin current in an electrical conductor with finite α_{SH} [99]. Since both, SHE and ISHE, rely on spin-orbit coupling, large α_{SH} are expected in heavy elements. From the experiment, one finds a large spin Hall angle in materials such as platinum (Pt), tantalum (Ta), tungsten (W), gold (Au), or alloys such as CuBi, with $|\alpha_{\text{SH}}| < 0.4$ [39, 69, 79, 85, 89, 121].

While a phenomenological description of the SHE has already been put forward by D'yakonov and Perel' [34] in 1971, interest into these effects was only sparked 3 decades later, when Hirsch [50] published his theoretical description of this effect and coined the term spin Hall effect. This ignited a series of publications on the SHE in

theory and experiment. Two very good review articles that cover all these theoretical and experimental observations have now been published by Hoffmann [51] and Sinova et al. [105].

7.4 Experimental Determination of the Spin Hall Angle

Before we discuss the experiments on the SHE (and ISHE), it is beneficial to first discuss the different steady-state conditions that can occur due to the implied boundary conditions in a sample. As the spin-up and spin-down electrons move in opposite transverse directions, we only obtain a transverse spin current (Fig. 7.3a). If we assume that the spins cannot exit the sample on the transverse edges of the sample, this spin current causes a spin accumulation on the length scale of the spin diffusion length of the material. In the steady-state, this spin accumulation gives rise to a gradient in the spin-dependent electrochemical potential, which opposes the transverse spin current generated by the SHE (Fig. 7.4a). In the end, we obtain a steady-state condition with no net transverse spin current flow, but with a spin accumulation at the sample edges. Assuming that one could realize a spin current short (as illustrated in Fig. 7.4b), which connects the two transverse sides of the sample, a finite transverse spin current flow will be maintained in the steady-state and the SHE will then effectively increase the longitudinal resistivity of the sample. This fact can be exploited for the detection of the SHE in spin Hall magnetoresistance experiments, as we will see later in this section.

Despite first theoretical work on the spin Hall effect in the early 1970s [34], it took several decades until much experimental effort has been put into the investigation of the spin Hall effect. One major challenge was the vanishing of the net transverse

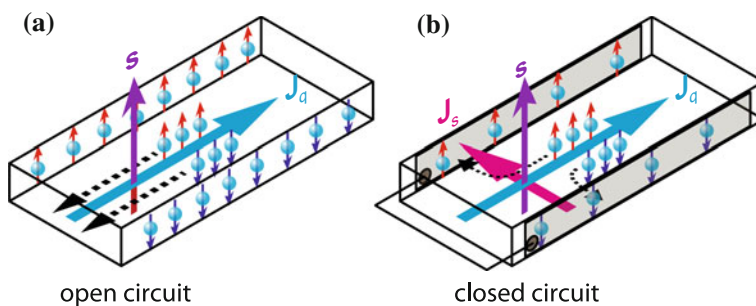


Fig. 7.4 **a** For an open spin circuit boundary condition (i.e. spins cannot exit at the transverse sides of the sample), we obtain in the steady-state a spin accumulation, which compensates the transverse spin current flow generated from the SHE. **b** In the case of a closed spin circuit boundary condition, the transverse spin current flow is maintained in the steady-state and causes an increase of the longitudinal resistivity (effective increase of the length of trajectory for the electrons). Adapted with permission from [1]

charge current, which made a direct electrical detection via an electric field like in the case of the AHE [45] impossible. However, over the course of the years, a couple of pioneering experimental work has been carried out. For example, Chazalviel [16] used electron spin resonance in non-magnetic semiconductors to detect an AHE-like signature of the net spin polarization generated by a microwave magnetic field.

After the theoretical publication by Hirsch [50], optical detection schemes were the first experiments to image the spin accumulation caused by the SHE in semiconducting materials. This approach has been pioneered by Kato et al. [60] and Wunderlich et al. [126] in the direct bandgap semiconductor GaAs. In the experiments by Kato et al. the magneto-optical Kerr effect was used to image the spin accumulation caused by the SHE in a semiconductor. In the experiment, the probing linearly polarized laser spot (with a photon energy close to the band gap of the semiconductor) was stepwise rastered across a strip of unstrained GaAs, while an electric field was applied to the strip, and the Kerr rotation of the reflected light was measured for each step. The obtained Kerr signal is only sizeable at the edges of the GaAs strip and has opposite sign at the two transverse edges. This is consistent with our picture of the spin accumulation caused by the SHE (compare Fig. 7.4a). Wunderlich et al. [126] used a different approach to detect the spin accumulation caused by the SHE. Here, the circular polarization of light generated by light emitting diodes fabricated at the edges of a GaAs strip were used to detect the spin accumulation. Both experimental results were the first proof for the existence of the SHE.

While optical detection schemes allow to image the spin accumulation in semiconducting materials, it is rather challenging to carry out such optical experiments in metals and especially to quantify the spin Hall angle from such experiments. Due to the fact that spin angular momentum is carried by electrons in electrical conductors an all-electrical detection technique appears desirable for a quantitative analysis. The basic experimental concept used for such an electrical detection is based on the ISHE, since here a charge current is generated by a spin current and the effect is the Onsager reciprocal of the SHE, such that the determination of the inverse spin Hall angle directly yields α_{SH} . In such experiments different techniques have been used to generate a pure spin current: in non-local spin valve experiments and spin Hall tunneling spectroscopy, a spin-polarized charge current emitted from a ferromagnet is used to generate a diffusive spin current. In spin pumping experiments a microwave excitation of the magnetization in a ferromagnet is used to drive a pure spin current across the interface into the NM. A different route is to quantify the amount of spin current generated by the SHE by measuring the spin-transfer torque imposed onto a ferromagnet by this spin current. For such experiments, spin-transfer torque induced ferromagnetic resonance or magnetization switching can be used for a direct measurement of the spin Hall effect. In addition, spin Hall magnetoresistance can be used to quantify the spin Hall effect. In the following we will describe these techniques in more detail.

7.4.1 Non-local Experiments

An important milestone for non-local measurement device concepts was established by Johnson and Silsbee [57] in 1985, by the experimental generation of a pure spin current from a spin polarized charge current in lateral nanostructures. In such structures as illustrated in Fig. 7.5a, a charge current is passed through a ferromagnetic metal contact (ferromagnet, FM) into a NM, which then generates a spin accumulation in the NM. This spin accumulation will diffuse in all directions within the NM, while the charge current used for the generation of the spin accumulation is only flowing in one direction. By geometric design in these lateral structures, one can then separate the charge current from the pure spin current. First experiments in this directions, where the detection of the pure spin current was realized via a second ferromagnetic contact, coined the term non-local spin valves and allowed to investigate the spin current transport in NMs [36, 53, 54, 63]. Valenzuela and Tinkham [116] pioneered this approach to quantify the spin Hall effect in lateral nanostructures. As illustrated in Fig. 7.5a, a spin-polarized charge current from a FM induces a spin accumulation in the NM. In their experiments an Al_2O_3 tunneling barrier was present between the FM and NM, and by applying an external magnetic field the magnetization of the FM was aligned along \mathbf{z} . The spin accumulation drives a diffusive pure spin current \mathbf{j}_s along \mathbf{x} , with a spin polarization $\mathbf{s} \parallel \mathbf{z}$. At the distance L_{SH} , a perpendicular NM bar (oriented along \mathbf{y}) crosses the NM path. This pure spin current is then transformed into a charge current flowing along \mathbf{y} via the ISHE. Due to open circuit boundary conditions this leads in the end to an electric field \mathbf{E}_{ISH} (compensating the transformed charge current), which is then electrically detected as a voltage V_{nl} . The measured non-local resistance $R_{\text{SH}} = V_{\text{nl}}/I$, where I is the

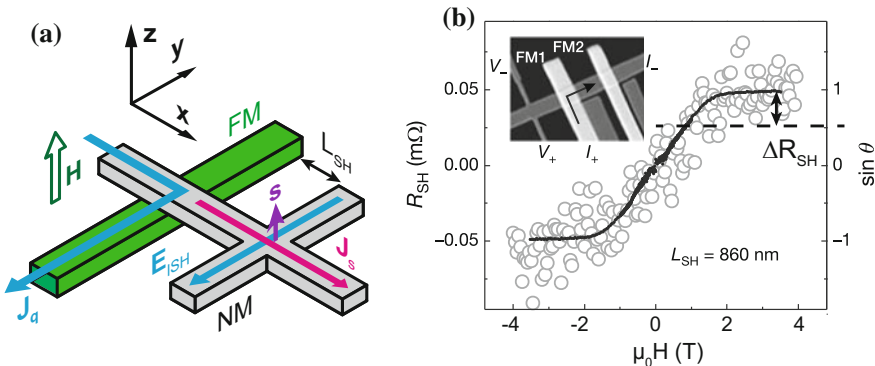


Fig. 7.5 Non-local detection of the ISHE: **a** Schematic illustration of the non-local detection scheme. A charge current is driven through a FM/NM contact, which induces a spin accumulation at the interface. The resulting diffusive spin current \mathbf{j}_s is then transformed into a charge current a distance L_{SH} away from the FM. **b** Non-local resistance signal as a function of the external magnetic field applied perpendicular to the sample plane. The inset shows an electron microscopy image of the actual device structure. Adapted with permission from [116]

charge current applied to the system is shown in Fig. 7.5b as a function of the applied external magnetic field. R_{SH} changes its sign upon field inversion, as the direction of the magnetization of the FM and thus the spin polarization \mathbf{s} are inverted, which also changes the sign of the detected ISHE voltage. Moreover, the signal saturates for large positive and negative fields and the curvature follows the magnetization orientation obtained from additional non-local spin valve experiments. For a quantitative extraction of α_{SH} one can then use [108, 116]:

$$\Delta R_{\text{SH}} = \frac{P}{t_{\text{NM}}\sigma_{\text{NM}}} \alpha_{\text{SH}} \exp(-L_{\text{SH}}/\lambda_{\text{sf}}), \quad (7.3)$$

where P is the spin-polarization of the electrically injected current, t_{NM} and σ_{NM} is the thickness and the conductivity of the NM. For the extraction of α_{SH} it is thus necessary to vary the separation of the ISHE detector and the FM (L_{SH}) and measure ΔR_{SH} for each distance, using an exponential fit to the data one can then determine the spin diffusion length λ_{sf} and the spin Hall angle α_{SH} . Valenzuela and Tinkham (see [116]) obtained $\alpha_{\text{SH}} = 2 \times 10^{-4}$ for Al at $T = 4.2$ K.

As evident from this discussion, it is necessary to determine first λ_{sf} to get quantitative values for α_{SH} . However, the design of the experiment allows this extraction of λ_{sf} with the very same measurement technique. The choice of materials is limited to such with a λ_{sf} that is larger than the length scales realizable by the lithography process (i.e. typically $\lambda_{\text{sf}} > 100$ nm). This makes especially studying materials with a large spin Hall angle a challenge, as due to the large spin-orbit interaction λ_{sf} is very likely to be small. A way to circumvent this issue is by utilizing a two step process, where two NMs (NM1, NM2) are used. First the spin current is injected into NM1, which has a large λ_{sf} and transported in the NM1 to a perpendicular strip of NM2 with a small λ_{sf} , but large α_{SH} for ISHE detection. This approach has been experimentally realized by Kimura et al. to quantify the spin Hall angle of Pt (NM2) using Cu (NM1) as the spin current conductor [64]. This approach also no longer requires the external magnetic field to be oriented along \mathbf{z} , because the spin current injected from NM1 into NM2 flows along \mathbf{z} such that \mathbf{s} has to be oriented along \mathbf{x} (Compare Fig. 7.5a) for maximum conversion efficiency via the ISHE. Thus the external magnetic field is now applied in-plane along \mathbf{x} . In this publication Kimura et al. [64] further showed that it is possible to detect the spin current generated by the spin Hall effect as a non-local voltage between the FM and the Cu leads, i.e. exchanging the contacts for charge current drive and voltage detection. Using both detection schemes the experimental reciprocity of SHE and ISHE has thus been proven. As already discussed, the usage of two or more NMs in such non-local experiments avoids applying the external magnetic field in the out-of-plane direction. For a single NM layer, FMs with a perpendicular magnetic anisotropy (magnetic easy axis along the surface normal) can be used as shown by Seki et al. [104] to completely avoid the application of an external magnetic field. Most experiments detect the induced charge current from the ISHE as an open-circuit voltage in these lateral structures, but it is also possible to detect the charge current directly, for example via loop structures [87].

Another important obstacle to master in the non-local SHE detection are additional voltage contributions originating from unavoidable non-local charge currents. These non-local charge currents become relevant due to the small dimensions of the sample, such that the charge current used as a drive also leaks into the non-local voltage detection. In principle, a careful analysis of R_{nl} as a function of L_{SH} should allow to separate the charge current contribution from the pure spin current contribution, as the relevant length scales should be different. While the charge current scales with the mean free path of the NM, the ISHE response scales with λ_{sf} . This problem is a major obstacle for the ISHE detection of a SHE generated pure spin current in double Hall bars, where contributions from the charge current are dominating the measured non-local voltage signal [75]. Special care should be taken in such non-local detection schemes to rule out any spurious contribution to the non-local voltage, when determining α_{SH} .

7.4.2 Spin Pumping

ISHE detection of a pure spin current is also used in the realm of spin pumping using FM/NM heterostructures. Here, the pure spin current is generated by exciting the magnetization of a ferromagnet out of equilibrium by microwave irradiation. Now, to relax back into the ground state, the magnetization has to change its angular momentum (difference indicated by the small grey arrow in Fig. 7.6a). While in the FM itself the angular momentum is in the end transferred into the crystal lattice, in FM/NM heterostructures an additional way of relaxing angular momentum of

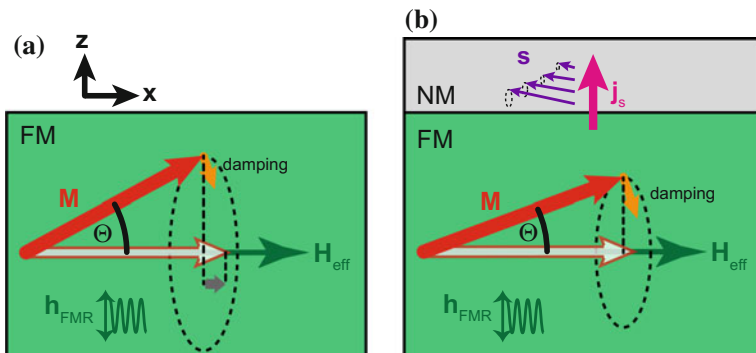


Fig. 7.6 Illustration of the spin pumping process in a FM/NM heterostructure. **a** Due to an external microwave driving field \mathbf{h}_{FMR} , the magnetization \mathbf{M} precesses around the effective magnetic field \mathbf{H}_{eff} . The two dashed lines indicate the difference in angular momentum between the non-equilibrium and equilibrium state of the magnetization. **b** If the FM is interfaced with a NM, excess angular momentum is transmitted via a spin current \mathbf{j}_s across the interface into the NM. In the NM the spin current decays over the lengthscale λ_{sf}

the magnetization is the emission of a pure spin current into the adjacent NM (see Fig. 7.6b). In spin pumping experiments the magnetization is driven out of equilibrium by applying a microwave excitation in a ferromagnetic resonance experiment. Another way of achieving such out-of-equilibrium magnetization states is the application of a thermal drive using a temperature gradient [9, 113, 114], which is then called the Spin Seebeck effect.

In more detail, in the steady-state the excitation via the microwave field and the relaxation (damping effects) of the magnetization have to balance each other, which leads to a precessional motion of the magnetization around its thermal equilibrium state, with a precession cone angle Θ (see Fig. 7.6a). The magnetization dynamics can be modeled using the Landau-Lifshitz-Gilbert (LLG) equation [80, 118]

$$\frac{d\mathbf{m}}{dt} = -\gamma\mu_0(\mathbf{m} \times \mathbf{H}_{\text{eff}}) + \alpha \left(\mathbf{m} \times \frac{d\mathbf{m}}{dt} \right), \quad (7.4)$$

with the gyromagnetic ratio γ , the normalised magnetization direction $\mathbf{m} = \mathbf{M}/|\mathbf{M}|$, and the so-called Gilbert damping parameter α describing viscous magnetization damping. The first term on the right hand side of (7.4) describes the precession of \mathbf{M} around an effective magnetic field \mathbf{H}_{eff} , which contains the external magnetic field, as well as contributions from magnetic anisotropy and demagnetizing fields from the sample shape. From the LLG equation the ferromagnetic resonance (FMR) condition can be calculated, i.e. the microwave frequency required to obtain a resonant absorption for a given \mathbf{H}_{eff} .

As can be seen from Fig. 7.6b, the excess angular momentum generated by the coherent microwave excitation is transferred across the FM/NM interface, and relaxes in the NM. The corresponding pure spin current across the interface is given by [110–112]

$$\mathbf{j}_s^{\text{pump}} = \frac{\hbar}{4\pi} \left\{ \text{Re}(g^{\uparrow\downarrow}) \left[\mathbf{m} \times \frac{d\mathbf{m}}{dt} \right] - \text{Im}(g^{\uparrow\downarrow}) \frac{d\mathbf{m}}{dt} \right\}, \quad (7.5)$$

here, $g^{\uparrow\downarrow}$ is the spin mixing conductance describing the available spin transport channels at the interface. As visible from the first term on the right hand side of (7.5), the spin current generated by spin pumping represents an additional Gilbert-like damping contribution, which will change the resonance line width of the ferromagnetic resonance (see also Fig. 7.6). By investigating the dependence of the ferromagnetic resonance line-width as a function of the FM thickness $g^{\uparrow\downarrow}$ can be determined from frequency dependent ferromagnetic resonance experiments. Such experiments showed that $g^{\uparrow\downarrow} \approx 10^{19} \text{ m}^{-2}$ for electrically conducting ferromagnets [2, 28, 121], as well as badly conducting or fully insulating ferromagnets such as magnetite (Fe_3O_4) or yttrium iron garnet ($\text{Y}_3\text{Fe}_5\text{O}_{12}$) and related garnets [14, 28, 49, 59, 101, 107]. These results suggest, that the spin current generated from spin pumping for different materials is identical, if the precession cone angle Θ is equal. In addition, spin pumping from insulating FMs is as efficient as spin pumping from electrically conducting FMs. Moreover, by taking the time average of (7.5) one finds that the pumped spin current has two contributions: one time independent contribution (DC spin current)

and one time dependent contribution (AC spin current) [110–112]. In most experiments using electrical detection schemes for the quantification of the spin Hall angle only the DC spin current component is used.

For the electrical detection of the pure spin current injected into the NM by spin pumping the ISHE is used (Fig. 7.7a) in so-called electrically detected spin pumping experiments. The pumped spin current flows along the surface normal of the heterostructure and the orientation of \mathbf{s} is determined by the magnetization orientation in the FM, with $\mathbf{s} \parallel -\mathbf{M}$ in typical ferromagnets [80]. Due to the ISHE (7.2) in the NM the pumped spin current is transformed into an electrical charge current, flowing in the NM plane. In the experiment this charge current is either detected directly, or the electric field, generated by the charge accumulation, is detected as a voltage signal ΔV in ferromagnetic resonance. As discussed in more detail in [28, 81, 82, 121], the magnitude of the spin pumping spin Hall voltage ΔV is given by

$$\frac{\Delta V}{L} = \frac{2e}{\hbar} \alpha_{\text{SH}} \frac{j_s \eta \lambda_{\text{sd}} \tanh\left(\frac{t_{\text{NM}}}{2\lambda_{\text{sd}}}\right)}{\sigma_{\text{FM}} t_{\text{FM}} + \sigma_{\text{NM}} t_{\text{NM}}} . \quad (7.6)$$

Here, σ_i and t_i are the conductivities and layer thicknesses of FM and NM, respectively, and η is the backflow parameter ($0 \leq \eta \leq 1$) accounting for a possible spin current backflow into the FM and is defined as [19, 56]:

$$\eta = \left[1 + 2\text{Re}(g^{\uparrow\downarrow}) \sigma_{\text{NM}} \lambda_{\text{sf}} \frac{e^2}{\hbar} \coth\left(\frac{t_{\text{NM}}}{\lambda_{\text{sf}}}\right) \right]^{-1} . \quad (7.7)$$

If $t_{\text{NM}} \gg \lambda_{\text{sf}}$ then $\eta = 1$ and the pumped spin current is completely absorbed in the NM.

Data from electrically detected spin pumping experiments at room temperature in a Fe/Pt thin film bilayer are shown in Fig. 7.7b–e [27]. For the experiments the sample was placed in the antinode of the microwave magnetic field of a commercial microwave cavity operating at a fixed frequency of 9.3 GHz. The FMR signal of the Fe layer, recorded with the external magnetic field applied as sketched in Fig. 7.7a, is shown as a solid line in panel (b). The DC voltage V_{DC} shown in Fig. 7.7c exhibits an identical Lorentzian line shape as the FMR signal and the magnetic field position coincides with the FMR signal. Upon inversion of the static external magnetic field orientation the FMR absorption remains unaltered (panel (d)). In contrast, a sign change is observed for the resonant peak in the V_{DC} signal, as evident from Fig. 7.7c, e, respectively. The inversion of magnetic field orientation results in an inversion of \mathbf{s} , and thus also an inversion of the ISHE charge current flow direction and provides an additional consistency check in the experiment [2, 5].

In most experiments, the line shape of V_{DC} is more complex than the simple Lorentzian line shape expected from the ISHE [81]. Additional contributions to V_{DC} originate from microwave rectification effects [12, 42, 58, 81]. Due to the precession of the magnetization at FMR conditions also the resistance of the FM varies with the microwave frequency due to AHE and anisotropic magnetoresistance contributions.

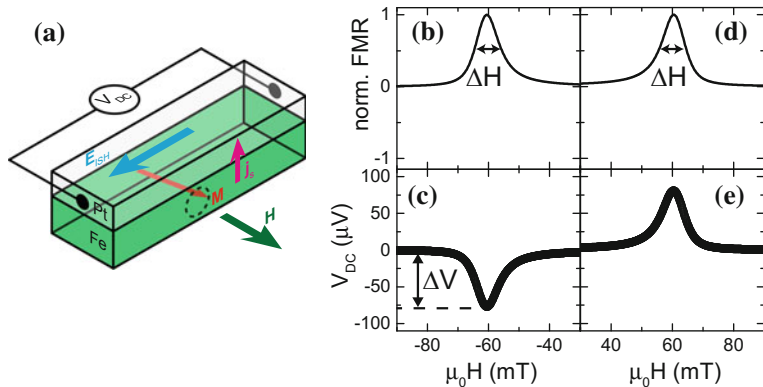


Fig. 7.7 Electrically detected spin pumping experiments on a Fe/Pt heterostructure. **a** Electrical detection scheme for the measurement of the spin current generated by the spin pumping effect. The spin current across the FM/NM interface is transformed into a charge current in the NM via the ISHE, which leads to a charge accumulation in the NM. This charge accumulation can then be detected as a voltage signal in V_{DC} . **b** Ferromagnetic resonance signal obtained for an external magnetic field sweep, while **(c)** shows the simultaneously detected V_{DC} . A maximum in V_{DC} is detected at the ferromagnetic resonance of the Fe layer. If the magnetic field direction is inverted, the ferromagnetic resonance signal remains unchanged **(d)**, while the polarity of V_{DC} is inverted **(e)**. Data taken from [27]

This time-varying resistivity then rectifies microwave-frequency charge currents, induced in the sample by the microwave irradiation. The resulting lineshape of the rectification signal is rather complex and careful evaluation of the experimental data is necessary to separate these contributions from the ISHE signal.

As already discussed, the pumped spin current also contains an AC component (see (7.5)). While the flow direction of this AC spin current is still along the surface normal in the FM/NM bilayers (see Fig. 7.6b), the spin polarization s varies with time and is oriented in the precession plane of the magnetization [56]. In first FMR experiments analyzing the dynamic coupling between two FM layers separated by a NM layer indirect evidence for the existence of this AC component has already been found [122]. A quantitative detection of such AC-spin currents is rather challenging, but has been achieved by using parametric driving [44] or self-calibrating techniques [119, 120]. From these first results, it is clear that the AC spin current is much larger than its DC counterpart. However, the experiments show that open questions like the frequency dependence of the spin Hall effect and phase correlations between the spin polarization of the spin current and the charge current generated by the ISHE need to be answered by future experiments.

As discussed previously, the spin pumping effect leads to an ISHE charge current flowing in the NM and also increases the FMR line-width. Ando et al. showed that also the inverse effect exists, i.e. a charge current in the NM influences the FMR line-width via a spin current generated by the SHE [4]. The experimental setup is identical to a spin pumping experiment only that in addition a charge current is applied to the

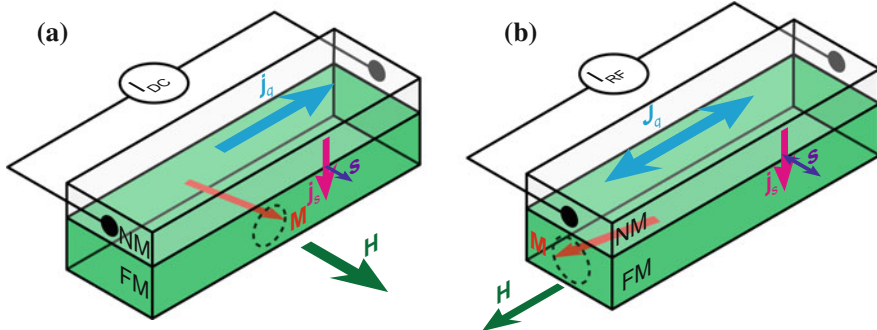


Fig. 7.8 Spin Hall effect induced magnetization dynamics. **a** Illustration of the setup for spin Hall damping enhancement. While the magnetization \mathbf{M} is driven into FMR by a microwave excitation, a charge current is driven simultaneously through the NM, where it is transformed into a spin current flowing across the interface into the FM. As the spin polarization \mathbf{s} and the precessing magnetization are not collinear an additional torque due to the spin current acts onto \mathbf{M} . **b** Experimental configuration for SHE induced spin-transfer torque ferromagnetic resonance. An RF charge current \mathbf{j}_q is applied to the FM/NM heterostructure, which is transformed into a spin current \mathbf{j}_s with a spin polarization \mathbf{s} . The spin current leads to an oscillating spin-transfer torque acting on the magnetization \mathbf{M} , which leads to a precession of \mathbf{M}

NM, while the magnetization is driven into FMR via an external microwave field (see Fig. 7.8a). The change of the FMR line-width as a function of the applied charge current is then measured. One should note that the static external magnetic field is also oriented here perpendicular to the charge current direction. In more detail, the spin-transfer torque τ_{STT} acting on \mathbf{M} due to the spin current, driven by the charge current in the NM, can be written as [4, 48, 68, 90]:

$$\tau_{\text{STT}} = -\gamma \frac{\hbar}{2e} j_q \left[\frac{\xi_{\text{DL}}}{M_s^2} \mathbf{M} \times (\mathbf{M} \times \mathbf{s}) - \frac{\xi_{\text{FL}}}{M_s} (\mathbf{M} \times \mathbf{s}) \right], \quad (7.8)$$

where M_s is the saturation magnetization of the FM. τ_{STT} consists of two contributions, the first term on the right hand side of (7.8) is called the damping-like torque, with ξ_{DL} describing its efficiency, the second term is called the field-like torque, with the efficiency ξ_{FL} . This naming convention originates from the two contributions in the LLG equation (7.4). The efficiencies (dimensionless parameters) are given by [90]:

$$\xi_{\text{DL}} = \alpha_{\text{SH}} \text{Re} \left[\frac{2g^{\uparrow\downarrow} \tanh\left(\frac{\hbar \omega_{\text{NM}}}{2\lambda_{\text{sf}}}\right)}{\frac{\sigma_{\text{NM}} \lambda_{\text{sf}} \hbar}{e^2} + 2g^{\uparrow\downarrow} \coth\left(\frac{\hbar \omega_{\text{NM}}}{\lambda_{\text{sf}}}\right)} \right], \quad (7.9)$$

$$\xi_{\text{FL}} = \alpha_{\text{SH}} \text{Im} \left[\frac{2g^{\uparrow\downarrow} \tanh\left(\frac{\hbar \omega_{\text{NM}}}{2\lambda_{\text{sf}}}\right)}{\frac{\sigma_{\text{NM}} \lambda_{\text{sf}} \hbar}{e^2} + 2g^{\uparrow\downarrow} \coth\left(\frac{\hbar \omega_{\text{NM}}}{\lambda_{\text{sf}}}\right)} \right]. \quad (7.10)$$

Here, h is the Planck constant. One now has to add τ_{STT} to the LLG equation (7.4), which then leads to a damping/antidamping contribution (neglecting the field-like torque due to the small imaginary part of the spin mixing conductance) in the magnetization configuration given here (see Fig. 7.8a). Indeed, Ando et al. [4] observed a change in the FMR line-width ΔH depending on the current polarity, if the external magnetic field is oriented perpendicular to the current direction, while there is no change in the FMR line-width, when the external magnetic field is oriented parallel to the current direction. A challenge for a quantitative analysis of the line-width changes are additional contributions like Joule heating and Oersted fields stemming from the applied charge current, that need to be included.

The physical concept of these experiments is taken a step further in spin Hall effect driven nano-oscillators [24, 31–33, 40, 46, 115]. Here, the magnetization in a FM/NM bilayer is driven by the spin-transfer torque of the spin current generated from a DC charge current in the NM into auto-oscillations, i.e. a continuous precessing motion (FMR), leading to an emission of microwave frequency signals. The occurrence of auto-oscillations requires large current densities in the NM layer, in lateral structures this is achieved in the experiment by structuring nm sized constrictions into the NM layer [32]. As the output power of a single device is rather small, the main challenge is to phase-lock several of these oscillators to obtain reasonable output powers, which currently limits the use in applications [8, 93]. It is worth noting that similar effects have been theoretically predicted for antiferromagnets, where the output frequency of such oscillators would be in the THz regime [17, 21, 29, 62]. An experimental proof of these theoretical conjectures would open up SHE induced spin currents for also driving dynamics in an antiferromagnet.

7.4.3 Spin-Transfer Torque Induced Ferromagnetic Resonance

The spin current generated from a charge current via the SHE can also be used to drive magnetization dynamics in FM/NM bilayers. As evident from (7.8), a spin-transfer torque is imposed by the spin polarization s of the SHE spin current, which acts as a driving force onto the magnetization [65, 68, 69, 74, 89, 96, 102].

In spin-transfer torque FMR a RF charge current is applied to the FM/NM bilayer with the magnetization oriented collinear with the charge current direction. As illustrated in Fig. 7.8b the RF charge current is transformed into a spin current via the SHE. As the spin polarization s and the magnetization M are aligned perpendicular to each other, this leads to an oscillatory spin-transfer torque acting on M (7.8). If the external applied magnetic field and the frequency of the RF charge current match the FMR condition, the magnetization starts to precess. Liu et al. [68] applied this technique to determine the spin Hall angle of Pt in NiFe/Pt bilayers. To detect the FMR motion of the magnetization, they measured the rectification voltage V_{mix} generated by the homodyne mixing of the time-varying magnetoresistance, due to the precess-

ing motion of the magnetization, with the RF charge current drive. The lineshape of V_{mix} contains both symmetric and antisymmetric Lorentzians for the NiFe/Pt sample, while the lineshape for the NiFe and NiFe/Cu control samples only contains an antisymmetric Lorentzian. Initially, it was assumed, that the antisymmetric contribution originates from the RF Oersted field generated by the RF charge current in the NM. In contrast, the symmetric lineshape is caused by the spin-transfer torque effect induced by the SHE in the NM. If the sample dimensions, conductivities of the NM and the FM layer, and the saturation magnetization of the FM are known, this allows to extract the spin Hall angle α_{SH} directly from such experiments. In the end, the ratio of the symmetric and antisymmetric Lorentzian amplitude is proportional to α_{SH} [68]. Liu et al. claim that this method is self-calibrating, as the torque generated by the SHE can be directly compared to the torque caused by the Oersted field of the RF charge current. However, it remains debatable whether only the SHE torque can cause a symmetric line shape or if other contributions like spin galvanic effects, due to the broken inversion-symmetry, lead to additional spin-transfer torque contributions [39]. Using this method Liu et al. determined α_{SH} for Pt ($|\alpha_{\text{SH,Pt}}| = 0.076$, [68]), Ta ($|\alpha_{\text{SH,Ta}}| = 0.12 \dots 0.15$, [69]) and β -phase W ($|\alpha_{\text{SH,W}}| = 0.30$, [89]) films.

The next logical step was to switch the magnetization direction in the FM via the spin-transfer torque. First experimental proof of magnetization switching has been presented by Miron et al. [74, 76] and Liu et al. [69]. A schematic sketch of the device used by Miron et al. [76] is shown in Fig. 7.9a. Here, a trilayer structure consisting of a ultrathin 0.6 nm Co layer sandwiched between a 3 nm thin Pt layer and a 1.6 nm thin AlO_x layer was used in the experiment. The Co layer exhibits a strong perpendicular magnetic anisotropy (easy axis along the surface normal), such that AHE measurements can be used to monitor the magnetization orientation (see Fig. 7.9c). In the spin torque switching experiments a charge current is applied to the Pt strip in \mathbf{x} direction. Due to the SHE this causes the injection of a spin current with the spin polarization along the \mathbf{y} direction. In their spin torque switching experiments the external magnetic field (applied along the \mathbf{z} direction) was stepwise swept. At each field step a positive and negative current pulse ($I_p = 2.58$ mA) (see Fig. 7.9b) is applied to the Pt strip and the AHE signal is then recorded. The result of this procedure is shown in Fig. 7.9d. For negative field values (-300 mT $< B < 0$ mT), positive current pulses switch the magnetization into the $+\mathbf{z}$ direction, while negative current pulses switch the magnetization into $-\mathbf{z}$ direction. For positive field values (0 mT $< B < 300$ mT), the situation is reversed. Initially, Miron et al. assumed that the switching of the magnetization is caused by a spin accumulation generated by the inverse spin galvanic effect [22, 37, 71, 77], caused by the broken inversion symmetry in the trilayer stack. However, further experiments showed that contributions of the SHE to the spin-transfer torque are not negligible [39]. In the experiments conducted by Liu et al. [69] a 1 nm $\text{Co}_{40}\text{Fe}_{40}\text{B}_{20}$ layer was sandwiched between a 4 nm thin Ta layer and a 1.6 nm thin MgO layer capped with a 1 nm thin Ta layer. AHE measurements were again used to trace the magnetization direction, at a certain critical threshold current the magnetization switches its orientation and causes a change in the sign of the AHE signal. This shows that in such NM/FM bilayers the

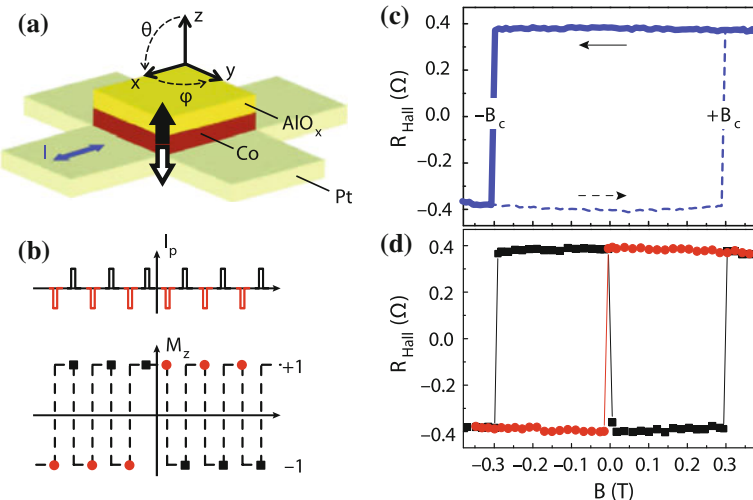


Fig. 7.9 Spin transfer torque switching experiments conducted by Miron et al. [74, 76]. **a** Illustration of the device used by Miron et al., the ultrathin Co layer is sandwiched between a thin Pt cross and a AlO_x layer, and exhibits a large perpendicular magnetic anisotropy (easy axis along **z**). **b** Applied current pulses as a function of time and corresponding magnetization orientation for the applied current pulses. **c** AHE signal obtained for the device using an external magnetic field sweep (field applied along **z**), at the coercive field $B_c = 300$ mT the magnetization orientation is reversed. **d** AHE signal obtained in a stepped field sweep, where at each field step a positive (black squares) and negative (red squares) current pulse is applied to the Pt along the **x** direction. Adapted with permission from [74]

magnetization direction of the FM can be influenced by the application of a charge current.

In these initial experiments on magnetization switching via SHE spin-transfer torque it was assumed that the reversal of the magnetization direction occurs in a uniform way. However, recent spatially- and time-resolved experiments show that in such structures the reversal is caused by domain wall nucleation and propagation [10]. Moreover, it has been shown that the spin torques generated from the SHE can also increase the domain wall velocities in similar structures as used for magnetization switching [35, 78, 97, 98]. It is important to emphasize here that the matching of domain walls with the correct chirality via interfacial Dzyaloshinskii-Moriya interaction to the spin-transfer torque via SHE and spin galvanic effects is important for these high domain wall velocities [61, 109]. However, for further improvement of such multilayers the role of additional contributions stemming from the broken inversion symmetry in these structures need to be quantitatively disentangled from SHE contributions, which is a rather difficult task in the experiment. Nevertheless, from an application point of view these high domain wall velocities could be used for racetrack memories [91, 92] and other magnetic memory applications. By further optimizing the multilayer structure even higher domain wall velocities have

been obtained in synthetic antiferromagnet structures [128]. Moreover, due to the importance of the chiral nature of the domain walls the physics used here is also applicable to Skyrmionic systems for either moving skyrmions [15, 100, 123] or for the generation of skyrmions [55].

7.4.4 Spin Hall Tunneling Spectroscopy

Inspired by the work on non-local SHE detection, Liu et al. [67] used the spin-polarized charge current flowing from a FM through a insulating barrier layer (I) into a NM to investigate the conversion of the injected spin current by the ISHE. They coined the term spin Hall effect tunneling spectroscopy for this measurement scheme.

In more detail, a charge current bias across a NM/I/FM tunnel junction (applied between contacts 1 and 3 in Fig. 7.10a) leads to a spin-polarized charge current flowing in the NM along **z**, with the spin polarization parallel to **M** (along the **x**-direction). The ISHE transforms this spin current into a charge current $j_{q,ISHE}$ flowing along the $-y$ direction and leads to the generation of an electric field along **y** (Leading to a voltage drop between the contacts 3 and 4). Liu et al. applied a differential resistance technique by applying a DC (I_{DC}) and an AC ($dI = 10 \mu\text{A}$, with a fixed modulation frequency of 1 kHz) charge current and detecting the AC voltage dV between contacts 2 and 4 via a Lock-In technique. The results obtained for Ta/MgO/CoFeB are

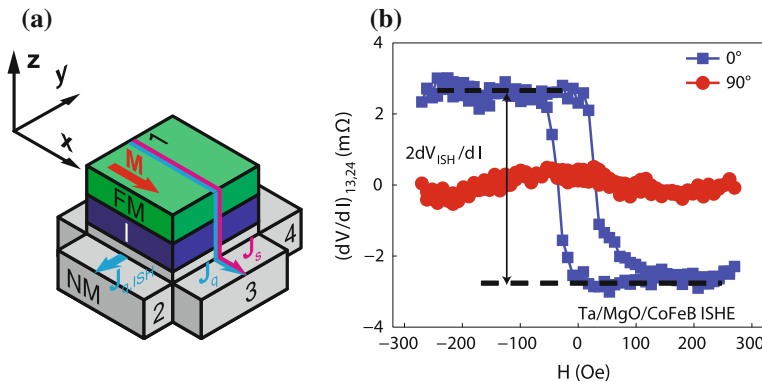


Fig. 7.10 **a** Illustration of the measurement geometry used by Liu et al. [67] for the detection of the ISHE. A spin-polarized charge current is injected from a FM through an insulating barrier layer (I) into the NM. The ISHE transforms the injected spin current j_s into a charge current $j_{q,ISHE}$, which can then be detected as an open-circuit voltage. 1, 2, 3, 4 define the contact leads used in the experiment. ISHE differential resistance signal as a function of the applied magnetic field obtained for a Ta/MgO/CoFeB **(b)** trilayer system. For 0° the external field points along **x**, while for 90° it is aligned along **y**. Only if the external magnetic field aligns **M** along **x** a hysteretic differential resistance is observed. Figures and data adapted with permission from [67]

shown in Fig. 7.10b. When the external magnetic field is swept along the \mathbf{x} -direction (blue squares, 0°), a hysteresis is observed in the differential resistance dV/dI , while no magnetic field dependence is observed when the field is applied along the \mathbf{y} -direction (red circles, 90°). This observation agrees with the vector product nature of the ISHE, as only for $\mathbf{s} \parallel \mathbf{x}$ the charge current will be oriented along $-\mathbf{y}$. Moreover, upon inversion of the magnetization direction the sign of the differential resistance is reversed. This confirms the ISHE effect as the origin of the differential resistance, as the direction of the charge current $\mathbf{j}_{q,\text{ISHE}}$ should be inverted upon inversion of \mathbf{s} . As a spin-polarized charge current is used for the generation of the spin current in the NM, similar to non-local experiments, this technique allows to quantify the spin Hall angle if the spin diffusion length of the NM is known. A unique feature of this experimental technique is the possibility to investigate the voltage bias dependence of the ISHE dV/dI by changing the applied I_{DC} . In principle, this should allow to disentangle the contributions from bulk ISHE in the NM and the spin galvanic effects (due to broken inversion symmetry) [22, 37, 71, 77] from surface states at the NM/I interface, as it is expected that both should have characteristically different bias dependence. However, further experiments are currently required to confirm this conjecture.

In addition, Liu et al. used the very same device geometry to also investigate the SHE of the NM. For such experiments a charge current \mathbf{j}_q is applied along the $-\mathbf{y}$ direction (between contacts 2 and 4, Fig. 7.10a). At the NM/I interface the SHE generated spin current leads to the generation of a spin accumulation. If \mathbf{M} of the FM is aligned parallel to \mathbf{s} , then the spin accumulation can be detected as a voltage across the tunnel junction between contacts 1 and 3. Similar to the results obtained in the ISHE configuration, dV/dI shows a hysteretic behaviour for $\mathbf{M} \parallel \mathbf{s}$, i.e. for magnetic fields sweeps along the \mathbf{x} direction. While no hysteresis is observed, if $\mathbf{M} \perp \mathbf{s}$. Moreover, the sign of dV/dI is inverted when the magnetization direction is reversed or Ta is exchanged with Pt.

These first proof-of-principle experiments are rather promising and may allow to investigate for example the influence of the bandstructure on the intrinsic spin Hall effect. Going a step further, Dankert et al. [30] utilized this measurement technique to investigate spin-polarized currents flowing on the surface of the topological insulator Bi_2Se_3 . In addition, theoretical calculations suggest that transverse voltage contributions can be also present in NM/I/FM heterostructures, where there is no spin-orbit coupling in the NM [72]. Moreover, in [18] theoretical calculations explore means to probe the magnon density of states in such tunneling structures.

7.4.5 Spin Hall Magnetoresistance

Last but not least, the spin Hall magnetoresistance (SMR) is also an effect that allows to investigate and quantify the spin Hall angle from magnetotransport experiments. As shown in Fig. 7.4a, b, when the transverse boundary conditions are changed from an open spin circuit to a closed spin circuit, the longitudinal resistance of the NM is

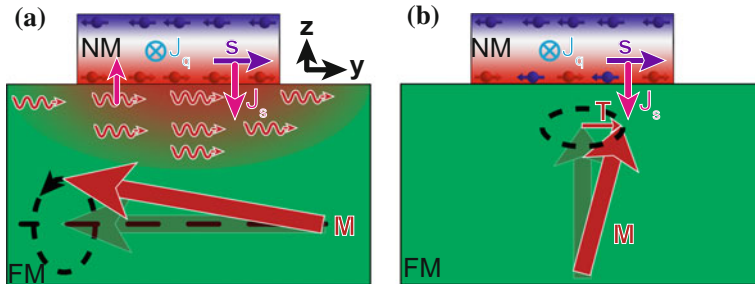


Fig. 7.11 Two different boundary conditions for SMR: **a** open spin circuit boundary condition, **b** closed spin circuit boundary condition

increased. In spin Hall magnetoresistance the boundary conditions are controlled by the magnetization direction of a FM in contact with the NM [1, 19, 20, 43, 73, 84, 117].

In the following we assume that the FM is an electrical insulator, which simplifies the discussion of the physical principles of SMR in FM/NM heterostructures. If a charge current \mathbf{j}_q is flowing in the NM a spin current \mathbf{j}_s is generated via the SHE, flowing along the \mathbf{z} -direction towards the FM/NM interface (Fig. 7.11a). As discussed previously, in the steady-state this leads to a spin accumulation at the transverse sides of the sample to compensate the transverse spin current flow. At the FM/NM interface the spin accumulation due to the SHE has a spin polarization pointing along \mathbf{y} . The spin accumulation at the NM/FM interface interacts with the magnetic order parameter in FM. This interaction depends on the orientation of \mathbf{M} relative to \mathbf{s} [11]. There are two limiting cases that need to be considered. First, if \mathbf{M} and \mathbf{s} are collinear an exchange of angular momentum via spin-transfer torque is not possible as $\mathbf{M} \times \mathbf{s} = 0$ (Fig. 7.11a, see also (7.8)). However, due to thermal fluctuations of \mathbf{M} a magnon accumulation is generated underneath the NM strip and diffuses into the FM. This leads to a small spin current flow across the NM interface. In theoretical models of the SMR this effect is normally neglected and one assumes that there is no spin current flow across the interface in this situation, which then corresponds to the open spin circuit boundary condition [19, 20]. But from very recent non-local, diffusive magnon transport experiments the existence of this magnon accumulation has been verified [11, 25, 26, 41, 66, 124, 130, 131]. Second, as illustrated in Fig. 7.11b, if $\mathbf{M} \perp \mathbf{s}$ spin angular momentum can be transferred over the interface into the FM (where it is then absorbed by the magnetic order parameter), such that a finite spin current \mathbf{j}_s flows into the FM and reduces the spin accumulation in the NM at the interface. The magnitude of \mathbf{j}_s is given by the spin-mixing conductance $g^{\uparrow\downarrow}$. In this situation, the closed spin circuit boundary condition is realized and the longitudinal resistance of the NM layer is increased. One should note, that as only one interface side of the NM allows the flow of a spin current this is still not representing the ideal closed spin circuit condition. This ideal condition may be realized by sandwiching the NM between two FMs [19].

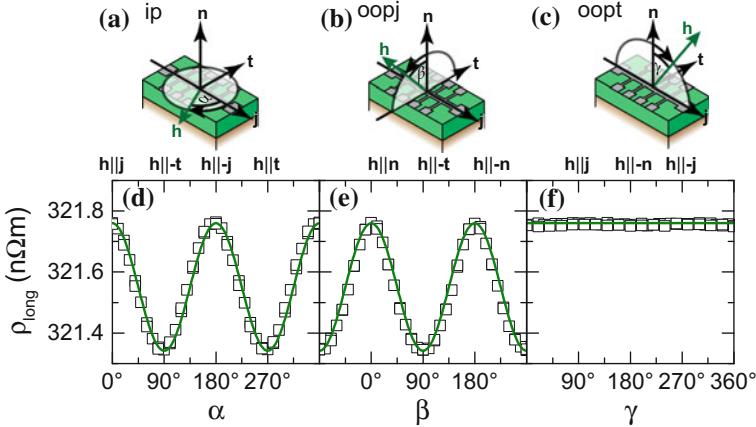


Fig. 7.12 Illustration of the three orthogonal rotation planes used in ADMR experiments: **a** ip rotation plane, **b** oopj rotation plane, **c** oopt rotation plane. Longitudinal resistivity as a function of magnetic field orientation obtained for a Pt (3.5 nm)/YIG (20 nm) heterostructure at $T = 300$ K and an external magnetic field magnitude $\mu_0 H = 1$ T for the ip (d), oopj (e), and oopt (f) rotation. The open squares are the data points, while the green lines are a simulation using (7.11). Data and figure adapted with permission from [1]

As evident from this qualitative description, the SMR depends on the orientation of \mathbf{M} relative to the spin polarization \mathbf{s} of the spin accumulation in the NM. As a reference frame we now use the three orthogonal directions, consisting of the current direction \mathbf{j} , the surface normal \mathbf{n} , and the transverse direction $\mathbf{t} = \mathbf{n} \times \mathbf{j}$ (see Fig. 7.12a). In this coordinate system \mathbf{s} is collinear with \mathbf{t} . The longitudinal resistivity ρ_{long} can thus be written as [19]:

$$\rho_{\text{long}} = \rho_0 + \rho_1 (1 - m_{\mathbf{t}}^2) , \quad (7.11)$$

where $m_{\mathbf{t}} = \mathbf{M}/M \cdot \mathbf{t}$ is the projection of the magnetization direction onto \mathbf{t} , ρ_i are resistivity parameters of the NM. For the SMR ratio ρ_1/ρ_0 one finds [19]:

$$\frac{\rho_1}{\rho_0} = \frac{\alpha_{\text{SH}}^2 (2\lambda_{\text{sf}}^2 \rho_{\text{NM}}) (t_{\text{NM}})^{-1} \text{Re} (g^{\uparrow\downarrow}) \tanh^2 \left(\frac{t_{\text{NM}}}{2\lambda_{\text{sf}}} \right)}{h e^{-2} + 2\lambda_{\text{sf}} \rho_{\text{NM}} \text{Re} (g^{\uparrow\downarrow}) \coth \left(\frac{t_{\text{NM}}}{\lambda_{\text{sf}}} \right)} . \quad (7.12)$$

Here, ρ_{NM} is the resistivity of the NM. The SMR ratio is proportional to α_{SH}^2 . Assuming $\alpha_{\text{SH}} \approx 0.1$, the expected relative resistance change is of the order of 1% for the SMR effect. Moreover, (7.12) allows to determine $|\alpha_{\text{SH}}|$ and λ_{sf} of the NM, if the SMR is measured as a function of the NM thickness and the spin mixing conductance is known [1, 117]. However, the sign of α_{SH} can not be determined due to the scaling of the SMR with α_{SH}^2 .

The unique symmetry of the SMR is reflected in angle dependent magnetoresistance (ADMR) measurements [1, 44, 84, 117]. In an ADMR experiment the external magnetic field is kept at fixed magnitude $\mu_0 H$, while the orientation of the

field direction \mathbf{h} with respect to the sample is changed. To distinguish the SMR from other magnetoresistance effects, like the anisotropic magnetoresistance, \mathbf{h} is rotated in three orthogonal rotation planes. In the in-plane (ip) rotation plane, \mathbf{h} rotates in the sample plane (perpendicular to the surface normal, cf. Fig. 7.12a). In the oopj rotation plane, the external magnetic field is rotated in the plane perpendicular to the current direction \mathbf{j} (Fig. 7.12b). In the oopt rotation plane, \mathbf{h} is rotated in the plane perpendicular to \mathbf{t} (Fig. 7.12c). From (7.11) and assuming that the magnetization is always aligned parallel to \mathbf{h} one expects that for the SMR only in the ip and oopj rotation planes a modulation of the longitudinal resistance with the field orientation should occur, while there should be no modulation in the oopt rotation plane. The results of ADMR measurements conducted on a Pt (3.5 nm)/yttrium iron garnet (YIG) (20 nm) heterostructure at $T = 300$ K and an external magnetic field magnitude $\mu_0 H = 1$ T from [1] are shown in Fig. 7.12d–f. Indeed, the longitudinal resistivity exhibits only for the oopj and ip rotation planes an angle-dependence. The angle-dependence of the SMR is qualitatively different from the one of a polycrystalline anisotropic magnetoresistance and allows to unambiguously identify the SMR as the physical origin of the observed MR [1, 44, 84, 117].

Initial experimental work on the SMR was focused on YIG/NM heterostructures, where the maximum SMR amplitude obtained up to now was $\rho_1/\rho_0 = 1.3 \times 10^{-3}$ [1]. Over the last years, the SMR effect was also observed in a variety of electrically insulating FMs [1, 52, 125], which confirms the universality of the SMR. Several groups also reported the experimental observation of the SMR in magnetically ordered systems that have a non-collinear spin texture, like in a spin-canted phase of a compensated ferrimagnet [38], in a material with spin spiral ordering [6], or an canted antiferromagnet [47]. These experiments thus show that not the net magnetization of a magnetically ordered system is relevant for the SMR, but each individual magnetic moment at the interface or even the relevant order parameter of the magnetically ordered system contribute to the SMR. A complete theoretical description for the SMR in this framework is still missing and could be tough to realize as magnetic domains may also play a crucial role in determining the magnitude of the SMR effect in such systems. Later experiments showed that the SMR also persists in metallic ferromagnets [7, 23, 86, 129] and can reach values of up to $\rho_1/\rho_0 = 3 \times 10^{-2}$.

7.5 Summary and Outlook

After several decades of effort from theory and experiment, the spin Hall effect and the inverse spin Hall effect have become important cornerstones in the field of pure spin current physics. The SHE allows to transform a charge current into a pure spin current, while the ISHE allows to electrically detect pure spin currents. As can be seen from this chapter, these concepts have lead to the discovery of entirely new physical phenomena. An important part that has been left out of this section are thermal effects, where thermal gradients are used to drive spin currents like in the

spin Seebeck effect [9, 113, 114]. Moreover, the SHE and ISHE have opened up novel application concepts ranging from energy harvesting applications, over new concepts for switching the magnetization direction in magnetic memories, to the generation of microwave and terahertz radiation [103].

For a deeper understanding of the SHE, a systematic investigation of the scaling of the spin Hall conductivity with the longitudinal charge conductivity, which spans several orders of magnitude in the conductivity is still missing. But such an investigation would be required to confirm that SHE and AHE are based on the very same microscopic mechanisms. One main challenge to accomplish this task is that interface effects can also be the origin of pure spin currents and it might be difficult to separate these contributions from the bulk SHE, because the short spin diffusion length requires already thin samples. The proposed quantum spin Hall effect [13] has initiated the quickly progressing field of topological insulators. In the future, these topological insulators might allow to realize dissipation free pure spin currents flowing in the edge states of such bulk insulators. Moreover, currently the high frequency limit of the SHE is heavily investigated. Utilizing the ISHE in FM/NM bilayers, efficient, broadband terahertz emitters have been realized [103]. Currently, most SHE experiments focus on metallic conductors, thus it might be beneficial to investigate the SHE in other materials more systematically like oxides [94, 95], anti-ferromagnets [88, 132–134] or even semiconducting materials [3, 106, 127], where the SHE was first discovered.

The field of SHE and ISHE physics is still in its early stages such that the underlying microscopic mechanisms in most of the observed phenomena are not completely understood and further exciting results are to be expected in the future. In the end, the SHE and ISHE will remain a very fruitful field for future theoretical and experimental studies.

Acknowledgements I would like to thank S. T. B. Goennenwein for all his help and support while writing this chapter. Moreover, helpful discussions with H. Huebl, R. Gross, and M. Weiler are gratefully acknowledged.

References

1. M. Althammer, S. Meyer, H. Nakayama, M. Schreier, S. Altmannshofer, M. Weiler, H. Huebl, S. Gräppls, M. Opel, R. Gross, D. Meier, C. Klewe, T. Kuschel, J.M. Schmalhorst, G. Reiss, L. Shen, A. Gupta, Y.T. Chen, G.E.W. Bauer, E. Saitoh, S.T.B. Goennenwein, Quantitative study of the spin Hall magnetoresistance in ferromagnetic insulator/normal metal hybrids. *Phys. Rev. B* **87**(22), 224401 (2013). <https://doi.org/10.1103/physrevb.87.224401>
2. K. Ando, E. Saitoh, Inverse spin-Hall effect in palladium at room temperature. *J. Appl. Phys.* **108**(11), 113925 (2010). <https://doi.org/10.1063/1.3517131>
3. K. Ando, E. Saitoh, Observation of the inverse spin Hall effect in silicon. *Nat. Commun.* **3**, 629 (2012). <https://doi.org/10.1038/ncomms1640>
4. K. Ando, S. Takahashi, K. Harii, K. Sasage, J. Ieda, S. Maekawa, E. Saitoh, Electric manipulation of spin relaxation using the spin Hall effect. *Phys. Rev. Lett.* **101**(3), 036601 (2008). <https://doi.org/10.1103/physrevlett.101.036601>

5. K. Ando, S. Takahashi, J. Ieda, Y. Kajiwara, H. Nakayama, T. Yoshino, K. Harii, Y. Fujikawa, M. Matsuo, S. Maekawa, E. Saitoh, Inverse spin-Hall effect induced by spin pumping in metallic system. *J. Appl. Phys.* **109**(10), 103913 (2011). <https://doi.org/10.1063/1.3587173>
6. A. Aqeel, N. Vlietstra, J.A. Heuver, G.E.W. Bauer, B. Noheda, B.J. van Wees, T.T.M. Palstra, Spin-Hall magnetoresistance and spin Seebeck effect in spin-spiral and paramagnetic phases of multiferroic CoCr₂O₄ films. *Phys. Rev. B* **92**, 224410 (2015). <https://doi.org/10.1103/physrevb.92.224410>
7. C.O. Avci, K. Garello, A. Ghosh, M. Gabureac, S.F. Alvarado, P. Gambardella, Unidirectional spin Hall magnetoresistance in ferromagnet/normal metal bilayers. *Nat. Phys.* **11**(7), 570–575 (2015). <https://doi.org/10.1038/nphys3356>
8. A.A. Awad, P. Dürrenfeld, A. Houshang, M. Dvornik, E. Iacocca, R.K. Dumas, J. Åkerman, Long-range mutual synchronization of spin Hall nano-oscillators. *Nat. Phys.* **13**, 292–299 (2017). <https://doi.org/10.1038/nphys3927>
9. G.E.W. Bauer, E. Saitoh, B.J. van Wees, Spin caloritronics. *Nat. Mater.* **11**(5), 391 (2012). <https://doi.org/10.1038/nmat3301>
10. M. Baumgartner, K. Garello, J. Mendil, C.O. Avci, E. Grimaldi, C. Murer, J. Feng, M. Gabureac, C. Stamm, Y. Acremann, S. Finizio, S. Wintz, J. Raabe, P. Gambardella, Spatially and time-resolved magnetization dynamics driven by spin-orbit torques. *Nat. Nanotechnol.* **12**(10), 980–986 (2017). <https://doi.org/10.1038/nnano.2017.151>
11. S.A. Bender, Y. Tserkovnyak, Interfacial spin and heat transfer between metals and magnetic insulators. *Phys. Rev. B* **91**, 140402 (2015). <https://doi.org/10.1103/physrevb.91.140402>
12. L. Berger, Generation of dc voltages by a magnetic multilayer undergoing ferromagnetic resonance. *Phys. Rev. B* **59**(17), 11465 (1999). <https://doi.org/10.1103/PhysRevB.59.11465>
13. B.A. Bernevig, T.L. Hughes, S.C. Zhang, Quantum spin Hall effect and topological phase transition in HgTe quantum wells. *Science* **314**(5806), 1757–1761 (2006). <https://doi.org/10.1126/science.1133734>
14. C. Burrowes, B. Heinrich, B. Kardasz, E.A. Montoya, E. Girt, Y. Sun, Y.Y. Song, M. Wu, Enhanced spin pumping at yttrium iron garnet/Au interfaces. *Appl. Phys. Lett.* **100**(9), 092403 (2012). <https://doi.org/10.1063/1.3690918>
15. F. Büttner, C. Moutafis, M. Schneider, B. Krüger, C.M. Günther, J. Geilhufe, C.V. Korff Schmising, J. Mohanty, B. Pfau, S. Schaffert, A. Bisig, M. Foerster, T. Schulz, C.A.F. Vaz, J.H. Franken, H.J.M. Swagten, M. Kläui, S. Eisebitt, Dynamics and inertia of skyrmionic spin structures. *Nat. Phys.* **11**(3), 225–228 (2015). <https://doi.org/10.1038/nphys3234>
16. J.N. Chazalviel, Spin-dependent Hall effect in semiconductors. *Phys. Rev. B* **11**(10), 3918–3934 (1975). <https://doi.org/10.1103/physrevb.11.3918>
17. J. Chciński, M. Frankowski, T. Stobiecki, Antiferromagnetic nano-oscillator in external magnetic fields. *Phys. Rev. B* **96**(17) (2017). <https://doi.org/10.1103/PhysRevB.96.174438>
18. W. Chen, M. Sigrist, D. Manske, Spin Hall effect induced spin transfer through an insulator. *Phys. Rev. B* **94**(10), 104412 (2016). <https://doi.org/10.1103/physrevb.94.104412>
19. Y.T. Chen, S. Takahashi, H. Nakayama, M. Althammer, S.T.B. Goennenwein, E. Saitoh, G.E.W. Bauer, Theory of spin Hall magnetoresistance. *Phys. Rev. B* **87**, 144411 (2013). <https://doi.org/10.1103/PhysRevB.87.144411>
20. Y.T. Chen, S. Takahashi, H. Nakayama, M. Althammer, S.T.B. Goennenwein, E. Saitoh, G.E.W. Bauer, Theory of spin Hall magnetoresistance (SMR) and related phenomena. *J. Phys. Condens. Matter* **28**(10), 103004 (2016). <https://doi.org/10.1088/0953-8984/28/10/103004>
21. R. Cheng, D. Xiao, A. Brataas, Terahertz antiferromagnetic spin Hall nano-oscillator. *Phys. Rev. Lett.* **116**(20), 207603 (2016). <https://doi.org/10.1103/physrevlett.116.207603>
22. A. Chernyshov, M. Overby, X. Liu, J.K. Furdyna, Y. Lyanda-Geller, L.P. Rokhinson, Evidence for reversible control of magnetization in a ferromagnetic material by means of spin-orbit magnetic field. *Nat. Phys.* **5**(9), 656–659 (2009). <https://doi.org/10.1038/nphys1362>
23. S. Cho, S.C. Baek, K.D. Lee, Y. Jo, B.G. Park, Large spin Hall magnetoresistance and its correlation to the spin-orbit torque in w/CoFeB/MgO structures. *Sci. Rep.* **5**, 14668 (2015). <https://doi.org/10.1038/srep14668>

24. M. Collet, X. de Milly, O. d' Allivy Kelly, V.V. Naletov, R. Bernard, P. Bortolotti, J.B. Youssef, V.E. Demidov, S.O. Demokritov, J.L. Prieto, M. Muñoz, V. Cros, A. Anane, G. de Loubens, O. Klein, Generation of coherent spin-wave modes in yttrium iron garnet microdisks by spin-orbit torque. *Nat. Commun.* **7**, 10377 (2016). <https://doi.org/10.1038/ncomms10377>
25. L.J. Cornelissen, J. Liu, R.A. Duine, J.B. Youssef, B.J. van Wees, Long-distance transport of magnon spin information in a magnetic insulator at room temperature. *Nat. Phys.* **11**(12), 1022–1026 (2015). <https://doi.org/10.1038/nphys3465>
26. L.J. Cornelissen, J. Shan, B.J. van Wees, Temperature dependence of the magnon spin diffusion length and magnon spin conductivity in the magnetic insulator yttrium iron garnet. *Phys. Rev. B* **94**, 180402 (2016). <https://doi.org/10.1103/physrevb.94.180402>
27. F.D. Czeschka, Spin currents in metallic nanostructures. Ph.D. thesis, Technische Universität München (2011)
28. F.D. Czeschka, L. Dreher, M.S. Brandt, M. Weiler, M. Althammer, I.M. Imort, G. Reiss, A. Thomas, W. Schoch, W. Limmer, H. Huebl, R. Gross, S.T.B. Goennenwein, Scaling behavior of the spin pumping effect in ferromagnet-platinum bilayers. *Phys. Rev. Lett.* **107**, 046601 (2011). <https://doi.org/10.1103/PhysRevLett.107.046601>
29. M.W. Daniels, W. Guo, G.M. Stocks, D. Xiao, J. Xiao, Spin-transfer torque induced spin waves in antiferromagnetic insulators. *New J. Phys.* **17**(10), 103039 (2015). <https://doi.org/10.1088/1367-2630/17/10/103039>
30. A. Dankert, J. Geurs, M.V. Kamalakar, S. Charpentier, S.P. Dash, Room temperature electrical detection of spin polarized currents in topological insulators. *Nano Lett.* **15**(12), 7976–7981 (2015). <https://doi.org/10.1021/acs.nanolett.5b03080>
31. V.E. Demidov, S. Urazhdin, H. Ulrichs, V. Tiberkevich, A. Slavin, D. Bather, G. Schmitz, S.O. Demokritov, Magnetic nano-oscillator driven by pure spin current. *Nat. Mater.* **11**, 1028–1031 (2012). <https://doi.org/10.1038/nmat3459>
32. V.E. Demidov, S. Urazhdin, A. Zholud, A.V. Sadovnikov, S.O. Demokritov, Nanoconstriction-based spin-Hall nano-oscillator. *Appl. Phys. Lett.* **105**(17), 172410 (2014). <https://doi.org/10.1063/1.4901027>
33. Z. Duan, A. Smith, L. Yang, B. Youngblood, J. Lindner, V.E. Demidov, S.O. Demokritov, I.N. Krivorotov, Nanowire spin torque oscillator driven by spin orbit torques. *Nat. Commun.* **5**, 5616 (2014). <https://doi.org/10.1038/ncomms6616>
34. M. Dyakonov, V. Perel, Current-induced spin orientation of electrons in semiconductors. *Phys. Lett. A* **35**(6), 459–460 (1971). [https://doi.org/10.1016/0375-9601\(71\)90196-4](https://doi.org/10.1016/0375-9601(71)90196-4)
35. S. Emori, U. Bauer, S.M. Ahn, E. Martinez, G.S.D. Beach, Current-driven dynamics of chiral ferromagnetic domain walls. *Nat. Mater.* **12**(7), 611–616 (2013). <https://doi.org/10.1038/nmat3675>
36. M. Erekhinsky, A. Sharoni, F. Casanova, I.K. Schuller, Surface enhanced spin-flip scattering in lateral spin valves. *Appl. Phys. Lett.* **96**(2), 022513 (2010). <https://doi.org/10.1063/1.3291047>
37. D. Fang, H. Kurebayashi, J. Wunderlich, K. Vyborny, L.P. Zarbo, R.P. Campion, A. Casiraghi, B.L. Gallagher, T. Jungwirth, A.J. Ferguson, Spin-orbit-driven ferromagnetic resonance. *Nat. Nanotechnol.* **6**, 413 (2011). <https://doi.org/10.1038/nnano.2011.68>
38. K. Ganzhorn, J. Barker, R. Schlitz, B.A. Piot, K. Ollefs, F. Guillou, F. Wilhelm, A. Rogalev, M. Opel, M. Althammer, S. Geprägs, H. Huebl, R. Gross, G.E.W. Bauer, S.T.B. Goennenwein, Spin Hall magnetoresistance in a canted ferrimagnet. *Phys. Rev. B* **94**, 094401 (2016). <https://doi.org/10.1103/physrevb.94.094401>
39. K. Garello, I.M. Miron, C.O. Avci, F. Freimuth, Y. Mokrousov, S. Blügel, S. Auffret, O. Boulle, G. Gaudin, P. Gambardella, Symmetry and magnitude of spin-orbit torques in ferromagnetic heterostructures. *Nat. Nanotechnol.* **8**(8), 587–593 (2013). <https://doi.org/10.1038/nnano.2013.145>
40. A. Giordano, M. Carpentieri, A. Laudani, G. Gubbiotti, B. Azzerboni, G. Finocchio, Spin-Hall nano-oscillator: a micromagnetic study. *Appl. Phys. Lett.* **105**(4), 042412 (2014). <https://doi.org/10.1063/1.4892168>
41. S.T.B. Goennenwein, R. Schlitz, M. Pernpeintner, K. Ganzhorn, M. Althammer, R. Gross, H. Huebl, Non-local magnetoresistance in YIG/Pt nanostructures. *Appl. Phys. Lett.* **107**(17), 172405 (2015). <https://doi.org/10.1063/1.4935074>

42. Y. Gui, N. Mecking, X. Zhou, G. Williams, C.M. Hu, Realization of a room-temperature spin dynamo: the spin rectification effect. *Phys. Rev. Lett.* **98**(10), 107602 (2007). <https://doi.org/10.1103/PhysRevLett.98.107602>
43. C. Hahn, G. de Loubens, O. Klein, M. Viret, V.V. Naletov, J.B. Youssef, Comparative measurements of inverse spin Hall effects and magnetoresistance in YIG/Pt and YIG/Ta. *Phys. Rev. B* **87**(17), 174417 (2013). <https://doi.org/10.1103/physrevb.87.174417>
44. C. Hahn, G. de Loubens, M. Viret, O. Klein, V.V. Naletov, J.B. Youssef, Detection of microwave spin pumping using the inverse spin Hall effect. *Phys. Rev. Lett.* **111**(21), 217204 (2013). <https://doi.org/10.1103/physrevlett.111.217204>
45. E.H. Hall, Anomalous Hall effect. *Philos. Mag.* **12** (1881)
46. A. Hamadeh, O. d'Allivy Kelly, C. Hahn, H. Meley, R. Bernard, A. Molpeceres, V. Naletov, M. Viret, A. Anane, V. Cros, S. Demokritov, J. Prieto, M. Muñoz, G. de Loubens, O. Klein, Full control of the spin-wave damping in a magnetic insulator using spin-orbit torque. *Phys. Rev. Lett.* **113**(19), 197203 (2014). <https://doi.org/10.1103/physrevlett.113.197203>
47. J.H. Han, C. Song, F. Li, Y.Y. Wang, G.Y. Wang, Q.H. Yang, F. Pan, Antiferromagnet-controlled spin current transport in SrMnO₃/Pt hybrids. *Phys. Rev. B* **90**, 144431 (2014). <https://doi.org/10.1103/physrevb.90.144431>
48. P.M. Haney, H.W. Lee, K.J. Lee, A. Manchon, M.D. Stiles, Current induced torques and interfacial spin-orbit coupling: semiclassical modeling. *Phys. Rev. B* **87**(17), 174411 (2013). <https://doi.org/10.1103/physrevb.87.174411>
49. B. Heinrich, C. Burrowes, E. Montoya, B. Kardasz, E. Girt, Y.Y. Song, Y. Sun, M. Wu, Spin pumping at the magnetic insulator (YIG)/normal metal (Au) interfaces. *Phys. Rev. Lett.* **107**(6), 066604 (2011). <https://doi.org/10.1103/PhysRevLett.107.066604>
50. J.E. Hirsch, Spin Hall effect. *Phys. Rev. Lett.* **83**(9), 1834–1837 (1999). <https://doi.org/10.1103/PhysRevLett.83.1834>
51. A. Hoffmann, Spin Hall effects in metals. *IEEE Trans. Magn.* **49**(10), 5172–5193 (2013). <https://doi.org/10.1109/tmag.2013.2262947>
52. M. Isasa, A. Bedoya-Pinto, S. Vélez, F. Golmar, F. Sánchez, L.E. Hueso, J. Fontcuberta, F. Casanova, Spin Hall magnetoresistance at Pt/CoFe₂O₄ interfaces and texture effects. *Appl. Phys. Lett.* **105**(14), 142402 (2014). <https://doi.org/10.1063/1.4897544>
53. F.J. Jedema, A.T. Filip, B.J. van Wees, Electrical spin injection and accumulation at room temperature in an all-metal mesoscopic spin valve. *Nature* **410**(6826), 345–348 (2001). <https://doi.org/10.1038/35066533>
54. Y. Ji, A. Hoffmann, J.S. Jiang, S.D. Bader, Spin injection, diffusion, and detection in lateral spin-valves. *Appl. Phys. Lett.* **85**(25), 6218–6220 (2004). <https://doi.org/10.1063/1.1841455>
55. W. Jiang, P. Upadhyaya, W. Zhang, G. Yu, M.B. Jungfleisch, F.Y. Fradin, J.E. Pearson, Y. Tserkovnyak, K.L. Wang, O. Heinonen, S.G.E. te Velthuis, A. Hoffmann, Blowing magnetic skyrmion bubbles. *Science* **349**(6245), 283–286 (2015). <https://doi.org/10.1126/science.aaa1442>
56. H. Jiao, G.E.W. Bauer, Spin backflow and ac voltage generation by spin pumping and the inverse spin Hall effect. *Phys. Rev. Lett.* **110**(21), 217602 (2013). <https://doi.org/10.1103/PhysRevLett.110.217602>
57. M. Johnson, R.H. Silsbee, Interfacial charge-spin coupling: injection and detection of spin magnetization in metals. *Phys. Rev. Lett.* **55**(17), 1790–1793 (1985). <https://doi.org/10.1103/physrevlett.55.1790>
58. H.J. Juretschke, Electromagnetic theory of dc effects in ferromagnetic resonance. *J. Appl. Phys.* **31**(8), 1401 (1960). <https://doi.org/10.1063/1.1735851>
59. Y. Kajiwara, K. Harii, S. Takahashi, J. Ohe, K. Uchida, M. Mizuguchi, H. Umezawa, H. Kawai, K. Ando, K. Takanashi, S. Maekawa, E. Saitoh, Transmission of electrical signals by spin-wave interconversion in a magnetic insulator. *Nature* **464**(7286), 262 (2010). <https://doi.org/10.1038/nature08876>
60. Y.K. Kato, R.C. Myers, A.C. Gossard, D.D. Awschalom, Observation of the spin Hall effect in semiconductors. *Science* **306**(5703), 1910–1913 (2004). <https://doi.org/10.1126/science.1105514>

61. A.V. Khvalkovskiy, V. Cros, D. Apalkov, V. Nikitin, M. Krounbi, K.A. Zvezdin, A. Anane, J. Grollier, A. Fert, Matching domain-wall configuration and spin-orbit torques for efficient domain-wall motion. *Phys. Rev. B* **87**(2) (2013). <https://doi.org/10.1103/PhysRevB.87.020402>
62. R. Khymyn, I. Lisenkov, V. Tiberkevich, B.A. Ivanov, A. Slavin, Antiferromagnetic THz-frequency Josephson-like oscillator driven by spin current. *Sci. Rep.* **7**, 43705 (2017). <https://doi.org/10.1038/srep43705>
63. T. Kimura, Y. Otani, Large spin accumulation in a permalloy-silver lateral spin valve. *Phys. Rev. Lett.* **99**(19), 196604 (2007). <https://doi.org/10.1103/physrevlett.99.196604>
64. T. Kimura, Y. Otani, T. Sato, S. Takahashi, S. Maekawa, Room-temperature reversible spin Hall effect. *Phys. Rev. Lett.* **98**(15), 156601 (2007). <https://doi.org/10.1103/physrevlett.98.156601>
65. S.I. Kiselev, J.C. Sankey, I.N. Krivorotov, N.C. Emley, R.J. Schoelkopf, R.A. Buhrman, D.C. Ralph, Microwave oscillations of a nanomagnet driven by a spin-polarized current. *Nature* **425**, 380–383 (2003)
66. J. Li, Y. Xu, M. Aldosary, C. Tang, Z. Lin, S. Zhang, R. Lake, J. Shi, Observation of magnon-mediated current drag in Pt/yttrium iron garnet/Pt(Ta) trilayers. *Nat. Commun.* **7**, 10858 (2016). <https://doi.org/10.1038/ncomms10858>
67. L. Liu, C.T. Chen, J.Z. Sun, Spin Hall effect tunnelling spectroscopy. *Nat. Phys.* **10**(8), 561–566 (2014). <https://doi.org/10.1038/nphys3004>
68. L. Liu, T. Moriyama, D. Ralph, R. Buhrman, Spin-torque ferromagnetic resonance induced by the spin Hall effect. *Phys. Rev. Lett.* **106**(3), 036601 (2011). <https://doi.org/10.1103/PhysRevLett.106.036601>
69. L. Liu, C.F. Pai, Y. Li, H.W. Tseng, D.C. Ralph, R.A. Buhrman, Spin-torque switching with the giant spin Hall effect of tantalum. *Science* **336**(6081), 555–558 (2012). <https://doi.org/10.1126/science.1218197>
70. A. Manchon, H.C. Koo, J. Nitta, S.M. Frolov, R.A. Duine, New perspectives for Rashba spin-orbit coupling. *Nat. Mater.* **14**(9), 871–882 (2015). <https://doi.org/10.1038/nmat4360>
71. A. Manchon, S. Zhang, Theory of spin torque due to spin-orbit coupling. *Phys. Rev. B* **79**(9), 094422 (2009). <https://doi.org/10.1103/physrevb.79.094422>
72. A. Matos-Abiague, J. Fabian, Tunneling anomalous and spin Hall effects. *Phys. Rev. Lett.* **115**(5), 056602 (2015). <https://doi.org/10.1103/physrevlett.115.056602>
73. S. Meyer, M. Althammer, S. Geprägs, M. Opel, R. Gross, S.T.B. Goennenwein, Temperature dependent spin transport properties of platinum inferred from spin Hall magnetoresistance measurements. *Appl. Phys. Lett.* **104**(24), 242411 (2014). <https://doi.org/10.1063/1.4885086>
74. I. Mihai Miron, G. Gaudin, S. Auffret, B. Rodmacq, A. Schuhl, S. Pizzini, J. Vogel, P. Gambardella, Current-driven spin torque induced by the Rashba effect in a ferromagnetic metal layer. *Nat. Mater.* **9**, 230–234 (2010). <https://doi.org/10.1038/nmat2613>
75. G. Mihajlović, J.E. Pearson, M.A. Garcia, S.D. Bader, A. Hoffmann, Negative nonlocal resistance in mesoscopic gold Hall bars: absence of the giant spin Hall effect. *Phys. Rev. Lett.* **103**(16), 166601 (2009). <https://doi.org/10.1103/physrevlett.103.166601>
76. I.M. Miron, K. Garello, G. Gaudin, P.J. Zermatten, M.V. Costache, S. Auffret, S. Bandiera, B. Rodmacq, A. Schuhl, P. Gambardella, Perpendicular switching of a single ferromagnetic layer induced by in-plane current injection. *Nature* **476**(7359), 189–193 (2011). <https://doi.org/10.1038/nature10309>
77. I.M. Miron, G. Gaudin, S. Auffret, B. Rodmacq, A. Schuhl, S. Pizzini, J. Vogel, P. Gambardella, Current-driven spin torque induced by the Rashba effect in a ferromagnetic metal layer. *Nat. Mater.* **9**, 230–234 (2010). <https://doi.org/10.1038/nmat2613>
78. I.M. Miron, T. Moore, H. Szambolics, L.D. Buda-Prejbeanu, S. Auffret, B. Rodmacq, S. Pizzini, J. Vogel, M. Bonfim, A. Schuhl, G. Gaudin, Fast current-induced domain-wall motion controlled by the Rashba effect. *Nat. Mater.* **10**(6), 419–423 (2011). <https://doi.org/10.1038/nmat3020>
79. M. Morota, Y. Niimi, K. Ohnishi, D.H. Wei, T. Tanaka, H. Kontani, T. Kimura, Y. Otani, Indication of intrinsic spin Hall effect in 4d and 5d transition metals. *Phys. Rev. B* **83**, 174405 (2011). <https://doi.org/10.1103/PhysRevB.83.174405>

80. A. Morrish, *The Physical Principles of Magnetism* (IEEE Press, New York, 2001)
81. O. Mosendz, J.E. Pearson, F.Y. Fradin, G.E.W. Bauer, S.D. Bader, A. Hoffmann, Quantifying spin Hall angles from spin pumping: experiments and theory. *Phys. Rev. Lett.* **104**(4), 046601 (2010). <https://doi.org/10.1103/PhysRevLett.104.046601>
82. O. Mosendz, V. Vlaminck, J.E. Pearson, F.Y. Fradin, G.E.W. Bauer, S.D. Bader, A. Hoffmann, Detection and quantification of inverse spin Hall effect from spin pumping in permalloy/normal metal bilayers. *Phys. Rev. B* **82**, 214403 (2010). <https://doi.org/10.1103/PhysRevB.82.214403>
83. N. Nagaosa, J. Sinova, S. Onoda, A.H. MacDonald, N.P. Ong, Anomalous Hall effect. *Rev. Modern Phys.* **82**(2), 1539–1592 (2010). <https://doi.org/10.1103/revmodphys.82.1539>
84. H. Nakayama, M. Althammer, Y.T. Chen, K. Uchida, Y. Kajiwara, D. Kikuchi, T. Ohtani, S. Geprägs, M. Opel, S. Takahashi, R. Gross, G.E.W. Bauer, S.T.B. Goennenwein, E. Saitoh, Spin Hall magnetoresistance induced by a nonequilibrium proximity effect. *Phys. Rev. Lett.* **110**, 206601 (2013). <https://doi.org/10.1103/physrevlett.110.206601>
85. Y. Niimi, Y. Kawanishi, D.H. Wei, C. Deranlot, H.X. Yang, M. Chshiev, T. Valet, A. Fert, Y. Otani, Giant spin Hall effect induced by skew scattering from bismuth impurities inside thin film CuBi alloys. *Phys. Rev. Lett.* **109**, 156602 (2012). <https://doi.org/10.1103/PhysRevLett.109.156602>
86. K. Olejník, V. Novák, J. Wunderlich, T. Jungwirth, Electrical detection of magnetization reversal without auxiliary magnets. *Phys. Rev. B* **91**(18), 180402 (2015). <https://doi.org/10.1103/physrevb.91.180402>
87. Y. Omori, F. Auvray, T. Wakamura, Y. Niimi, A. Fert, Y. Otani, Inverse spin Hall effect in a closed loop circuit. *Appl. Phys. Lett.* **104**(24), 242415 (2014). <https://doi.org/10.1063/1.4884520>
88. Y. Ou, S. Shi, D.C. Ralph, R.A. Buhrman, Strong spin Hall effect in the antiferromagnet PtMn. *Phys. Rev. B* **93**(22) (2016). <https://doi.org/10.1103/PhysRevB.93.220405>
89. C.F. Pai, L. Liu, Y. Li, H.W. Tseng, D.C. Ralph, R.A. Buhrman, Spin transfer torque devices utilizing the giant spin Hall effect of tungsten. *Appl. Phys. Lett.* **101**(12), 122404 (2012). <https://doi.org/10.1063/1.4753947>
90. C.F. Pai, Y. Ou, L.H. Vilela-Leão, D.C. Ralph, R.A. Buhrman, Dependence of the efficiency of spin Hall torque on the transparency of Pt/ferromagnetic layer interfaces. *Phys. Rev. B* **92**(6), 064426 (2015). <https://doi.org/10.1103/physrevb.92.064426>
91. S. Parkin, S.H. Yang, Memory on the racetrack. *Nat. Nanotechnol.* **10**(3), 195–198 (2015). <https://doi.org/10.1038/nnano.2015.41>
92. S.S.P. Parkin, M. Hayashi, L. Thomas, Magnetic domain-wall racetrack memory. *Science* **320**(5873), 190–194 (2008). <https://doi.org/10.1126/science.1145799>
93. V. Puliafito, A. Giordano, A. Laudani, F. Garesci, M. Carpentieri, B. Azzerboni, G. Finocchio, Scalable synchronization of spin-Hall oscillators in out-of-plane field. *Appl. Phys. Lett.* **109**(20), 202402 (2016). <https://doi.org/10.1063/1.4967842>
94. Z. Qiu, T. An, K. Uchida, D. Hou, Y. Shiomi, Y. Fujikawa, E. Saitoh, Experimental investigation of spin Hall effect in indium tin oxide thin film. *Appl. Phys. Lett.* **103**(18), 182404 (2013). <https://doi.org/10.1063/1.4827808>
95. Z. Qiu, D. Hou, T. Kikkawa, K.I. Uchida, E. Saitoh, All-oxide spin Seebeck effects. *Appl. Phys. Express* **8**(8), 083001 (2015). <https://doi.org/10.7567/APEX.8.083001>
96. D.C. Ralph, M.D. Stiles, Spin transfer torques. *JMMM* **320**(7), 1190–1216 (2008)
97. K.S. Ryu, L. Thomas, S.H. Yang, S. Parkin, Chiral spin torque at magnetic domain walls. *Nat. Nanotechnol.* **8**(7), 527–533 (2013). <https://doi.org/10.1038/nnano.2013.102>
98. K.S. Ryu, S.H. Yang, S. Parkin, Experimentally tunable chiral spin transfer torque in domain wall motion. *New J. Phys.* **18**(5), 053027 (2016). <https://doi.org/10.1088/1367-2630/18/5/053027>
99. E. Saitoh, M. Ueda, H. Miyajima, G. Tatara, Conversion of spin current into charge current at room temperature: inverse spin-Hall effect. *Appl. Phys. Lett.* **88**(18), 182509 (2006). <https://doi.org/10.1063/1.2199473>

100. J. Sampaio, V. Cros, S. Rohart, A. Thiaville, A. Fert, Nucleation, stability and current-induced motion of isolated magnetic skyrmions in nanostructures. *Nat. Nanotechnol.* **8**(11), 839–844 (2013). <https://doi.org/10.1038/nnano.2013.210>
101. C. Sandweg, Y. Kajiwara, A. Chumak, A. Serga, V. Vasyuchka, M. Jungfleisch, E. Saitoh, B. Hillebrands, Spin pumping by parametrically excited exchange magnons. *Phys. Rev. Lett.* **106**(21), 216601 (2011). <https://doi.org/10.1103/PhysRevLett.106.216601>
102. M. Schreier, T. Chiba, A. Niedermayr, J. Lotze, H. Huebl, S. Geprägs, S. Takahashi, G.E.W. Bauer, R. Gross, S.T.B. Goennenwein, Current-induced spin torque resonance of a magnetic insulator. *Phys. Rev. B* **92**(14), 144411 (2015). <https://doi.org/10.1103/physrevb.92.144411>
103. T. Seifert, S. Jaiswal, U. Martens, J. Hannegan, L. Braun, P. Maldonado, F. Freimuth, A. Kronenberg, J. Henrizi, I. Radu, E. Beaurepaire, Y. Mokrousov, P.M. Oppeneer, M. Jourdan, G. Jakob, D. Turchinovich, L.M. Hayden, M. Wolf, M. Münzenberg, M. Kläui, T. Kampfrath, Efficient metallic spintronic emitters of ultrabroadband terahertz radiation. *Nat. Photon.* **10**(7), 483–488 (2016). <https://doi.org/10.1038/nphoton.2016.91>
104. T. Seki, Y. Hasegawa, S. Mitani, S. Takahashi, H. Imamura, S. Maekawa, J. Nitta, K. Takanashi, Giant spin Hall effect in perpendicularly spin-polarized FePt/Au devices. *Nat. Mater.* **7**(2), 125–129 (2008). <https://doi.org/10.1038/nmat2098>
105. J. Sinova, S.O. Valenzuela, J. Wunderlich, C. Back, T. Jungwirth, Spin Hall effects. *Rev. Modern Phys.* **87**(4), 1213–1260 (2015). <https://doi.org/10.1103/revmodphys.87.1213>
106. T.D. Skinner, K. Olejnik, L.K. Cunningham, H. Kurebayashi, R.P. Campion, B.L. Gallagher, T. Jungwirth, A.J. Ferguson, Complementary spin-Hall and inverse spin-galvanic effect torques in a ferromagnet/semiconductor bilayer. *Nat. Commun.* **6**, 6730 (2015). <https://doi.org/10.1038/ncomms7730>
107. Y. Sun, H. Chang, M. Katabek, Y.Y. Song, Z. Wang, M. Jantz, W. Schneider, M. Wu, E. Montoya, B. Kardasz, B. Heinrich, S.G.E. te Velthuis, H. Schultheiss, A. Hoffmann, Damping in yttrium iron garnet nanoscale films capped by platinum. *Phys. Rev. Lett.* **111**(10), 106601 (2013). <https://doi.org/10.1103/PhysRevLett.111.106601>
108. S. Takahashi, S. Maekawa, Spin current in metals and superconductors. *J. Phys. Soc. Jpn.* **77**(3), 031009 (2008). <https://doi.org/10.1143/jpsj.77.031009>
109. A. Thiaville, S. Rohart, M. Ju, V. Cros, A. Fert, Dynamics of Dzyaloshinskii domain walls in ultrathin magnetic films. *EPL (Europhys. Lett.)* **100**(5), 57002 (2012). <https://doi.org/10.1209/0295-5075/100/57002>
110. Y. Tserkovnyak, A. Brataas, G.E.W. Bauer, Enhanced gilbert damping in thin ferromagnetic films. *Phys. Rev. Lett.* **88**(11), 117601 (2002). <https://doi.org/10.1103/PhysRevLett.88.117601>
111. Y. Tserkovnyak, A. Brataas, G.E.W. Bauer, Spin pumping and magnetization dynamics in metallic multilayers. *Phys. Rev. B* **66**, 224403 (2002). <https://doi.org/10.1103/PhysRevB.66.224403>
112. Y. Tserkovnyak, A. Brataas, G.E.W. Bauer, B.I. Halperin, Nonlocal magnetization dynamics in ferromagnetic heterostructures. *Rev. Modern Phys.* **77**(4), 1375–1421 (2005). <https://doi.org/10.1103/RevModPhys.77.1375>
113. K. Uchida, S. Takahashi, K. Harii, J. Ieda, W. Koshiba, K. Ando, S. Maekawa, E. Saitoh, Observation of the spin Seebeck effect. *Nature* **455**(7214), 778–781 (2008). <https://doi.org/10.1038/nature07321>
114. K. Uchida, J. Xiao, H. Adachi, J. Ohe, S. Takahashi, J. Ieda, T. Ota, Y. Kajiwara, H. Umezawa, H. Kawai, G.E.W. Bauer, S. Maekawa, E. Saitoh, Spin Seebeck insulator. *Nat. Mater.* **9**(11), 894–897 (2010). <https://doi.org/10.1038/nmat2856>
115. H. Ulrichs, V.E. Demidov, S.O. Demokritov, W.L. Lim, J. Melander, N. Ebrahim-Zadeh, S. Urazhdin, Optimization of Pt-based spin-Hall-effect spintronic devices. *Appl. Phys. Lett.* **102**(13), 132402 (2013). <https://doi.org/10.1063/1.4799492>
116. S.O. Valenzuela, M. Tinkham, Direct electronic measurement of the spin Hall effect. *Nature* **442**(7099), 176–179 (2006)

117. N. Vlietstra, J. Shan, V. Castel, B.J. van Wees, J.B. Youssef, Spin-Hall magnetoresistance in platinum on yttrium iron garnet: dependence on platinum thickness and in-plane/out-of-plane magnetization. *Phys. Rev. B* **87**(18), 184421 (2013). <https://doi.org/10.1103/physrevb.87.184421>
118. S.V. Vonsovskii, *Ferromagnetic Resonance* (Pergamon Press, New York, 1960)
119. D. Wei, M. Obstbaum, M. Ribow, C.H. Back, G. Woltersdorf, Spin Hall voltages from a.c. and d.c. spin currents. *Nat. Commun.* **5** (2014). <https://doi.org/10.1038/ncomms4768>
120. M. Weiler, J.M. Shaw, H.T. Nembach, T.J. Silva, Phase-sensitive detection of spin pumping via the ac inverse spin Hall effect. *Phys. Rev. Lett.* **113**(15), 157204 (2014). <https://doi.org/10.1103/physrevlett.113.157204>
121. M. Weiler, G. Woltersdorf, M. Althammer, H. Huebl, S.T.B. Goennenwein, Spin pumping and spin currents in magnetic insulators. Recent advances in magnetic insulators—from spintronics to microwave applications, in *Solid State Physics*, vol. 64, chap. 5, ed. by M. Wu, A. Hoffmann (Academic Press, 2013), pp. 123–156
122. G. Woltersdorf, O. Mosendz, B. Heinrich, C.H. Back, Magnetization dynamics due to pure spin currents in magnetic double layers. *Phys. Rev. Lett.* **99**(24), 246603 (2007). <https://doi.org/10.1103/PhysRevLett.99.246603>
123. S. Woo, K. Litzius, B. Krüger, M.Y. Im, L. Caretta, K. Richter, M. Mann, A. Krone, R.M. Reeve, M. Weigand, P. Agrawal, I. Lemesh, M.A. Mawass, P. Fischer, M. Kläui, G.S.D. Beach, Observation of room-temperature magnetic skyrmions and their current-driven dynamics in ultrathin metallic ferromagnets. *Nat. Mater.* **15**(5), 501–506 (2016). <https://doi.org/10.1038/nmat4593>
124. H. Wu, C.H. Wan, X. Zhang, Z.H. Yuan, Q.T. Zhang, J.Y. Qin, H.X. Wei, X.F. Han, S. Zhang, Observation of magnon-mediated electric current drag at room temperature. *Phys. Rev. B* **93**(6) (2016). <https://doi.org/10.1103/physrevb.93.060403>
125. H. Wu, Q. Zhang, C. Wan, S.S. Ali, Z. Yuan, L. You, J. Wang, Y. Choi, X. Han, Spin Hall magnetoresistance in CoFe₂O₄/Pt films. *IEEE Trans. Magn.* **51**(11), 1–4 (2015). <https://doi.org/10.1109/tmag.2015.2433060>
126. J. Wunderlich, B. Kaestner, J. Sinova, T. Jungwirth, Experimental observation of the spin-Hall effect in a two-dimensional spin-orbit coupled semiconductor system. *Phys. Rev. Lett.* **94**(4), 047204 (2005). <https://doi.org/10.1103/physrevlett.94.047204>
127. J. Wunderlich, B.G. Park, A.C. Irvine, L.P. Zarbo, E. Rozkotova, P. Nemec, V. Novak, J. Sinova, T. Jungwirth, Spin Hall effect transistor. *Science* **330**(6012), 1801–1804 (2010). <https://doi.org/10.1126/science.1195816>
128. S.H. Yang, K.S. Ryu, S. Parkin, Domain-wall velocities of up to 750 m s^{−1} driven by exchange-coupling torque in synthetic antiferromagnets. *Nat. Nanotechnol.* **10**(3), 221–226 (2015). <https://doi.org/10.1038/nnano.2014.324>
129. S.S.L. Zhang, G. Vignale, Theory of unidirectional spin Hall magnetoresistance in heavy-metal/ferromagnetic-metal bilayers. *Phys. Rev. B* **94**(14), 140411 (2016). <https://doi.org/10.1103/physrevb.94.140411>
130. S.S.L. Zhang, S. Zhang, Magnon mediated electric current drag across a ferromagnetic insulator layer. *Phys. Rev. Lett.* **109**, 096603 (2012). <https://doi.org/10.1103/physrevlett.109.096603>
131. S.S.L. Zhang, S. Zhang, Spin convertance at magnetic interfaces. *Phys. Rev. B* **86**, 214424 (2012). <https://doi.org/10.1103/physrevb.86.214424>
132. W. Zhang, W. Han, S.H. Yang, Y. Sun, Y. Zhang, B. Yan, S.S.P. Parkin, Giant facet-dependent spin-orbit torque and spin Hall conductivity in the triangular antiferromagnet IrMn₃. *Sci. Adv.* **2**(9), e1600759–e1600759 (2016). <https://doi.org/10.1126/sciadv.1600759>
133. W. Zhang, M.B. Jungfleisch, F. Freimuth, W. Jiang, J. Sklenar, J.E. Pearson, J.B. Ketterson, Y. Mokrousov, A. Hoffmann, All-electrical manipulation of magnetization dynamics in a ferromagnet by antiferromagnets with anisotropic spin Hall effects. *Phys. Rev. B* **92**(14) (2015). <https://doi.org/10.1103/PhysRevB.92.144405>
134. W. Zhang, M.B. Jungfleisch, W. Jiang, J.E. Pearson, A. Hoffmann, F. Freimuth, Y. Mokrousov, Spin hall effects in metallic antiferromagnets. *Phys. Rev. Lett.* **113**(19) (2014). <https://doi.org/10.1103/PhysRevLett.113.196602>

Chapter 8

Weyl Semimetals



Bo Wan, Hai-Zhou Lu and Xiangang Wan

Abstract Currently, the topological behavior in condensed matter system is a hot topic. As a new class of topological quantum material, Weyl semimetals (WSM) have attracted extensive interest. In this Book chapter, we review the basic concepts of WSM: the semimetallic states are topologically protected, with corresponding Fermi arcs surface states. We also summarize the unique transport properties and the recent progress in this field.

8.1 Introduction

The topological properties of electronic bands in certain condensed-matter system have received significant attentions since 1980s. One of the most important progress recently is the discovery of the topological insulator (TI) [1–3]. According to the momentum-space topology of the bulk band structure, insulators are classified by a topological invariant that takes different values for TI than for ordinary insulators [1–3]. Since the topological invariant must change across the interface between a TI and topologically trivial insulators, TI always has metallic edge or surface states [1–3]. If the energy gap of the system is not closed, the topological invariant cannot be changed by any continuous modification of the Hamiltonian describing the system. Thus the band gap makes the topological ground state insensitive to small perturbations, and usually people believe the gapless system cannot have interesting topological features.

B. Wan · X. Wan (✉)

National Laboratory of Solid State Microstructures, School of Physics, Collaborative Innovation Center of Advanced Microstructures, Nanjing University, Nanjing 210093, China
e-mail: xgwan@nju.edu.cn

B. Wan · H.-Z. Lu

Institute for Quantum Science and Engineering and Department of Physics, South University of Science and Technology of China, Shenzhen 518055, China

H.-Z. Lu

Shenzhen Key Laboratory of Quantum Science and Engineering, Shenzhen 51805, China

In 2011 [4], a theoretical paper has shown that due to the interplay of electron correlations and strong spin-orbit interactions of $5d$ electron, the Fermi surface of pyrochlore iridates is formed by the crossing points of two non-degenerate linearly dispersing energy bands. As a result, the low-energy electronic excitation of these materials can be described by the Weyl equation [5]. Thus these systems have been coined as Weyl Semimetals (WSM) [4, 6]. Though being metals without a band gap, WSM still have topological invariants, and broaden the classification of topological phases of matter beyond insulators. In contrast to TI where only the surface states are interesting, both bulk and surface states of WSM are topologically non-trivial [4, 6]. Due to the unique bulk Weyl fermion and the surface Fermi Arcs, WSM displays many unusual physical phenomena, such as negative magnetoresistance, topological anomalous Hall effect, chiral magnetic effects and many other novel quantum behaviors. Thus due to these unique physical properties and great potential in applications, recently WSM becomes one of the central research subjects of condensed matter physics [7, 8]. In this book chapter, we will briefly summarize the progress of WSM.

8.2 Topological Bulk States

The first class of materials being predicted to be WSM was the pyrochlore iridates [4]. Pyrochlore iridates have the general formula $A_2\text{Ir}_2\text{O}_7$, where A = yttrium or a lanthanide element [4]. Early experiments show that with increasing radius of the A ion, $A_2\text{Ir}_2\text{O}_7$ change from insulator to metal. For example, $\text{Y}_2\text{Ir}_2\text{O}_7$ is an insulator [9] but with increasing the ionic radius at the A -site, the system eventually becomes metallic for $\text{Nd}_2\text{Ir}_2\text{O}_7$ [10], while $\text{Pr}_2\text{Ir}_2\text{O}_7$ shows strong Kondo behavior [11]. Moreover, it has been found that temperature will result in an insulator-to-metal transition associated with abnormal magnetic behavior without structural change [12].

Both Ir and A atoms are located on a network of corner-sharing tetrahedra, the lattice of pyrochlore iridates is thus highly magnetically geometrical frustration. Below the transition temperatures pyrochlore iridates exhibit a considerable difference in the temperature dependence of the magnetization measured under field-cooled conditions (FC) and zero-field-cooled conditions (ZFC) [9]. While, there is no magnetic hysteresis loop and sharp anomaly in specific heat data [9]. Thus $A_2\text{Ir}_2\text{O}_7$ had been suggested as the spin-glass-like compounds below the transition temperatures [9]. However, a detailed theoretical study reveals that the magnetic state of $A_2\text{Ir}_2\text{O}_7$ is a quite simple non-collinear all-in/all-out configuration (AIAO), where all moments point to or away from the centers of the tetrahedron [4]. This AIAO state is consistent with the absence of magnetic hysteresis in experiments [9]. Numerical results also show that the energy bands near the Fermi level are very sensitive to the orientation of magnetic moments, meanwhile the total energy difference between different magnetic configuration is very small [4]. Therefore, one can expect that external magnetic field may significantly affect the magnetic response and the conductivity of pyrochlore iridates. Although a conclusive experimental evidence is still lacking

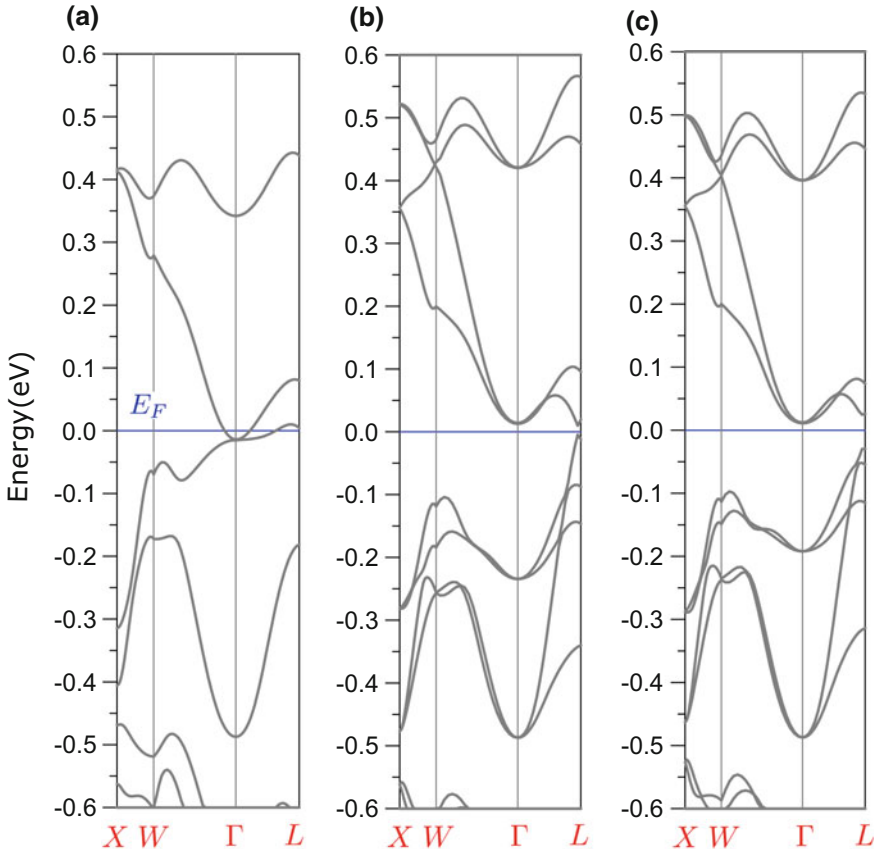


Fig. 8.1 Evolution of electronic band structure of $\text{Y}_2\text{Ir}_2\text{O}_7$. **a** The result from LDA + SOC calculation, **b** LSDA + U + SOC result with $U = 2.0$ eV, **c** LSDA + U + SOC result with $U = 1.5$ eV. For **b** and **c**, the magnetic order is AIAO. The Weyl point is located at the general k-point in case **c**, and is not visible along any high symmetry lines

due to the poor resolution of neutron scattering measurement for iridium compounds, there are a lot of works that support the theoretical prediction about AIAO magnetic configuration [13–15].

Based on a tight-binding model, Pesin and Balents propose that the non-magnetic phase of the pyrochlore iridates is a topological Mott insulator, which has gapless surface spin-only excitations [16]. As shown in Fig. 8.1a, LDA + SOC (local density approximation plus spin orbit coupling) calculation gives a metallic solution [4]. The low energy 8 bands in Fig. 8.1a are the $J_{\text{eff}} = 1/2$ states. At the Γ point (i.e., Brillouin zone center), the tight-binding result shows that these bands appear with degeneracies 4, 2, 2, consequently becomes insulator [16]. However, in non-magnetic LDA + SOC calculations (see Fig. 8.1a), the degeneracies of these bands are 2, 4, 2,

which is necessarily metallic with 4 levels filled. Thus, one needs either a structural transition or a magnetic order to result in an insulating phase.

While the magnetic pattern remains AIAO, the electronic properties change with correlation strength. Considering the effect of Coulomb repulsion, LSDA + U + SOC (where LSDA means spin polarized local spin density approximation and U is the electronic correlation of Ir-5d orbits) calculation clearly demonstrate that the electronic band structure along high-symmetry lines appears to be insulating as shown in Fig. 8.1b, c. It is well known that LDA + U method uses a Hartree Fock approximation for electronic Coulomb repulsion, thus the numerical band gap usually decreases with decreasing the parameter U [17]. However, a very strange electronic feature appears in the band structure. The band gap of $\text{Y}_2\text{Ir}_2\text{O}_7$ seems to increase with decreasing U from 2.0 to 1.5 eV as shown in Fig. 8.1.

It is worth to mention that the AIAO magnetic configuration preserves inversion symmetry. Thus by calculating the band parity, one can explore the evolution of the electronic band behavior, consequently study the possible novel properties related with the above mentioned abnormal band structure. The Time Reversal Invariant Momenta (TRIMs) (Time Reversal Invariant Momenta) are invariant under inversion. Thus one can label electronic bands by its parity eigenvalues $\xi = \pm 1$. For pyrochlore iridates, TRIMs in the Brillouin zone (BZ) correspond to the $\Gamma = (0, 0, 0)$, and $X, Y, Z [= 2\pi/a(1, 0, 0)$ and permutations] points and four L points $[\pi/a(1, 1, 1)$ and equivalent points]. For the top four occupied bands, the calculated parities at eight TRIMs are shown (in order of increasing energy) in Table 8.1. Regardless all L points are equivalent by symmetry, the choice of inversion center at an Iridium site singles out one of them, L' , and the parities at L' and the other three L points are the opposite of one another. Numerical results show that for the AIAO magnetic configuration, the parities do not change above $U > U_c \sim 1.8$ eV. The calculated parities (with $U = 2$ eV) is shown in the top row of Table 8.1. It is readily seen that these parities are the same as for a site-localized picture of this phase, thus can be adiabatically transformed into an atomic insulator (AI). Smoothly connect to AI, one can call it as the Mott phase. On the other hand, as shown in Fig. 8.1c the LSDA + U + SO calculation with smaller $U = 1.5$ eV also gives insulating result. It is interesting to notice that the phase with U less than 1.8 eV is not an extension of the Mott insulator. There is a change of parities as shown in Table 8.1, which indicates a phase transition has occurred between $U = 1.5$ and 2.0 eV. Comparing with $U = 1.5$ case, for $U = 2.0$ eV, an unoccupied state and an occupied state with opposite parities have switched places at the L points. It can be proven that only one of the two phases adjacent to the U where this parities change happens can be insulating [4]. The large U phase is smoothly connected to a gapped Mott phase, thus the phase with smaller U must be the non-insulating one. A detailed k - p analysis about the case of $U = 1.5$ eV shows that there is a three dimension (3D) electronic band crossing located around the k -vector $(0.52, 0.52, 0.3)\frac{2\pi}{a}$ [4]. There are also 23 additional electronic band crossing points in the BZ. All related by symmetry, the 24 band crossing points in the whole BZ thus have exactly the same energy. There is no other band crossing the Fermi level, and the numerical calculation show that the chemical potential is exactly at the band-crossing energy. Thus the bulk Fermi surface is just a collection

Table 8.1 Numerical parities of states at Time Reversal Invariant Momenta (TRIMs) for several electronic phases of the iridates. The calculations are done by LSDA + U + SO scheme with AIAO magnetic order. Only the top four filled states are shown in order of increasing energy

Phase	Γ	X, Y, Z	L'	$L \times 3$
$U = 2.0$, AIAO (Mott)	+++	---	---	-+++
$U = 1.5$, AIAO (Weyl)	+++	---	---	-+-

of 24 Fermi points. The density of states (DOS) around the Fermi level behave like $DOS(E) \propto E^2$, where E is the energy respect to the Fermi level. The small DOS makes it an electrical insulator at zero temperature, which is consistent with experimental results [9].

Without the time reversal symmetry, the electronic bands forming the touching point in pyrochlore iridates are non-degenerate. Thus for $A_2\text{Ir}_2\text{O}_7$, the effective Hamiltonian in the vicinity of a crossing point \mathbf{k}_0 is [4]:

$$H_W = \sum_{i=1}^3 \mathbf{q} \sigma_i \cdot \mathbf{v}_i, \quad (8.1)$$

where σ_i are the three Pauli matrices and energy is measured from the Fermi level, $\mathbf{q} = \mathbf{k} - \mathbf{k}_0$ and. The velocity vectors \mathbf{v}_i are generically non-vanishing and linearly independent. Thus around the node, system has a cone-like energy dispersion $\Delta E = \pm \sqrt{\sum_{i=1}^3 (\mathbf{q} \cdot \mathbf{v}_i)^2}$. It is worth to mention that the above equation is closely related to the Weyl equation in particle physics [5]. Thus, these electronic band crossing points are referred as Weyl points and the quasiparticles near them are reminiscent of Weyl fermions [4, 6]. Weyl fermions have a definite right- or left-handed chirality and by combining in pairs of opposite chirality, a massless Dirac fermion appears [18]. Similarly, one can assign a *chirality* (or chiral charge) $c = \pm 1$ to the Weyl points defined as $c = \text{sign}(\mathbf{v}_1 \cdot \mathbf{v}_2 \times \mathbf{v}_3)$. Thus the electronic band touching points related by inversion symmetry have opposite chirality. As shown in the above equation, the 2×2 Pauli matrices appear, thus the Weyl particles are two component fermions. In contrast to regular four component Dirac fermions, it is not possible to introduce a mass gap [18]. Thus the Weyl nodes are topologically robust. According to the theorem of Nielsen and Ninomiya, Weyl points should occur in pairs of opposite chirality. The only way for these nodes to disappear is if they meet with another Weyl points with opposite chiral charge.

The stability of Weyl points can been understood in the following discussion: a very general Hamiltonian for any two non-degenerate bands system is

$$H = \begin{pmatrix} A(k) & B(k) + iC(k) \\ B(k) - iC(k) & -A(k) \end{pmatrix},$$

Fermi Arc Surface States

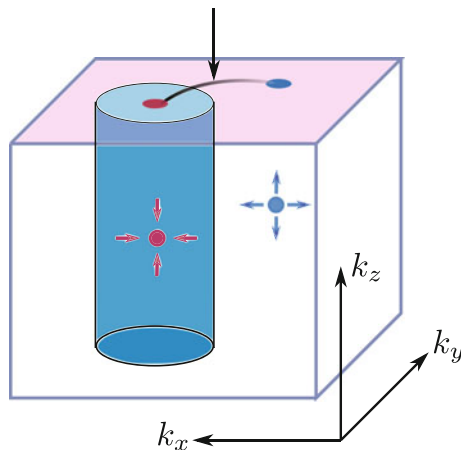


Fig. 8.2 Illustration of surface states arising from bulk Weyl points. For simplicity, only a pair of Weyl points with opposite chirality are shown. The imaginary cylinder in momentum space has unit Chern number, due to the Berry monopole at the Weyl point. Hence a surface state must arise, as shown schematically in the same plot. When the Fermi energy is at the Weyl point, a Fermi arc is present which connects the surface momenta of the projected bulk Weyl points of opposite chirality

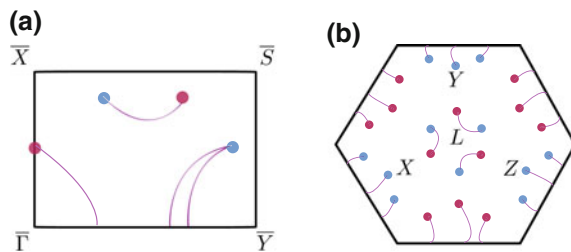
and the eigenvalues are $E(k) = \pm\sqrt{A^2(k) + B(k)^2 + C(k)^2}$. The existence of a band touching point requires three equations $A(k) = 0$, $B(k) = 0$ and $C(k) = 0$. The independent parameters for a 3D system are three (namely k_x , k_y and k_z). This does not guarantee an electronic band degenerate point, but once such a band degeneracy has appeared, any small perturbation for the Hamiltonian will only slightly shift the location of the band crossing point, and one can always adjust k_x , k_y and k_z to satisfy the three equations [19]. Only when the Weyl points with opposite chirality meet and annihilate, the system can become an insulator.

It is worth to emphasise that the WSM are rather different from the 3D Dirac Semimetal (DSM). As just discussed, the Weyl points are topological objects and robust against any perturbations regardless of symmetry. On the other hand, with time reverse symmetry and inversion symmetry, the Dirac Semimetal still requires additional spatial symmetry [20–23].

8.3 Fermi Arc Surface States

One of the most striking features of WSM is that it has topological Fermi Arc surface states [4]. As a twofold band degenerate points, the Weyl points behave like ‘magnetic’ monopoles in momentum space whose charge is given by the chirality. As a band crossing point, the Weyl point is actually a source of “Berry flux” rather than

Fig. 8.3 The Fermi arc surface states from tight-binding calculations. The left panel corresponds to the (110) surface of the pyrochlore iridate $\text{Y}_2\text{Ir}_2\text{O}_7$. The right is (111) surface



magnetic flux [24]. The Berry connection, a vector potential in momentum space, is defined by $\mathcal{A}(\mathbf{k}) = \sum_{n=1}^N i \langle u_{n\mathbf{k}} | \nabla_{\mathbf{k}} | u_{n\mathbf{k}} \rangle$ where N is the index for occupied bands. The Berry curvature can be calculated by $\mathcal{F} = \nabla_{\mathbf{k}} \times \mathcal{A}$ [24].

It is easy to show that the band topology associated with the Weyl point results in a novel topological states in certain surfaces. Consider a curve in the surface Brillouin zone girding the projection of the bulk Weyl point, which is traversed counterclockwise as one change the parameter $\eta: 0 \rightarrow 2\pi$; $\mathbf{k}_\eta = (k_x(\eta), k_y(\eta))$ (see Fig. 8.2). We show that the energy ϵ_η of a surface state at momentum \mathbf{k}_η crosses $E = 0$. With η and k_z treated as two momentum, $H(\eta, k_z) = H(\mathbf{k}_\eta, k_z)$ can be interpreted as the gapped Hamiltonian of a two dimensional system. The two periodic parameters k_z, η constitute a geometry of the surface of a torus in momentum space. For this two dimensional band structure, the Chern number is given by the integration: $\frac{1}{2\pi} \int \mathcal{F} dk_z d\eta$, which, similar to magnetic monopole, corresponds to the density of “monopoles” enclosed within the torus. Chern number can also be obtained by summing the chirality of the enclosed Weyl nodes. Further considering a unitary net chirality, this indicates one single Weyl node enclosed within the torus. Such two dimensional subsystem is a quantum Hall insulator with unit Chern number. Defined on the half space $z < 0$, a chiral edge state is expected as the subsystem corresponds to setting the quantum Hall state on a cylinder. The energy ϵ_η spans the band gap of the subsystem as λ varies. Therefore, this surface state crosses zero energy somewhere on the surface Brillouin zone \mathbf{k}_η . Such a state could be obtained for every curve enclosing the Weyl point. Thus, at zero energy, there is a Fermi line, which terminates at the Weyl points, connecting Weyl points with different chirality in the surface Brillouin zone (see Fig. 8.2). Clearly, the net chirality of the Weyl points enclosed in the (k_z, η) torus was a pivotal initial condition to determine the number of these states. If Weyl points with opposite chirality line up along the k_z direction, there is a cancellation and no surface states are expected.

To verify these theoretical considerations, one can construct a tight-binding model which has features as shown in the electronic structure calculations for $\text{Y}_2\text{Ir}_2\text{O}_7$ [4]. The bands near the Fermi energy are contributed by the Ir- t_{2g} orbitals, thus only the Ir- t_{2g} states had been considered in the model. The Iridium atoms form a tetrahedral network, each pair of nearest neighboring (NN) atoms forms three bonds: one σ -like bond and two π -like bonds. We denote the hopping integrals for these bond as t and t' respectively. To simulate the appearance of Weyl points, it is essential to include next-nearest neighbor (NNN) interactions between t_{2g} orbitals which are

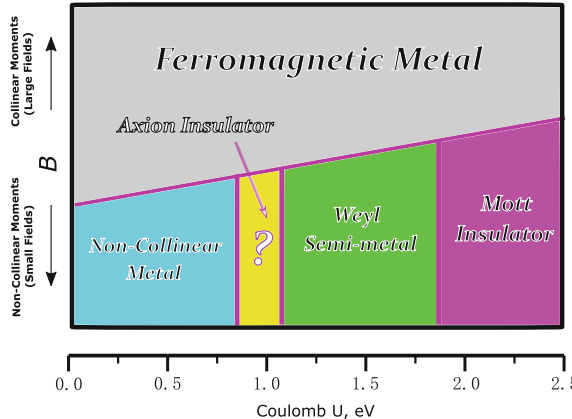


Fig. 8.4 Schematic diagram of predicted phase diagram for pyrochlore iridates including Mott insulator, Weyl semimetal, Axion insulator and non-collinear metals in small magnetic fields. The horizontal axis indicates the strength of interaction among Ir 5d electrons while the vertical axis corresponds to the external magnetic fields. The external field can trigger a transition out of the noncollinear AIAO ground state

denoted as t'' . With the setup parameter system with $t = 0.2$, $t' = 0.5t$, $t'' = -0.2t$, on-site spin-orbit coupling equal to $2.5t$ and the applied on-site “Zeeman” splitting of $0.1t$ between states parallel and antiparallel to the local quantization axis within all-in/all-out (AIAO) configuration, one can model both the bulk Weyl semimetal state and its surface state in a straightforward way. Based on this model, one can calculate the surface states for a slab, leading to surface states for both the front and back surface. The calculated Fermi arc surface states at (110) and (111) plane are shown in Fig. 8.3.

Sharply contrast this with the surface states of conventional system, which form a closed loop in momentum space, the Fermi arcs in WSM terminate at the projected location of the bulk Weyl points [4]. Thus detecting the Fermi arcs by angle-resolved photoemission spectroscopy (ARPES) experiments provides a smoking gun for the presence of the WSM phase.

The basic results for pyrochlore iridates are summarized in the phase diagram Fig. 8.4 [4]. With increasing U , WSM will change to Mott insulator. On the other hand, decreasing U results in another topological phase transition and the WSM becomes Axion insulator, which has magneto-electric parameter $\theta = \pi$ [4]. As shown in Fig. 8.4, U value is the key parameter to determine the novel phase in pyrochlore iridates. Based on the constrained random phase approximation calculation, the values of U have been obtained between 1.4 and 2.4 eV for 5d electron [25]. As mentioned above, the U is depend on the radii of the ion at A site. Thus, the above topological phase transition may occur by changing the lanthanide element at A site.

8.4 Topological Anomalous Quantum Hall Effects

Similar with Dirac Semimetal, WSM also has an anomalous response to a magnetic field [26]. This can be illustrated by the following 3D two-band model

$$H_{\vec{k}} = [2t_x(\cos k_x - \cos k_0) + m(2 - \cos k_y - \cos k_z)]\sigma_x + 2t_y \sin k_y \sigma_y + 2t_z \sin k_z \sigma_z, \quad (8.2)$$

where σ is Pauli matrix. This model breaks time-reversal symmetry, and there are two Weyl points located at $\vec{P} = \pm(k_0, 0, 0)$. The Hamiltonian $H_{\vec{k}}$ with the \vec{k} at a k_z -fixed plane in the bulk BZ can be considered as the Hamiltonian of a two-dimensional system. If $k_x \neq \pm k_0$, this 2D system is fully gapped, and has a well-defined Chern number C_{k_x} . It is easy to prove that $C_{k_x} = 1$ if $k_x \in (-k_0, k_0)$ and $C_{k_x} = 0$ when k_x is not between two Weyl points. Consequently, the 2D Hall conductance is

$$\begin{aligned} \sigma_{xy}^{2D}(k_z) &= \frac{e^2}{h} \text{ if } k_z \in (-k_0, k_0) \\ \sigma_{xy}^{2D}(k_z) &= 0 \text{ if } k_z \notin (-k_0, k_0) \end{aligned}$$

the net Hall conductivity of this 3D system is therefore

$$\sigma_{xy} = \int \frac{dk_z}{2\pi} \sigma_{xy}^{2D}(k_z) = \frac{e^2 k_0}{\pi h}$$

For a general case, the Hall conductivity is also simply proportional to the distance between the Weyl points, and is independent of all other material properties [26].

8.5 Magneto-Transport Phenomena in Weyl Semimetal

8.5.1 Effective Model

To illustrate the physics of transport in WSM, the following two-node minimal Hamiltonian [27], which has an identical structure as that for A -phase of ^3He superfluids [28], is introduced

$$\mathcal{H} = A(k_x \sigma_x + k_y \sigma_y) + \mathcal{M}_k \sigma_z, \quad (8.3)$$

where σ are the Pauli matrices, $\mathcal{M}_k = M_0 - M_1(k_x^2 + k_y^2 + k_z^2)$, $\mathbf{k} = (k_x, k_y, k_z)$ is the wave vector and A, M_0, M_1 are all model parameters. When $M_0 M_1 > 1$, the up- and down-bands intersects at $\mathbf{k} = (0, 0, k_0^\pm)$, where $k_0^\pm = \pm\sqrt{M_0/M_1}$. Under this condition, the model is in the regime of WSM phase and could be rewritten as

$$\mathcal{H} = A(k_x\sigma_x + k_y\sigma_y) + M(k_0^2 - \mathbf{k}^2)\sigma_z, \quad (8.4)$$

still A , M , k_0 are model parameters. (8.4) has the following energy spectrum

$$E_{\pm} = \pm\sqrt{M^2(k_0^2 - \mathbf{k}^2)^2 + A^2(k_x^2 + k_y^2)}, \quad (8.5)$$

where $k_0 = |k_0^{\pm}|$. Along the line of $k_x = k_y = 0$, the energy dispersion is $\tilde{E}_{\pm} = \pm M|k_0^2 - k_z^2|$. In the vicinity of Weyl nodes $\mathbf{k} = (0, 0, k_0^{\pm})$, (8.4) reduces to two separated local models of chiral Weyl fermions

$$\mathcal{H}^{\eta} = \mathbf{M}^{\eta} \cdot \boldsymbol{\sigma},$$

where $\eta = \pm$ describes the chirality of each Weyl node and $\mathbf{M}^{\eta} = (A\tilde{k}_x, A\tilde{k}_y, -\eta 2Mk_0\tilde{k}_z)$. $(\tilde{k}_x, \tilde{k}_y, \tilde{k}_z)$ denotes the effective wave vector measured from each Weyl node. In the next, this model had been use to illustrate full topological properties, including Berry curvature, Fermi arcs etc.

8.5.2 Topological Properties

The topological aspects of the above model could be revealed from the calculations of Berry curvature, Chern number and Fermi arcs [4, 24, 29, 30]. The Berry flux could be calculated with the definition given in the previous section. For the two-node model (8.4), the Berry curvature of the up band can be expressed as

$$\mathcal{F}(\mathbf{k}) = \frac{A^2 M}{E_+^3} \left(k_x k_x, k_z k_y, \frac{1}{2} (k_z^2 - k_0^2 - k_x^2 - k_y^2) \right),$$

from which one can easily see that there are two singularities at $(0, 0, k_0^{\pm})$. The chirality of each Weyl node can be found through an integral over the Fermi surface enclosing the Weyl node, which yields opposite “charges” $\mp \text{sgn}(M)$ at $(0, 0, k_0^{\pm})$. Such topological charges could be considered as “magnetic monopole” in the momentum space.

In the minimal model (8.4), according to the previous sections, the Chern number is well defined for a given k_z with the definition $n_c(k_z) = -(1/2\pi) \iint dk_x dk_y \mathcal{F}(\mathbf{k}) \cdot \hat{z}$ in the k_x - k_y plane, and is calculated as [30]

$$n_c(k_z) = -\frac{1}{2} [\text{sgn}[M(k_0^2 - k_z^2)] + \text{sgn}(M)],$$

which equals $-\text{sgn}(M)$ in the interval $-k_0 < k_z < k_0$ and becomes 0 otherwise. According to the bulk-boundary correspondence, the non-zero Chern number corresponds to the Fermi arcs as the k_z -dependent edge states.

There are several ways to find the Fermi arc surface states, for example the calculation for a large slab. Here is another avenue through solving (8.4) with an open boundary. Without loss of generality, assuming the wave functions vanishes at an open boundary at $y = 0$, the dispersion of surface states is given by

$$E^{\text{sur}}(k_x, k_z) = \text{sgn}(M) A k_x,$$

and the corresponding wave function is expressed as

$$\Psi_{k_x, k_z}^{\text{sur}}(\mathbf{r}) = C e^{i(k_x x + k_z z)} \begin{bmatrix} \text{sgn}(M) \\ 1 \end{bmatrix} (e^{\kappa_1 y} - e^{\kappa_2 y}),$$

where C is a normalization factor and $\kappa_i = A/2|M| \mp \sqrt{(A/2M)^2 - (k_0^2 - k_x^2 - k_z^2)}$. The Fermi arcs could exist in the conditions: (1) $\kappa_i > 0$, and (2) $\kappa_i = a \mp ib$ with $a, b > 0$. Note that in both conditions $k_0^2 - k_x^2 - k_z^2 > 0$, hence, the solution of Fermi surface states are constrained in the circle $k_x^2 - k_z^2 < k_0^2$.

As has been proven, the two-node model provides a generic description for Weyl semimetals, including the band touching, opposite chirality, monopoles of Berry curvature, topological charges, and Fermi arcs.

8.5.3 Landau Bands

Magnetoresistance measures the change of the electric resistance of a solid due to external magnetic field. Under an external magnetic field along z direction, the energy spectrum is quantized into a set of one-dimensional (1D) Landau bands dispersing with k_z . Adopting the Landau gauge, the vector potential expressed as $\mathbf{A} = (-yB, 0, 0)$, the Landau bands solutions of the minimal model could be solved analytically with the eigenvalues [27]

$$E_\nu(k_z) = \begin{cases} \omega/2 - M_0 + M_1 k_z^2, & \text{for } \nu = 0, \\ \omega/2 \pm \sqrt{M_\nu^2 + \nu \xi^2}, & \text{for } \nu \geq 1, \end{cases}$$

where $\omega = 2M/\ell_B^2$, $\xi = \sqrt{2}A/\ell_B$ and the magnetic length $\ell_B = \sqrt{\hbar/eB}$. The eigenstates for $\nu \geq 1$ are

$$|\nu, k_x, k_z, +\rangle = \begin{bmatrix} \cos(\frac{\theta}{2})|\nu-1\rangle \\ \sin(\frac{\theta}{2})|\nu\rangle \end{bmatrix} |k_x, k_z\rangle, \quad (8.6)$$

$$|\nu, k_x, k_z, -\rangle = \begin{bmatrix} \sin(\frac{\theta}{2})|\nu-1\rangle \\ -\cos(\frac{\theta}{2})|\nu\rangle \end{bmatrix} |k_x, k_z\rangle, \quad (8.7)$$

and for $\nu = 0$ is

$$|0, k_x, k_z\rangle = \begin{bmatrix} 0 \\ |0\rangle \end{bmatrix} |k_x, k_z\rangle,$$

where $\cos(\theta) = \mathcal{M}_v / \sqrt{\mathcal{M}_v + v\xi^2}$ and the corresponding wave functions are found as

$$\psi_{k_x, k_z}^v(\mathbf{r}) = \frac{C_v}{L_x L_z \ell_B} e^{ik_x x} e^{ik_z z} e^{-\frac{\xi^2}{2}} \mathcal{H}_v(\xi),$$

where $C_v = 1/\sqrt{v! 2^v \sqrt{\pi}}$, L_x L_z are the sample size in x- and z- directions, respectively, and $\xi = (y - k_x \ell_B^2)/\ell_B$. As the dispersion are not explicit functions of k_x , the number of different k_x represents the Landau degeneracy $N_L = 1/(2\pi\ell_B^2) = eB/h$ in a unit area in the $x - y$ plane. These analytical Landau band solutions for the minimal model in an external magnetic field provide a concrete terrace to study the magneto-transport properties of WSM.

8.5.4 Magneto-Transport Phenomena

Due to the chiral anomaly, WSM exhibits highly anisotropic negative longitudinal magnetoresistance [31–37]. This novel magneto-transport phenomenon had been attributed to the presence of Weyl points and the associated chiral anomaly. Proposed in relativistic field theory [38, 39], chiral anomaly had been used to describe the current associated with the breaking of a global chiral symmetry, and a chiral current is defined by the difference between currents with different chiralities (usually indexed by Left and Right). The first proposal of realizing chiral anomaly in condensed matter physics was given by Nielsen and Ninomiya [40, 41], where they used a one-dimensional model in the quantum limit. Based on a two band model, they revealed that an external electric field would drive electrons to higher levels in one band and lower in the other. Such process is, in a way, treated as “creation” of charges with left chirality and “annihilation” of the right ones. Therefore, the chiral current in their model is not-conserved under a external electric field and chiral anomaly appears in lattice. In WSM, the nodes with linear dispersion always occur in pairs and carry opposite chiralities. And the nodes serve as monopoles of Berry curvature in momentum space [28] with the fluxes of Berry curvature flow from one monopole to the other. Along the direction that connects two monopoles, external parallel electric and magnetic fields would pump the electrons from one monopole to the other, which leads to the chiral anomaly (also known as Adler-Bell-Jackiw anomaly or triangle anomaly).

Study of magnetotransport properties is one of the research focuses in Weyl semimetals. Explorations of transport experiments on WSM have been performed in a number of series of materials, including BiSb alloy [42, 43], TaAs-family [44–48] etc. To further understand the physics of novel magneto-transport properties in WSM, in the following subsections, we are going to discuss schematic calculations of

longitudinal magnetoconductivity. Magnetoconductivity can be classified into three regimes according to the strength of parallel magnetic fields, from the quantum limit to near zero field. In the strong fields, namely only the lowest Landau band is partially occupied (the quantum limit), the chiral anomaly had been suggested as the reason of negative magnetoresistance in several previous works. However as shown in the following, besides the contribution from chiral anomaly, the novel behavior of magneto-transport in WSM may also comes from many details like Fermi velocity and scattering mechanisms. While for weak magnetic field, non-trivial Berry curvature and chiral anomaly in WSM may give rise to negative magnetoresistance. In near zero field regime, an exotic transport known as weak antilocalization effect would lead to a positive magnetoresistance.

8.5.4.1 Strong Magnetic Fields: The Quantum Limit

Several theoretical works claimed that a negative longitudinal magnetoresistance (or positive magnetoconductivity) should be observed in magneto-transport experiments on WSM due to the existence of chiral anomaly [31, 33, 49]. However, the magnetoconductivity is always negative in the strong magnetic fields experiments. Thus, by fully considering the magnetic dependence of the Fermi velocity, a systematic calculation on the conductivity of topological semimetals had been performed [27]. The results show that high field positive magnetoconductivity may not be a dramatic signature of chiral anomaly. Along the z direction, the semiclassical Drude conductivity could be expressed using the formula [50]

$$\sigma_{zz} = \frac{e^2 \hbar}{2\pi L_x L_y L_z} \sum_{k_x, k_z} (v_0^z)^2 G_0^R G_0^A,$$

where $-e$ is the electron charge, L_i is the sample length along i -direction, and $v_0^z = \partial E_{k_z}^0 / \hbar \partial k_z$ is the velocity along z -direction for a state with vector k_z in the lowest Landau band, which could be obtained from the results in the previous section. $G_0^{R/A} = 1/(E_F - E_{k_z}^0 \pm i\hbar/2\tau^0)$ are the retarded/advanced Greens function, with τ^0 the lifetime of a state in the lowest Landau band with wave vector k_x, k_z . Using self-consistent Born approximation for τ^0 and short-range delta scattering potential $U(\mathbf{r}) = \sum_i u_i \delta(\mathbf{r} - \mathbf{R}_i)$ with delta correlated $\langle U(\mathbf{r})U(\mathbf{r}') \rangle = V_{imp} \delta(\mathbf{r} - \mathbf{r}')$, where V_{imp} is field-independent scattering parameter, one can obtain the following formula for magnetoconductivity in the quantum limit

$$\sigma_{zz} = \frac{e^2}{h} \frac{(\hbar v_F^0)^2}{V_{imp}}.$$

If neglecting the field-dependence of Fermi velocity, a B -independent conductivity was concluded, which is consistent with the previous work in which the velocity is considered as constant [51]. In an ideal WSM with fixed carrier density, when the

field dependence of Fermi velocity is included, the magnetoconductivity is always negative in the electron-doped regime, while positive in the hole-doped case. Moreover the magnetoconductivity is negative and with linear dependence in B for a WSM with fixed Fermi energy. Thus positive magnetoconductivity may not be the definite signature of chiral anomaly.

Another extraordinary work presented by Goswami et al. [52] shows that the emergence of the axial anomaly in 3D generic metals does not guarantee the existence of negative longitudinal magnetoresistance through a systematic calculation of the longitudinal magnetoconductivity in the quantum limit using the Boltzmann equation, for both short-range neutral and long-range ionic impurity scattering processes. Specifically, for the case of WSM, they started from a toy model on a tetragonal lattice

$$\mathcal{H} = 2t_{\perp,1} [\sin(k_x a)\sigma_x + \sin(k_y a)\sigma_y] - \{2t_{\perp,2} \times [2 - \cos(k_x a) - \cos(k_y a)] + 2t_z \cos(k_z c) - \Delta\} \sigma_3, \quad (8.8)$$

where a, c are lattice parameters for a and c axis, respectively, and $t_{\perp,i}, t_z$ are hopping terms. For studying the Landau bands in WSM, apply an external magnetic field along z -direction and choose the Landau gauge $\mathbf{A} = (0, Bx, 0)$, the Hamiltonian in (8.8) becomes

$$\mathcal{H} \approx \hbar v_{\perp} [-i \partial_x \sigma_x + (k_y - eBx/\hbar) \sigma_y] - [2t_z \cos(k_z c) - \Delta] \sigma_z, \quad (8.9)$$

from which the dispersion of Landau bands can be easily solved

$$\epsilon_N = \begin{cases} -2t_z \cos(k_z c) + \Delta, & \text{for } N = 0, \\ \text{sgn}(\alpha) \left[\epsilon_0^2 + 2N \frac{\hbar^2 v_{\perp}^2}{\ell_B^2} \right]^{1/2}, & \text{for } N \geq 1. \end{cases}$$

After tremendous calculations, they found that at half-filling, the zero-range point impurities lead to a constant longitudinal magnetoconductivity, whereas the neutral Gaussian impurities give rise to a B -linear one (when $\ell_B^2 < 2a^2$). Furthermore, in a system away from half-filling, zero-range point impurities lead to a $\cos^2(B_0/2B)$, where B_0 is the magnetic field reaching the quantum limit, and the short-range Gaussian scatterings still give rise to a B -linear one. In their work, it is also stated that the magnetic field dependence of the Fermi velocity of lowest Landau band and the transport lifetime should be considered.

Combine these arguments together, one can conclude that the positive magnetoconductivity in WSM in strong magnetic fields could not be simply the result from chiral anomaly. More detailed attentions should be taken into account explaining such novel transport property besides the chiral anomaly.

8.5.4.2 Weak Magnetic Fields: Negative Magnetoresistance

The nontrivial Berry curvature can couple the velocity of electrons to an external magnetic field, leading to a correction chiral current linearly proportional to the field. The correlation of chiral currents further contributes to an extra conductivity that quadratically grows with increasing magnetic field, which is parallel to applied electric field. This B^2 positive conductivity in weak parallel magnetic fields is rare in non-ferromagnetic materials, can serve as one of the transport features of topological semimetals. To further understand the physics of negative magnetoresistance in weak magnetic field, we give two different demonstrations. The first starts with semiclassical equation of motion proposed by Niu et al. [30, 53, 54]

$$\begin{aligned}\dot{\mathbf{r}} &= \mathbf{v} + \dot{\mathbf{k}} \times \mathcal{F}_k, \\ \hbar \dot{\mathbf{k}} &= e\mathbf{E} + e\dot{\mathbf{r}} \times \mathbf{B}.\end{aligned}\quad (8.10)$$

The second term in the first equation indicates that electron can acquire an anomalous velocity correction term that is proportional to the Berry curvature \mathcal{F}_k in the presence of electric field. This anomalous velocity is related to a number of different transport phenomenons. Iterating $\dot{\mathbf{r}}$ and $\dot{\mathbf{k}}$ gives

$$\begin{aligned}\dot{\mathbf{r}} &= \left(1 + \frac{e}{\hbar} \mathbf{B} \cdot \mathcal{F}_k\right)^{-1} \left[\mathbf{v} + \frac{e}{\hbar} \mathbf{E} \times \mathcal{F}_k + \frac{e}{\hbar} (\mathcal{F}_k \cdot \mathbf{v}) \mathbf{B} \right], \\ \hbar \dot{\mathbf{k}} &= \left(1 + \frac{e}{\hbar} \mathbf{B} \cdot \mathcal{F}_k\right)^{-1} \left[e\mathbf{E} + e\mathbf{v} \times \mathbf{B} + \frac{e^2}{\hbar} (\mathbf{E} \cdot \mathbf{B}) \mathcal{F}_k \right].\end{aligned}$$

In the framework of linear response theory, with small \mathbf{B} and $E = 0$, the velocity reduces to

$$\dot{\mathbf{r}} = \mathbf{v} + \frac{e}{\hbar} (\mathcal{F}_k \cdot \mathbf{v}) \mathbf{B},$$

where the second term is the additional velocity term induced by non-trivial Berry curvature. Since conductivity is defined as a current-current correlation [58], the linear B -related velocity would give B^2 conductivity, or in the parallel fields negative magnetoresistance.

The other demonstration is more complicated based on solving coupled diffusive equations, where the coupling is between total and chiral charges. This calculation is first proposed by Burkov et al. [33, 55]. Introduce a Weyl Hamiltonian

$$\mathcal{H}(\mathbf{k}) = v_F \tau^z (\hat{z} \times \sigma \cdot \mathbf{k}) + b \sigma^z + \hat{\Delta}(\mathbf{k}),$$

where $\hat{\Delta}(\mathbf{k}) = \Delta_S \tau^x + \frac{\Delta_D}{2} (\tau^+ e^{ik_z d} + H.c.)$, σ and τ are Pauli matrices describing spin and pseudospin degrees of freedom, b is the splitting of spin induced by magnetic impurities. This model describes topological insulator and band insulator multilayers doped with random magnetic impurities, Δ_S and Δ_D are tunneling matrix elements

between the same or different topological insulator layers. Calculating the diffusion propagator with the eigenvectors obtained by solving the Hamiltonian, and project it into the subspace of total-chiral charge, one could have the inverse diffusion propagator

$$\mathcal{D}^{-1}(q, \Omega) = \begin{pmatrix} -i\Omega\tau_t + Dq^2\tau_t & -iq\Gamma\tau_t \\ -iq\Gamma\tau_t & -i\Omega\tau_t + \tau_t/\tau_c + Dq^2\tau_t \end{pmatrix},$$

where t/c denotes total or chiral charges, τ_i are the transport time of corresponding charges scattered by random magnetic impurities, and D is the diffusive constant in z direction, Γ is the coupling coefficient between total and chiral charges linearly proportional to B . We have ignore the detailed expressions for D and Γ since they are irrelevant for the physics under consideration. This inverse diffusion propagator can be transformed into the following coupled diffusive equations

$$\begin{aligned} \frac{\partial n_t}{\partial t} &= D \frac{\partial^2 n_t}{\partial z^2} + \Gamma \frac{\partial n_c}{\partial z}, \\ \frac{\partial n_c}{\partial t} &= D \frac{\partial^2 n_c}{\partial z^2} - \frac{n_c}{\tau_c} + \Gamma \frac{\partial n_t}{\partial z}, \end{aligned} \quad (8.11)$$

where n_t and n_c are densities for total and chiral charges, respectively. τ_c is the relaxation rate of chiral charges, which is the result of chiral anomaly in Weyl semimetal. Since the total charge is conserved, assuming the total charge density is uniform, using $\partial n_t / \partial t = -\nabla \cdot \mathbf{j}_t$, one could have an expression for the total charge current

$$\mathbf{j}_t = -\frac{\sigma_0}{e} \frac{\partial \mu_t}{\partial z} - \frac{e^2 B}{2\pi^2} \delta \mu_c,$$

where μ_i are the total and chiral electrochemical potentials and σ_0 is the usual zero-field Drude conductivity. The first term is the usual current response to the gradient of the electrochemical potential. The second term is the outcome of the chiral anomaly in Weyl semimetals. Further assume that there is a uniform steady total current density in the z -direction in the system, the final expression for the longitudinal magnetoconductivity is

$$\sigma_z z = \sigma_0 + \chi(\tau_c) B^2,$$

where $\chi(\tau_c)$ is proportional to τ_c and inversely to the density of states around Fermi energy. Since $\Gamma \propto B$, the second term shows a B^2 magnetoconductivity or negative quadratic field dependent magnetoresistance induced by chiral anomaly in weak magnetic fields.

8.5.4.3 Near Zero Field: Weak Antilocalization

As the magnetic field further decreases approaching near zero, weak antilocalization effect, which occurs in disordered metals as a transport phenomena [56], should be taken into consideration. At low temperatures, the mean free path of electrons is much shorter than the sample size and phase coherence length, phase coherence of electrons could be still maintained during scatterings. In this quantum diffusive regime, a correction to the conductivity arises as a result of the quantum interference between closed and time-reversed loops that circle regions in which one or more impurities are present. If the correction of quantum interference is positive, it gives a weak antilocalization emendation to the conductivity. This correction can be suppressed by applying a magnetic field to break the time reversal symmetry, leading to a negative magnetoconductivity, or positive magnetoresistivity, as the signature for the weak antilocalization. The previous work [57] studied the weak localization and antilocalization using Feynman diagram techniques, in which disorder and interaction are treated as perturbations in the linear response theory of the conductivity. The result shows that the quantum interference gives the main contribution to the magnetoconductivity. For a single valley of Weyl fermions, the low-temperature magnetoconductivity is proportional to $-\sqrt{B}$, where B is the applied magnetic field along arbitrary direction. In the presence of weak intervalley scatterings, such magnetoconductivity is from the weak antilocalization (WAL) of Weyl fermions. In near zero magnetic fields, this dependence always overwhelms the positive B^2 magnetoconductivity from chiral anomaly. Moreover, strong intervalley scattering and correlation can lead to a transition from the weak antilocalization to weak localization, during which magnetoconductivity changes sign from $-\sqrt{B}$ to \sqrt{B} in the strong limit of intervalley correlation and scattering. The results are in a good agreement with experiment performed previously [42].

8.6 Materials Realization

Since the discovery of the Fermi arc surface state and the first proposal to realize WSM in pyrochlore irdates [4], where 24 pairs of Weyl points emerge as the system undergoes an correlation induced phase transition, the number of proposed magnetic WSM has increased dramatically. Based on first-principles calculation, ferromagnetic compound HgCr_2Se_4 had been proposed as a WSM with a single pair of Weyl nodes separated in BZ [60]. HgCr_2Se_4 has quite simple ferromagnetic (FM) magnetic configuration and its band structure and magnetic properties are not sensitive to the choice of on-site Coulomb interaction parameter U . Experiments show that its Curie temperature T_c is high (around 106–120 K), and its saturated moment is around $5.64 \mu_B/f.u.$ [61, 62]. Theoretical work proposes that the Weyl nodes in HgCr_2Se_4 carry Chern number ± 2 , and the quantum anomalous Hall effect can be realized in its quantum-well structure [60]. Motivated by this theoretical proposal, detailed

transport studies have been performed. Experiment finds that HgCr_2Se_4 has nearly full spin-polarized current, which indicates its half-metallicity [63].

A multilayer-heterostructure material, consisting of alternating layers of a 3D topological insulator and an ordinary insulator, had been predicted as a WSM with just two Weyl points [64]. Numerical calculations also reveal that spinel osmium (CaOs_2O_4 and SrOs_2O_4) is a ferromagnetic compound and may be a WSM or Axion insulator depending on the on-site Coulomb correlation U [65]. $\text{Hg}_{1-x-y}\text{Cd}_x\text{Mn}_y\text{Te}$ in a magnetic field had been suggested as a WSM with two nodes in an experimentally reasonable region of the phase diagram [66]. Its Hall conductivity is proportional to the average Mn ion spin, strongly temperature dependent and shows an unusual magnetic field angle dependence [66]. Unfortunately, to preserve the properties of the magnetic WSM, one need a sample which has quite large magnetic domains. Thus it is a highly challenging problem to experimentally verify the above theoretical proposal about the magnetic WSM.

As mention above, the topological stability of the Weyl points crucially requires that the involved bands are non-degenerate. Thus to obtain a WSM one need break either time reversal symmetry [4] or inversion symmetry [59, 89]. In addition to the time-reversal symmetry-breaking materials, several inversion symmetry-breaking compounds have been proposed as WSM. A WSM phase have been found in a superlattice system formed by HgTe/CdTe multilayer structure [89]. It had been suggested between the normal insulator and the topological insulator phases, a WSM phase exists for a finite range of the system parameters and exhibits a finite number of Weyl points with robust band touching at the Fermi level [89]. Theoretical work suggests that trigonal Te and Se undergo insulating-semimetallic-metallic transitions under pressure, and the semimetallic phase is a WSM with multiple Weyl nodes near the Fermi level [90]. By studying the problem of phase transitions from three-dimensional topological to normal insulators without inversion symmetry, a robust WSM had been suggested in the solid solutions $\text{LaBi}_{1-x}\text{Sb}_x\text{Te}_3$ and $\text{LuBi}_{1-x}\text{Sb}_x\text{Te}_3$ for $x \approx 38.5\text{--}41.9\%$ and $x \approx 40.5\text{--}45.1\%$, respectively [91]. There are also several other proposals for realization of WSM. Unfortunately, none of them had been definitely confirmed to be a WSM.

In 2015, two research groups simultaneously theoretically predicted the existence of WSM in the noncentrosymmetric and non-magnetic transition-metal monophosphides: TaAs , TaP , NbP and NbAs [67, 68]. TaAs crystalizes in a body-centered tetragonal lattice system, the space group is $I4_1md$ (C_{4v}). TaAs family compounds contain two mirror planes, namely, M_x and M_y [67, 68]. The $Z\Gamma$ plane in BZ possess mirror symmetry, thus the energy bands within this plane can be classified in terms of the mirror eigenvalues ± 1 . The calculations without spin-orbital coupling show that the two bands that cross along the Z to Γ line belong to opposite mirror eigenvalues [67]. Combining with the time reversal symmetry, this band inversion guarantees a nodal line in the $Z\Gamma$ plane [69]. Considering SOC, the first-principles calculation shows that the $Z\Gamma$ plane becomes fully gapped [67, 68]. To explore the possible band crossing at general k point is very important.

For the material with inversion symmetry, the presence of Weyl point can be justified by parities of occupied bands at all the TRIM [4, 70, 71]. Without inversion

symmetry, one cannot use the parity criterion for TaAs family compounds. On the other hand, with mirror planes M_x and M_y , mirror Chern number (MCN) can directly reveal whether TaAs hosts Weyl points in the BZ or not [67]. Based on the Wilson-loop method, the MCNs for the two mirror planes had been calculated, and the numerical results confirm that Weyl points exist in the TaAs band structure [67].

The exact positions of Weyl points can be determined by calculating the Berry flux through a closed surface enclosing a Weyl point. The Berry curvature integration can be done based on a computational scheme proposed by Fukui et al. [72]. One can define a small cubic region surrounding each Weyl point. A quantity $\gamma_{P_l,s}^n$, which is called the field strength, is defined as [72, 73]:

$$\gamma_{P_l,s}^n = \text{Im} \log(\langle n(\mathbf{k}_l, s) | n(\mathbf{k}_l + \mathbf{u}_1, s) \rangle \langle n(\mathbf{k}_l + \mathbf{u}_1, s) | n(\mathbf{k}_l + \mathbf{u}_1 + \mathbf{u}_2, s) \rangle \langle n(\mathbf{k}_l + \mathbf{u}_1 + \mathbf{u}_2, s) | n(\mathbf{k}_l + \mathbf{u}_2, s) \rangle \langle n(\mathbf{k}_l + \mathbf{u}_2, s) | n(\mathbf{k}_l, s) \rangle)$$

where \mathbf{k}_l is a vector at l th mesh point, $s = 1-6$ denotes the six faces of the cube, \mathbf{u}_1 and \mathbf{u}_2 are vectors between nearest mesh points for the two directions of the \mathbf{k} vector on the surface of the cube, P_l is l th smallest closed path passing by the points \mathbf{k}_l and its nearest mesh point. In this formula, the Chern number can be obtained through the summation over a mesh of phases $\gamma_{P_l,s}^n$: $C_n = \sum_{P_l,s} \gamma_{P_l,s}^n$. The Bloch wave functions $|n(\mathbf{k}_l, s)\rangle$ are given from the first-principles calculations.

By employing dense k -mesh on each of the six faces of the small cube, two nonequivalent Weyl points had been found out [67, 68]. There are 24 Weyl points in total: 8 Weyl points on the $k_z = 0$ plane, and 16 Weyl points away from the $k_z = 0$ plane. The Weyl points in the $k_z = 0$ plane are about 2 meV above the Fermi energy and form eight tiny hole pockets, while the others are about 21 meV below the Fermi level to form 16 electron pockets [67, 68]. Regardless of the quite complicated patterns for the Fermi surfaces, the Fermi arc structures on both (001) and (100) surfaces had also been identified theoretically [67, 68]. Unlike previous predictions, these compound are stoichiometric and does not depend on fine-tuning chemical composition. Moreover, different with the proposed magnetic WSM which requires magnetic ordering in sufficiently large domains, TaAs family naturally break the inversion symmetry. Thus these compounds are ideal for the ARPES measurements.

The theoretical prediction of WSM in TaAs family compounds had been quickly confirmed by subsequent experiments. Several groups have reported the direct observation of the bulk Weyl points and the surface Fermi arcs by ARPES in TaAs [74-77], NbAs [78], TaP [79, 80], and NbP [81]. The observations of Fermi arc, the hallmark of WSM [4], unambiguously confirm the emergence of WSM in these compounds. As discussed above, according to quantum field theory, the appearance of Weyl points near the Fermi level will cause novel transport phenomena related to chiral anomaly. This novel property had also been confirmed by experiments [44, 45]. For most metals, usually the resistivity increases under an external magnetic field. While under parallel electric and magnetic fields, TaAs displays a negative magnetoresistance, namely this compound becomes more conductive as a magnetic field is applied along the direction of the current for certain ranges of the field strength [44, 45].

This maybe a signature of the chiral anomaly, and indicates the existence of WSM. Moreover, Analysis of the Shubnikov de Haas (SdH) oscillations suggests that the Berry phase accumulated along the cyclotron orbits is π . This again indicates the existence of Weyl points [44].

Due to the fact that not all Weyl nodes in TaAs are symmetry related, 24 Weyl nodes are close to but not exactly at the Fermi level. Moreover, there are also trivial Fermi pockets at the Fermi level in addition to the Weyl nodes [67, 68]. Thus the linear-B negative magnetoresistance [31, 82], the emergent supersymmetry [83] and others [84], have not been experimentally observed in TaAs family. Therefore, it is urgent to search for ideal Weyl semimetals with all Weyl nodes exactly residing at the Fermi level. Based on first-principles calculation, chalcopyrites CuTlSe₂, AgTlTe₂, AuTlTe₂, and ZnPbAs₂ had been predicted as ideal WSM [85]. These compounds have largely separated Weyl points and uncovered Fermi arcs, consequently are amenable to experimental detections [85]. HgTe and half-Heusler compounds had also been suggested as ideal WSM under a broad range of in-plane compressive strain [86]. With Weyl nodes located exactly at the Fermi level and without coexisting trivial Fermi surfaces, these ideal WSMs provide perfect playground of intriguing Weyl semimetals and potential applications for low-power and high-speed electronics.

8.7 Type-II Weyl Semimetals

In the above mentioned WSM, refers to type-I WSM, the low energy excitation is analogs of the relativistic Weyl fermion from high energy physics. Thus these WSM respect Lorentz symmetry and around the Weyl points their band structure have the typical conical dispersion as shown in Fig. 8.5. There is also type-II WSM [92], with also crossing points formed by two non-degenerate linearly dispersing energy bands. However as shown in Fig. 8.5, the Weyl node in type-II WSM appears at the contact of electron and hole pockets and exhibits a strongly tilted conical band structure dispersion with a nonvanishing density of states (DOS) [92, 93]. In contrast, type-I WSM has a pointlike Fermi surface and a vanishing DOS at Fermi level. Thus different with type-I WSM, type-II WSM violates Lorentz and has no counterparts in high energy physics [92, 93].

The first realistic type-II WSM proposed by theorists is WTe₂ [92]. WTe₂ is a layered transition metal dichalcogenides material [94]. This compound has an extremely large positive magnetoresistance (MR) at low temperatures and the MR remains unsaturated even at extremely high applied magnetic fields of 60T [94]. A perfect balance between the electron and hole populations [94] and novel spin textures at Fermi surface [95] may be the source of these unique MR effects. Moreover, under pressure WTe₂ displays dome-shaped superconductivity [96, 97].

The crystal structure of WTe₂ is orthorhombic with space group $Pmn2_1$ (C_{2v}^7). Without including SOC, the first-principles calculation reveals that WTe₂ has 16 band crossing points, eight of them locate at the $k_z = 0$ plane and the others locate at low symmetry points [92]. SOC will eliminate the band crossing points at the

low symmetry points. As the case of TaAs [67, 68], by computing the integral of the Berry curvature on a closed surface in k space, eight Weyl points had been confirmed, and all of them located at the $k_z = 0$ plane [92]. The eight Weyl nodes in WTe₂ can be classified to two types: WP1 and WP2. The WP1 is slightly (0.052 eV) above the Fermi level, and its coordinate is (0.121, 0.038, 0) (in units of reciprocal lattice constants). While WP2 is 0.058 eV higher than Fermi energy, and the coordinate is (0.124, 0.045, 0). The other six Weyl points can be easily obtained by lattice symmetry [92]. Numerical results show that when the Fermi level is tuned to the energy of Weyl point, two electron pockets touches two hole pockets at the positions of the Weyl point. This is sharply in contrast with the Type-I WSM, in which the Fermi surface is point-like.

The nature of Weyl point can be checked by considering the following Hamiltonian [92]

$$H(k) = \sum_{i=x,y,z} k_i A_{i0} + \sum_{i,j=x,y,z} k_i A_{ij} \sigma_j,$$

where k is the wave vector, A is a 3×3 coefficient matrix, and $\vec{\sigma}$ are the Pauli matrices. The energy spectrum of this Hamiltonian is

$$\varepsilon_{\pm}(k) = \sum_{i=x,y,z} k_i A_{i0} \pm \sqrt{\sum_{j=x,y,z} \left(\sum_{i=x,y,z} k_i A_{ij} \right)^2} = T(k) \pm U(k).$$

It is clear that this band structure has a Weyl point at $k = 0$, and $T(k)$ tilts the Weyl cone consequently breaks the Lorentz invariance. For type-I Weyl point, $T(k)$ always less than $U(k)$, consequently $\varepsilon_{\pm}(k) = 0$ occurs only at $k = 0$ point. However, if $T(k) > U(k)$ at particular region in BZ, the equation of $\varepsilon_{\pm}(k) = 0$ has solutions not only at $k = 0$ but also at certain other k points. Consequently the Fermi surface becomes open electron and hole pockets, which touches at Weyl point [92]. This kind of Weyl point had been referred as type-II Weyl point, and the materials with type-II Weyl point around the Fermi level had been coined as type-II WSM [92]. And the theoretical work suggests that WTe₂ is a type-II WSM [92].

It is very known that Fermi surface plays important role in the response to external fields. Thus type-II WSM give rise to many new properties. In contrast to a type-I WSM, which exhibits a chiral anomaly for any direction of the magnetic field, the chiral anomaly appears in a type-II WSM only when the direction of the magnetic field is within a cone where $|T(k)| > |U(k)|$ [92]. If the field direction is outside this cone, then the Landau-level spectrum is gapped and has no chiral zero mode [92].

It had been suggested that regardless of the field strength for type-II Weyl node, there always exists a critical angle between the B field and the tilt, at which the Landau level spectrum collapses [98]. Moreover, before the collapse, magneto-optical spectrum displays interesting properties, including the invariable presence of intraband peaks, the absence of absorption tails, and the special anisotropic field dependence [98]. It had also been proposed that type-II WSM possess a modified anomalous

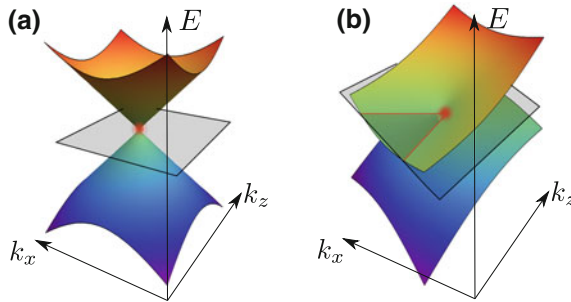


Fig. 8.5 A schematic demonstration of dispersion along k_x - k_z plane in Type-I and Type-II Weyl semimetals. In both diagrams, the grey planes indicate the position of Fermi energy and the red dot denotes the Weyl point. **a** Type-I Weyl semimetal; **b** Type-II Weyl semimetal and the red lines correspond to edge of electron pockets (hole pockets are not shown in this diagram)

Hall conductivity [99]: Induced by the strongly tilted conical spectrum in type-II WSM, the Hall conductivity is not universal and can change sign as a function of the parameters quantifying the tilts [99].

Moreover, Type-II WSM display a novel momentum-space Klein tunneling [101]. Since electrons and holes in graphene system have different chirality, quantum tunnelling in these materials becomes highly anisotropic, qualitatively different from the case of normal, non-relativistic electrons. Thus massless Dirac fermions in graphene allow a close realization of Klein's paradox—unimpeded penetration of relativistic particles through high and wide potential barriers [100]. With both electron and hole pockets at Fermi surface, type-II WSM exhibits novel magnetic quantum oscillations [101]. Tunneling between the electron and hole pockets in a magnetic field is the momentum space counterpart of Klein tunneling at a p-n junction in real space [101]. This magnetic breakdown happens at a characteristic field strength that vanishes when the Fermi level approaches the Weyl point. And depending on connected or disconnected pairs of Weyl cones, type-II WSM displays qualitatively different quantum oscillations on the direction of the magnetic field [101].

Owing to its intriguing physical properties like nonsaturating positive magnetoresistance and being possibly a type-II WSM, WTe₂ attract a lot of research attention. The magneto-transport of WTe₂ had been measured by several groups [102–104]. The notable negative longitudinal magnetoresistance, which may relate with the chiral anomaly in WSM, had been observed [102–104]. The negative longitudinal magnetoresistance displays strong planar orientation dependence with the absence along the tungsten chains [102]. This is consistent with the feature of a type-II WSM [92]. Moreover, experiment reveals that the negative longitudinal magnetoresistance in WTe₂ can be tuned by gate voltage [102]. This may be attributed to the fact that Fermi energy pass through the Weyl points [102]. These experimental results strongly indicate the existence of type-II Weyl point in WTe₂.

Due to the existence of multiple pockets in a limited momentum space, the full electronic structure picture of WTe₂ remains controversial [95, 105–107]. Recently,

by using laser-based ARPES with high energy and momentum resolutions, Wang *et al.* explore the electronic structure of WTe₂[108]. Their experimental results show good agreement with the band structure calculations, provide electronic signatures that are consistent with a type-II Weyl state in WTe₂[108]. Unfortunately the Weyl points lie about 50 meV above the Fermi energy and the distance between a pair of Weyl points is only about 0.7% of the reciprocal lattice vector length [92], thus for WTe₂ the definite experimental evidence on type-II WSM is still lacking.

Based on first-principles calculation, T_d phase MoTe₂, which is isostructural to WTe₂, had been proposed as type-II WSM [109, 110]. Numerical results reveal MoTe₂ has four pairs of Weyl points, and these Weyl points is only slightly above (~ 6 meV) the Fermi energy [109, 110]. The distance between the predicted Weyl points is around 4% of the reciprocal lattice in MoTe₂. This is six times larger than that of WTe₂. Due to the large Weyl point separation, the Fermi arcs surface state can be easily accessed by ARPES [109, 110]. A series of strain-driven topological phase transitions in MoTe₂ had also been suggested [109, 110]. Theoretical calculation also reveals that Mo-doped WTe₂ is a type-II WSM [111]. The positions of the Weyl points and length of the Fermi arc can be adiabatically tuned as a function of Mo doping. A 2% Mo doping is sufficient to stabilize the WSM phase not only at low temperatures but also at room temperatures [111] and a moderate doping can induce long Fermi arc [111]. By pump-probe ARPES, the band structure above Fermi energy had been accessed, and a topological Fermi arc had been directed observed [112]. The excellent agreement between theoretical simulation and experimental measurement confirm that these system are indeed type-II WSM [112].

However, the band structures of WTe₂ and MoTe₂ are very complicated and the arrangement of Weyl points is sensitive to small changes in the crystal structure, which, in turn, is sensitive to temperature [92, 113]. Thus it is crucially important to find the materials with robust separated Weyl nodes. Numerical results predict that transition metal diphosphides MoP₂ and WP₂ is type-II WSM [114]. The crystal structure of these materials is different from the previously reported ditellurides. With relatively simple band structures, MoP₂ and WP₂ have four pairs of type-II Weyl points [114]. Neighboring Weyl points have the same chirality, which makes the type-II WSM phase robust against small perturbations of the crystalline lattice. Due to the peculiar arrangement of the Weyl points, the Fermi arcs is quite long, making them readily accessible in ARPES [114]. Strongly robust type-II Weyl points had also been predicted existed at Ta₃S₂ [115] and TaIrTe₄ [116]. The Fermi arc in Ta₃S₂ is about twice larger than the measured value in TaAs and 20 times larger than the predicted value in WTe₂ [115], while Fermi arcs of TaIrTe₄ is extend to about 1/3 of the surface BZ [116].

8.8 Outlook

As a new states of matter, WSM have attracted intense research interest, and a lot of other novel properties had been suggested. In the limit of weak internode scattering,

WSM exhibit nonlocal transport behaviors [117]. The unusual Fermi arc surface states of WSM display nontrivial quantum oscillations signature [118]. Because Weyl fermion quasiparticles are naturally spin-momentum locked and superconductivity in these materials may exhibit non-Abelian statistics [119–121], they may also be exploited to realize new applications, such as in spintronics and quantum computers. The photoinduced anomalous Hall effects [87] and significant photocurrents behavior [88] had also been proposed.

Weyl fermions were conjectured in the 1920s by the mathematician Hermann Weyl [5], and played a crucial role in the development of quantum field theory and the Standard Model but has not yet been observed as a fundamental particle in Nature. With Weyl fermions as its low-energy quasiparticle excitations, WSM thus has attracted intense research interest not only at condensed matter system, but also many other field. The Weyl points had been theoretically predicted and experimentally observed at photonic crystal [122, 123]. The bulk Weyl magnon with chiral magnon surface states forming arcs at finite energy had been suggested [124]. Lorentz-violating type-II Weyl fermions had been proposed at acoustic system [125]. Recently, the so-called new fermion, with [126] or without [127–129] counterparts in high energy physics, had been discussed.

Acknowledgements This work was supported by NSFC (Grants No. 11525417, No. 51721001, and No. 11574127), Guangdong Innovative and Entrepreneurial Research Team Program (Grant No. 2016ZT06D348), the National Key R & D Program (Grant No. 2016YFA0301700), and the Science, Technology and Innovation Commission of Shenzhen Municipality (Grant No. ZDSYS20170303165926217).

References

1. M.Z. Hasan, C.L. Kane, Rev. Mod. Phys. **82**, 3045 (2010)
2. X.L. Qi, S.C. Zhang, Rev. Mod. Phys. **83**, 1057 (2011)
3. Y. Ando, J. Phys. Soc. Jpn. **82**, 102001 (2013)
4. X. Wan, A.M. Turner, A. Vishwanath, S.Y. Savrasov, Phys. Rev. B **83**, 205101 (2011)
5. H. Weyl, Zeitshrift fur Physik **56**, 330 (1929)
6. L. Balents, Physics **4**, 36 (2011)
7. T.O. Wehling, A.M. Black-Schaffer, A.V. Balatsky, Adv. Phys. **63**, 1 (2014)
8. N.P. Armitage, E.J. Mele, A. Vishwanath, [arXiv:1705.01111](https://arxiv.org/abs/1705.01111) (2017)
9. N. Taria, M. Wakushima, Y. Hinatsu, J. Phys. Condens. Matter **13**, 5527 (2001)
10. K. Matsuhira et al., J. Phys. Soc. Jpn. **76**, 043706 (2007)
11. S. Nakatsuji, Phys. Rev. Lett. **96**, 087204 (2006). Y. Machida et al., Nature **463**, 210 (2011)
12. K. Matsuhira et al., J. Phys. Soc. Jpn. **80**, 094701 (2011)
13. S.M. Disseler, Phys. Rev. B **89**, 140413 (2014). H. Liu et al., Solid State Commun. **179**, 1 (2014)
14. J.J. Ishikawa, E.C.T. O'Farrell, S. Nakatsuji, Phys. Rev. B **85**, 245109 (2012)
15. E.Y. Ma et al., Science **350**, 538 (2015)
16. D.A. Pesin, L. Balents, Nature Phys. **6**, 376 (2010)
17. G. Kotliar, S.Y. Savrasov, K. Haule, V.S. Oudovenko, O. Parcollet, C.A. Marianetti, Rev. Mod. Phys. **78**, 865 (2006)
18. D. Lurie, *Particles and Fields* (Wiley, New York, 1968)

19. A.M. Turner, A. Vishwanath, [arXiv:1301.0330](https://arxiv.org/abs/1301.0330) (2013)
20. S.M. Young, S. Zaheer, J.C.Y. Teo, C.L. Kane, E.J. Mele, A.M. Rappe, Phys. Rev. Lett. **108**, 140405 (2012)
21. Z. Wang, Y. Sun, X.-Q. Chen, C. Franchini, G. Xu, H. Weng, X. Dai, Z. Fang, Phys. Rev. B **85**, 195320 (2012)
22. Z. Wang, H. Weng, Q. Wu, X. Dai, Z. Fang, Phys. Rev. B **88**, 125427 (2013)
23. Y. Du, B. Wan, D. Wang, L. Sheng, C.-G. Duan, X. Wan, Sci. Rep. **5**, 14423 (2015)
24. D. Xiao, M.-C. Chang, Q. Niu, Rev. Mod. Phys. **82**, 1959 (2010)
25. R. Arita, J. Kuneš, A.V. Kozhevnikov, A.G. Eguiluz, M. Imada, Phys. Rev. Lett. **108**, 086403 (2012)
26. K.-Y. Yang, Y.-M. Lu, Y. Ran, Phys. Rev. B **84**, 075129 (2011)
27. H.-Z. Lu, S.-B. Zhang, S.-Q. Shen, Phys. Rev. B **92**, 045203 (2015)
28. G.E. Volovik, *The Universe in a Helium Droplet* (Clarendon Press, 2003)
29. Y. Hatsugai, Phys. Rev. Lett. **71**, 3697 (1993)
30. H.-Z. Lu, W.-Y. Shan, W. Yao, Q. Niu, S.-Q. Shen, Phys. Rev. B **81**, 115407 (2010)
31. D.T. Son, B.Z. Spivak, Phys. Rev. B **88**, 104412 (2013)
32. D.E. Kharzeev, H.U. Yee, Phys. Rev. B **88**, 115119 (2013)
33. A.A. Burkov, Phys. Rev. Lett. **113**, 247203 (2014)
34. D.T. Son, N. Yamamoto, Phys. Rev. Lett. **109**, 181602 (2012)
35. M.A. Stephanov, Y. Yin, Phys. Rev. Lett. **109**, 162001 (2012)
36. K. Landsteiner, E. Megías, F. Pena-Benitez, Phys. Rev. Lett. **107**, 021601 (2011)
37. M.-C. Chang, M.-F. Yang, Phys. Rev. B **91**, 115203 (2015)
38. S.L. Adler, Phys. Rev. **177**, 2426 (1969)
39. J.S. Bell, R. Jackiw, Il Nuovo Cimento A **60**, 47 (1969)
40. H.B. Nielsen, M. Ninomiya, Phys. Lett. B **130**, 389 (1983)
41. H.B. Nielsen, M. Ninomiya, Nucl. Phys. B **185**, 20 (1981)
42. H.J. Kim et al., Phys. Rev. Lett. **111**, 246603 (2013)
43. K.S. Kim, H.J. Kim, M. Sasaki, Phys. Rev. B **89**, 195137 (2014)
44. X.C. Huang et al., Phys. Rev. X **5**, 031023 (2015)
45. C.L. Zhang et al., Nat. Commun. **7**, 10735 (2016)
46. C. Zhang et al., Phys. Rev. B **92**, 041203 (2015)
47. F. Arnold et al., Nat. Commun. **7**, 11615 (2016)
48. C.-L. Zhang et al., Nat. Phys. **13**, 979 (2017)
49. E.V. Gorbar, V.A. Miransky, I.A. Shovkovy, Phys. Rev. B **89**, 085126 (2014)
50. S. Datta, *Electronic Transport in Mesoscopic Systems* (Cambridge University Press, 1997)
51. V. Aji, Phys. Rev. B **85**, 241101 (2012)
52. P. Goswami, J.H. Pixley, S.D. Sarma, Phys. Rev. B **92**, 075205 (2015)
53. M.-C. Chang, Q. Niu, Phys. Rev. Lett. **75**, 1348 (1995)
54. J.-H. Zhou, H. Jiang, Q. Niu, J.-R. Shi, Chin. Phys. Lett. **30**, 027101 (2013)
55. A.A. Burkov, Phys. Rev. B **91**, 245157 (2015)
56. P.A. Lee, T.V. Ramakrishnan, Rev. Mod. Phys. **57**, 287 (1985)
57. H.-Z. Lu, S.-Q. Shen, Phys. Rev. B **92**, 035203 (2015)
58. G.D. Mahan, *Many-Particle Physics* (Plenum Press, 1990)
59. S. Murakami, New J. Phys. **9**, 356 (2007)
60. G. Xu, H. Weng, Z. Wang, X. Dai, Z. Fang, Phys. Rev. Lett. **107**, 186806 (2011)
61. P.K. Baltzer, H.W. Lehmann, M. Robbins, Phys. Rev. Lett. **15**, 493 (1965)
62. P.K. Baltzer, P.J. Wojtowicz, M. Robbins, E. Lopatin, Phys. Rev. **151**, 367 (1966)
63. T. Guan, C. Lin, C. Yang, Y. Shi, C. Ren, Y. Li, H. Weng, X. Dai, Z. Fang, S. Yan, P. Xiong, Phys. Rev. Lett. **115**, 087002 (2015)
64. A.A. Burkov, L. Balents, Phys. Rev. Lett. **107**, 127205 (2011)
65. X. Wan, A. Vishwanath, S.Y. Savrasov, Phys. Rev. Lett. **108**, 146601 (2012)
66. D. Bulmash, C.-X. Liu, X.-L. Qi, Phys. Rev. B **89**, 081106 (2014)
67. H. Weng, C. Fang, Z. Fang, B.A. Bernevig, X. Dai, Phys. Rev. X **5**, 011029 (2015)
68. S.-M. Huang et al., Nat. Commun. **6**, 7373 (2015)

69. G. Bian et al., *Nat. Commun.* **7**, 10556 (2015)
70. A.M. Turner, Y. Zhang, R.S.K. Mong, A. Vishwanath, *Phys. Rev. B* **85**, 165120 (2012)
71. T.L. Hughes, E. Prodan, B.A. Bernevig, *Phys. Rev. B* **83**, 245132 (2011)
72. T. Fukui, Y. Hatsugai, H. Suzuki, *J. Phys. Soc. Jpn.* **74**, 6 (2005)
73. M. Taillefumier, V.K. Dugaev, B. Canals, C. Lacroix, P. Bruno, *Phys. Rev. B* **78**, 155330 (2008)
74. B.Q. Lv et al., *Phys. Rev. X* **5**, 031013 (2015)
75. B.Q. Lv et al., *Nat. Phys.* **11**, 724 (2015)
76. S.-Y. Xu et al., *Science* **349**, 613 (2015)
77. L.X. Yang et al., *Nat. Phys.* **11**, 728 (2015)
78. S.-Y. Xu et al., *Nat. Phys.* **11**, 748 (2015)
79. N. Xu et al., *Nat. Commun.* **7**, 11006 (2016)
80. S.-Y. Xu et al., *Sci. Adv.* **1**, 1501092 (2015)
81. D.F. Xu et al., *Chin. Phys. Lett.* **32**, 107101 (2015)
82. S.-B. Zhang, H.-Z. Lu, S.-Q. Shen, *New J. Phys.* **18**, 053039 (2016)
83. S.-K. Jian, Y.-F. Jiang, H. Yao, *Phys. Rev. Lett.* **114**, 237001 (2015)
84. P. Hosur, X. Qi, *CR Phys.* **14**, 857 (2013)
85. J. Ruan, S.-K. Jian, D. Zhang, H. Yao, H. Zhang, S.-C. Zhang, D. Xing, *Phys. Rev. Lett.* **116**, 226801 (2016)
86. J. Ruan, S.-K. Jian, H. Yao, H. Zhang, S.-C. Zhang, D. Xing, *Nat. Commun.* **7**, 11136 (2016)
87. C.-K. Chan, P.A. Lee, K.S. Burch, J.H. Han, Y. Ran, *Phys. Rev. Lett.* **116**, 026805 (2016)
88. C.-K. Chan, N.H. Lindner, G. Refael, P.A. Lee, *Phys. Rev. B* **95**, 041104 (2017)
89. G.B. Halasz, L. Balents, *Phys. Rev. B* **85**, 035103 (2012)
90. M. Hirayama, R. Okugawa, S. Ishibashi, S. Murakami, T. Miyake, *Phys. Rev. Lett.* **114**, 206401 (2015)
91. J. Liu, D. Vanderbilt, *Phys. Rev. B* **90**, 155316 (2014)
92. A.A. Soluyanov et al., *Nature* **527**, 495 (2015)
93. Y. Xu, F. Zhang, C. Zhang, *Phys. Rev. Lett.* **115**, 265304 (2015)
94. M.N. Ali et al., *Nature* **514**, 205 (2014)
95. J. Jiang et al., *Phys. Rev. Lett.* **115**, 166601 (2015)
96. X.-C. Pan et al., *Nat. Commun.* **6**, 7805 (2015)
97. D. Kang et al., *Nat. Commun.* **6**, 7804 (2015)
98. Z.-M. Yu, Y. Yao, S.A. Yang, *Phys. Rev. Lett.* **117**, 077202 (2016)
99. A.A. Zyuzin, R.P. Tiwari, *JETP Lett.* **103**, 717 (2016)
100. M.I. Katsnelson, K.S. Novoselov, A.K. Geim, *Nat. Phys.* **2**, 620 (2006)
101. T.E. O'Brien, M. Diez, C.W.J. Beenakker, *Phys. Rev. Lett.* **116**, 236401 (2016)
102. Y. Wang et al., *Nat. Commun.* **7**, 13142 (2016)
103. E. Zhang et al., *Nano Lett.* **17**, 878 (2017)
104. Y.-Y. Lv et al., *Phys. Rev. Lett.* **118**, 096603 (2017)
105. I. Pletikosić, Mazhar N. Ali, A.V. Fedorov, R.J. Cava, T. Valla, *Phys. Rev. Lett.* **113**, 216601 (2014)
106. P.L. Cai et al., *Phys. Rev. Lett.* **115**, 057202 (2015)
107. Z. Zhu et al., *Phys. Rev. Lett.* **114**, 176601 (2015)
108. C. Wang et al., *Phys. Rev. B* **94**, 241119 (2016)
109. Y. Sun, S.-C. Wu, M.N. Ali, C. Felser, B. Yan, *Phys. Rev. B* **92**, 161107 (2015)
110. Z. Wang et al., *Phys. Rev. Lett.* **117**, 056805 (2016)
111. T.-R. Chang et al., *Nat. Commun.* **7**, 10639 (2016)
112. I. Belopolski et al., *Nat. Commun.* **7**, 13643 (2016)
113. M. Udagawa, E.J. Bergholtz, *Phys. Rev. Lett.* **117**, 086401 (2016)
114. G. Autes, D. Gresch, M. Troyer, A.A. Soluyanov, O.V. Yazyev, *Phys. Rev. Lett.* **117**, 066402 (2016)
115. G. Chang et al., *Sci. Adv.* **2**, e1600295 (2016)
116. K. Koepernik et al., *Phys. Rev. B* **93**, 201101 (2016)

117. S.A. Parameswaran, T. Grover, D.A. Abanin, D.A. Pesin, A. Vishwanath, *Phys. Rev. X* **4**, 031035 (2014)
118. A.C. Potter, I. Kimchi, A. Vishwanath, *Nat. Commun.* **5**, 5161 (2014)
119. P. Hosur, X. Dai, Z. Fang, X.-L. Qi, *Phys. Rev. B* **90**, 045130 (2014)
120. G. Bednik, A.A. Zyuzin, A.A. Burkov, *Phys. Rev. B* **92**, 035153 (2015)
121. Y. Li, F.D.M. Haldane, [arXiv:1510.01730](https://arxiv.org/abs/1510.01730) (2015)
122. L. Lu, L. Fu, J.D. Joannopoulos, M. Soljacic, *Nat. Photon.* **7**, 294 (2013)
123. L. Lu et al., *Science* **349**, 622 (2015)
124. F.-Y. Li, Y.-D. Li, Y.B. Kim, L. Balents, Y. Yu, G. Chen, *Nat. Commun.* **7**, 12691 (2016)
125. Z. Yang, B. Zhang, *Phys. Rev. Lett.* **117**, 224301 (2016)
126. F. Tang, X. Luo, Y. Du, Y. Yu and X. Wan, [arXiv:1612.05938](https://arxiv.org/abs/1612.05938) (2016)
127. B. Bradlyn, J. Cano, Z. Wang, M.G. Vergniory, C. Felser, R.J. Cava, B.A. Bernevig, *Science* **353**, 6299 (2016)
128. B.Q. Lv et al., *Nature* **546**, 627 (2017)
129. H. Weng, C. Fang, Z. Fang, X. Dai, *Phys. Rev. B* **94**, 165201 (2016)

Chapter 9

Symmetry and Topology in Antiferromagnetic Spintronics



Libor Šmejkal and Tomáš Jungwirth

Abstract Antiferromagnetic spintronics focuses on investigating and using antiferromagnets as active elements in spintronics structures. Last decade advances in relativistic spintronics led to the discovery of the staggered, current-induced field in antiferromagnets. The corresponding Néel spin-orbit torque allowed for efficient electrical switching of antiferromagnetic moments and, in combination with electrical readout, for the demonstration of experimental antiferromagnetic memory devices. In parallel, the anomalous Hall effect was predicted and subsequently observed in antiferromagnets. A new field of spintronics based on antiferromagnets has emerged. We will focus here on the introduction into the most significant discoveries which shaped the field together with a more recent spin-off focusing on combining antiferromagnetic spintronics with topological effects, such as antiferromagnetic topological semimetals and insulators, and the interplay of antiferromagnetism, topology, and superconductivity in heterostructures.

L. Šmejkal (✉)

Institut für Physik, Johannes Gutenberg-Universität, Staudinger Weg 7,
55128 Mainz, Germany
e-mail: smejkall@fzu.cz

L. Šmejkal · T. Jungwirth

Institute of Physics, Academy of Sciences of the Czech Republic,
Cukrovarnická 10, 162 00 Praha 6 Prague, Czech Republic
e-mail: jungw@fzu.cz

L. Šmejkal

Faculty of Mathematics and Physics, Department of Condensed Matter Physics,
Charles University, Ke Karlovu 5., 12116 Praha 2 Prague, Czech Republic

T. Jungwirth

School of Physics and Astronomy, University of Nottingham, University Park,
Nottingham NG7 2RD, UK

9.1 Introduction

The phase of matter can be characterized by symmetry and topology [1, 2]. For certain effects, symmetry provides the basic condition to occur while topology can add exceptional robustness. A text-book example is the Hall effect enabled by the broken time-reversal symmetry (\mathcal{T}) in the applied magnetic field. The exact discrete resistance values in the quantum Hall effect (QHE), unperturbed by disorder, are then a consequence of the topological Landau level form of the electronic structure in a strong quantizing magnetic field [3]. In this chapter, we show how the fundamental concepts of symmetry and topology apply to antiferromagnetic spintronics [4].

We start our chapter by briefly illustrating the symmetry and topology principles on three key functionalities of spintronic memory devices, namely the retention, reading, and writing of magnetic information [5, 6]. Side by side we compare in this introductory section how the principles apply when considering the more conventional ferromagnetic and the emerging antiferromagnetic spintronic devices.

Ferromagnetism can (and often does) lower the symmetry of the crystal, depending on the direction of magnetic moments. For example, a rotation along a certain crystal axis remains a symmetry operation when moments are aligned with the axis but the symmetry is broken when the moments are perpendicular to the rotation axis. It implies that reorientation of ferromagnetic moments can, in the presence of spin-orbit coupling (SOC), change the electronic structure and by this the total energy. This is the origin of the magnetocrystalline anisotropy energy (MAE) barrier that supports the non-volatile storage in spintronic memories [5]. The same symmetry principle and corresponding magnetic storage functionality apply equally to antiferromagnets (AFs) [4]. On top of that, the lack of a net magnetic moment and suppressed dipolar fields make the storage in AFs less sensitive to magnetic fields and allow for denser integration of memory bits than in ferromagnets. Apart from binary storage, AFs naturally host series of different stable multi-domain reconfigurations which is suitable for integrated memory-logic or neuromorphic computation devices [7–10].

Anisotropic resistance, i.e. the sensitivity of electronic transport to the current direction, requires broken cubic symmetry. Ferromagnetism where spins align with a specific crystal axis always breaks cubic symmetry. This implies that ferromagnets can have the anisotropic resistance. Here typically the leading dependence of the resistance on current direction is when measured with respect to the magnetization axis. The effect called (spontaneous) anisotropic magnetoresistance (AMR) is known for more than 150 years [12] and provides arguably the most straightforward means for electrically detecting different directions of ferromagnetic moments. AMR was used, e.g., in the first generation of magnetoresistive field sensors for hard-disk read-heads or for electrical readout in the first generation of magnetic random access memories (MRAMs) [13]. The same symmetry argument applies to the AMR in AFs where it has been used to demonstrate electrical readout in experimental memory devices, as shown in Fig. 9.1 [7–9, 14, 15]. On the other hand, AMR in AFs is not suitable for external magnetic field sensing because of the lack of the net magnetic moment.

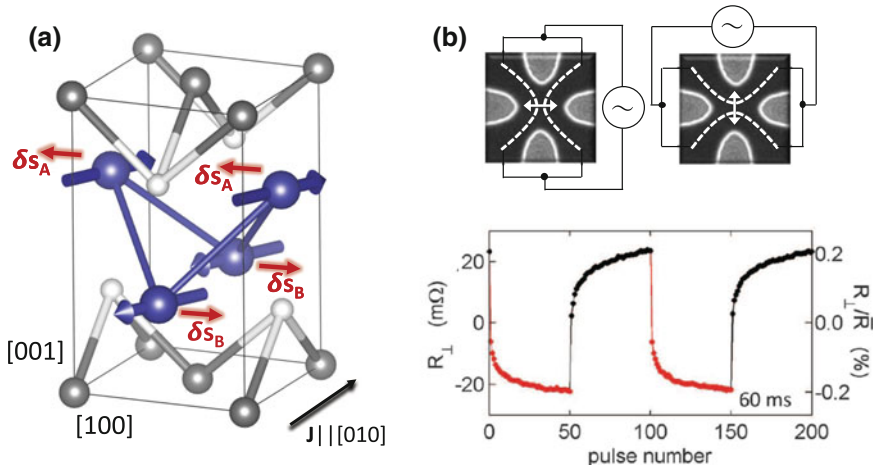


Fig. 9.1 Discovery of the manipulation of the antiferromagnetic order via electric currents. **a** The crystal structure of the CuMnAs AF with marked non-equilibrium spin polarisations δs generated by the current J applied along the [010] direction. **b** The reorientation of the moments is observed in the microbars of the CuMnAs. The writing current is applied along one of two orthogonal directions and generates a spin-orbit field which reorients the moments along the perpendicular direction to the applied current. In the bottom panel, we show the anisotropic magnetoresistance signal corresponding to the reorientation of the Néel order parameter. Panel (b) adapted from [7, 11]

Another transport effect that can be used to internally detect magnetic moments of a conductor is the anomalous Hall effect (AHE). It can occur in crystals with magnetic space groups whose symmetry allows for the presence of a net magnetic moment. Remarkably, this symmetry argument holds independently of whether the system indeed has a ferromagnetic moment or is in a fully compensated antiferromagnetic state. While the AHE in ferromagnets was discovered more than 100 years ago [17], its experimental demonstration in AFs, shown in Fig. 9.2, is one of the most recent developments in spintronics [16, 142, 143].

Unlike time-reversal, the symmetry operation of space-inversion (\mathcal{P}) does not rotate the axial magnetic moment vector which implies that ferromagnets cannot have a combined \mathcal{PT} -symmetry. This removes the Kramers \mathcal{PT} -symmetry protection of the spin-up/spin-down degeneracy of electronic bands. As a result, electrons moving in the unequal spin-up and spin-down bands have different resistivities. In ferromagnetic bilayers this leads to different resistance states for parallel and antiparallel alignments of moments in the two layers and the corresponding giant/tunnelling magnetoresistance (GMR/TMR) effects [5]. These phenomena, that tend to be stronger than the AMR, are used in modern hard disk read-heads and MRAMs.

Different resistivities in spin-up and spin-down transport channels in a ferromagnet can be also used to filter an unpolarised current passing through the ferromagnetic layer by suppressing one spin-component of the electrical current. The resulting spin-polarized current filtered through such a ferromagnetic polarizer can exert a spin transfer torque (STT) on the adjacent ferromagnetic layer and switch its magnetic

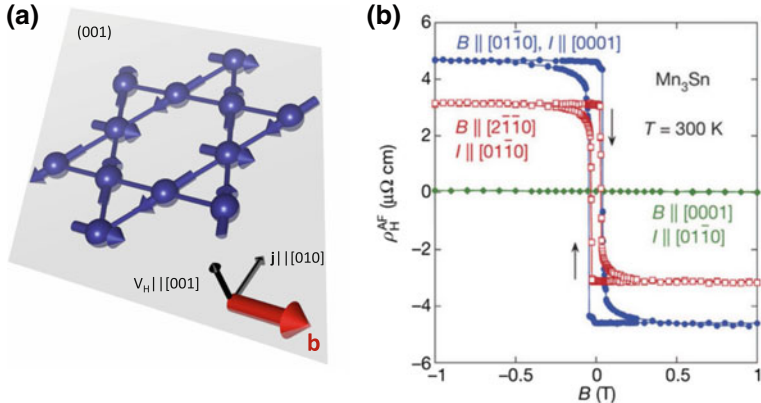


Fig. 9.2 Observation of the anomalous Hall effect in noncollinear AFs. **a** The noncollinear magnetic order on the kagome lattice in the Mn_3Sn breaks the time reversal symmetry and allows for the net magnetization in the [100] direction. Although the net moment is almost perfectly compensated, a strong emergent magnetic field, e.g. Berry curvature **b**, along the [100] direction generates a large anomalous Hall effect in the perpendicular, (001), plane. **b** The measured Hall resistivity ρ_H^{AF} obtained by subtracting the signal from the small net moment and ordinary Hall effect. The panel **(b)** adapted from [16]

moment [18]. This reversible electrical writing method is used in the latest generation of MRAMs.

There is no equivalent counterpart of the two-spin-channel GMR/TMR or STT phenomena in AFs with equal spin-up and spin-down bands. On the other hand, AFs can have the combined \mathcal{PT} -symmetry which opens a possibility of the Dirac crossing of two doubly-degenerate bands, as shown in Fig. 9.3a [19, 20]. The topological protection of these Dirac points can be turned on and off by changing other symmetries of the antiferromagnetic crystal, e.g., via changing the direction of the antiferromagnetic Néel vector. This could enable very large topological AMR effects in AFs and remedy the absence of the two-spin-channel GMR/TMR.

In time-reversal symmetric paramagnets, degeneracy of states with opposite spins and opposite crystal momenta occurs, while the states at a given crystal momentum can be spin split when the spatial inversion symmetry is broken. As a result, the crystal can develop a net spin polarization in a non-equilibrium, current-carrying state. When these spin Hall or Edelstein effects occur at an inversion-asymmetric interface between a paramagnet and a ferromagnet, or inside a ferromagnetic crystal that lacks inversion symmetry, they can induce a spin-orbit torque (SOT) in the ferromagnet [21, 22]. The charge to spin conversion efficiency driving the SOT can outperform that of the STT and is explored as a prospect writing mechanism for future fast MRAMs. A particularly large charge to spin conversion efficiency is expected to occur in time-reversal symmetric topological insulators (TIs) whose 2D surfaces host Dirac cones with the spins locked perpendicular to the 2D momenta [23]. The ultimate charge to spin conversion efficiency would then occur in 1D surface states of 2D TIs, the so called quantum spin Hall states [24], with opposite electron spins locked to the opposite crystal momenta at a given 1D edge.

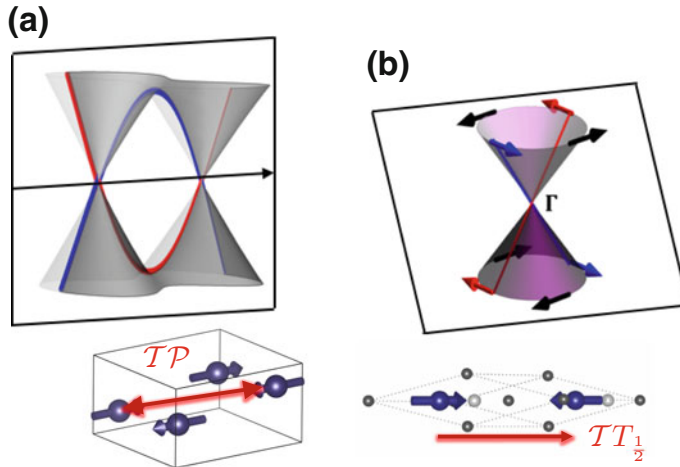


Fig. 9.3 Concepts of topological antiferromagnetic structures in crystal momentum space. **a** The antiferromagnetic effective time reversal symmetry \mathcal{TP} combining time reversal and spatial inversion can protect the Dirac semimetal state. The exemplar crystal structure of orthorhombic CuMnAs is shown in the inset. **b** The antiferromagnetic effective time reversal symmetry $\mathcal{TT}_{\frac{1}{2}}$ combining time reversal and half-unit cell translation can protect the topological insulator. The GdPtBi candidate is drawn in the inset

A direct counterpart of the SOT is observed in AFs that break the \mathcal{T} symmetry and the \mathcal{P} symmetry but have the combined \mathcal{PT} symmetry. In these antiferromagnetic crystals, a global electrical current induces a staggered non-equilibrium spin polarization that is commensurate with the staggered equilibrium Néel order [25]. The phenomenon was used to demonstrate, in combination with AMR, experimental antiferromagnetic memory devices with electrical writing and readout [7]. Because of the THz-scale antiferromagnetic resonance, compared to the GHz-scale ferromagnetic resonance, SOT switching in antiferromagnetic memory devices was demonstrated with writing current pulses as short as 1 ps [11]. Moreover, since it is again the \mathcal{PT} -symmetry that enables the antiferromagnetic SOT, it is potentially compatible with the large topological AMR [20]. Recently electrical switching of Mn_2 Au was also observed accompanied by a large AMR [28]. The role of thermal activation [144] and crystal orientation [145] for the SOT was also investigated.

Another class of AFs, with no symmetry counterparts in ferromagnets, has the combined $\mathcal{TT}_{\frac{1}{2}}$ -symmetry, where $T_{\frac{1}{2}}$ is the translation by a half of the magnetic unit cell. This symmetry allows in principle for TIs with spin-momentum locked surface states, despite the breaking of the \mathcal{T} symmetry by the magnetic order, as illustrated in Fig. 9.3b [26]. Overall, an antiferromagnetic order can occur in 1421 magnetic space groups out of which only 275 allow also for the ferromagnetic order. Similarly, the 122 magnetic point groups are all compatible with the antiferromagnetic order out of which only 31 also support ferromagnetic states. This not only underlines why antiferromagnetism is more common than ferromagnetism and spans the whole range

of materials from insulators to superconductors but also highlights how much is the symmetry and topology playground enlarged by including AFs. We are just beginning to unravel what new spintronics phenomena and functionalities this may offer. In Sect. 9.2 we give a brief overview of symmetry and topology concepts in condensed matter systems. In Sect. 9.3 we discuss in more detail antiferromagnetic topological semimetals, Chern insulators, and TIs. Topological spintronic phenomena in AFs are reviewed in Sects. 9.4 and 9.5 gives a brief summary of the Chapter.

9.2 Antiferromagnets: Symmetry and Topology

The phases of matter can be classified by Landau symmetry breaking mechanism. In an AF, Néel vector breaks the rotational symmetry present in the paramagnetic state. The order parameter is the Néel vector and SOC determines the particular direction(s) of the magnetic moments in crystal, the so-called easy axes, corresponding to the lowest MAE. While certain AFs tends to be to a very good approximation isotropic Heisenberg magnets, e.g. Mn_2Au AF can have in-plane MAE at the level of $10\text{ }\mu\text{eV}$ per formula unit [27, 28], noncollinear Mn_3Sn AF was reported to have MAE of 0.1 eV per formula unit [29, 30], and a giant MAE of 10 meV per formula unit was predicted in noncollinear IrMn_3 [31].

The discoveries in the 1980s in the theory of superfluid vortices, QHE, or dislocation defects revealed an additional label of the phases different from the symmetry, based on topology [32]. The phases can be characterized by an integer topological index which does not change upon continuous transformations of the Hamiltonian and thus supports the relative robustness of a topological phase. For instance, the topological invariants in TIs are the Z_2 indices, which in simple centrosymmetric non-magnetic TIs are related to counting the number of parities at time-reversal invariant crystal momenta [1]. Dirac semimetals (DSMs), such as graphene, are protected by the vorticity around the Dirac point [33]. The DSMs protected by crystalline symmetry can be assigned a topological index by subtracting this crystalline symmetry eigenvalues of the conduction and valence band along the line in Brillouin zone (BZ) invariant under this symmetry. Red and blue lines in Fig. 9.3a illustrate the symmetry eigenvalues with an opposite sign.

We note that TIs and semimetals represent a symmetry protected topological order [34]. For instance, AF DSMs or TIs require the presence of the \mathcal{PT} or $\mathcal{T}T_{1/2}$ symmetry as illustrated in Fig. 9.3a, b. Weyl semimetals (WSM) and Chern insulators are protected by Chern numbers. WSM can be realized in system with broken \mathcal{PT} symmetry, while Chern insulators materialize in systems with broken \mathcal{T} symmetry as we explain further. The slices of constant wavevector component k_z between two Weyl points in simple model WSM [35] (with \mathcal{PT} symmetry broken by breaking \mathcal{T} symmetry, Fig. 9.4a) can be thought of as Chern insulators, whose examples are QHE or quantum anomalous Hall effect (QAHE). If we use the Bloch ansatz, the Chern number of a $k_z = \text{const.}$ plane reads,

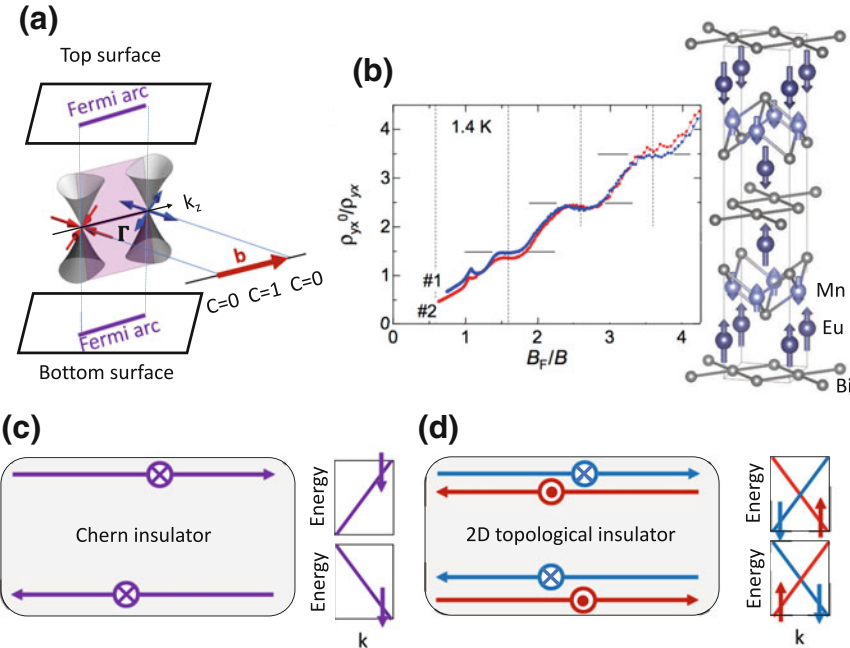


Fig. 9.4 Topological edge states and transport. **a** Fermi arcs in Weyl semimetal. **b** The realization of quantum Hall effect as seen in quantized transversal resistivity in EuMnBi_2 AF [37]. **c** The edge states in Chern insulator. **d** Spin polarised edge states in quantum spin Hall effect. Panel (b) adapted from [37]

$$\mathcal{C} = \frac{1}{2\pi} \int dk_x dk_y b_z(\mathbf{k}), \quad (9.1)$$

where the Berry curvature has a meaning of an emergent magnetic field \mathbf{b} in the crystal momentum space and quantifies the underlying topology of the wavefunction [33]:

$$\mathbf{b}(\mathbf{k}) = -\text{Im} \langle \partial_{\mathbf{k}} u(\mathbf{k}) | \times | \partial_{\mathbf{k}} u(\mathbf{k}) \rangle. \quad (9.2)$$

The topological index of a Weyl point can be defined as a Chern number of a closed surface surrounding the Weyl point, which can be calculated due to the Gauss theorem as a difference between two Chern numbers along the line connecting the Weyl points:

$$\mathcal{Q} = \mathcal{C}(k_{z,W} + \delta) - \mathcal{C}(k_{z,W} - \delta) = \frac{1}{2\pi} \int_{\delta S} d^2k \mathbf{n} \cdot \mathbf{b}(\mathbf{k}). \quad (9.3)$$

Here δS is a small sphere surrounding the Weyl point at $k_{z,W}$, \mathbf{n} is the surface normal vector, and \mathcal{C} is the Chern number of the plane slightly below and above the Weyl point $k_{z,W} \pm \delta$. Thus the Chern number is nonzero along the k_z between the two Weyl points and zero outside as marked in Fig. 9.4a.

The Berry curvature acts as a source and sink at the Weyl points as we illustrate in Fig. 9.4a and consequently the two Weyl points along k_z have $\mathcal{Q} = +1$, and -1 . Topological phases in the crystal momentum space are very often accompanied by quantized or almost quantized and low dissipation transport properties and nontrivial surface states [1, 36]. In Fig. 9.4b we show the quantized Hall plateaus in EuMnBi₂ AF [37]. The Chern insulator exhibits quantized Hall conductivity: $\sigma_{xy} = \frac{e^2}{h}\mathcal{C}$. On the other hand, quantum spin Hall effect (QSHE) in the 2D TI shows a quantized spin Hall conductivity $\sigma_{xy}^S = 2\frac{e^2}{h}$. In a Chern insulator, chiral edge states arise (single spin polarized electrons), which are in fact 1D Weyl fermions of a given chirality [38], as we show in Fig. 9.4c. In 2D TIs, helical edge states are observed (two counter-propagating perfectly polarized currents with opposite spins) as we illustrate in Fig. 9.4d. In contrast, a WSM exhibits surface BZ Fermi arcs for the constant k_z in-between Weyl points as we show in Fig. 9.4a. The stacked Fermi arcs from chiral edge states of QAHE subsystems yield almost quantized Hall conductivity: $\sigma_{xy} = \frac{e^2}{h}\frac{\delta k_W}{\pi}$, where δk_W is the distance between the Weyl points in the BZ. In Sect. 9.3 we will discuss in detail possible realizations of topological semimetals, Chern insulators, and TIs in AFs.

9.2.1 Magnetic Symmetry and Spintronics Effects

The potential presence of long-range ordered antiferromagnetic textures and spintronics effects in AFs is determined by magnetic symmetries. Magnetic point groups (MPGs) [39] are obtained from the ordinary point groups by adding an additional antiunitary operation \mathcal{T} whose application reverses the direction of magnetic moments. Antiferromagnetic order can be in principle found in all 122 MPGs. The colorless MPGs, the so called category I [39] (see an example of a MPG I in Fig. 9.5), are those which do not contain the operation \mathcal{T} at all and there are 32 of them which is the same number as the number of nonmagnetic classical point groups. The grey magnetic point groups (category II [39]) contains \mathcal{T} as an element of the magnetic symmetry group. There is also 32 of them obtained from the category I by adding the \mathcal{T} operation. Antiferromagnetic order may appear in this category since the point groups can be obtained from the magnetic space groups by removing all nontrivial unit cell translations. Thus antiferromagnetic sublattices connected by a combination of nontrivial translation T and time reversal fall into this category and we show in Fig. 9.5 (MPG II) exemplar FeSe AF structure with the $\mathcal{T}T_{\frac{1}{2}}$ operation. Finally, the category III black and white MPGs contain \mathcal{T} only in a combination with another point group symmetry (mirror, or rotation). There are 58 of them and we show in Fig. 9.5 (MPG III) three antiferromagnetic examples (from left): A DSM AF crystal [20], a WSM AF crystal [40] and a WSM AF crystal with a nonzero AHE [41].

The form of spintronics linear response tensors is obtained by the application of magnetic symmetries. The Neumann principle states that *any physical observable of a system must exhibit symmetry of the point group of the system* [39]. A special role

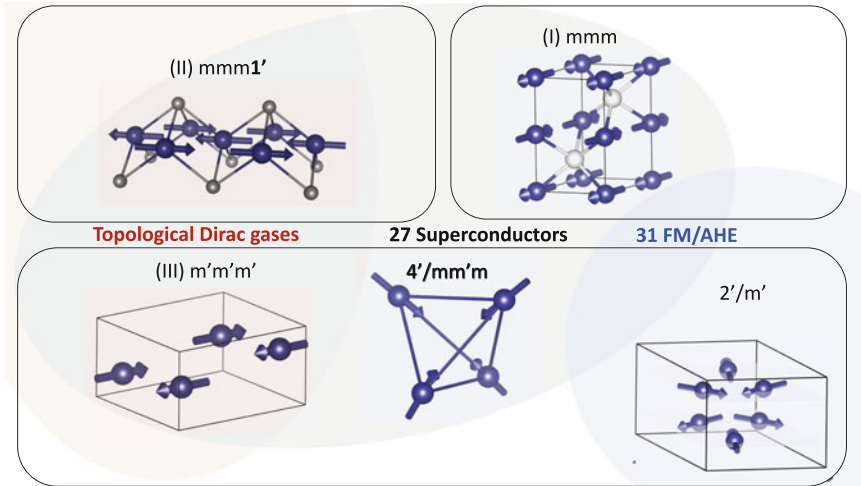


Fig. 9.5 Classical magnetic point groups (MPGs) and exemplar AFs. (I) White MPG example of a layered AF MnTe. (II) Grey MPG and zig-zag antiferromagnet FeSe. (III) Black and white MPG. Three different types (from left): \mathcal{PT} AF CuMnAs, centrosymmetric AF with 3Q magnetic order and prohibited anomalous Hall effect (AHE)—IrMn [42] or pyrochlore AF [40], and centrosymmetric AF with nonzero AHE, Mn₃Ge. The three colors represent overlap of the antiferromagnetic symmetries allowing for Dirac quasiparticles, superconductivity, and AHE

Table 9.1 Spatial inversion and time reversal transformations of tensors

Tensor rank	Even (scalar, matrix)				Odd (vector, 3rd rank)			
Time reversal \mathcal{T}	+		-		+		-	
Spatial inversion \mathcal{P}	+(polar)	-(axial)	+(polar)	-(axial)	-(polar)	+(axial)	-(polar)	+(axial)
\mathcal{PT}	+	-	-	+	-	+	+	-
Exemplar tensor	AMR		σ_{ij}^{AHE}			σ_{ij}^S		b

is played by \mathcal{T} and \mathcal{P} symmetries which define the basic transformation properties of tensors as shown in Table 9.1. For the conductivity σ_{ij} and spin Hall conductivity σ_{ij}^S analysis, it is sufficient to use the magnetic Laue group [43]. σ_{ij} and σ_{ij}^S do not change sign under spatial inversion and thus this symmetry can be omitted leading to only 32 magnetic Laue groups to investigate [44]. In contrast, the SOT torkance tensor τ_{ij} changes sign under spatial inversion and thus non-centrosymmetric lattice sites are required and all 122 MPGs have to be considered [45, 46]. This procedure leads to the conclusion that in the MPG from category I, and III there are in total 31 MPGs which allow for uncompensated moments, ferrimagnetism, ferromagnetism and also a nonzero AHE conductivity σ_{ij}^{AHE} . In Fig. 9.5 (MPG III)—right panel we show a corresponding example of the non-collinear AF structure of Mn₃Ge.

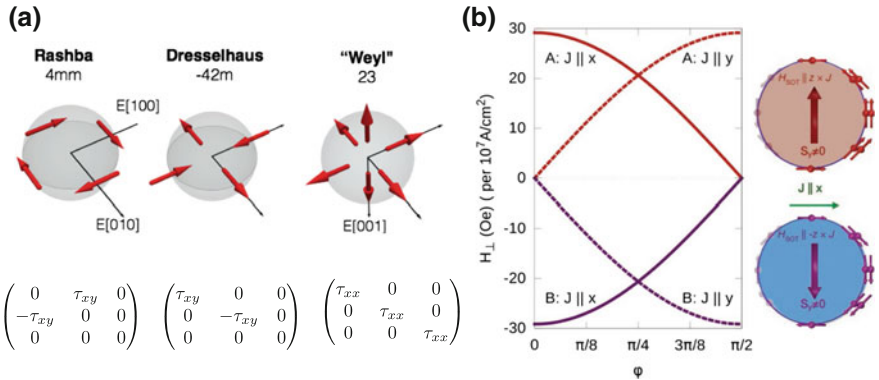


Fig. 9.6 The symmetry of spin-orbit fields. **a** All possible nonequilibrium spin polarization at noncentrosymmetric positions in crystals can be decomposed into combinations of Rashba, Dresselhaus, or Weyl spin texture. **b** Example of realistic calculation of the spin-orbit fields induced by electric current in tetragonal CuMnAs. The symmetry of the fields was confirmed in experiment [7]. Panel (b) adapted from [7].

The torkance tensor is defined by $\mathbf{t} = \tau \mathbf{E}$ [47], where \mathbf{t} is a torque generated by an applied electric field \mathbf{E} . The Onsager reciprocal for SOT is the inverse SOT obtained by interchanging the perturbation and response and both effects can be described by the torkance tensor [48]. SOT can be decomposed into part even in magnetization part \mathbf{t}_E and an odd part \mathbf{t}_O : $\mathbf{t} = \mathbf{t}_E + \mathbf{t}_O$. There are 21 non-centrosymmetric point groups which allow for a global or local current-induced nonequilibrium spin polarisation, and thus for SOT, in the lowest order that is independent of magnetization [49]. Spin-orbit fields generating the SOT can be decomposed into a combination of Rashba, Dresselhaus, and Weyl symmetry as shown in Fig. 9.6a. The AF variants of SOT can be found in AFs with non-centrosymmetric magnetic sublattices connected by crystalline symmetries as we illustrate on the example of the CuMnAs AF in Fig. 9.6b [7, 20, 25, 28]. Here the dominating SOT is driven by a staggered effective current-induced field of Rashba symmetry and the magnetic sublattices are connected via \mathcal{PT} symmetry [20]. Wimmer et al. [45] list forms of torkance tensors for all 122 MPGs.

There are also 21 MPGs which contain combined \mathcal{PT} symmetry and can host Dirac quasiparticles as we explain in Sect. 9.3. Other effects can be treated analogically. For instance, the magneto-optical Kerr effect [50] and anomalous Nernst effect [51, 52] were predicted and observed in non-collinear AFs as well. Also, this scheme can be applied to the layer-resolved quantities in heterostructures, e.g. the layer-resolved conductivity [43].

Finally, AF order can coexist with superconductivity as we illustrate in Fig. 9.5 by the grey shaded ellipse and examples are the iron-based superconductors [53]. More complicated magnetic structures such as spin spirals, spin density waves, and skyrmions may not allow to be described completely in the classical MPG framework. Gopalan and Litvin [54] have shown the possibility of new hidden symmetries, an

example being local roto-inversion. This operation does not rotate the whole crystal but just a finite subset while unchanging its MPG. The novel magnetic counterpart symmetries might be also relevant for the complete description of antiferromagnetic structures.

9.2.2 Electronic Structure and Band Touchings

Antiferromagnetic exchange interactions arise as a result of the complex interplay among the electrons. Different types of exchange interactions are possible, e.g., direct, indirect, superexchange, or itinerant exchange. The electronic structure of AFs is thus very often complicated and requires the inclusion of correlation and many particle effects. A realistic insight into the electronic structure and the existence of the antiferromagnetic phase can be determined by the density functional theory (DFT). In DFT, the interacting many-particle problem is mapped onto non-interacting electrons in an effective Kohn-Sham potential. Hohenberg and Kohn have shown that the ground-state properties of the effective electronic gas are uniquely determined by the electronic density. The reformulation of the problem as a variational one tremendously decreases the macroscopic $\sim 10^{23}$ degree of freedom to just 3—the spatial coordinates of the electronic density. In a magnetic system with a strong relativistic SOC, the magnetic relativistic “spin-only” (neglected diamagnetic effects [55]) Kohn-Sham-Dirac Hamiltonian reads [55]:

$$H_{\text{KSD}} = c\alpha \cdot \mathbf{p} + \beta mc^2 + V^{\text{eff}}(\mathbf{r}) - \mathbf{m}(\mathbf{r}) \cdot \mathbf{B}^{\text{eff}}(\mathbf{r}), \quad (9.4)$$

where $\mathbf{p} = -i\hbar\nabla$ is a momentum, V^{eff} and \mathbf{B}^{eff} is the spin independent part of the potential and the exchange-correlation magnetic field, α, β are 4×4 Dirac matrices, \mathbf{m} is spin density, and the electronic density is obtained from $n(\mathbf{r}) = \sum \Psi_i^\dagger(\mathbf{r})\Psi_i(\mathbf{r})$ [55]. The Kohn-Sham potential is not known exactly and has to be approximated, e.g., by the local density approximation (LDA) or generalized gradient approximation (GGA) [56]. The set of equations for the electronic wavefunctions and Kohn-Sham potential is solved iteratively. The procedure yields ground state wavefunctions and Hamiltonian from which other quantities, e.g., linear response coefficients can be calculated. For instance in Fig. 9.8b we show electronic bands of the orthorhombic AF CuMnAs as calculated within GGA [20].

AF systems are often correlated and disordered. Electronic correlations can be treated within DFT+Hubbard U, or DFT+dynamical mean field theory (DMFT). We show the generalized band structure of an AF BaFe₂As₂ calculated by DFT+DMFT in Fig. 9.7b. The effects of disorder can be captured by the supercell technique [56] or coherent potential approximation [56] as was demonstrated, for instance, for disordered Mn₂Au AF [28].

Symmetries impose constraints on the electronic spectrum, including the existence and protection of band touchings. The palette of quasiparticles in solids is more rich than the three types of high energy physics excitations: Weyl, Dirac and Majorana

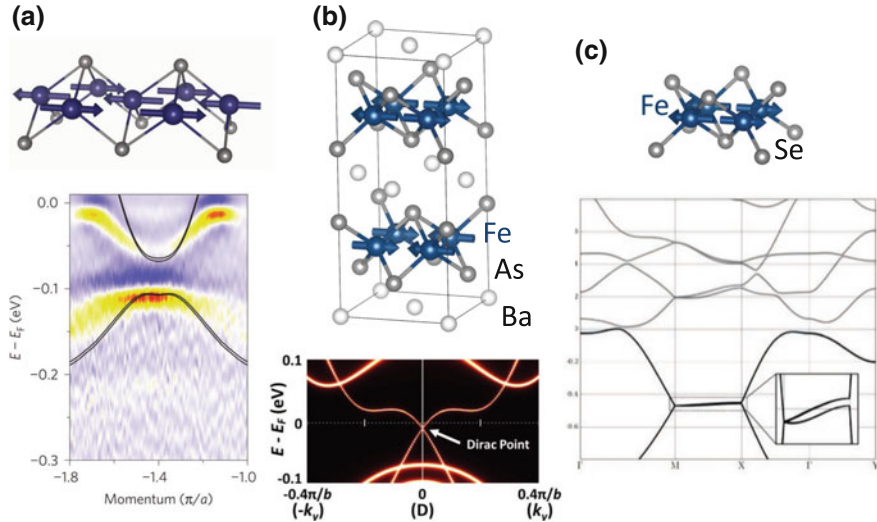


Fig. 9.7 Dirac quasiparticles in iron-based AF superconductors. **a** Realization of QSHE in a monolayer of FeSe AF. Angle resolved photoemission spectroscopy data overlayed with *ab initio* bands [53]. **b** Topological quasi-2D Dirac quasiparticles in BaFe₂As₂ AF. **c** Single Dirac cone at M point in FeSe monolayer AF with a stripe order. Panel (a) adapted from [53], panel (b) from [66], and panel (c) from [78]

fermions [35]. This is because of the more complex crystalline symmetries that are not present in the high energy vacuum [57, 58]. In the next Section we illustrate how the effective Hamiltonian arises for Dirac and Weyl quasiparticles in an AF.

9.3 Topological Antiferromagnetic Phases

Topological magnetic phases can be found in heterostructures with antiferromagnetic elements as well as in bulk AFs. In Table 9.2, we list promising topological AFs for spintronics together with the status of theoretical predictions and experimental observations of topological state or spintronics effects.

9.3.1 Low Dimensional Dirac Antiferromagnets and Superconductors

Introducing magnetism into TIs is known to modify the spin texture of the Dirac quasiparticles [73]. Magnetism can couple to TIs either by creating the magnetically doped TI (MTI) [73], or by proximity coupling between the TI and magnetic order in

Table 9.2 Topological antiferromagnets

AF	Phase	T_N	Space group	Representative effect
FeSe	QSHE [53]		P4/nmm	Superconductivity
GdPtBi	[26, 59, 60]/Weyl [61]	9 [62]	F43m	Large thermopower, AHE [62]
SrMnBi ₂	Dirac metal [63]	290 [63]	I4/mmm	Angular dependent magnetoresistance [64]
CaMnBi ₂	Dirac metal	300 [65]	P4/nmm	Dirac fermions coupled to magnetism [65]
EuMnBi ₂	Dirac metal	22 ^a [37]	I4/mmm	QHE controlled by magnetism [37]
BaFe ₂ As ₂	2D Dirac metal	[66]	I4/mmm	Superconductivity [66]
CuMnAs	<i>Dirac semimetal</i> [19, 20, 67]	~400 [67]	Pnma	<i>TopoMIT, TopoAMR</i> [20]
X ₂ Ir ₂ O ₇	Weyl semimetal [40, 68]		Fd $\bar{3}$ m	TopoMIT [69], <i>wealth of topo. phases</i> [40, 70]
Mn ₃ Sn	Weyl (semi)metal [71, 72]	430 [16]	P63/mmc	AHE controlled by magnetic field [16]

^aItalic font marks theoretical prediction. Normal font marks existing experimental signatures.

heterostructures [74]. AF order was shown to increase the critical temperature of the adjacent MTIs in the MTI/AF CrSb/MTI heterostructure [75]. Improved performance of the SOT in terms of larger spin Hall angles and lower critical currents was achieved in the TI/ferrimagnetic CoTb alloys with the AF coupled Co and Tb sublattices [76, 77].

The first TI AF was predicted in systems with combined $\mathcal{T}T_{1/2}$ symmetry [26]. GdPtBi AF was suggested as a possible candidate, as we show in Fig. 9.3b. GdPtBi was up to date not confirmed as a TI due to the low resolution of data obtained by the angle resolved photoemission spectroscopy (ARPES) [79]. However, signatures of the coexistence of a 2D TI (Fig. 9.4c), and a superconducting state in hole-doped and electron-doped antiferromagnetic monolayers of FeSe were demonstrated [53]. FeSe belongs to the metallic building block of the iron-based high- T_C superconductors. Remarkably, the combined effects of SOC, substrate strain, and electronic correlations can induce band inversion and QSHE edge states, as we show in Fig. 9.7a [53]. Creating a p-n junction across FeSe and attaching two ferromagnetic electrodes can generate Majorana zero modes at the interfaces [80]. Majorana states are considered for a possible use in quantum computing [81] and are addressed in Chap. 12 of this book.

One of the first systems explored for observing Dirac quasiparticles in condensed matter beyond graphene were the SrMnBi₂ type AFs. The electronic structure of these systems is governed by the quasi-2D square Bi planes. The Bi states create close to the Fermi level massive Dirac quasiparticles. High mobilities, and Fermi velocities, and pseudospin structure of wavefunctions are reminiscent of graphene properties. In contrast to graphene, however, the quasiparticles are highly anisotropic

with anisotropy factor of ~ 8 [64]. Several of these types of AFs were reported in recent years including SrMnBi_2 [64], or CaMnBi_2 [65]. The systems belong to the 112-type pnictides where the antiferromagnetism and Dirac quasiparticles might coexist also with superconductivity. Related systems, e.g. YbMnBi_2 , were inconclusively [38] reported to be either WSM [82, 83] or DSM [84, 85]. Most likely the collinear AF order cants in, e.g., the $(\text{Sr}, \text{Yb})\text{MnBi}_2$ alloy [86] where the double band degeneracy breaks and Weyl points might emerge. Despite many recent studies, more accurate and detailed measurements are needed to reveal the detailed nature of Dirac quasiparticles in these systems. Finally, in the sister compound, EuMnBi_2 AF, the half-integer QHE was reported controllable by the strength of an external magnetic field, as we showed in Fig. 9.4b. EuMnBi_2 contains at very low temperatures two antiferromagnetic sublattices. The presence of QHE was linked to the confinement of the massive Dirac quasiparticles by the spin-flop at the Eu AF sites [37].

Recently the high temperature superconducting 122-type pnictide Ba - and SrFe_2As_2 AFs showed signatures of topological Dirac quasiparticles in the infrared spectra in high magnetic fields. In Fig. 9.7b we show the state-of-the-art DFT+DMFT calculation of quasi-2D Dirac cones close to the Fermi level which are consistent with the observed Landau level spectra and density of states [66]. When the Fermi states are dominated by Dirac quasiparticles, the topological semimetal is achieved. Electron filling enforced semimetals with a single Dirac cone were predicted theoretically in 2D model AFs [78]. In Fig. 9.7c we show the single Dirac cone at the M point in the BZ of the monolayer of the FeSe AF with a stripe order. The quasi-low dimensional systems and heterostructures, however, suffer from fragile magnetism and low critical temperatures. In two following subsection, we describe possible room temperature 3D Dirac and Weyl semimetal AFs.

9.3.2 3D Dirac Semimetal Antiferromagnets

Dirac quasiparticles are allowed in doubly-degenerate bands [33] realized in systems invariant under \mathcal{PT} symmetry.

The low energy Hamiltonian might maintain an effective Dirac form [35, 87, 88], corresponding to the Dirac Hamiltonian (9.4) [38, 88, 89]:

$$\mathcal{H}_D(\mathbf{k}) = \begin{pmatrix} \hbar v_F \mathbf{k} \cdot \boldsymbol{\sigma} & m \\ m & -\hbar v_F \mathbf{k} \cdot \boldsymbol{\sigma} \end{pmatrix}. \quad (9.5)$$

Here v_F is the Fermi velocity, $\mathbf{k} = \mathbf{q} - \mathbf{q}_0$ is the crystal momentum measured from the Dirac point at \mathbf{q}_0 , m is the mass (in units of energy), and $\boldsymbol{\sigma}$ is the vector of Pauli matrices. The energy dispersion gives massive Dirac cones,

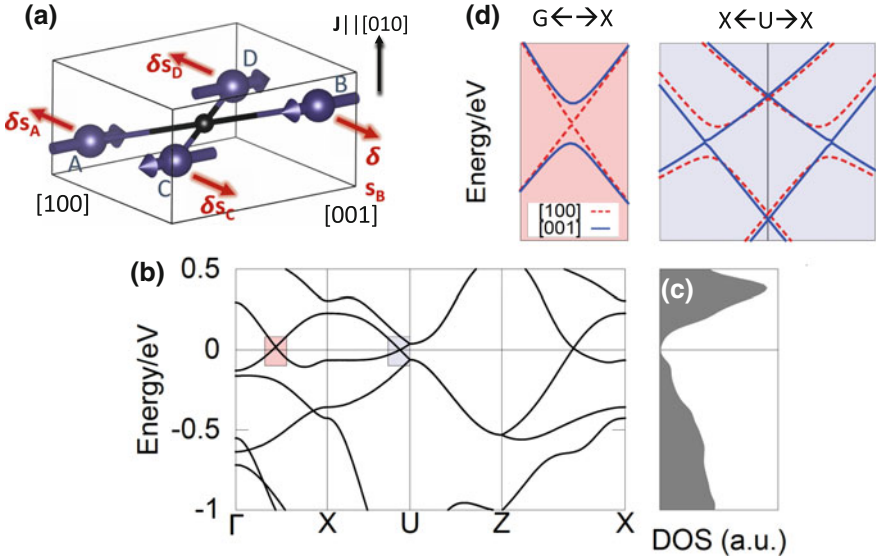


Fig. 9.8 Antiferromagnetic Dirac semimetals, spin-orbit torques, and metal-insulator transition. **a** Unit cell of orthorhombic CuMnAs AF with marked \mathcal{PT} symmetry center (black sphere) and nonequilibrium spin polarizations δs for current applied along the [010]. **b** Band structure of the CuMnAs AF calculated *ab initio* without SOC. **c** The density of states. **d** Detail of Dirac quasiparticles in CuMnAs as calculated *ab initio* with SOC switched on. Panel (a) adapted from [90], and panels (b–d) adapted from [20]

$$E(\mathbf{k}) = \pm \hbar v_F \sqrt{k_x^2 + k_y^2 + k_z^2 + \left(\frac{m}{\hbar v_F}\right)^2}. \quad (9.6)$$

The mass term can be removed by the presence of an additional crystalline symmetry, and in this case $\mathcal{H}_D(\mathbf{k})$ describes the four-fold degenerate band touching [88, 89] of a 3D DSM as we show in Fig. 9.8b on the band dispersion of an antiferromagnetic DSM orthorhombic CuMnAs with a high Néel temperature of ~ 400 K [67].

The 3D DSM state cannot occur in ferromagnets because \mathcal{T} -symmetry breaking prevents double band degeneracy. However, a topological crystalline 3D DSM was predicted in an AF, namely in the orthorhombic phase of CuMnAs [19, 20]. The unit cell of the orthorhombic CuMnAs contains four Mn sublattices that are connected in pairs by the \mathcal{PT} symmetry [19, 20] as we show in Fig. 9.8a. Although individually the \mathcal{P} and \mathcal{T} symmetries are broken, the preserved combined \mathcal{PT} symmetry ensures the double band degeneracy over the whole BZ. In the calculation with a switched-off SOC (see Fig. 9.8b), we observe three Dirac points at the Fermi level along the Γ -X, X-U, and Z-X lines which are part of the nodal line protected by the \mathcal{PT} symmetry. The Dirac quasiparticles are 3D as can be seen from the

quadratically vanishing DOS at the Fermi level/Dirac point as we show in Fig. 9.8c. In the presence of SOC and for the Néel order along the [001] axis, the nodal lines become gapped except for the two Dirac points along the UXU line, as we show in Fig. 9.8d. The Dirac points are protected by the non-symmorphic screw axis symmetry $\mathcal{S}_z = \{2_z | (\frac{1}{2}, 0, \frac{1}{2})\}$ [19, 20] and are connected via nontrivial surface states [19]. The topological invariants and surface states can be linked to the crystalline symmetry protecting the degeneracy and even in the non-magnetic DSM, the surface states are in general less stable than in WSM and strongly depend on the crystalline orientation at the surface termination [87, 91]. The easy axis in orthorhombic CuMnAs tends to be along [100] according to *ab initio* calculation [20], however, we will discuss in the next section the possibility of reorienting the Néel vector.

The orthorhombic CuMnAs AF is an attractive *hydrogen atom* for magnetic DSMs induced by band inversion since only a single pair of Dirac points appears near the Fermi level of the *ab initio* band structure. However, presumably, the correlation and disorder effects prevented the observation of Dirac quasiparticles in non-stoichiometric CuMnAs to date [92, 93].

9.3.3 Weyl Semimetal Antiferromagnets

In solids, quite often at least one of the \mathcal{P} or \mathcal{T} symmetries is broken and thus the double band degeneracy is lifted. When the two non-degenerate bands are touching close to the Fermi level a 3D WSM can be formed (Chapter 8 is concerned with WSM in greater detail).

WSM is described by the generalized two-band Weyl Hamiltonian [88, 89]:

$$\mathcal{H}_W(\mathbf{k}) = \varepsilon_0 \pm \hbar v_F (\mathbf{q} - \mathbf{q}_0) \cdot \boldsymbol{\sigma}, \quad (9.7)$$

where the first term corresponds to the tilting of the Weyl cone and $\mathbf{k} = \mathbf{q} - \mathbf{q}_0$. Weyl points always come in pairs with opposite topological charges. Dimensionality is important here. Because the Weyl points are 3D objects in the BZ, the effective Hamiltonian uses all three Pauli matrices. Thus any small perturbation expressed without loss of generality as a linear combination of these three Pauli matrices just shifts but not gaps the Weyl point. We illustrate this on the dispersion around the Weyl points for a perturbation of a form $m\sigma_z$,

$$E(\mathbf{k}) = \varepsilon_0 \pm \hbar v_F \sqrt{k_x^2 + k_y^2 + \left(k_z + \frac{m}{\hbar v_F}\right)^2}. \quad (9.8)$$

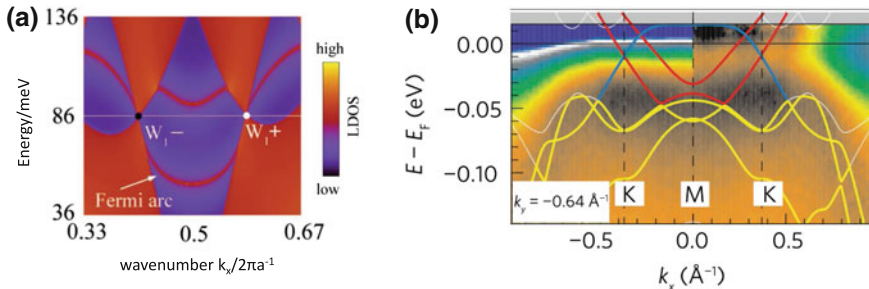


Fig. 9.9 Antiferromagnetic Weyl semimetal and surface Fermi arcs. **a** *Ab initio* calculation of Fermi arcs in Mn_3Sn AF. **b** ARPES of Weyl points in Mn_3Sn close to the Fermi level overlayed with *ab initio* band structure. Panel (a) adapted from [41] and panel (b) from [72]

WSM states can be found in nonmagnetic, ferromagnetic [94, 95] or antiferromagnetic solids, where the \mathcal{PT} symmetry is broken. A WSM state was observed in non-centrosymmetric non-magnetic mono-pnictides of the TaAs type [96–98]. TaAs is well described by the DFT single quasiparticle picture. Despite numerous predictions, the true magnetic WSM remained for a long time experimentally elusive [72]. The reason is that the magnetic system is very often also strongly correlated, disordered, and the symmetry breaking is provided by the complex collective phenomenon—magnetism. Antiferromagnetic candidates include pyrochlore irridates [40] like the $\text{Eu}_2\text{Ir}_2\text{O}_7$ [68], or YbMnBi_2 AF which were suggested to be either the WSM [82, 83] or the DSM [84, 85].

Weyl fermions were proposed also in non-collinear AFs Mn_3Ge and Mn_3Sn [99, 100] (see Fig. 9.2a) [71]. These AFs are potentially appealing for spintronics due to the measured large AHE, established magnetic structure, and Néel temperatures reaching 365–420 K. The structure of Mn_3Ge and Mn_3Sn crystals is built from stacked kagome planes along the [001] axis, as we show in the right panel in Fig. 9.5 (MPG III). These AFs have a relatively weak magnetic anisotropy, reaching 0.1 meV per formula unit for Mn_3Sn [29, 30] due to the vanishing second and fourth order MAE of the inverted triangular AF structure on the kagome lattice [101, 102]. The magnetic order can be thus reoriented by low external magnetic fields. Kuroda et al. [72] reports reorientation fields of ~ 200 Gauss. The net magnetic moment reaches $0.005 \mu\text{B}$ per unit cell [102]. In spite of the weak anisotropy of the inverted chiral structure, the materials show relatively high stability against thermal fluctuations. Also, a possibility to influence the in-plane chiral AF magnetic structure by a spin-filtering effect was reported [103].

Mn_3Ge and Mn_3Sn were predicted to exhibit several different types of Weyl points in their metallic bandstructure coexisting with trivial bands close to the Fermi level [41]. The Weyl points found by tracking the Berry curvature in the BZ are tilted, thus of the so-called type-II [104] PRL 115, 265304 (2015). The Fermi arc surface states—the hallmark of a WSM—were predicted by first-principles calculations of the local density of states (LDOS) as we show in Fig. 9.9a [71]. The tilting of the Weyl

points does not influence the Berry curvature, however, the electron and hole pockets due to the tilting influence the transport effects, particularly they can renormalize the almost perfectly quantized AHE [105]. Signatures of these band crossings were reported recently in an ARPES study of Mn_3Sn AF [72], as we show in Fig. 9.9b. Weyl band crossings were found along MK or $M'K$ lines depending on the orientation of the triangular magnetic texture stabilized by an external magnetic field [72]. A comparison between DFT and ARPES points towards strong electron correlations in the Mn 3d bands as seen in the strong renormalization of the bands in ARPES in Fig. 9.9b. In the next Section, we describe in detail the AHE in Mn_3Ge and Mn_3Sn and its relation to Weyl points.

9.4 Topological Antiferromagnetic Spintronics Effects

Topological variants of common magnetotransport effects and their novel cousins can potentially offer large signal to noise ratios important for reading signals in spintronics nanodevices. Again, we will demonstrate that very often the unique anti-ferromagnetic symmetries are of vital importance for certain topological spintronics effects to occur, such as topological AMR or AHE.

9.4.1 Large Magnetoresistance and Chiral Anomaly

Application of a magnetic field perpendicular to the current flow results in a positive magnetoresistance, defined as

$$\text{MR} = \frac{\rho(B) - \rho(0)}{\rho(0)}, \quad (9.9)$$

where $\rho(H)$ is the resistivity in a magnetic field B , as commonly observed in metals, semimetals, and semiconductors. However, in a topological semimetal with Weyl quasiparticles, a negative magnetoresistance might occur, attributed to a chiral anomaly. In the original proposal for a condensed matter realization of the chiral anomaly, Nielsen and Ninomiya [106] considered a chiral Weyl linear dispersion of the zero-th Landau levels. Application of an electric field parallel to the magnetic field generates an imbalance between the zero Landau levels of opposite chiralities. This axial current leads to a positive magnetoconductivity [38]:

$$\sigma(B) = \sigma + \frac{e^4 B^2}{4\pi^4 g(E_F)}, \quad (9.10)$$

where $g(E_F)$ is the density of states at the Fermi level. Remarkably, this expression can be derived both in the quantum limit or in the semi-classical framework without

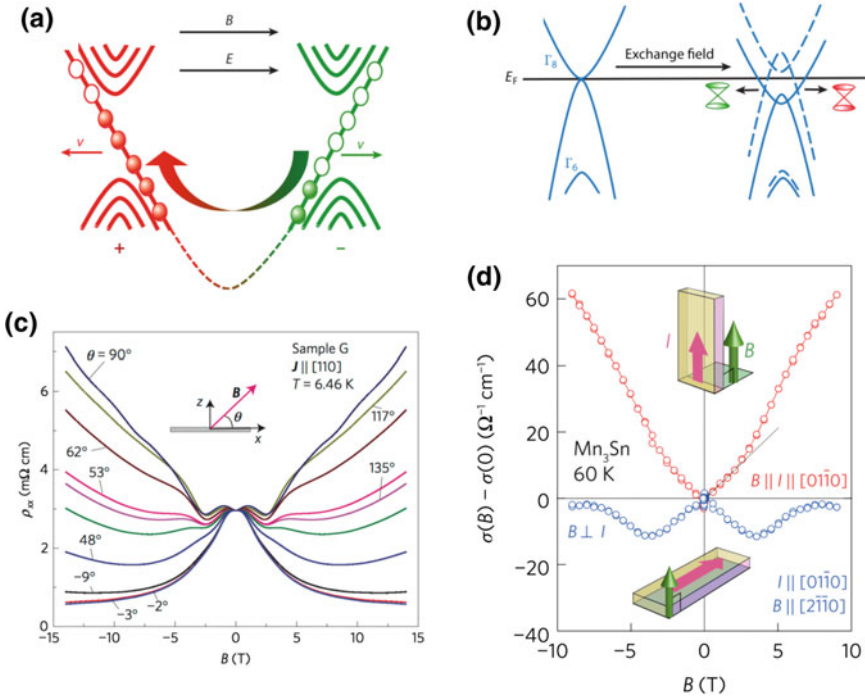


Fig. 9.10 Possible observation of a chiral anomaly in magnetically induced Weyl semimetal and antiferromagnetic Weyl semimetal. **a** Cartoon of the chiral anomaly principle. **b** A magnetically induced Weyl semimetal in GdPtBi. **c** Observed negative magnetoresistance in GdPtBi. **d** Observed positive magnetoconductance in the Mn_3Sn AF. Panels (a, b) adapted from [107], panel (c) from [61], and panel (d) from [72]

introducing Landau levels [38]. We illustrate the chiral anomaly with Weyl fermions in Fig. 9.10a.

The negative magnetoresistance became accepted as the signature of the presence of linearly dispersing topological quasiparticles, and was possibly observed for instance in GdPtBi [61], which is a quadratic gapless semiconductor. In the magnetic field, the fourfold degenerate band-touching splits and pairs of Weyl points are created as we illustrate in schematics in Fig. 9.10b. Rotating the external magnetic field from out-of-plane to in-plane (see Fig. 9.10c) changes the magnetoresistance from positive to negative. Positive non-saturating magnetoconductance was observed recently also in the Mn_3Sn AF [72]. Alternative sources of positive magnetoconductance such as current jetting and weak localization were carefully ruled out in this study. The positive magnetoconductance in Mn_3Sn is linear in a magnetic field which was attributed to the type-II Weyl fermions [72] in contrast to the quadratic magnetoresistance observed in type-I (non-tilted) Weyl semimetals [108]. The detailed role of topological quasiparticles in the negative and large non-saturating magnetoresistance remains to be clarified [104, 109–111]. Here the first step was made by

ab initio [112] and transport studies [113] of Weyl points in strong magnetic fields signaling the importance of linear dispersion for the observation of negative magnetoresistance. In strong magnetic fields, the negative magnetoresistance disappears which was attributed to the gapping of Weyl points by the Zeeman splitting.

9.4.2 *Topological Phase Transitions and Anisotropic Magnetoresistance in Antiferromagnetic Systems*

Topological phase transitions were experimentally demonstrated in heterostructures with TIs and AFs [75, 114] or systems with an artificially engineered AF coupling [115, 146]. AF CrSb/TI (Bi,Sb)₂Te₃/AF CrSb heterostructure shows spikes in the magnetoresistance which were attributed to a topological phase transition of Dirac quasiparticles at the interfaces [114]. A MTI/TI/MTI heterostructure was reported for a presumed topological phase transition between QAHE state and axion insulator (quantized topological magnetoelectric effect) by switching the magnetic order in the MTI from ferromagnetic to antiferromagnetic by an external magnetic field or electric gating [115, 116]. Albeit at mK temperatures, the phase transition yields very large magnetoresistance or electroresistance changes corresponding to switching on and off the quantized conductivity plateau $h/e^2 \sim 25, 8 \text{ k}\Omega$ [115, 116]. The QAHE effect was to date observed only at mK temperatures [36]. Searching for novel mechanism and material candidates with a more robust, controllable and room temperature QAHE states represents an important direction of future research in topological spintronics. Here for instance, QAHE induced by electrical gating was predicted in Sr₂FeOsO₆ AF [117].

The prediction of tuning the Néel order parameter by the Néel SOT or gating in antiferromagnetic DSMs opens the possibility of using the topological metal-insulator transition (TopoMIT) in a bulk AF [20, 90]. The origin of these effects is in the sensitivity of Dirac crossing hybridizations on the orientation of the Néel vector in the orthorhombic magnetic crystalline symmetry, as shown in Fig. 9.8d. In the presence of SOC, only for the Néel vector along the [001] axis, protected Dirac fermions emerge. All the other Néel vector orientations lead to a gapped spectrum at the Fermi level [20]. The transport counterpart of the topoMIT was predicted to be the topological anisotropic magnetoresistance (topoAMR) [20]. The topoAMR can be extremely large and is understood as a limiting case of the crystalline AMR. In Fig. 9.11a we show the tetragonal lattice of a minimal model of the DSM AF [20]. The corresponding Hamiltonian reads $H_{\mathbf{k}} = -2t\tau_x \cos \frac{k_x}{2} \cos \frac{k_y}{2} - t'(\cos k_x + \cos k_y) + \lambda\tau_z(\sigma_y \sin k_x - \sigma_x \sin k_y) + \tau_z J_n \boldsymbol{\sigma} \cdot \mathbf{n}$, where first two terms are first and second neighbor hoppings, third term is a staggered SOC, last term is AF s-d type exchange and τ , and σ are Pauli matrices corresponding to orbital and spin-degree of freedom, respectively. The longitudinal conductivity is calculated from the Boltzmann formula in the limit of a small spectral broadening Γ :

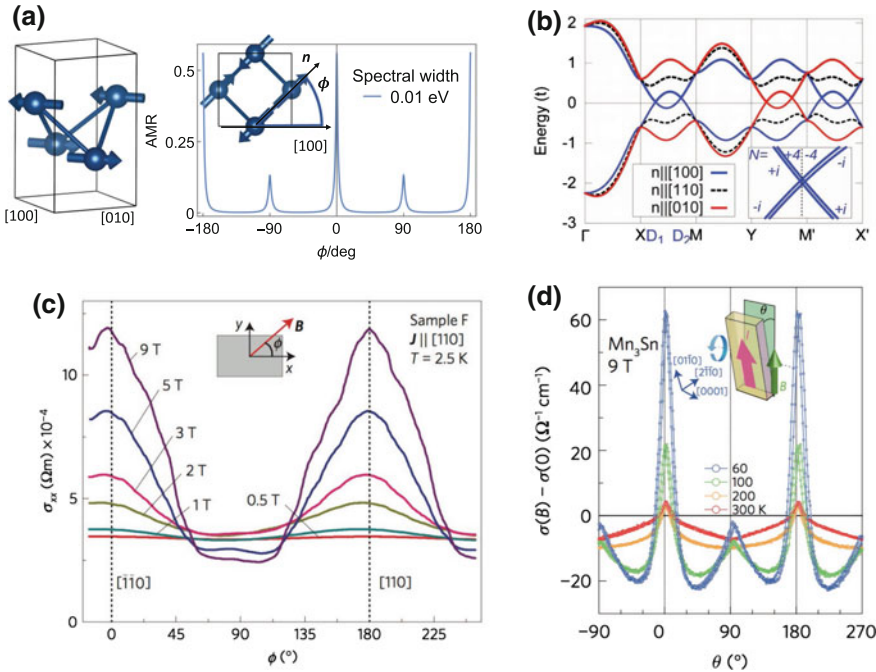


Fig. 9.11 Extreme anisotropies in magnetoresistance effects in topological semimetals. **a** Large topological anisotropic magnetoresistance in a tetragonal AF Dirac semimetal model. **b** Band structure of the model Dirac AF. **c** Angular dependence of magnetoresistance in a magnetically induced Weyl semimetal GdPtBi. **d** Angular dependence of magnetoresistance in AF Weyl semimetal Mn_3Sn . Panel (b) adapted from [20], panel (c) from [61], and panel (d) from [72]

$$\sigma_{xx}(\phi) = \frac{e^2}{\hbar 4\Gamma L^2} \sum_{\mathbf{k}n} \frac{\partial E_{\mathbf{k}n}}{\partial k_x} \frac{\partial E_{\mathbf{k}n}}{\partial k_x} \delta(E - E_F), \quad (9.11)$$

where L is the size of the system, and ϕ is the angle between [100] axis and magnetization. The AMR is defined as:

$$\text{AMR} = -\frac{\sigma_{xx}(\phi) - \sigma}{\sigma}, \quad (9.12)$$

where σ is the average conductivity within the plane. In Fig. 9.11a we show the angular dependence of the AMR in this model [118]. In Fig. 9.11b we show the band structure of the model. For the Néel vector orientations [100] and [010], preserving the glide mirror planes of the system [20], the Dirac points are gapless and conduct. Once the Néel vector is rotated away from these high symmetry axes, the crystalline symmetries are broken, Dirac bands hybridize and gap opens. Consequently the conductivity decreases exponentially. The sharp peaks in the angular dependence are very different when comparing to the standard harmonic AMR dependence in ferromagnetic alloys. Also the origin is very distinct. The topoAMR originates in Fermi

surface topology changes instead of scattering effects responsible for the standard AMR. The difference in conductivity between the [100] and [010] direction originates in the anisotropy of the Dirac cones. The orthorhombic CuMnAs was predicted as the realistic material candidate based on *ab initio* calculations [20]. The interplay of the Dirac points and topoAMR with disorder, interaction effects, and nonequilibrium currents needs to be carefully addressed to potentially make the effect relevant for real spintronics device applications. Foreseen applications include topological transistors or memories [90]. Since the control of the Néel vector can be achieved either by the Néel SOT due to the applied current or due to the tuning of the MAE by electric gating, the effect is presumably more favorable for spintronics than the MIT manipulated by external magnetic field in pyrochlores [69] or AF topological semimetal candidate NdSb [119]. Although this topoAMR due to the MIT was not experimentally discovered yet, analogical effects controlled by external magnetic field were observed in WSMs.

In GdPtBi, Weyl point positions are sensitive to the orientation of the applied magnetic field [61]. This leads in turn to a pronounced angular dependence of the magnetoconductance, as we show in Fig. 9.11c. The changes in magnetoconductance are attributed to the varying angle between the crystalline axis and the Zeeman field what is in contrast to the behavior predicted for the AF DSM CuMnAs. The spikes in magnetoconductance have been measured also in the correlated WSM AF Mn₃Sn as we illustrate in Fig. 9.11d [72]. Here the magnetic order is controlled by the relatively weak external magnetic field. The reorientation of the moments changes the local symmetry and possibly redistributes the Weyl points close to the Fermi level [72]. Importantly, the spikes in magnetoconductance persist to temperatures ~ 100 K, despite the WSM is highly correlated and disordered. These temperatures are much higher temperatures than the reported QAHE critical temperatures of ~ 10 mK.

9.4.3 Anomalous Hall Effect in Noncollinear Antiferromagnets

AHE (discussed also in Chap. 6) refers to the transversal electric current generation in the magnet subjected to an applied longitudinal electric field. The anomalous Hall conductivity is for the magnetization along z axis the antisymmetric part of the conductivity tensor:

$$\sigma_{\text{AHE}} = \frac{\sigma_{xy} - \sigma_{yx}}{2}. \quad (9.13)$$

For a long time, the AHE was considered to scale with the magnetization: $\rho_H = R_0 H_z + R_S M_z$, where the first part corresponds to the ordinary Hall effect due to the external magnetic field H_z , and the second term is the AHE due to the \mathcal{T} symmetry breaking due to the magnetization M_z , and R_0 , and R_S are ordinary and (spontaneous) anomalous Hall coefficients, respectively. AHE was traditionally attributed to the simultaneous presence of \mathcal{T} symmetry breaking by the ferromagnetism and SOC. Thus, naively, one would expect that the AHE must vanish in AFs because of

the compensation moments of the opposite sublattices. Indeed, this picture is valid in simple AFs where the combination of \mathcal{T} symmetry with another crystalline symmetry forces the AHE to vanish. Typical examples include collinear AFs with \mathcal{PT} or $\mathcal{T}T_{1/2}$ symmetries which we discussed in the context of the Dirac quasiparticles and TIs. Remarkably, the AHE was observed in systems with a negligible net magnetization and without the necessity for SOC. Interestingly, already Haldane pointed out in 1988 [120] the possibility of the quantized AHE in honeycomb lattice with complex hoppings with a staggered potential and Shindou et al. [121] later demonstrated the nonzero AHE in a model calculation in AHE induced by distorting the FCC lattice with 3Q AF order. More recently Hua Chen et al. [122] and Kübler and Felser [99] predicted a large AHE in noncollinear AFs with a negligible net moment. Presumably, the large MAE in Mn_3Ir AF makes it impossible to orient the magnetic domains and thus prevents the experimental detection of the AHE in this compound.

However, Mn_3Ge and Mn_3Sn have a much smaller MAE. AHE from the AF texture, ρ_H^{AF} , was indeed observed in these compounds by carefully subtracting the Hall effect originating from the external field, $R_0 H_z$, and from the small ferromagnetic moment, $R_S M$ [16, 123]:

$$\rho_H = R_0 H_z + R_S M + \rho_H^{AF}, \quad (9.14)$$

where M is the net magnetization. The experimental value of the AHE in Mn_3Ge is $\sigma_{xz} \approx 380 \Omega^{-1} \text{cm}^{-1}$ [124] while the *ab initio* calculation from Berry curvature gives $\sigma_{xz} \approx 330 \Omega^{-1} \text{cm}^{-1}$ [71]. The noncollinear AF order on the kagome lattice breaks the time-reversal symmetry as we show in Fig. 9.12a, b. For the AF structure in Fig. 9.12a [102, 124] there is an effective time reversal symmetry $\mathcal{T}\mathcal{M}_x$ (\mathcal{M}_x is the mirror (100) plane symmetry) which gives $\sigma_{yz} = 0$, and the emergent magnetic field lies along $\mathbf{B} \parallel [010]$, and only $\sigma_{xz} \neq 0$. In contrast, for the chiral texture in Fig. 9.12b [102, 124], the effective $\mathcal{T}\mathcal{G}_y$ symmetry (\mathcal{G}_y is the glide mirror plane $\{\mathcal{M}_y | (0, 0, \frac{1}{2})\}$) implies $\sigma_{xz} = 0$, the emergent magnetic field points along $\mathbf{B} \parallel [100]$, and only $\sigma_{zy} \neq 0$. Furthermore, independent on the in-plane orientation, there is an effective time reversal symmetry $\mathcal{T}\mathcal{M}_z$ (\mathcal{M}_z is the mirror (001) plane symmetry) making the component $\sigma_{xy} = 0$. The symmetry analysis is consistent with the experimental data measured on Mn_3Sn and Mn_3Ge and presented in Figs. 9.2b and 9.12c. In conclusion, the spin-orbit entangled bands generate a large fictitious magnetic field in the crystal momentum space parallel to the direction of the field stabilizing the triangular order, and the AHE takes place in the plane perpendicular to the field.

The emergent magnetic field was estimated to be very large, of the order of ~ 200 T in Mn_3Ge [124]. Although the Mn_3Ge and Mn_3Sn were predicted to host Weyl points close to the Fermi level, the *ab initio* calculation of the AHE shows that the largest contributions come from BZ regions not related to any identified Weyl points, but rather from spin-orbit entangled avoided crossings [100]. A recent study by Felser and Kübler [126], however, demonstrates the possibility of propagation of Fermi sea Weyl points in Mn_3Ge and Mn_3Sn to the Fermi surface-quasiparticle transport [127, 128]. Finally, AHE was recently observed also in Mn_3Pt (isostructural to $IrMn_3$) and it was switched on and off by the piezoelectric effect transferred from the ferroelectric $BaTiO_3$ substrate [143].

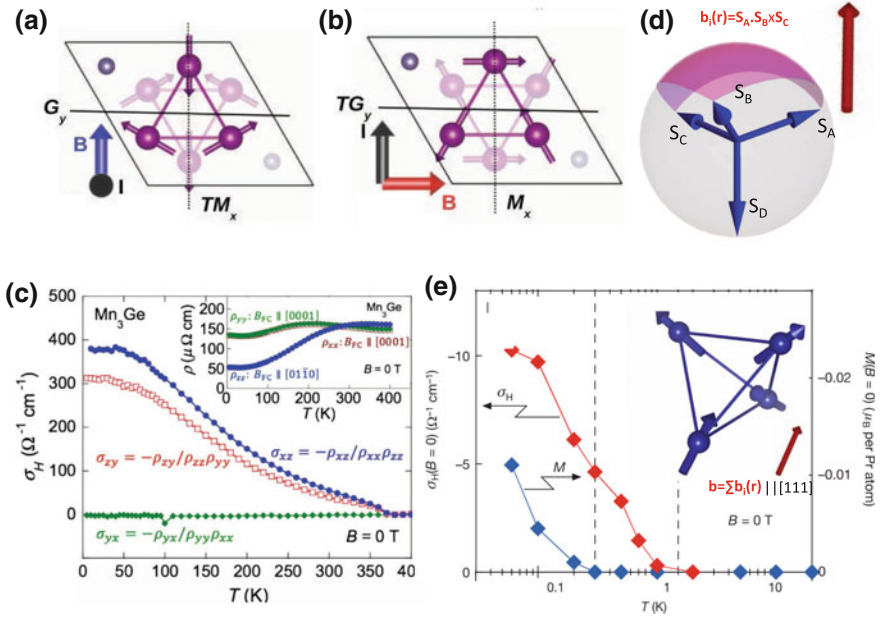


Fig. 9.12 Anomalous and topological Hall effects in chiral AFs. Two chiral inverted AF structure stabilized by an external magnetic field along **a** [010], and **b** [100] direction. **c** Measured temperature dependence of AHE in Mn_3Ge originating from AF texture. **d** Spin chirality and non-coplanar magnetic moments of an antiferromagnetic candidate for the quantum topological Hall effect. **e** Topological Hall effect observed in the spin liquid state on a pyrochlore lattice—fragment shown in the inset. Panels (a, b) adapted from [88], panel (c) from [124], and panel (e) from [125]

9.4.4 Topological Hall Effects and Antiferromagnetic Skyrmions

In the topological Hall effect, the role of SOC is overtaken by the spin chirality. We show in Fig. 9.12d the spin chirality generating a nonzero Berry curvature. Spin chirality is nonzero in non-coplanar spins, in contrast, it vanishes in coplanar non-collinear antiferromagnetic structures of, e.g., Mn_3Ge and Mn_3Sn . The spin chirality generates a fictitious magnetic field (see red arrow in Fig. 9.12d), $\hat{\mathbf{m}} \cdot (\partial_x \hat{\mathbf{m}} \times \partial_y \hat{\mathbf{m}})$. This field acting on the Bloch electrons generates a Hall response. The topological Hall effect and the AHE can be possible to experimentally disentangled by analyzing the disorder dependence [129]. The topological Hall effect was initially reported in antiferromagnetic pyrochlore iridates (see Fig. 9.12e) [125] and later in MnSi chiral antiferromagnetic alloys [130, 131]. We note that the effect does not imply in this case a correspondence to a topological invariant, in sharp contrast to the topological Hall effect in skyrmions. However, in the quantum topological Hall effect proposed for the non-coplanar AF $\text{K}_{0.5}\text{RhO}_2$ [132], with its magnetic sublattices shown schematically in Fig. 9.12d, the topological charge occurs in the momentum space as in the QAHE.

The topological Hall effect from a skyrmion spin texture is associated with a topological winding number of the skyrmion [116]. It is important to distinguish it from the skyrmion Hall effect which refers to the deflection of skyrmion center due to the Magnus force. The Magnus force is according to micromagnetic calculations not present in AF skyrmions, which implies that AF skyrmions might move in straight lines [133]. This is favorable when considering skyrmions for storing information in racetracks. Finally, the topological Hall effect in AF skyrmions with a compensating sublattices vanishes, while the topological spin Hall effect can be still sizable and can be used to detect an AF skyrmion [134, 135]. Chapters 1, 4, and 5 of this book are devoted to skyrmions.

9.5 Summary

Antiferromagnetic spintronics has been recently established as a new branch of magnetism [4, 88, 136, 137]. In parallel, last few years have seen progress in coupling magnetism with topological states of matter, giving rise to a new spin-off: topological spintronics [138]. We have shown that AF order might play an important role in topological spintronics due to the unique AF symmetries [90]. While signatures of correlated AF WSM were already observed [72], other topological AF phases remain to be discovered. The large signal to noise ratio was reported in magnetoresistance signals of topological semimetals [20, 72]. Further theoretical and experimental progress will possibly lead to topological spintronics effects improving the reading and writing signals in AFs [90]. The progress in writing efficiency due to the nontrivial topologies is in its infancy, although an increase of the spin Hall angle in TI/MTI [139, 140] or TI/ferrimagnetic systems [76, 77] was already reported and novel mechanisms for dissipationless SOT were suggested [141]. Here we focused on the state-of-the-art effects which were predicted, and some of them already experimentally confirmed, in antiferromagnetic systems. The unique AF symmetries and the abundance of AF allow for other research directions to emerge such as topological superconductivity in AFs and spintronics based on antiferromagnetic skyrmions [90].

Acknowledgements We acknowledge support from the Ministry of Education of the Czech Republic Grants LM2015087 and LNSM-LNSpin, the Grant Agency of the Czech Republic Grant No. 14-37427, and the EU FET Open RIA Grant No. 766566.

References

1. M.Z. Hasan, C. Kane, Rev. Mod. Phys. **82**(4), 3045 (2010). <https://doi.org/10.1103/RevModPhys.82.3045>, <http://link.aps.org/doi/10.1103/RevModPhys.82.3045>
2. F.D.M. Haldane, Rev. Mod. Phys. **89**(4), 040502 (2017). <https://doi.org/10.1103/RevModPhys.89.040502>, <https://link.aps.org/doi/10.1103/RevModPhys.89.040502>

3. T.H. Hansson, M. Hermanns, S.H. Simon, S.F. Viefers, Rev. Mod. Phys. **89**(June), 025005 (2017). <https://doi.org/10.1103/RevModPhys.89.025005>, arXiv:1601.01697, <http://dx.doi.org/10.1103/RevModPhys.89.025005>
4. T. Jungwirth, X. Marti, P. Wadley, J. Wunderlich, Nat. Nanotechnol. **11**(3), 231 (2016). <https://doi.org/10.1038/nnano.2016.18>, <http://dx.doi.org/10.1038/nnano.2016.18>
5. C. Chappert, A. Fert, F.N. Van Dau, Nat. Mater. **6**(11), 813 (2007). <https://doi.org/10.1038/nmat2024>, <http://www.ncbi.nlm.nih.gov/pubmed/17972936>
6. A.D. Kent, D.C. Worledge, Nat. Nanotechnol. **10**(3), 187 (2015). <https://doi.org/10.1038/nnano.2015.24>, <http://www.nature.com/articles/nnano.2015.24%5Cnpapers3://publication/doi/10.1038/nnano.2015.24>
7. P. Wadley, B. Howells, J. Elezny, C. Andrews, V. Hills, R.P. Campion, V. Novak, K. Olejnik, F. Maccherozzi, S.S. Dhesi, S.Y. Martin, T. Wagner, J. Wunderlich, F. Freimuth, Y. Mokrousov, J. Kuneš, J.S. Chauhan, M.J. Grzybowski, A.W. Rushforth, K.W. Edmonds, B.L. Gallagher, T. Jungwirth, Science **351**(6273), 587 (2016). <https://doi.org/10.1126/science.aab1031>, arXiv:1503.03765, <http://www.sciencemag.org/cgi/doi/10.1126/science.aab1031>
8. D. Kriegner, K. Výborný, K. Olejník, H. Reichlová, V. Novák, X. Marti, J. Gazquez, V. Saidl, P. Němec, V.V. Volobuev, G. Springholz, V. Holý, T. Jungwirth, Nat. Commun. **7**, 11623 (2016). <https://doi.org/10.1038/ncomms11623>, <http://www.nature.com/doifinder/10.1038/ncomms11623>
9. K. Olejník, V. Schuler, X. Marti, V. Novak, Z. Kaspar, P. Wadley, R.P. Campion, K.W. Edmonds, B.L. Gallagher, J. Garces, M. Baumgartner, P. Gambardella, T. Jungwirth, Nat. Commun. **8**, 15434 (2017). <https://doi.org/10.1038/ncomms15434>
10. W.A. Borders, H. Akima, S. Fukami, S. Moriya, S. Kurihara, Y. Horio, S. Sato, H. Ohno, Appl. Phys. Express **10**, 013007 (2017)
11. K. Olejník, T. Seifert, Z. Kaspar, V. Novak, P. Wadley, R.P. Campion, M. Baumgartner, P. Gambardella, P. Nemec, J. Wunderlich, J. Sinova, M. Muller, T. Kampfrath, T. Jungwirth, Science Advances **4**(3), 3566 (2018). arXiv:1711.08444
12. W. Thomson, Proc. R. Soc. Lond. **8**, 546 (1856). <https://doi.org/10.1098/rspl.1856.0144>
13. J. Daughton, Thin Solid Film. **216**, 162 (1992). [https://doi.org/10.1016/0040-6090\(92\)90888-1](https://doi.org/10.1016/0040-6090(92)90888-1)
14. B.G. Park, J. Wunderlich, X. Martí, V. Holý, Y. Kurosaki, M. Yamada, H. Yamamoto, A. Nishide, J. Hayakawa, H. Takahashi, A.B. Shick, T. Jungwirth, Nat. Mater. **10**(5), 347 (2011). <https://doi.org/10.1038/nmat2983>, <http://www.ncbi.nlm.nih.gov/pubmed/21399629>, <http://www.nature.com/doifinder/10.1038/nmat2983>
15. X. Marti, I. Fina, C. Frontera, J. Liu, P. Wadley, Q. He, R.J. Paull, J.D. Clarkson, J. Kudrnovský, I. Turek, J. Kuneš, D. Yi, J.H. Chu, C.T. Nelson, L. You, E. Arenholz, S. Salahuddin, J. Fontcuberta, T. Jungwirth, R. Ramesh, Nat. Mater. **13**(4), 367 (2014). <https://doi.org/10.1038/nmat3861>, <http://www.ncbi.nlm.nih.gov/pubmed/24464243>
16. S. Nakatsuji, N. Kiyohara, T. Higo, Nature **527**, 212 (2015). <https://doi.org/10.1038/nature15723>
17. E. Hall, Philos. Mag. Ser. 5 **12**(74), 157 (1881). <https://doi.org/10.1080/14786448108627086>
18. D. Ralph, M. Stiles, J. Magn. Magn. Mater. **320**(7), 1190 (2008). <https://doi.org/10.1016/j.jmmm.2007.12.019>, <http://linkinghub.elsevier.com/retrieve/pii/S0304885307010116>
19. P. Tang, Q. Zhou, G. Xu, S.C. Zhang, Nat. Phys. **12**, 1100 (2016). <https://doi.org/10.1038/NPHYS3839>
20. L. Šmejkal, J. Železný, J. Sinova, T. Jungwirth, Phys. Rev. Lett. **118**(10), 106402 (2017). <https://doi.org/10.1103/PhysRevLett.118.106402>, <http://link.aps.org/doi/10.1103/PhysRevLett.118.106402>
21. J. Sinova, S.O. Valenzuela, J. Wunderlich, C.H. Back, T. Jungwirth, Rev. Mod. Phys. **87**(4), 1213 (2015). <https://doi.org/10.1103/RevModPhys.87.1213>, <http://link.aps.org/doi/10.1103/RevModPhys.87.1213>
22. F. Hellman, A. Hoffmann, Y. Tserkovnyak, G.S.D. Beach, E.E. Fullerton, C. Leighton, A.H. MacDonald, D.C. Ralph, D.A. Arena, H.A. Durr, P. Fischer, J. Grollier, J.P. Heremans, T. Jungwirth, A.V. Kimel, B. Koopmans, I.N. Krivorotov, S.J. May, A.K. Petford-Long, J.M.

Rondinelli, N. Samarth, I.K. Schuller, A.N. Slavin, M.D. Stiles, O. Tchernyshyov, A. Thiaville, B.L. Zink, Rev. Mod. Phys. **89**(2), 025006 (2017). <https://doi.org/10.1103/RevModPhys.89.025006>, arXiv:1607.00439

23. A.R. Mellnik, J.S. Lee, A. Richardella, J.L. Grab, P.J. Mintun, M.H. Fischer, A. Vaezi, A. Manchon, E.A. Kim, N. Samarth, D.C. Ralph, Nature **511**(7510), 449 (2014). <https://doi.org/10.1038/nature13534>, <http://www.nature.com/doifinder/10.1038/nature13534>

24. A. Roth, C. Brüne, H. Buhmann, L.W. Molenkamp, J. Maciejko, X.L. Qi, S.C. Zhang, Science **325**, 294 (2009). <https://doi.org/10.1126/science.1174736>, <http://www.ncbi.nlm.nih.gov/pubmed/19608911>

25. J. Železný, H. Gao, K. Výborný, J. Zemen, J. Mašek, A. Manchon, J. Wunderlich, J. Sinova, T. Jungwirth, Phys. Rev. Lett. **113**(15), 157201 (2014). <https://doi.org/10.1103/PhysRevLett.113.157201>, <http://link.aps.org/doi/10.1103/PhysRevLett.113.157201>

26. R.S.K. Mong, A.M. Essin, J.E. Moore, Phys. Rev. B **81**(24), 245209 (2010). <https://doi.org/10.1103/PhysRevB.81.245209>, <http://link.aps.org/doi/10.1103/PhysRevB.81.245209>

27. A.B. Shick, S. Khmelevskyi, O.N. Mryasov, J. Wunderlich, T. Jungwirth, Phys. Rev. B **81**(21), 212409 (2010). <https://doi.org/10.1103/PhysRevB.81.212409>, <http://link.aps.org/doi/10.1103/PhysRevB.81.212409>

28. S.Y. Bodnar, L. Šmejkal, I. Turek, T. Jungwirth, O. Gomonay, J. Sinova, A.A. Sapozhnik, H.J. Elmers, M. Kláui, M. Jourdan, Nature Communications **9**(348) (2018). arXiv:1706.02482

29. L.M. Sandratskii, J. Kübler, Phys. Rev. Lett. **76**(26), 4963 (1996). <https://doi.org/10.1103/PhysRevLett.76.4963>, <http://link.aps.org/doi/10.1103/PhysRevLett.76.4963>, <http://journals.aps.org/prl/abstract/10.1103/PhysRevLett.76.4963>

30. T.F. Duan, W.J. Ren, W.L. Liu, S.J. Li, W. Liu, Z.D. Zhang, Appl. Phys. Lett. **107**(8), 82403 (2015). <https://doi.org/10.1063/1.4929447>

31. L. Szunyogh, B. Lazarovits, L. Uvdardi, J. Jackson, U. Nowak, Phys. Rev. B-Condens. Matter Mater. Phys. **79**(2), 020403(R) (2009). <https://doi.org/10.1103/PhysRevB.79.020403>

32. T. David, in *Topological Quantum Numbers In Nonrelativistic Physics* (World Scientific Publishing Company, 1998). <https://books.google.cz/books?id=BgbtCgAAQBAJ>

33. B. Bernevig, T. Hughes, in *Topological Insulators and Topological Superconductors* (Princeton University Press, 2013). <https://books.google.de/books?id=wOn7JHSSxrsC>

34. M. Hermanns, pp. 1–24 (2017). arXiv:1702.01525

35. O. Vafek, A. Vishwanath, Ann. Rev. Condens. Matter Phys. **5**(1), 83 (2014). <https://doi.org/10.1146/annurev-conmatphys-031113-133841>, arXiv:1306.2272, <http://www.annualreviews.org/doi/10.1146/annurev-conmatphys-031113-133841>

36. J. Wang, S.C. Zhang, Nat. Mater. **16**(11), 1062 (2017). <https://doi.org/10.1038/nmat5012>, <http://www.nature.com/doifinder/10.1038/nmat5012>

37. H. Masuda, H. Sakai, M. Tokunaga, Y. Yamasaki, A. Miyake, J. Shiogai, S. Nakamura, S. Awaji, A. Tsukazaki, H. Nakao, Y. Murakami, T.h. Arima, Y. Tokura, S. Ishiwata, Sci. Adv. **2**(1), e1501117 (2016). <https://doi.org/10.1126/sciadv.1501117>, <http://advances.sciencemag.org/cgi/doi/10.1126/sciadv.1501117>

38. N.P. Armitage, E.J. Mele, A. Vishwanath, Rev. Mod. Phys. **90**, 015001 (2018)

39. C. Bradley, A. Cracknell, The mathematical theory of symmetry in solids: representation theory for point groups and space groups, in *Oxford Classic Texts in the Physical Sciences* (OUP Oxford, 2010). https://books.google.cz/books?id=lMdNv_wbu2IC

40. X. Wan, A.M. Turner, A. Vishwanath, S.Y. Savrasov, Phys. Rev. B **83**(20), 205101 (2011). <https://doi.org/10.1103/PhysRevB.83.205101>, <http://link.aps.org/doi/10.1103/PhysRevB.83.205101>

41. H. Yang, Y. Sun, Y. Zhang, W.J. Shi, S.S.P. Parkin, B. Yan, New J. Phys. **19**(1), 015008 (2017). <https://doi.org/10.1088/1367-2630/aa5487>, arXiv:1608.03404, <http://stacks.iop.org/1367-2630/19/i=1/a=015008?key=crossref.8be483e90a7a8a1a6e931152b5976b48>

42. A. Kohn, A. Kovács, R. Fan, G.J. McIntyre, R.C.C. Ward, J.P. Goff, Sci. Rep. **3**, 2412 (2013). <https://doi.org/10.1038/srep02412>, <http://www.ncbi.nlm.nih.gov/articlerender.fcgi?artid=3740276&tool=pmcentrez&rendertype=abstract>, <http://www.nature.com/articles/srep02412>

43. M. Seemann, D. K  dderitzsch, S. Wimmer, H. Ebert, Phys. Rev. B—Condens. Matter Mater. Phys. **92**(15) (2015). <https://doi.org/10.1103/PhysRevB.92.155138>
44. W.H. Kleiner, Phys. Rev. **142**(2), 318 (1966)
45. S. Wimmer, K. Chadova, M. Seemann, D. K  dderitzsch, H. Ebert, Phys. Rev. B **94**(5) (2016). <https://doi.org/10.1103/PhysRevB.94.054415>
46. J. Zelezny, H. Gao, A. Manchon, F. Freimuth, Y. Mokrousov, J. Zemen, J. Masek, J. Sinova, T. Jungwirth, Phys. Rev. B **95**, 014403 (2017). <https://doi.org/10.1103/PhysRevB.95.014403>
47. F. Freimuth, S. Bl  gel, Y. Mokrousov, Phys. Rev. B **90**, 174423 (2014). <https://doi.org/10.1103/PhysRevB.90.174423>, <http://link.aps.org/doi/10.1103/PhysRevB.90.174423>
48. F. Freimuth, S. Bl  gel, Y. Mokrousov, Phys. Rev. B **92**(6), 064415 (2015). <https://doi.org/10.1103/PhysRevB.92.064415>, <http://journals.aps.org/prb/abstract/10.1103/PhysRevB.92.064415>
49. C. Ciccarelli, L. Anderson, V. Tshitoyan, A.J. Ferguson, F. Gerhard, C. Gould, L.W. Molenkamp, J. Gayles, J.   zezn  , L.   mejkal, Z. Yuan, J. Sinova, F. Freimuth, T. Jungwirth, Nat. Phys. **12**(9), 855 (2016). <https://doi.org/10.1038/nphys3772>, <http://www.nature.com/doifinder/10.1038/nphys3772>
50. W. Feng, G.Y. Guo, J. Zhou, Y. Yao, Q. Niu, Phys. Rev. B **92**(14), 144426 (2015). <https://doi.org/10.1103/PhysRevB.92.144426>, <http://link.aps.org/doi/10.1103/PhysRevB.92.144426>
51. M. Ikhlas, T. Tomita, T. Koretsune, M.T. Suzuki, D. Nishio-Hamane, R. Arita, Y. Otani, S. Nakatsuji, Nat. Phys. **13**, 1085–1090 (2017). <https://doi.org/10.1038/nphys4181>, <http://www.nature.com/doifinder/10.1038/nphys4181>
52. G. Li, B. Yan, Z. Wang, K. Held, Phys. Rev. B **95**(3), 035102 (2017). <https://doi.org/10.1103/PhysRevB.95.035102>, <http://journals.aps.org/prb/abstract/10.1103/PhysRevB.95.035102>
53. Z.F. Wang, H. Zhang, D. Liu, C. Liu, C. Tang, C. Song, Y. Zhong, J. Peng, F. Li, C. Nie, L. Wang, X.J. Zhou, X. Ma, Q.K. Xue, F. Liu, Nat. Mater. **15**(September), 968 (2016). <https://doi.org/10.1038/nmat4686>, <http://www.nature.com/doifinder/10.1038/nmat4686>
54. V. Gopalan, D.B. Litvin, Nat. Mater. **10**(5), 376 (2011). <https://doi.org/10.1038/nmat2987>, <http://dx.doi.org/10.1038/nmat2987>
55. P. Strange, Relativistic quantum mechanics: with applications in condensed matter and atomic physics, (Cambridge University Press, 1998). <https://books.google.de/books?id=sdVrBM2w0OwC>
56. R. Prasad, Electronic structure of materials, (Taylor & Francis, 2013). <https://books.google.de/books?id=8s3VygAACAAJ>
57. B.J. Wieder, Y. Kim, A.M. Rappe, C.L. Kane, Phys. Rev. Lett. **116**(18), 186402 (2016). <https://doi.org/10.1103/PhysRevLett.116.186402>, <http://link.aps.org/doi/10.1103/PhysRevLett.116.186402>
58. B. Bradlyn, J. Cano, Z. Wang, M.G. Vergniory, C. Felser, R.J. Cava, B.A. Bernevig, Science **353**(6299), aaf5037 (2016). <https://doi.org/10.1126/science.aaf5037>, <http://www.sciencemag.org/cgi/doi/10.1126/science.aaf5037>
59. C. Li, J.S. Lian, Q. Jiang, Phys. Rev. B **83**(23), 235125 (2011). <https://doi.org/10.1103/PhysRevB.83.235125>, <http://link.aps.org/doi/10.1103/PhysRevB.83.235125>
60. Z. Li, H. Su, X. Yang, J. Zhang, Phys. Rev. B **91**(23), 235128 (2015). <https://doi.org/10.1103/PhysRevB.91.235128>, <http://link.aps.org/doi/10.1103/PhysRevB.91.235128>
61. M. Hirschberger, S. Kushwaha, Z. Wang, Q. Gibson, S. Liang, C.A. Belvin, B.A. Bernevig, R.J. Cava, N.P. Ong, Nat. Mater. **15**(11), 1161 (2016). <https://doi.org/10.1038/nmat4684>, [arXiv:1602.07219](http://arxiv.org/abs/1602.07219), <http://dx.doi.org/10.1038/nmat4684>, <http://www.nature.com/doifinder/10.1038/nmat4684>
62. T. Suzuki, R. Chisnell, A. Devarakonda, Y.T. Liu, W. Feng, D. Xiao, J.W. Lynn, J.G. Checkelsky, Nat. Phys. **12**(July), 1119 (2016). <https://doi.org/10.1038/nphys3831>, <http://www.nature.com/doifinder/10.1038/nphys3831>
63. J. Park, G. Lee, F. Wolff-Fabris, Y.Y. Koh, M.J. Eom, Y.K. Kim, M.A. Farhan, Y.J. Jo, C. Kim, J.H. Shim, J.S. Kim, Phys. Rev. Lett. **107**(12), 126402 (2011). <https://doi.org/10.1103/PhysRevLett.107.126402>, <http://link.aps.org/doi/10.1103/PhysRevLett.107.126402>

64. K. Wang, D. Graf, H. Lei, S.W. Tozer, C. Petrovic, Phys. Rev. B-Condens. Matter Mater. Phys. **84**(22), 220401(R) (2011). <https://doi.org/10.1103/PhysRevB.84.220401>
65. Y.F. Guo, A.J. Princep, X. Zhang, P. Manuel, D. Khalyavin, I.I. Mazin, Y.G. Shi, A. T. Boothroyd, Phys. Rev. B **90**, 075120 (2014)
66. Z.G. Chen, L. Wang, Y. Song, X. Lu, H. Luo, C. Zhang, P. Dai, Z. Yin, K. Haule, G. Kotliar, Phys. Rev. Lett. **119**(9), 096401 (2017). <https://doi.org/10.1103/PhysRevLett.119.096401>, arXiv:1709.00203, <http://dx.doi.org/10.1103/PhysRevLett.119.096401>
67. F. Máca, J. Mašek, O. Stelmakhovich, X. Martí, H. Reichlová, K. Uhlírová, P. Beran, P. Wadley, V. Novák, T. Jungwirth, J. Magn. Magn. Mater. **324**(8), 1606 (2012). <https://doi.org/10.1016/j.jmmm.2011.12.017>, <http://linkinghub.elsevier.com/retrieve/pii/S0304885311008900>
68. A.B. Sushkov, J.B. Hofmann, G.S. Jenkins, J. Ishikawa, S. Nakatsuji, S. Das Sarma, H.D. Drew, Phys. Rev. B-Condens. Matter Mater. Phys. **92**(24), 241108(R) (2015). <https://doi.org/10.1103/PhysRevB.92.241108>
69. Z. Tian, Y. Kohama, T. Tomita, H. Ishizuka, T.H. Hsieh, J.J. Ishikawa, K. Kindo, L. Balents, S. Nakatsuji, Nat. Phys. **12**(November), 134 (2015). <https://doi.org/10.1038/nphys3567>, <http://www.nature.com/doifinder/10.1038/nphys3567>
70. T. Kondo, M. Nakayama, R. Chen, J.J. Ishikawa, E.G. Moon, T. Yamamoto, Y. Ota, W. Malae, H. Kanai, Y. Nakashima, Y. Ishida, R. Yoshida, H. Yamamoto, M. Matsunami, S. Kimura, N. Inami, K. Ono, H. Kumigashira, S. Nakatsuji, L. Balents, S. Shin, Nat. Commun. **6**, 10042 (2015). <https://doi.org/10.1038/ncomms10042>, arXiv:1510.07977, <http://www.nature.com/doifinder/10.1038/ncomms10042>
71. H. Yang, Y. Sun, Y. Zhang, W.J. Shi, S.S.P. Parkin, B. Yan, New J. Phys. **19**(1), 015008 (2017). <https://doi.org/10.1088/1367-2630/aa5487>, <http://stacks.iop.org/1367-2630/19/i=1/a=015008?key=crossref.8be483e90a7a8a1a6e931152b5976b48>
72. K. Kuroda, T. Tomita, M.T. Suzuki, C. Bareille, A.A. Nugroho, P. Goswami, M. Ochi, M. Ikhlas, M. Nakayama, S. Akebi, R. Noguchi, R. Ishii, N. Inami, K. Ono, H. Kumigashira, A. Varykhalov, T. Muro, T. Koretsune, R. Arita, S. Shin, T. Kondo, S. Nakatsuji, Nat. Mater. **16**, 1090–1095 (2017). <https://doi.org/10.1038/nmat4987>, arXiv:1710.06167
73. S.Y. Xu, M. Neupane, C. Liu, D. Zhang, A. Richardella, L. Andrew Wray, N. Alidoust, M. Leandersson, T. Balasubramanian, J. Sánchez-Barriga, O. Rader, G. Landolt, B. Slomski, J. Hugo Dil, J. Osterwalder, T.R. Chang, H.T. Jeng, H. Lin, A. Bansil, N. Samarth, M. Zahid Hasan, Nat. Phys. **8**(8), 616 (2012). <https://doi.org/10.1038/nphys2351>, <http://dx.doi.org/10.1038/nphys2351>
74. F. Katmis, V. Lauter, F.S. Nogueira, B.A. Assaf, M.E. Jamer, P. Wei, B. Satpati, J.W. Freeland, I. Eremin, D. Heiman, P. Jarillo-Herrero, J.S. Moodera, Nature **533**(7604), 513 (2016). <https://doi.org/10.1038/nature17635>, <http://www.nature.com/nature/journal/v533/n7604/full/nature17635.html>
75. Q.L. He, X. Kou, A.J. Grutter, G. Yin, L. Pan, X. Che, Y. Liu, T. Nie, B. Zhang, S.M. Disseler, B.J. Kirby, W. Ratcliff II, Q. Shao, K. Murata, X. Zhu, G. Yu, Y. Fan, M. Montazeri, X. Han, J.A. Borchers, K.L. Wang, Nat. Mater. **16**(1), 94 (2016). <https://doi.org/10.1038/nmat4783>, arXiv:1605.04854, <http://www.nature.com/doifinder/10.1038/nmat4783>
76. J. Finley, L. Liu, Phys. Rev. Appl. **6**(5), 054001 (2016). <https://doi.org/10.1103/PhysRevApplied.6.054001>, <https://link.aps.org/doi/10.1103/PhysRevApplied.6.054001>
77. J. Han, A. Richardella, S. Siddiqui, J. Finley, N. Samarth, L. Liu, Phys. Rev. Lett. **119**, 077702 (2017). [arXiv:1703.07470](https://doi.org/10.1103/PhysRevLett.119.077702)
78. S.M. Young, B.J. Wieder, Phys. Rev. Lett. **118**, 186401 (2017). [arXiv:1609.06738](https://doi.org/10.1103/PhysRevLett.118.186401)
79. C. Liu, Y. Lee, T. Kondo, E.D. Mun, M. Caudle, B.N. Harmon, S.L. Bud, P.C. Canfield, A. Kaminski, Phys. Rev. B **83**, 205133 (2011). <https://doi.org/10.1103/PhysRevB.83.205133>
80. W.F. Tsai, H. Lin, Nat. Mater. **15**, 927–928 (2016). <https://doi.org/10.1038/nmat4700>
81. C.W.J. Beenakker, L. Kouwenhoven, Nat. Phys. **12**(7), 618 (2016). <https://doi.org/10.1038/nphys3778>, <http://www.nature.com/doifinder/10.1038/nphys3778>
82. S. Borisenko, D. Evtushinsky, Q. Gibson, A. Yaresko, T. Kim, M.N. Ali, B. Buechner, M. Hoesch, R.J. Cava, (2015). <https://doi.org/10.1017/CBO9781107415324.004>

83. M. Chinotti, A. Pal, W.J. Ren, C. Petrovic, L. Degiorgi, Phys. Rev. B **94**(24), 245101 (2016). <https://doi.org/10.1103/PhysRevB.94.245101>, <https://link.aps.org/doi/10.1103/PhysRevB.94.245101>
84. A. Wang, I. Zaliznyak, W. Ren, L. Wu, D. Graf, V.O. Garlea, Phys. Rev. B **94**, 165161 (2016). <https://doi.org/10.1103/PhysRevB.94.165161>
85. D. Chaudhuri, B. Cheng, A. Yaresko, Q.D. Gibson, R.J. Cava, N.P. Armitage, Phys. Rev. B **96**, 075151 (2017). [arXiv:1701.08693](https://arxiv.org/abs/1701.08693)
86. J.Y. Liu, J. Hu, Q. Zhang, D. Graf, H.B. Cao, S.M. Radmanesh, D.J. Adams, Y.L. Zhu, G.F. Cheng, X. Liu, W.A. Phelan, J. Wei, M. Jaime, F. Balakirev, D.A. Tennant, J.F. DiTusa, I. Chiorescu, L. Spinu, Z.Q. Mao. Nat. Mater. **16**(9), 905 (2017). <https://doi.org/10.1038/nmat4953>
87. B.J. Yang, N. Nagaosa, Nat. Commun. **5**, 4898 (2014). <https://doi.org/10.1038/ncomms5898>, <http://dx.doi.org/10.1038/ncomms5898>
88. L. Šmejkal, T. Jungwirth, J. Sinova, Phys. Status Solidi-Rapid Res. Lett. **11**(4) (2017). <https://doi.org/10.1002/pssr.201700044>, [arXiv:1702.07788](https://arxiv.org/abs/1702.07788), <http://dx.doi.org/10.1002/pssr.201700044>
89. A.A. Burkov, Nat. Mater. **15**(11), 1145 (2016). <https://doi.org/10.1038/nmat4788>, [arXiv:1610.07866](https://arxiv.org/abs/1610.07866), <http://www.nature.com/doifinder/10.1038/nmat4788%5Cn>
90. L. Šmejkal, Y. Mokrousov, B. Yan, A.H. MacDonald, Nature Physics **14**, 242–251 (2018). [arXiv:1706.00670](https://arxiv.org/abs/1706.00670)
91. M. Kargarian, M. Randeria, Y.M. Lu, Proce. Nat. Acad. Sci. **113**(31), 8648 (2016). <https://doi.org/10.1073/pnas.1524787113>, <http://www.pnas.org/cgi/content/short/113/31/8648>
92. E. Emmanouilidou, H. Cao, P. Tang, X. Gui, C. Hu, B. Shen, J. Wu, S.C. Zhang, W. Xie, N. Ni, Phys. Rev. B **96**, 224405 (2017). [arXiv:1708.09340](https://arxiv.org/abs/1708.09340)
93. X. Zhang, S. Sun, H. Lei, Phys. Rev. B **96**, 235105 (2017). [arXiv:1709.03394](https://arxiv.org/abs/1709.03394)
94. G. Xu, H. Weng, Z. Wang, X. Dai, Z. Fang, Phys. Rev. Lett. **107**(18), 186806 (2011). <https://doi.org/10.1103/PhysRevLett.107.186806>, <http://link.aps.org/doi/10.1103/PhysRevLett.107.186806>
95. Z. Wang, M.G. Vergniory, S. Kushwaha, M. Hirschberger, E.V. Chulkov, A. Ernst, N.P. Ong, R.J. Cava, B.A. Bernevig, Phys. Rev. Lett. **117**(23), 236401 (2016). <https://doi.org/10.1103/PhysRevLett.117.236401>, [arXiv:1603.00479](https://arxiv.org/abs/1603.00479), <http://link.aps.org/doi/10.1103/PhysRevLett.117.236401>
96. S.Y. Xu, I. Belopolski, N. Alidoust, M. Neupane, G. Bian, C. Zhang, R. Sankar, G. Chang, Z. Yuan, C.C. Lee, S.M. Huang, H. Zheng, J. Ma, D.S. Sanchez, B. Wang, A. Bansil, F. Chou, P.P. Shibayev, H. Lin, S. Jia, M.Z. Hasan, Science **349**(6248), 613 (2015). <https://doi.org/10.1126/science.aaa9297>, <http://www.sciencemag.org/cgi/doi/10.1126/science.aaa9297>
97. B.Q. Lv, H.M. Weng, B.B. Fu, X.P. Wang, H. Miao, J. Ma, P. Richard, X.C. Huang, L.X. Zhao, G.F. Chen, Z. Fang, X. Dai, T. Qian, H. Ding, Phys. Rev. X **5**(3), 031013 (2015). <https://doi.org/10.1103/PhysRevX.5.031013>
98. L.X. Yang, Z.K. Liu, Y. Sun, H. Peng, H.F. Yang, T. Zhang, B. Zhou, Y. Zhang, Y.F. Guo, M. Rahn, D. Prabhakaran, Z. Hussain, S.K. Mo, C. Felser, B. Yan, Y.L. Chen, Nat. Phys. **11**(9), 728 (2015). <https://doi.org/10.1038/nphys3425>, <http://www.nature.com/doifinder/10.1038/nphys3425>
99. J. Kübler, C. Felser, Europhys. Lett. (EPL) **108**(6), 67001 (2014). <https://doi.org/10.1209/0295-5075/108/67001>, <http://stacks.iop.org/0295-5075/108/i=6/a=67001?key=crossref.7fc151e16858620dbeae03d11c5917a6>
100. Y. Zhang, Y. Sun, H. Yang, J. Železný, S.P.P. Parkin, C. Felser, B. Yan, Phys. Rev. B **95**(7), 075128 (2017). <https://doi.org/10.1103/PhysRevB.95.075128>, [arXiv:1610.04034](https://arxiv.org/abs/1610.04034), <http://link.aps.org/doi/10.1103/PhysRevB.95.075128>
101. T. Nagamiya, S. Tomiyoshi, Y. Yamaguchi, Solid State Commun. **42**(5), 385 (1982). [https://doi.org/10.1016/0038-1098\(82\)90159-4](https://doi.org/10.1016/0038-1098(82)90159-4), <http://linkinghub.elsevier.com/retrieve/pii/0038109882901594>
102. S. Tomiyoshi, Y. Yamaguchi, J. Phys. Soci. Jpn. **51**(8), 2478 (1982), <http://journals.jps.jp/doi/abs/10.1143/JPSJ.51.2478#WK-Vf2a3ROQ.mendeley>

103. H. Fujita, Phys. Status Solidi-Rapid Res. Lett. **11**(4), 1600360 (2017). <https://doi.org/10.1002/pssr.201600360>
104. A.A. Soluyanov, D. Gresch, Z. Wang, Q. Wu, M. Troyer, X. Dai, B.A. Bernevig, Nature **527**(7579), 495 (2015). <https://doi.org/10.1038/nature15768>, <http://dx.doi.org/10.1038/nature15768>, <http://www.nature.com/doifinder/10.1038/nature15768>
105. A.A. Zyuzin, R.P. Tiwari, JETP Lett. **103**(11), 717 (2016). <https://doi.org/10.1134/S002136401611014X>, <http://link.springer.com/10.1134/S002136401611014X>
106. H.B. Nielsen, M. Ninomiya, Phys. Lett. B **130**(6), 389 (1983). [https://doi.org/10.1016/0370-2693\(83\)91529-0](https://doi.org/10.1016/0370-2693(83)91529-0)
107. B. Yan, C. Felser, Ann. Rev. Condens. Matter Phys. **8**, 337 (2017). <https://doi.org/10.1146/annurev-conmatphys-031016-025458>. [arXiv:1611.04182](https://arxiv.org/abs/1611.04182)
108. V.A. Zyuzin, Phys. Rev. B **95**, 245128 (2017). <https://doi.org/10.1103/PhysRevB.95.245128>
109. M.N. Ali, J. Xiong, S. Flynn, J. Tao, Q.D. Gibson, L.M. Schoop, T. Liang, N. Haldolaarachchige, M. Hirschberger, N.P. Ong, R.J. Cava, Nature **514**(7521), 205 (2014). <https://doi.org/10.1038/nature13763>, <http://www.ncbi.nlm.nih.gov/pubmed/25219849>
110. I. Pletikosic, M.N. Ali, A.V. Fedorov, R.J. Cava, T. Valla, Phys. Rev. Lett. **113**(21), 216601 (2014). <https://doi.org/10.1103/PhysRevLett.113.216601>
111. T. Khouri, U. Zeitler, C. Reichl, W. Wegscheider, N.E. Hussey, S. Wiedmann, J.C. Maan, Phys. Rev. Lett. **117**(25), 256601 (2016). <https://doi.org/10.1103/PhysRevLett.117.256601>, <https://journals.aps.org/prl/abstract/10.1103/PhysRevLett.117.256601>
112. P. Kim, J.H. Ryoo, C.H. Park, Phys. Rev. Lett. **119**, 266401 (2017). [arXiv:1707.01103](https://arxiv.org/abs/1707.01103)
113. Q.R. Zhang, B. Zeng, D. Rhodes, S. Memaran, T. Besara, R. Sankar, F. Chou, N. Alidoust, S.Y. Xu, I. Belopolski, M.Z. Hasan, L. Balicas, pp. 1–24 (2017), <https://arxiv.org/pdf/1705.00920.pdf>
114. Q.L. He, G. Yin, L. Yu, A.J. Grutter, L. Pan, X. Kou, X. Che, G. Yu, T. Nie, B. Zhang, Q. Shao, K. Murata, X. Zhu, Y. Fan, X. Han, B.J. Kirby, K.L. Wang, Arxiv preprint (2016). [arXiv:1612.01661](https://arxiv.org/abs/1612.01661)
115. M. Mogi, M. Kawamura, R. Yoshimi, A. Tsukazaki, Y. Kozuka, N. Shirakawa, K.S. Takahashi, M. Kawasaki, Y. Tokura, Nat. Mater. **16**, 516–521 (2017). <https://doi.org/10.1038/NMAT4855>
116. Y. Tokura, M. Kawasaki, N. Nagaosa, Nat. Phys. **13**, 1056–1068 (2017). <https://doi.org/10.1038/NPHYS4274>
117. X.Y. Dong, S. Kanungo, B. Yan, C.X. Liu, Phys. Rev. B **94**(24), 245135 (2016). <https://doi.org/10.1103/PhysRevB.94.245135>, <http://link.aps.org/doi/10.1103/PhysRevB.94.245135>
118. K. Yamamoto, L. Smejkal, T. Jungwirth, J. Sinova, unpublished
119. N. Wakeham, E.D. Bauer, M. Neupane, F. Ronning, Phys. Rev. B-Condens. Matter Mater. Phys. **93**(20), 205152 (2016). <https://doi.org/10.1103/PhysRevB.93.205152>
120. F.D.M. Haldane, Phys. Rev. Lett. **61**(18), 2015 (1988). <https://doi.org/10.1103/PhysRevLett.61.2015>, <http://link.aps.org/doi/10.1103/PhysRevLett.61.2015>
121. R. Shindou, N. Nagaosa, Phys. Rev. Lett. **87**(11), 116801 (2001). <https://doi.org/10.1103/PhysRevLett.87.116801>, <http://link.aps.org/doi/10.1103/PhysRevLett.87.116801>
122. H. Chen, Q. Niu, A.H. MacDonald, Phys. Rev. Lett. **112**, 017205 (2014). <https://doi.org/10.1103/PhysRevLett.112.017205>, <http://link.aps.org/doi/10.1103/PhysRevLett.112.017205>
123. A.K. Nayak, J.E. Fischer, Y. Sun, B. Yan, J. Karel, A.C. Komarek, C. Shekhar, N. Kumar, W. Schnelle, J. Kübler, C. Felser, S.S.P. Parkin, Sci. Adv. **2**(4), e1501870 (2016). <https://doi.org/10.1126/sciadv.1501870>, <http://advances.science.org/cgi/doi/10.1126/sciadv.1501870>
124. N. Kiyohara, T. Tomita, S. Nakatsuji, Phys. Rev. Appl. **5**, 064009 (2016). <https://doi.org/10.1103/PhysRevApplied.5.064009>. [arXiv:1511.04619](https://arxiv.org/abs/1511.04619), <http://dx.doi.org/10.1103/PhysRevApplied.5.064009>
125. Y. Machida, S. Nakatsuji, S. Onoda, T. Tayama, T. Sakakibara, Nature **463**(7278), 210 (2010). <https://doi.org/10.1038/nature08680>, <http://dx.doi.org/10.1038/nature08680>
126. J. Kübler, C. Felser, Europhys. Lett. (EPL) **120**(4), (2018) . [arXiv:1711.03891](https://arxiv.org/abs/1711.03891)

127. F. Haldane, Phys. Rev. Lett. **93**(20), 206602 (2004). <https://doi.org/10.1103/PhysRevLett.93.206602>, <http://link.aps.org/doi/10.1103/PhysRevLett.93.206602>
128. D. Gosálbez-Martínez, I. Souza, D. Vanderbilt, Phys. Rev. B **92**(8), 085138 (2015). <https://doi.org/10.1103/PhysRevB.92.085138>, <https://link.aps.org/doi/10.1103/PhysRevB.92.085138>
129. N. Kanazawa, Y. Onose, T. Arima, D. Okuyama, K. Ohoyama, S. Wakimoto, K. Kakurai, S. Ishiwata, Y. Tokura, Phys. Rev. Lett. **106**(15), 156603 (2011). <https://doi.org/10.1103/PhysRevLett.106.156603>, <http://link.aps.org/doi/10.1103/PhysRevLett.106.156603>
130. C. Sürgers, G. Fischer, P. Winkel, H.V. Löhneysen, Nat. Commun. **5**, 3400 (2014). <https://doi.org/10.1038/ncomms4400>, <http://www.ncbi.nlm.nih.gov/pubmed/24594621>
131. C. Sürgers, W. Kittler, T. Wolf, H.v. Löhneysen, AIP Adv. **6**(5), 055604 (2016). <https://doi.org/10.1063/1.4943759>, <arXiv:1601.01840>, <http://aip.scitation.org/doi/10.1063/1.4943759>
132. J. Zhou, Q.F. Liang, H. Weng, Y.B. Chen, S.H. Yao, Y.F. Chen, J. Dong, G.Y. Guo, Phys. Rev. Lett. **116**(25), 256601 (2016). <https://doi.org/10.1103/PhysRevLett.116.256601>
133. J. Barker, O.A. Tretiakov, Phys. Rev. Lett. **116**(14), 147203 (2016). <https://doi.org/10.1103/PhysRevLett.116.147203>, <http://link.aps.org/doi/10.1103/PhysRevLett.116.147203>
134. P.M. Buhl, F. Freimuth, S. Blügel, Y. Mokrousov, Phys. Status Solidi (RRL)—Rapid Res. Lett. **11**(4), 1700007 (2017). <https://doi.org/10.1002/pssr.201700007>, <arXiv:1701.03030>, <http://doi.wiley.com/10.1002/pssr.201700007>
135. B. Göbel, A. Mook, J. Henk, I. Mertig, Phys. Rev. B **96**(6), 060406 (2017). <https://doi.org/10.1103/PhysRevB.96.060406>, <arXiv:1707.05267>, <http://stacks.iop.org/1367-2630/19/i=6/a=063042?key=crossref.8e79cf18fd05a715d017f8a5fb97a762>, <http://link.aps.org/doi/10.1103/PhysRevB.96.060406>
136. A.H. MacDonald, M. Tsui, Philos. Trans. R. Soc. A: Math. Phys. Eng. Sc. **369**(1948), 3098 (2011). <https://doi.org/10.1098/rsta.2011.0014>, <http://www.ncbi.nlm.nih.gov/pubmed/21727116>, <http://rsta.royalsocietypublishing.org/cgi/doi/10.1098/rsta.2011.0014>
137. D. Sander, S.O. Valenzuela, D. Makarov, C.H. Marrows, E.E. Fullerton, P. Fischer, J. McCord, P. Vavassori, S. Mangin, P. Pirro, B. Hillebrands, A.D. Kent, T. Jungwirth, O. Gutfleisch, C.G. Kim, A. Berger, J. Phys. D Appl. Phys. **50**, 363001 (2017). <http://iopscience.iop.org/0022-3727/50/36/363001>
138. Y. Fan, K.L. Wang, SPIN **06**(02), 1640001 (2016). <https://doi.org/10.1142/S2010324716400014>, <http://www.worldscientific.com/doi/abs/10.1142/S2010324716400014>
139. Y. Fan, P. Upadhyaya, X. Kou, M. Lang, S. Takei, Z. Wang, J. Tang, L. He, L.T. Chang, M. Montazeri, G. Yu, W. Jiang, T. Nie, R.N. Schwartz, Y. Tserkovnyak, K.L. Wang, Nat. Mater. **13**(7), 699 (2014). <https://doi.org/10.1038/nmat3973>, <http://www.ncbi.nlm.nih.gov/pubmed/24776536>
140. Y. Fan, K.L. Wang, X. Kou, P. Upadhyaya, Q. Shao, L. Pan, M. Lang, X. Che, J. Tang, M. Montazeri, K. Murata, L.T. Chang, M. Akyol, G. Yu, T. Nie, K.L. Wong, J. Liu, Y. Wang, Y. Tserkovnyak, K.L. Wang, Nat. Nanotechnol. **11**, 352 (2016). <https://doi.org/10.1038/nnano.2015.294>, <arXiv:1511.07442>, <http://www.worldscientific.com/doi/abs/10.1142/S2010324716400014>
141. J.P. Hanke, F. Freimuth, C. Niu, S. Blügel, Y. Mokrousov, Nature Communications **8**, 1479 (2017). <http://arxiv.org/1701.08050>
142. A.K. Nayak, J.E. Fischer, Y. Sun, B. Yan, J. Karel, A.C. Komarek, C. Shekhar, N. Kumar, W. Schnelle, J. Kübler, C. Felser, S.S.P. Parkin, Sci. Adv. **2**(4), e1501870 (2016)
143. Z.Q. Liu, H. Chen, J.M. Wang, J.H. Liu, K. Wang, Z.X. Feng, H. Yan, X.R. Wang, C.B. Jiang, J.M.D. Coey, A.H. MacDonald, Nature Electronics **1**, 172–177 (2018)
144. M. Meinert, D. Graulich, T. Matalla-Wagner, Phys. Rev. Applied **9**, 064040 (2018)
145. X.F. Zhou, J. Zhang, F. Li, X.Z. Chen, G.Y. Shi, Y.Z. Tan, Y.D. Gu, M.S. Saleem, H.Q. Wu, F. Pan, C. Song Phys. Rev. Applied **9**, 054028 (2018)
146. Di Xiao, Jue Jiang, Jae-Ho Shin, Wenbo Wang, Fei Wang, Yi-Fan Zhao, Chaoxing Liu, Wu Weida, Moses H. W. Chan, Nitin Samarth, Cui-Zu Chang. Phys. Rev. Lett. **120**, 056801 (2018)

Chapter 10

Magnons



Sergej O. Demokritov

Abstract Spin waves and their quanta magnons are the dynamic eigen-exitations of a magnetic system. They provide the basis for the description of spatial and temporal evolution of the magnetization distribution of a magnetic object. The unique features of spin waves such as the possibility to carry spin information over relatively long distances, the possibility to achieve sub-micrometer wavelength at microwave frequencies, and controllability by electronic signal via magnetic fields make these waves uniquely suited for implementation of novel integrated electronic devices characterized by high speed, low power consumption, and extended functionalities. It is important to notice that contrary to photons and phonons magnons possess an anisotropic dispersion. The energy/frequency of a magnons depends not only on the absolute value of the wave vector of the magnon, but also on its angle relative to the orientation of the static magnetization.

10.1 Introduction

10.1.1 Spin Waves and Magnons

Bloch [1] has theoretically introduced the concept of spin waves in 1930. He considered theoretically from the point of view of quantum mechanics a chain of exchange-coupled spins. By analyzing low-amplitude deviations of spins from their equilibrium orientations he has found that these deviations were dynamic and propagating nature. Holstein and Primakoff [2] and Dyson [3] developed a generalized theory of spin waves and took into account not only the exchange, but also magnetic dipole interaction between spins and their Zeeman energy in the external magnetic field. In the late 1950s the term for the quanta of spin waves—magnons—was introduced. It is important to notice that contrary to photons and phonons magnons possess an

S. O. Demokritov (✉)

Institute for Applied Physics and Center for Nanotechnology,
University of Münster, Münster, Germany

e-mail: demokrit@uni-muenster.d

anisotropic dispersion. The energy/frequency of a magnons depends not only on the absolute value of the wave vector of the magnon, but also on its angle relative to the orientation of the static magnetization. This dependence is determined by the anisotropic magnetic dipole interaction.

Magnons are able to carry spin information, they can have sub-micrometer wavelength at the frequencies in the interval of 1–100 GHz, their excitation and propagation can be controlled electronically by applied magnetic fields. All these features allow creation of magnonic devices that can be used for implementation of novel high speed and low power consumption integrated electronic circuits. The emerging field of magnonics [4–7] describes application of magnons for electronic operations such as logics, signal processing, neuromorphic calculations. An impressive development in spintronics and nanomagnetism opened new horizons for magnonics. Let us here mention the recent discovery of the spin-transfer torque (STT) [8–10] and the spin-Hall effect (SHE) [11–13]. Both these effects brought about innovative device geometries and functionalities [14–18].

The development of magnonics demonstrates an increasing importance of magnetic systems with reduced dimensionality for spin-wave studies. In fact, the $T^{3/2}$ Bloch was predicted for three-dimensional magnets in the 1930s. Since 1950s the scientists paid the major attention to quasi-two-dimensional objects (films and multilayers). This development resulted in the discovery of spin resonances [19, 20], non-reciprocal Damon-Eshbach mode [21, 22] and the exchange interlayer coupling [23]. In 1990s, quasi-one-dimensional stripes became the most actively studied magnetic systems. As a result, lateral quantization of spin waves [24] as well as the edge modes [25, 26] were discovered. Approximately the same time the spin-torque effect [8, 9] was theoretically predicted. Together with development of new techniques for nano-fabrication, this allowed for investigation of zero-dimensional objects such as spin-torque nano-oscillators [27–33]. Approximately 10 years later room-temperature Bose-Einstein condensation—a coherent macroscopic quantum state of magnons—was discovered [34].

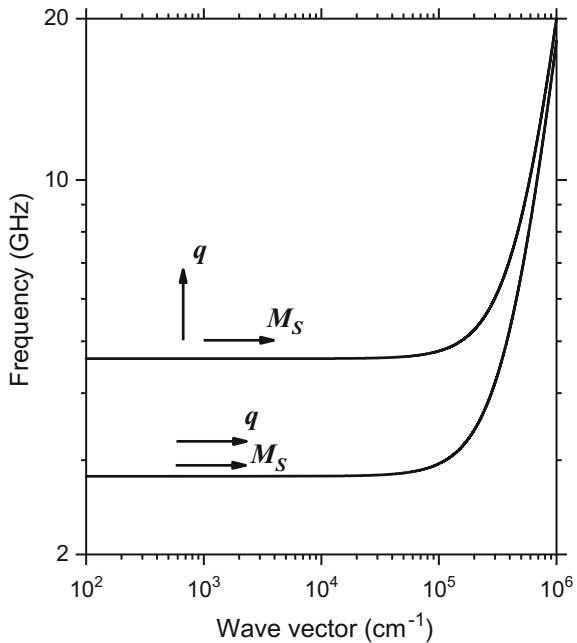
10.1.2 Magnons in Three and Two Dimensions

The Landau-Lifshitz torque equation, which describes dynamics of the magnetization in a ferromagnet is as follows [35]:

$$\frac{1}{\gamma} \frac{d\mathbf{M}}{dt} = \mathbf{M} \times \mathbf{H}_{\text{eff}} \quad (10.1)$$

where $\mathbf{M} = \mathbf{M}_S + \mathbf{m}(\mathbf{R}, t)$ with \mathbf{M}_S and $\mathbf{m}(\mathbf{R}, t)$ being the vectors of the saturation and the (small) variable magnetization, correspondingly, γ is the gyromagnetic ratio for the electron spin. $\mathbf{H}_{\text{eff}} = -\delta W/\delta\mathbf{M}$ is the effective magnetic field calculated from the energy function W , where all the relevant interactions have been taken into account. For the case of an unbounded 3D ferromagnetic medium the time- and the

Fig. 10.1 Magnon spectrum in a bulk ferromagnet at $H = 1\text{kOe}$. The material parameters $4\pi M_s = 1.75\text{ kg}$ and $A = 3.6 \times 10^{-7}\text{ erg/cm}$ correspond to the values of Yttrium Iron Garnet



space dependence of $\mathbf{m}(\mathbf{R}, t)$ can be expanded in a series of plane spin waves (having a 3D wave vector \mathbf{q}), corresponding to magnon modes:

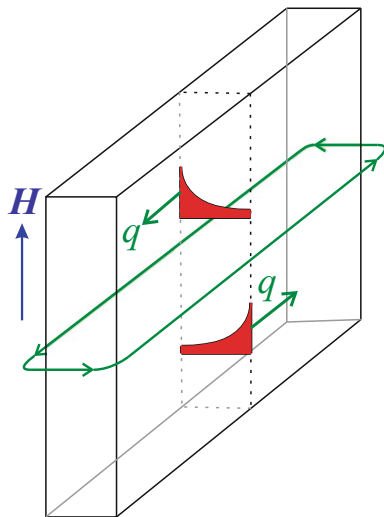
$$\mathbf{m}(\mathbf{R}, t) = \sum_{\mathbf{q}} \mathbf{m}_q \exp(i\mathbf{q}\mathbf{R}) \quad (10.2)$$

Note here, that although $\mathbf{m}(\mathbf{R}, t)$ is small with respect to the saturation magnetization, we consider here the situation, where the quantum population numbers for all magnon modes are large, and a quasi-classical description can be applied. The magnon frequency in an unbounded ferromagnetic medium is given by the Herring-Kittel formula [36]

$$\omega = 2\pi f = \gamma \left[\left(H + \frac{2A}{M_s} q^2 \right) \left(H + \frac{2A}{M_s} q^2 + 4\pi M_s \sin^2 \theta_q \right) \right]^{1/2} \quad (10.3)$$

where A is the exchange stiffness constant, H is the applied magnetic field, and θ_q is the angle between \mathbf{q} and \mathbf{M}_s . Analyzing (10.3), one can clearly distinguish between the contribution of the Zeeman- (H), the exchange ($2Aq^2/M_s$) and the magnetic dipole ($4\pi M_s \sin^2 \theta$) interactions. As illustrated in Fig. 10.1, for small q (the exchange can be neglected) the magnon frequency is independent of q . It depends solely on θ_q demonstrating, an anisotropic spectrum. In contrast, for large q one has an almost isotropic spectrum of the exchange magnons [1].

Fig. 10.2 Schematics of the propagation of the Damon-Eshbach modes. Modes are localized at the surfaces, and the modes at the opposite surfaces propagate in the opposite directions



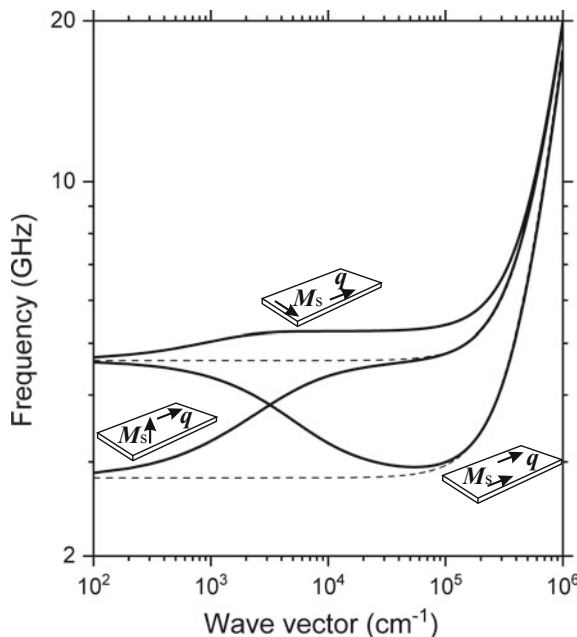
The transition from 3D to 2D can be made if one considers a magnetic film with a finite thickness d . In this case, since the translational invariance along the direction normal to the film surfaces (axis x) is broken, the 3D wave vector is represented as a sum of a 2D continuous in-plane wave vector \mathbf{q}_{\parallel} and quantized wave vector $(n\pi/w)\mathbf{e}_x$ along the film thickness w , while $\mathbf{R} = \mathbf{R}_{\parallel} + x\mathbf{e}_x$. Then, (10.2) changes to: $\mathbf{m}(\mathbf{R}, t) = \sum_{\mathbf{q}_{\parallel}, p} \mathbf{m}_p(x) \exp(i\mathbf{q}_{\parallel}\mathbf{R}_{\parallel})$. If the exchange is neglected, for the lowest thickness mode propagating perpendicular to H one has the dispersion equation derived by Damon and Eshbach for the dipolar surface mode [21]:

$$\omega_{DE}(q_y d) = 2\pi f_{DE}(q_y d) = \gamma [H(H + 4\pi M_S) + (2\pi M_S)^2 (1 - \exp(-2q_y d))]^{1/2}. \quad (10.4)$$

The mode profile of such a mode depicted in Fig. 10.2 is described by an exponential function with a maximum at one of the interfaces of the film $\mathbf{m}(x) = \mathbf{m}_0 \exp(-qx)$. Moreover, the mode is nonreciprocal: it propagates in one direction only, whereas, as shown in Fig. 10.2, the mode at the opposite interface propagates in the opposite direction. Together, if synchronized, these two modes build a nontrivial topological object.

It is possible to obtain an approximate general (quite complex) expression for different magnon modes a magnetic film of a finite thickness with different absolute values and directions of \mathbf{q} and to build a two-dimensional magnon dispersion surface [37]. Figure 10.3 illustrates the general typology of the lowest quasi-uniform magnon modes in the quasi-2D case of a magnetic film for different mutual orientations between \mathbf{q}_{\parallel} and \mathbf{M}_S . Three different geometries are shown. If \mathbf{M}_S is in the film plane and \mathbf{q}_{\parallel} is perpendicular to \mathbf{M}_S , the above-mentioned Damon-Eshbach (DE) mode exists. If \mathbf{q}_{\parallel} and \mathbf{M}_S are collinear in the film plane, a mode with a negative dispersion

Fig. 10.3 Typology of magnon modes in a magnetic film for different orientations of the magnetization, M_S and the in-plane wave vector, q as indicated (solid lines). The dash lines represent the bulk spectrum for comparison. The numerical data correspond to a YIG film with the thickness of 5 μm and the internal magnetic field of 1 kOe



at small wave vectors, the so-called backward volume (BV) mode, exists. Finally, if the magnetization M_S is perpendicular to the film plane, the existing mode is the so-called forward volume (FV) mode.

10.2 Brillouin Light Scattering—A Powerful Tool for Investigation of Magnons

There are several techniques for investigation of magnons: ferromagnetic resonance (FMR) [38], time resolved Kerr magnetometry [26, 39–41], Brillouin light scattering spectroscopy (BLS) [42–44] and neutron scattering [45] are mostly used. The choice of the technique strongly depends on the wave vector and the frequency of magnons under study. FMR, for example, is appropriate for magnons with zero- or small wave vectors, whereas neutron scattering is sensitive to magnons with high frequencies and wave vectors comparable with that of the Brillouin zone. BLS has a number of advantages for magnonic studies. It combines the possibility to study magnons with wave vectors $0\text{--}10^6 \text{ cm}^{-1}$ and in the frequency range of 1–500 GHz with an extremely high sensitivity.

The BLS process can be considered as absorption/emission of a magnon with the wave vector q and the frequency ω by a mono-energetic photon (visible light, usually green line 532 nm) with the wave vector q_I and frequency $\omega_I = c q_I$. Due

to the momentum and energy conservation laws, the photon increases/decreases its energy and momentum, correspondingly:

$$\hbar\omega_S = \hbar(\omega_I \pm \omega) \quad \hbar\mathbf{q}_S = \hbar(\mathbf{q}_I \pm \mathbf{q}) \quad (10.5)$$

the measured frequency shift of the scattered light provides the frequency of the magnon. It is also evident from (10.5) that the difference between the two wave vectors $\mathbf{q}_S - \mathbf{q}_I$, is equal to the wave vector \mathbf{q} of the magnon. Changing the scattering geometry one can sweep the value of q and measure the corresponding $\omega(q)$. Note here that the maximum accessible wave vector $q = 2q_I$, which corresponds to the backscattering geometry. The BLS intensity from a magnon state is directly proportional to the magnon occupation number, or, in classical language, to the corresponding dynamic magnetization squared.

The momentum conservation law, given by (10.5), follows from the translation invariance of the infinite medium. However, for a thin film, this invariance is broken along the direction normal to the film surfaces. Therefore, only the in-plane wave vector is conserved in the light scattering experiments. Correspondingly, if the in-plane translational invariance of the magnetic film is broken by patterning, the in-plane wave vector is no longer fully conserved in the BLS process. In the case of a magnon mode localized in a long stripe, the only conserved component is the component along the stripe axis. Finally, if the confinement takes place in all three dimensions, no conservation laws for wave vectors can be applied in accordance with the above uncertainty principle. One should perform a Fourier analysis of the 3D-distribution of the dynamic magnetization of a particular mode in the real space to calculate its contribution to the BLS intensity.

A complimentary approach is the micro-focus BLS (μ BLS) [43]. Here the light is focused into a diffraction-limited spot. Direct spatial imaging of the magnon intensity is realized by two-dimensional rastering of the probing spot over the sample surface. For reliable two-dimensional imaging of magnons, the spatial resolution of μ BLS is of crucial importance, which is found to be about 250 nm for the wavelength of 532 nm. The approach of the near-field optical microscopy resolution of about 50 nm [46]. However, in this case the setup has a much worse sensitivity.

In agreement with the uncertainty principle, high spatial resolution of the μ BLS technique is incompatible with the wave vector resolution. Thus, the information about the wavelength of the studied magnons is lost. However, this drawback can be eliminated by mapping the phase of the scattered light, which is directly correlated to the phase of the magnetization oscillations in the magnon mode. The phase-resolution technique was first applied for a macro-BLS apparatus [47] and was later adapted for μ BLS [48, 49].

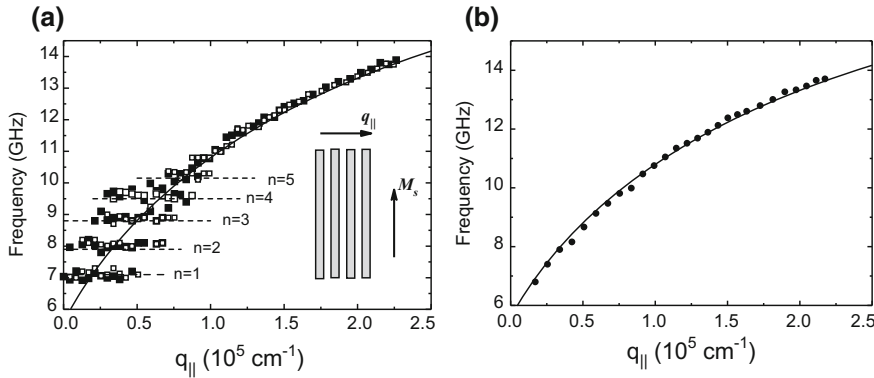


Fig. 10.4 **a** Magnon dispersion curves obtained for an array of permalloy stripes with a stripe thickness of 20 nm, a width of 1.8 μm and a separation of 0.7 μm (open symbols) and 2.2 μm (solid symbols) at $H_e = 500$ Oe. The dash horizontal lines indicate the results of calculations with the quantized wave vectors, determined by the quantization numbers n as indicated. **b** The magnon dispersion of a permalloy film with a thickness of 20 nm at $H_e = 500$ Oe. The solid lines in (a) and (b) are the result of calculation based on (10.4)

10.3 Laterally Confined Magnons

10.3.1 *Lateral Quantization of Magnons in Magnetic Stripes*

Mathieu et al. [24] and Jorwick et al. [50] investigated magnons confined in arrays of permalloy stripes and observed several dispersionless magnon modes. By varying the in-plane wave vector q_{\parallel} , oriented perpendicular to the stripes, the corresponding dispersion was obtained as displayed in Fig. 10.4a (cf. with the spectrum of a continuous film in Fig. 10.4b). The spectrum shows a disintegration of the continuous dispersion of an infinite film into several discrete, resonance-like modes with a frequency spacing of about 0.9 GHz. Since no significant dependence on the stripes separation was found, the mode splitting is purely caused by the quantization of the magnons in a single 1D element.

After these two pioneering works, many studies on the magnon lateral quantization has followed [51, 52].

10.3.2 *Edge Magnons*

Until now, we neglected demagnetizing factors and implied that the internal magnetic field is homogeneous. If, however, the field is directed along the width of a stripe, the internal field is strongly inhomogeneous, in particular, it is almost zero close to the edges of the stripes [53, 54]. Magnons in this case are affected not only by the

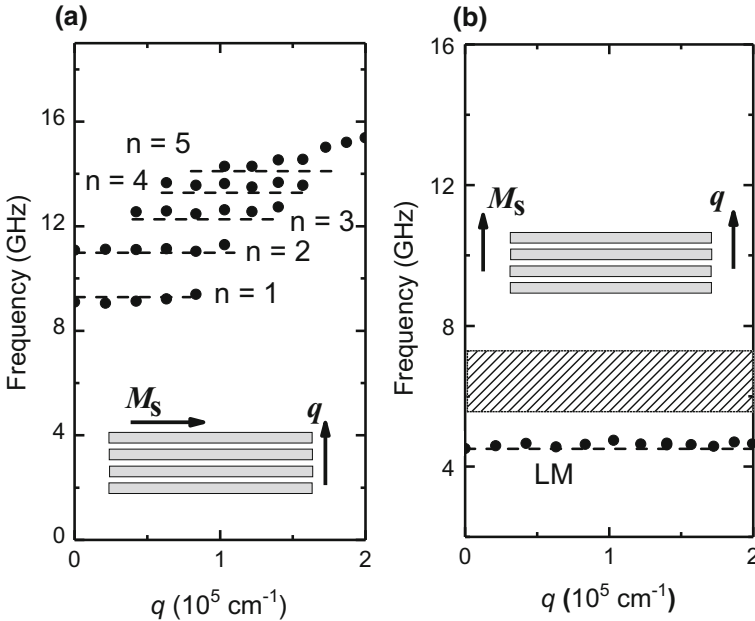


Fig. 10.5 Spin wave dispersion of the stripe array measured at $H_e = 500$ Oe for **a** the DE geometry with the quantization numbers of the quantized modes as indicated and **b** the BV-geometry. In the latter case, the shadowed region represents the band of non-localized modes, whereas LM indicates the localized mode. The dash lines represent the results of calculation

confinement effects, but also by the above inhomogeneity as illustrated by Fig. 10.5 showing the magnon dispersions of the same array of stripes in two geometries: $q \perp M_S$ (DE) and $q \parallel M_S$ (BV). In fact, Fig. 10.5a representing the DE-geometry is very similar to Fig. 10.4a, resembling a typical “staircase” dispersion. In contrast, the dispersion presented in Fig. 10.5b (BV-geometry) contains a broad band in the frequency range 5.5–7.5 GHz. This is due to the fact that the spin-wave group velocity in the BV-geometry is smaller than that in the DE-geometry. Therefore, although the quantized in the k -space w is the same for the both geometries, the frequency separation is in the BV-geometry is much smaller, and many unresolved peaks build the band. Additionally, a separate, low frequency, dispersionless mode with a frequency near 4.6 GHz (indicated as “LM” in Fig. 10.5b) is observed over the entire accessible wave vector range ($q_{\max} = 2.5 \times 10^5 \text{ cm}^{-1}$) with almost constant intensity. This is a direct confirmation of a strong lateral localization of the mode within a region with a width of $\Delta z = 2\pi/q_{\max} = 250 \text{ nm}$. It is clear that a low frequency of the observed mode indicates that the mode is localized near the edges of the elements, where the internal field vanishes [54].

A quantitative analysis of the observed edge mode has been performed in [25]. Its frequency f can be found using a formalism similar to that for the potential well in quantum mechanics:

$$2 \int q(H(z), f) dz + \Delta\psi_1 + \Delta\psi_2 = 2r\pi \quad (10.6)$$

for $r = 1$, whereas $q(H(z), f)$ is found from the magnon dispersion in the film, and $\Delta\psi_1, \Delta\psi_2$ are the phase jumps at the left and right turning points of the well.

The higher order magnon modes with $r > 1$ having their frequencies above 5.3 GHz are not localized under the used experimental conditions. In the experiment, they show the broad band, since the frequency difference between the neighboring modes is below the experimental frequency resolution. Note here, that several localized modes can be observed at higher fields [55].

10.3.3 Magnon Beams in Waveguides

The lateral quantization of magnons and the edge magnon modes reveal themselves also in properties of magnonic waveguides, where two components of the wave vector are of importance: one, continuously varying component along the waveguide and another one, quantized due to the finite width of the waveguide, as illustrated in Fig. 10.6. In fact, if the quantized components q_z^n are known, the spectrum of the waveguide modes can be obtained from the two-dimensional dispersion surface [37] as illustrated in Fig. 10.6a by the curves labeled as DE₁-DE₃, where the number just labels the number of antinodes in the corresponding mode. For the sake of clearness we project these curves onto the frequency- q_y plane, as shown in Fig. 10.6b, keeping in mind that the different curves correspond to different q_z^n . As seen from Fig. 10.6a, the considered modes propagate perpendicular to H_e , i.e. they are analogues of the DE mode in an extended film, their dispersion curves are shifted to lower frequencies with respect to that of the unconfined DE mode. The shift increases with the increase of the mode number, resembling the backward dispersion of the BV-modes (Fig. 10.6a).

The data of Fig. 10.6b show that the dispersion spectrum of waveguide modes supports multimode propagation of magnons at all frequencies above f_0 . For example, for a given excitation frequency f_1 , one simultaneously excites a number of modes with different longitudinal wave vectors q_y . Neglecting magnon attenuation, the spatial distribution of the magnon density can be described as an interference of all these modes:

$$I(y, z) = \left| \sum_n A_n \sin\left(\frac{n\pi}{w}\left(z + \frac{w}{2}\right)\right) \exp(-iq_n y) \right|^2 \quad (10.7)$$

where A_n are the amplitudes of the modes and q_n are their longitudinal wave vectors at the given excitation frequency (see Fig. 10.6b). Figure 10.7 illustrates the beam profiles calculated using (10.7) for different ratios between the amplitudes A_n . If one implies that only the fundamental mode with $n = 1$ (Fig. 10.7a) is present, the intensity distribution is uniform along the direction of the beam propagation, whereas

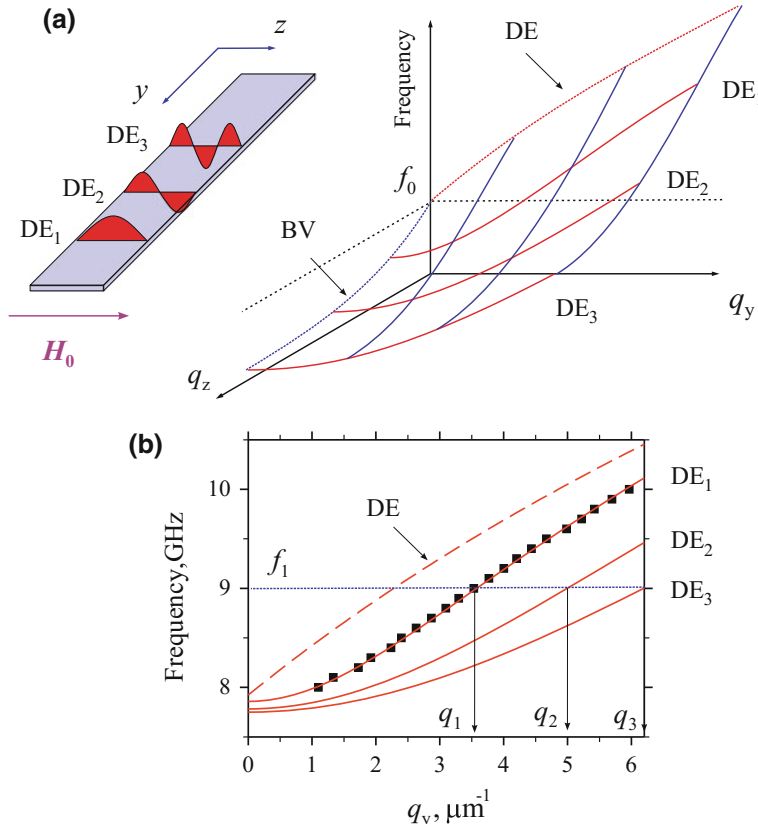


Fig. 10.6 **a** Two-dimensional dispersion spectrum of spin waves in an extended in-plane magnetized ferromagnetic film. Inset shows the geometry of the stripe waveguide and transverse profiles of the dynamic magnetization for normal waveguide modes. **b** Calculated (solid lines) and measured (symbols) dispersion curves for a waveguide with the width $w = 800$ nm and the thickness $d = 20$ nm magnetized by the static field $H_c = 900$ Oe. Dashed curve shows the dispersion curve for Damon-Eshbach mode in an extended film

in the transverse direction it shows a half-sine profile. If the fundamental mode and the mode with $n = 2$ co-propagate (Fig. 10.7b) the beam profile shows a “snake”-like pattern. Moreover, as seen from Fig. 10.7c, if the fundamental mode and the mode with $n = 3$ co-propagate, one observes a periodic spatial beating pattern. In such a beam, the density of magnons is periodically concentrated in the middle of the waveguide. One can call this effect “spin-wave focusing” analogously to light focusing in optics [56]. Figure 10.8a showing a typical measured magnon intensity map for a $2.4 \mu\text{m}$ wide and 36 nm thick Py waveguide clearly demonstrates this effect (compare with Fig. 10.7c). In order to highlight the details of the interference pattern in Fig. 10.8a, the spatial decay of magnons (see solid symbols Fig. 10.8b) is numerically compensated by multiplying the experimental data by $\exp(2y/\xi)$, where

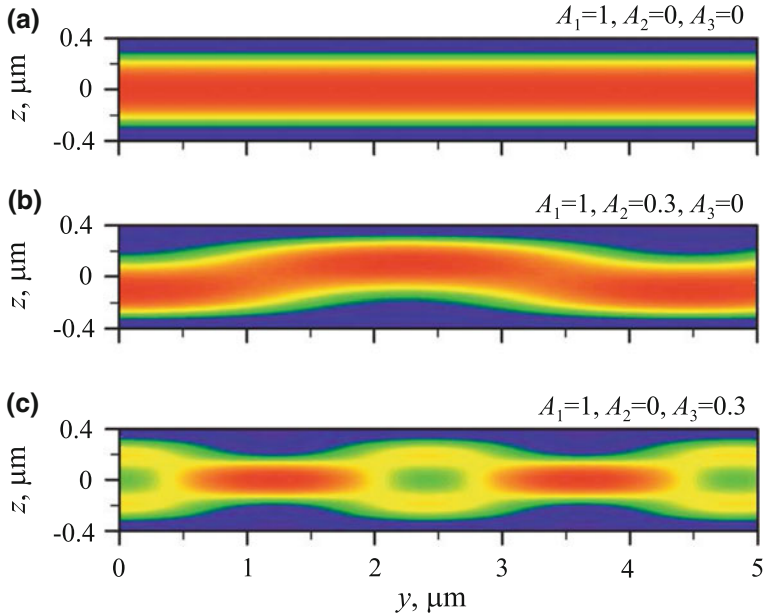


Fig. 10.7 Interference patterns for the three lowest-order waveguide modes calculated for different ratios between their amplitudes, as labeled. Calculations were performed for the waveguide with the width of 800 nm and the thickness of 20 nm magnetized by the field $H_e = 900$ Oe

$\xi = 6.4 \mu\text{m}$ is the magnon decay length, determined directly from the data shown in Fig. 10.8b. Figure 10.8b also illustrates the modulation of the beam width caused by the focusing.

In the above discussion on the normal waveguide modes, we neglected the non-uniformity of the magnetic field inside the waveguide caused by the demagnetization effects, since the waveguide magnetized along its axis was considered. Following to [53], the internal field in a magnetic stripe magnetized perpendicular to its axis is as follows:

$$H_i(z) = H_e - \frac{4\pi M_s}{\pi} \left[\text{atan} \left(\frac{d}{2z+w} \right) - \text{atan} \left(\frac{d}{2z-w} \right) \right] \quad (10.8)$$

as illustrated Fig. 10.9a. Figure 10.9b shows decay-compensated magnon intensity maps obtained using an excitation signal at the frequencies below the FMR frequency $f_0 = 10$ GHz for the used experimental conditions. The data of Fig. 10.9b clearly indicate that magnons do not occupy the entire cross-section of the waveguide. Contrary, they build two narrow beams with the submicrometer width frequency-dependent spatial positions, as predicted by the simple qualitative model. Further analysis (see Fig. 10.9c) demonstrates that, for the applied frequencies, the widths

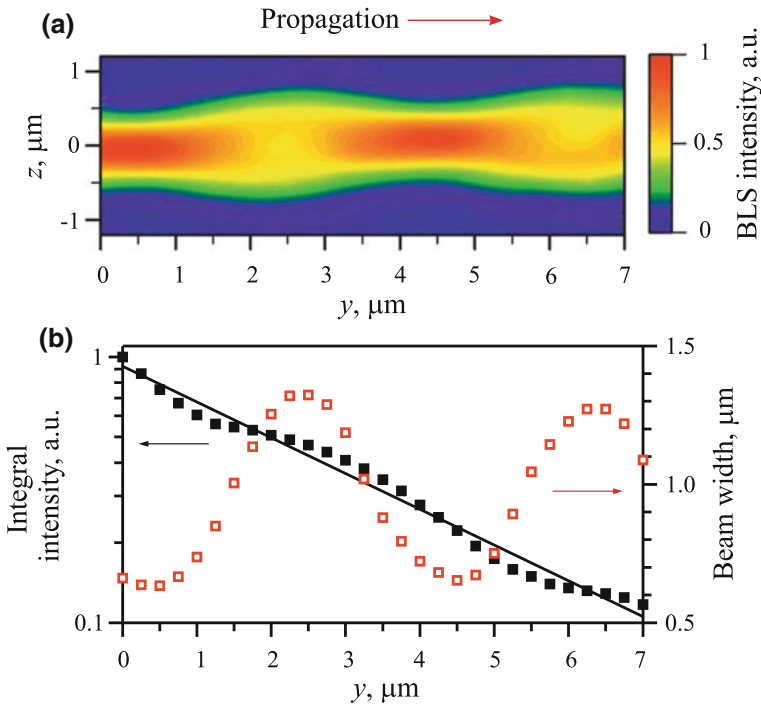


Fig. 10.8 **a** Measured map of the magnon intensity for a waveguide with the width of $2.4 \mu\text{m}$ and the thickness of 36 nm magnetized by the field of 900 Oe . Excitation frequency is 9.4 GHz . Spatial decay of spin waves is numerically compensated. **b** Solid symbols—BLS intensity integrated across the transverse waveguide section versus the propagation coordinate in the log-linear scale. Line is the exponential fit to the experimental data. Open symbols—transverse width of the magnon beam measured at one half of the maximum intensity versus the propagation coordinate

of the beams vary in the range $400\text{--}500 \text{ nm}$. Contrarily, the distance between their centers monotonously decreases with increasing frequency from 1.4 to $0.8 \mu\text{m}$.

10.3.4 Control and Manipulation with Magnon Beams

One of the great advantages of magnon beams for implementation of signal-processing devices is the possibility to control the propagation of the beams by the applied magnetic field and on this way to manipulate their propagation. The implementation of this mechanism on the macroscopic scale requires creation of magnetic fields in large volumes making this approach extremely space- and power-consuming. The downscaling of spin-wave devices provides a route for overcoming this drawback, since, in microscopic systems, a sufficiently large control magnetic field can be created by using electric currents [49]. However, a more elegant way to

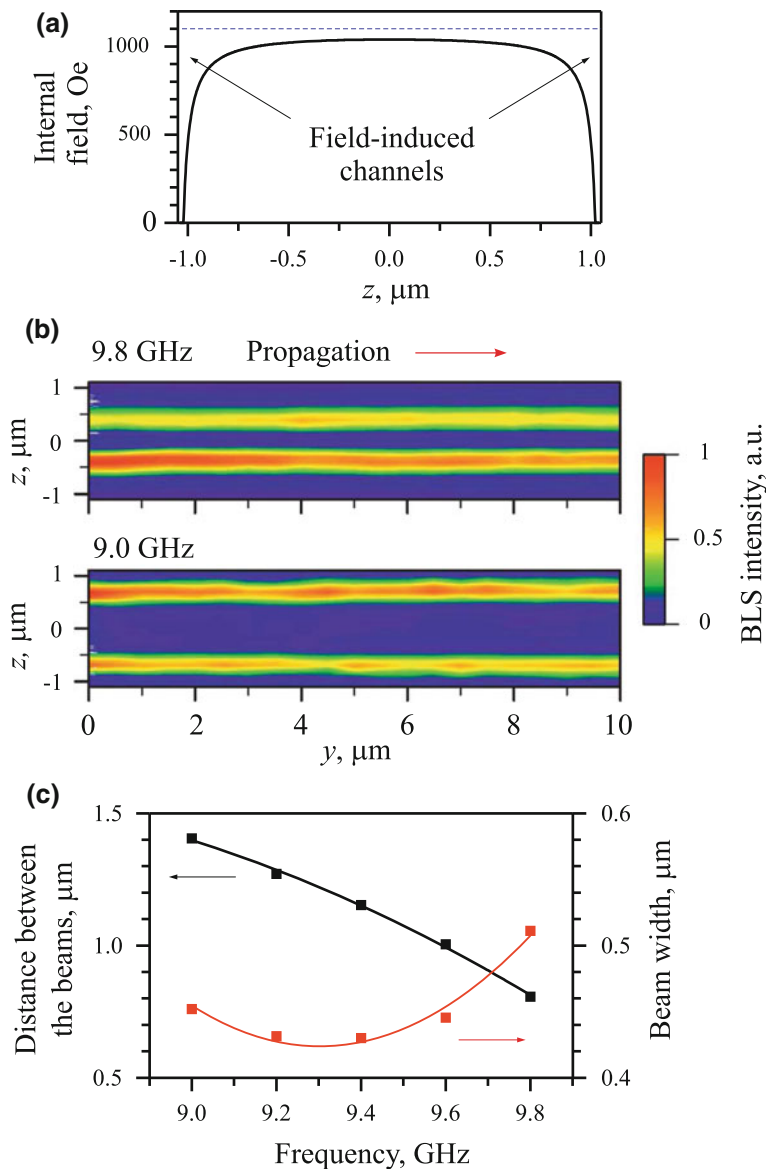


Fig. 10.9 **a** Calculated distribution of the internal static magnetic field across the width of a waveguide with the width of $2.1 \mu\text{m}$ and the thickness of 20 nm magnetized by the static field of 1100 Oe . Horizontal dashed line marks the value of the external magnetic field. **b** Measured maps of the magnon intensity for two excitation frequencies, as labeled. Spatial decay of spin waves is numerically compensated. **c** Distance between the centers of the magnon beams and their transverse width measured at one half of the maximum intensity versus the magnon frequency

control magnonic beams is to manipulate the internal field using the shape anisotropy of the waveguide by varying the ratio between the width and the thickness of the waveguide [57, 58].

Figure 10.10a illustrates a waveguide with the varying width and a constant thickness of $d = 36$ nm. The width w varies from 1.3 to 2.4 μm over a transition region with the length L , resulting, according to (10.8), in a spatial variation of the internal field. The field changes from 870 Oe in the narrow part of the waveguide to 950 Oe in its wide part (Fig. 10.10b). This variation, in its turn shifts the dispersion curves of the fundamental center waveguide mode in the two parts by about 500 MHz (Fig. 10.10c). For the excitation frequency positioned between the cut-off frequencies of the two parts of the waveguide from 8.7 to 9.2 GHz (f_1 in Fig. 10.10c), the center mode propagating in the narrow part of the waveguide cannot pass into the wide part. Instead, it is transformed into the edge mode, whose frequency range is located below that of the center modes. Figure 10.10d illustrates this transformation. It shows two magnon density maps measured for the excitation frequencies of 8.7 and 9.1 GHz, clearly demonstrating the conversion of the center mode into two narrow magnon beams with frequency-dependent spatial separation. Since the two beams propagate in the separate channels induced by the internal field, they are independent from each other. Therefore, the observed transformation can be used for implementation of a magnonic splitter.

When the frequency of magnons is larger than cut-off frequencies in both parts of the waveguide (f_2 in Fig. 10.10c), in the waveguides with the long transition region ($L = 3 \mu\text{m}$ in Fig. 10.10e), the propagation of magnons from the narrow to the wide part is quasi-adiabatic. It is only accompanied by the increase in the wavelength, while the spatial structure of the magnon beam remains unchanged. However, in systems with shorter transitions (e.g., $L = 1 \mu\text{m}$ in Fig. 10.10e), the propagation is accompanied by an appearance of an intensity pattern with a non-trivial topology. This fact is apparently connected with interference of different propagating modes in a strongly non-uniform internal field.

10.4 Magnons and the Spin Transfer Torque Effect

Since the first demonstration [27, 29–31, 59, 60] that spin-polarized electric currents can excite magnetization dynamics due to the spin transfer torque (STT) effect [8, 9], a lot of studies were performed on the dynamic spin torque phenomena. The ability of dc currents to control magnetization precession with microwave frequencies is very important for the generation of microwave signals [61–65] and propagating magnons [18, 32, 66–68] in magnetic nanocircuits. Local generation of magnons using electronic signals is of great importance for nanomagnonics, where propagating magnons serve as the carriers for the transmission and processing of signals, pattern recognition on nanoscale, and logic operations [5–7].

Initially, STT phenomena have been studied in 0D-nanodevices based on the metallic magnetic structures, where STT is induced by the electric current flowing

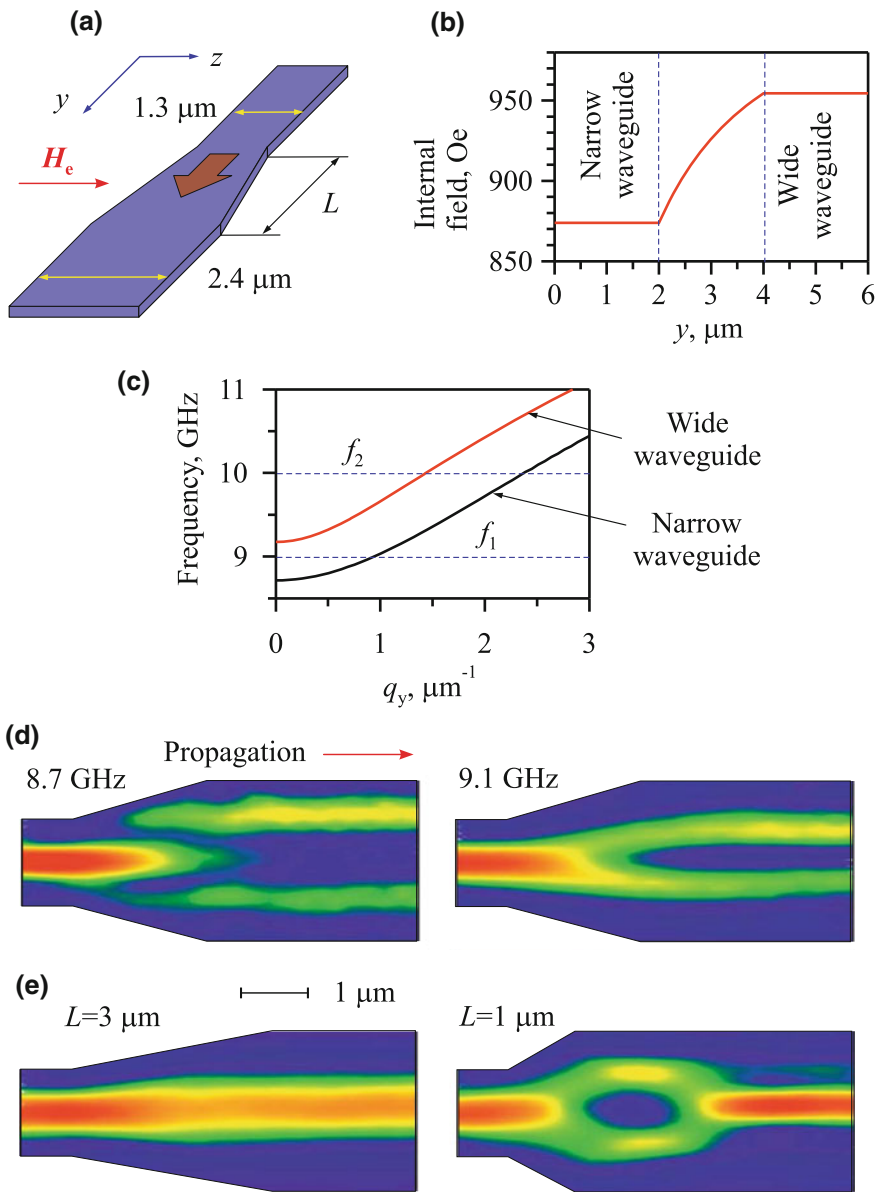


Fig. 10.10 **a** Schematic of a magnon waveguide with a varying width. **b** Calculated distribution of the internal static magnetic field in the section along the axis of the waveguide with the thickness of 36 nm and the geometrical parameters given in (a). The external static magnetic field $H_e = 1000$ Oe. **c** Calculated dispersion curves for the fundamental center waveguide mode in the wide and the narrow parts of the waveguide. **d** Maps of the magnon intensity measured at the excitation frequencies of 8.7 and 9.1 GHz, as labeled. Width of the transition region $L = 2 \mu\text{m}$. **e** Maps of the magnon intensity measured at the excitation frequency of 9.7 GHz in waveguides with $L = 3$ and $1 \mu\text{m}$, as labeled. In (d) and (e) the spatial decay of spin waves is numerically compensated

through a multilayer consisting of a “fixed” magnetic spin-polarizer and the “free” active magnetic layer, separated by a non-magnetic spacer. In these structures, the electric charges must cross the active magnetic layer to excite its magnetization dynamics. To enable current flow through the active magnetic layers, STT devices operating with spin-polarized electric current require that current-carrying electrodes are placed both on top and on the bottom of the spin valve. To keep the electric current below a reasonable limit, the devices should have sub-100-nm dimensions in both lateral directions.

One can avoid these shortcomings using pure spin currents—flows of spin without directional transfer of electrical charge. Since in this case, the electrical current does not flow through the active magnetic layer, the Joule heating and electromigration effects are reduced. Finally, one can use insulating magnetic materials such as Yttrium Iron Garnet (YIG) [14, 69] for implementation of STT devices.

Among physical mechanisms used to create pure spin currents, one should mention the spin-Hall effect (SHE) [11–13, 70], the nonlocal spin injection (NLSI) [71, 72], the spin Seebeck effect [73, 74], and the Rashba–Edelstein effect [75, 76]. Here we will focus on SHE and NLSI, since they effectively can excite coherent magnetization oscillations and magnonic beams. SHE is usually large in non-magnetic materials with strong spin-orbit interaction, such as Pt, W and Ta. By passing an electrical current through these materials a spin current in the direction perpendicular to the charge flow is produced [13, 70]. If a bilayer containing a SHE layer and an adjacent ferromagnetic film, the spin current flows through the interface into the ferromagnet and exerts STT on its magnetization [77]. Important to notice that SHE can exert STT on ferromagnets over extended areas. Indeed, in such bilayer the in-plane current flows through the bilayer, SHE injects the spin current over the entire area of the sample, which can reach macroscopic sizes [77]. One can use this feature to control the spatial decay of propagating magnons in waveguides, if the natural magnetic damping is partially compensated by STT.

The effect of pure spin current on the magnetization is similar to that of spin-polarized electric currents. Both can be described by the Slonczewski’s STT term [10] included into the Landau–Lifshitz–Gilbert equation:

$$\frac{d\mathbf{M}}{dt} = -\gamma \mathbf{M} \times \mathbf{H}_{\text{eff}} + \frac{\alpha}{M_s} \mathbf{M} \times \frac{d\mathbf{M}}{dt} + \frac{\beta}{M_s^2} \mathbf{M} \times (\mathbf{M} \times \hat{\mathbf{s}}) \quad (10.9)$$

where α is the Gilbert damping parameter, β is the strength of STT, proportional to the spin current density, and $\hat{\mathbf{s}}$ is the unit vector in the direction of the spin-current polarization. All other notations are similar to those of (10.1) and (10.2). In fact, (10.9) is an extension of (10.1), which takes into account magnetic damping and the STT effect. Within this model, the third term is mathematically very similar to the second one. Correspondingly, one expects that spin current with an appropriate polarization can reduce magnetic damping of propagating spin waves. It should be mentioned, that an additional, a field-like torque also follows from the theory (see, e.g., [61] and references herein). However, this torque is responsible for modification of the spin-

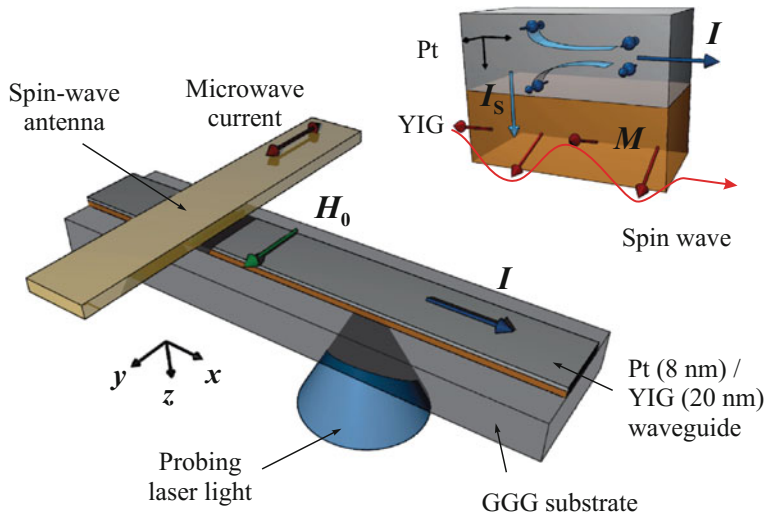


Fig. 10.11 Schematic of the experiment on compensation of the magnon damping by pure spin current. Inset illustrates the generation of the pure spin current by the spin-Hall effect

wave frequencies. We, in contrast, are mainly interested in damping compensation of spin waves. Therefore, we neglect this term in our discussion.

10.4.1 Spin Transfer Torque Effect and Damping Compensation

The above compensation has been recently demonstrated experimentally [78]. Figure 10.11 shows the schematic of the test devices. They are based on a 20 nm thick YIG film grown on Gadolinium Gallium Garnet (GGG) (111) substrate. The film is covered by an 8 nm thick layer of Pt. The YIG/Pt bilayer is patterned into a waveguide with the width of 1 μm . The waveguide is magnetized by the static magnetic field $H_0 = 1000$ Oe applied along its width. A dc electrical current I flowing in the plane of the Pt film is converted by the SHE into the transverse spin accumulation (see inset in Fig. 10.11). The associated pure spin current I_S is injected into the YIG film resulting in a spin-transfer torque on its magnetization.

The magnon beam was excited by applying a microwave current to an inductive antenna. The beam was mapped using μ BLS by rastering the probing laser spot over the surface of the waveguide. Figure 10.12a shows a representative map of the BLS intensity, proportional to the local density in the magnon beam. As seen from these data, the magnon beam propagates along the waveguide nearly uniformly without changing its transverse profile (inset in Fig. 10.12a), which is a clear signature of the single-mode propagation regime caused by the strong separation of the transverse

modes in a narrow waveguide. The magnon density of the beam decreases by only 60% over the propagation path of 10 μm . To characterize the decay length ξ of the beam and its dependence on the current, we plot in Fig. 10.12b the dependences of the magnon density on the propagation coordinate obtained for different dc currents in the Pt layer. These data show that magnons in the waveguide experience well-defined exponential decay (note the logarithmic vertical scale) $\sim \exp(-2y/\xi)$. As seen from the Figure, ξ strongly increases with increasing dc current, as expected for the effect of spin current on the effective magnetic damping.

Figure 10.12c summarizes the results of the spatially-resolved measurements. The decay length monotonously increases with the increasing $I < I_C$ and then shows an abrupt decrease at $I > I_C$ in contradiction to naive expectations that for large values of I the magnetic damping should be overcompensated by the spin current, and the propagating spin wave should be amplified. This experimental observation can be attributed to the strong scattering of the propagating magnons from large-amplitude current-induced magnetic fluctuations.

10.4.2 Spin-Torque- and Spin-Hall- Nanooscillators

The STT effect discussed above is of particular importance for magnetic systems fully confined in all three directions. A pure spin current, injected into a ferromagnetic layer through a nanocontact exerts a torque on the magnetization, leading to a strongly localized microwave-frequency precession of magnetization, which can be considered as a 0D magnonic mode. This phenomenon can serve as a basis for the development of tunable nanometer-size microwave oscillators, the so-called spin-torque nano-oscillators (STNO) [27, 29–31, 59, 60]. Since the spin precession excited in a magnetic nanocontact is usually surrounded by a 2D film or is coupled to a 1D waveguide, it may radiate propagating magnons. All these makes the phenomena connected with the STT-driven magnetization dynamics multifarious and intriguing.

Let us consider an STNO shown in Fig. 10.13 [32]. The device is formed by a nanocontact on an extended Permalloy (Py) film. The nanocontact is shaped as an elliptical nanopillar formed by the nanopatterned polarizing $\text{Co}_{70}\text{Fe}_{30}$ layer and a Cu spacer. A dc current I flowing from the polarizer to the Py film induces local magnetization oscillations in this film. Figure 10.14 shows density maps of magnons emitted by STNO at $I = 5$ mA, measured for different in-plane directions of the applied field \mathbf{H}_e using μBLS . As seen in Fig. 10.14, the emission mainly occurs in the direction perpendicular to the in-plane field, regardless of its orientation with a decay length of the emitted magnons below 500 nm. One sees in Fig. 10.14d an essential difference between the intensity of spin waves along two opposite directions. This fact is connected with the influence of the circular Oersted field of the current flowing through the nanocontact. In fact, on one side of the nanocontact the Oersted is parallel to the uniform applied field \mathbf{H}_e , whereas on the opposite side of the nanocontact it is antiparallel to \mathbf{H}_e . Further studies [18, 66, 79] have shown that the magnons emitted

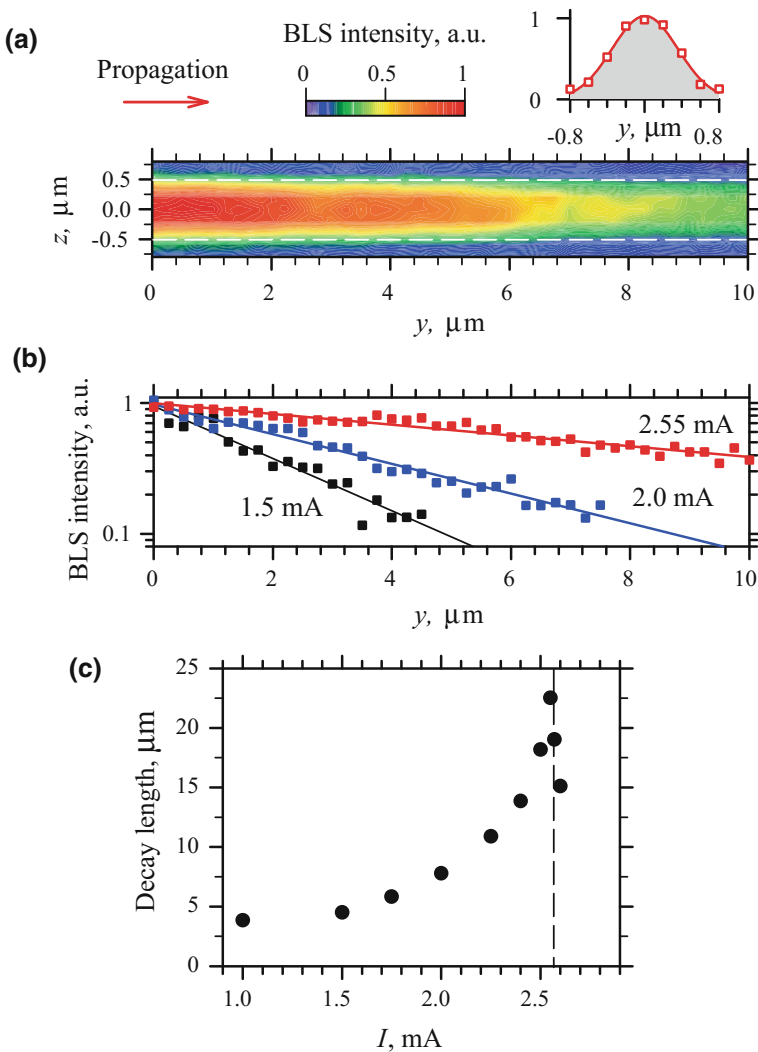


Fig. 10.12 **a** Normalized spatial intensity map of the propagating spin wave excited by the antenna. The map was recorded for $I = 2.55$ mA. The mapping was performed by rastering the probing spot over the area 1.6×10 μm, which is larger than the waveguide width of 1 μm. Dashed lines show the edges of the waveguide. Inset shows the transverse profile of the magnon intensity. **b** Dependences of the magnon intensity on the propagation coordinate for different currents, as labeled, in the log-linear scale. Lines show the exponential fit of the experimental data. **c** Current dependences of the decay length. Vertical dashed line marks I_C . The data were obtained at $H_e = 1000$ Oe

in these experiments have an evanescence nature, since their frequency were slightly below the magnon spectrum of the surrounding Py film.

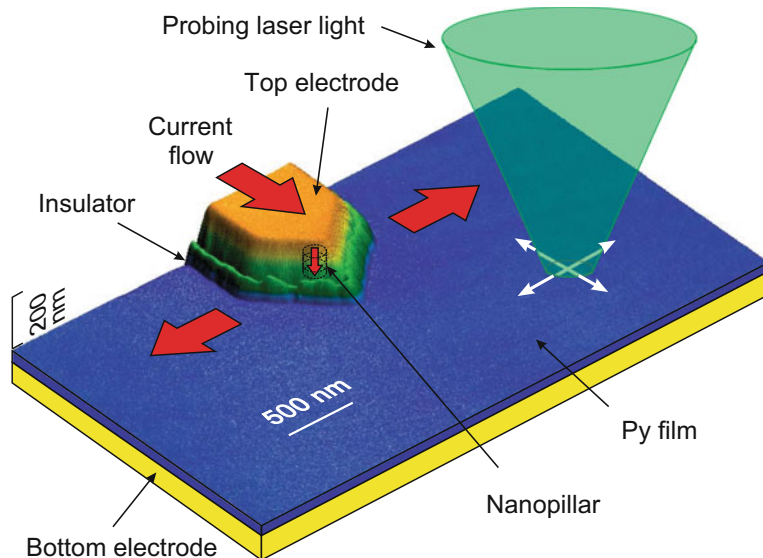


Fig. 10.13 Schematic of the studied STNO with an AFM image superimposed. The devices consist of an extended 6-nm thick Permalloy free layer and an elliptical nanopillar formed by a 9-nm thick Co₇₀Fe₃₀ polarizing layer and a 3-nm thick Cu spacer. The nanopillar is located close to the edge of the top electrode enabling optical access to the free layer for BLS microscopy. Magnetic precession in the device is induced by dc current flowing from the polarizer to the free layer. The spatially resolved detection of spin waves is accomplished by focusing the probing laser light into a 250 nm spot, which is rastered over the surface of the Py film

As demonstrated in Fig. 10.15, microwave parametric pumping can be used as a mechanism for the transfer of the generated microwave energy into the desirable spectral range above the FMR frequency [79]. In this study, an additional microwave current with its frequency slightly above the double frequency of the auto-emitted waves was applied to the nanocontact. Due to parametric effects (see [79] for details) an additional spin wave with a higher frequency and a larger decay length was formed. This approach enables an increase of the decay length of 540 nm for the auto-emission to 940 nm for the pumping-induced emission. Moreover, the phenomenon of the pumping-induced emission does not disturb the unique directionality found for the emission in the auto-oscillation regime, as illustrated by Fig. 10.15.

Another possibility to inject angular momentum into a magnetic system is utilization of pure spin currents. As it has been already mentioned above, pure spin current has numerous advantages compared to spin-polarized electric current as far as the excitation of large-amplitude 0D magnon modes is concerned. A complete compensation of damping by the spin current appears to be a straightforward extension of the damping reduction. However, as the compensation point is approached, additional nonlinear damping emerges due to the coupling between different dynamical modes enhanced simultaneously by the spin current, preventing the onset of

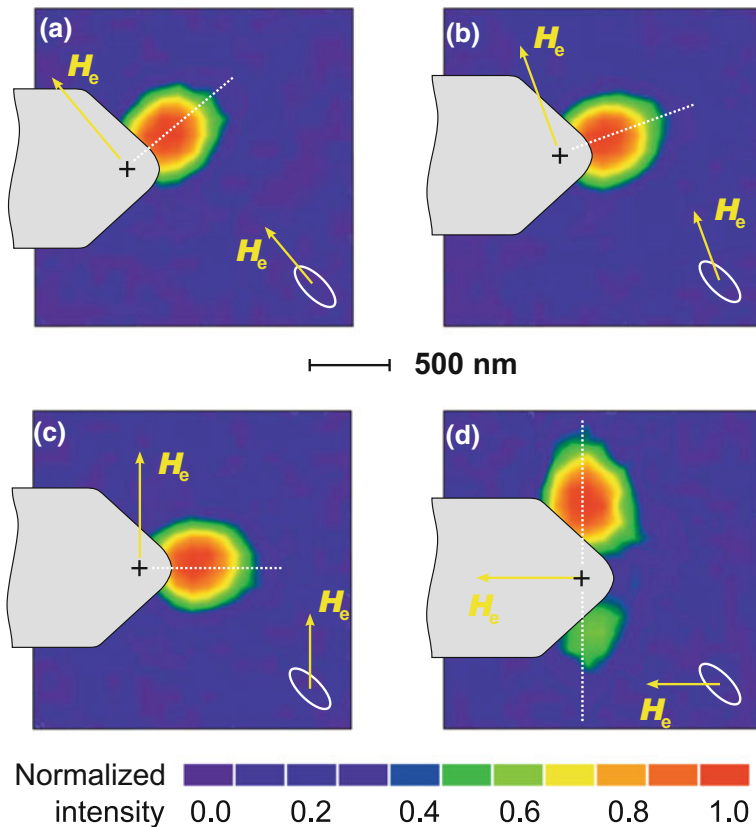


Fig. 10.14 Normalized color-coded intensity maps of magnons emitted by the STNO, recorded at different angles φ between the in-plane magnetic field $H_e = 900$ Oe and the easy axis of the elliptical nanopillar: **a** $\varphi = 5^\circ$, **b** $\varphi = 25^\circ$, **c** $\varphi = 45^\circ$, **d** $\varphi = -45^\circ$. The bias current is $I = 5$ mA. The schematic of the top electrode is superimposed on each map, with a cross indicating the location of the nanowire. The intensity maps acquired at $I = 0$ were subtracted to eliminate the contribution from the thermal magnons. Arrows show the direction of the static magnetic field, and the dashed lines indicate the direction of the magnon emission

auto-oscillation. Since magnon-magnon scattering rates are proportional to the populations of the corresponding modes, detrimental effects of the mode coupling can be avoided by selectively suppressing all the modes, except for the ones that can be expected to auto-oscillate. To achieve selective suppression, in the described experiments, the frequency-dependent damping caused by the magnon radiation was used. To take advantage of this radiative damping, the spin current was locally injected into an extended magnetic film. In fact, the local spin current enhances a large number of magnon modes, but those having higher frequencies, and, consequently, higher group velocities, quickly escape from the active region, which results in their efficient suppression by the radiation losses.

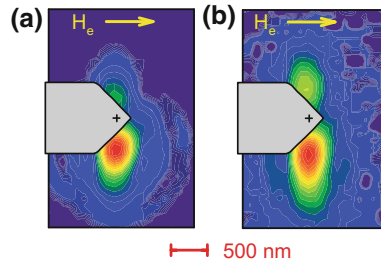


Fig. 10.15 Pseudocolor spatial intensity maps of the emitted magnons, acquired at $I = 5$ mA. A schematic of the top electrode and a cross indicating the location of the nanocontact is superimposed on each map. **a** Magnon auto-emission, in the absence of the external pumping microwaves. **b** Magnon emission under influence of parametric pumping. Note an extended magnon propagation area for **(b)**

The scheme of the experiment with pure spin current is shown in Fig. 10.16a [33]. The studied device is formed by a bilayer of a 8 nm thick film of Pt and a 5 nm thick film of Py patterned into a disk with a diameter of 4 μ m. Two 150 nm thick Au electrodes with sharp points separated by a 100 nm wide gap are placed on top of the bilayer, forming an in-plane point contact. Since the sheet resistance of the Au electrodes is much smaller than that of the bilayer, the electrical current induced by voltage between the electrodes is strongly localized in the gap, as illustrated in Fig. 10.16b. Due to the spin-Hall effect, the electric current creates a pure spin current flowing into Py, which exerts STT on its magnetization. As a result, the damping is compensated, and the magnon modes are enhanced.

Figure 10.17 shows the BLS spectra obtained with the probing spot positioned in the center of the gap between the electrodes, at different values of the dc current I . At $I = 0$, the BLS spectrum exhibits a broad peak corresponding to incoherent thermal magnetization fluctuations in the Py film (Fig. 10.17a). As this thermal peak grows with increasing current, its rising front becomes increasingly sharper than the trailing front, consistent with the preferential enhancement of the low-frequency modes. Analysis of the dependence of the frequency-integrated BLS intensity on current (Fig. 10.17b) shows that the intensity of magnetic fluctuations diverges as the current approaches a critical value of $I_c \approx 16.1$ mA. In contrast to systems driven by spatially uniform spin currents [80], the intensity of fluctuations does not saturate as the current approaches I_c , indicating that the processes preventing the onset of auto-oscillations are avoided.

At $I \geq I_c$, a new peak highlighted in Fig. 10.17a by shadowing appears in the BLS spectrum below the thermal peak. Since this peak is not present in the thermal fluctuation spectrum, we can conclude that it corresponds to a new auto-oscillation mode that does not exist at $I < I_c$. The peak rapidly grows and then saturates above 16.3 mA (Fig. 10.17c, d). Comparing the spectra for $I = 16.1$ mA and 16.3 mA, we see that the onset of auto-oscillations is accompanied by a decrease in the intensity of thermal fluctuations, suggesting that the energy of the spin current is mainly chan-

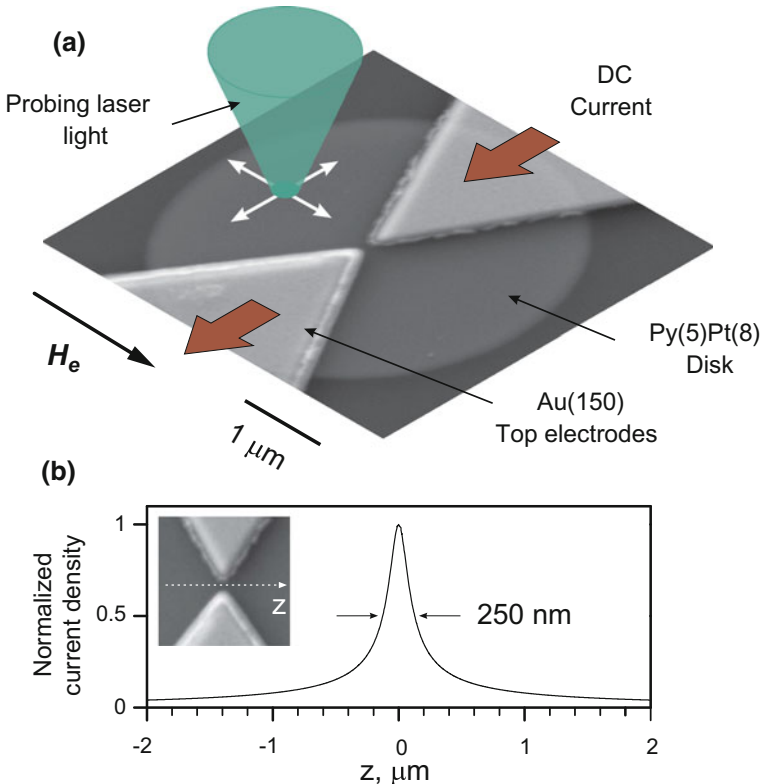


Fig. 10.16 **a** Scanning-electron microscopy image of the test spin-Hall nano-oscillator. The device consists of a 4 μm diameter disk formed by a 8 nm-thick Pt on the bottom and a 5 nm-thick Py layer on top, covered by two pointed Au(150 nm) electrodes separated by a 100 nm gap. **b** Normalized calculated distribution of current through the section of the device shown in the inset by a dashed line

nelled into the auto-oscillation mode. Note that the linewidth in the spectra shown in Fig. 10.17a, c is determined by the spectral resolution of our optical technique under usual conditions. Additional measurements at our instrument's ultimate spectral resolution of 60 MHz show that the actual linewidth in the saturated regime is below this value, suggesting a high degree of coherence of the observed auto-oscillation mode.

The frequency of the auto-oscillation peak monotonically decreases with increasing I (Fig. 10.17d). We note that the generated frequency is significantly below the frequencies of magnetic fluctuations even at the onset of auto-oscillations. We draw three important conclusions based on this observation. First, the auto-oscillation mode does not belong to the linear magnon spectrum. Second, this mode is formed abruptly at the onset current, and not by gradual reduction of frequency from the magnon spectrum due to the red nonlinear frequency shift. Third, since the energy

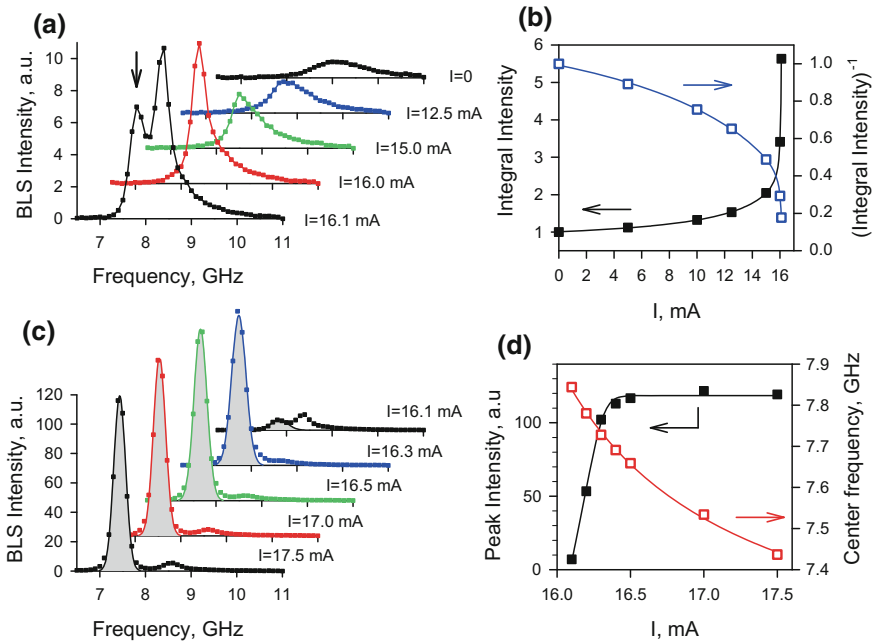


Fig. 10.17 **a** BLS spectra of thermal fluctuation amplified by the spin current at currents below the onset of auto-oscillation. **b** Integral intensity of amplified thermal fluctuations and its inverse versus current. Both dependencies are normalized by their values at $I = 0$. **c** BLS spectra of the magnetization auto-oscillation driven by the spin current. Filled areas are the results of fitting by the Gaussian function. Note, that the spectral widths are determined by the resolution of the BLS setup. **d** The intensity and the center frequency of the auto-oscillation peak versus current. Curves are guides for the eye

can be radiated only by propagating magnons and there are no available magnon spectral states at the auto-oscillation frequency, the auto-oscillation mode is not influenced by the radiation losses.

To determine the spatial profile of the auto-oscillation mode, we performed two-dimensional mapping of the auto-oscillation mode using μ BLS, as shown in Fig. 10.18. The auto-oscillations are localized in a very small area in the gap between the electrodes with the estimated size of the auto-oscillation region being less than 100 nm, significantly smaller than the characteristic size of the current localization (Fig. 10.16b). Therefore, we conclude that the auto-oscillation area is determined not by the spatial localization of the driving current, but by the nonlinear self-localization processes defining the geometry of a standing spin-wave “bullet” [81]. We emphasize that the observed quick saturation of the intensity of the auto-oscillation peak above the onset and its monotonic red frequency shift are the intrinsic characteristics of the “bullet” mode. Only one “bullet” mode exists at the frequency of the auto-oscillations and this frequency is well separated from the continuous spectrum of non-localized

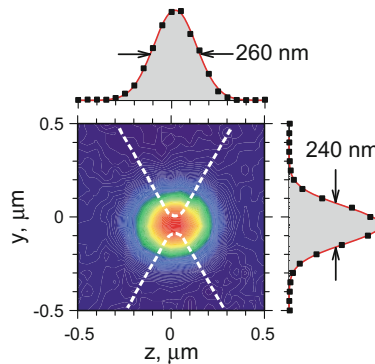


Fig. 10.18 Normalized color-coded map of the measured BLS intensity over the auto-oscillation area, and two orthogonal sections through its center. Symbols are the experimental data, and filled areas under solid curves are the results of fitting by a Gaussian function. Dashed lines on the map show the contours of the top electrodes. The data were recorded at $I = 16.2$ mA

spin waves. Therefore, our findings provide strong evidence that auto-oscillations involve only a single mode in the studied system.

10.4.3 STNO as Sources of Magnons

Although STNOs can excite magnons, it is, in general, difficult to achieve frequency matching of STNO with the propagating magnons, since the large-amplitude magnon modes in STNOs are frequency shifted due to nonlinear effects with respect to characteristic frequencies of propagating magnons. However, if one uses a magnonic waveguide of a particular geometry as described below, efficient matching between such waveguides and STNOs can be achieved. This matching is realized by taking advantage of the dipolar magnetic field within the waveguide, which acts on propagating magnon modes [18].

Figure 10.19a shows the layout of the studied device. A point-contact STNO comprises a multilayer Cu(4)/Co₇₀Fe₃₀(4)/Au(150) fabricated on top of an extended 5 nm-thick Permalloy (Py) film. Additionally, the device incorporates a 5 nm thick and 200 nm wide Co₇₀Fe₃₀ nanostripe below the Py film. The device is magnetized by a static magnetic field $H_e = 800\text{--}1200$ Oe applied in the plane of the Py film perpendicular to the CoFe nanostripe.

Figure 10.19b shows the characteristics of the oscillation of STNO determined by the standard electronic spectroscopy measurements. Above the onset current of about 3.5 mA, both the amplitude and the frequency of the auto-oscillations exhibit a smooth dependence on current, indicating a single-mode operation of the STNO. Correspondingly, Fig. 10.19c shows representative BLS spectra recorded with the probing laser spot positioned above the CoFe nanostripe. While propagating magnons

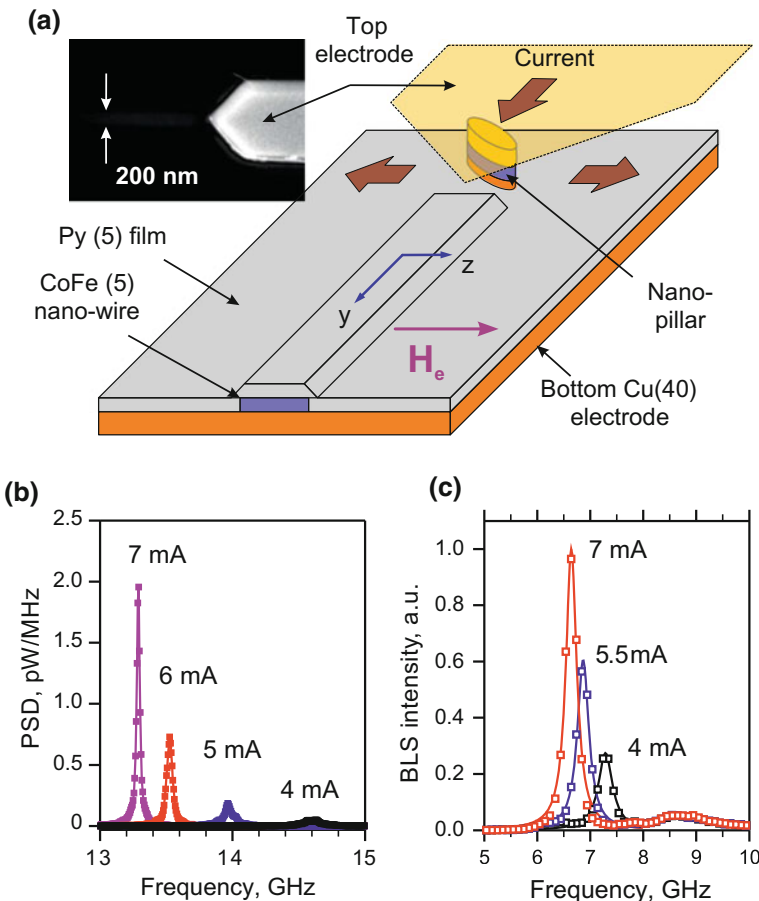


Fig. 10.19 **a** Layout of the studied STNO with an incorporated waveguide. Inset: SEM micrograph of the device. H_e is the static magnetic field. Numbers in parentheses indicate the thicknesses of the layers in nanometres. **b** Spectra of the current-induced oscillations of the STNO measured by a spectrum analyzer at different driving dc currents, as indicated. **c** BLS spectra recorded at different driving currents measured by positioning the probing laser spot on the nano-waveguide. Note, that the spectral widths are determined by the resolution of the BLS setup

are clearly detected above the CoFe nanostripe, no signals were detected away from the nanostripe. This observation indicates that the STNO can efficiently generate magnons, propagating along the CoFe nanostripe, but a radiation of magnons into the free Py film is inefficient.

To understand this phenomenon, one has to consider the effects of the dipolar field of the CoFe nanostripe on the internal field in the magnetic layers. Similar to magnonic waveguides, the internal field is significantly reduced in the magnetic film in the region of the CoFe nanostripe, as compared to that away from the nanostripe.

The reduction of the internal field results in lowering of the local magnon spectrum, creating a one-dimensional channel with allowed magnon frequencies below the bottom of the spectrum in the free Py film. Low-frequency magnons excited by STNO are directionally guided along the CoFe nanostripe, since there are no states available at these frequencies in the free Py film.

The measured propagation characteristics of magnons in the nano-waveguide are illustrated in Fig. 10.20. Figure 10.20a shows the normalized spatial map of the BLS intensity, which is proportional to the local magnon intensity. The map was recorded at a constant dc current of 5 mA by rastering the probing laser spot over a 1.6 μm by 1.6 μm area with the step size of 100 nm. To highlight the transverse profile of the propagating wave, the spatial decay in the direction of propagation was compensated by normalizing the signal with the integral over the transverse section of the map (along the z -coordinate). The map of Fig. 10.20a clearly shows that the spin wave energy is concentrated entirely in the nano-waveguide, i.e. magnons are guided by the field-induced channel without noticeable losses associated with the radiation of energy into the surrounding free Py film.

The BLS intensity integrated over the transverse section of the map exhibits a simple exponential spatial decay in the direction of propagation (shown on the log scale in Fig. 10.20b). By fitting the data of Fig. 10.20b with the function $\exp(-2y/\xi)$, we obtain $\xi = 1.3 \mu\text{m}$. We note that this value is close to the best spin-wave propagation characteristics obtained in low-loss Py films with comparable thickness, despite the higher dynamical losses expected due to the stronger damping in CoFe.

By analyzing transverse cross-sections of the BLS intensity map (Fig. 10.20c), we determine the transverse full width at half maximum w of the spin wave intensity distribution for different positions along the waveguide. The obtained value $w = 320 \text{ nm}$ is independent of the propagation coordinate (Fig. 10.20d), which confirms that the magnons are efficiently localized in the waveguide without spreading out. We note that the measured spatial profile (Fig. 10.20c) represents a convolution of the actual profile of the magnon intensity with the distribution of intensity in the diffraction-limited probing light spot whose estimated diameter is 250 nm. The value $w = 320 \text{ nm}$ is therefore in a reasonable agreement with the measured waveguide width of 200 nm (inset in Fig. 10.19a). It is important to emphasize here that although Fig. 10.20 clearly demonstrates that spin waves are propagating within the waveguide only, it has no information about modes propagating in the waveguide, since the width of the waveguide is smaller than the diameter of the optical beam. However, micromagnetic simulations indicate that the nanooscillator excites the low-frequency edge modes of the waveguide,

10.5 Bose-Einstein Condensation Magnons

Bose-Einstein condensation (BEC), predicted by Einstein [82] in 1925, is one of the most intriguing quantum phenomena, since it allows one to observe coherent

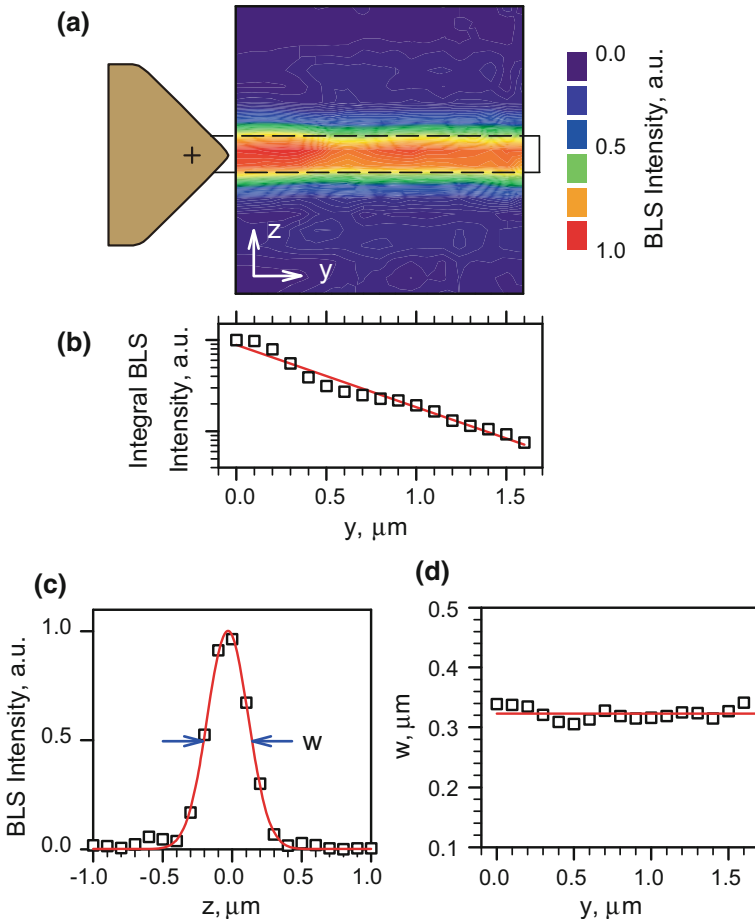


Fig. 10.20 **a** Normalized decay-compensated spatial map of the magnon intensity. The positions of the top device electrode and the CoFe nanostripe are schematically shown. **b** Measured dependence of the integral magnon intensity on the propagation coordinate (symbols), on the log-linear scale. The line shows the result of the fitting of the experimental data by the exponential function. **c** Distribution of the magnon intensity in the section transverse to the nano-waveguide. Symbols are experimental data, curve is a fit by the Gaussian function. w is the full width at half maximum of the transverse intensity profile. **d** Dependence of w on the propagation coordinate. Symbols are experimental data, horizontal line is the mean value

quantum effects on the macroscopic scale (for review see, e.g., [83]). Although BEC was experimentally observed for different equilibrium (liquid He^4 [84, 85], ultra-cold atoms [86, 87], magnetic triplons [88]) as well as non-equilibrium (excitons [89], polaritons [90–92], magnons [34, 93], photons [94]) ensembles of bosonic particles, the experimental investigation of spatially coherent structures in BECs remains an attractive albeit a challenging task for researchers.

For the simplest case of a very weak, but non-zero interaction between magnons, BEC can be understood as follows: as the temperature of the boson gas T decreases at a given density N , or, vice versa, the density increases at a given temperature, the chemical potential, μ , describing the gas increases. On the other hand, μ cannot be larger than the minimum energy of the bosons ε_{\min} . The condition $\mu(N, T) = \varepsilon_{\min}$ defines the critical temperature $T_c(N)$ or the critical density $N_c(T)$. If the density of the particles in the system is larger than N_c , BEC takes place: the gas is spontaneously divided into two fractions: (i) particles with the density N_c distributed over the entire spectrum of possible boson states; (ii) a coherent ensemble of particles accumulated in the lowest state with $\varepsilon = \varepsilon_{\min}$. Exactly this scenario was realized in a gas of magnons [34]. As illustrated in Fig. 10.21a, magnons in YIG film were pumped using microwave parametric pumping: a microwave photon of a frequency $2f_p$ creates two primary magnons with frequencies f_p and opposite wave vectors. The created primary magnons then thermalized and accumulated close to the minimum of the magnon spectrum. Figure 10.21b shows the measured BLS spectra of magnons in YIG films under parametric pumping, illustrating the distribution of magnons over the states. One observes that already at $t = 200$ ns after the start of the pumping, the distribution of magnons away from the minimum energy saturates and show no further changes, whereas the peak corresponding to the minimum demonstrates a dramatic growth for $t > 200$ ns. It clearly means that for $t > 200$ ns (almost) all pumped magnons occupy the lowest state after thermalization [95]. Important to note that the width of the peak in Fig. 10.21b is determined by the spectral resolution of BLS. Further experiments [96] revealed that the intrinsic width of the peak is three orders of the magnitude smaller (about 1 MHz) confirming a high temporal coherence of the magnon condensate.

The most unambiguous way to investigate spatial coherence of a BEC is an interference experiment [97]. Since the lowest-energy magnon state is doubly degenerate (Fig. 10.21a), the condensation spontaneously occurs at two non-zero values of the wave vector $k = \pm k_{\text{BEC}}$, resulting in formation of two condensates. The interference of the wave-functions of the condensates forms a real-space standing wave of the total condensate density:

$$|\Psi|^2 = |\psi_+ \exp(ik_{\text{BEC}}z) + \psi_- \exp(-ik_{\text{BEC}}z)|^2 \propto \cos(2k_{\text{BEC}}z) \quad (10.10)$$

Figure 10.22 shows the results of a two-dimensional mapping of the BLS intensity, which is proportional to the total density of the condensate. The map accumulated across an $8 \times 5 \mu\text{m}^2$ area of the YIG film over several days, clearly demonstrates a periodic pattern along the direction of the static magnetic field created because of the interference of the two condensates. The obtained spatial period of the pattern $0.9 \pm 0.1 \mu\text{m}$, agrees well with the period $0.92 \mu\text{m}$ calculated based on the known value $k_{\text{BEC}} = 3.4 \times 10^4 \text{ cm}^{-1}$ [98]. Note here, that a long-term (several days) stability of the patterns indicates not only a high spatial coherence of each condensate, but also their mutual phase-locking.

Another interesting feature of the interference pattern in Fig. 10.22 is the presence of persistent topological defects marked by dashed circles. These fork-like defects

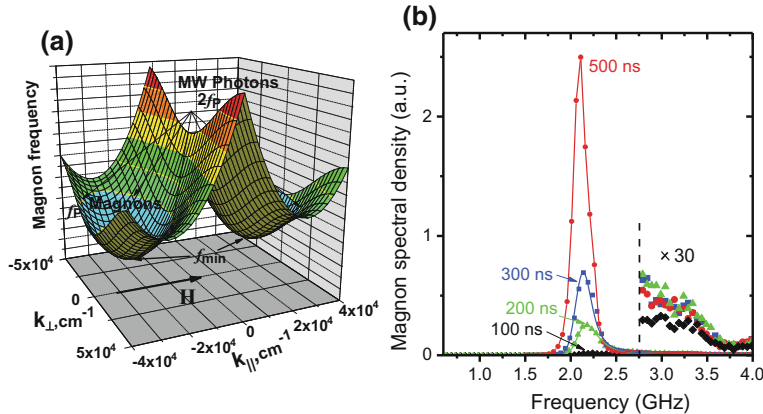
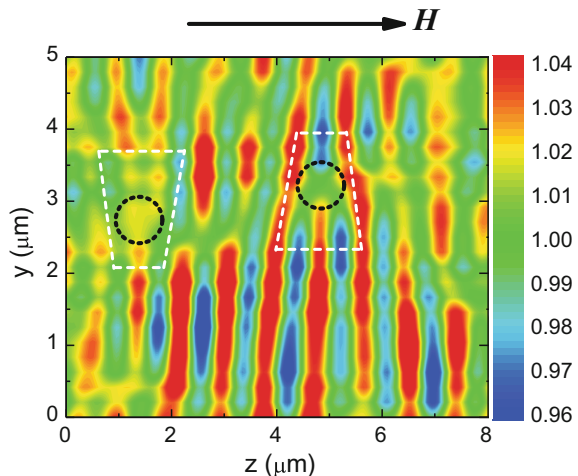


Fig. 10.21 **a** Calculated dispersion spectrum of magnons in an in-plane magnetized YIG film. k_{\parallel} and k_{\perp} correspond to the components of the magnon wave vector parallel and perpendicular to the static magnetic field, respectively. The arrows illustrate the process of parametric pumping of magnons. Note two degenerated minima. **b** BLS magnon spectra at different delay times after start of the pumping, as indicated

Fig. 10.22 Measured two-dimensional spatial map of the BLS intensity proportional to the condensate density. Note a periodic structure resulting from interference between two condensates. Dashed circles show the positions of topological defects in the standing-wave pattern corresponding to persistent quantized vortices



correspond to singularities of the phase of the individual wave-functions ψ_+ and ψ_- . To illustrate this, we draw contours around the defects and calculate the phase shift over them. It is obvious that the phase is constant as one moves along a red or dark blue line in the map and that the phase changes by 2π , as one moves from a red (blue) line to the neighboring one. When calculating the phase shift over the shown contours according to these rules, one gets 2π in either ψ_+ and ψ_- for both defects. The theoretical analysis [97] based on the generalized Ginzburg-Landau equations shows that these defects correspond to two quantized persistent vortices, each of

them existing in one condensate component only. These structures are analogous to half vortices (fractional vortices) of two-component atomic BECs created by phase imprinting [99].

10.6 Conclusion and Outlook

Concluding this Chapter, I would like to emphasize that it is far from fully covering the field of magnonic research. The main goal of the Chapter is to present to the reader the concept of magnons as quanta of propagating excitations in magnetic media, the fundamental ideas of spin waves and magnons, their similarities and differences to widely known waves as light and sound. In fact, the main difference is that due to contribution of the relativistic anisotropic magnetic dipole interaction, the frequency/energy of spin waves/magnons depends not only the absolute value of its wave vector, but on its direction as well. Thus, the dispersion law of magnons is anisotropic, that results in numerous exciting physical phenomena spanning from existence of the surface Damon-Eshbach mode to Bose-Einstein condensation of magnons. We have also learnt how the development of the spin-wave studies was following the development of magnetic technologies: from bulk via films and multi-layers to laterally confined structures. An important new aspect of magnonic research, which appears about the turn of the century, is the interaction of magnons with spin-polarized electric and pure spin currents. This development brought about a lot of new physics as discussed in the Chapter.

However, the very recent development connected with consequences of the Dzyaloshinskii-Moriya interaction (DMI) [100, 101] on spin wave properties are beyond this review, just because this field is too young for any review. Here I just would like to note several key words and references. In fact, the DMI appears in low-symmetry (breaking the inverse symmetry) materials, with a strong spin orbit coupling. Since phenomenologically it can be described as antisymmetric exchange interaction, it is responsible for the spontaneous formation skyrmionic structures [102, 103] as well as stabilization domain walls with a given handedness [104] with significant consequences on domain wall mobilities. It was also predicted [105] and then experimentally observed [106], that such an antisymmetric interaction results in an asymmetric magnon dispersion. Another interesting effect of the DMI on spin waves is the magnon Hall effect [107, 108], since it revealed nontrivial topologies of the magnon dispersion laws. Finally, the existence of topological nontrivial edge magnons suggests that topological magnon insulators may be created, which is important for future spintronics applications [109].

Another important topic, which was not addressed in this Chapter is spin-wave propagation in magnonic crystals. Similarly to photonic crystals in optics [110], the artificial magnonic crystals [111–114] represent one of the important functional elements of magnonic circuits. They are—spin-wave propagation media, where the characteristics of waves are tailored by using spatially periodic modulation of magnetic properties. Let us emphasize that an important new feature of magnonic crystals with

respect to photonic crystals is connected with fast controllability of magnetic systems by using, for example, non-uniform magnetic fields. This controllability allows realization of reconfigurable magnonic crystals, whose properties can be changed on demand. Without going into details, let us transfer the reader to recent comprehensive reviews on the topic [115, 116].

References

1. F. Bloch, Zur Theorie des Ferromagnetismus. *Z. Phys.* **61**, 206–219 (1930)
2. T. Holstein, H. Primakoff, Field dependence of the intrinsic domain magnetization of a ferromagnet. *Phys. Rev.* **58**, 1098 (1940)
3. F.J. Dyson, General theory of spin-wave interactions. *Phys. Rev.* **102**, 1217 (1956)
4. S. Neusser, D. Grundler, Magnonics: spin waves on the nanoscale. *Adv. Mater.* **21**, 2927–2932 (2009)
5. V.V. Kruglyak, S.O. Demokritov, D. Grundler, Magnonics. *J. Phys. D: Appl. Phys.* **43**, 264001 (2010)
6. B. Lenk, H. Ulrichs, F. Garbs, M. Mnzenberg, The building blocks of magnonics. *Phys. Rep.* **507**, 107 (2011)
7. A.V. Chumak, V.I. Vasyuchka, A.A. Serga, B. Hillebrands, *Nat. Phys.* **11**, 453–461 (2015)
8. J.C. Slonczewski, Current-driven excitation of magnetic multilayers. *J. Magn. Magn. Mater.* **159**, L1–L7 (1996)
9. L. Berger, Emission of spin waves by a magnetic multilayer traversed by a current. *Phys. Rev. B* **54**, 9353–9358 (1996)
10. J.C. Slonczewski, Excitation of spin waves by an electric current. *J. Magn. Magn. Mater.* **195**, L261–L268 (1999)
11. M.I. Dyakonov, V.I. Perel, Possibility of orienting electron spins with current. *Sov. Phys. JETP Lett.* **13**, 467–469 (1971)
12. J.E. Hirsch, Spin Hall effect. *Phys. Rev. Lett.* **83**, 1834–1837 (1999)
13. A. Hoffmann, Spin Hall effects in metals. *IEEE Trans. Magn.* **49**, 5172–5193 (2013)
14. Y. Kajiwara et al., Transmission of electrical signals by spin-wave interconversion in a magnetic insulator. *Nature* **464**, 262–266 (2010)
15. Z. Wang, Y. Sun, M. Wu, V. Tiberkevich, A. Slavin, Control of spin waves in a thin film ferromagnetic insulator through interfacial spin scattering. *Phys. Rev. Lett.* **107**, 146602 (2011)
16. V.E. Demidov, S. Urazhdin, A.B. Rinkevich, G. Reiss, S.O. Demokritov, Spin Hall controlled magnonic microwaveguides. *Appl. Phys. Lett.* **104**, 152402 (2014)
17. K. An et al., Control of propagating spin waves via spin transfer torque in a metallic bilayer waveguide. *Phys. Rev. B* **89**, 140405(R) (2014)
18. S. Urazhdin, V.E. Demidov, H. Ulrichs, T. Kendziorczyk, T. Kuhn, J. Leuthold, G. Wilde, S.O. Demokritov, Nanomagnonic devices based on the spin-transfer torque. *Nat. Nanotech.* **9**, 509–513 (2014)
19. C. Kittel, Excitation of spin waves in a ferromagnet by uniform RF field. *Phys. Rev.* **110**, 1295 (1958)
20. M.H. Seavey Jr., E. Tannenwald, Direct observation of spin wave resonance. *Phys. Rev. Lett.* **1**, 168 (1958)
21. R.W. Damon, J.R. Eshbach, Magnetostatic modes of a ferromagnet slab. *J. Phys. Chem. Solids* **19**, 308–320 (1961)
22. P. Grunberg, F. Metawe, Light scattering from bulk and surface spin waves in EuO. *Phys. Rev. Lett.* **39**, 1561 (1977)
23. P. Grunberg, R. Schreiber, Y. Pang, M.B. Brodsky, H. Sowers, Layered magnetic structures: evidence for antiferromagnetic coupling of Fe layers across Cr interlayers. *Phys. Rev. Lett.* **57**, 2442 (1986)

24. C. Mathieu, J. Jorwick, A. Frank, S.O. Demokritov, A.N. Slavin, B. Hillebrands, B. Bartenlian, C. Chappert, D. Decanini, F. Rousseaux, E. Cambrill, Lateral quantization of spin waves in micron size magnetic wires. *Phys. Rev. Lett.* **81**, 3968 (1998)
25. J. Jorwick, S.O. Demokritov, B. Hillebrands, D. Berkov, N.L. Gorn, K. Guslienko, A.N. Slavin, Spin wave wells in nonellipsoidal micrometer size magnetic elements. *Phys. Rev. Lett.* **88**, 047204 (2002)
26. J. Park, D.M. Eames, J. Engebretson, A. Berezovsky, P. Crowell, *Phys. Rev. Lett.* **89**, 277201 (2002)
27. M. Tsoi et al., Excitation of a magnetic multilayer by an electric current. *Phys. Rev. Lett.* **80**, 4281–4284 (1998)
28. M. Tsoi, A.G.M. Jansen, J. Bass, W.C. Chiang, V. Tsoi, P. Wyder, Generation and detection of phase-coherent current-driven magnons in magnetic multilayers. *Nature* **406**, 46 (2000)
29. S.I. Kiselev et al., Microwave oscillations of a nanomagnet driven by a spin-polarized current. *Nature* **425**, 380–383 (2003)
30. W.H. Rippard, M.R. Pufall, S. Kaka, S.E. Russek, T.J. Silva, Direct-current induced dynamics in Co₉₀Fe₁₀/Ni₈₀Fe₂₀ point contacts. *Phys. Rev. Lett.* **92**, 027201 (2004)
31. I.N. Krivorotov, N.C. Emley, J.C. Sankey, S.I. Kiselev, D.C. Ralph, R.A. Buhrman, Time-domain measurements of nanomagnet dynamics driven by spin-transfer torques. *Science* **307**, 228 (2005)
32. V.E. Demidov, S. Urazhdin, S.O. Demokritov, Direct observation and mapping of spin waves emitted by spin-torque nano-oscillators. *Nat. Mater.* **9**, 984–988 (2010)
33. V.E. Demidov et al., Magnetic nano-oscillator driven by pure spin current. *Nat. Mater.* **11**, 1028–1031 (2012)
34. S.O. Demokritov, V.E. Demidov, O. Dzyapko, G.A. Melkov, A.A. Serga, B. Hillebrands, A.N. Slavin, Bose-Einstein condensation of quasi-equilibrium magnons at room temperature under pumping. *Nature* **443**, 430–433 (2006)
35. L.D. Landau, E.M. Lifshitz, Theory of the dispersion of magnetic permeability in ferromagnetic bodies. *Phys. Z. Sowjet.* **8**, 153 (1935)
36. C. Herring, C. Kittel, On the theory of spin waves in ferromagnetic media. *Phys. Rev.* **81**, 869 (1951)
37. B.A. Kalinikos, A.N. Slavin, Theory of dipole-exchange spin wave spectrum for ferromagnetic films with mixed exchange boundary conditions. *J. Phys. C* **19**, 7013 (1986)
38. B. Heinrich, R. Urban, G. Woltersdorf, *J. Appl. Phys.* **91**, 7523 (2002)
39. W.K. Hieber, A. Stankiewicz, M.R. Freeman, *Phys. Rev. Lett.* **79**, 1134 (1997)
40. A. Barman, V.V. Kruglyak, R.J. Hicken, J.M. Rowe, A. Kundrotaita, J. Scott, M. Rahman, Imaging the dephasing of spin wave modes in a square thin film magnetic element. *Phys. Rev. B* **69**, 174426 (2004)
41. Y. Acremann, C.H. Back, M. Buess, O. Portmann, A. Vaterlaus, D. Pescia, H. Melchior, Imaging precessional motion of the magnetization vector. *Science* **290**, 492 (2000)
42. S.O. Demokritov, B. Hillebrands, A.N. Slavin, Brillouin light scattering studies of confined spin waves: linear and nonlinear confinement. *Phys. Rep.* **348**, 441 (2001)
43. S.O. Demokritov, V.E. Demidov, Micro-Brillouin light scattering spectroscopy of magnetic nanostructures. *IEEE Trans. Magn. Adv. Magn.* **44**, 6 (2008)
44. V.E. Demidov, S.O. Demokritov, Magnonic waveguides studied by microfocus Brillouin light scattering. *IEEE Trans. Magn.* **51**, 8578 (2015)
45. B.T.M. Willis, C.J. Carlile, *Experimental Neutron Scattering* (Oxford University Press, Oxford, 2009)
46. J. Jersch, V.E. Demidov, H. Fuchs, K. Rott, P. Krzysteczko, J. Munchenberger, G. Reiss, S.O. Demokritov, Mapping of localized spin-wave excitations by near-field Brillouin light scattering. *Appl. Phys. Lett.* **97**, 152502 (2010)
47. A.A. Serga, T. Schneider, B. Hillebrands, S.O. Demokritov, M. Kostylev, Phase-sensitive Brillouin light scattering spectroscopy from spin-wave packets. *Appl. Phys. Lett.* **89**, 063506 (2006)

48. K. Vogt, H. Schultheiss, S.J. Hermsdoerfer, P. Pirro, A.A. Serga, B. Hillebrands, All-optical detection of phase fronts of propagating spin waves in a Ni81Fe19 microstripe. *Appl. Phys. Lett.* **95**, 182508 (2009)
49. V.E. Demidov, S. Urazhdin, S.O. Demokritov, Control of spin-wave phase and wavelength by electric current on the microscopic scale; *Appl. Phys. Lett.* **95**, 262509 (2009)
50. J. Jorwick, S.O. Demokritov, C. Mathieu, B. Hillebrands, B. Bartenlian, C. Chappert, F. Rousseaux, A. Slavin, Brillouin light scattering from quantized spin waves in micron-size magnetic wires. *Phys. Rev. B* **60**, 15194 (1999)
51. G. Gubbiotti, O. Kazakova, G. Carlotti, M. Hanson, P. Vavassori, Spin-wave spectra in nanometric elliptical dots arrays. *IEEE Trans. Magn.* **39**, 2750 (2003)
52. J. Jorwick, S.O. Demokritov, B. Hillebrands, B. Bartenlian, C. Chappert, D. Decanini, F. Rousseaux, E. Cambril, Spin wave quantization and dynamic coupling in micron-size circular magnetic dots. *Appl. Phys. Lett.* **75**, 3859 (1999)
53. R.I. Joseph, E. Schliemann, Demagnetizing field in nonellipsoidal bodies. *J. Appl. Phys.* **36**, 1579–1593 (1965)
54. P. Bryant, H. Suhl, Thin-film magnetic patterns in an external field. *Appl. Phys. Lett.* **54**, 2224 (1989)
55. C. Bayer, S.O. Demokritov, B. Hillebrands, A.N. Slavin, Spin wave wells with multiple states created in small magnetic elements. *Appl. Phys. Lett.* **82**, 607 (2003)
56. V.E. Demidov, S.O. Demokritov, K. Rott, J. Krzysteczk, G. Reiss, Self-focusing of spin waves in Permalloy microstripes. *Appl. Phys. Lett.* **91**, 252504 (2007)
57. V.E. Demidov, J. Jersch, S.O. Demokritov, K. Rott, J. Krzysteczk, G. Reiss, Transformation of propagating spin-wave modes in microscopic waveguides with variable width. *Phys. Rev. B* **79**, 054417 (2009)
58. V.E. Demidov, M. Kostylev, K. Rott, J. Mnchenberger, G. Reiss, S.O. Demokritov, Excitation of short-wavelength spin waves in magnonic waveguides. *Appl. Phys. Lett.* **99**, 082507 (2011)
59. E. Myers, D.C. Ralph, J.A. Katine, R.N. Louie, R.A. Buhrman, Current-induced switching of domains in magnetic multilayer devices. *Science* **285**, 867–870 (1999)
60. J.A. Katine, F.J. Albert, R.A. Buhrman, E.B. Myers, D.C. Ralph, Current-driven magnetization reversal and spin-wave excitations in Co/Cu/Co pillars. *Phys. Rev. Lett.* **84**, 3149–3152 (2000)
61. D.C. Ralph, M.D. Stiles, Spin transfer torques. *J. Magn. Magn. Mater.* **320**, 1190–1216 (2008)
62. T.J. Silva, W.H. Rippard, Developments in nano-oscillators based upon spin-transfer point-contact devices. *J. Magn. Magn. Mater.* **320**, 1260–1271 (2008)
63. A. Brataas, A.D. Kent, H. Ohno, Current-induced torques in magnetic materials. *Nat. Mater.* **11**, 372 (2012)
64. N. Locatelli, V. Cros, J. Grollier, Spin-torque building blocks. *Nat. Mater.* **13**, 11 (2014)
65. T. Chen, R.K. Dumas, A. Eklund, K. Muduli, A. Houshang, A.A. Awad, P. Duerrenfeld, B.G. Malm, A. Rusu, J. Akerman, Spin-torque and spin-Hall nano-oscillators. *IEEE Trans. Magn.* **99**, 1 (2016)
66. M. Madami et al., Direct observation of a propagating spin wave induced by spin-transfer torque. *Nat. Nanotech.* **6**, 635–638 (2011)
67. A. Houshang, E. Iacocca, P. Duerrenfeld, S.R. Sani, J. Akerman, R.K. Dumas, Spin-wave-beam driven synchronization of nanocontact spin-torque oscillators. *Nat. Nanotech.* **11**, 280–286 (2016)
68. V.E. Demidov, S. Urazhdin, R. Liu, B. Divinskiy, A. Telegin, S.O. Demokritov, Excitation of coherent propagating spin waves by pure spin currents. *Nat. Commun.* **7**, 10446 (2016)
69. J. Xiao, G.E.W. Bauer, Spin-wave excitation in magnetic insulators by spin-transfer torque. *Phys. Rev. Lett.* **108**, 217204 (2012)
70. T. Jungwirth, J. Wunderlich, K. Olejnik, Spin Hall effect devices. *Nat. Mater.* **11**, 382 (2012)
71. F.J. Jedema, A.T. Filip, B.J. van Wees, Electrical spin injection and accumulation at room temperature in an all-metal mesoscopic spin valve. *Nature* **410**, 345–348 (2001)
72. Y. Otani, T. Kimura, Manipulation of spin currents in metallic systems. *Philos. Trans. R. Soc. Lond. Ser. A* **369**, 3136–3149 (2011)

73. K. Uchida, S. Takahashi, K. Harii, J. Ieda, W. Koshibae, K. Ando, S. Maekawa, E. Saitoh, Observation of the spin Seebeck effect. *Nature* **455**, 778–781 (2008)
74. K. Uchida, J. Xiao, H. Adachi, J. Ohe, S. Takahashi, J. Ieda, T. Ota, Y. Kajiwara, H. Umezawa, H. Kawai, G.E.W. Bauer, S. Maekawa, E. Saitoh, Spin Seebeck insulator. *Nat. Mater.* **9**, 894–897 (2010)
75. V.M. Edelstein, Spin polarization of conduction electrons induced by electric current in two-dimensional asymmetric electron systems. *Solid State Commun.* **73**, 233–235 (1990)
76. A. Chernyshov, M. Overby, X. Liu, J.K. Furdyna, Y. Lyanda-Geller, L.P. Rokhinson, Evidence for reversible control of magnetization in a ferromagnetic material by means of spin-orbit magnetic field. *Nat. Phys.* **5**, 656–659 (2009)
77. K. Ando, S. Takahashi, K. Harii, K. Sasage, J. Ieda, S. Maekawa, E. Saitoh, Electric manipulation of spin relaxation using the spin Hall effect. *Phys. Rev. Lett.* **101**, 036601 (2008)
78. M. Evelt et al., High-efficiency control of spin-wave propagation in ultra-thin Yttrium Iron Garnet by the spin-orbit torque. *Appl. Phys. Lett.* **108**, 172406 (2016)
79. V.E. Demidov, S. Urazhdin, V. Tiberkevich, A. Slavin, S.O. Demokritov, Control of spin-wave emission from spin-torque nano-oscillators by microwave pumping. *Phys. Rev. B* **83**, 060406 (R) (2011)
80. V.E. Demidov et al., Control of magnetic fluctuations by spin current. *Phys. Rev. Lett.* **107**, 107204 (2011)
81. A. Slavin, V. Tiberkevich, Spin wave mode excited by spin-polarized current in a magnetic nanocontact is a standing self-localized wave bullet. *Phys. Rev. Lett.* **95**, 237201 (2005)
82. A. Einstein, Quantentheorie des einatomigen idealen Gases. *Sitz. Ber. Preuss. Akad. Wiss.* **1**, 3–8 (1925)
83. L.P. Pitaevskii, S. Stringari, *Bose-Einstein Condensation*. International Series of Monographs on Physics 116 (Clarendon Press, 2003)
84. P. Kapitza, Viscosity of liquid helium below the λ -point. *Nature* **141**, 74 (1938)
85. J.F. Allen, A.D. Misener, Flow of liquid helium II. *Nature* **141**, 75 (1938)
86. M.H. Anderson, J.R. Ensher, M.R. Matthews, C.E. Wieman, E.A. Cornell, Observation of Bose-Einstein condensation in a Dilute Atomic Vapor. *Science* **269**, 198–201 (1995)
87. K.B. Davis et al., Bose-Einstein condensation in a gas of sodium atoms. *Phys. Rev. Lett.* **75**, 3969–3973 (1995)
88. T. Giamarchi, Ch. Regg, O. Tchernyschyov, Bose-Einstein condensation in magnetic insulators. *Nat. Phys.* **4**, 198–204 (2008)
89. L.V. Butov, A.L. Ivanov, A. Imamoglu, P.B. Littlewood, A.A. Shashkin, V.T. Dolgopolov, K.L. Campman, A.C. Gossard, Stimulated scattering of indirect excitons in coupled quantum wells: signature of a degenerate Bose-gas of excitons. *Phys. Rev. Lett.* **86**, 5608–5611 (2001)
90. J. Kasprzak et al., Bose-Einstein condensation of exciton polaritons. *Nature* **443**, 409–414 (2006)
91. R. Balili, V. Hartwell, D. Snoke, L. Pfeiffer, K. West, Bose-Einstein condensation of microcavity polaritons in a trap. *Science* **316**, 1007–1010 (2007)
92. A. Amo et al., Collective fluid dynamics of a polariton condensate in a semiconductor microcavity. *Nature* **457**, 291–295 (2009)
93. YuM Bunkov, G.E. Volovik, Bose-Einstein condensation of magnons in superfluid ^3He . *J. Low Temp. Phys.* **150**, 135–144 (2008)
94. J. Klaers, J. Schmitt, F. Vewinger, M. Weitz, Bose-Einstein condensation of photons in an optical microcavity. *Nature* **468**, 545–548 (2010)
95. V.E. Demidov, O. Dzyapko, S.O. Demokritov, G.A. Melkov, A.N. Slavin, Thermalization of a parametrically driven magnon gas leading to Bose-Einstein condensation. *Phys. Rev. Lett.* **99**, 037205 (2007)
96. O. Dzyapko, P. Nowik-Boltyk, B. Koene, V.E. Demidov, J. Jersch, A. Kirilyuk, T. Rasing, S.O. Demokritov, High-resolution magneto-optical Kerr effect spectroscopy of magnon Bose-Einstein condensate. *IEEE Magn. Lett.* **7**, 3501805 (2016)
97. P. Nowik-Boltyk, O. Dzyapko, V.E. Demidov, N.G. Berloff, S.O. Demokritov, Spatially non-uniform ground state and quantized vortices in a two-component Bose-Einstein condensate of magnons. *Sci. Rep.* **2**, 482 (2012)

98. V.E. Demidov, O. Dzyapko, M. Buchmeier, T. Stockhoff, G. Schmitz, G.A. Melkov, S.O. Demokritov, Magnon kinetics and Bose-Einstein condensation studied in phase space. *Phys. Rev. Lett.* **101**, 257201 (2008)
99. M.R. Matthews, B.P. Anderson, P.C. Haljan, D.S. Hall, C.E. Wieman, E.A. Cornell, Vortices in a Bose-Einstein condensate. *Phys. Rev. Lett.* **83**, 2498 (1999)
100. I.A. Dzyaloshinsky, Thermodynamic theory of ‘weak’ ferromagnetism of antiferromagnetics. *J. Phys. Chem. Solids* **4**, 241–255 (1958)
101. T. Moriya, New mechanism of anisotropic superexchange interaction. *Phys. Rev. Lett.* **4**, 228–230 (1960)
102. M. Bode, M. Heide, K. von Bergmann, P. Ferriani, S. Heinze, G. Bihlmayer, A. Kubetzka, O. Pietzsch, S. Blügel, R. Wiesendanger, Chiral magnetic order at surfaces driven by inversion asymmetry. *Nature* **447**, 190–193 (2007)
103. S. Mühlbauer, B. Binz, F. Jonietz, C. Pfleiderer, A. Rosch, A. Neubauer, R. Georgii, P. Böni, Skyrmion lattice in a chiral magnet. *Science* **323**, 915–919 (2009)
104. G. Chen, T. Ma, A.T. N'Diaye, H. Kwon, C. Won, Y. Wu, A.K. Schmid, Tailoring the chirality of magnetic domain walls by interface engineering. *Nat. Commun.* **4**, 2671 (2013)
105. L. Uvdardi, L. Szunyogh, Chiral asymmetry of the spin-wave spectra in ultrathin magnetic films. *Phys. Rev. Lett.* **102**, 207204 (2009)
106. Kh Zakeri, Y. Zhang, J. Prokop, T.-H. Chuang, N. Sakr, W.X. Tang, J. Kirschner, Asymmetric spin-wave dispersion on Fe(110): direct evidence of the Dzyaloshinskii-Moriya interaction. *Phys. Rev. Lett.* **104**, 137203 (2010)
107. Y. Onose, T. Ideue, H. Katsura, Y. Shiomi, N. Nagaosa, Y. Tokura, Observation of the magnon Hall effect. *Science* **329**, 297–299 (2010)
108. R. Matsumoto, S. Murakami, Theoretical prediction of a rotating magnon wave packet in ferromagnets. *Phys. Rev. Lett.* **106**, 197202 (2011)
109. L. Zhang, J. Ren, J.-S. Wang, B. Li, Topological magnon insulator in insulating ferromagnet. *Phys. Rev. B* **87**, 144101 (2013)
110. J.D. Joannopoulos, S.G. Johnson, J.N. Winn, R.D. Meade, *Photonic Crystals—Molding the Flow of Light* (Princeton University Press, Princeton, 2008)
111. B. Lenk, H. Ulrichs, F. Garbs, M. Münzenberg, The building blocks of magnonics. *Phys. Rep.* **507**, 107–136 (2011)
112. G. Gubbiotti, S. Tacchi, M. Madami, G. Carlotti, A.O. Adeyeye, M. Kostylev, Brillouin light scattering studies of planar metallic magnonic crystals. *J. Phys. D Appl. Phys.* **43**, 264003 (2010)
113. S.A. Nikitov, D.V. Kalyabin, I.V. Lisenkov, A. Slavin, YuN Barabanenkov, S.A. Osokin, A.V. Sadovnikov, E.N. Beginin, M.A. Morozova, YuA Filimonov, YuV Khivintsev, S.L. Vysotsky, V.K. Sakharov, E.S. Pavlov, Magnonics: a new research area in spintronics and spin wave electronics. *Phys.-Usp.* **58**, 1002 (2015)
114. S. Tacchi, G. Gubbiotti, M. Madami, G. Carlotti, Brillouin light scattering studies of 2D magnonic crystals. *J. Phys.: Condens. Matter* **29**, 073001 (2017)
115. M. Krawczyk, D. Grundler, Review and prospects of magnonic crystals and devices with reprogrammable band structure. *J. Phys.: Condens. Matter* **26**, 123202 (2014)
116. A.V. Chumak, T. Neumann, A.A. Serga, B. Hillebrands, M.P. Kostylev, Magnonic crystals for data processing. *J. Phys. D: Appl. Phys.* **42**, 205005 (2009)

Chapter 11

Spin Transfer Torque Driven Magnetodynamical Solitons



Johan Åkerman

Abstract The recent progress in generating high spin current densities in magnetic nanostructures has made it possible to excite unprecedented magnon densities from which a range of novel magnetodynamical solitons, such as spin wave bullets, magnetic droplets, and dynamical skyrmions can nucleate. In this chapter, these magnetodynamical solitons, and the devices where they can be created and observed - so-called spin torque and spin Hall nano-oscillators are discussed in detail. The solitons form under conditions of magnon-magnon attraction, which arises when the magnetodynamics exhibits negative non-linearity, and the resulting particle-like objects exhibit a rich dynamics including Brownian motion, drift instabilities, perimeter eigenmode excitations, and merging. While originally only observed indirectly using microwave spectroscopy, these solitons can now also be observed directly using scanning transmission x-ray microscopy.

11.1 Introduction

The first description of a soliton phenomenon—although not called that at the time—was given by John Scott Russell in 1834. He observed how a propagating water wave, created in between a drawn boat and the side of the narrow Union Canal in Scotland, would, after the boat had stopped, continue on its own without any apparent loss of shape or speed and only the slightest loss of amplitude. He followed the wave for some 10–15 minutes during which it had travelled about 1–2 miles. He called it a “Wave of translation” and intrigued by this chance encounter, spent significant time and effort to reproduce and study this phenomenon in a wave tank. He described a number of properties typical of solitons: (*i*) the waves were stable over very long

J. Åkerman (✉)

Department of Physics, University of Gothenburg, 412 96 Gothenburg, Sweden
e-mail: johan.akerman@physics.gu.se

J. Åkerman

Materials and Nanophysics, KTH Royal Institute of Technology, 164 40 Kista, Sweden

distances, in contrast to normal waves that would either flatten out, or break; (*ii*) their speed depended on their size, and their width on the water depth; (*iii*) waves would never merge, instead a bigger and faster wave would travel through a smaller and slower one; (*iv*) a wave too big for the depth of water would separate into two individual waves.

It is intuitively clear that such solitons are intrinsically dynamic and require dynamics for their existence. Any attempt at forming a stable static structure out of liquid water is bound to relax back to the energetically favored uniform state of a flat water surface. However, if the coupling between the microscopic entities of the system is strong, such as in a magnetic material, so-called topological solitons, also called topological defects, can be statically stable. Examples include domain walls, vortices, bubbles, and skyrmions, which are stable objects due to topological constraints. Their stability is either related to the energy cost of moving the topological defect to a nearby boundary, or breaking the coupling between two neighboring spins. Nothing prevents dynamical solitons to also have topology, and the dynamics can also help in stabilizing otherwise unstable topological defects (see e.g. dynamical skyrmions below).

Magnetodynamical solitons were first experimentally demonstrated in thick YIG films [1]. It required substantial pumping power and relied on the very low damping of YIG to reach sufficient spin wave densities. The orders of magnitude higher damping in metal based systems, make such approaches ineffective. However, the advent of spin transfer torque [2, 3] opened up an entirely different route towards very high SW densities. Using very high densities of spin polarized currents through nano-pillars or nano-contacts, it is possible to locally overcome the high damping of ferromagnetic metals and create a magnetic medium with gain. The spin wave intensity in such a system will grow exponentially in time until non-linear damping effects finally limits the growth and a steady auto-oscillatory state of a very high local spin wave intensity is reached. Depending on the magnetic anisotropy of the system and of the applied magnetic field, a number of different magnetodynamical solitons can then form.

This chapter is organized as follows. In Sect. 11.2, the basics of spin transfer torque generated auto-oscillations is covered briefly. In Sect. 11.3, the spin wave bullet and its experimental demonstration in different systems is described. Section 11.4 describes the magnetic droplet in perpendicular anisotropy systems in detail. Finally, Sect. 11.5 describes the dynamical skyrmion, i.e. a magnetodynamical soliton with non-zero topology.

11.2 Spin Transfer Torque Driven Spin Wave Auto-oscillations

Last year marked the 20th anniversary of the publication of two ground-breaking papers by Slonczewski [2] and Berger [3], describing the spin transfer torque (STT) phenomenon. Although Berger had already discussed the possibility for STT in the late 1970s [4, 5] and in 1985 demonstrated STT-driven domain wall motion in millimeter-wide films using rather extreme currents (45 A) [6], and Slonczewski had

developed the theory for spin-current-driven exchange coupling in magnetic tunnel junctions (MTJs) [7], their two papers in 1996 described how a current flowing perpendicularly to the plane of a magnetic metal multilayer should be able to reorient the magnetization direction in one of the layers. Their predictions were hence directly amenable to device fabrication at a time when giant magnetoresistance (GMR) [8, 9] multilayers were being readied for hard drive read-head production and the first high-quality MTJs had just appeared [10, 11].

Although it took a few years before STT driven magnetization switching and precession were experimentally demonstrated [12–14], the fundamental and technological impact of this phenomenon has been profound. Modern day magnetoresistive random-access memory (MRAM), programmed using STT from a direct current through the MTJ memory cell, is beginning to replace toggle MRAM [15, 16], and so-called spin torque nano-oscillators for microwave signal generation and detection are close to actual applications.

11.2.1 *Spin Currents and Spin Transfer Torque*

We will here only briefly describe the nature, origin, and consequences of spin currents. For in-depth STT reviews, please see [17, 18]. For more in-depth reviews of STT-based MRAM and STNOs, see [19–23] and [24, 25].

In the general case, a spin current is a 3×3 tensor describing the flow, in three spatial dimensions, of spin vectors, in three-dimensional spin space. As the spin of the electron is associated with a magnetic moment in real space, one often pictures the spin current as a flow of tiny magnetic moments. In most technologically relevant device geometries, the situation can often be simplified to a one-dimensional flow of three-, or sometimes even two-, dimensional spins.

Spin currents can be generated in many ways, e.g. from a spin-polarized charge current through a ferromagnetic material, from spin pumping due to a precessing magnetization [26], from the spin Hall effect (see below), from the spin Seebeck effect, and from rapid demagnetization. In non-magnetic metals, spin currents are carried by the charge carriers, in magnetic insulators by spin waves (magnons), and in magnetic metals by both.

Spin transfer torque (STT) arises when a spin current is non-collinear with the local magnetization. This torque may be gradual and spread out over a long distance, e.g. when spin-polarized electrons flow through a domain wall and rotate with the local magnetization, or it can be very abrupt, as in current-perpendicular-to-plane spin valves and MTJs when a spin current from one ferromagnetic layer enters a second ferromagnetic layer with a non-collinear magnetization direction. In metallic system [27–29], STT is dominated by so-called in-plane or damping-like torque, i.e. it has a component that (time-averaged) is either parallel or anti-parallel to the ordinary damping torque. In MTJs, there is also a substantial so-called field-like torque component perpendicular to the damping torque such that it has the same effect as an applied magnetic field [28, 30–32].

11.2.2 The Spin Hall Effect

The spin Hall effect (SHE), first described by D'yakonov and Perel' in 1971 [33, 34], experienced a renaissance when Hirsch revisited the problem in 1999 [35], which subsequently lead to its first experimental demonstration in 2004 [36, 37]. In contrast to the combined spin and charge current generated when carriers traverse a ferromagnetic material, the SHE can produce a pure spin current, typically in a direction perpendicular to the charge current. The pure spin current can then exert substantial STT on any adjacent magnetic layer, which can be used for magnetic switching [38, 39] and magnetization precession [40, 41]. The SHE can be viewed as a limiting case of the anomalous Hall effect (AHE) [42, 43], which was proposed by Edwin Hall in 1881 when he applied his earlier discovery of the ordinary Hall effect (HE) [44] to ferromagnetic metals and found that this effect could be ten times greater than in nonmagnetic metals. The SHE is simply a limiting case of the AHE in materials without any spontaneous magnetization but with substantial spin-orbit coupling. Without any spin imbalance in the nonmagnetic material, the asymmetric spin-dependent scattering does not result in any Hall voltage. What it does result in, however, is a net spin current transverse to the charge current and, in a steady state, the build-up of spin accumulation zones at the edges of the conductor, which can be directly observed by optical means [36, 37] and which is used in spin-current-driven devices. For recent in-depth reviews of the SHE and its origins, please see [45, 46].

11.2.3 The Landau-Lifshitz-Gilbert-Slonczewski Equation

For most practical purposes, the magnitude of the magnetization vector \mathbf{M} in a ferromagnet is always equal to the saturation magnetization M_S (notable exceptions include rapid demagnetization and operation close to the Curie temperature). Its direction can, however, vary internally and this variation can be static, as in a domain wall, or dynamic, as in spin waves. The magnetization dynamics is described by the so-called Landau-Lifshitz-Gilbert (LLG) equation, first introduced by Landau and Lifshitz [47] in 1935 and in 1955 modified by Gilbert [48], who added a friction-like phenomenological damping parameter α . In 1996, Slonczewski added a STT term [2], and the final Landau-Lifshitz-Gilbert-Slonczewski (LLGS) equation then becomes:

$$\frac{\partial \mathbf{M}}{\partial t} = \gamma [\mathbf{H}_{eff} \times \mathbf{M}] + \mathbf{T}_\alpha + \mathbf{T}_S. \quad (11.1)$$

where the first term describes conservative Larmor precession around the effective field \mathbf{H}_{eff} , the second term describes the Gilbert damping torque, and the last term \mathbf{T}_S is the Slonczewski STT. \mathbf{H}_{eff} is the sum of the externally applied field, the magneto-dipolar field, an anisotropy field, the exchange field, and, in the presence of a drive current, the Oersted field:

$$\mathbf{H}_{eff} = \mathbf{H}_a + \mathbf{H}_{dip} + \mathbf{H}_k + \mathbf{H}_{ex} + \mathbf{H}_{oe}. \quad (11.2)$$

11.2.4 Non-linear Spin Wave Auto-oscillations

Auto-oscillations [49] can happen in any system having an intrinsic resonance, such as an organ pipe or a violin string. If the violin string is plucked, i.e. the system is subjected to an impulse function, the resonance gets excited until various sources of damping restores the original uniform, non-sounding, state. If one provides a constant source of energy larger than this damping, such as the friction from a bow, the string can auto-oscillate on its resonance indefinitely.

In the case of a violin string, the frequency is independent of the amplitude of the oscillation and this type of auto-oscillator is therefore linear. To change the frequency of a given string, the violinist instead has to use a finger to change the length of the oscillating part. Spin wave auto-oscillators are however highly *non-linear*, i.e. their frequency is *dependent* on the amplitude of oscillation. The non-linearity stems from how the internal terms in H_{eff} , i.e. H_{dip} , H_k , and H_{ex} , depend on the oscillation amplitude. As a simplified example, we here consider a macrospin approximation of an auto-oscillating easy-plane magnetization saturated normal to the film plane. To reach saturation, the applied field must overcome the demagnetization field. During auto-oscillation, the local magnetization processes around the applied field and as the oscillation amplitude increases, so does the opening angle away from the film normal. As the demagnetization field is proportional to the M_z component of the auto-oscillating magnetization, it decreases with increasing opening angle, which in turn makes the total H_{eff} increase. As a consequence, in this Slonczewski geometry, the frequency will increase with amplitude, and since the oscillation amplitude increases with current the so-called non-linearity, df/dI , is positive.

It can however be shown [50] that the non-linearity will decrease if the internal magnetization angle deviates from the normal and for angles closer to the plane, df/dI can also be negative. As we will see in the following, a negative non-linearity can have dramatic consequences as it leads to self-localization of the auto-oscillating spin waves when their frequency falls below the SW gap of the extended film.

11.2.5 Spin Torque and Spin Hall Effect Nano-oscillators

Spin torque and spin Hall nano-oscillators (STNOs and SHNOs) come in a wide variety of structures and layouts (Fig. 11.1). The first demonstrations of so-called magnetic point-contacts relied on a highly sharpened metallic tip to make electrical contact, with an area of about 10^2 nm^2 , to an extended multilayer film [12, 51, 52]. For better fabrication control and reliability, lithographically defined nano-contact STNOs are now preferred [13, 53–56]. In both types of devices, it is only the current injection site that is nanoscopic, and the magnetic films remain extended. In nano-pillar STNOs [14, 57], on the other hand, all of the magnetic layers are patterned through, which ensures that all of the electric current passes through the entire multilayer stack, typically resulting in lower threshold current densities ($< 10^7 \text{ A/cm}^2$),

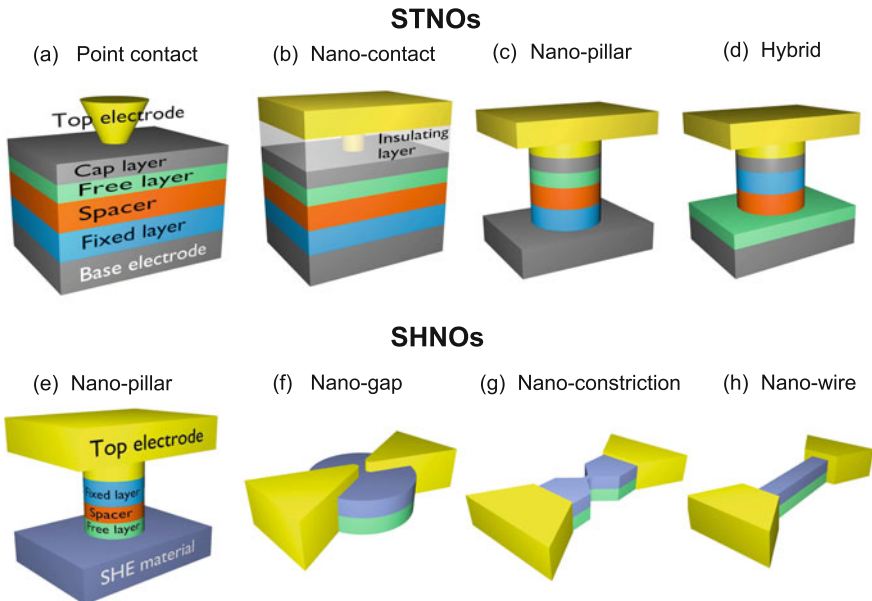


Fig. 11.1 a-d Different structures and layouts of spin torque nano-oscillators (STNOs), where the “free” and “fixed” layers are ferromagnetic and separated by either a metallic spacer or a thin dielectric acting as a tunneling barrier. **e-h** Different structures and layouts of spin Hall nano-oscillators (SHNOs). (From [25] with permission)

compared to nano-contacts (10^8 – 10^9 A/cm 2). Hybrid STNOs, i.e. a nanopillar fabricated on top of an extended film, have also been demonstrated [58, 59].

In a similar manner, SHNOs can be categorized into four geometries. In the three-terminal nanopillar geometry, the magnetic free layer is patterned on top of an extended layer of the SHE-generating normal metal [39, 40]. In another approach one utilizes a nanogap between two highly conductive Au electrodes, injecting a high current density into a nanosized region of an extended FM/Pt bilayer [41, 60]. In more recent nanoconstriction-based SHNOs, both the FM and the Pt (or W) layer are patterned into a constriction [61–64]. Similar confinement of the SHE-induced spin current has been demonstrated in a nanowire geometry [65]. The benefits of the latter two device geometries include easier fabrication and direct optical access to the entire magnetodynamically active region.

11.3 Spin Wave Bullets

The term spin wave bullet was inspired by its optical analogue, the Light Bullet [66], theoretically predicted by Silberberg in 1990, but experimentally observed well after the SW bullet in 2005.

11.3.1 *Macroscopic Spin Wave Bullets*

Macroscopic, millimeter-sized, SW bullets were for the first time experimentally observed in antenna based experiments on thick ($7\text{ }\mu\text{m}$) YIG films [67]. Short-lived high intensity SW packets were excited using 29 ns long microwave pulses and their spatial and temporal evolution was monitored using a Brillouin Light Scattering (BLS) microscope. The high-intensity SW packets exhibited clear self-focusing, shrinking more than 50% in both lateral directions and retaining its minimum size as long as the SW intensity stayed over a certain threshold value.

11.3.2 *Nanoscopic Spin Wave Bullets in STNOs*

Although not described as such, STT generated nanoscopic SW bullets were first observed in nano-contact STNOs in in-plane magnetic field by Rippard et al. [53, 55], where they made a number of experimental observations, which conflicted with Slonczewski's original predictions for propagating SWs: (i) a much lower threshold current for auto-oscillations than theoretically predicted, (ii) an auto-oscillating frequency below the FMR frequency instead of above, and (iii) a further red-shift in the frequency as the current increased. As discussed in the next section, these are all specific traits of SW bullets.

In an angular dependence study, Bonetti et al. subsequently demonstrated the existence of a critical out-of-plane magnetization angle above which only propagating SWs are observed [68–70] and below which both propagating SWs and SW bullets can be generated [71, 72]. While small nano-contacts ($\approx 40\text{ nm}$) only can sustain one of the two modes at any given time, rapid mode hopping between propagating SWs and SW bullets were observed. However, in larger nano-contacts, a single nano-contact can drive both modes simultaneously, with their respective intensity maxima at opposite sides of the nano-contact [73, 74]. In both large and small nano-contacts, these phenomena are to a large extent governed by the strong Oersted field in the nano-contact vicinity.

11.3.3 *Direct Observation of Nanoscopic Spin Wave Bullets*

The main auto-oscillating mode in nano-gap SHNOs in in-plane fields is the spin wave bullet, as first demonstrated by Demidov et al. [41]. The auto-oscillation frequency is well below the FMR frequency and direct BLS observations also reveal a spatial distribution of SWs consistent with an auto-oscillating region much smaller (100 nm) than the spatial resolution of the BLS microscope (250 nm).

To improve on the spatial resolution, other techniques, such as scanning transmission X-ray microscopy (STXM) have been employed. The direct observation of

a possible spin wave bullet was reported by Bonetti et al. [75] where they also were able to follow the average time-evolution of the precessing spins using a stroboscopic method.

11.4 Magnetic Droplets

11.4.1 *Magnon Drops and Magnetic Droplets*

Magnetic droplets derive their name from magnon drops, which are conservative magnetodynamical solitons first described by Ivanov and Kosevich in thin films with perpendicular anisotropy and zero SW damping [76, 77]. Magnon drops can be of any size, but since they require a loss-less medium, they have not yet been experimentally demonstrated.

Given their requirement for an unrealistic zero-damping magnetic material, magnon drops remained a theoretical curiosity until it was realized by Hoefer and coworkers that the active region underneath a nano-contact could serve as an effective magnetic medium with zero damping [78]. They showed both analytically and numerically that STT can nucleate and sustain a condensed state of magnons even in a magnetic material with significant damping, such as magnetic metals.

11.4.2 *Experimental Demonstrations of Magnetic Droplets*

The first experimental demonstration of magnetic droplets [79] was reported by Mohseni et al. in so-called orthogonal STNOs [81] where the Co/Ni multilayer free layer had strong PMA and the fixed layer was made of easy-plane Co. These results were later confirmed by Macia et al. using NiFe as the fixed layer [82]. The nucleation of a droplet is observed as a large drop in microwave frequency, an increase in the microwave power, an increase of the STNO resistance, and a sign change of its magnetoresistance (Fig. 11.2). Sometimes the nucleation is also accompanied by microwave noise in a lower frequency range of about 0.1–2 GHz and even auto-modulation.

In contrast to the original droplet theory developed for spin valve stacks where both the free and the fixed layer were assumed to have perpendicular anisotropy, the droplet nucleation current was experimentally found to have a non-trivial field dependence (Fig. 11.3). As discussed in detail in [80], the droplet nucleation current in an orthogonal spin valve can be very well reproduced using one term linear in field and another inversely proportional to the field, plus a constant,

$$I_n = \alpha \mathcal{A}H + \frac{\mathcal{B}}{H} + \mathcal{C}. \quad (11.3)$$

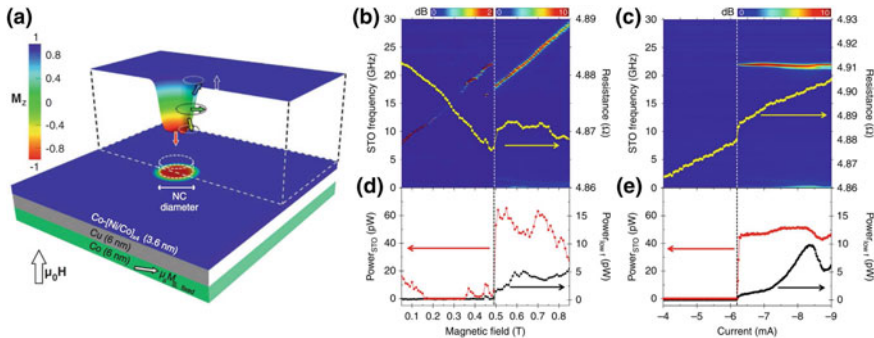


Fig. 11.2 **a** Schematic of a nano-contact spin torque oscillator based on an orthogonal spin valve with an in-plane Co fixed layer and a [Co/Ni] free layer with its easy axis along the film normal. Above the stack is shown a cartoon of the magnetization of the droplet, with the color indicating the degree of reversal and the arrows showing the local precession of the spins. (Adapted from [79]). **b** Power spectral density (PSD) and device resistance (R) versus magnetic field showing a sharp drop in frequency, a dramatic increase in power, and a resistance step when the droplet nucleates at about 0.49 T. **c** PSD and R versus current again showing a dramatic increase in microwave power and a resistance step when the droplet forms at about -6.2 mA. **d**, **e** Microwave power in the fundamental peak and at low frequency showing that the droplet is accompanied by the appearance of low-frequency microwave noise. (Adapted from [80] with permission)

In orthogonal STNOs, a perpendicular field tilts the fixed layer orientation by an angle θ , defined with respect to the film normal, consistent with a hard axis reversal condition $\cos(\theta) = H/M_{s,p}$ (valid until saturation, i.e. for $H \leq M_{s,p}$). This is hence the origin of the term inversely proportional to the field. As the field further increases, the usual field dependent Slonczewski criterion for a STT-driven spin wave instability gradually takes over. For fields above fixed layer saturation, only this field-dependent term survives. Similar nucleation phase diagrams were observed also for NiFe fixed layers [83].

11.4.3 Drift Instability and Auto-modulation

In a perpendicular field and with a completely saturated fixed layer, the droplet finds itself in a circularly symmetric field landscape and remains stable underneath the nanocontact. However, if either the field or the fixed layer magnetization (or both) are tilted away from the film normal, the effective field landscape becomes distorted and the droplet shifts away from the nanocontact center [78]. If the non-uniformity is increased beyond a certain critical value this shift can be large enough to eventually dislodge, which allows the droplet to propagate away from the nanocontact, losing amplitude to damping until it finally decays completely. If the current is above the threshold for droplet nucleation, a new droplet can again form underneath the nanocontact and the process can repeat itself indefinitely.

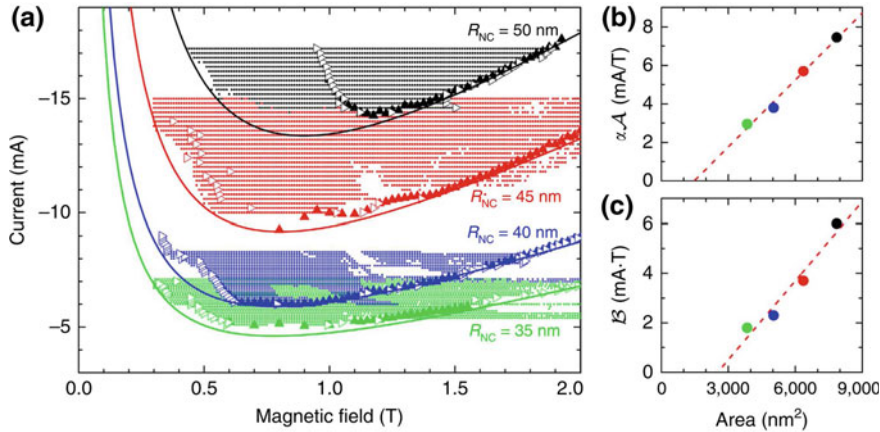


Fig. 11.3 **a** Droplet nucleation boundary determined experimentally from field sweeps (empty triangles), current sweeps (solid triangles), and from the presence of low-frequency microwave noise (solid circles) for devices with different NC radii R_{NC} . Fits using (11.3) are shown by solid lines using the same color code for each R_{NC} . The coefficients \mathcal{A} and \mathcal{B} are shown in **b** and **c** as a function of NC area utilizing the same color code as shown in (a). (Adapted from [80] with permission)

Figure 11.4a shows an example of this process [83]. First a stable droplet is allowed to nucleate in a uniform effective field landscape. Then the applied field is tilted away from the normal about 8° , which induces enough non-uniformity to make the droplet move away from the nanocontact and finally dissipate entirely. Within a few nanoseconds a new droplet forms but almost immediately succumbs to the same drift instability. While this process can have a well-defined periodicity at zero temperature, thermal fluctuations induces large variations in the droplet life-time which leads to the generation of low-frequency microwave noise instead of a well-defined frequency.

Well-defined sub-GHz frequencies can however still be observed at room temperature and even lead to auto-modulation of the main precession signal, as shown in Fig. 11.4b where both first and second order modulation sidebands are clearly observable although no external modulation was provided [79]. This auto-modulating behavior was reproduced by micromagnetic simulations if the parameters were adjusted such that the droplet performed a periodic translational motion *without* leaving the nanocontact. It is however noteworthy that while droplet nucleation is highly reproducible from device to device, auto-modulation displays a much greater variability, sometimes not showing at all, which corroborates that the details of the effective field landscape, typically affected by nanocontact imperfections, govern this behavior.

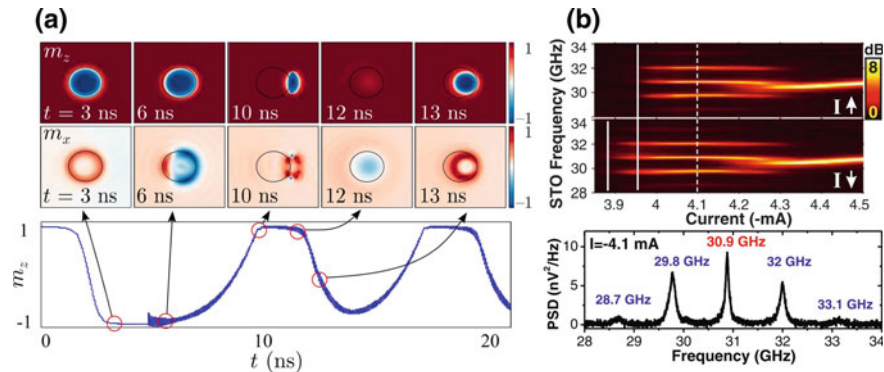


Fig. 11.4 **a** Micromagnetic simulations of a droplet, first ($t < 5$ ns) in a perpendicular field and then in a field tilted about 8° away from the film normal. In the tilted field the droplet shifts away from the nanocontact center and finally dislodges and dissipates away, after which a new droplet can form (From [83] with permission). **b** Auto-modulation of the droplet precession frequency showing both first and second order upper and lower modulation sidebands. (Adapted with permission from [79])

11.4.4 Breathing and Droplet Perimeter Modes

Already the first experimental demonstration of droplets showed evidence of droplet breathing related to fundamental modes of the droplet perimeter. It was later worked out, both analytically and using micromagnetic simulations, that the driving mechanism for this excitation of the perimeter eigenmodes is parametric pumping by the fundamental spin precession itself.

Figure 11.5a–f show spatial map snapshots of the free layer magnetization during micromagnetic simulations of a droplet in a perpendicular field and with a fixed layer that is saturated along the film normal. The top row shows the droplet at three different fields and at currents just above droplet nucleation threshold. In all cases, the droplet is highly stable, the perimeter follows the nanocontact edge closely, and all spins precess in phase. The main effects of the increasing applied field is a linear increase in the precession frequency and a slight reduction of the droplet size due to its increasing Zeeman energy.

The situation changes dramatically if the current is increased an order of magnitude (Fig. 11.5d–f). The droplet perimeter is now strongly excited on eigenmodes with $n = 3 - 5$ as the field increases. Figure 11.5g shows the frequency of the generated microwave signal as a function of applied field at this higher current. Two qualitatively different types of regimes can be observed: (i) an unperturbed droplet with a frequency that closely follows a linear dependence (dashed line) given by theory, and (ii) three regions where the $n = 3 - 5$ perimeter eigenmodes are excited. In these regions, the frequency of precession is close to twice that of the excited perimeter mode, which indicates that the fundamental precession drives the eigenmodes through parametric excitation. It also appears that the interaction between

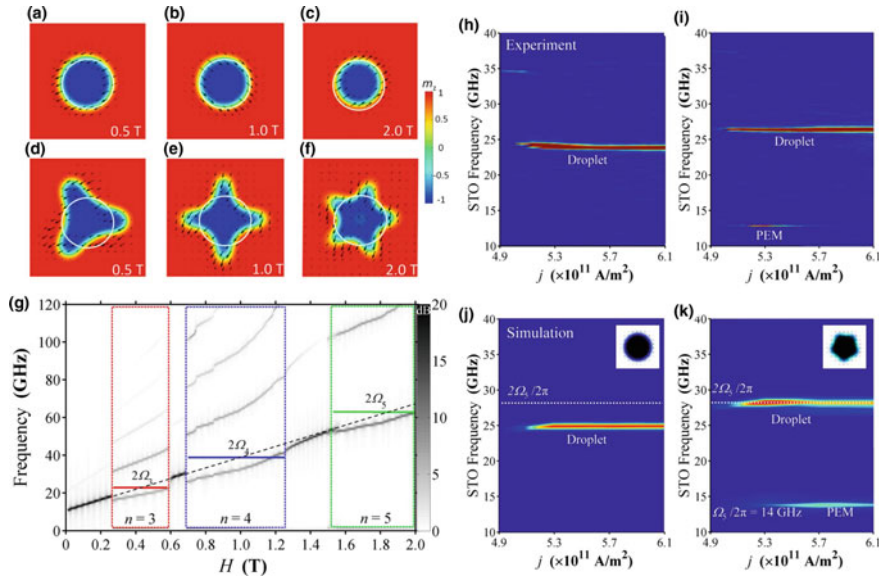


Fig. 11.5 **a–c** Micromagnetically simulated droplets versus increasing perpendicular field and at a current just above the nucleation threshold. The main effects of the magnetic field is a linear increase of the precession frequency and a slight compression of the droplet due to its increasing Zeeman energy. **d–f** Same simulated device at a higher current, now showing strong eigenmodes of the perimeter, with mode number increasing with field. **g** The microwave frequency of the same device highlighting the three regions where the eigenmodes are excited. In each case, the precession frequency and twice the eigenmode frequency (indicated by straight colored lines) overlap, suggesting parametric excitation. **h–i** Experimental power spectral density data for a STNO measured at two different fields, where the second plots shows the appearance of a perimeter eigenmode excitation at half the precession frequency. **j–k** Micromagnetic simulations of a similar device reproducing the overall behavior and indicating that a fifth order eigenmode is likely excited. (Adapted with permission from [84])

the fundamental precession and the perimeter modes leads to mode hybridization, as evidenced by a reduction of the droplet frequency and the appearance of a large number of higher harmonics.

In experiments, the drive current can typically not be increased an order of magnitude above the nucleation threshold, and observations of excited perimeter modes are rare [79, 84]. Figure 11.5h–i shows one device where an additional frequency at about half the droplet frequency appears for certain field and current conditions. The micromagnetic simulations indicate that a fifth order perimeter eigenmode is excited in this particular case.

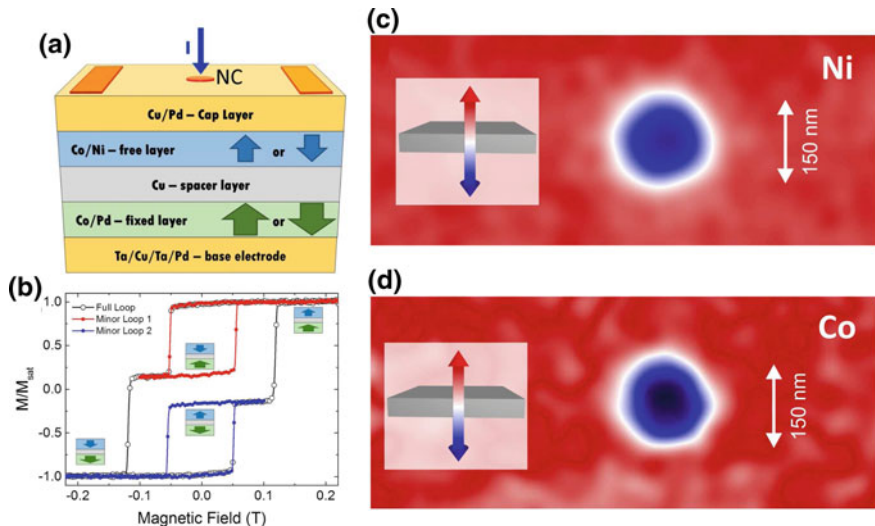


Fig. 11.6 **a** Schematic of the all-perpendicular STNO. **b** Major and minor hysteresis loops showing well defined square switching of both the free and the fixed layer, indicating strong perpendicular anisotropy in both. **c** Direct STXM observation of a fully reversed droplet using the Ni edge. **d** Direct STXM observation of the same droplet using the Co edge (normalized to the Co content in the free layer). (Adapted from [85] with permission)

11.4.5 Direct Microscopic Observation of Magnetic Droplets

Direct imaging of magnetic droplets has proven difficult. Due to their small size, the preferred technique is again STXM, which requires that devices be fabricated on X-ray transparent SiN membranes and that the top contact providing current to the nanocontact be as thin as possible. The devices must then survive several hours of operation in a vacuum where heat dissipation is much less effective. Finally, the measurement is made even more challenging since stable droplets require a perpendicular field and a fully saturated fixed layer. The first attempts at direct observations of droplets were made on orthogonal spin valves, where the applied field (0.7 T) was possibly not sufficient to fully saturate the NiFe fixed layer. While a region of reduced moment along the z axis could be observed, which in principle is consistent with a droplet core, the degree of reversal (25°) was much less than the expected (close to) full reversal. In addition, the observed region of reduced moment was highly irregular, in particular at higher current. Both observations are consistent with the droplet suffering from drift instabilities, i.e. a droplet is only present underneath the nanocontact for part of the time-averaged STXM measurement resulting in an apparent reduction of the core reversal, and the droplet drifting away from the nanocontact leads to an irregular apparent shape of the region of reduced moment.

Very recently, droplets have also been realized in STNOs where *both* the free and the fixed layer have their remanent states along the film normal [85]. In such

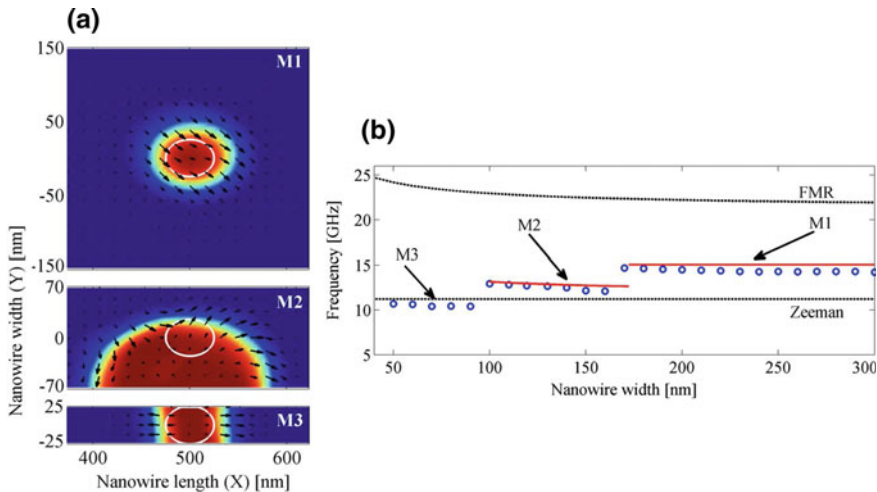


Fig. 11.7 **a** Top view snapshots of the free layer magnetization in a micromagnetic simulation of an all-perpendicular nano-contact STNO where the lateral extension of the free layer has been consecutively reduced in the y direction. M1: Ordinary droplet. M2: Edge droplet. M3: Quasi-1D droplet. **b** Droplet frequency at threshold as a function of the nanowire width. (Adapted from [86] with permission)

all-perpendicular STNOs, the requirement of a strong perpendicular field for stable droplets is greatly relaxed, which both makes the experimental set-up less complicated and reduces the required drive current. Thanks to the symmetric effective field landscape (neither the field nor the fixed layer magnetization are tilted) any droplet drift instability should be suppressed. As a consequence, STXM measurements on both the Ni and the Co edges yield a fully reversed droplet with a well-defined circular perimeter (Fig. 11.6). Somewhat unexpectedly, the droplet size was found to be about twice as large as the nanocontact, which was interpreted as mainly due to lateral current spread in the STNO making the effective nanocontact area larger.

11.4.6 Edge and 1-Dimensional Magnetic Droplets

Droplets have also been studied in reduced dimensions where simulations of droplets in magnetic nanowires suggest that the droplet can interact with the nanowire sides to first form a so-called edge droplet, where the droplet is only attached to one side of the wire, and a 1-dimensional droplet, if the nanowire width is further reduced (Fig. 11.7). The edge droplet has the form of half a disk, i.e. it is essentially forming one half of a much larger droplet, consistent with the microwave frequency of such a larger droplet. The 1-dimensional droplet corresponds to two precessing domain walls, continuously transforming between Bloch and Néel walls as their spins precess.

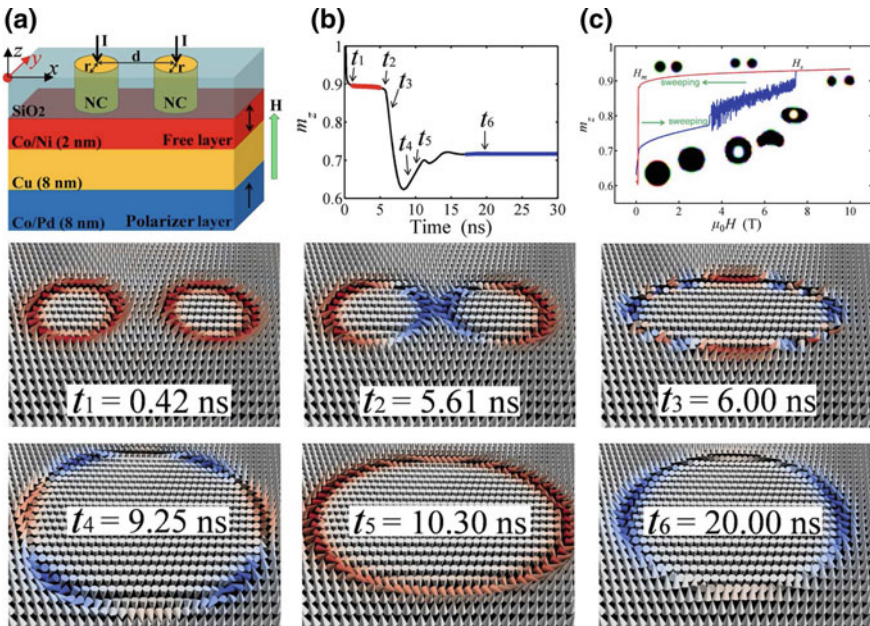


Fig. 11.8 **a** Schematic of two nano-contacts fabricated on top of an orthogonal spin valve stack. **b** Temporal evolution of the total moment along the z direction of the simulation area showing how two individual droplets have formed at t_1 and remain stable for about 5 ns until their mutual interaction make them coalesce at about $t_1 = 6$ ns. The spatial profiles of the droplets and their interactions can be followed in the six panels labelled with the corresponding times $t_1 - t_6$. **c** The merged droplet can be broken up by applying a very strong perpendicular field and to reform another merged droplet, the field must again be reduced. (Adapted from [87] with permission)

11.4.7 Interacting and Merging Droplets

As nano-contacts can be fabricated very close to each other, it is in principle possible to nucleate two or more droplets and study their mutual interactions. While this has not yet been done experimentally, numerical simulations indicate that two adjacent droplets can interact through their precessing spins and merge to form a much larger droplet spanning both original nano-contacts (Fig. 11.8) [87]. This is a hysteretic process as the merged droplet is highly stable. By increasing the magnetic field to several Tesla, the merged droplet can eventually be broken up into two individual droplets when the Zeeman energy of the large merged droplet becomes prohibitive (Fig. 11.8c).

11.5 Topological Magnetodynamical Solitons

11.5.1 Adding Topology to Magnon Drops

The theoretical possibility of adding topology to magnetodynamical solitons in ultra-thin magnetic films with strong perpendicular anisotropy and zero SW damping has been discussed by Ivanov and coworkers [88, 89]. In contrast to the non-topological magnon drop, where all spins precess in phase, the spins in the topological counterpart all precess at the same frequency, but have a finite phase shift along the perimeter to form bound states with an integral phase shift of $2\pi n$ along the perimeter. As a consequence, the topological version has a slightly higher energy than the topologically trivial drop.

11.5.2 Dynamically Stabilized Skyrmions

With the advent of (static) nano-skyrmions in thin magnetic films with both strong PMA and Dzyaloshinskii-Moriya interaction (DMI) [90–93], the possibility of adding topology to magnetic droplets was investigated by Zhou et al. [94]. As in the conservative case, it was shown that topological versions can indeed be realized in numerical simulations, and that DMI is not required for their stability—the precessional state provides the stability whether or not DMI is present. This is hence in stark contrast to the static nano-skyrmion, which requires a very high DMI to be stable [92]. From a skyrmion point of view, dynamics is hence a *third* mechanism, in addition to magnetostatics and DMI, for stability.

Figure 11.9 shows a micromagnetic simulation of an all-perpendicular nano-contact STNO where the free layer also has substantial DMI. The simulation starts at a current level where only an ordinary droplet with topological number $S = 0$ is nucleated (t_2). While a stable droplet has all its spin precessing in phase with zero topological density at all points, the large DMI favors a chiral magnetic structure, perturbs the droplet perimeter, and induces a substantial topological density at opposing sides of the droplet (t_3 and t_4). These perturbations increase with current density and when the drive current is increased the original droplet becomes unstable and transforms into a *topological* magnetodynamical soliton, a so-called dynamical skyrmion, with $S = 1$ ($t_5 - t_7$). When the current is again reduced, the dynamical skyrmion remains stable, now at a higher frequency. If the current is further decreased, SW damping takes over and the dynamical skyrmion collapses into a uniform ferromagnetic state.

The dynamical skyrmion shows a number of drastically different properties compared to the droplet. There is now a finite phase shift between spins along the perimeter, such that a full 2π rotation is acquired along the perimeter length. The size of the dynamical skyrmion breathes with the precession frequency as the magnetization texture continually transform between a vortex and a hedgehog skyrmion

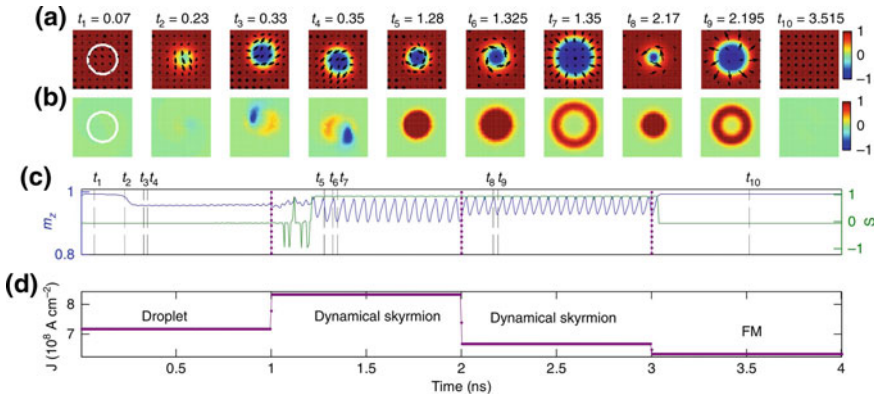


Fig. 11.9 **a** Snapshot top views of the magnetic state of the free layer in an all-perpendicular nano-contact STNO with substantial DMI. The white circle outlines the nano-contact. The color scale shows the m_z component of the magnetization and the black arrows indicate its in-plane orientation and magnitude. **b** Snapshots of the topological density over the same simulation area as in **(a)**. **c** Plots of the m_z component of the free layer magnetization overlayed on a plot of the topological number (the integrated topological density) S . **d** The current density applied during the simulation and labels high-lighting the magnetic state of the free layer. (From [94] with permission)

character. The breathing amplitude is proportional to the DMI, which favors expansion of the hedgehog texture, but wants to minimize the extension of the vortex texture. The strong breathing provides a route to efficient generation of microwave signals since a large part of the spins involved in the breathing experiences a full parallel-to-antiparallel reversal and hence make use of all the available magnetoresistance.

11.5.3 Possible Experimental Demonstrations of Dynamical Skyrmions

There is so far only one report on the experimental demonstration of dynamical skyrmions [95]. In nano-gap SHNOs based on Pt/[Co/Ni]₆ multilayers, Liu et al. observe a well-defined microwave signal well below the FMR spectrum. The signal is at some field and current combinations accompanied by pronounced auto-modulated sidebands. Since all observations, however, are also consistent with the nucleation and auto-modulation of a droplet, additional experiments will be needed to claim with confidence that a dynamical skyrmion has indeed been observed. One potential way forward would be to study how the observed auto-oscillation locks to microwave fields of different symmetries [94].

11.6 Conclusions and Outlook

The possibility to drive very high intensity local spin currents in spin torque and spin Hall nano-oscillators have opened up a realm of new possibilities to realize and observe magnetodynamical solitons on the nano-scale. In this work we have reviewed the present state-of-the-art with particular focus on spin wave bullets and magnetic droplets. It is safe to say that the full potential of these novel objects is far from exhausted. With the possibility of direct soliton observation using techniques such as STXM and high-sensitivity electrical studies using MTJs, the future promises a continued increasing understanding and quite likely the discovery of both novel magnetodynamical solitons and novel effects based on them.

Acknowledgements Discussions with M. Ahlberg, A. A. Awad, S. Chung, R. K. Dumas, M. Dvornik, A. Houshang, S. M. Mohseni, R. Khymyn, and Y. Zhou are gratefully acknowledged. Work funded by The Swedish Research Council, The Knut and Alice Wallenberg Foundation, and the Gärden Gustafsson Foundation.

References

1. B.A. Kalinikos, N.G. Kovshikov, A.N. Slavin, Envelope solitons and modulation instability of dipole-exchange magnetization waves in yttrium iron garnet films. Sov. Phys. JETP **67**(2), 303–312 (1988)
2. J. Slonczewski, Current-driven excitation of magnetic multilayers. J. Magn. Magn. Mater. **159**(1-2), L1–L7 (1996). ISSN: 03048853, [https://doi.org/10.1016/0304-8853\(96\)00062-5](https://doi.org/10.1016/0304-8853(96)00062-5)
3. L. Berger, Emission of spin waves by a magnetic multilayer traversed by a current. Phys. Rev. B **54**(13), 9353–9358 (1996). ISSN: 0163-1829
4. L. Berger, Low-field magnetoresistance and domain drag in ferromagnets. J. Appl. Phys. **49**(3), 2156 (1978). ISSN: 00218979, <https://doi.org/10.1063/1.324716>
5. L. Berger, Domain drag effect in the presence of variable magnetic field or variable transport current. J. Appl. Phys. **50**(B3), 2137 (1979). ISSN: 00218979, <https://doi.org/10.1063/1.327083>
6. P.P. Freitas, L. Berger, Observation of s-d exchange force between domain walls and electric current in very thin Permalloy films. J. Appl. Phys. **57**(4), 1266–1269 (1985). <https://doi.org/10.1063/1.334524>
7. J.C. Slonczewski, Conductance and exchange coupling of two ferromagnets separated by a tunneling barrier. Phys. Rev. B **39**, 6995–7002 (1989). <https://doi.org/10.1103/PhysRevB.39.6995>
8. M.N. Baibich et al., Giant magnetoresistance of (001)Fe/(001)Cr magnetic superlattices. Phys. Rev. Lett. **61**(21), 2472 (1988). <https://doi.org/10.1103/PhysRevLett.61.2472>
9. G. Binasch et al., Enhanced magnetoresistance in layered magnetic structures. Phys. Rev. B **39**(7), 4828–4830 (1989)
10. T. Miyazaki, N. Tezuka, Giant magnetic tunneling effect in Fe/Al₂O₃/Fe junction. J. Magn. Magn. Mater. **139**, L231 (1995)
11. J.S. Moodera et al., Large magnetoresistance at room temperature in ferromagnetic thin film tunnel junctions. Phys. Rev. Lett. **74**(16), 3273 (1995)
12. M. Tsoi et al., Excitation of a magnetic multilayer by an electric current. Phys. Rev. Lett. **80**, 4281–4284 (1998). <https://doi.org/10.1103/PhysRevLett.80.4281>
13. E.B. Myers et al., Current-induced switching of domains in magnetic multilayer devices. Science **285**(5429), 867–870 (1999). <https://doi.org/10.1126/science.285.5429.867>

14. J.A. Katine et al., Current-driven magnetization reversal and spin-wave excitations in Co/Cu/Co pillars. *Phys. Rev. Lett.* **84**, 3149–3152 (2000). <https://doi.org/10.1103/PhysRevLett.84.3149>
15. J. Åkerman, Toward a universal memory. *Science* **743**(9), 508–510 (2005)
16. B.N. Engel et al., A 4-Mb toggle MRAM based on a novel bit and switching method. *IEEE Trans. Magn.* **41**(1), 132–136 (2005). ISSN: 0018-9464, <https://doi.org/10.1109/TMAG.2004.840847>
17. D. Ralph, M. Stiles, Spin transfer torques. *J. Magn. Magn. Mater.* **320**(7), 1190–1216 (2008). ISSN: 03048853, <https://doi.org/10.1016/j.jmmm.2007.12.019>
18. J.Z. Sun, D.C. Ralph, Magnetoresistance and spin-transfer torque in magnetic tunnel junctions. *J. Magn. Magn. Mater.* **320**(7), 1227–1237 (2008). ISSN: 03048853, <https://doi.org/10.1016/j.jmmm.2007.12.008>
19. J.A. Katine, E.E. Fullerton, Device implications of spin-transfer torques. *J. Magn. Magn. Mater.* **320**(7), 1217–1226 (2008). ISSN: 03048853, <https://doi.org/10.1016/j.jmmm.2007.12.013>
20. T.J. Silva, W.H. Rippard, Developments in nano-oscillators based upon spin-transfer point-contact devices. *J. Magn. Magn. Mater.* **320**(7), 1260–1271 (2008). ISSN: 0304-8853, <https://doi.org/10.1016/j.jmmm.2007.12.022>
21. J.-V. Kim, Spin-torque oscillators. *Solid State Phys.* **63**, 217–294 (2012). ISSN: 00811947, <https://doi.org/10.1016/B978-0-12-397028-2.00004-7>
22. K.L. Wang, J.G. Alzate, P. Khalili Amiri, Low-power non-volatile spintronic memory: STT-RAM and beyond. *J. Phys. D: Appl. Phys.* **46**(7), 074003 (2013). ISSN: 0022-3727, <https://doi.org/10.1088/0022-3727/46/7/074003>
23. N. Locatelli, V. Cros, J. Grollier, Spin-torque building blocks. *Nat. Mater.* **13**(1), 11–20 (2014)
24. A. Slavin, V. Tiberkevich, Nonlinear auto-oscillator theory of microwave generation by spin-polarized current. *IEEE Trans. Magn.* **45**(4), 1875–1918 (2009)
25. T. Chen et al., Spin-torque and spin-Hall nano-oscillators. *Proc. IEEE* **104**(10), 1919–1945 (2016). ISSN: 0018-9219, <https://doi.org/10.1109/JPROC.2016.2554518>, arXiv:1512.03162, <http://ieeexplore.ieee.org/document/7505988/%20>, <http://arxiv.org/abs/1512.03162%20>, <http://ieeexplore.ieee.org/lpdocs/epic03/wrapper.htm?arnumber=7505988>
26. A. Brataas et al., Spin battery operated by ferromagnetic resonance. *Phys. Rev. B* **66**(6), 060404(R) (2002). ISSN: 0163-1829, <https://doi.org/10.1103/PhysRevB.66.060404>
27. M.D. Stiles, A. Zangwill, Anatomy of spin-transfer torque. *Phys. Rev. B* **66**, 014407 (2002). <https://doi.org/10.1103/PhysRevB.66.014407>
28. K. Xia et al., Spin torques in ferromagnetic/normal-metal structures. *Phys. Rev. B* **65**, 220401 (2002). <https://doi.org/10.1103/PhysRevB.65.220401>
29. M. Zwierzycki et al., First-principles study of magnetization relaxation enhancement and spin transfer in thin magnetic films. *Phys. Rev. B* **71**, 064420 (2005). <https://doi.org/10.1103/PhysRevB.71.064420>
30. I. Theodonis et al., Anomalous bias dependence of spin torque in magnetic tunnel junctions. *Phys. Rev. Lett.* **97**, 237205 (2006). <https://doi.org/10.1103/PhysRevLett.97.237205>
31. R. Matsumoto et al., Spin-torque diode measurements of MgO-based magnetic tunnel junctions with asymmetric electrodes. *Appl. Phys. Express* **4**(6), 063001 (2011)
32. J.C. Sankey et al., Measurement of the spin-transfer-torque vector in magnetic tunnel junctions. *Nat. Phys.* **4**(1), 67–71 (2008). ISSN: 1745-2473, <https://doi.org/10.1038/nphys783>
33. M.I. D'yakonov, V.I. Perel', Possibility of orienting electron spins with current. *Sov. Phys. JETP Lett.* **13**(11), 467 (1971)
34. M.I. Dyakonov, V.I. Perel, Current-induced spin orientation of electrons in semiconductors. *Phys. Lett. A* **35**(6), 459–460 (1971). ISSN: 03759601, [https://doi.org/10.1016/0375-9601\(71\)90196-4](https://doi.org/10.1016/0375-9601(71)90196-4)
35. J.E. Hirsch, Spin Hall effect induced by resonant scattering on impurities in metals. *Phys. Rev. Lett.* **83**(15), 1834 (1999). ISSN: 1079-7114
36. Y.K. Kato et al., Observation of the spin Hall effect in semiconductors. *Science* **306**(5703), 1910–1913 (2004). ISSN: 0036-8075, <https://doi.org/10.1126/science.1105514>
37. J. Wunderlich et al., Experimental observation of the spin-Hall effect in a two-dimensional spin-orbit coupled semiconductor system. *Phys. Rev. Lett.* **94**(4), 047204 (2005). ISSN: 00319007, <https://doi.org/10.1103/PhysRevLett.94.047204>, arXiv: 0410295 [cond-mat]

38. I.M. Miron et al., Perpendicular switching of a single ferromagnetic layer induced by in-plane current injection. *Nature* **476**(7359), 189–193 (2011). ISSN: 0028-0836, <https://doi.org/10.1038/nature10309>
39. L. Liu et al., Spin-torque switching with the giant spin Hall effect of tantalum. *Science* **336**(6081), 555–558 (2012). ISSN: 1095-9203, <https://doi.org/10.1126/science.1218197>
40. L. Liu et al., Magnetic oscillations driven by the spin Hall effect in 3-terminal magnetic tunnel junction devices. *Phys. Rev. Lett.* **109**(18), 186602 (2012). ISSN: 0031-9007, <https://doi.org/10.1103/PhysRevLett.109.186602>
41. V.E. Demidov et al., Magnetic nano-oscillator driven by pure spin current. *Nat. Mater.* **11**(12), 1028–1031 (2012). ISSN: 1476-1122
42. E.H. Hall, On the possibility of transvers currents in ferromagnets. *Philos. Mag.* **12**, 157–172 (1881)
43. N. Nagaosa et al., Anomalous Hall effect. *Rev. Mod. Phys.* **82**(2), 1539–1592 (2010). ISSN: 0034-6861, <https://doi.org/10.1103/RevModPhys.82.1539>, arXiv: 0904.4154
44. E.H. Hall, On a new action of the magnet on electric currents. *Am. J. Math.* **2**(287), 287–292 (1879). ISSN: 0028-0836, <https://doi.org/10.1038/021361a0>
45. A. Hoffmann, Spin Hall effects in metals. *IEEE Trans. Magn.* **49**(10), 5172–5193 (2013). ISSN: 0018-9464, <https://doi.org/10.1109/TMAG.2013.2262947>
46. J. Sinova et al., Spin Hall effects. *Rev. Mod. Phys.* **87**, 1213–1260 (2015). <https://doi.org/10.1103/RevModPhys.87.1213>
47. L. Landau, E. Lifshitz, On the theory of the dispersion of magnetic permeability in ferromagnetic bodies. *Phys. Z. Sowjetunion* **8**, 153–169 (1935)
48. T.L. Gilbert, A Lagrangian formulation of the gyromagnetic equation of the magnetization field. *Phys. Rev.* **100**, 1243 (1955)
49. A. Jenkins, Self-oscillation. *Phys. Rep.* **525**(2), 167–222 (2013). ISSN: 03701573, <https://doi.org/10.1016/j.physrep.2012.10.007>
50. A.N. Slavin, P. Kabos, Approximate theory of microwave generation in a current-driven magnetic nanocontact magnetized in an arbitrary direction. *IEEE Trans. Magn.* **41**(4), 1264–1273 (2005). <https://doi.org/10.1109/TMAG.2005.845915>
51. M. Tsoi et al., Generation and detection of phase-coherent current driven magnons in magnetic multilayers. *Nature* **406**(6791), 46–48 (2000). ISSN: 0028-0836
52. J.Z. Sun, Current-driven magnetic switching in manganite trilayer junctions. *J. Magn. Magn. Mater.* **202**(1), 157–162 (1999). ISSN: 0304-8853, [https://doi.org/10.1016/S0304-8853\(99\)00289-9](https://doi.org/10.1016/S0304-8853(99)00289-9)
53. W.H. Rippard, M.R. Pufall, T.J. Silva, Quantitative studies of spinmomentum-transfer-induced excitations in Co/Cu multilayer films using point-contact spectroscopy. *Appl. Phys. Lett.* **82**(8), 1260 (2003). ISSN: 00036951, <https://doi.org/10.1063/1.1556168>
54. M.R. Pufall, W.H. Rippard, T.J. Silva, Materials dependence of the spin-momentum transfer efficiency and critical current in ferromagnetic metal/Cu multilayers. *Appl. Phys. Lett.* **83**(2), 323–325 (2003). <https://doi.org/10.1063/1.1590432>
55. W.H. Rippard et al., Direct-current induced dynamics in Co90Fe10/Ni80Fe20 point contacts. *Phys. Rev. Lett.* **92**, 027201 (2004). <https://doi.org/10.1103/PhysRevLett.92.027201>
56. R.K. Dumas et al., Recent advances in nanocontact spin-torque oscillators. *IEEE Trans. Magn.* **50**(6), 4100107 (2014). ISSN: 0018-9464, <https://doi.org/10.1109/TMAG.2014.2305762>
57. S.I. Kiselev et al., Microwave oscillations of a nanomagnet driven by a spin-polarized current. *Nature* **425**(6956), 380–383 (2003). ISSN: 0028-0836
58. V.E. Demidov, S. Urazhdin, S.O. Demokritov, Direct observation and mapping of spin waves emitted by spin-torque nano-oscillators. *Nature Mater.* **9**(12), 984–988 (2010). ISSN: 1476-1122, <https://doi.org/10.1038/nmat2882>
59. E.R. Evarts, M.R. Pufall, W.H. Rippard, Continuous film vs. device-level ferromagnetic resonance in magnetic tunnel junction thin films. *J. Appl. Phys.* **113**(8), 083903 (2013). <https://doi.org/10.1063/1.4793589>
60. M. Ranjbar et al., CoFeB-Based spin Hall nano-oscillators. *IEEE Magn. Lett.* **5**, 3000504 (2014). <https://doi.org/10.1109/LMAG.2014.237515>

61. V.E. Demidov et al., Nanoconstriction-based spin-Hall nano-oscillator. *Appl. Phys. Lett.* **105**(17), 172410 (2014). <https://doi.org/10.1063/1.4901027>
62. H. Mazraati et al., Low operational current spin Hall nano-oscillators based on NiFe/Wbilayers. *Appl. Phys. Lett.* **109**(24), 242402 (2016). ISSN: 0003-6951, <https://doi.org/10.1063/1.4971828>
63. P. Dürrenfeld et al., A 20 nm spin Hall nano-oscillator. *Nanoscale* **9**(3), 1285–1291 (2017). ISSN: 2040-3364, <https://doi.org/10.1039/C6NR07903B>, <http://xlink.rsc.org/?DOI=C6NR07903B>
64. A.A. Awad et al., Long-range mutual synchronization of spin Hall nanooscillators. *Nat. Phys.* **13**(3), 292–299 (2017). ISSN: 1745-2473, <https://doi.org/10.1038/nphys3927>, <https://doi.org/10.1038/nphys3927>
65. Z. Duan et al., Nanowire spin torque oscillator driven by spin orbit torques. *Nat. Commun.* **5**, 5616 (2014). ISSN: 2041-1723, <https://doi.org/10.1038/ncomms6616>
66. Y. Silberberg, Collapse of optical pulses. *Opt. Lett.* **15**(22), 1282 (1990). ISSN: 0146-9592, <https://doi.org/10.1364/OL.15.001282>, <http://www.osapublishing.org/abstract.cfm?uri=ol-15-22-1282>, <https://www.osapublishing.org/ol/fulltext.cfm?uri=ol-15-22-1282>, <https://www.osapublishing.org/abstract.cfm?URI=ol-15-22-1282>
67. S.O. Demokritov, B. Hillebrands, A.N. Slavin, Brillouin light scattering studies of confined spin waves: linear and nonlinear confinement (2001). [https://doi.org/10.1016/S0370-1573\(00\)00116-2](https://doi.org/10.1016/S0370-1573(00)00116-2)
68. M. Madami et al., Direct observation of a propagating spin wave induced by spin-transfer torque. *Nat. Nanotech.* **6**, 635 (2011). <https://doi.org/10.1038/nnano.2011.140>
69. M. Madami et al., Propagating spin waves excited by spin-transfer torque: a combined electrical and optical study. *Phys. Rev. B* **92**, 024403 (2015). <https://doi.org/10.1103/PhysRevB.92.024403>
70. A. Houshang et al., Spin-wave-beam driven synchronization of nanocontact spin-torque oscillators. *Nat. Nanotech.* **11**(3), 280–286 (2016). ISSN: 1748-3387, <https://doi.org/10.1038/nnano.2015.280>
71. S. Bonetti et al., Experimental evidence of self-localized and propagating spin wave modes in obliquely magnetized current-driven nanocontacts. *Phys. Rev. Lett.* **105**, 217204 (2010). <https://doi.org/10.1103/PhysRevLett.105.217204>
72. S. Bonetti et al., Power and line width of propagating and localized modes in nanocontact spin-torque oscillators. *Phys. Rev. B* **85**(17), 174427 (2012). ISSN: 1098-0121, <https://doi.org/10.1103/PhysRevB.85.174427>
73. R.K. Dumas et al., Spin-wave-mode coexistence on the nanoscale: a consequence of the oersted-field-induced asymmetric energy landscape. *Phys. Rev. Lett.* **110**, 257202 (2013). <https://doi.org/10.1103/PhysRevLett.110.257202>
74. G. Consolo et al., Non-stationary excitation of two localized spin-wave modes in a nano-contact spin torque oscillator. *J. Appl. Phys.* **114**(15), 153906 (2013)
75. S. Bonetti et al., Direct observation and imaging of a spin-wave soliton with p-like symmetry. *Nat. Commun.* **6**, 8889 (2015). ISSN: 2041-1723, <https://doi.org/10.1038/ncomms9889>
76. B.A. Ivanov, A.M. Kosevich, Bound states of a large number of magnons in a ferromagnet with a single-ion anisotropy. *Soviet J. Exp. Theor. Phys.* **45**, 1050 (1977)
77. A.M. Kosevich, B.A. Ivanov, A.S. Kovalev. Magnetic solitons. *Phys. Rep.* **194**(3-4), 117–238 (1990). ISSN: 03701573, [https://doi.org/10.1016/0370-1573\(90\)90130-T](https://doi.org/10.1016/0370-1573(90)90130-T), <http://linkinghub.elsevier.com/retrieve/pii/037015739090130T>
78. M.A. Hoefer, T.J. Silva, M.W. Keller, Theory for a dissipative droplet soliton excited by a spin torque nanocontact. *Phys. Rev. B* **82**, 054432 (2010). <https://doi.org/10.1103/PhysRevB.82.054432>
79. S.M. Mohseni et al., Spin torque-generated magnetic droplet solitons. *Science* **339**(6125), 1295–1298 (2013). ISSN: 0036-8075, <https://doi.org/10.1126/science.1230155>

80. S. Chung et al., Magnetic droplet nucleation boundary in orthogonal spin-torque nano-oscillators. *Nat. Commun.* **7**, 11209 (2016). ISSN: 2041-1723, <https://doi.org/10.1038/ncomms11209>, <http://www.nature.com/ncomms/2016/160418/ncomms11209/abs/ncomms11209.html>, <http://www.nature.com/doifinder/10.1038/ncomms11209>
81. S.M. Mohseni et al., High frequency operation of a spin-torque oscillator at low field. *Phys. Status Solidi Rapid Res. Lett.* **5**(12), 432–434 (2011). ISSN: 18626254, <https://doi.org/10.1002/pssr.201105375>
82. F. Macià, D. Backes, A.D. Kent, Stable magnetic droplet solitons in spin-transfer nanocontacts. *Nat. Nanotech.* **9**, 992–996 (2014). ISSN: 1748-3387, <https://doi.org/10.1038/nnano.2014.255>
83. S. Lendínez et al., Observation of droplet soliton drift resonances in a spin-transfer-torque nanocontact to a ferromagnetic thin film. *Phys. Rev. B* **92**(17), 174426 (2015). ISSN: 1098-0121, <https://doi.org/10.1103/PhysRevB.92.174426>, eprint: 1507.08218, <http://link.aps.org/doi/10.1103/PhysRevB.92.174426>
84. D. Xiao et al., Parametric autoexcitation of magnetic droplet soliton perimeter modes. *Phys. Rev. B* **95**(2), 024106 (2017). ISSN: 2469-9950. <https://doi.org/10.1103/PhysRevB.95.024106>, eprint: 1610.06650, <http://link.aps.org/doi/10.1103/PhysRevB.95.024106>
85. S. Chung et al., Direct observation of Zhang-Li torque expansion of magnetic droplet solitons. *Phys. Rev. Lett.* **120**, 217204 (2018). <https://doi.org/10.1103/PhysRevLett.120.217204>
86. E. Iacocca et al., Generation linewidth of mode-hopping spin torque oscillators. *Phys. Rev. B* **89**, 054402 (2014). <https://doi.org/10.1103/PhysRevB.89.054402>
87. D. Xiao et al., Merging droplets in double nanocontact spin torque oscillators. *Phys. Rev. B* **93**(9), 094431 (2016). ISSN: 2469-9950, <https://doi.org/10.1103/PhysRevB.93.094431>, <http://link.aps.org/doi/10.1103/PhysRevB.93.094431>
88. B.A. Ivanov, C.E. Zaspel, I.A. Yastremsky, Small-amplitude mobile solitons in the two-dimensional ferromagnet. *Phys. Rev. B* **63**(13), 134413 (2001). ISSN: 0163-1829, <https://doi.org/10.1103/PhysRevB.63.134413>, <http://link.aps.org/doi/10.1103/PhysRevB.63.134413>
89. B. Ivanov et al., Finite energy solitons in highly anisotropic two dimensional ferromagnets. *Phys. Rev. B* **74**(22), 1–17 (2006). ISSN: 1098-0121, <https://doi.org/10.1103/PhysRevB.74.224422>, <http://link.aps.org/doi/10.1103/PhysRevB.74.224422>
90. I. Dzyaloshinskii, Thermodynamic theory of “Weak” ferromagnetism in antiferromagnetic substances. *Sov. Phys. JETP* **5**(6), 1259–1272 (1957)
91. T. Moriya, New mechanism of anisotropic superexchange interaction. *Phys. Rev. Lett.* **4**, 228–230 (1960). <https://doi.org/10.1103/PhysRevLett.4.228>, <http://link.aps.org/doi/10.1103/PhysRevLett.4.228>
92. J. Sampaio et al., Nucleation, stability and current-induced motion of isolated magnetic skyrmions in nanostructures. *Nat. Nanotechnol.* **8**(11), 839–844 (2013). ISSN: 1748-3387, <https://doi.org/10.1038/nnano.2013.210>, <http://www.ncbi.nlm.nih.gov/pubmed/24162000%20>, <http://www.nature.com/doifinder/10.1038/nnano.2013.210>
93. S. Tacchi et al., Interfacial Dzyaloshinskii-Moriya interaction in Pt/CoFeB films: effect of the heavy-metal thickness. *Phys. Rev. Lett.* **118**(14), 147201 (2017). ISSN: 0031-9007, <https://doi.org/10.1103/PhysRevLett.118.147201>, eprint: 1604.02626
94. Y. Zhou et al., Dynamically stabilized magnetic skyrmions. *Nat. Commun.* **6**, 8193 (2015). ISSN: 2041-1723, <https://doi.org/10.1038/ncomms9193>, <http://www.nature.com/doifinder/10.1038/ncomms9193>
95. R.H. Liu, W.L. Lim, S. Urazhdin, Dynamical skyrmion state in a spin current nano-oscillator with perpendicular magnetic anisotropy. *Phys. Rev. Lett.* **114**(13), 137201 (2015). ISSN: 0031-9007, <https://doi.org/10.1103/PhysRevLett.114.137201>, arXiv: 1312.6343, <http://link.aps.org/doi/10.1103/PhysRevLett.114.137201>

Chapter 12

Majorana States



Jeffrey C. Y. Teo

Abstract The main goal of this chapter is to introduce the basic concepts of Majorana fermions and zero energy Majorana bound states, and their origin from topology, magnetism and superconductivity. This chapter gears towards young researchers at their early developing stage in their career, and for the most parts, the central ideas are presented in a self-contained manner without assuming professional background knowledge other than fundamental quantum mechanics and solid state physics.

The main goal of this chapter is to introduce the basic concepts of Majorana fermions and zero energy Majorana bound states, and their origin from topology, magnetism and superconductivity. This chapter gears towards young researchers at their early developing stage in their career, and for the most parts, the central ideas are presented in a self-contained manner without assuming professional background knowledge other than fundamental quantum mechanics and solid state physics. For the more experienced readers, this chapter perhaps can serve as a supplementary to the more advanced review texts by [1–9] among others.

Noticing the incompatibility between Schrödinger's description of quantum mechanics [10] and Einstein's theory of special relativity [11], Paul A. M. Dirac in 1928 revised the quantum theory of relativistic electrons [12]. One of the many ground-breaking consequences of the theory is the prediction of anti-particles, which carry the same spin-exchange statistics but opposite conserved charge (such as electric charge) as their partners. In 1937, right before his mysterious disappearance, Ettore Majorana proposed a symmetrical theory of electron and positron [13] that described self-conjugate particles, now known as Majorana fermions, which are their own anti-particle. None of the elementary fermions in the standard model are Majorana fermions because they all carry gauge charges, and the hypothetical right-handed sterile neutrinos, which may have a Majorana mass, have not been observed.

J. C. Y. Teo (✉)

Department of Physics, University of Virginia, Charlottesville, VA, USA
e-mail: jteo@virginia.edu

Sitting at the opposite end of the energy spectrum, condensed electronic matter, such as a superconductor or a quantum Hall state, often involve strong correlation and quantum entanglement. These characteristics can facilitate fractionalization and the emergent of Majorana fermions.

This chapter focuses on the origin and mechanism for Majorana fermion (MF) and zero energy Majorana bound state (MBS) to appear in a quantum electronic medium. In Sect. 12.2, we first describe the theoretical manifestation of MF and MBS in time reversal breaking topological superconductors (TSC) [14–16]. We review the Kitaev p -wave topological superconducting chain model [17] and some of its recent material realizations [18–21]. We summarize the chiral $p_x + ip_y$ superconductor in two dimensions and explain its chiral Majorana fermion edge mode as well as vortex zero energy MBS [22–27]. In Sect. 12.3, we move to inhomogeneous heterostructures [28–34], where electronic materials with distinct orders are juxtaposed and MF and MBS arise at point and line junctions sandwiched between different materials. Before embarking on these areas, we first begin with a brief review of the relevant background.

12.1 Background and Motivation

Magnetization and conventional s -wave superconductivity are competing orders. For instance, the magnetization order parameter $\hat{S}_z = c_\uparrow^\dagger c_\uparrow - c_\downarrow^\dagger c_\downarrow$ anti-commutes with the s -wave superconducting pairing order parameter $\hat{\Delta} = c_\uparrow c_\downarrow$, i.e. $\hat{S}_z \hat{\Delta} = -\hat{\Delta} \hat{S}_z$. In general, one does not expect a ground state to be a simultaneous eigenstate of \hat{S}_z and $\hat{\Delta}$. Therefore, loosely speaking, a ground state with large magnetization $\langle GS| \hat{S}_z | GS \rangle \sim 1$ must have vanishing pairing because $\langle GS| \hat{\Delta} | GS \rangle \sim \langle GS| \hat{\Delta} \hat{S}_z | GS \rangle = -\langle GS| \hat{S}_z \hat{\Delta} | GS \rangle \sim -\langle GS| \hat{\Delta} | GS \rangle$. Moreover, magnetization and pairing have opposite characteristics regarding charge conservation and time reversal symmetry. While \hat{S}_z commutes with the number operator $\hat{n} = c_\uparrow^\dagger c_\uparrow + c_\downarrow^\dagger c_\downarrow$, $\hat{\Delta}$ anti-commutes with \hat{n} and thus a superconducting ground state must be a superposition of quantum states with different numbers of (Cooper pairs of) electrons. On the other hand, time reversal (TR) symmetry flips spins

$$\mathcal{T} c_\uparrow \mathcal{T}^{-1} = -c_\downarrow, \quad \mathcal{T} c_\downarrow \mathcal{T}^{-1} = c_\uparrow \quad (12.1)$$

and therefore pairing is even under TR $\mathcal{T} \hat{\Delta} \mathcal{T}^{-1} = \hat{\Delta}$ while magnetization is odd under TR $\mathcal{T} \hat{S}_z \mathcal{T}^{-1} = -\hat{S}_z$. In this section, we will consider superconductors beyond the conventional s -wave regime. In particular, we will focus on superconductors that violate TR symmetry. This can be a result of an applied magnetic field, an asymmetric p -wave pairing order parameter, or proximity with a ferromagnet or anti-ferromagnet.

A Bardeen-Cooper-Schrieffer (BCS) superconductor [35, 36] is described by a mean-field theory where the charge $U(1)$ conservation symmetry, $c_j \rightarrow e^{i\phi} c_j$, is

spontaneously broken by the non-zero ground state expectation value of pairing $\tilde{\Delta}_{ij} = \langle GS | c_i c_j | GS \rangle \neq 0$. It is facilitated by an attractive interaction, which can be mediated by phonons for example, that under the mean-field approximation becomes

$$-u_{ij} c_i^\dagger c_i c_j^\dagger c_j + h.c. \longrightarrow u_{ij} \tilde{\Delta}_{ij} c_i^\dagger c_j^\dagger + h.c. \quad (12.2)$$

where the i, j indices represent a combination of spin, orbital, and position degrees of freedom. The dynamics of quasiparticle excitations of the superconductor is described by the mean-field Hamiltonian

$$\hat{H}_{\text{BCS}} = \hat{H}_0 - \epsilon_f \sum_i c_i^\dagger c_i + \sum_{ij} \Delta_{ij} c_i^\dagger c_j^\dagger + h.c. \quad (12.3)$$

where ϵ_f is the Fermi energy, and we have absorbed the interaction strength u_{ij} into the pairing parameter $\Delta_{ij} = u_{ij} \tilde{\Delta}_{ij}$. Here the first term \hat{H}_0 of (12.3) is a kinetic term describing the metallic state. It could be a quadratic Hamiltonian $p^2/2m$ in the nearly free electron limit, or a tight binding model

$$\hat{H}_0 = \sum_{ij} t_{ij} c_i^\dagger c_j + h.c. \quad (12.4)$$

where t_{ij} is the hopping amplitude for an electron to tunnel from site j to site i on a lattice.

Electron operators in momentum space $c_\lambda(\mathbf{k})$ can be defined using operators in real space $c_\lambda(\mathbf{r})$ using the Fourier transform $c_\lambda(\mathbf{r}) = \int \frac{d^d \mathbf{k}}{(2\pi)^d} e^{i\mathbf{k} \cdot \mathbf{r}} c_\lambda(\mathbf{k})$, where $\lambda = 1, \dots, n$ encodes some local degrees of freedom such as spin, orbital and lattice basis. The integration is taken over the momentum space \mathbb{R}^d for a continuum system or the Brillouin zone (BZ) for a lattice periodic system, where d is the dimension of the system. We choose the following Nambu vector notation that combines the creation and annihilation operators

$$\xi(\mathbf{k}) = \left(c_\lambda(\mathbf{k}), i(\sigma_y)_{\lambda\lambda'} c_{\lambda'}^\dagger(-\mathbf{k}) \right)^T \quad (12.5)$$

where σ_y is the Pauli matrix $\begin{pmatrix} 0 & -i \\ i & 0 \end{pmatrix}$ that acts on spin \uparrow, \downarrow . The BCS Hamiltonian (12.3) takes the following form in momentum space

$$\hat{H}_{\text{BCS}} = \int \frac{d^d \mathbf{k}}{(2\pi)^d} \xi(\mathbf{k})^\dagger H_{\text{BdG}}(\mathbf{k}) \xi(\mathbf{k}) \quad (12.6)$$

where $H_{\text{BdG}}(\mathbf{k})$ is a $(2n) \times (2n)$ hermitian matrix known as the Bogoliubov-de Gennes (BdG) Hamiltonian. The Nambu doubling (12.5) is artificial and the anti-commutation relation of fermion operators requires the BdG Hamiltonian matrix (12.6) to satisfy a particle-hole (PH) symmetry:

$$\Xi^{-1} H_{\text{BdG}}(\mathbf{k}) \Xi = \sigma_y \tau_y H_{\text{BdG}}(\mathbf{k})^* \sigma_y \tau_y = -H_{\text{BdG}}(-\mathbf{k}) \quad (12.7)$$

where $\Xi = \sigma_y \tau_y \mathcal{K}$ is the PH operator, \mathcal{K} is the complex conjugation operator, and τ_y is the Pauli matrix $\begin{pmatrix} 0 & -i \\ i & 0 \end{pmatrix}$ that acts on the Nambu degrees of freedom (c, c^\dagger) . It is worth noticing that $\Xi^2 = 1$ and the PH symmetry corresponds to class D of the Altland-Zirnbauer classification of band theories [37].

The BdG Hamiltonian of a BCS superconductor is similar to the Bloch Hamiltonian of a band insulator. Its quasiparticle excitations $\psi(\mathbf{k}) = \xi(\mathbf{k})^\dagger \mathbf{u}(\mathbf{k}) = \sum_{\lambda=1}^n u^\lambda(\mathbf{k}) c_\lambda^\dagger(\mathbf{k}) + u^{n+\lambda}(\mathbf{k}) c_\lambda(-\mathbf{k})$ are represented by eigenvectors $\mathbf{u}(\mathbf{k}) = (u_1(\mathbf{k}), \dots, u_{2n}(\mathbf{k}))$ of the BdG Hamiltonian, $H_{\text{BdG}}(\mathbf{k}) \mathbf{u}(\mathbf{k}) = E(\mathbf{k}) \mathbf{u}(\mathbf{k})$. The excitation requires a finite amount of energy $|E(\mathbf{k})| \geq \Delta_{\text{gap}}$, where $\Delta_{\text{gap}} > 0$ is the smallest amount of energy necessary to excite the ground state.

The PH symmetry of the BdG Hamiltonian (12.7) has two consequences. First, the energy bands are also particle-hole symmetric in the sense that if $E(\mathbf{k})$ is an energy eigenvalue at \mathbf{k} , then $-E(\mathbf{k})$ is also an energy eigenvalue at $-\mathbf{k}$. Second, the energy bands and the eigenstates are redundant. The Nambu doubling (12.5) implies that a “hole” excitation at \mathbf{k} is equivalent to a “particle” at $-\mathbf{k}$, i.e.

$$\psi(\mathbf{k})^\dagger = \Xi \psi(-\mathbf{k}) \Xi^{-1}. \quad (12.8)$$

Therefore, the “negative” energy bands are actually “holes” of the positive energy ones. As a matter of fact, there is no excitation with “negative” energy. As the BdG quasiparticle $\psi(\mathbf{k})$ is a linear superposition of the creation and annihilation operator, it does not transform under the $U(1)$ symmetry and is not associated to an electric charge. However, it carries fermionic statistics and obeys the Pauli’s exclusion principle.

The finite energy gap Δ_{gap} refers to the smallest energy required to excite a BdG quasiparticle $\psi(\mathbf{k})$ in the *bulk* of the superconductor. The wavefunction of $\psi(\mathbf{k})$ is a delocalized plane wave in all directions. When the system has defects or boundaries, there can be additional low energy BdG excitations that are localized and carry energies below the bulk energy gap Δ_{gap} . In this section, we are interested in these mid-gap defect or boundary excitations that are “topologically” protected [3, 6, 8] and stable against perturbations. In particular we focus on the manifestation of protected Majorana fermions (MF) [13, 38] and zero energy Majorana bound states (MBS) [1–5, 7, 9].

Zero energy BdG quasiparticles (also known as zero modes) are special in a particle-hole symmetric system, $\Xi \hat{H} \Xi^{-1} = -\hat{H}$. Suppose ψ_0 is a zero mode so that $[\hat{H}, \psi_0] = 0$, and suppose it is the only zero mode localized at the defect or boundary. The PH symmetry implies $\Xi \psi_0 \Xi^{-1}$ is also a zero mode. However, since the PH symmetry is local, it does not change the localization position, and therefore ψ_0 and $\Xi \psi_0 \Xi^{-1}$ are actually identical.¹ On the other hand, the Nambu doubling (12.5) and the particle-hole symmetry (c.f. 12.8) require the zero mode to be hermitian or self-conjugate

$$\psi_0^\dagger = \Xi \psi_0 \Xi^{-1} = \psi_0. \quad (12.9)$$

¹The quantum phase difference $e^{i\phi}$ between the two can be absorbed by a gauge redefinition $\psi_0 \rightarrow e^{i\phi/2} \psi_0$.

Equation (12.9) is one the defining conditions of a Majorana fermion zero mode.² Written in terms of the original electron operators, the Majorana zero mode takes the superposition form $\psi_0 = u_j c_j + u_j^* c_j^\dagger$. From the fermionic anticommutation relations

$$\{c_i, c_j\} = c_i c_j + c_j c_i = 0, \quad \{c_i, c_j^\dagger\} = c_i c_j^\dagger + c_j^\dagger c_i = \delta_{ij}, \quad (12.10)$$

the Majorana operator squares to a constant $\psi_0^2 = 2|\mathbf{u}|^2$, which we normalize to unity, $\psi_0^2 = 1$.

Now suppose there are multiple Majorana fermion zero modes $\gamma_1, \dots, \gamma_{2N}$. The fermion exchange statistics requires Majorana operators to mutually anticommute. Together with the normalization $\gamma_m^2 = 1$, they follow the algebraic relationship

$$\{\gamma_l, \gamma_m\} = 2\delta_{lm}. \quad (12.11)$$

One can group them in pairs and define n Dirac fermions $d_l = (\gamma_{2l-1} + i\gamma_{2l})/2$, which satisfies the anticommutation relations (12.10). Each Dirac fermion is associated a two-level system or a quantum bit (qubit) spanned by $|0\rangle = d_l|1\rangle$ and $|1\rangle = d_l^\dagger|0\rangle$, which are eigenstates of the number operator $\hat{n}_l = d_l^\dagger d_l$. Together, they generate a degenerate zero energy Hilbert space of dimension 2^n , where quantum states are superpositions of the tensor product states $|\{n_l\}\rangle = \dots \otimes |n_l\rangle \otimes |n_{l+1}\rangle \otimes \dots$, for $n_l = 0, 1$.

At this point, it is opportune to clarify the terminology we are going to use in this section and distinguish between Majorana fermion (MF) and zero energy Majorana bound state (MBS). The previous discussion of zero energy BdG quasiparticle ψ_0 applies to excitation localized at either (i) a point defect, or (ii) an open system with a boundary edge or surface. Zero energy MBS refers to the first case, where a zero mode is bound to a point with a wavefunction exponentially localized in all directions. A MBS is protected if it is the only zero energy BdG quasiparticle localized at that point, and there are no other BdG excitations (localized or not) near zero energy. Figure 12.1a shows the density of state (DOS) plot of a generic BdG Hamiltonian with a single MBS at zero energy. There are no states near zero energy except the MBS (shown as a spike in DOS at $E = 0$) and the extended bulk states appears at energy larger than Δ_{gap} . The zero energy MBS is protected against any perturbation that does not close the bulk energy gap. It cannot gain a non-zero energy, otherwise the particle-hole symmetry would imply another opposite energy BdG state which however, is non-existing.

In the second case, the zero mode ψ_0 extends in the form of a plane wave in the direction(s) parallel to the boundary. Figure 12.1b, c shows the edge or surface energy

²If there are multiple zero modes, there exists an orthogonal transformation that rotates to a new basis where all zero modes are self-conjugate (12.9). For instance, given a zero mode ψ_0 which is not self-conjugate, one can define the self-conjugate zero modes $\psi_0 + \Xi\psi_0^\dagger, i\psi_0 - i\Xi\psi_0^\dagger$. This process can be repeated until all zero modes are self-conjugate.

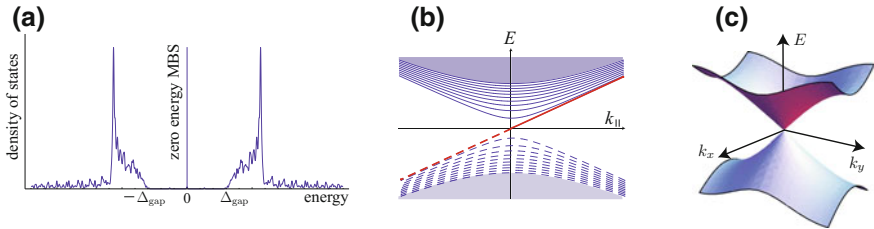


Fig. 12.1 Energy spectrum of zero energy Majorana bound state (MBS) and Majorana fermion (MF). **a** Density of states of a BdG Hamiltonian with a MBS at zero energy. **b** Energy spectrum of a 2D BdG Hamiltonian in a semi-infinite geometry with an open edge. Blue bands represent bulk states, red band represents the chiral MF localized along the edge. **c** Energy spectrum of the MF surface state of a TR symmetric 3D topological superconductor

spectra of a topological system. There are BdG excitation states arbitrarily close to zero energy in the thermodynamic limit. We refer to these low-energy extended BdG excitations as Majorana fermions (MF). With the appropriate edge or surface boundary conditions, these Majorana fermions can also admit states at exactly zero energy. However, as they are not bounded and localized at a point. We only refer to them as Majorana zero modes but not Majorana bound states (MBS).

Zero energy Majorana bound states (MBS) are desirable. Unlike local qubits in a system of spins for example, it takes two MBS to form a qubit. If the MBS are far away with exponentially small wavefunction overlap, the quantum information is stored non-locally in space. This means that the qubit is protected against accidental measurement by local perturbations, or in other words, this enables a long lifetime of quantum coherence. On the other hand, a qubit can be read off by determining the fermion parity $|0\rangle$ or $|1\rangle$ when a pair of MBS is brought together. Moreover, MBS are *non-Abelian* quasiparticles in the sense that mutual exchange and braiding operations do not commute with one another. This allows us to design quantum gates out of unitary adiabatic operations that form the basis of a topological quantum computer (TQC) [39–44]. The non-local nature of MBS demonstrates quantum entanglement. An entangled state $(|00\rangle + |11\rangle)/\sqrt{2}$ can be prepared for instance from a pure state $|00\rangle$ through an MBS exchange operation.

12.2 Time Reversal Breaking Topological Superconductors

We discuss the topological classification of characterization of superconductors in one and two dimensions that do not preserve time reversal (TR) symmetry [3, 6, 8, 14–16]. We show these topological superconductors (TSC) can support zero energy Majorana bound states (MBS) [1, 2, 4, 5, 7, 9]. Section 12.2.1 covers one dimensional TSC. This includes the Kitaev’s p -wave superconducting chain [17] and the superconducting spin-orbit coupled nanowire [18–21]. Section 12.2.2 studies two

dimensional TR breaking TSC and focuses on the prototype $p_x + ip_y$ TSC [22–26], which carries chiral edge Majorana fermion (MF) and vortex bound MBS. Section 12.3 considers superconducting heterostructures [28–34], where MBS are located at point junctions between topological insulating, superconducting, and magnetic domains. A discussion on the classification and characterization of topological point defects [3, 32, 33] in superconducting media will be given at the end.

12.2.1 Topological Superconductors in One Dimension

Previously, we introduced the BdG description of a BCS mean-field superconductor (12.6). As a consequence of the artificial Nambu doubling (12.5), the BdG Hamiltonian $H_{\text{BdG}}(\mathbf{k})$ has a particle-hole (PH) symmetry (12.7). We begin with the example of the Kitaev’s p -wave superconducting wire model before we move on to a more recent application of superconducting spin-orbit coupled nanowire.

12.2.1.1 Kitaev’s p -Wave Superconducting Chain

A one dimensional metallic wire can be mimicked by a lattice Dirac fermion model. Suppose there is a spinless electron degree of freedom c_r on each site r on a simple 1D chain. The tight-binding Hamiltonian $\hat{H}_0 = \frac{t}{2} \sum_r c_r^\dagger c_{r+1} + h.c.$, which consists of nearest neighbor electron hoppings, has a periodic energy spectrum $E(k) = t \cos k$. With partial electron filling, it models a 1D metal with a Fermi energy ϵ_f between $\pm t$. Suppose there is some uniform attractive interaction between nearest neighbors that, under a mean-field analysis, breaks charge $U(1)$ conservation spontaneously. The BCS Hamiltonian takes the form

$$\hat{H}_{\text{BCS}} = \hat{H}_0 - \epsilon_f \sum_r c_r^\dagger c_r + \Delta \sum_r c_r^\dagger c_{r+1}^\dagger + h.c. \quad (12.12)$$

where $\Delta \sim \langle c_r c_{r+1} \rangle$ is the uniform (r independent) superconducting pairing parameter. Since the system is spinless and the pairing is odd under inversion $r \rightarrow -r$, Δ is p -wave.

Using the Fourier and Nambu transformation (c.f. (12.5)),

$$c(k) = \int_{-\pi}^{\pi} \frac{dk}{2\pi} e^{ikr} c(r), \quad \xi(k) = (c(k), c^\dagger(-k))^T \quad (12.13)$$

the BdG Hamiltonian (c.f. (12.6)) takes the 2×2 matrix form

$$H_{\text{BdG}}(k) = (t \cos k - \epsilon_f) \tau_z + \Delta \sin k \tau_y \quad (12.14)$$

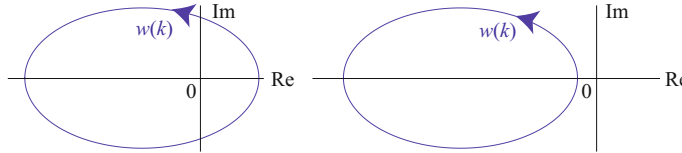


Fig. 12.2 The trajectory of $w(k) = (t \cos k - \epsilon_f) + i \Delta \sin k$ on the complex plane when (left) $|\epsilon_f| < |t|$, the winding number is 1, or (right) $|\epsilon_f| > |t|$, the winding number is 0

where $\tau_z = \begin{pmatrix} 1 & 0 \\ 0 & -1 \end{pmatrix}$ and $\tau_y = \begin{pmatrix} 0 & -i \\ i & 0 \end{pmatrix}$ act on the Nambu c, c^\dagger degree of freedom. The Hamiltonian is PH symmetric, $\Xi H_{\text{BdG}}(k) \Xi^{-1} = -H_{\text{BdG}}(-k)$ where $\Xi = \tau_x \mathcal{K}$ the PH operator. The p -wave superconductor has a BdG excitation spectrum $E(k) = \sqrt{(t \cos k - \epsilon_f)^2 + (\Delta \sin k)^2}$, and has an excitation energy gap $\Delta_{\text{gap}} = \min\{E(k)\}$ which is non-zero unless the chain is completely filled or empty, i.e. $\epsilon_f = \pm t$.

The Kitaev's model (12.14) [17] is a topological superconductor in one dimension. It is protected by a Chern-Simons topological invariant. We begin with the “occupied” states of (12.14). One choice of the “negative energy” eigenstate is of the form $\mathbf{u}(k) = (-1 + e^{i\theta(k)}, 1 + e^{i\theta(k)})/2$, where $\theta(k)$ is the argument of the complex number $w(k) = (t \cos k - \epsilon_f) + i \Delta \sin k$. The Berry connection is defined to be the differential 1-form

$$\mathcal{A}(k) \equiv \langle \mathbf{u}(k) | \frac{d}{dk} \mathbf{u}(k) \rangle dk = \langle \mathbf{u}(k) | \frac{d}{d\theta} \mathbf{u}(k) \rangle d\theta = -\frac{i}{2} d\theta. \quad (12.15)$$

The Chern-Simons invariant in this case is the integral

$$\text{CS}_1 = \frac{i}{\pi} \int_{k=-\pi}^{k=\pi} \mathcal{A}(k) = \frac{1}{2\pi} \int_{k=-\pi}^{k=\pi} d\theta(k) = \theta(k = \pi) - \theta(k = -\pi). \quad (12.16)$$

The integral $\int d\theta/2\pi$ in (12.16) is also known as a winding number. It counts how many times the complex number $w(k)$ winds around the origin as k goes from $-\pi$ to π (See Fig. 12.2). Therefore we have

$$\text{CS}_1 = \begin{cases} 1, & \text{for } |\epsilon_f| < |t| \\ 0, & \text{for } |\epsilon_f| > |t| \end{cases} \quad (12.17)$$

Of course, since we began with a partially filled metallic chain with ϵ_f between $\pm t$, the Kitaev's p -wave superconducting model has a non-trivial Chern-Simons invariant and is topological. The second case when $|\epsilon_f| > t$, the chain is completely filled or empty to begin with. The system therefore connects to an insulating state, which in one dimension must also connect to the trivial atomic limit where all electrons are atomically localized.

The Berry connection (12.15), and consequently the Chern-Simons invariant (12.16), is gauge dependent. One can choose another eigenstate that differs from the origin by a gauge transformation $\mathbf{u}'(k) = e^{i\varphi(k)} \mathbf{u}(k)$, where $e^{i\varphi(k+2\pi)} = e^{i\varphi(k)}$ is

some k -dependent periodic quantum phase. The new eigenstate $\mathbf{u}'(k)$ is continuous and defines a new Berry connection

$$\mathcal{A}'(k) = \langle \mathbf{u}'(k) | d\mathbf{u}'(k) \rangle = \mathcal{A}(k) - i d\varphi(k). \quad (12.18)$$

This modifies the Chern-Simons invariant

$$CS'_1 = CS_1 + \frac{1}{\pi} \int_{k=-\pi}^{k=\pi} d\varphi(k). \quad (12.19)$$

The correction term is *twice* of the winding number for the gauge transformation $e^{i\varphi(k)}$ and changes the invariant by an even integer. Hence, the Chern-Simons invariant (12.16) is well-defined only up to even integers. On the other hand, it also tells us that the two scenarios (12.17) cannot be related by any gauge transformation.

One may ask if one can introduce a perturbation that changes the value of the Chern-Simons invariant continuously away from 0 or 1 (modulo 2). If this were possible, one might be able to continuously deform and connect the BdG Hamiltonians between the two limits $|\epsilon_f| > t$ and $|\epsilon_f| < t$. Fortunately, the particle-hole symmetry and the energy gap force the Chern-Simons invariant (12.16) to take an integral value. Here we sketch a proof. First, the PH symmetry flips between the “positive” and “negative” BdG bands. The “positive” energy eigenstates $\mathbf{v}(k) = \Xi \mathbf{u}(-k)$ associates a new Berry connection $\mathcal{A}^{(+)}(k)$, which is opposite to the one constructed before from “negative” eigenstates.

$$\begin{aligned} \mathcal{A}^{(+)}(k) &= \langle \mathbf{v}(k) | \frac{d}{dk} \mathbf{v}(k) \rangle dk = \langle \Xi \mathbf{u}(-k) | \frac{d}{dk} \Xi \mathbf{u}(-k) \rangle dk \\ &= \langle \mathbf{u}(-k) | \frac{d}{dk} \mathbf{u}(-k) \rangle^* dk = -\mathcal{A}(-k). \end{aligned} \quad (12.20)$$

Here, the first identity in the second line holds because the PH operator is antiunitary (i.e. $\langle \Xi \mathbf{w}_1 | \Xi \mathbf{w}_2 \rangle = \langle \mathbf{w}_1 | \mathbf{w}_2 \rangle^*$) and local (i.e. spatially independent [$\frac{d}{dk}, \Xi = 0$]). The minus sign in the last identity comes from the fact that the Berry connection \mathcal{A} is purely imaginary, $\mathcal{A}^* = -\mathcal{A}$. However, as inversion $k \rightarrow -k$ changes the orientation of momentum space, it adds a minus sign to the momentum integration in the Chern-Simons invariant (12.16). Therefore the Chern-Simons invariant defined from the “positive” eigenstates is actually identical to the one from the “negative” eigenstates, $CS_1^{(+)} = CS_1$.

Second, the Chern-Simons invariants from the “positive” and “negative” eigenstates should add up to zero (modulo 2). This is because

$$CS_1^{(+)} + CS_1 = \frac{i}{\pi} \int_{k=-\pi}^{k=\pi} \mathcal{A}^{(+)}(k) + \mathcal{A}(k) = \frac{i}{\pi} \int_{k=-\pi}^{k=\pi} \text{Tr}(\mathcal{A}^{\text{tot}}(k)) \quad (12.21)$$

where $\mathcal{A}_{mn}^{\text{tot}}(k) = \langle \mathbf{u}_m(k) | d\mathbf{u}_n(k) \rangle$ is the 2×2 total Berry connection constructed by both “positive” and “negative” eigenstates, $\mathbf{u}_1(k) = \mathbf{u}(k)$, $\mathbf{u}_2(k) = \mathbf{v}(k)$. However, $U(k) = (\mathbf{u}_1(k), \mathbf{u}_2(k))$ is simply a unitary basis transformation and the sum above is just the winding number

$$\text{CS}_1^{(+)} + \text{CS}_1 = \frac{i}{\pi} \int_{k=-\pi}^{k=\pi} \text{Tr} \left(U(k) \frac{d}{dk} U(k) \right) dk = 2 \times \frac{i}{2\pi} \int_{k=-\pi}^{k=\pi} dk \frac{d}{dk} \log \det U(k). \quad (12.22)$$

It counts *twice* the number of times the complex number $\det U(k)$ goes around the origin as k goes from $-\pi$ to π . In other words, $\text{CS}_1^{(+)} + \text{CS}_1$ must be an even integer. Combining with the previous observation that the two Chern-Simons invariants are actually identical, we see that CS_1 must be an integer. Lastly, we notice that the definition of the Chern-Simons invariant (12.16) requires the energy eigenstate $\mathbf{u}(k)$ to be continuous. This holds only when there is a non-vanishing energy gap so that the “positive” band never crosses the “negative” one.

To summarize, the PH symmetry and energy gap require the Chern-Simons invariant (12.16) to be an integer. However, there is a gauge ambiguity as a large gauge transformation can change the value by any even integer (see (12.19)). Therefore, there are actually only two distinct values of $\text{CS}_1 = 0, 1$ modulo 2, where the parity (evenness or oddness) of the Chern-Simons invariant is a gauge independent quantity. We refer to this type of invariants as a \mathbb{Z}_2 -invariant, where $\mathbb{Z}_2 = \{0, 1\}$ is the binary group that follows the rule of addition $1 + 1 \equiv 0$ modulo 2. It characterizes the *topology* of the BCS superconductor. As CS_1 will not be altered by any energy gap preserving perturbation and deformation, a topological superconductor with $\text{CS}_1 = 1$ can never be adiabatically connected to a trivial superconductor with $\text{CS}_1 = 0$.

Now that we have established the bulk topology of the Kitaev’s p -wave superconducting wire, we move on to its non-trivial signature at the boundary. First, we rewrite the model (12.12). Decomposing the Dirac electron operator at site r into real and imaginary Majorana components $c_r = (\gamma_{2r-1} + i\gamma_{2r})/2$, in the limit when $t = 2\Delta$, (12.12) becomes

$$\hat{H}_{\text{Kitaev}} = \sum_{r=1}^n i\epsilon_f \gamma_{2r-1} \gamma_{2r} + i t \gamma_{2r} \gamma_{2r+1}. \quad (12.23)$$

This is the Majorana fermion (MF) version of the Su-Schrieffer-Heeger model of polyacetylene [45], which is built out of Dirac fermions. The Fermi energy ϵ_f term corresponds to intra-unitcell MF coupling while the kinetic electron tunneling and pairing term t corresponds to inter-unitcell MF coupling.

The distinction between the topological case with $\text{CS}_1 = 1$ when $|\epsilon_f| < |t|$ and the trivial case with $\text{CS}_1 = 0$ when $|\epsilon_f| > |t|$ is revealed at the boundary of the 1D chain. In the topological case, the inter-cell coupling is stronger than the intra-cell coupling (see Fig. 12.3). A boundary therefore terminates at a strong bond and this leaves behind a dangling boundary state at each end. For example in the limit $\epsilon_f = 0$,

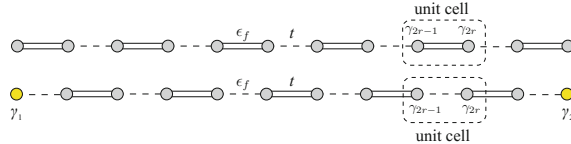


Fig. 12.3 The Kitaev's Majorana chain model (12.23). (Top) The trivial case when $\epsilon_f > t$ with no boundary states. (Bottom) The topological case when $\epsilon_f < t$ with zero energy boundary MBS γ_1 and γ_{2n}

the boundary MF γ_1 and γ_{2n} are completely decoupled from the rest of the chain, i.e. $[\hat{H}_{\text{Kitaev}}, \gamma_1] = [\hat{H}_{\text{Kitaev}}, \gamma_{2n}] = 0$, and correspond to zero energy MBS localized at the two ends. In the trivial limit where $t = 0$ and $\epsilon_f > 0$, MF are completely dimerized within unitcells and there are no zero energy boundary states.

These boundary MBS are *topologically* protected. Their presence is a direct consequence of the bulk topology, namely the non-vanishing Chern-Simons invariant $CS_1 = 1$. They are robust against *any* energy preserving perturbations. This is because as long as there is a bulk energy gap, there are no extended quantum states near zero energy to hybridize with the MBS. In other words, there are no low energy channels for the zero energy boundary MBS to escape and the wave function of the zero mode must be exponentially localized at the boundary. For example, if one perturbs about half-filling by turning on the Fermi energy ϵ_f , as long as $|\epsilon_f| < |t|$, there is always a Majorana zero mode (i.e. $[\hat{H}_{\text{Kitaev}}, \tilde{\gamma}] = 0$)

$$\tilde{\gamma} = \frac{1}{\mathcal{N}} \sum_{r=0}^{\infty} \left(\frac{\epsilon_f}{t} \right)^r \gamma_{2r+1} \quad (12.24)$$

in the thermodynamic semi-infinite geometry $n \rightarrow \infty$, for $\mathcal{N} = \sqrt{\sum_{r=0}^{\infty} (\epsilon_f/t)^{2r}}$ a normalization constant so that $\tilde{\gamma}^2 = 1$. The wave function of $\tilde{\gamma}$ has an exponentially decaying tail $\sim e^{-r/l}$ with the localization length $l = 1/\log(t/\epsilon_f)$.

The boundary spectrum of a 1D superconductor in general consists of multiple mid-gap Majorana zero modes $\tilde{\gamma}_1, \dots, \tilde{\gamma}_s$. They are however not all protected against boundary perturbation as they can acquire finite energy u by pair annihilation $\delta H = iu\tilde{\gamma}_i\tilde{\gamma}_j$. The PH symmetry requires the same number of “positive” energy states and “negative” ones. Thus, when s is even, the zero modes can be paired up and removed, whereas when s is odd, there is at least one MBS at zero energy remaining. The number parity (evenness or oddness) of MBS at a boundary defines a \mathbb{Z}_2 analytic index, $\text{ind}_{\text{bdry}} \equiv s \bmod 2$. In general, a one dimensional superconducting model is either adiabatically connected to the topological case with $CS_1 = 1$ or the trivial case with $CS_1 = 0$. Since boundary MBS cannot escape during adiabatic deformation, the Chern-Simons invariant is a \mathbb{Z}_2 topological index that corresponds to the analytic boundary signature,

$$\text{ind}_{\text{bdry}} \equiv \text{CS}_1 \pmod{2}. \quad (12.25)$$

This identification of a boundary analytic index and a bulk topological invariant is an example of a *bulk-boundary correspondence*.

Lastly, we notice that the bulk Chern-Simons invariant also applies when there are translation symmetry breaking disorder. Equation (12.16) can be re-defined in real space

$$\text{CS}_1 = 2\mathcal{T}(P\hat{r}P^{-1}) \pmod{2}, \quad (12.26)$$

where the real-space position operator \hat{r} is represented by the momentum differential operator id/dk after Fourier transform, P is the projection operator onto the “negative” BdG states, and \mathcal{T} is the operator trace that includes the momentum integral $i \int dk/2\pi$. $\langle \hat{r} \rangle = \mathcal{T}(P\hat{r}P^{-1})$ locates the average center position of the Wannier wave function of the “negative” BdG bands, i.e. the ground state. It is well-defined only up to integers because the value can be shifted by any integral amount by lattice translations (or momentum dependent gauge transformations). The PH symmetry forces $\langle \hat{r} \rangle$ to take either integral or half-integral values. In the trivial case such as the top diagram of Fig. 12.3, it takes integral value as the Wannier center (i.e. the strong bond) is located at a unitcell, while in the topological case (see the bottom diagram of Fig. 12.3), it takes half-integral value since the Wannier center is located between unitcells.

12.2.1.2 Superconducting Spin-Orbit Coupled Nanowire

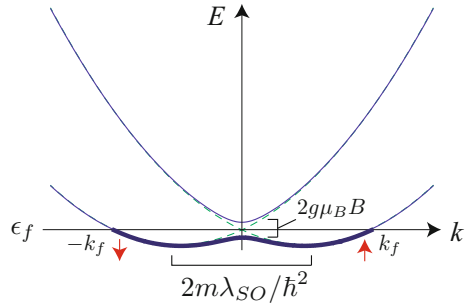
Superconductivity normally arises in a three dimensional material, but it can also be induced on an one dimensional wire that is in proximity with a bulk 3D superconductor. These proximity induced superconducting wires can be topological and support boundary zero energy Majorana bound states (MBS). Previously, we discussed the Kitaev’s p -wave superconducting chain, which is a topological model built out of spinless electrons. In reality, electrons have spin, and the Kramers’ theorem dictates that BdG states must be doubly degenerate in any time reversal symmetric system. Therefore, a system that support a single (or odd number of) zero energy MBS must breaks time reversal. This can be realized by a nanowire with strong spin-orbit coupling (SOC) under an external magnetic field or internal magnetization [18–21].

The normal metallic state of the SOC nanowire is described by the Hamiltonian

$$H_0(k) = \frac{\hbar^2 k^2}{2m} + \lambda_{SO} k \sigma_x + g \mu_B B \sigma_z \quad (12.27)$$

where the Pauli matrices σ ’s act on spin, and λ_{SO} is the SOC strength. The third term is the Zeeman energy from an external magnetic field pointing in a direction perpendicular to spin-orbit direction. Equivalently, the third term can also be generated by an internal magnetization. The energy spectrum is shown in Fig. 12.4. The SOC

Fig. 12.4 The energy spectrum of the SOC nanowire under a magnetic field (12.27). Dashed line represents the case when the magnetic field is absent



displaces the parabolic bands according to spins \uparrow, \downarrow with respect to σ_x , and the magnetic field introduces a Zeeman splitting at zero momentum. If the Fermi energy ϵ_f is located mid-Zeeman gap around 0, there is a pair of counter-propagating modes at $\pm k_f$ with opposite spins (in the limit $B \ll \lambda_{SO}$). This mimics the helical edge modes of a quantum spin Hall insulator [46–50].

Now when the SOC nanowire is in proximity of a bulk s -wave superconductor, its electronic state acquires a proximity-induced pairing Δ and is described by the BdG Hamiltonian

$$H_{\text{BdG}}(k) = \left[\left(\frac{\hbar^2 k^2}{2m} - \epsilon_f \right) + \lambda_{SO} k \sigma_x \right] \tau_z + g \mu_B B \sigma_z + \Delta \tau_x \quad (12.28)$$

where the Pauli matrices $\tau_{x,z}$ acts on the Nambu (c, c^\dagger) degrees of freedom (12.5). As a consistency check, we see that the Hamiltonian has a PH symmetry with respect to the PH operator $\Xi = \sigma_y \tau_y \mathcal{K}$ so that $\Xi H_{\text{BdG}}(k) \Xi^{-1} = -H_{\text{BdG}}(-k)$. The magnetic Zeeman term is the only term that violates time reversal symmetry, or otherwise the Hamiltonian would be TR symmetric, $\mathcal{T} H_{\text{BdG}}(k) \mathcal{T}^{-1} = H_{\text{BdG}}(-k)$ where $\mathcal{T} = i \sigma_y \mathcal{K}$ is the TR operator. The magnetic Zeeman term commutes and therefore competes with the pairing term. This agrees with the conventional competing theory of superconductivity and magnetism. However in this case, due to the helical (spin-momentum locked) nature of the 1D electronic modes, there is a region where magnetism and superconductivity can coexist.

To simplify the problem, we notice that the Hamiltonian (12.28) has an accidental chiral symmetry, $\sigma_x \tau_y H_{\text{BdG}}(k) \sigma_x \tau_y = -H_{\text{BdG}}(k)$. This means that it takes an off-block diagonal form under a basis transformation

$$\begin{aligned} \tilde{H}_{\text{BdG}}(k) &= U H_{\text{BdG}}(k) U^\dagger = \begin{pmatrix} 0 & h(k) \\ h(k)^\dagger & 0 \end{pmatrix}, \quad U = \frac{1}{\sqrt{2}} \begin{pmatrix} -i & 0 & 0 & 1 \\ 0 & -i & 1 & 0 \\ i & 0 & 0 & 1 \\ 0 & i & 1 & 0 \end{pmatrix}, \\ h(k) &= - \left(\frac{\hbar^2 k^2}{2m} - \epsilon_f \right) \mathbb{1}_2 - (\lambda_{SO} k - i \Delta) \mu_x - g \mu_B B \mu_z \quad (12.29) \end{aligned}$$

where $\mu_{x,z}$ are Pauli matrices acting on the new basis and $\mathbb{1}_2$ is the 2×2 identity matrix. The superconducting wire has a finite energy gap unless the determinant

$$\det(h(k)) = -(g\mu_B B)^2 + \Delta^2 + \epsilon_f^2 + \frac{\hbar^4 k^4}{4m^2} - k^2 \left(\frac{\hbar\epsilon_f}{m} + \lambda_{SO}^2 \right) - 2i\Delta\lambda_{SO}k \quad (12.30)$$

vanishes. In the presence of SOC and proximity-induced pairing, $\lambda_{SO}, \Delta \neq 0$, the energy gap closes at $k = 0$ when $(g\mu_B B)^2 = \Delta^2 + \epsilon_f^2$. This separates the (i) weak field phase $g\mu_B|B| < \sqrt{\Delta^2 + \epsilon_f^2}$ from (ii) the strong-field phase $g\mu_B|B| > \sqrt{\Delta^2 + \epsilon_f^2}$.

Next we show that the two phases are topologically distinct. This requires us to solve for the eigenstates of the BdG Hamiltonian and compute the Chern-Simons invariant (12.16). First, we notice that \tilde{H}_{BdG} squares to the block diagonal form $\text{diag}(hh^\dagger, h^\dagger h)$, where the hermitian Laplacians $L(k) = h(k)h(k)^\dagger$ and $L'(k) = h(k)^\dagger h(k)$ are positive definite. Suppose $\mathbf{x}_1(k), \mathbf{x}_2(k)$ are the normalized eigenvectors for the first Laplacian so that $L(k)\mathbf{x}_j(k) = \epsilon_j(k)^2\mathbf{x}_j(k)$, where $\epsilon_1(k)^2, \epsilon_2(k)^2$ are the positive eigenvalues. They generate the “negative” energy eigenvectors of the BdG Hamiltonian

$$\tilde{H}_{\text{BdG}}(k)\mathbf{u}_j(k) = -\epsilon_j(k)\mathbf{u}_j(k), \quad \mathbf{u}_j(k) = \frac{1}{\sqrt{2}} \begin{pmatrix} \mathbf{x}_j(k) \\ -\epsilon_j(k)^{-1}h(k)^\dagger\mathbf{x}_j(k) \end{pmatrix}. \quad (12.31)$$

The Berry connection is given by

$$\text{Tr}(\mathcal{A}(k)) = \langle \mathbf{u}_j(k) | d\mathbf{u}_j(k) \rangle = \text{Tr}(X(k)^\dagger dX(k)) + \frac{1}{2} \text{Tr}(h^\dagger(k)^{-1} dh^\dagger(k)) \quad (12.32)$$

where $X(K) = (\mathbf{x}_1(k), \mathbf{x}_2(k))$ is unitary. The first term can be absorbed and canceled by a gauge transformation $\mathcal{A} \rightarrow X\mathcal{A}X^\dagger + XdX^\dagger$. The Chern-Simons invariant (12.16) in a multi-band model generalizes to

$$\begin{aligned} \text{CS}_1 &= \frac{i}{\pi} \int_{k=-\infty}^{k=\infty} \text{Tr}(\mathcal{A}(k)) \bmod 2 \\ &= \frac{i}{2\pi} \int_{k=-\infty}^{k=\infty} \text{Tr}(h^\dagger(k)^{-1} dh^\dagger(k)) = \frac{i}{2\pi} \int_{k=-\infty}^{k=\infty} d \log \det h^\dagger(k) \end{aligned} \quad (12.33)$$

which counts the number of times the complex number $\det(h^\dagger(k))$ in (12.30) winds around the origin as k runs from $-\infty$ to ∞ .

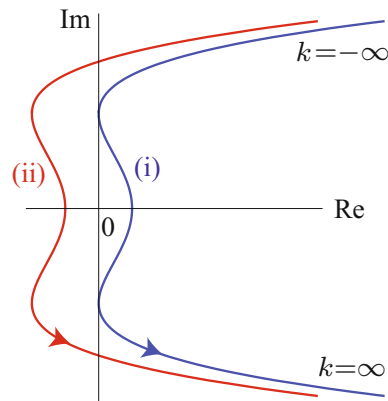
Figure 12.5 shows the trajectory of $\det(h(k)) = |\det(h(k))|e^{i\vartheta(k)}$ for (i) the weak field phase $g\mu_B|B| < \sqrt{\Delta^2 + \epsilon_f^2}$ and (ii) the strong field phase $g\mu_B|B| > \sqrt{\Delta^2 + \epsilon_f^2}$. When $k \rightarrow \pm\infty$, the $\hbar^4 k^4/4m^2$ term in (12.30) dominates and therefore $\vartheta(k \rightarrow \pm\infty) = 0$. For finite k , the imaginary piece $-2i\Delta\lambda_{SO}k$ in (12.30) brings the phase

Fig. 12.5 The trajectory of $\det(h(k))$ in (12.30) on the complex plane for (i) the weak field phase

$$g\mu_B|B| < \sqrt{\Delta^2 + \epsilon_f^2}$$

(ii) the strong field phase

$$g\mu_B|B| > \sqrt{\Delta^2 + \epsilon_f^2}$$



ϑ away from π . The winding number depends on the sign of $\det(h(k=0)) = (g\mu_B B)^2 - \Delta^2 - \epsilon_f^2$. In the weak field phase, $\det(h(k=0)) > 0$ and the path can be deformed and contracted along the negative real axis without crossing the origin. On the contrary, in the strong field phase, $\det(h(k=0)) < 0$ and the path winds once around the origin.

$$\text{CS}_1 = \begin{cases} 0, & \text{for } g\mu_B|B| < \sqrt{\Delta^2 + \epsilon_f^2} \\ 1, & \text{for } g\mu_B|B| > \sqrt{\Delta^2 + \epsilon_f^2} \end{cases} \pmod{2} \quad (12.34)$$

This shows that the strong field phase is topological whereas the weak field phase is trivial.

Next we consider zero energy boundary BdG states of the superconducting SOC nanowire. In a semi-infinite geometry where the nanowire occupies the positive real axis $x > 0$, a normalizable boundary state takes the decaying form $\mathbf{u}_0 \sim e^{-\kappa x}$ where $l = 1/\text{Re}(\kappa) > 0$ is the localization length. It is a zero mode if it is a zero eigenvector of the BdG Hamiltonian $H_{\text{BdG}}(i\kappa)\mathbf{u}_0 = 0$, and represents the MBS $\tilde{\gamma} = \mathbf{u}_0 \cdot \boldsymbol{\xi}(i\kappa)$. In other words, a zero mode corresponds to a solution to the polynomial equation $\det(h(i\kappa)) = 0$ on the analytic-continued complex momentum half-plane $k = i\kappa$, for $\text{Im}(k) > 0$. Using (12.30), we see that if k is a complex root of $\det(h(k))$, then so is $-k^*$. This means that complex roots usually come in pairs except when $k = -k^*$ lives on the imaginary axis. The number parity (evenness or oddness) of roots on the momentum half-plane is therefore determined along the positive imaginary axis. From (12.30), we see that the determinant has a single (or odd number of) root if $\det(h(i\kappa))$ changes sign between $\kappa = 0$ and $\kappa = \infty$. This is the case if and only if $g\mu_B|B| > \sqrt{\Delta^2 + \epsilon_f^2}$, i.e. the strong field topological phase (Fig. 12.6).

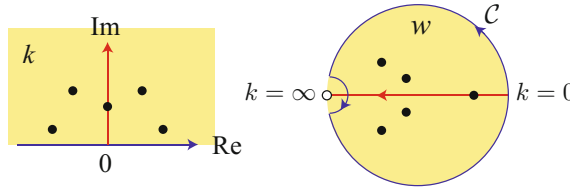


Fig. 12.6 Mobiüs transformation $w = (i - k)/(i + k)$ from the upper-half complex momentum plane to the unit disc. Black dots \bullet (white dots \circ) represent zeros (resp. poles) of $\det(h(k))$

$$\text{ind}_{\text{bdry}} = \text{number of MBS} = \begin{cases} 0, & \text{for } g\mu_B|B| < \sqrt{\Delta^2 + \epsilon_f^2} \\ 1, & \text{for } g\mu_B|B| > \sqrt{\Delta^2 + \epsilon_f^2} \end{cases} \pmod{2}. \quad (12.35)$$

We recover the index theorem (12.25) by comparing and identifying (12.34) and (12.35). In fact, one can show that the identification of ind_{bdry} and CS_1 in the general scenario without using the particular polynomial form of $\det(h(k))$ in (12.30). We use the Mobiüs transformation $w(k) = (i - k)/(i + k)$ to map the upper half complex k plane to the unit disc, where w lives (see Fig. 12.6). The Chern-Simons integral (12.33) becomes the closed integral

$$\text{CS}_1 = \frac{i}{2\pi} \oint_{\mathcal{C}} d\log \det h^\dagger(w) = \text{number of zeros enclosed in } \mathcal{C} \pmod{2} \quad (12.36)$$

along the unit circle. The closed loop \mathcal{C} is defined to go around the point $w = -1$ (i.e. $k = \infty$) so that the pole of $\det h^\dagger(w)$ is avoided and there are no poles enclosed by \mathcal{C} . Equation (12.36) thus directly relates the Chern-Simons invariant CS_1 and the number of boundary zero modes ind_{bdry} .

We conclude the discussion on superconducting SOC nanowires by reporting some recent progress in transport theory and experiments [20, 51–57]. We consider a SOC nanowire where the proximity-induced superconductivity is turned on (off) along the right (resp. left) segment, i.e. $\Delta(x) = \Delta\theta(x)$ for $\theta(x)$ the unit step function that vanishes along the negative x -axis. The normal metallic segment ($x < 0$) is treated as a lead. A bias potential V_b is put across the wire if there is a jump of chemical potential between the lead and the superconducting wire, $\epsilon(x) = \epsilon + eV_b(1 - \theta(x))$.

Electric transport is dictated by the scattering at the junction that describe the probability of transmission and backscattering. We are interested in bias V_b smaller than the superconducting gap, so that at zero temperature, there is no mid-gap extended transmission channels in the superconducting segment. There are two ways an electron injected from the normal lead can be backscattered at the junction. First, analogous to the conventional metal-insulator junction, the normal backscattering bounces an incoming electron to an outgoing electron in the reverse direction along the normal lead. Since there is no net charge transfer, this process does not contribute to electric

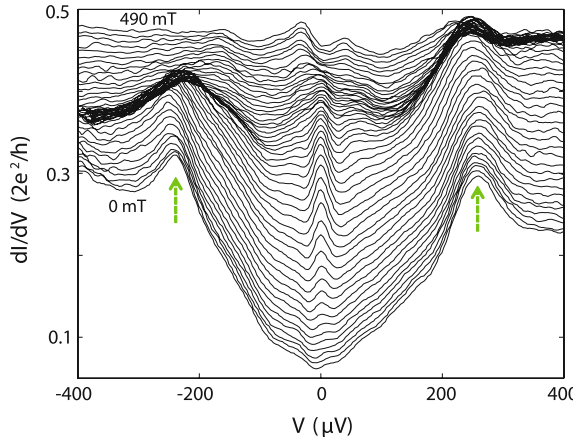


Fig. 12.7 An excerpt from the Science journal paper by [51]. Magnetic field-dependent spectroscopy. dI/dV versus V at 70 mK taken at different B fields (from 0 to 490 mT in 10-mT steps; traces are offset for clarity, except for the lowest trace at $B = 0$). Arrows indicate the induced gap peaks

transport. Second, the incoming electron can be backscattered into an outgoing hole while the superconducting segment absorbs a charge $2e$ Cooper pair into the condensate. This process is called an Andreev reflection, and each of such channels corresponds to the differential electric conductance $\sigma = dI/dV = (2e^2/h)|S_{eh}|^2$, where $|S_{eh}|^2$ is the electron-hole backscattering probability.

First, we consider the trivial case where the superconducting segment is in the weak field phase $g\mu_B|B| < \sqrt{\Delta^2 + \epsilon_f^2}$. In the simplest scenario that there is no boundary localized mode near zero energy, the only wavefunctions near Fermi level are those corresponds to normal backscattering, $\psi(x) = (1 - \theta(x))(\psi_{k_f,\uparrow}(x) + e^{i\phi}\psi_{-k_f,\downarrow})$, where $\psi_{k_f,\uparrow}, \psi_{-k_f,\downarrow}$ are the incoming and outgoing electron wavefunctions at Fermi energy. Thus there is no electric conductance near zero bias.³

Next we move onto the topological case where the superconducting segment is in the strong field phase $g\mu_B|B| > \sqrt{\Delta^2 + \epsilon_f^2}$. We assume a single boundary Majorana zero mode $\tilde{\gamma}(x) = \sum_{\sigma=\uparrow,\downarrow} \xi_{\sigma}(x)c_{\sigma}(x) + \xi_{\sigma}^*(x)c_{\sigma}^{\dagger}(x)$, for $x > 0$, where $c_{\sigma}(x), c_{\sigma}^{\dagger}(x)$ are electron annihilation and creation operators, and $\xi_{\sigma}(x) \sim e^{-\kappa x}$ are the wavefunctions localized at the boundary. Recall the Majorana condition $\tilde{\gamma} = \tilde{\gamma}^{\dagger}$ requires equal contributions from electrons and hole, i.e. conjugate wavefunction coefficients of c and c^{\dagger} . By matching wavefunctions continuously across the junction, the wavefunction along the normal lead is also an equal weight superposition of

³Even if there are accidental mid-gap BdG-states, they are not particle-hole symmetric and their wavefunctions carry unequal weights between electron and hole. Consequently, the electric conductance $\sigma = (2e^2/h)|S_{eh}|^2$ will be smaller than the quantized value $2e^2/h$.

electron and hole. In other words, the electron-hole backscattering probability is $|S_{eh}|^2 = 1$ and there is a differential electric conductance $\sigma = 2e^2/h$ at zero bias.

When plotting σ against the bias voltage V_b , one expects a peak at zero bias with $\sigma = 2e^2/h$ for the topological case. We notice that the conductance quantization relies on the Majorana condition (12.9), which is a consequence of the particle-hole symmetry at zero energy. Figure 12.7 is an excerpt from the transport experiment performed by [51] proximity-induced superconducting SOC InSb wire. It shows a zero bias peak of differential electric conductance for a strong enough the magnetic field. There are other experiments, such as those by [20, 53, 54, 57], that show similar transport signatures. $2e^2/h$ quantization of the zero bias conductance was not achieved until very recently [58] thanks to improvements in materials and experimental designs.

Before concluding this subsection, we notice that there are alternative measurable signatures of protected Majorana zero modes in 1D topological superconductors. In particular, the resonant tunneling of single electrons between two normal leads separated by a 1D topological superconducting island can be mediated by the pair of Majorana zero modes at the two ends. Even when the mesoscopic superconducting island is long and the Majorana wavefunctions do not overlap, the single-electron resonant tunneling can be facilitated by charging energy alone (through a second order perturbative process) without involving the gapped BdG-quasiparticle states in the superconducting bulk. Consequently, the Coulomb-blockade conductance should show oscillations with period of a single electric charge [59–62], whereas the period should be $2e$ for trivial superconductors. Experimental observations have recently been made [63] and are qualitatively consistent with this picture of electron teleportation via Majorana bound states.

12.2.2 Topological Superconductors in Two Dimensions

Similar to the one dimension case, topological superconductors in higher dimensions are systems that cannot be adiabatically connected to a trivial s -wave superconductor. In this section, we are going to focus on time reversal breaking topological superconductors that support vortex and boundary Majorana modes. At the end we will also briefly mention their counterparts in three dimensions as well as time reversal symmetric cases.

We are interested in superconductors within the BCS mean-field regime where excitations are described by a BdG Hamiltonian $H_{\text{BdG}}(\mathbf{k})$ (c.f. 12.6), where $\mathbf{k} \in BZ$ is the lattice momentum in the two dimensional Brillouin zone. Due to the Nambu doubling (e.g. (12.5) for a spinful system), the Hamiltonian has a particle-hole symmetry (12.7) and belongs to class D of the Altland-Zirnbauer classification of band theories [37]. In two dimensions, these superconductors are topologically \mathbb{Z} -classified [3, 6, 8, 14–16]. This means that there is an integer—the first Chern number Ch_1 —associated with any 2D BCS superconductors with a finite pairing gap [24, 25, 64]. Two superconductors can be adiabatically connected without closing

the bulk gap if and only if their Chern numbers are identical. Ch_1 is a topological quantity that depends on the bulk quantum ground state, but also has non-trivial analytic consequences along system boundary. It corresponds to the number of chiral Majorana fermion (MF) channels along an edge. Despite being electrically neutral, these boundary modes carry energy current and correspond to non-trivial quantum thermal Hall conductances [24, 65, 66]. This integral invariant is also intimately related to vortex bound zero energy Majorana bound states (MBS). The number parity (even or odd) of vortex MBS is identical (modulo 2) to the product between Ch_1 and the vorticity [23–26, 33].

We begin with the prototype topological superconductor, the chiral spinless $p_x + ip_y$ -wave superconductor [23–25, 27, 36, 64, 67–69]. In the discrete lattice limit, it can be modeled by the BdG Hamiltonian

$$H_{\text{BdG}}^0(\mathbf{k}) = \Delta(\sin k_x \tau_x + \sin k_y \tau_y) + [t(\cos k_x + \cos k_y) - \epsilon_f] \tau_z, \quad (12.37)$$

where the τ 's are Pauli matrices acting on the Nambu annihilation-creation degrees of freedom (c, c^\dagger). The t term describes the Kinetic Hamiltonian of a metal on a square lattice with spectrum $E_{\text{metal}}(\mathbf{k}) = t(\cos k_x + \cos k_y)$, where t is the nearest neighbor hopping amplitude $t \sum_{\langle \mathbf{r}, \mathbf{r}' \rangle} c_{\mathbf{r}}^\dagger c_{\mathbf{r}'}$. ϵ_f is the Fermi energy, which is set to 0 at half-filling. We consider partially filled band so that the Fermi energy lies between the band edges, i.e. $2|t| > |\epsilon_f|$. As the model is spinless, there is no conventional local s -wave pairing $c_\uparrow c_\downarrow$. Δ represents a non-local superconducting pairing $\Delta \sum_{\mathbf{r}} i c_{\mathbf{r}} c_{\mathbf{r}+\mathbf{e}_x} + c_{\mathbf{r}} c_{\mathbf{r}+\mathbf{e}_y} + h.c.$ between nearest neighbors. There is a finite pairing gap except when the Fermi energy is zero, $\epsilon_f = 0$, where there are two massless Majorana fermions at momenta $X = (\pi, 0)$ and $X' = (0, \pi)$. In the continuum limit, a $p_x + ip_y$ superconductor can be represented by spinless quadratic theory

$$H_{\text{BdG}}^0(\mathbf{k}) = \Delta(k_x \tau_x + k_y \tau_y) + \left(\frac{\hbar^2 k^2}{2m} - \epsilon_f \right) \tau_z, \quad (12.38)$$

where the Fermi energy ϵ_f is positive. For the moment, the $p_y + ip_x$ pairings Δ in both of these cases are chosen to be real. The PH operator is $\Xi = \tau_x \mathcal{K}$ for both (12.37) and (12.38), where \mathcal{K} is the complex conjugation operator.

The Hamiltonians take the form $H(\mathbf{k}) = \mathbf{h}(\mathbf{k}) \cdot \vec{\tau}$, where $\mathbf{h}(\mathbf{k})$ is a non-zero vector in three dimensions (except when the lattice band is completely filled or empty at $2|t| = |\epsilon_f|$). The excitation energy of the BdG quasiparticle is $E(\mathbf{k}) = |\mathbf{h}(\mathbf{k})|$. Expressing the vector in spherical coordinates $\mathbf{h} = |\mathbf{h}|(\sin \theta \cos \phi \mathbf{e}_x + \sin \theta \sin \phi \mathbf{e}_y + \cos \theta \mathbf{e}_z)$, the eigenstate with “negative” energy is $\mathbf{u}(\mathbf{k}) = (-\sin(\theta(\mathbf{k})/2), e^{i\phi} \cos(\theta(\mathbf{k})/2))^T$. The Berry connection in the 1D case was defined in (12.15) and is now generalized to

$$\mathcal{A}(\mathbf{k}) = \langle \mathbf{u}(\mathbf{k}) | \nabla_{\mathbf{k}} \mathbf{u}(\mathbf{k}) \rangle \cdot d\mathbf{k} = \frac{i}{2} [1 + \cos \theta(\mathbf{k})] d\phi(\mathbf{k}). \quad (12.39)$$

The Berry curvature is the momentum-space analogue of the magnetic field $\mathbf{B} = \nabla \times \mathbf{A}$ (or $B_z = \partial_x A_y - \partial_y A_x$ in 2D), and is defined to be the differential

$$\mathcal{F}(\mathbf{k}) = d\mathcal{A}(\mathbf{k}) = (\partial_{k_x} \mathcal{A}_y - \partial_{k_y} \mathcal{A}_x) dk_x \wedge dk_y = \frac{i}{2} \sin \theta(\mathbf{k}) d\theta(\mathbf{k}) \wedge d\phi(\mathbf{k}). \quad (12.40)$$

Here the wedge product \wedge is anti-symmetric and generalizes the cross product \times for 3D vectors. For instance, $dk_x \wedge dk_y = -dk_y \wedge dk_x$, $d\theta \wedge d\phi = -d\phi \wedge d\theta$, and $dk_x \wedge dk_x = dk_y \wedge dk_y = d\theta \wedge d\theta = d\phi \wedge d\phi = 0$. Up to the $i/2$ factor, the Berry curvature is identical to the solid-angle area form $d\text{vol}|_{\mathbb{S}^2} = \sin \theta d\theta \wedge d\phi$ of the unit 2-sphere \mathbb{S}^2 where $\hat{\mathbf{h}} = \mathbf{h}/|\mathbf{h}|$ lives. It can be written in the coordinates free expression

$$\mathcal{F}(\mathbf{k}) = \frac{i}{2} \hat{\mathbf{h}}(\mathbf{k}) \cdot [d\hat{\mathbf{h}}(\mathbf{k}) \wedge d\hat{\mathbf{h}}(\mathbf{k})] = \frac{i}{2} \hat{\mathbf{h}}(\mathbf{k}) \cdot [\partial_{k_x} \hat{\mathbf{h}}(\mathbf{k}) \times \partial_{k_y} \hat{\mathbf{h}}(\mathbf{k})] dk_x \wedge dk_y. \quad (12.41)$$

Just like the Gauss-Bonnet theorem

$$\chi(\Sigma) = 2 - 2g(\Sigma) = \frac{1}{2\pi} \oint_{\Sigma} K dA \quad (12.42)$$

that relates the Gaussian curvature K and the genus $g(\Sigma)$ —number of “holes”—of a closed orientable surface Σ (e.g. $g = 0$ for a sphere \mathbb{S}^2 and $g = 1$ for a torus T^2), the first Chern number

$$\text{Ch}_1 = \frac{i}{2\pi} \oint_{BZ} \mathcal{F}(\mathbf{k}) \quad (12.43)$$

is an integer-valued topological invariant for the superconducting ground state. In the present case, the integral also takes the form

$$\text{Ch}_1 = \frac{-1}{4\pi} \oint_{BZ} \sin \theta(\mathbf{k}) d\theta(\mathbf{k}) \wedge d\phi(\mathbf{k}) = \frac{-1}{4\pi} \oint_{BZ} \hat{\mathbf{h}}(\mathbf{k}) \cdot [d\hat{\mathbf{h}}(\mathbf{k}) \wedge d\hat{\mathbf{h}}(\mathbf{k})], \quad (12.44)$$

which is also known as a winding number. This counts the net solid-angle (in units of 4π) covered by the normal vector $\hat{\mathbf{h}}(\mathbf{k})$ as momentum $\mathbf{k} = (k_x, k_y)$ runs through the lattice Brillouin zone $BZ = [-\pi, \pi] \times [-\pi, \pi]$ or the continuum momentum space $BZ = \mathbb{R}^2$. In other words, (12.44) is the winding number (c.f. (12.16) for the 1D case) that counts the number of times the momentum space BZ wraps around the unit sphere \mathbb{S}^2 by the map $\hat{\mathbf{h}} : BZ \rightarrow \mathbb{S}^2$. Equivalently, Ch_1 is the momentum space version of a skyrmion (see Fig. 12.8).

In the lattice case (12.37), depending on the sign of the Fermi energy ϵ , the Fermi circle either encloses the origin $\Gamma = (0, 0)$ or the corner point $M = (\pi, \pi)$ in the Brillouin zone (see Fig. 12.8a). We assume the hopping t is negative so that in the

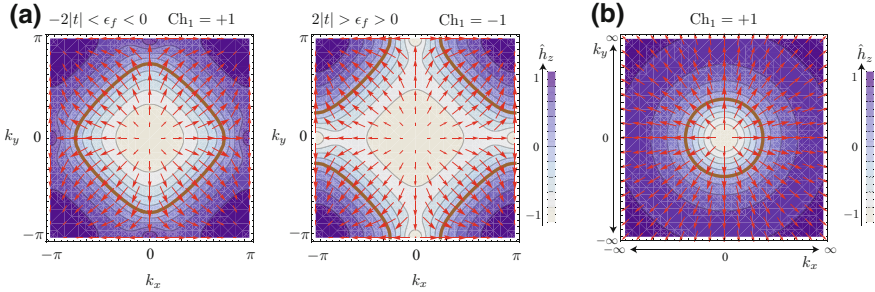


Fig. 12.8 The BdG Hamiltonian $H(\mathbf{k}) = \mathbf{h}(\mathbf{k}) \cdot \vec{\tau}$ represented in \mathbf{k} -space for **a** the lattice model (12.37) and **b** the continuum model (12.38). $\hat{\mathbf{h}} = \mathbf{h}/|h| = (\hat{h}_x, \hat{h}_y, \hat{h}_z)$. Red arrows represent the x, y components of $\hat{\mathbf{h}}$, color contours represent the z component of $\hat{\mathbf{h}}$. Solid brown lines represent the Fermi circles in the metallic states where $\hat{h}_z = 0$

metallic state, there is an electron pocket around Γ and a hole pocket around M . $h_z = t(\cos k_x + \cos k_y) - \epsilon_f$ vanishes on the Fermi circles, along which the x, y components $(h_x, h_y) = (\Delta \sin k_x, \Delta \sin k_y)$ winds by 2π . In the $\epsilon_f < 0$ case, the Fermi circle encloses the γ electron pocket where h_z is negative. In the $\epsilon_f > 0$, it encloses the M hole pocket where h_z is positive. Thus the two cases have opposite orientations and skyrmion number $\text{Ch}_1 = \pm 1$. In the continuum case (12.38), there is similarly a 2π winding of the vector $(h_x, h_y) = (\Delta k_x, \Delta k_y)$ around the Fermi circle where $h_z = \hbar^2 k^2 / 2m - \epsilon_f = 0$. The Fermi circle encloses an electron pocket where $h_z < 0$ (see Fig. 12.8b). Thus the Chern number is $\text{Ch}_1 = 1$.

In the general case, the Hamiltonian H_{BdG} can be a $2N \times 2N$ matrix. The Berry connection is defined by the $N \times N$ matrix-valued 1-form $\mathcal{A}_{mn}(\mathbf{k}) = \langle \mathbf{u}_m(\mathbf{k}) | d\mathbf{u}_n(\mathbf{k}) \rangle$, where $\mathbf{u}_m(\mathbf{k})$, for $m = 1, \dots, N$, are orthonormal eigenvectors of $H_{\text{BdG}}(\mathbf{k})$ with “negative” energies. The Berry curvature is defined in a similar manner as the field strength of a $U(N)$ gauge theory $\mathcal{F} = d\mathcal{A} + \mathcal{A} \wedge \mathcal{A}$ except now it is in momentum space. The $\mathcal{A} \wedge \mathcal{A}$ piece does not contribute to the Chern number, which is now defined by

$$\text{Ch}_1 = \frac{i}{2\pi} \oint_{BZ} \text{Tr}(\mathcal{F}(\mathbf{k})). \quad (12.45)$$

As the trace of the Berry curvature is invariant under any gauge transformation $\mathbf{u}_n(\mathbf{k}) \rightarrow \mathbf{u}_n g_{mn}(\mathbf{k})$ for $g = (g_{mn})_{N \times N}$ a unitary matrix, the Chern invariant is gauge independent. As a matter of fact, the Chern number is an obstruction to a global eigen-frame $\mathbf{u}_m(\mathbf{k})$, i.e. there is no continuous globally-defined orthonormal $\mathbf{u}_m(\mathbf{k})$ for the “negative” bands when the Chern number is non-vanishing.⁴ However $\text{Tr}(\mathcal{F}(\mathbf{k}))$

⁴The orthonormal frame corresponds to a N -dimensional subspace $\mathcal{V}_{\mathbf{k}} = \text{span}\{\mathbf{u}_m(\mathbf{k})\}_{m=1, \dots, N}$ for each \mathbf{k} . The collection of these subspaces is known as a *vector bundle* $\mathcal{V} = \coprod_{\mathbf{k} \in BZ} \mathcal{V}_{\mathbf{k}}$. The vector bundle is trivial if it decomposes into a cartesian product $\mathcal{V} \cong BZ \times \mathbb{C}^N$, which is the case if and only if there is a global continuous eigen-frame $\mathbf{u}_m(\mathbf{k})$. Otherwise, the vector bundle is topological. For the mathematics of vector bundles and their classification, we refer the readers to [70–72].

is still globally-defined continuously over the entire Brillouin zone. To understand this, we use the analogy of magnetic monopoles [73]. The Chern number counts the “magnetic” flux in momentum space, which is identical to the number of enclosed “magnetic” monopoles. When it is non-trivial, there is no globally defined non-singular “vector” potentials but the “magnetic” field is still physical and continuously defined everywhere. The Chern number (12.45) is quantized in integers for the same reason magnetic monopoles are quantized.

The Chern invariant (12.45) is non-zero only when time reversal (TR) symmetry is broken. For the spinless lattice and continuum examples (12.37) and (12.38), TR is represented by the complex conjugation operator $\mathcal{T} = \mathcal{K}$. Recall a TR symmetric BdG Hamiltonian obeys $\mathcal{T} H_{\text{BdG}}(\mathbf{k}) \mathcal{T}^{-1} = H_{\text{BdG}}(-\mathbf{k})$. TR is therefore broken by the τ_x pairing terms in (12.37) and (12.38). In general, since TR is anti-unitary and the Berry curvature \mathcal{F}_{mm} is purely imaginary, TR reverses $\text{Tr}(\mathcal{F}(\mathbf{k})) \rightarrow \text{Tr}(\mathcal{F}(-\mathbf{k}))^* = -\text{Tr}(\mathcal{F}(-\mathbf{k}))$. As parity flips $\mathbf{k} \rightarrow -\mathbf{k}$ in 2D preserves orientation, after taking the momentum integration, TR requires $\text{Ch}_1 = -\text{Ch}_1$, which holds only when the Chern number is trivial. Thus, a topological superconductor of this kind must break time reversal symmetry.

12.2.2.1 Chiral Majorana Edge Modes

We now focus on the boundary of the 2D superconductor. Although there is a finite bulk excitation energy gap, due to the non-trivial topological nature of the ground state, there are gapless modes localized along the system edge that can be excited by an arbitrarily small energy. Figure 12.9 show the energy spectrum of the chiral $p_x + ip_y$ superconductor in (a) an open lattice slab geometry where system is infinitely long in the x -direction but has a finite length L in y , or (b) a semi-infinite continuum geometry where $(x, y) \in (-\infty, \infty) \times [0, \infty)$.

First, we describe the boundary modes for the lattice model (12.37) in a slab geometry. Figure 12.9a shows the energy spectrum when the square lattice is put on an open strip with $L = 20$ atomic sites along the y -axis. Rewriting (12.37) by the inverse

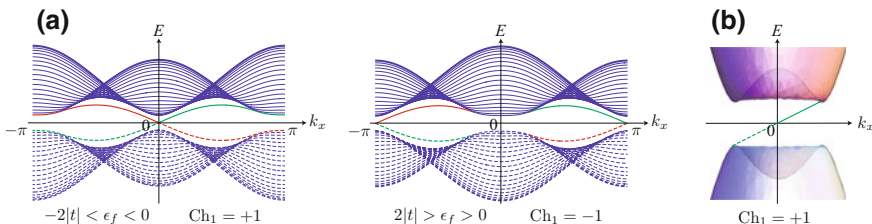


Fig. 12.9 Chiral Majorana edge modes of $p_x + ip_y$ superconductors for **a** the lattice model (12.37) in a slab geometry, and **b** the continuum model (12.38) in a semi-infinite geometry. Blue bands represent bulk BdG states. **a** Red (Green) bands represent boundary Majorana fermion modes localized along the open bottom (top) edge

Fourier transform $c_{k_x,y} = \int \frac{dk_y}{2\pi} e^{-ik_y y} c_{k_x,k_y}$, $\hat{H}_{\text{BCS}} = \int \frac{dk_x}{2\pi} \sum_{y,y'=1}^L \xi_{k_x,y}^\dagger H_{\text{BdG}}^0(k_x)_{yy'} \xi_{k_x,y'}$, for $\xi_{k_x,y} = (c_{k_x,y}, c_{-k_x,y}^\dagger)^T$ and

$$H_{\text{BdG}}^0(k_x)_{yy'} = [\Delta \sin k_x \tau_x + (t \cos k_x - \epsilon_f) \tau_z] \delta_{yy'} + \left[\frac{1}{2} (\Delta i \tau_y + t \tau_z) \delta_{y,y'+1} + \text{h.c.} \right], \quad (12.46)$$

the energy spectrum is obtained by diagonalizing the $2L \times 2L$ BdG Hamiltonian as a function of k_x . The “negative” bands, shown as dashed lines, are redundant and are coming from the artificial Nambu doubling in the BdG construction. The bulk bands (blue lines) corresponds to the gapped excitation states that extend in both x and y directions. The edge bands (red and green lines) are energy spectra of the gapless boundary modes that are localized along the (resp. bottom and top) edges. There are topological distinctions between (i) the $\epsilon_f < 0$ case, where $\text{Ch}_1 = +1$, and (ii) the $\epsilon_f > 0$ case, where $\text{Ch}_1 = -1$. Firstly the *chiralities*—the propagating directions—of the edge modes are reversed. Focusing on the top edge for instance, system (i) carries a right-moving boundary mode, while system (ii) carries a left-moving one. Secondly the momenta of the zero modes are different. The anti-unitary PH symmetry requires zero energy edge modes to have momentum $K_x = 0$ or π so that the lattice translation phase $T_x = e^{iK_x} = \pm 1$ is real. System (i) supports an edge zero mode at 0 momentum, while system (ii) supports that at π . These two distinctions have different topological origins.

Second, we describe the boundary modes for the continuum model (12.38) in a semi-infinite geometry. The continuous spectrum in Fig. 12.9b corresponds to the gapped BdG excitations in the bulk. It can be obtained from the 2D BdG spectrum by collapsing k_y since translation symmetry in y is broken by the open edge along the x -axis. Similar to the lattice case, there are gapless right-moving boundary modes. They are solutions to the differential equations

$$\left[\Delta \left(k_x \tau_x - i \frac{d}{dy} \tau_y \right) + \left(\frac{\hbar^2 k_x^2}{2m} - \frac{\hbar^2}{2m} \frac{d^2}{dy^2} - \epsilon_f \right) \tau_z \right] \mathbf{u}_m(k_x, y) = E_m(\mathbf{k}_x) \mathbf{u}_m(k_x, y) \quad (12.47)$$

by replacing $k_y \leftrightarrow -id/dy$ in (12.38). The wavefunctions $\mathbf{u}_m(k_x, y)$ are normalizable and obey the boundary condition $\mathbf{u}_m(k_x, 0) = 0$. In particular, we demonstrate the zero mode wavefunction $\mathbf{u}_0(0, y) = (u_1(y), u_2(y))^T$ at $k_x = 0$. Putting $E_0(k_x = 0) = 0$, (12.47) requires $DD^\dagger u_i = D^\dagger Du_i = 0$ for

$$D = \frac{\hbar^2}{2m} \frac{d^2}{dy^2} + \Delta \frac{d}{dy} + \epsilon_f, \quad D^\dagger = \frac{\hbar^2}{2m} \frac{d^2}{dy^2} - \Delta \frac{d}{dy} + \epsilon_f. \quad (12.48)$$

Assuming $\Delta > 0$, there is a normalizable zero solution $u_i \sim e^{-\kappa y}$ with $\text{Re}(\kappa) > 0$ for D but not for D^\dagger . The zero mode takes the real form $\mathbf{u}_0(0, y) = (u(y), u(y))^T$, where

$$u(y) = \frac{1}{\mathcal{N}} e^{-m\Delta y/\hbar^2} \sin \left(y \sqrt{\frac{2m\epsilon_f}{\hbar^2} - \frac{m^2\Delta^2}{\hbar^4}} \right) \text{ or } \frac{1}{\mathcal{N}} e^{-m\Delta y/\hbar^2} \sinh \left(y \sqrt{\frac{m^2\Delta^2}{\hbar^4} - \frac{2m\epsilon_f}{\hbar^2}} \right) \quad (12.49)$$

depending on the sign of $2\hbar^2\epsilon_f/m - \Delta^2$, where \mathcal{N} is some normalization constant. It is no coincident that the zero mode is a real eigenvector of τ_x . It satisfies the Majorana condition (12.9), $\Xi \mathbf{u}_0 = \tau_x \mathcal{K} \mathbf{u}_0 = \mathbf{u}_0$. For small k_x so that the k_x^2 term in (12.47) is unimportant, $\mathbf{u}_0(k_x, y)$ has energy $E_0(k_x) = \Delta k_x$. We notice in passing that if the Chern number is reversed, say by substituting a $-p_x + ip_y$ pairing $\Delta(-k_x\tau_x + k_y\tau_y)$ in (12.38), the chiralities of the edge modes will also be reversed.

In general, the boundary modes have a low-energy effective (1 + 1)D free Majorana fermion (MF) description

$$\mathcal{L} = \sum_{a=1}^{N_R} i\hbar\psi_R^a(\partial_t + v\partial_x)\psi_R^a + \sum_{b=1}^{N_L} i\hbar\psi_L^b(\partial_t - v\partial_x)\psi_L^b, \quad (12.50)$$

where $\psi_{R/L}$ are right (resp. left) moving MF, i.e. $\psi_{R/L} = \psi_{R/L}^\dagger$. To be precise, the MF are the Fourier transforms $\psi(x) \sim \int_{-\Lambda}^{\Lambda} dk_x e^{-ik_x x} \mathbf{u}_0(k_x) \cdot \boldsymbol{\xi}(k_x)$, where $\boldsymbol{\xi}$ is the Nambu vector (12.5) of electron operators, \mathbf{u}_0 is the eigenvector of BdG Hamiltonian, such as (12.46) and (12.47), corresponding to the chiral Majorana mode, and Λ is a small momentum cut-off. Although being electrically neutral, each Majorana channel carries an energy current I_T^1 and corresponds to the differential thermal conductance $|\kappa^1| = d|I_T^1|/dT = c^1(\pi^2 k_B^2/3h)T$, where T is temperature and $c^1 = 1/2$ is the *central charge* of a Majorana fermion conformal field theory [74]. In the multi-fermion theory (12.50), since counter-propagating channels carry opposite energy currents, the overall differential thermal conductance along the edge is [24, 65, 66]

$$\kappa = \frac{dI_T}{dT} = c \frac{\pi^2 k_B^2}{3h} T, \quad \text{where } c = \frac{N_R - N_L}{2} \quad (12.51)$$

is known as the *chiral central charge* [24]. The numbers $N_{R/L}$ of right/left-moving Majorana fermions are not protected and are unstable against backscattering $\delta\mathcal{H} = im\psi_R^a\psi_L^b$, which pair annihilates ψ_R^a and ψ_L^b and remove them from the low-energy effective theory when the mass m is big. Thus the numbers can change by an arbitrary amount $(N_R, N_L) \rightarrow (N_R + N', N_L + N')$. The chiral central charge c in (12.51), on the other hand, is a unidirectional transport quantity and is robust against edge perturbations.

This thermal response quantity (12.51), or equivalently the imbalance between right and left-moving Majorana edge channels, corresponds exactly to the bulk topological invariant (12.45)

$$2c = N_R - N_L = \text{Ch}_1. \quad (12.52)$$

This index theorem that identified the boundary analytic spectral flow quantity and the bulk topological quantity was mathematically proven by [75–77]. It was applied in the context of integer quantum Hall effect [78–82] and two dimensional topological superconductors [24, 25, 64]. We refer the interested readers to the existing review texts in the literature, such as [27, 72]. We notice in passing that as the transport quantity does not rely on translation symmetry, there should be an alternative definition of the Chern number that does not involve momentum and can be applied in disordered system. Analog to the 1D case where the Chern-Simons invariant takes the real space form (12.26), the Chern number (12.45) can be rewritten as [24, 83–85]

$$\text{Ch}_1 = 2\pi i \mathcal{T} (P [[\hat{x}, P], [\hat{y}, P]]) . \quad (12.53)$$

Here P is the projection operator to the BdG states with “negative” energy, \hat{x} and \hat{y} are the position operators, and \mathcal{T} is the operator trace.

Equation (12.52) is not the only bulk-boundary correspondence involved in a topological superconductor. Recall in Sect. 12.2.1, we discussed the Chern-Simons \mathbb{Z}_2 -invariant (12.16) that classified topological superconductors in one dimension. The same invariant applies on any 1D cycles inside the 2D momentum space that are closed under the PH flip $\mathbf{k} \rightarrow -\mathbf{k}$. For example, in a 2D lattice Brillouin zone, the 1-cycles $\mathcal{C}_x = BZ|_{k_y=\pi}$ and $\mathcal{C}_y = BZ|_{k_x=\pi}$ that run along the k_y and k_x directions on the zone boundary define two additional *weak* topological \mathbb{Z}_2 -invariants

$$\nu_{x,y} = \frac{i}{\pi} \oint_{\mathcal{C}_{x,y}} \text{Tr}(\mathcal{A}(\mathbf{k})) \quad \text{modulo 2.} \quad (12.54)$$

The index theorem (12.25) then dictates the number parity (even or odd) of zero modes at edge momentum π . For example, when $\epsilon_f < 0$, the lattice model (12.37) has trivial weak indices $\nu_x = \nu_y = 0$, and therefore there is no protected zero energy boundary state at $k_x = \pi$ in Fig. 12.9a. On the contrary, when $\epsilon_f > 0$, the Fermi circle encloses the corner point M in the BZ , and the lattice model (12.37) has non-trivial weak indices $\nu_x = \nu_y = 1$. In this case, we see that in Fig. 12.9a, the boundary mode is shifted and the zero energy state is now located at $k_x = \pi$.

Lastly, we give a brief list of some proposals and findings in materials. For a more complete description, we refer the readers to the review texts such as [27, 36, 68, 69]. Liquid helium-3 thin film in its time reversal breaking superfluid A-phase is an example of a chiral $p_x + ip_y$ superconductor [64, 86–88]. Superconducting strontium ruthenate (Sr_2RuO_4) is a plausible candidate of a topological superconductor with $\text{Ch}_1 = 2$ because of spin degeneracy. It shows signatures of time reversal breaking and odd parity spin triplet pairing [89–92]. However, the precise pairing and topological nature is still under debate [93–95]. A chiral $p_x + ip_y$ superconductor can also be obtained in a Chern insulator (a.k.a. a quantum anomalous Hall state) [96], such as chromium doped bismuth antimony telluride thin film [97], under strong proximity-induced superconducting pairing [98–101].

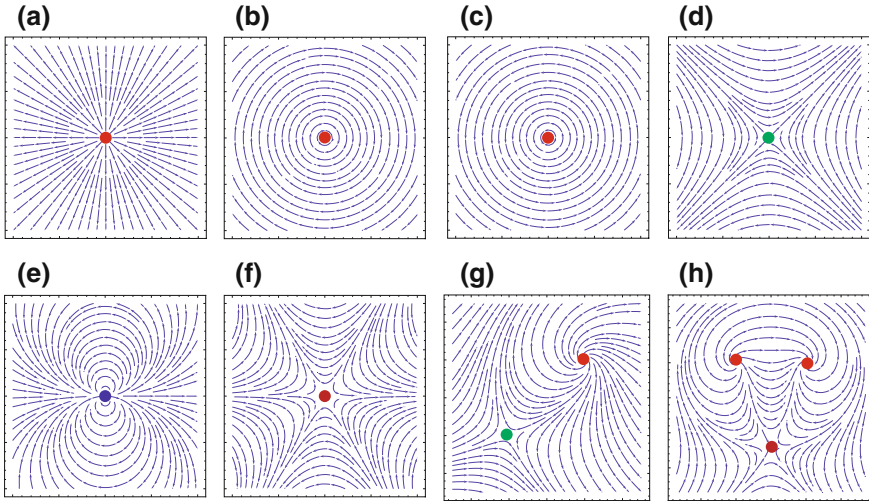


Fig. 12.10 Pairing phases in superconducting vortices. Vector represents the parameters (Δ_x, Δ_y) . **a, b, c** Vortices with vorticity $\nu = 1$. **d** $\nu = -1$. **e** $\nu = 2$. **f** $\nu = -2$. **g** Vortex dipole with $\nu = \pm 1$. **h** Vortex triplet with $\nu = 1$ and $\nu = -2$

12.2.2.2 Vortex Bound Majorana Zero Modes

Chiral topological superconductors in two dimensions support zero energy Majorana bound states (MBS) at quantum flux vortices [23–26, 102]. The superconducting pairing parameter in the BCS mean-field description $\Delta c_i c_j + h.c.$ is a complex order parameter $\Delta = \Delta_x + i\Delta_y = |\Delta|e^{i\varphi}$, where φ is called the superconducting phase. A superconducting vortex—known as a Caroli-de Gennes–Matricon vortex—in 2D is a topological point defect where the pairing parameter $\Delta(\mathbf{r})$ spatially modulates and the pairing phase winds non-trivially around the defect point [35, 36, 103]. The vorticity is the winding number

$$\nu = \frac{1}{2\pi i} \oint_{\mathcal{C}} d\varphi(\mathbf{r}) \quad (12.55)$$

where \mathcal{C} is a (right-handed) loop going once around the vortex. Examples are drawn in Fig. 12.10.

The vorticity corresponds to the monodromy Berry phase $e^{i\pi\nu}$ when an electron orbits once around the vortex. This is because the phase winding $\Delta \rightarrow \Delta e^{2\pi i\nu}$ in the BCS Hamiltonian $\Delta c_i c_j + h.c.$ can be absorbed into the electron operator $c_i \rightarrow c_i e^{i\pi\nu}$. Since ν is an integer, $e^{i\pi\nu} = e^{-i\pi\nu} = \pm 1$, and the same monodromy phase also applies to BdG quasiparticles $\psi \rightarrow \psi e^{i\pi\nu}$, which are linear superpositions of c and c^\dagger . In a type-II superconductor which supports flux vortices, the superconducting coherent length is shorter than the London penetration depth, and magnetic fluxes

are confined along the vortex core. Associating the monodromy phase with the gauge holonomy [104],

$$\pi\nu = \frac{e}{\hbar c} \oint_C \mathbf{A} \cdot d\mathbf{l} = 2\pi \frac{\Phi_B}{\phi_0} \quad (12.56)$$

for $\phi_0 = hc/e$ the magnetic flux quantum, magnetic flux along superconducting vortices are quantized in $\Phi_B = \nu\phi_0/2$.

We consider vortices in the chiral $p_x + ip_y$ superconductor continuum model (12.37). We first put the model in a disc geometry. We assume the radius is much longer than the localization length κ of the edge modes near zero energy, so that locally, the edge modes propagate approximately along a straight line. The model has a rotation symmetry $R_\theta H_{\text{BdG}}^0(\mathbf{k}) R_\theta^\dagger = H_{\text{BdG}}^0(r_\theta \mathbf{k})$, where $R_\theta = e^{i\theta\tau_z/2}$ acts on Nambu space (c, c^\dagger) and $r_\theta = e^{i\theta\sigma_y}$ acts on momentum space \mathbf{k} . We saw previously that when the edge terminates along the x -axis, the edge mode \mathbf{u}_0 is an eigenvector of τ_x . In general, when the boundary terminates along an edge with a tangent angle θ from the x -axis, the edge mode is rotated by $R_\theta \mathbf{u}_0$ and is an eigenvector of $\tau_\theta = R_\theta \tau_x R_\theta^\dagger$. When the edge mode circles once around the disc boundary, it accumulates a minus sign $\mathbf{u}_0 \rightarrow R_{2\pi} \mathbf{u}_0 = -\mathbf{u}_0$. This minus sign is identical to the 2π twist phase of a fermion, and is a consequence of the fermionic nature of the BdG excitation. In other words, the low-energy MF description (12.50) takes an anti-periodic boundary condition when put on a closed ring geometry.

The boundary condition has non-trivial consequences on the boundary modes. It requires the translation phase $T_L = e^{ik_{\parallel}L}$ to be -1 , where T_L is the translation operator that takes the MF ψ once around the boundary ring, L is the circumference, and k_{\parallel} is the edge momentum of the edge mode. Thus k_{\parallel} is quantized in $(2l+1)\pi/L$, where l is an integer. As the zero energy state is located at $k_{\parallel} = 0$ which is forbidden by the anti-periodic boundary condition, it is not admissible. The boundary condition can be modified by passing flux vortices across the superconducting bulk. When the total vorticity is ν , due to the additional monodromy phase, the boundary condition is now $T_L = e^{ik_{\parallel}L} = -e^{i\pi\nu}$. In particular, there is a zero mode along the boundary if and only if ν is odd. In the more general case, when there are multiple boundary MF channels ψ_R^a, ψ_L^b , the boundary condition applies to all of them, and there will be $N_R + N_L$ zero modes if ν is odd. As the Chern number $\text{Ch}_1 = N_R - N_L$ in (12.52) dictates the number of MF channels along the boundary, the following index counts the number parity (even or odd) of boundary zero modes

$$\text{ind}_{\text{vrtx}} = \nu \text{Ch}_1 \text{ modulo } 2. \quad (12.57)$$

We notice that the finite disc geometry puts the chiral superconducting model in a closed system with a closed Hilbert space. Majorana zero modes must come in pairs because it takes two of them to form a two-level system (c.f. the discussion below (12.11)). If there is an odd number of zero modes on the boundary, there must also be an odd number of them in the bulk. However, there is a finite pairing energy gap everywhere in the bulk except at the vortex cores where the Δ vanishes.

This ensures there must be an odd number of zero energy MBS localized at vortices. The index (12.57) therefore also counts the number parity of MBS at a vortex with vorticity ν . This was applied in the context of fractional quantum Hall states [105–107] and chiral superconductors [24, 27, 102]. The index theorem was verified by [33] in the general setting by identifying it with a Chern-Simons invariant

$$\text{ind}_{\text{vrtx}} = \text{CS}_3 \equiv \frac{1}{4\pi^2} \int_{BZ \times \mathbb{S}^1} \text{Tr} \left(\mathcal{A} \wedge d\mathcal{A} + \frac{2}{3} \mathcal{A} \wedge \mathcal{A} \wedge \mathcal{A} \right) \pmod{2}. \quad (12.58)$$

Here $\mathcal{A}_{\mathbf{k},\mathbf{r}}^{mn} = \langle \mathbf{u}_{\mathbf{k},\mathbf{r}}^m | d\mathbf{u}_{\mathbf{k},\mathbf{r}}^n \rangle$ is the Berry connection constructed from the “negative” eigenstates of the defect Hamiltonian $H_{\text{BdG}}(\mathbf{k}, \mathbf{r})$, where \mathbf{r} is the spatial parameter far away from the vortex core that slowly modulates the BdG Hamiltonian. The integral is taken over momentum $\mathbf{k} \in BZ$ and the angle parameter $\theta \in \mathbb{S}^1$ that circles once around the vortex in real space.

We now demonstrate and reproduce the vortex zero mode in the continuum $p_x + ip_y$ model discussed by [22, 67]. When there is a vortex with vorticity ν at the origin, assuming that $\Delta(\mathbf{r}) = |\Delta_\infty| e^{i\nu\theta}$, where θ is the polar angle, and $r = |\mathbf{r}|$ is much longer than the London penetration depth, the BdG Hamiltonian (12.38) is modified to

$$\hat{H}_{\text{BdG}} = -i|\Delta_\infty| e^{i\nu\theta\tau_z/2} (\partial_x \tau_x + \partial_y \tau_y) e^{-i\nu\theta\tau_z/2} - \left(\frac{\hbar^2}{2m} \nabla^2 + \epsilon_f \right) \tau_z \quad (12.59)$$

by replacing momentum with the differential operator $\mathbf{k} \leftrightarrow -i\nabla$. While preserving the PH symmetry, (12.59) can be deformed into

$$e^{i\nu\theta\tau_z/2} H_{\text{BdG}}^0(-i\nabla) e^{-i\nu\theta\tau_z/2} = \hat{H}_{\text{BdG}} + \frac{\hbar^2}{2m} \left(\frac{\nu^2}{4r^2} + \frac{i\nu}{2r} \partial_\theta \right) \tau_z, \quad (12.60)$$

for H_{BdG}^0 the vortexless Hamiltonian, by continuously turning on the last correction term. When $\nu = 2n$ is even, one can absorb the spatial dependence by the gauge transformation $\mathbf{u} \rightarrow e^{in\theta\tau_z} \mathbf{u}$. Thus, the energy spectrum of (12.60) is identical to that of a vortexless system, which has an energy gap. Since the number parity of zero modes cannot change during a PH preserving deformation, (12.59) must have even number of zero modes, if they exist at all.

When $\nu = 2n + 1$ is odd, the transformation $\mathbf{u} \rightarrow e^{i\nu\theta\tau_z/2} \mathbf{u}$ is discontinuous as it introduces a branch cut where the BdG states switch sign. Applying the continuous gauge transformation $\mathbf{u} \rightarrow e^{in\theta\tau_z} \mathbf{u}$ reduces the problem to $\nu = 1$. We now seek a solution to the zero energy differential equation $\hat{H}_{\text{BdG}} \mathbf{u}_0(\mathbf{r}) = 0$ when $\nu = 1$. Using the PH symmetry and the Majorana condition (12.9), $\mathbf{u}_0 = (u, u^*)^T$ and it obeys

$$\left(\frac{\hbar^2}{2m} \nabla^2 + \epsilon_f \right) u + 2|\Delta_\infty| e^{-i\theta/2} \partial_z e^{-i\theta/2} u^* = 0 \quad (12.61)$$

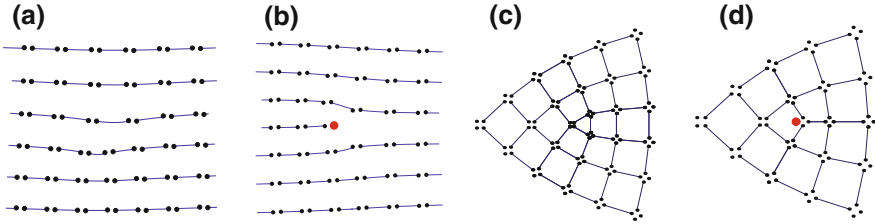


Fig. 12.11 Dislocations (**a**, **b**) and disclinations (**c**, **d**) in 2D weak topological superconductors. Zero energy Majorana bound states (MBS) are present and highlighted in red for (**b**, **d**). Each dot represents a Majorana fermion (MF)

where $\partial_{\bar{z}} = (\partial_x + i\partial_y)/2 = e^{i\theta}(\partial_r + i\partial_\theta/r)/2$. We assume u is real and is θ -independent. The differential equation becomes

$$\left[\frac{\hbar^2}{2m} \left(\partial^2 + \frac{1}{r} \partial_r \right) + \epsilon_f + |\Delta_\infty| \left(\partial_r + \frac{1}{2r} \right) \right] u(r) = 0. \quad (12.62)$$

Substituting $u(r) = \chi(r) e^{-m|\Delta_\infty|r/\hbar^2}$,

$$\left[\partial_r^2 + \frac{1}{r} \partial_r + \frac{2m}{\hbar^2} \left(\epsilon_f - \frac{m|\Delta_\infty|^2}{2\hbar^2} \right) \right] \chi(r) = 0 \quad (12.63)$$

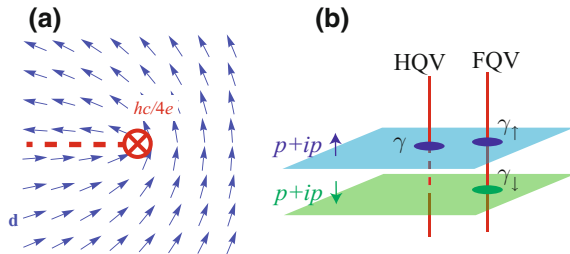
which has the solution

$$\chi(r) = \begin{cases} J_0(x), & \text{if } \epsilon_f > \frac{m|\Delta_\infty|^2}{2\hbar^2} \\ I_0(x), & \text{if } \epsilon_f < \frac{m|\Delta_\infty|^2}{2\hbar^2} \\ \log(r/l), & \text{if } \epsilon_f = \frac{m|\Delta_\infty|^2}{2\hbar^2} \end{cases}, \quad \text{for } x = r \sqrt{\frac{2m}{\hbar^2} \left| \epsilon_f - \frac{m|\Delta_\infty|^2}{2\hbar^2} \right|} \quad (12.64)$$

where J_0 and I_0 are the Bessel function and modified Bessel function that are non-singular when $x \rightarrow 0$. The wavefunction $u(r)$ is finite as $r \rightarrow \infty$ and is normalizable if $\epsilon > 0$, in which case there is a vortex zero mode.

Pairing vortices are not the only kind of topological point defects in 2D superconductors. Here we briefly mention other types of defects that intertwine additional symmetry breaking orders with the pairing order and bulk topology. Consequently, these defects can also host protected zero energy MBS. First, we recall that the boundary MBS of a 1D topological superconductor can be understood by a dimer model of MF (see Fig. 12.3). This line of thought can be generalized in two dimensions. Figure 12.11 shows Majorana dimer models in 2D. (a, b) are arrays of the Kitaev's superconducting chains, where along each chain MF couple between unit cells. (c, d) represent a generalized MF dimer model on a square lattice with four MF per site. MF is coupled to the nearest neighboring sites and the square lattice model has a fourfold rotation symmetry. Each one contains a lattice topological defect, either a dislocation or a disclination [108, 109]. In (b, d), there is an unbonded MF at each

Fig. 12.12 **a** Spatial configuration of the **d**-vector around a half-quantum vortex (HQV) of a spin triplet $p_x + ip_y$ superconductor. **b** Zero energy Majorana bound state (MBS) of a half-quantum vortex and a full quantum vortex



defect center and it corresponds to a zero energy MBS. The defect bound state is a consequence of the mixing of lattice translation and/or rotation order with the symmetry protected topology in the superconductor. For instance, with lattice translation symmetry, superconductors in 2D are enriched with the two weak \mathbb{Z}_2 topological indices (12.54). They combine together to form the \mathbb{Z}_2 -valued reciprocal vector $\mathbf{G} = \nu_x \mathbf{b}_x + \nu_y \mathbf{b}_y$, where $\mathbf{b}_{x,y}$ are the primitive reciprocal lattice vectors. There is a protected dislocation MBS if the dislocation Burgers vector \mathbf{B} is aligned in a way so that the following \mathbb{Z}_2 -index

$$\text{ind}_{\text{dislocation}} = \frac{1}{2\pi} \mathbf{G} \cdot \mathbf{B} \bmod 2 \quad (12.65)$$

is non-trivial [33, 110–113]. Similar index theorems are proposed to characterize disclination MBS [113–115].

Second, we briefly discuss the mixing of rotation and charge $U(1)$ symmetry breaking order, and there corresponding half-quantum vortex (HQV) [116–119]. In particular we focus on the spin-triplet $p_x + ip_y$ superconducting model of Sr_2RuO_4

$$H_0(\mathbf{k}) = \Delta(\boldsymbol{\sigma} \cdot \mathbf{d})(k_x \tau_x + k_y \tau_y) + \left(\frac{\hbar^2 k^2}{2m} - \epsilon_f \right) \tau_z, \quad (12.66)$$

where σ (τ) acts on spin (Nambu) degree of freedom, the BdG states is arranged according to the Nambu vector $(c_\uparrow, c_\downarrow, c_\downarrow^\dagger, -c_\uparrow^\dagger)$, and the PH operator is $\Xi = \sigma_y \tau_y \mathcal{K}$. The three-dimensional unit **d**-vector breaks spin rotation symmetry by specifying a spin direction. Here we assume **d** lies on the xy -plane where the quasi-2D material lives. The model has an artificial spin symmetry $S = (\boldsymbol{\sigma} \cdot \mathbf{d})\sigma_y$, and each of the $S = \pm 1 = \leftarrow, \rightarrow$ sectors corresponds to a chiral $p_x + ip_y$ superconducting model (12.38). The total Chern number is therefore $\text{Ch}_1 = 2$ and there are two MBS γ_\leftarrow and γ_\rightarrow at a full quantum vortex (FQV) with $\Phi_B = \phi_0/2$. They are not protected at zero energy and can pair annihilate by spin mixing or a magnetic field $\delta H = iu\gamma_\leftarrow\gamma_\rightarrow$.

On the other hand, a HQV with magnetic flux $\Phi_B = \phi_0/4$ consists of a π -rotation of the pairing phase as well as the **d**-vector about the z -axis (see Fig. 12.12a). Neither the pairing π -vortex nor the spin π -disclination alone are allowed point defects as both require an extended branch cut where the spin triplet pairing function changes sign.

They are allowed and confined together because the two signs cancel. The HQV is represented by the defect Hamiltonian

$$H(\mathbf{k}, \mathbf{r}) = e^{i\theta(\tau_z + \sigma_z)/4} |\Delta(r)| \sigma_x (k_x \tau_x + k_y \tau_y) e^{-i\theta(\tau_z + \sigma_z)/4} + \left(\frac{\hbar^2 k^2}{2m} - \epsilon_f \right) \tau_z, \quad (12.67)$$

where θ is the angular parameter around the vortex, and $\mathbf{k} \leftrightarrow -i\nabla$. Notice that (12.67) commutes with $\Sigma = \sigma_z \tau_z$ and the problem decomposes into the $\Sigma = \pm 1 = \uparrow, \downarrow$ sector. Effectively the HQV acts as a quantum vortex acting only on one of the two spin sectors where τ_z and σ_z have the same sign. This gives a single protected zero energy MBS as shown in Fig. 12.12b.

We notice in passing that the protected MBS at a dislocation, a disclination, or a HQV all have the same topological origin and are universally characterized by the Chern-Simons \mathbb{Z}_2 -invariant (12.58) [33].

12.2.2.3 Time Reversal Symmetric Variations

We conclude this section by briefly digressing to time reversal symmetric topological superconductors in one, two and three dimensions [3, 6, 8, 14–16]. The physical time reversal (TR) operator in a spinful system squares to $\mathcal{T}^2 = -1$. The Kramers theorem guarantees Majorana zero modes, if they exist, must come in pairs. The BdG mean-field Hamiltonian of a time reversal symmetric BCS superconductor belongs to class DIII according to the band theory description by [37]. Topological superconductors of this kind are \mathbb{Z}_2 classified in one and two dimensions, and are \mathbb{Z} classified in three dimensions.

In one and two dimensions, TR symmetric topological superconductors can be constructed by taking TR pairs $H_{\text{total}} = H_{\uparrow} \oplus H_{\downarrow}$, where $H_{\downarrow} = \mathcal{T} H_{\uparrow} \mathcal{T}^{-1}$ and H_{\uparrow} has the same structure as the spinless Kitaev's p -wave superconducting chain (12.14) or the chiral $p_x + ip_y$ superconductor (12.37) respectively. Because of the spin degeneracy, the boundary Majorana spectra of these models are doubled. In the 1D case, there is a pair (or in general odd number of pairs) of boundary zero energy MBS γ_{\uparrow} and γ_{\downarrow} which are related by TR, $\mathcal{T} \gamma_{\uparrow} \mathcal{T}^{-1} = -\gamma_{\downarrow}$ and $\mathcal{T} \gamma_{\downarrow} \mathcal{T}^{-1} = \gamma_{\uparrow}$. They are protected from pair annihilation $\delta H = iu\gamma_{\uparrow}\gamma_{\downarrow}$ as it breaks TR. Therefore, they are pinned at zero energy and cannot be removed unless the bulk gap closes. In the 2D case, the two spin sectors have opposite Chern numbers and chiralities. The TR symmetric $(p_x + ip_y) \uparrow \otimes (p_x - ip_y) \downarrow$ superconductor has helical edge modes, which consist of a pair of counter-propagating Majorana fermions with opposite spins. The low-energy effective boundary theory is

$$\mathcal{L} = i\hbar\psi_R^{\uparrow}(\partial_t + v\partial_x)\psi_R^{\uparrow} + i\hbar\psi_L^{\downarrow}(\partial_t - v\partial_x)\psi_L^{\downarrow}, \quad (12.68)$$

where TR switches $\mathcal{T}\psi_R^\uparrow\mathcal{T}^{-1} = -\psi_L^\downarrow$ and $\mathcal{T}\psi_L^\downarrow\mathcal{T}^{-1} = \psi_R^\uparrow$. These MF cannot acquire a mass because the backscattering term $\delta\mathcal{H} = im\psi_R^\uparrow\psi_L^\downarrow$ violates TR. Although chiral TR breaking superconductors in 2D are \mathbb{Z} classified by the Chern number, helical TR symmetric superconductors are only \mathbb{Z}_2 classified. For instance, two pairs of helical boundary MF are unstable against the TR symmetric backscattering $\delta\mathcal{H} = im(\psi_R^{\uparrow,1}\psi_L^{\downarrow,2} + \psi_L^{\downarrow,1}\psi_R^{\uparrow,2})$.

While there are no non-trivial strong topologies for TR breaking class D superconductors in three dimensions, TR symmetric ones are \mathbb{Z} classified. A prototype is given by the continuum model of liquid ^3He in its superfluid B-phase [15, 16, 27, 120–124]

$$H_{\text{BdG}}(\mathbf{k}) = \hbar v \mathbf{k} \cdot \boldsymbol{\sigma} \tau_x + \left(\frac{\hbar^2 k^2}{2m} - \epsilon_f \right) \tau_z \quad (12.69)$$

where $\mathbf{k} \in \mathbb{R}^3$ lives in the 3D momentum space, $\sigma_{x,y,z}$ act on spins, and the Nambu vector is arranged according to $(c_\uparrow(\mathbf{k}), c_\downarrow(\mathbf{k}), c_\downarrow^\dagger(-\mathbf{k}), -c_\uparrow^\dagger(-\mathbf{k}))$. The PH and TR operators are $\Xi = \sigma_y \tau_y \mathcal{K}$ and $\mathcal{T} = i \sigma_y \mathcal{K}$. The combination of the two leads to a chiral symmetry $\Gamma_5 = -i \Xi \mathcal{T} = \tau_y$, which anticommutes with H_{BdG} . The non-singular Dirac operator

$$g(\mathbf{k}) \equiv P_- H_{\text{BdG}} P_+^\dagger = \left(\frac{\hbar^2 k^2}{2m} - \epsilon_f \right) \mathbb{1} + i \hbar v \mathbf{k} \cdot \boldsymbol{\sigma}, \quad (12.70)$$

where P_\pm is the 4×2 projection matrices onto the eigenspace of $\Gamma_5 = \pm 1$ and $\mathbb{1}$ is the 2×2 identity matrix, corresponds to a unit winding number

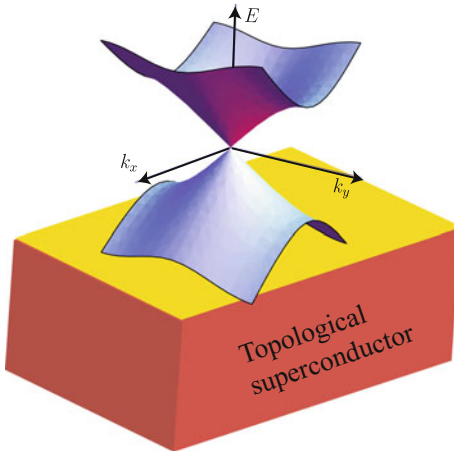
$$\nu = \frac{i}{48\pi^3} \int_{\mathbb{R}^3} \text{Tr} \left[(g(\mathbf{k})^{-1} dg(\mathbf{k}))^{\wedge 3} \right]. \quad (12.71)$$

The system's surface hosts a massless Majorana fermion (c.f. its spectrum in Fig. 12.13)

$$\mathcal{L} = i \hbar \psi (\partial_t \mathbb{1} + v \sigma_x \partial_x + v \sigma_z \partial_y) \psi, \quad (12.72)$$

where the MF $\psi = (\psi_\uparrow, \psi_\downarrow)$ is protected by TR which flips $\mathcal{T}\psi\mathcal{T}^{-1} = i\sigma_y\psi$ and forbids the mass term $im\psi_\uparrow\psi_\downarrow$. Similar surface states can also be supported on an electronic topological superconductor [125–128]. Unlike the 2D case which is \mathbb{Z}_2 classified, 3D topological superconductors are \mathbb{Z} classified. Surface MF with the same helicity—the sign $\text{sgn}(\det(M))$ of the general spin-momentum locked Hamiltonian $H_{\text{surf}} = M_{ij} \sigma_i \partial_j$ where $i = x, z$, $j = x, y$ and M is real symmetric non-singular—cannot mutually annihilate without breaking TR symmetry. For instance, the TR symmetric mixing term between two surface MF with same helicity $\delta\mathcal{H} = iu(\psi_{\uparrow,1}\psi_{\downarrow,2} + \psi_{\downarrow,1}\psi_{\uparrow,2})$ merely displaces the two MF in momentum space without gapping any of them.

Fig. 12.13 Linear energy spectrum of the massless surface Majorana fermion on a time reversal symmetric class DIII topological superconductor



12.3 Superconducting Heterostructures and Topological Defects

Previously, we discussed zero energy Majorana bound states (MBS) at the boundaries of topological superconductors in one dimension (Sect. 12.2.1) and chiral Majorana fermion (MF) along the edges of topological superconductors in two dimensions (Sect. 12.2.2). In this section, we focus on the realization of MBS and MF in superconducting heterostructures in two and three dimensions. These are point or line junctions sandwiched between different materials with distinct orders, such as insulators, magnets or superconductors.

12.3.1 Majorana Bound States at Topological Point Junctions

12.3.1.1 Superconducting QSHI Edge and Fermion Parity Pump

We begin with the edge of a quantum spin Hall insulator (QSHI) [46–50, 129]. The two dimensional band insulating system can be described by the Bloch Hamiltonian model on a square lattice

$$H_{\text{QSHI}}(\mathbf{k}) = \lambda (\sin k_x \sigma_x + \sin k_y \sigma_y) \mu_x + (m + 2t - t \cos k_x - t \cos k_y) \mu_z \quad (12.73)$$

where σ and μ are Pauli matrices acting on spin and orbital degrees of freedom. It is time reversal (TR) symmetric, $\mathcal{T}H(\mathbf{k})\mathcal{T}^{-1} = H(-\mathbf{k})$ for $\mathcal{T} = i\sigma_y\mathcal{K}$. $t > 0$ is a hopping parameter in a tight binding model, $m + 2t$ gives an onsite energy difference between the orbitals, λ is a spin-orbit coupling strength, and the Fermi energy ϵ_f is

set near zero inside the gap. The topological QSHI phase lies on the region where $-4t < m < 0$ have opposite signs, and the trivial insulating phase lies outside this region. This model Hamiltonian can be block diagonalized $H = H_+ \oplus H_-$ according to the artificial spin-orbit symmetry $\sigma_z \mu_z = \pm 1$. In the topological phase, each of the two sectors is a Chern insulator [96, 97], which is the insulating analogue of the $p_x + ip_y$ superconductor (see Sect. 12.2.2). The Chern number (12.43) constructed by the valence states of H_+ (H_-) is $\text{Ch}_1 = 1$ ($\text{Ch}_1 = -1$), and corresponds to a chiral Dirac edge channel that propagates to the right (left).

The helical Dirac edge fermions are described by the low-energy effective Bloch theory

$$H_{\text{edge}}(k_x) = \lambda k_x \sigma_x \quad (12.74)$$

where in this case the edge is along the x -axis. The counter-propagating Dirac channels $c_{R\rightarrow}, c_{L\leftarrow}$ can acquire either a TR breaking mass $g\mu_B B c_{R\rightarrow}^\dagger c_{L\leftarrow}$ or a charge $U(1)$ breaking s -wave pairing gap $\Delta c_{R\rightarrow} c_{L\leftarrow}$. The TR breaking mass $g\mu_B B$ can be introduced by a Zeeman magnetic field or by putting the QSHI edge next to a magnetic insulator. The pairing Δ can be introduced by proximity with a superconductor. These two orders can be put together in the BdG description

$$H_{\text{edge-BdG}}(k_x) = (\lambda k_x \sigma_x - \epsilon_f) \tau_z + g\mu_B B \sigma_z + \Delta \tau_x, \quad (12.75)$$

where the Nambu vector is arranged according to $(c_R(k_x), c_L(k_x), c_L^\dagger(-k_x), -c_R^\dagger(-k_x))$. The PH operator is $\sigma_y \tau_y \mathcal{K}$, and TR is still $\mathcal{T} = i\sigma_y \mathcal{K}$. Equation (12.75) has the same structure as the superconducting spin-orbit coupled wire model (12.28) except that the $\hbar^2 k^2 / 2m$ term is missing. One can follow the same derivation below (12.28) and deduce that there is a energy gap closing topological phase transition at $g\mu_B |B| = \sqrt{\Delta^2 + \epsilon_f^2}$ that separates (i) the weak field phase for $g\mu_B |B| < \sqrt{\Delta^2 + \epsilon_f^2}$ from (ii) the strong field phase for $g\mu_B |B| > \sqrt{\Delta^2 + \epsilon_f^2}$.⁵ We assume ϵ_f is small so that the weak field phase is connected to the superconducting edge and the strong field phase is connected to the magnetic edge.

In a heterostructure where the magnetic domain is adjacent to the superconducting one along the QSHI edge (see Fig. 12.14a) [30, 130], the BdG model (12.75) has spatially modulated parameters $g\mu_B B(x)$ and $\Delta(x)$ so that the edge changes from a weak field phase (i) to a strong field one (ii) across the junction. We demonstrate the MBS in the simple limit $\epsilon_f = 0$. Equation (12.75) has an artificial symmetry $S = \sigma_z \tau_x$ in this case. The Hamiltonian can be block diagonalized according the sign of S , $H = H^{(+)} \oplus H^{(-)}$, where

$$H_{\text{edge-BdG}}^{(\pm)}(k_x, x) = \lambda k_x \tilde{\sigma}_x + [g\mu_B B(x) \pm \Delta(x)] \tilde{\sigma}_z, \quad (12.76)$$

⁵Contrary to the SOC wire model, by computing the Chern-Simons invariant (12.33) here, the weak field phase (i.e. the superconducting edge) is topological while the strong field phase (i.e. the magnetic edge) is trivial.

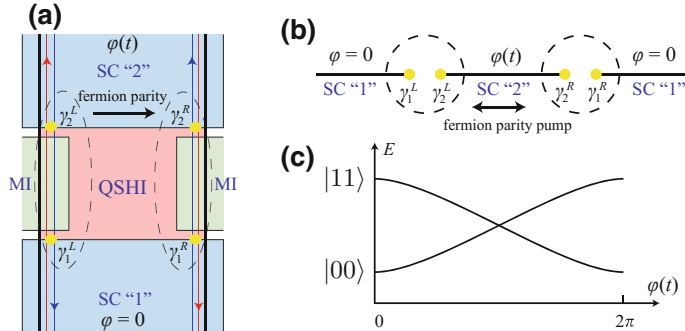


Fig. 12.14 Zero energy Majorana bound states (MBS) and fermion parity pump controlled by superconducting phase $\varphi(t)$. **a** Quantum spin Hall insulator (QSHI)—magnetic insulator (MI)—superconductor (SC) heterostructures that host MBS γ (yellow dots). Helical edge modes (blue and red lines) are gapped by MI and SC islands. MBS γ_2^L and γ_1^R changes signs after a 2π cycle of SC phase evolution. A single (or an odd number of) fermion is pump between the left and right systems. **b** Phase evolution of a topological superconducting wire with Hamiltonian (12.80). **c** Energy level crossing between opposite fermion parity states during a 2π phase cycle

and $\tilde{\sigma}$ are Pauli matrices acting on the new basis. Assuming that $B, \Delta \leq 0$, the edge domain wall transition is captured only by $H^{(-)}$ since $g\mu_B B(x) + \Delta(x)$ never changes sign for $H^{(+)}$. Writing $M(x) = g\mu_B B(x) - \Delta(x)$, the $H^{(-)}$ sector is identical to the Jackiw-Rebbi model [131]. In the thermodynamic limit where the magnetic and superconducting islands are large, we approximate the junction by assuming that $M(x)$ asymptotically approaches the values $\lim_{x \rightarrow +\infty} M(x) = M_{+\infty} > 0$ and $\lim_{x \rightarrow -\infty} M(x) = M_{-\infty} < 0$. The zero energy soliton solution to $H^{(-)}(k_x \leftrightarrow -i\partial_x)$ is given by

$$\mathbf{u}_0(x) = \frac{e^{-i\pi/4}}{\mathcal{N}} \exp\left(-\frac{1}{\lambda} \int_0^x M(x') dx'\right) \begin{pmatrix} 1 \\ i \end{pmatrix} \quad (12.77)$$

where \mathcal{N} is some normalization constant. The wavefunction is exponentially localized on both sides with the localization length $l_{\pm} \sim \lambda/|M_{\pm\infty}|$. Or in operator form in the original basis, the MBS is

$$\gamma_0(x) = \frac{1}{\mathcal{N}'} \exp\left(-\frac{1}{\lambda} \int_0^x M(x') dx'\right) [e^{-i3\pi/4} c_R(x) + e^{-i\pi/4} c_L(x) + h.c.] \quad (12.78)$$

The heterostructure in Fig. 12.14a has four magnet—superconductor junctions along QSHI edges. Each one of them hosts a zero energy MBS $\gamma_{1,2}^{L,R}$, where L, R label the two edges and 1, 2 label the two superconducting sides. We pair the MBS (dashed circles) to form the Dirac operators $d_L = (\gamma_1^L + i\gamma_2^L)/2$ and $d_R = (\gamma_1^R + i\gamma_2^R)/2$. Each one corresponds to a two-level system $|0\rangle, |1\rangle = d^\dagger|0\rangle$ of opposite fermion

parity states. When the width of the magnets are comparable to the localization length $l \sim \lambda/g\mu_B B$, MBS can couple across the magnetic edges as their wavefunctions overlap. Electron tunneling processes correspond to the perturbation away from zero energy

$$\delta\mathcal{H} = -it (\gamma_1^L \gamma_2^L + \gamma_1^R \gamma_2^R) \quad (12.79)$$

that, when $t > 0$, favors the ground state $|00\rangle = |0\rangle_L \otimes |0\rangle_R$. Figure 12.14b represents a simplification of Fig. 12.14a where the line segments represent the topological superconducting QSHI edge. The middle segment in Fig. 12.14b corresponds to the top superconductor “2” of Fig. 12.14a when joining the QSHI edge on the left and right sides together.

The superconducting phase difference between “2” and “1” can be tuned by connecting the top and bottom superconductors in a superconducting quantum interference device (SQUID) geometry [132]. The fermion parity pump physics only depends on the phase difference and we assume the bottom superconducting phase is fixed at $\varphi = 0$. During an adiabatic evolution of the top superconducting phase $\varphi(t)$, the top superconducting edge is modeled by the BdG Hamiltonian

$$\begin{aligned} H_{\text{edge-BdG}}(k_x, \varphi(t)) &= e^{i(\varphi(t)-\varphi(0))\tau_z/2} H_{\text{edge-BdG}}(k_x, \varphi(0)) e^{-i(\varphi(t)-\varphi(0))\tau_z/2} \\ &= (\lambda k_x \sigma_x - \epsilon_f) \tau_z + g\mu_B B \sigma_z + \Delta (\cos \varphi(t) \tau_x + \sin \varphi(t)). \end{aligned} \quad (12.80)$$

After a phase cycle where $\varphi(t)$ winds by 2π (or equivalently an insertion of the half-flux quantum ϕ_0 across the SQUID), the Hamiltonian (12.80) goes back to its initial form but the boundary zero modes acquire an extra phase $\gamma_2^{L,R} = \xi^T \mathbf{u}_0 \rightarrow \xi^T e^{i(\varphi(T)-\varphi(0))\tau_z/2} \mathbf{u}_0 = -\gamma_2^{L,R}$ for $\xi = (c_R, c_L, c_L^\dagger, -c_R^\dagger)$ the Nambu vector. As a result, the Dirac operators are conjugated $d_{L,R} \leftrightarrow d_{L,R}^\dagger$ after the cycle. Equivalently, the adiabatic cycle can be projectively represented (up to a $U(1)$ -phase) by the unitary operation $U = e^{\pi\gamma_2^L \gamma_2^R/2} = \gamma_2^L \gamma_2^R$ so that

$$U \gamma_1^{L,R} U^\dagger = \gamma_1^{L,R}, \quad U \gamma_2^{L,R} U^\dagger = -\gamma_2^{L,R}, \quad U d_{L,R} U^\dagger = d_{L,R}^\dagger. \quad (12.81)$$

If the initial state is the ground state $|00\rangle = |0\rangle_L \otimes |1\rangle_R$, after the cycle it becomes (up to a $U(1)$ -phase)

$$U|00\rangle = -(d_L - d_L^\dagger)(d_R - d_R^\dagger)|00\rangle = -d_L^\dagger d_R^\dagger|00\rangle = -|11\rangle, \quad (12.82)$$

which is the excited state of $\delta\mathcal{H}$ in (12.79).

Despite there being a pairing gap in the superconducting edge, (12.82) suggests that a unit of Dirac fermion is pumped between L and R during the adiabatic cycle. As the ground state and excited state of $\delta\mathcal{H}$ is connected by the adiabatic evolution, there must be an energy level crossing (or odd number of them) during the process (see Fig. 12.14c). This fermion parity pump (first proposed by [17]) has a topological nature. It is the superconducting version of the adiabatic charge pump across an

insulator [133], except that such pairing cycles are \mathbb{Z}_2 classified [33]. This is because the number of fermions can only be counted modulo 2 in a superconductor with a condensate of Cooper pairs.

12.3.1.2 Superconducting Vortex MBS on Topological Insulator Surface

We switch gears from QSHI in two dimensions to topological insulators (TI) in three dimensions [134–139]. The bulk Hamiltonian can be modeled by the lattice Bloch Hamiltonian

$$H_{\text{TI}}(\mathbf{k}) = \lambda(\sin k_x \sigma_x + \sin k_y \sigma_y + \sin k_z \sigma_z) \mu_x + (m + 3t - t \cos k_x - t \cos k_y - t \cos k_z) \mu_z \quad (12.83)$$

which extends the 2D QSHI in (12.73). We assume, for simplicity, $t > 0 > m > -2t$ so that (12.83) is in the strong topological phase (1; 000) with trivial weak indices. The model reduces to the QSHI model (12.73) when restricting to the TR symmetric $k_x k_y$, $k_y k_z$ and $k_z k_x$ momentum planes in the 3D Brillouin zone. Consequently, when terminating the system along a surface boundary, say the xy -plane, the QSHI model along the $k_x k_z$ bulk momentum plane guarantees that there is a pair of helical Dirac boundary modes on the surface k_x momentum axis. The same happens to the surface k_y axis. They can be put together and effectively described by the gapless surface Dirac fermion Hamiltonian

$$H_{\text{Surface}}(\mathbf{k}_{\parallel}) = \lambda(k_x \sigma_x + k_y \sigma_y) \quad (12.84)$$

in low energy and first order in momentum (see Fig. 12.15 for its energy spectrum).

Just like in the QSHI case, the surface Dirac fermion is protected by TR and the linear crossing is protected by the Kramers' theorem. It can acquire a mass by breaking either TR or charge $U(1)$ symmetry. Here we consider surface s -wave pairing $\Delta = \Delta_0 e^{i\varphi} = \Delta_x + i\Delta_y$, for $\Delta_0 > 0$, induced by proximity with a superconductor. The BdG surface Hamiltonian is

$$H_{\text{BdG-Surface}}(\mathbf{k}_{\parallel}, \varphi) = [\lambda(k_x \sigma_x + k_y \sigma_y) - \epsilon_f] \tau_z + \Delta_x \tau_x + \Delta_y \tau_y \quad (12.85)$$

where the Nambu vector is arranged according to $(c_{\uparrow}(\mathbf{k}_{\parallel}), c_{\downarrow}(\mathbf{k}_{\parallel}), c_{\downarrow}^{\dagger}(-\mathbf{k}_{\parallel}), -c_{\uparrow}^{\dagger}(-\mathbf{k}_{\parallel}))$. The PH operator is $\Xi = \sigma_y \tau_y \mathcal{K}$ and the TR operator is $\mathcal{T} = i\sigma_y \mathcal{K}$, which is broken by the Δ_y pairing. For simplicity, we consider zero fermi energy $\epsilon_f = 0$.

When compared with the chiral $p_x + ip_y$ topological superconductor discussed in Sect. 12.2.2, due to the spin-momentum locking and the π Berry phase around the surface Fermi circle, a superconducting vortex on the TI surface hosts protected zero energy MBS [29, 31, 52] despite the pairing being s -wave. This was first discovered by [140] in the context of zero modes in a vortex-fermion system with a chiral

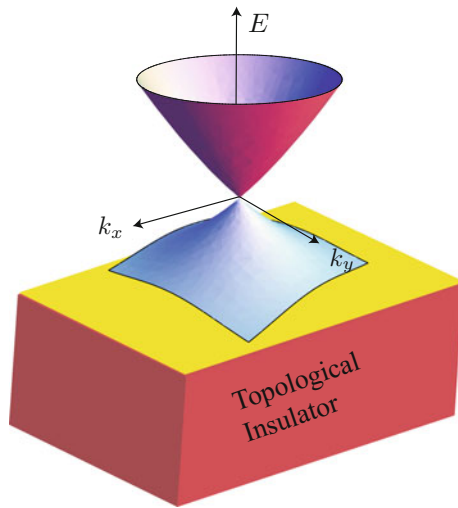


Fig. 12.15 Linear energy spectrum of the massless surface Dirac fermion on a time reversal symmetric class AII topological insulator

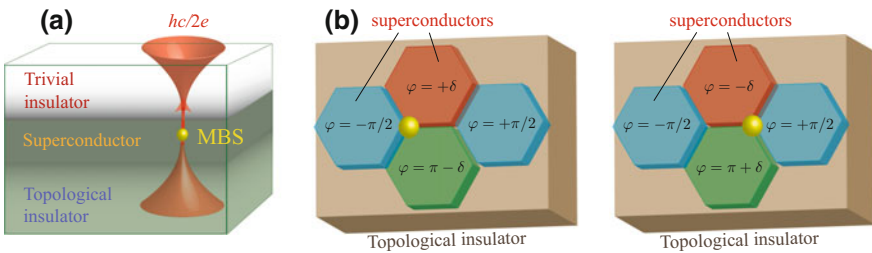


Fig. 12.16 **a** Zero energy Majorana bound state (MBS) at a superconducting vortex core on the surface of a topological insulator (TI). **b** Superconducting phase patterns on TI surface that host MBS (orange balls) at tri-junctions

symmetry. We consider a pairing vortex $\Delta(\mathbf{r}) = \Delta_0 e^{i\nu\theta}$, where ν is the vorticity, θ is the polar angle about the vortex on the surface and $r = |\mathbf{r}|$ is much longer than the London penetration depth. Similar to the previous $p_x + ip_y$ case, even vortices with $\nu = 2n$ are topologically connected to the vortexless case by a gauge transformation e^{int_z} , and therefore zero modes, if they exist, must come in pairs and are not protected. We focus on the primitive vortex where $\nu = 1$ and $\Phi_B = \phi_0/2$ (see Fig. 12.16a). The model has an artificial chiral symmetry $\Gamma_5 = \sigma_z \tau_z$, which anticommutes with (12.85) when $\epsilon_f = 0$ and distinguishes the spins, $\Gamma_5 = 1$ for \uparrow or -1 for \downarrow . The Hamiltonian $\hat{H}_{\text{BdG-surface}} = -i\lambda(\partial_x \sigma_x + \partial_y \sigma_y)\tau_z + \Delta_0(\cos \theta \tau_x + \sin \theta \tau_y)$ decomposes into the off-diagonal Dirac operators under the new basis

$$U \hat{H}_{\text{BdG-surface}} U^{-1} = \begin{pmatrix} 0 & D \\ D^\dagger & 0 \end{pmatrix}, \quad U \Gamma_5 U^{-1} = \begin{pmatrix} -\mathbb{1} & 0 \\ 0 & \mathbb{1} \end{pmatrix}, \quad U = \begin{pmatrix} 0 & 1 & 0 & 0 \\ 0 & 0 & 1 & 0 \\ 1 & 0 & 0 & 0 \\ 0 & 0 & 0 & 1 \end{pmatrix}. \quad (12.86)$$

The Dirac operator

$$D^\dagger = \begin{pmatrix} -2i\lambda\partial_z & \Delta_0 e^{-i\theta} \\ \Delta_0 e^{i\theta} & 2i\lambda\partial_{\bar{z}} \end{pmatrix} = e^{-i\theta\tilde{\sigma}_z} \begin{pmatrix} -i\lambda(\partial_r - i\partial_\theta/r) & \Delta_0 \\ \Delta_0 & i\lambda(\partial_r + i\partial_\theta/r) \end{pmatrix} \quad (12.87)$$

has the normalizable zero mode $\mathbf{u}_0(r) \sim e^{-\Delta_0 r/\lambda} (e^{i\pi/4}, e^{-i\pi/4})^T$, where $\tilde{\sigma}_z$ is the Pauli matrix in the new basis. Or back in the Nambu basis, the MBS has the operator form

$$\gamma_0(\mathbf{r}) = \frac{1}{\mathcal{N}} e^{-\Delta_0 r/\lambda} (e^{i\pi/4} c_\downarrow(\mathbf{r}) + e^{-i\pi/4} c_\downarrow^\dagger(\mathbf{r})) \quad (12.88)$$

where \mathcal{N} is some normalization constant. It has negative chirality $\Gamma_5 = -1$ as it involves only \downarrow spin.

Equation (12.88) is the only zero mode in this problem. In general the analytic index of the chiral symmetric model—which is defined by the difference (i.e. chirality)

$$\begin{aligned} \text{ind}_{\text{vrtx}} &= \dim \ker(D) - \dim \ker(D^\dagger) \\ &= \# \text{ positive chiral zero modes} - \# \text{ negative chiral zero modes} \end{aligned} \quad (12.89)$$

where $\dim \ker$ counts the number of linearly independent zero modes of the Dirac operator—is identified with a topological index [72, 141–146]. To see this, we notice (12.89) equals the heat kernel $\mathcal{T}(\Gamma_5 e^{-t\hat{H}^2})$ where t is an arbitrary positive parameter and

$$H^2 = \hat{H}_{\text{BdG-surface}}^2 = -\lambda^2 \nabla^2 + |\Delta(\mathbf{r})|^2 + \lambda \epsilon^{ij} \partial^k \Delta_i(\mathbf{r}) \sigma_k \tau_j \quad (12.90)$$

is the square of the vortex Hamiltonian with a general spatially winding pairing $\Delta(\mathbf{r}) = \Delta_x(\mathbf{r}) + i\Delta_y(\mathbf{r})$, for $i, j, k = x, y = 1, 2$ and ϵ^{ij} the antisymmetric tensor. All non-zero energy states come in $\pm E$ pairs, $| -E \rangle = \Gamma_5 | +E \rangle$, as $\Gamma_5 \hat{H} = -\hat{H} \Gamma_5$. Thus $\langle E | \Gamma_5 e^{-t\hat{H}^2} | E \rangle = 0$ for any $E \neq 0$ and does not contribute to the heat kernel. On the other hand, the zero energy subspace can be decomposed according to chirality $\Gamma_5 = \pm 1$, and therefore the heat kernel counts the overall chirality (12.89) of the zero modes.

Next we express the wavefunction with energy E_n in Fourier basis, $\psi_n(\mathbf{r}) = \int \frac{d^2\mathbf{k}}{(2\pi)^2} \psi_n(\mathbf{k}) e^{i\mathbf{k} \cdot \mathbf{r}}$, where $\psi_n = (\psi_n^1, \psi_n^2, \psi_n^3, \psi_n^4)^T$. Using the completeness relation $\sum_n \psi_n^a(\mathbf{k}) \psi_n^b(\mathbf{k}')^* = \delta(\mathbf{k} - \mathbf{k}') \delta^{ab}$, the heat kernel becomes

$$\begin{aligned} \mathcal{T} \left(\Gamma_5 e^{-t\hat{H}^2} \right) &= \sum_n \int d^2\mathbf{r} \int \frac{d^2\mathbf{k}}{(2\pi)^2} \frac{d^2\mathbf{k}'}{(2\pi)^2} \psi_n(\mathbf{k})^\dagger e^{-i\mathbf{k}\cdot\mathbf{r}} \Gamma_5 e^{-t\hat{H}^2} e^{i\mathbf{k}'\cdot\mathbf{r}} \psi_n(\mathbf{k}') \\ &= \int d^2\mathbf{r} \int \frac{d^2\mathbf{k}}{(2\pi)^2} \text{Tr} \left[\Gamma_5 e^{-t(\lambda^2 k^2 + |\Delta(\mathbf{r})|^2 + \lambda \epsilon^{ij} \partial^k \Delta_i(\mathbf{r}) \sigma_k \tau_j)} \right], \end{aligned} \quad (12.91)$$

where Tr is now the 4×4 matrix trace and we have replaced $-\nabla^2 \leftrightarrow k^2$ in Fourier space.

Expanding the exponential in series of t , due to the traceless Γ_5 , the lowest order non-vanishing term is

$$\text{Tr} \left[\Gamma_5 e^{-t\lambda \epsilon^{ij} \partial^k \Delta_i(\mathbf{r}) \sigma_k \tau_j} \right] = -t^2 \lambda^2 \text{Tr} (\mathbb{1}_4) \det (\partial^k \Delta_i(\mathbf{r})) + O(t^3), \quad (12.92)$$

where $\mathbb{1}_4$ is the 4×4 identity matrix. To evaluate the integral, we compactify the real space and pairing space to the sphere $\mathbb{S}^2 = \mathbb{R}^2 \cup \{\infty\}$ and assume the pairing vanishes at the vortex core $\Delta(0) = 0$ and diverges at infinity $\Delta(\infty) = \infty$.⁶ The determinant relates the measure $d\Delta_x d\Delta_y = \det(\partial^k \Delta_i) d^2\mathbf{r}$ between real space and pairing space. The heat kernel becomes the Gaussian integral

$$\mathcal{T} \left(\Gamma_5 e^{-t\hat{H}^2} \right) = \int \nu d\Delta_x d\Delta_y \int \frac{d^2\mathbf{k}}{(2\pi)^2} e^{-t(\lambda^2 k^2 + |\Delta|^2)} \left(-4t^2 \lambda^2 + O(t^3) \right) = -\nu + O(t), \quad (12.93)$$

where ν is the winding number (12.55) of the pairing phase. Since we have already identified the heat kernel with the analytic index (12.89), which takes discrete integral value, (12.93) should be t -independent. Taking $t \rightarrow 0$, we recover the Atiyah-Singer index theorem

$$\text{ind}_{\text{vrtx}} = -\nu. \quad (12.94)$$

In the physical scenario where the chiral Γ_5 symmetry is only accidental, positive and negative chiral (i.e. spin) zero modes can mix and pair annihilate. In fact, chirality cannot be defined when the Γ_5 /spin symmetry is absent when $\epsilon_f \neq 0$, but the vorticity ν modulo 2 still defines a \mathbb{Z}_2 -invariant that corresponds to the number parity of vortex MBS for small ϵ_f . The index theorem (12.94) resembles (12.57) for vortices in chiral $p_x + ip_y$ superconductors in two dimensions, and it is not a coincidence. Firstly, both formulas apply to special cases that simplify and derive from the general Chern-Simons invariant (12.58), which topologically characterizes all superconducting point defects in 2D [33]. Secondly, as we will see in the subsequent subsection, a quasi-2D TI slab with superconducting top surface and magnetic bottom surface

⁶In reality the pairing strength plateaus $\Delta(\mathbf{r}) = |\Delta_\infty| e^{i\varphi(\mathbf{r})}$ for $|\mathbf{r}| \gg 0$ far away from the vortex. However, because of the non-trivial winding of the phase, $\Delta(\mathbf{r})$ cannot be compactified or otherwise it would be discontinuous at ∞ . We deform the model and let the pairing strength plateaus up to some long length scale L until it eventually diverges at ∞ . In this case after compactifying both real and pairing spaces $\mathbb{S}^2 = \mathbb{R}^2 \cup \{\infty\}$, the pairing function $\Delta : \mathbb{S}^2 \rightarrow \mathbb{S}^2$ is continuous.

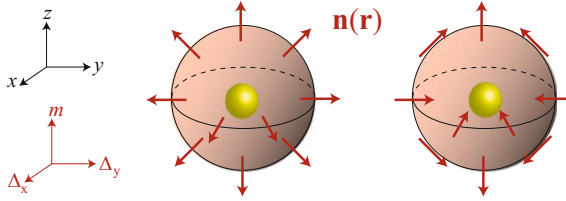


Fig. 12.17 Hedgehog point defect configurations in real space of the order parameter vector $\mathbf{n}(\mathbf{r}) = (\Delta_x(\mathbf{r}), \Delta_y(\mathbf{r}), m(\mathbf{r}))$ (red vector field) that have unit winding number (12.97) and host protected Majorana bound state (yellow balls)

is topologically equivalent to a chiral topological superconductor with odd Chern number. Equations (12.94) and (12.57) therefore have an identical topological origin although the pairing orders and the BdG Hamiltonians are drastically different.

Equation (12.94) applies to the general scenario where the phase winding can be highly non-uniform. Figure 12.16b shows a mesoscopic superconducting pairing phase pattern on the surface of a TI proposed by [29]. The honeycomb lattice pattern consists of superconducting hexagon plaquettes \bigcirc_j , each with a constant pairing phase φ_j (mod 2π), separated from adjacent plaquettes by Josephson line junctions. The surface Dirac fermion underneath each hexagonal superconductor is gapped by proximity effect. A line junction generically does not carry protected gapless electronic channels unless the phase difference across the junction is π , where it hosts a pair of helical Majorana modes (to be discussed in the subsequent subsection). If the phase difference $|\varphi_1 - \varphi_2|$ between two adjacent islands is smaller than π , we assume the phase connects across the junction along the shortest path on the $U(1)$ phase circle. There is a zero energy MBS at a tri-junction if the phase winds by 2π around the three neighboring superconducting islands. The two configurations in Fig. 12.16b host MBS at two different tri-junctions. By manipulating the phase parameter δ , one can control the phase winding around each tri-junction and therefore the position of the MBS. When $\delta = 0$, the MBS can leak through the low-energy channels along the π junction and move from one tri-junction to another. The ability to manipulate the position of MBS is essential for the implementation of braiding operations.

Lastly, we remark that superconducting TI heterostructures are systems in three dimensions. The previous discussion, which focuses on the TI surface, is valid because the low-energy electronic degrees of freedom is frozen in the vertical z -direction by the large energy gap in the bulk insulator and the superconductor. There should be a more complete topological defect theory that captures the MBS physics in three dimensions [32, 147]. Here we briefly describe the topological point defect in a 3D setting. The BdG Hamiltonian that extends away from the TI surface takes the following form

$$H_{\text{BdG-TI-SC}}(\mathbf{k}) = (H_{\text{TI}}(\mathbf{k}) - \epsilon_f) \tau_z + \Delta_x \tau_x + \Delta_y \tau_y, \quad (12.95)$$

where H_{TI} is the TI model (12.83). The mass term $m(\mathbf{r})$ in H_{TI} changes sign across the TI surface from the topological to the trivial insulator. The superconductor pairing $\Delta(\mathbf{r}) = |\Delta(\mathbf{r})|e^{i\varphi(\mathbf{r})} = \Delta_x(\mathbf{r}) + i\Delta_y(\mathbf{r})$ has support near the TI surface and its phase winds by multiple of 2π around a vortex. Since the topological band inversion happens at zero momentum, the relevant small momentum physics can be captured by the continuum limit

$$H_{\text{BdG-TI-SC}}(\mathbf{k}, \mathbf{r}) = \left[\lambda \mathbf{k} \cdot \boldsymbol{\sigma} \mu_x + \left(m(\mathbf{r}) + \frac{tk^2}{2} \right) \mu_z - \epsilon_f \right] \tau_z + \Delta_x(\mathbf{r}) \tau_x + \Delta_y(\mathbf{r}) \tau_y \quad (12.96)$$

where \mathbf{k} now lives on the momentum space \mathbb{R}^3 . Here the k^2 term is kept only for regularization in the bulk TI, and can be dropped in the context of topological point defect. We assume again for simplicity that $\epsilon_f = 0$ so that the model has a $\Gamma_5 = \mu_y \tau_z$ chiral symmetry. [140] and [141–146] showed in such situations, the overall chirality of zero energy bound states (c.f. (12.89)) is identical to the number of times the combined order parameter vector $\mathbf{n}(\mathbf{r}) = |\mathbf{n}(\mathbf{r})| \hat{\mathbf{n}}(\mathbf{r}) = (\Delta_x(\mathbf{r}), \Delta_y(\mathbf{r}), m(\mathbf{r}))$ winds around the defect point. The winding number is

$$\nu = \frac{1}{2\pi} \oint_{\mathbb{S}^2} \hat{\mathbf{n}}(\mathbf{r}) \cdot [\mathbf{d}\hat{\mathbf{n}}(\mathbf{r}) \wedge \mathbf{d}\hat{\mathbf{n}}(\mathbf{r})] \quad (12.97)$$

(c.f. the momentum space version (12.44)). Equation (12.97) reduces to the vorticity (12.55) of surface pairing when there is a TI transition across the surface so that the mass term $m(\mathbf{r})$ switches sign along the z -axis. The parameter vector $\mathbf{n}(\mathbf{r})$ can be represented by a vector field in real space. Figure 12.17 shows hedgehog configurations of the vector that correspond to point defects with winding number $\nu = 1$ and host protected MBS. The index theorem in 3D (or higher dimensions in general) can also be proven using a heat kernel similar to the one in the 2D case. For small finite ϵ_f that breaks the chiral symmetry, the number parity of MBS can be shown to be identical to a Chern-Simons \mathbb{Z}_2 -invariant [32].

12.3.2 Majorana Channels Along Topological Line Junctions

12.3.2.1 Chiral Majorana Channels in Topological Heterostructures

We start with the TI surface Dirac fermion (12.84). It can acquire a magnetic mass $g\mu_B B$ by breaking TR or a s -wave superconducting mass Δ by breaking charge $U(1)$ symmetry. These mass terms can be introduced by proximity effect when the TI surface is put in contact with a magnetic insulator or a s -wave superconductor. The BdG Hamiltonian of the surface Dirac fermion is

$$H_{\text{BdG-surface}}(\mathbf{k}_\parallel) = [\lambda(k_x \sigma_x + k_y \sigma_y) - \epsilon_f] \tau_z + g\mu_B B \sigma_z + \Delta \tau_x, \quad (12.98)$$

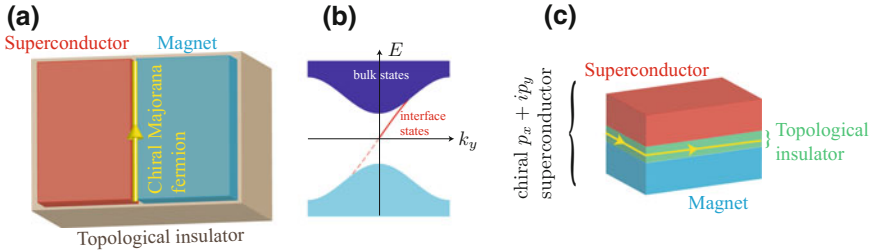


Fig. 12.18 **a** A superconductor—magnet domain wall on a topological insulator surface that host a chiral Majorana fermion (yellow line) along the line interface. **b** The energy dispersion (red curve) of the chiral Majorana fermion channel. **c** A quasi-2D topological insulator slab with superconducting and magnetic surfaces

which is an extension of the QSHI edge BdG model (12.75) by the vertical term $\lambda k_y \sigma_y \tau_z$. We consider a domain wall on the TI surface separating (i) a superconducting domain with $g\mu_B|B| < \sqrt{\Delta^2 + \epsilon_f^2}$ and (ii) a magnetic domain with $g\mu_B|B| > \sqrt{\Delta^2 + \epsilon_f^2}$ (see Fig. 12.18a) [52, 55]. We assume without loss of generality that the domain wall is parallel to the y -direction so that the mass terms $B(x)$, $\Delta(x)$ varies along the x -axis. Horizontal momentum is replaced by the differential operator $k_x \leftrightarrow -i\partial_x$ but momentum k_y is still a good quantum number.

The derivation of the zero mode at $k_y = 0$ is identical to that in the QSHI case in Sect. 12.3.1.1. For the simple case when $\epsilon_f = 0$, The zero mode (12.78) is exponentially localized at the line junction. It is a positive eigenstate of $\sigma_y \tau_z$, and therefore when the $\lambda k_y \sigma_y \tau_z$ term is included when $k_y \neq 0$, (12.78) becomes the chiral Majorana fermion (MF) that has energy dispersion $E(k_y) = +\lambda k_y$ (see Fig. 12.18b). The chiral MF has the same low-energy behavior as the one we have seen along the edge of a chiral $p_x + ip_y$ superconductor in Sect. 12.2.2. For instance, it is electrically neutral but carries the thermal response in (12.51) with chiral central charge $c = 1/2$. For a general TI with an odd number of surface Dirac fermions, there may be multiple number of chiral MF species along a superconductor—magnet interface. The number must however be odd and the chiral central charge must still be a half-integer.

It is no coincidence that the low-energy degrees of freedom along the superconductor—magnet interface is identical to that of the edge of a 2D topological superconductor. In fact, the two problems can be mapped on to each other. First the 3D heterostructure can be deformed into a quasi-2D slab geometry (see Fig. 12.18c), where a TI slab is sandwiched between a superconductor and a magnet. We assume the slab is still thick enough to forbid electron tunneling between the top and bottom TI surfaces. The low-energy BdG description of this geometry is decomposed into the top and bottom surfaces, $H_{\text{BdG-slab}} = H_{\text{BdG-top}} \oplus H_{\text{BdG-bottom}}$.

$$\begin{aligned} H_{\text{BdG-top}}(\mathbf{k}_\parallel) &= [\lambda(k_x\sigma_x + k_y\sigma_y) - \epsilon_f] \tau_z + \Delta\tau_x \\ H_{\text{BdG-bottom}}(\mathbf{k}_\parallel) &= [\lambda(k_x\sigma_x + k_y\sigma_y) - \epsilon_f] \tau_z + g\mu_B B\sigma_z. \end{aligned} \quad (12.99)$$

The top surface is TR symmetric and does not contribute to the Chern number (12.45). The bottom surface is doubled by the Nambu c, c^\dagger construction. It can be decomposed into two sectors according to $\tau_z = \pm 1$, each being a two-band model and of the form $H_\pm = \mathbf{h}_\pm \cdot \boldsymbol{\sigma} = \pm\lambda(k_x\sigma_x + k_y\sigma_y) \pm \epsilon_f + g\mu_B B\sigma_z$. For $|\epsilon_f| < g\mu_B|B|$, the bottom surface is insulating, and each sector corresponds to Chern/skyrmion number $\pm 1/2$ (depending on the sign of B) because $\hat{\mathbf{h}}_\pm$ covers exactly half of the Bloch sphere.⁷ The BdG slab model therefore has overall Chern number $\text{Ch}_1 = \pm 1$ and corresponds to a single chiral Majorana edge channel.

Going back to the TI surface geometry in Fig. 12.18a, the line defect can also be described in a three dimensional setting in (12.95) and (12.96) by taking $\Delta = \Delta_x$ and turning off Δ_y . The mass terms $m(\mathbf{r})$ changes sign along the z -axis across the TI surface. The difference between the magnetic and superconducting masses, $M(\mathbf{r}) = g\mu_B B(\mathbf{r}) - \Delta(\mathbf{r})$, changes sign along the x -axis from the magnet to the superconductor. When \mathbf{r} is far away from the line interface (the y -axis), these mass terms modulate slowly in space and we can treat \mathbf{r} as an adiabatic parameter. The 3D defect Hamiltonian $H_{\text{BdG-TI-SC}}(\mathbf{k}, \mathbf{r})$ defines a Berry connection $\mathcal{A}_{ab}(\mathbf{k}, \mathbf{r}) = \langle u_a(\mathbf{k}, \mathbf{r}) | du_b(\mathbf{k}, \mathbf{r}) \rangle$ using its “negative” energy states u_a . The corresponding Berry curvature is defined similar to a non-Abelian $U(N)$ -gauge theory, $\mathcal{F} = d\mathcal{A} + \mathcal{A} \wedge \mathcal{A}$. The topology of the line defect is characterized by the second Chern number [33]

$$\text{Ch}_2 = \frac{-1}{8\pi^2} \int_{BZ \times \mathbb{S}^1} \text{Tr}(\mathcal{F} \wedge \mathcal{F}) \quad (12.100)$$

where BZ is the Brillouin zone/momentum space and \mathbb{S}^1 is a (right-handed) circle that wraps around the line defect once in real space. In general, this integral index is identical to the net *chirality* of the Majorana channels enclosed by the circle, i.e. the difference between the number of forward and backward moving MF, or equivalently twice of the overall chiral central charge. In the TI surface case in (12.95) and (12.96), when $|\epsilon_f| < g\mu_B|B|$, $|\Delta|$, (12.100) can be simplified by integrating out momentum into the winding number

$$\nu = \frac{1}{2\pi} \oint_{\mathbb{S}^1} \varepsilon_{ij} \hat{\mathbf{n}}_i \partial_\theta \hat{\mathbf{n}}_j d\theta, \quad (12.101)$$

where $\hat{\mathbf{n}} = (\hat{n}_1, \hat{n}_2)$ is the unit direction of mass vector $\mathbf{n} = (m, M)$, and θ circles once around the line defect in real space. ν counts the number of times \mathbf{n} is rotated

⁷The Nambu doubled BdG theory of the bottom surface can be regularized at large momentum by adding $\varepsilon k^2 \sigma_z \tau_z$, for instance, ε could be $\hbar^2/2m$. Depending on the relative sign of ε and B , the Chern numbers of the $(+, -)$ sectors are now $(\pm 1, 0)$ or $(0, \pm 1)$ as $\hat{\mathbf{h}}_\pm$ cover either the entire Bloch sphere or nothing at all.

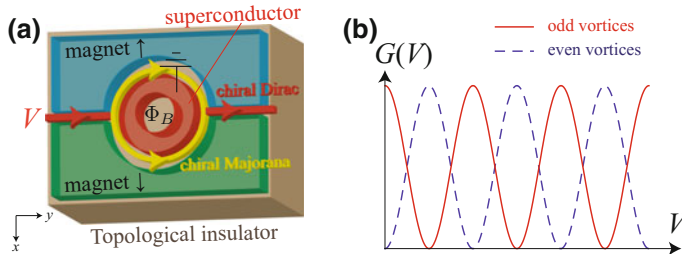


Fig. 12.19 **a** A Mach-Zehnder interferometer with a magnetic flux $\Phi_B = n_v \phi_0/2$ across the grounded superconducting region (red island). V is the electric potential difference between the chiral Dirac lead and the superconductor. **b** Electric conductance $G(V)$ versus V when n_v is odd or even

in one orbit around the line defect. In the heterostructure in Fig. 12.18, this number is 1 and corresponds to a single chiral MF along the line interface.

12.3.2.2 Charge Transport and Interferometry

Chiral Majorana modes and zero energy MBS have non-trivial charge transport consequences. Theoretical proposals in the context of TI heterostructures were pioneered by [52, 55, 56]. Here we briefly review the Mach-Zehnder interferometer involving magnetic and superconducting domains on a TI surface (see Fig. 12.19a). The superconducting region is in the form of a compact disk/annulus with a magnetic flux quantized in $\Phi_B = n_v \phi_0/2$ passing through, where $\phi_0 = hc/e$ is the magnetic flux quantum. From the previous discussion in Sect. 12.3, we have seen that vortices with odd n_v host odd number of protected zero energy MBS. Its presence has non-trivial holonomical effects on orbiting fermions.

The superconducting disk is sandwiched between two magnetic insulating domains with opposite orientations. As a result, there are a pair of chiral Majorana channels (represented by yellow directed lines in Fig. 12.19a) running along the top and bottom semi-circular interfaces. The pair of Majorana channels join at the two tri-junctions where the superconductor region terminates and sits next to a pair of time reversal conjugate copies of magnetic regions. As the pair of MF channels $\psi_{\text{top}}, \psi_{\text{bottom}}$ are co-propagating, they join into a chiral Dirac fermion channel $d = (\psi_{\text{top}} + i\psi_{\text{bottom}})/2$ (red directed lines in Fig. 12.19a) along the interface between the opposite magnetic domains [33].⁸ Assuming the proximity-induced superconducting pairing does not extend to the magnetic domains, the chiral Dirac channel carries electric charge transport.

⁸The chiral Dirac interface fermion between time reversal conjugate magnetic TI surface domains can be illustrated by solving the Bloch Hamiltonian $H_{\text{surface}}(\mathbf{k}_{\parallel}) = \lambda(k_x \sigma_x + k_y \sigma_y) + g\mu_B B(x) \sigma_z$ for $k_x \leftrightarrow -i\partial_x$ and $B(x)$ changes sign across the domain wall along the y -axis. The derivation is similar to that of the Jackiw-Rebbi model (12.76) and is carried out in the context of a BdG model later in (12.103).

We consider the electric current I under a potential difference V between the incoming chiral Dirac channel and the superconductor domain. The differential conductance $G(V) = dI/dV$ depends on the total flux $\Phi_B = n_v\phi_0/2$ across the superconductor domain, where n_v is an integer and $\phi_0 = hc/e$ is the magnetic flux quantum. n_v is also total vorticity ν of all the flux vortices passing the superconductor, and recall from (12.94) (also see Fig. 12.16), n_v modulo 2 counts the number parity of protected zero energy MBS on the superconducting TI surface. However, we assume all vortices are far away from the magnetic interface so that the vortex MBS wave functions do not overlap with that of the chiral MF channels. In this case, as the hybridization between vortex MBS and interface MF is unimportant, we ignore the vortex zero modes and focus only on the low-energy modes along the line interfaces.

Assuming the potential eV and temperature $k_B T$ are small when compared to the proximity-induced pairing gap in the superconducting surface domain, electrons near the Fermi level from the chiral Dirac channels cannot tunnel as BdG quasiparticles into the superconductor. Electric charge transport between the chiral Dirac leads and the superconductor is generated by Andreev reflection processes, where incoming Dirac electron $d^{(in)} = (\psi_{\text{top}}^{(in)} + i\psi_{\text{bottom}}^{(in)})/2$ is scattered into an outgoing Dirac hole $d^{(out)} = (\psi_{\text{top}}^{(out)} - i\psi_{\text{bottom}}^{(out)})/2$ while leaking a charge $2e$ Cooper pair into the superconductor. This process is facilitated, for instance, by an odd number of vortices n_v between the top and bottom paths so that it corresponds to the phase difference $(-1)^{n_v}$ between the two MF $\psi_{\text{top}}, \psi_{\text{bottom}}$. Another origin of phase difference $e^{ik\delta L}$ is from the path difference $\delta L = L_{\text{top}} - L_{\text{bottom}}$ between the top and bottom semi-circular line interfaces, where $k = eV/\hbar v_M$ is the momentum of the MF given a potential V . Combining these together, the differential conductance takes the oscillating form (see Fig. 12.19b)

$$G(V) = \frac{2e^2}{h} |S_{eh}|^2 = \frac{2e^2}{h} \sin^2 \left(\frac{n_v\pi}{2} + \frac{eV\delta L}{2\hbar v_M} \right) \quad (12.102)$$

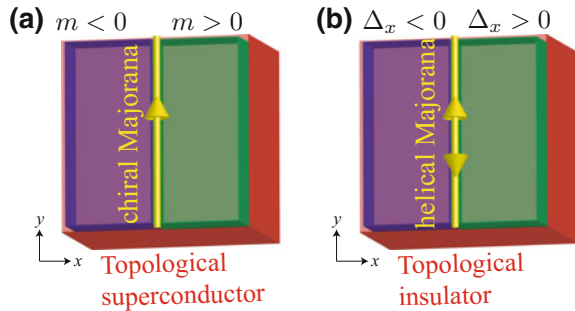
predicted by [52], where $|S_{eh}|^2$ is the scattering probability from an electron to a hole. Similar predictions were also proposed in [55, 56]. For instance, when $V = 0$, $G(0)$ is trivial when n_v is even, or is $2e^2/h$ when n_v is odd (c.f. the zero-bias charge transport in superconducting SOC wire in Sect. 12.2.1).

12.3.2.3 Majorana Channels in Other Heterostructures

We briefly report other types of topological heterostructures that support chiral or helical MF channels along line interfaces. First we start with the class DIII TR symmetric topological superconductor model in three dimensions we discussed before in (12.69). The massless surface MF $\psi = (\psi_{\uparrow}, \psi_{\downarrow})$ is described by the effective low-energy BdG Hamiltonian

$$H_{\text{surface-MF}}(\mathbf{k}_{\parallel}, \mathbf{r}) = \hbar v(k_x\sigma_x + k_y\sigma_z) - m(x)\sigma_y \quad (12.103)$$

Fig. 12.20 **a** Chiral Majorana channel (yellow directed line) between time reversal breaking and conjugate massive domains on the surface of a class DIII topological superconductor. **b** Helical Majorana channel (yellow double directed line) across a π -junction on a topological insulator surface



(c.f. (12.72) and Fig. 12.13), where the TR and PH operators are $\mathcal{T} = i\sigma_y\mathcal{K}$ and $\Xi = \mathcal{K}$, and the mass term $m(x)$ breaks TR. We consider a domain wall on the surface where the mass term $m(x)$ changes sign across a line interface taken along the y -axis, i.e. $\lim_{x \rightarrow \pm\infty} \text{sgn}(m(x)) = \pm 1$ (see Fig. 12.20a).

Replacing $k_x \leftrightarrow -i\partial_x$ and focusing on $k_y = 0$, (12.103) has the identical structure as the Jackiw-Rebbi model in (12.76) [131]. Following similar derivation, (12.103) has the eigenvector wave function solution $\mathbf{u}_0(x, k_y) \propto e^{-\int_0^x m(x')dx'/\hbar v} (1, 0)^T$ which corresponds to the MF $\gamma_0(x, k_y) \propto e^{-\int_0^x m(x')dx'/\hbar v} \psi_\uparrow(x, k_y)$ and has the chiral dispersion $E_0(k_y) = +\hbar v k_y$. This shows that the TR conjugate massive domain wall sandwiches a single chiral Majorana channel along the line interface [33, 148]. We notice in passing that the BdG model (12.103) has the same matrix operator structure as the Bloch Hamiltonian that describes the TR conjugate magnetic domain wall of the Dirac surface state of a TI (Fig. 12.19). In this case, $\mathbf{u}_0(x, k_y)$ represents a chiral Dirac fermion instead.

We have seen earlier in (12.101) that chiral MF channels can arise as vortices of the order parameter $\mathbf{n}(\mathbf{r}) = (m(\mathbf{r}), g\mu_B B(\mathbf{r}) - \Delta_x(\mathbf{r}))$ in the three dimensional model (12.96). Here we explore chiral MF along pairing vortices in superconducting Dirac/Weyl (semi)metals.⁹ The simplest Dirac (semi)metal [149–155] consists of two Weyl fermions $\mathbf{c}_\mu = (c_{\mu,\uparrow}, c_{\mu,\downarrow})$, for $\mu = \pm 1$, with opposite chiralities. They can be described by the low-energy effective Bloch Hamiltonian

$$H_{\text{Dirac-3D}}(\mathbf{k}) = \hbar v \mathbf{k} \cdot \boldsymbol{\sigma} \mu_z \quad (12.104)$$

where $\boldsymbol{\sigma}$ acts on spins and $\mu_z = \pm 1$ labels the two Weyl species. There is already an abundant pool of semimetallic materials, such as TaAs, Cd₃As₂, Na₃Bi that support Dirac/Weyl fermions near Fermi energy [156–168] among many more. There has been theoretical discussions as well as experimental observations of superconductivity in Dirac metals, such as [169, 170]. Here we consider a superconducting Dirac

⁹Here we do not make the distinction between Dirac and Weyl (semi)metals because they both consist of pairs of Weyl fermions with opposite chiralities. We do not pay attention to their spatial symmetry origins and their locations in momentum space.

metal with intra-Weyl-species s -wave pairing [171, 172]. It has the BdG description

$$H_{\text{BdG-Dirac}}(\mathbf{k}, \mathbf{r}) = (\hbar v \mathbf{k} \cdot \boldsymbol{\sigma} \mu_z - \epsilon_f) \tau_z + \Delta_x^s(\mathbf{r}) \tau_x + \Delta_y^s(\mathbf{r}) \tau_y + \Delta_x^a(\mathbf{r}) \mu_z \tau_x + \Delta_y^a(\mathbf{r}) \mu_z \tau_y \quad (12.105)$$

under the Nambu Basis $\xi(\mathbf{k}) = (\mathbf{c}(\mathbf{k}), -i\sigma_y \mathbf{c}^\dagger(-\mathbf{k}))$. The pairing parameters can be grouped into $\Delta^\pm = \Delta_x^\pm + i\Delta_y^\pm = |\Delta^\pm| e^{i\varphi_\pm}$, for $\Delta_{x,y}^\pm = \Delta_{x,y}^s \pm \Delta_{x,y}^a$, so that each one of them acts only on the Weyl fermion species $\mu = \pm$. A pairing vortex of $\Delta^\pm(\mathbf{r})$ is therefore characterized by the two vorticities (ν_+, ν_-) , where $\nu_\pm = \oint d\varphi_\pm / 2\pi$. The net chirality of the vortex, i.e. the difference between the number N_R of forward moving MF and the number N_L of backward moving ones (c.f. (12.52)), is

$$2c = N_R - N_L = \nu_+ - \nu_- \quad (12.106)$$

where c is the chiral central charge that dictates low-temperature thermal transport (12.51). Equation (12.106) is a special case of the index theorem proven by [75–77]. The difference $\nu_+ - \nu_-$ can also be shown to be identical to the second Chern number (12.100) defined by “negative” energy states of the defect Hamiltonian (12.105). The proof of (12.106) will be omitted, but the readers should be able to derive the chiral MF vortex solution themselves using previous techniques. For instance, (12.105) can be block-diagonalized according to Weyl fermion species $\mu_z = \pm 1$. Assuming the vortex is along the z -direction and focusing at $k_z = 0$, the Hamiltonian of each Weyl species sector is simply the Jackiw-Rossi model (c.f. (12.85)).

Lastly, we go back to the superconducting pattern on TI surface in Fig. 12.16 that host MBS at tri-junctions. We indicated earlier that the MBS can move from one tri-junction to a nearby one when the phase difference between two neighboring superconducting islands is tuned to π . We model the π -junction using the BdG surface Hamiltonian (12.85) (see Fig. 12.20b). We restrict to real pairing so that $H_{\text{BdG-surface}}(\mathbf{k}_\parallel) = [\lambda(k_x \sigma_x + k_y \sigma_y) - \epsilon_f] \tau_z + \Delta_x(x) \tau_x$ is TR symmetric (recall $\mathcal{T} = i\sigma_y \mathcal{K}$). We also assume the junction lies along the y -axis and the real pairing Δ_x changes sign across the junction. For simplicity, we consider $\epsilon_f = 0$. The Hamiltonian now commutes with the artificial symmetry $S = \sigma_z \tau_x$ and can be block-diagonalized according to $S = \pm 1$. One can check that each of the 2×2 block has the form of (12.103) and therefore hosts a chiral MF along the line interface. The two $S = \pm$ sectors are however TR conjugate because $\mathcal{T}S = -S\mathcal{T}$. TR symmetry requires the two chiral MF from the $S = \pm$ sectors to propagate in the opposite direction, and form a pair of *helical* MF channels. Similar to the helical Dirac edge modes of a QSHI, helical MF modes are protected by the Kramers’ theorem as $\mathcal{T}^2 = -1$ and are robust against any single-body interactions that preserves the bulk energy gap and TR symmetry. On the other hand, the deviation δ away from real pairing on the superconducting pattern on TI surface in Fig. 12.16 introduces the TR breaking

Δ_y . The MF along the line junction then acquire a TR breaking mass and the zero energy MBS is pushed to either the left or the right of the line junction depending on the sign of δ .

12.4 Summary

In this chapter, we studied Majorana fermions (MF) and zero energy Majorana bound states (MBS) in topological superconductors (TSC) in one, two and three spatial dimensions. The main goal was to understand the conditions for their appearances and their relationships with bulk topologies. The primary focus was on single protected Majorana modes, which required time reversal (TR) symmetry to be broken and in many cases facilitated by magnetism that coexisted with superconductivity to certain extent. The chapter was divided into two parts. Section 12.2 concentrated on homogeneous TSC, while Sect. 12.3 addressed non-uniform superconducting heterostructures. In both situations, protected MF could emerge as defect bound states that localized along low-dimensional structures.

In Sect. 12.2.1, we studied TSC in one dimension. Zero energy MBS were supported and located at the two ends of the 1D superconductor. This was theoretically understood by the Kitaev's p -wave superconducting chain model and was applied to superconducting spin-orbit coupled nanowires. Relevant recent experimental observations and their theoretical principles were reported. In Sect. 12.2.2, we studied TSC in two dimensions. Chiral $p_x + ip_y$ TSC was shown to carry chiral MF edge modes that could only propagate in a single direction. Pairing vortices were shown to host zero energy MBS. TR symmetric versions of TSC were briefly introduced at the end.

In Sect. 12.3.1, we studied MBS at point junctions in heterostructures. This included (i) the interface sandwiched between a superconducting segment and a (anti)ferromagnetic segment along the helical edge of a 2D quantum spin Hall insulator, and (ii) the superconducting vortex on the surface of a topological insulator. In Sect. 12.3.2, we studied 1D MF along line junctions in heterostructures. We showed chiral MF could run along line interfaces where materials with different topologies and orders meet in three dimensions. Possible consequences in transport were reviewed.

Contemporary research in Majorana physics is primarily fueled by its promising prospect in topological quantum computing. This relies on the non-Abelian nature of Majorana zero modes that allows non-local quantum information storage and non-commuting unitary quantum operations. Regretfully, these interesting topics are out of the scope of this chapter and this book, but hopefully, for the readers who have not been exposed to these ideas, they will still be convinced that Majorana is compellingly remarkable.

Acknowledgements I am in debt to Prof. Charlie Kane, who was my Ph.D advisor and introduced the concepts of Majorana and topological insulators and superconductors to me during my graduate years. In addition, I also thank all my research collaborators, in particular Ching-Kai Chiu, Eduardo

Fradkin, Liang Fu, Taylor Hughes, and Shinsei Ryu, who not only made significant contributions to the advancement in Majorana physics but also had valuable impact on my academic development. Last but not least, I am grateful to all my students, especially Syed Raza, who went through the manuscript and provided helpful feedback. This chapter is supported by the National Science Foundation under Grant No. DMR 1653535.

References

1. J. Alicea, *Rep. Prog. Phys.* **75**, 076501 (2012). <https://doi.org/10.1088/0034-4885/75/7/076501>
2. C.W.J. Beenakker, *Annu. Rev. Condens. Matter Phys.* **4**, 113 (2013). <https://doi.org/10.1146/annurev-conmatphys-030212-184337>
3. C.-K. Chiu, J.C.Y. Teo, A.P. Schnyder, S. Ryu, *Rev. Mod. Phys.* **88**, 035005 (2016). <https://doi.org/10.1103/RevModPhys.88.035005>
4. S. Das Sarma, M. Freedman, C. Nayak, *Npj Quantum Inf.* **1**, 15001 (2015). <https://doi.org/10.1038/npjqi.2015.1>
5. S.R. Elliott, M. Franz, *Rev. Mod. Phys.* **87**, 137 (2015). <https://doi.org/10.1103/RevModPhys.87.137>
6. M.Z. Hasan, C.L. Kane, *Rev. Mod. Phys.* **82**, 3045 (2010). <https://doi.org/10.1103/RevModPhys.82.3045>
7. M. Leijnse, K. Flensberg, *Semicond. Sci. Technol.* **27**(12), 124003 (2012). <https://doi.org/10.1088/0268-1242/27/12/124003>
8. X.-L. Qi, S.-C. Zhang, *Rev. Mod. Phys.* **83**, 1057 (2011). <https://doi.org/10.1103/RevModPhys.83.1057>
9. T.D. Stanescu, S. Tewari, *J. Phys. Condens. Matter* **25**, 233201 (2013), <http://stacks.iop.org/0953-8984/25/i=23/a=233201>
10. E. Schrödinger, *Phys. Rev.* **28**, 1049 (1926). <https://doi.org/10.1103/PhysRev.28.1049>
11. A. Einstein, *Ann. der Phys.* **322**(10), 891 (1905). <https://doi.org/10.1002/andp.19053221004>
12. P.A.M. Dirac, *Proc. R. Soc. Lond. A: Math. Phys. Eng. Sci.* **117**(778), 610 (1928). <https://doi.org/10.1098/rspa.1928.0023>
13. E. Majorana, *Il Nuovo Cimento* (1924–1942) **14**(4), 171 (1937). <https://doi.org/10.1007/BF02961314>
14. A. Kitaev, *AIP Conf. Proc.* **1134**, 22 (2008). <https://doi.org/10.1063/1.3149495>
15. X.-L. Qi, T.L. Hughes, S. Raghu, S.-C. Zhang, *Phys. Rev. Lett.* **102**, 187001 (2009). <https://doi.org/10.1103/PhysRevLett.102.187001>
16. A.P. Schnyder, S. Ryu, A. Furusaki, A.W.W. Ludwig, *Phys. Rev. B* **78**, 195125 (2008). <https://doi.org/10.1103/PhysRevB.78.195125>
17. A.Y. Kitaev, *Phys.-Usp.* **44**, 131 (2001). <https://doi.org/10.1070/1063-7869/44/10S/S29>
18. A. Cook, M. Franz, *Phys. Rev. B* **84**, 201105 (2011). <https://doi.org/10.1103/PhysRevB.84.201105>
19. R.M. Lutchyn, J.D. Sau, S. Das Sarma, *Phys. Rev. Lett.* **105**, 077001 (2010). <https://doi.org/10.1103/PhysRevLett.105.077001>
20. S. Nadj-Perge, I.K. Drozdov, J. Li, H. Chen, S. Jeon, J. Seo, A.H. MacDonald, B.A. Bernevig, A. Yazdani, *Science* **346**, 602 (2014). <https://doi.org/10.1126/science.1259327>
21. Y. Oreg, G. Refael, F. von Oppen, *Phys. Rev. Lett.* **105**, 177002 (2010). <https://doi.org/10.1103/PhysRevLett.105.177002>
22. V. Gurarie, L. Radzihovsky, *Phys. Rev. B* **75**, 212509 (2007b). <https://doi.org/10.1103/PhysRevB.75.212509>
23. D.A. Ivanov, *Phys. Rev. Lett.* **86**, 268 (2001). <https://doi.org/10.1103/PhysRevLett.86.268>
24. A. Kitaev, *Ann. Phys.* **321**(1), 2 (2006). <https://doi.org/10.1016/j.aop.2005.10.005>

25. N. Read, D. Green, Phys. Rev. B **61**, 10267 (2000). <https://doi.org/10.1103/PhysRevB.61.10267>
26. G.E. Volovik, Pisma Zh. Eksp. Teor. Fiz. **70**, 601 (1999). <https://doi.org/10.1134/1.568223>
27. G.E. Volovik, *The Universe in a Helium Droplet* (Oxford University Press, 2003)
28. C.-K. Chiu, M.J. Gilbert, T.L. Hughes, Phys. Rev. B **84**(14), 144507 (2011). <https://doi.org/10.1103/PhysRevB.84.144507>
29. L. Fu, C.L. Kane, Phys. Rev. Lett. **100**, 096407 (2008). <https://doi.org/10.1103/PhysRevLett.100.096407>
30. L. Fu, C.L. Kane, Phys. Rev. B **79**, 161408(R) (2009a). <https://doi.org/10.1103/PhysRevB.79.161408>
31. P. Hosur, P. Ghaemi, R.S.K. Mong, A. Vishwanath, Phys. Rev. Lett. **107**(9), 097001 (2011). <https://doi.org/10.1103/PhysRevLett.107.097001>
32. J.C.Y. Teo, C.L. Kane, Phys. Rev. Lett. **104**, 046401 (2010a). <https://doi.org/10.1103/PhysRevLett.104.046401>
33. J.C.Y. Teo, C.L. Kane, Phys. Rev. B **82**, 115120 (2010b). <https://doi.org/10.1103/PhysRevB.82.115120>
34. J.-P. Xu, C. Liu, M.-X. Wang, J. Ge, Z.-L. Liu, X. Yang, Y. Chen, Y. Liu, Z.-A. Xu, C.-L. Gao, D. Qian, F.-C. Zhang, J.-F. Jia, Phys. Rev. Lett. **112**, 217001 (2014). <https://doi.org/10.1103/PhysRevLett.112.217001>
35. P.G. De Gennes, *Superconductivity Of Metals And Alloys* (Westview Press, 1999)
36. A.J. Leggett, *Quantum Liquids: Bose Condensation and Cooper Pairing in Condensed-Matter Systems* (Oxford University Press, 2006)
37. A. Altland, M.R. Zirnbauer, Phys. Rev. B **55**, 1142 (1997). <https://doi.org/10.1103/PhysRevB.55.1142>
38. F. Wilczek, Nat. Phys. **5**, 614 (2009). <https://doi.org/10.1038/nphys1380>
39. M. Freedman, A. Kitaev, M. Larsen, Z. Wang, Bull. Am. Math. Soc. **40**, 31 (2002). <https://doi.org/10.1090/S0273-0979-02-00964-3>
40. A. Kitaev, Ann. Phys. **303**, 2 (2003). [https://doi.org/10.1016/S0003-4916\(02\)00018-0](https://doi.org/10.1016/S0003-4916(02)00018-0)
41. C. Nayak, S.H. Simon, A. Stern, M. Freedman, S. Das Sarma, Rev. Mod. Phys. **80**, 1083 (2008). <https://doi.org/10.1103/RevModPhys.80.1083>
42. J. Preskill, *Topological Quantum Computation*, <http://www.theory.caltech.edu/~preskill/ph219/topological.pdf> (2004)
43. R. Walter Ogburn, J. Preskill, Topological quantum computation, in *Quantum Computing and Quantum Communications: First NASA International Conference, QCQC'98 Palm Springs, California, USA February 17–20, 1998 Selected Papers*, ed. by C.P. Williams (Springer, Berlin, Heidelberg, 1999), pp. 341–356. https://doi.org/10.1007/3-540-49208-9_31
44. Z. Wang, *Topological Quantum Computation* (American Mathematics Society, 2010)
45. W.P. Su, J.R. Schrieffer, A.J. Heeger, Phys. Rev. B **22**, 2099 (1980). <https://doi.org/10.1103/PhysRevB.22.2099>
46. C.L. Kane, E.J. Mele, Phys. Rev. Lett. **95**, 226801 (2005a). <https://doi.org/10.1103/PhysRevLett.95.226801>
47. C.L. Kane, E.J. Mele, Phys. Rev. Lett. **95**, 146802 (2005b). <https://doi.org/10.1103/PhysRevLett.95.146802>
48. I. Knez, C.T. Rettner, S.-H. Yang, S.S.P. Parkin, L. Du, R.-R. Du, G. Sullivan, Phys. Rev. Lett. **112**, 026602 (2014). <https://doi.org/10.1103/PhysRevLett.112.026602>
49. M. König, S. Wiedmann, C. Brüne, A. Roth, H. Buhmann, L. Molenkamp, X.-L. Qi, S. Zhang, Science **318**, 766 (2007). <https://doi.org/10.1126/science.1148047>
50. C. Liu, T.L. Hughes, X.-L. Qi, K. Wang, S.-C. Zhang, Phys. Rev. Lett. **100**, 236601 (2008). <https://doi.org/10.1103/PhysRevLett.100.236601>
51. V. Mourik, K. Zuo, S. Frolov, S. Plissard, E. Bakkers, L. Kouwenhoven, Science **336**, 1003 (2012). <https://doi.org/10.1126/science.1222360>
52. A.R. Akhmerov, J. Nilsson, C.W.J. Beenakker, Phys. Rev. Lett. **102**, (2009). <https://doi.org/10.1103/PhysRevLett.102.216404>

53. A. Das, Y. Ronen, Y. Most, Y. Oreg, M. Heiblum, H. Shtrikman, *Nat. Phys.* **8**, 887 (2012). <https://doi.org/10.1038/nphys2479>
54. M.T. Deng, C.L. Yu, G.Y. Huang, M. Larsson, P. Caroff, H.Q. Xu, *Nano Lett.* **12**, 6414 (2012). <https://doi.org/10.1021/nl303758w>
55. L. Fu, C.L. Kane, *Phys. Rev. Lett.* **102**, 216403 (2009b). <https://doi.org/10.1103/PhysRevLett.102.216403>
56. K.T. Law, P.A. Lee, T.K. Ng, *Phys. Rev. Lett.* **103**, 237001 (2009). <https://doi.org/10.1103/PhysRevLett.103.237001>
57. L.P. Rokhinson, X. Liu, J. K. Furdyna, *Nat. Phys.* **8**, 795 (2012). <https://doi.org/10.1038/nphys2429>
58. H. Zhang, C.-X. Liu, S. Gazibegovic, D. Xu, J.A. Logan, G. Wang, N. van Loo, J.D.S. Bommer, M.W.A. de Moor, D. Car, R.L.M.O. het Veld, P.J. van Veldhoven, S. Koelling, M.A. Verheijen, M. Pendharkar, D.J. Pennachio, B. Shojaei, J.S. Lee, C.J. Palmstrom, E.P.A.M. Bakkers, S. Das Sarma, L.P. Kouwenhoven, *Nature* **556**, 74 (2018). <https://doi.org/10.1038/nature26142>
59. L. Fu, *Phys. Rev. Lett.* **104**, 056402 (2010). <https://doi.org/10.1103/PhysRevLett.104.056402>
60. B. van Heck, R.M. Lutchyn, L.I. Glazman, *Phys. Rev. B* **93**, 235431 (2016). <https://doi.org/10.1103/PhysRevB.93.235431>
61. R. Hützen, A. Zazunov, B. Braunecker, A.L. Yeyati, R. Egger, *Phys. Rev. Lett.* **109**, 166403 (2012). <https://doi.org/10.1103/PhysRevLett.109.166403>
62. J.D. Sau, B. Swingle, S. Tewari, *Phys. Rev. B* **92**, 020511 (2015). <https://doi.org/10.1103/PhysRevB.92.020511>
63. S.M. Albrecht, A.P. Higginbotham, M. Madsen, F. Kuemmeth, T.S. Jespersen, J. Nygård, P. Krogstrup, C.M. Marcus, *Nature* **531**, 206 (2016). <https://doi.org/10.1038/nature17162>
64. G.E. Volovik, *JETP Lett.* **55**, 368 (1992), http://www.jetpletters.ac.ru/ps/1273/article_19263.shtml
65. A. Cappelli, M. Huerta, G.R. Zemba, *Nucl. Phys. B* **636**(3), 568 (2002). [https://doi.org/10.1016/S0550-3213\(02\)00340-1](https://doi.org/10.1016/S0550-3213(02)00340-1)
66. C.L. Kane, M.P.A. Fisher, *Phys. Rev. B* **55**, 15832 (1997). <https://doi.org/10.1103/PhysRevB.55.15832>
67. V. Gurarie, L. Radzihovsky, *Ann. Phys.* **322**(1), 2 (2007). <https://doi.org/10.1016/j.aop.2006.10.009>
68. M. Sigrist, K. Ueda, *Rev. Mod. Phys.* **63**, 239 (1991). <https://doi.org/10.1103/RevModPhys.63.239>
69. D.I. Uzunov, Theory of ferromagnetic unconventional superconductors with spin-triplet electron pairing, in *Superconductors—Materials, Properties and Applications*, ed. by A. Gabovich, Chapter 17 (InTech, 2003), pp. 415–440. <https://doi.org/10.5772/48579>
70. M. Atiyah, *K-Theory* (Westview Press, 1994)
71. H.B. Lawson, M.-L. Michelsohn, *Spin Geometry* (Princeton University Press, 1990)
72. M. Nakahara, *Geometry, Topology and Physics*, 2nd edn. Graduate Student Series in Physics (Taylor & Francis, 2003), <http://www.amazon.ca/exec/obidos/redirect?tag=citeulike09-20&path=ASIN/0750306068>
73. J.D. Jackson, *Classical Electrodynamics* 3rd edn. (Wiley, New York, 1999)
74. P. Di Francesco, P. Mathieu, D. Senechal, *Conformal Field Theory* (Springer, New York, 1999)
75. M.F. Atiyah, V.K. Patodi, I.M. Singer, *Math. Proc. Camb. Philos. Soc.* **77**(1), 43 (1975a). <https://doi.org/10.1017/S0305004100049410>
76. M.F. Atiyah, V.K. Patodi, I.M. Singer, *Math. Proc. Camb. Philos. Soc.* **78**(3), 405 (1975b). <https://doi.org/10.1017/S0305004100051872>
77. M.F. Atiyah, V.K. Patodi, I.M. Singer, *Math. Proc. Camb. Philos. Soc.* **79**(1), 71 (1976). <https://doi.org/10.1017/S0305004100052105>
78. B.I. Halperin, *Phys. Rev. B* **25**, 2185 (1982). <https://doi.org/10.1103/PhysRevB.25.2185>
79. Y. Hatsugai, *Phys. Rev. Lett.* **71**, 3697 (1993). <https://doi.org/10.1103/PhysRevLett.71.3697>
80. R.B. Laughlin, *Phys. Rev. B* **23**, 5632 (1981). <https://doi.org/10.1103/PhysRevB.23.5632>

81. H. Schulz-Baldes, J. Kellendonk, T. Richter, J. Phys. A: Math. Gen. **33**(2), L27 (2000), <http://stacks.iop.org/0305-4470/33/i=2/a=102>
82. D.J. Thouless, M. Kohmoto, M.P. Nightingale, M. den Nijs, Phys. Rev. Lett. **49**, 405 (1982). <https://doi.org/10.1103/PhysRevLett.49.405>
83. J. Bellissard, A. van Elst, H. Schulz-Baldes, J. Math. Phys. **35**(10), 5373 (1994). <https://doi.org/10.1063/1.530758>
84. T.A. Loring, M.B. Hastings, EPL (Europhysics Lett.) **92**(6), 67004 (2010), <http://stacks.iop.org/0295-5075/92/i=6/a=67004>
85. E. Prodan, H. Schulz-Baldes, J. Funct. Anal. **271**(5), 1150 (2016). <https://doi.org/10.1016/j.jfa.2016.06.001>
86. P.W. Anderson, P. Morel, Phys. Rev. **123**, 1911 (1961). <https://doi.org/10.1103/PhysRev.123.1911>
87. A.J. Leggett, Rev. Mod. Phys. **47**, 331 (1975). <https://doi.org/10.1103/RevModPhys.47.331>
88. G.E. Volovik, JETP Lett. **93**(2), 66 (2011). <https://doi.org/10.1134/S0021364011020147>
89. G.M. Luke, Y. Fudamoto, K.M. Kojima, M.I. Larkin, J. Merrin, B. Nachumi, Y.J. Uemura, Y. Maeno, Z.Q. Mao, Y. Mori, H. Nakamura, M. Sigrist, Nature **394**, 558 (1998). <https://doi.org/10.1038/29038>
90. K.D. Nelson, Z.Q. Mao, Y. Maeno, Y. Liu, Science **306**(5699), 1151 (2004). <https://doi.org/10.1126/science.1103881>
91. T.M. Rice, M. Sigrist, J. Phys.: Condens. Matter **7**, L643 (1995). <https://doi.org/10.1088/0953-8984/7/47/002>
92. J. Xia, Y. Maeno, P.T. Beyersdorf, M.M. Fejer, A. Kapitulnik, Phys. Rev. Lett. **97**, 167002 (2006). <https://doi.org/10.1103/PhysRevLett.97.167002>
93. J.R. Kirtley, C. Kallin, C.W. Hicks, E.-A. Kim, Y. Liu, K.A. Moler, Y. Maeno, K.D. Nelson, Phys. Rev. B **76**, 014526 (2007). <https://doi.org/10.1103/PhysRevB.76.014526>
94. Y. Maeno, T.M. Rice, M. Sigrist, Phys. Today **54**, 42 (2001). <https://doi.org/10.1063/1.1349611>
95. S. Raghu, A. Kapitulnik, S.A. Kivelson, Phys. Rev. Lett. **105**, 136401 (2010). <https://doi.org/10.1103/PhysRevLett.105.136401>
96. F.D.M. Haldane, Phys. Rev. Lett. **61**, 2015 (1988). <https://doi.org/10.1103/PhysRevLett.61.2015>
97. C.-X. Liu, S.-C. Zhang, X.-L. Qi, Annu. Rev. Condens. Matter Phys. **7**, 301 (2016). <https://doi.org/10.1146/annurev-conmatphys-031115-011417>
98. Q.L. He, L. Pan, A.L. Stern, E.C. Burks, X. Che, G. Yin, J. Wang, B. Lian, Q. Zhou, E.S. Choi, K. Murata, X. Kou, Z. Chen, T. Nie, Q. Shao, Y. Fan, S.-C. Zhang, K. Liu, J. Xia, K.L. Wang, Science **357**(6348), 294 (2017). <https://doi.org/10.1126/science.aag2792>
99. A. Iii, K. Yada, M. Sato, Y. Tanaka, Phys. Rev. B **83**, 224524 (2011). <https://doi.org/10.1103/PhysRevB.83.224524>
100. X.-L. Qi, T.L. Hughes, S.-C. Zhang, Phys. Rev. B **82**, 184516 (2010). <https://doi.org/10.1103/PhysRevB.82.184516>
101. J. Wang, Q. Zhou, B. Lian, S.-C. Zhang, Phys. Rev. B **92**, 064520 (2015). <https://doi.org/10.1103/PhysRevB.92.064520>
102. M. Stone, R. Roy, Phys. Rev. B **69**, 184511 (2004). <https://doi.org/10.1103/PhysRevB.69.184511>
103. C. Caroli, P.G. de Gennes, J. Matricon, Phys. Lett. **9**, 307 (1964). [https://doi.org/10.1016/0031-9163\(64\)90375-0](https://doi.org/10.1016/0031-9163(64)90375-0)
104. J.J. Sakurai, *Modern Quantum Mechanics*, 2nd edn. (Addison Wesley, 1994), <http://www.amazon.com/exec/obidos/redirect?tag=citeulike07-20&path=ASIN/0201539292>
105. M.E. Cage, K. Klitzing, A. Chang, F. Duncan, M. Haldane, R. Laughlin, A. Pruisken, D. Thouless, R.E. Prange, S.M. Girvin, *The Quantum Hall Effect* (Springer Science & Business Media, Berlin, 2012)
106. E. Fradkin, *Field Theories of Condensed Matter Physics*, 2nd edn. (Cambridge University Press, 2013)

107. N. Read, G. Moore, Nucl. Phys. B **360**, 362 (1991). [https://doi.org/10.1016/0550-3213\(91\)90407-O](https://doi.org/10.1016/0550-3213(91)90407-O)
108. P.M. Chaikin, T.C. Lubensky, *Principles of Condensed Matter Physics* (Cambridge University Press, 2000)
109. D.R. Nelson, *Defects and Geometry in Condensed Matter Physics* (Cambridge University Press, 2002)
110. D. Asahi, N. Nagaosa, Phys. Rev. B **86**, 100504(R) (2012). <https://doi.org/10.1103/PhysRevB.86.100504>
111. T.L. Hughes, H. Yao, X.-L. Qi, Phys. Rev. B **90**, 235123 (2014). <https://doi.org/10.1103/PhysRevB.90.235123>
112. Ran, Y. (2010), arXiv:1006.5454 [cond-mat.str-el]
113. J.C. Teo, T.L. Hughes, Annu. Rev. Condens. Matter Phys. **8**(1), 211 (2017). <https://doi.org/10.1146/annurev-conmatphys-031016-025154>
114. W.A. Benalcazar, J.C.Y. Teo, T.L. Hughes, Phys. Rev. B **89**, 224503 (2014). <https://doi.org/10.1103/PhysRevB.89.224503>
115. J.C.Y. Teo, T.L. Hughes, Phys. Rev. Lett. **111**, 047006 (2013). <https://doi.org/10.1103/PhysRevLett.111.047006>
116. S.B. Chung, H. Bluhm, E.-A. Kim, Phys. Rev. Lett. **99**, 197002 (2007). <https://doi.org/10.1103/PhysRevLett.99.197002>
117. S. Das Sarma, C. Nayak, S. Tewari, Phys. Rev. B **73**, 220502 (2006). <https://doi.org/10.1103/PhysRevB.73.220502>
118. J. Jang, D.G. Ferguson, V. Vakaryuk, R. Budakian, S.B. Chung, P.M. Goldbart, Y. Maeno, Science **331**(6014), 186 (2011). <https://doi.org/10.1126/science.1193839>
119. M.M. Salomaa, G.E. Volovik, Phys. Rev. Lett. **55**, 1184 (1985). <https://doi.org/10.1103/PhysRevLett.55.1184>
120. S.B. Chung, S.-C. Zhang, Phys. Rev. Lett. **103**, 235301 (2009). <https://doi.org/10.1103/PhysRevLett.103.235301>
121. S. Murakawa, Y. Tamura, Y. Wada, M. Wasai, M. Saitoh, Y. Aoki, R. Nomura, Y. Okuda, Y. Nagato, M. Yamamoto, S. Higashitani, K. Nagai, Phys. Rev. Lett. **103**, 155301 (2009). <https://doi.org/10.1103/PhysRevLett.103.155301>
122. S. Murakawa, Y. Wada, Y. Tamura, M. Wasai, M. Saitoh, Y. Aoki, R. Nomura, Y. Okuda, Y. Nagato, M. Yamamoto, S. Higashitani, K. Nagai, J. Phys. Soc. Jpn. **80**, 013602 (2011). <https://doi.org/10.1143/JPSJ.80.013602>
123. S. Ryu, A.P. Schnyder, A. Furusaki, A.W.W. Ludwig, New J. Phys **12**, 065010 (2010), <http://stacks.iop.org/1367-2630/12/i=6/a=065010>
124. Y. Wada, S. Murakawa, Y. Tamura, M. Saitoh, Y. Aoki, R. Nomura, Y. Okuda, Phys. Rev. B **78**, 214516 (2008). <https://doi.org/10.1103/PhysRevB.78.214516>
125. L. Fu, E. Berg, Phys. Rev. Lett. **105**, 097001 (2010). <https://doi.org/10.1103/PhysRevLett.105.097001>
126. Y.S. Hor, A.J. Williams, J.G. Checkelsky, P. Roushan, J. Seo, Q. Xu, H.W. Zandbergen, A. Yazdani, N.P. Ong, R.J. Cava, Phys. Rev. Lett. **104**, 057001 (2010). <https://doi.org/10.1103/PhysRevLett.104.057001>
127. S. Sasaki, M. Kriener, K. Segawa, K. Yada, Y. Tanaka, M. Sato, Y. Ando, Phys. Rev. Lett. **107**, 217001 (2011). <https://doi.org/10.1103/PhysRevLett.107.217001>
128. L.A. Wray, S.-Y. Xu, Y. Xia, Y.S. Hor, D. Qian, A.V. Fedorov, H. Lin, A. Bansil, R.J. Cava, M.Z. Hasan, Nat. Phys. **6**, 855 (2010). <https://doi.org/10.1038/nphys1762>
129. B.A. Bernevig, T.L. Hughes, S.-C. Zhang, Science **314**(5806), 1757 (2006). <https://doi.org/10.1126/science.1133734>
130. J. Nilsson, A.R. Akhmerov, C.W.J. Beenakker, Phys. Rev. Lett. **101**, 120403 (2008). <https://doi.org/10.1103/PhysRevLett.101.120403>
131. R. Jackiw, C. Rebbi, Phys. Rev. D **13**, 3398 (1976). <https://doi.org/10.1103/PhysRevD.13.3398>
132. J.C. Gallop, *SQUIDs, the Josephson Effects and Superconducting Electronics* (CRC Press, 1991)

133. D.J. Thouless, Phys. Rev. B **27**, 6083 (1983). <https://doi.org/10.1103/PhysRevB.27.6083>
134. L. Fu, C.L. Kane, E.J. Mele, Phys. Rev. Lett. **98**, 106803 (2007). <https://doi.org/10.1103/PhysRevLett.98.106803>
135. D. Hsieh, D. Qian, L. Wray, Y. Xia, Y.S. Hor, R.J. Cava, M.Z. Hasan, Nature **452**, 970 (2008). <https://doi.org/10.1038/nature06843>
136. J.E. Moore, L. Balents, Phys. Rev. B **75**, 121306(R) (2007). <https://doi.org/10.1103/PhysRevB.75.121306>
137. X.-L. Qi, T.L. Hughes, S.-C. Zhang, Phys. Rev. B **78**, 195424 (2008). <https://doi.org/10.1103/PhysRevB.78.195424>
138. R. Roy, Phys. Rev. B **79**, 195322 (2009). <https://doi.org/10.1103/PhysRevB.79.195322>
139. Y. Xia, D. Qian, D. Hsieh, L. Wray, A. Pal, H. Lin, A. Bansil, D. Grauer, Y.S. Hor, R.J. Cava, M.Z. Hasan, Nat. Phys. **5**, 398 (2009). <https://doi.org/10.1038/nphys1274>
140. R. Jackiw, P. Rossi, Nucl. Phys. B **190**, 681 (1981). [https://doi.org/10.1016/0550-3213\(81\)90044-4](https://doi.org/10.1016/0550-3213(81)90044-4)
141. M.F. Atiyah, G.B. Segal, Ann. Math. **87**, 531 (1968). <https://doi.org/10.2307/1970716>
142. M.F. Atiyah, I.M. Singer, Bull. Am. Math. Soc. **69**, 422 (1963), <http://www.ams.org/journals/bull/1963-69-03/S0002-9904-1963-10957-X/home.html>
143. M.F. Atiyah, I.M. Singer, Ann. Math. **87**, 484 (1968a). <https://doi.org/10.2307/1970715>
144. M.F. Atiyah, I.M. Singer, Ann. Math. **87**, 546 (1968b). <https://doi.org/10.2307/1970717>
145. M.F. Atiyah, I.M. Singer, Ann. Math. **93**, 119 (1971a). <https://doi.org/10.2307/1970756>
146. M.F. Atiyah, I.M. Singer, Ann. Math. **93**, 139 (1971b). <https://doi.org/10.2307/1970757>
147. M. Freedman, M.B. Hastings, C. Nayak, X.-L. Qi, K. Walker, Z. Wang, Phys. Rev. B **83**, 115132 (2011). <https://doi.org/10.1103/PhysRevB.83.115132>
148. X.-L. Qi, E. Witten, S.-C. Zhang, Phys. Rev. B **87**, 134519 (2013). <https://doi.org/10.1103/PhysRevB.87.134519>
149. A.A. Burkov, L. Balents, Phys. Rev. Lett. **107**, 127205 (2011). <https://doi.org/10.1103/PhysRevLett.107.127205>
150. A.A. Burkov, M.D. Hook, L. Balents, Phys. Rev. B **84**, 235126 (2011). <https://doi.org/10.1103/PhysRevB.84.235126>
151. S. Murakami, New J. Phys. **9**, 356 (2007). <https://doi.org/10.1088/1367-2630/9/9/356>
152. O. Vafek, A. Vishwanath, Annu. Rev. Condens. Matter Phys. **5**(1), 83 (2014). <https://doi.org/10.1146/annurev-conmatphys-031113-133841>
153. X. Wan, A.M. Turner, A. Vishwanath, S.Y. Savrasov, Phys. Rev. B **83**, 205101 (2011). <https://doi.org/10.1103/PhysRevB.83.205101>
154. Z. Wang, Y. Sun, X.-Q. Chen, C. Franchini, G. Xu, H. Weng, X. Dai, Z. Fang, Phys. Rev. B **85**, 195320 (2012). <https://doi.org/10.1103/PhysRevB.85.195320>
155. S.M. Young, S. Zaheer, J.C.Y. Teo, C.L. Kane, E.J. Mele, A.M. Rappe, Phys. Rev. Lett. **108**, 140405 (2012). <https://doi.org/10.1103/PhysRevLett.108.140405>
156. S. Borisenko, Q. Gibson, D. Evtushinsky, V. Zabolotnyy, B. Büchner, R.J. Cava, Phys. Rev. Lett. **113**, 027603 (2014). <https://doi.org/10.1103/PhysRevLett.113.027603>
157. X. Huang, L. Zhao, Y. Long, P. Wang, D. Chen, Z. Yang, H. Liang, M. Xue, H. Weng, Z. Fang, X. Dai, G. Chen, Phys. Rev. X **5**, 031023 (2015). <https://doi.org/10.1103/PhysRevX.5.031023>
158. S. Jeon, B.B. Zhou, A. Gyenis, B.E. Feldman, I. Kimchi, A.C. Potter, Q.D. Gibson, R.J. Cava, A. Vishwanath, A. Yazdani, Nat. Mater. **13**, 851 (2014). <https://doi.org/10.1038/nmat4023>
159. T. Liang, Q. Gibson, M.N. Ali, M. Liu, R.J. Cava, N.P. Ong, Nat. Mater. **14**(3), 280 (2015). <https://doi.org/10.1038/nmat4143>
160. Z.K. Liu, J. Jiang, B. Zhou, Z.J. Wang, Y. Zhang, H.M. Weng, D. Prabhakaran, S.-K. Mo, H. Peng, P. Dudin, T. Kim, M. Hoesch, Z. Fang, X. Dai, Z.X. Shen, D.L. Feng, Z. Hussain, Y.L. Chen, Nat. Mater. **13**, 677 (2014a). <https://doi.org/10.1038/nmat3990>
161. Z.K. Liu, B. Zhou, Y. Zhang, Z.J. Wang, H.M. Weng, D. Prabhakaran, S.-K. Mo, Z.X. Shen, Z. Fang, X. Dai, Z. Hussain, Y.L. Chen, Science **343**(6173), 864 (2014b). <https://doi.org/10.1126/science.1245085>

162. B.Q. Lv, H.M. Weng, B.B. Fu, X.P. Wang, H. Miao, J. Ma, P. Richard, X.C. Huang, L.X. Zhao, G.F. Chen, Z. Fang, X. Dai, T. Qian, H. Ding, *Phys. Rev. X* **5**, 031013 (2015a). <https://doi.org/10.1103/PhysRevX.5.031013>
163. B.Q. Lv, N. Xu, H.M. Weng, J.Z. Ma, P. Richard, X.C. Huang, L.X. Zhao, G.F. Chen, C.E. Matt, F. Bisti, V.N. Strocov, J. Mesot, Z. Fang, X. Dai, T. Qian, M. Shi, H. Ding, *Nat. Phys.* **11**(9), 724 (2015b). <https://doi.org/10.1038/nphys3426>
164. M. Neupane, S.-Y. Xu, R. Sankar, N. Alidoust, G. Bian, C. Liu, I. Belopolski, T.-R. Chang, H.-T. Jeng, H. Lin, A. Bansil, F. Chou, M.Z. Hasan, *Nat. Commun.* **5**, 3786 (2014). <https://doi.org/10.1038/ncomms4786>
165. Z. Wang, H. Weng, Q. Wu, X. Dai, Z. Fang, *Phys. Rev. B* **88**, 125427 (2013). <https://doi.org/10.1103/PhysRevB.88.125427>
166. S.-Y. Xu, I. Belopolski, N. Alidoust, M. Neupane, G. Bian, C. Zhang, R. Sankar, G. Chang, Z. Yuan, C.-C. Lee, S.-M. Huang, H. Zheng, J. Ma, D.S. Sanchez, B. Wang, A. Bansil, F. Chou, P.P. Shibayev, H. Lin, S. Jia, M.Z. Hasan, *Science* **349**(6248), 613 (2015a). <https://doi.org/10.1126/science.aaa9297>
167. S.-Y. Xu, C. Liu, S.K. Kushwaha, R. Sankar, J.W. Krizan, I. Belopolski, M. Neupane, G. Bian, N. Alidoust, T.-R. Chang, H.-T. Jeng, C.-Y. Huang, W.-F. Tsai, H. Lin, P.P. Shibayev, F.-C. Chou, R.J. Cava, M.Z. Hasan, *Science* **347**(6219), 294 (2015b). <https://doi.org/10.1126/science.1256742>
168. C. Zhang, S.-Y. Xu, I. Belopolski, Z. Yuan, Z. Lin, B. Tong, N. Alidoust, C.-C. Lee, S.-M. Huang, H. Lin, M. Neupane, D.S. Sanchez, H. Zheng, G. Bian, J. Wang, C. Zhang, T. Neupert, M. Zahid Hasan, S. Jia, *Nat. Commun.* **7**, 10735 (2016). <https://doi.org/10.1038/ncomms10735>
169. L. Aggarwal, A. Gaurav, G.S. Thakur, Z. Haque, A.K. Ganguli, G. Sheet, *Nat. Mater.* **15**, 32 (2016). <https://doi.org/10.1038/nmat4455>
170. S. Kobayashi, M. Sato, *Phys. Rev. Lett.* **115**, 187001 (2015). <https://doi.org/10.1103/PhysRevLett.115.187001>
171. P.L.e.S. Lopes, J.C.Y. Teo, S. Ryu, *Phys. Rev. B* **95**, 235134 (2017). <https://doi.org/10.1103/PhysRevB.95.235134>
172. M.-J. Park, J.C.Y. Teo, M.J. Gilbert, To appear soon (2017)

Index

A

- Ab initio calculations, 203
- AC spin pumping, 220
- Angle dependent magnetoresistance, 228
- Anisotropic magnetoresistance, 268, 269, 286, 287
- Annihilation, 86
- Anomalous Hall effect, 177–179, 181, 188, 189, 192, 201, 202, 204, 267, 269, 270, 272, 275, 288
- Anomalous quantum Hall effect, 247
- Anomalous velocity, 178
- Antiferromagnet, 267, 268, 272, 275, 280, 282, 288
- Antivortex, 75–83, 94, 110
- Antivortices, 78
- Artificial structures, 133
- Atiyah-Singer index theorem, 396
- Auto-oscillation, 336, 338, 339, 341, 351

B

- Backward volume mode, 303
- Band structure, 107, 110
- Bandwidths, 110
- BCS superconductor, 360, 366, 374, 387
- Berry curvature, 245, 248–251, 253, 257, 259
- Berry phase and Berry curvature, 177–185, 188–192, 197, 198, 200–202
- Bloch point (hedgehog), 2, 5, 37
- Bloch points, 155, 160, 161
- Bloch wall, 47, 48, 53, 54, 61, 70

- Bogoliubov-de Gennes Hamiltonian, 359–363, 365, 369–371, 374, 375, 377–380, 384, 392, 397, 398, 402, 404
- Bose-Einstein condensation, 300, 325, 329
- Brillouin light scattering (BLS), 126, 303
- Bulk-boundary correspondence, 368, 381

C

- Chern number, 178, 194–196, 244, 245, 248, 255, 257, 272, 273
- Chern-Simons invariant, 364–368, 370, 372, 381, 384, 390, 396
- Chiral anomaly, 250–252, 254, 255, 257–260, 284, 285
- Circularity, 75, 76, 79, 81, 83, 85, 87, 88, 91, 97, 111
- Collective motions, 109
- Core diameters, 83
- Coupled vortices, 96, 101
- Creation of skyrmions, 136, 138
- Critical velocity, 95
- Cross-tie wall, 78
- Cubic chiral magnets, 151–153, 158–160, 168

D

- Damon-Eshbach mode, 300, 302, 308, 329
- Demagnetization energy, 82
- Density functional theory (DFT), 277
- Density of state, 361, 362
- Dirac semimetal, 271, 272, 279–281, 287
- Dispersion relation, 105

Dispersions of gyrationary waves, 103
 Dissipation tensor, 90
 Domain wall, 1–5, 9–15, 20, 21, 23–33, 35, 37, 41–47, 49, 50, 53–70
 Dzyaloshinskii-Moriya interaction (DMI), 1–3, 5, 15, 18, 21, 24, 29, 30, 32, 34–37, 118, 329

E
 Eigenfrequencies, 98
 Eigenmodes, 97
 Electrically detected spin pumping, 219
 Exchange energy, 82
 Extrinsic scattering transport mechanisms, 211

F
 Fermi arcs, 239, 240, 246, 248, 249, 257, 258, 261
 Ferromagnetic resonance, 218, 303
 First-principle calculations, 255, 256, 258
 Forward volume mode, 303

G
 Gauss-Bonnet theorem, 376
 Geometric phase, 178
 Giant magnetoresistance, 269
 Gilbert damping parameter, 90
 Gyration, 87, 91
 Gyrationary switching, 95
 Gyrationary waves, 107
 Gyrotropic force, 52, 53, 56–60, 66
 Gyrotropic mode, 87, 89–91, 97, 104, 110
 Gyrovector, 90

H
 Hall micromagnetometry, 85
 Hall resistivity, 177, 178, 184, 185
 High-frequency absorption measurements, 102
 Hole, 360, 373, 374, 376, 377, 402
 Homotopy, 4–10, 13, 15, 23
 Hysteresis, 85

I
 Impurity scattering, 182
 Initial motion, 89
 Interaction strength, 97
 Interfacial Dzyaloshinskii-Moriya interaction (DMI), 118
 Intrinsic band structure Hall effect, 211
 Inverse spin Hall effect, 212
 Isolated antivortex, 79
 Isolated magnetic vortex, 78
 Isolated vortex, 82

J
 Jackiw-Rebbi model, 391, 401, 403

K
 Kerr microscopy, 125, 128, 130, 132, 134, 135, 137, 140, 141
 Kitaev model, 358, 362–364, 385
 Kramers' theorem, 368, 393, 404

L
 Landau-Lifshitz-Gilbert (LLG) equation, 17, 51, 54, 87–89, 218, 314
 Lorentz transmission electron microscopy (LTEM), 130, 172

M
 Magnetic droplet, 336, 342, 347, 348, 350, 352
 Magnetic force microscopy (MFM), 130, 152–154, 160
 Magnetic phase diagrams, 152–154, 157, 158, 163, 164, 166–168
 Magnetic point group, 271, 274, 275
 Magnetic tunnel junction (MTJ), 336
 Magnetic vortices, 76
 Magnetically doped topological insulator (MTI), 278, 286, 291
 Magnetization, 82
 Magneto-crystalline magnetic anisotropy, 178, 186
 Magnetocrystalline anisotropy, 268
 Magnetodynamical, 336, 342, 350, 352
 Magnetoresistive random-access memory (MRAM), 336
 Magnon, 299–329
 Magnonic crystals, 107
 Magnonic vortex crystal, 75, 96, 103, 107, 110
 Magnonic vortex crystals, 99
 Magnon transport, 227
 Majorana bound state, 357, 360–362, 368, 374, 375, 382, 385, 386, 389, 391, 394, 397, 405
 Majorana fermion, 357, 360–363, 366, 375, 380, 385, 387–389, 399, 405
 Meron, 1, 3, 5, 10, 13, 15–17, 37
 Metastable skyrmion phase, 152, 155, 156
 Micro-focused BLS, 304
 Micromagnetic model, 82
 Micromagnetic simulations, 89
 Monopoles in reciprocal space, 184
 Motion of skyrmions, 138, 139, 141

N
 Néel wall, 47, 57, 59, 70

Negative magnetoresistance, 240, 251, 253, 257, 258
Neumann principle, 274
Non-collinear magnets, 178, 186, 200, 202
Nonlinear oscillator model, 92
Non local resistance measurements, 215
Non-local spin Hall effect, 215
Non-local spin valves, 215
Nonparabolic Thiele model, 92
Non trivial topology, 151, 152, 154
Normal modes, 104
Nucleation, 86

O

Onsager reciprocity, 212
Orbital magnetism, 178, 200, 202, 204

P

Perpendicular magnetic anisotropy, 216
Photoemission electron microscopy (PEEM), 130
Photonic crystal, 329, 330
Point group, 274
Polarization, 75, 76, 80, 81, 84, 87, 89, 91, 93–95, 98–110
Polarization configurations, 100
Polarization patterns, 108
Polarization state, 102
Pure spin current, 209, 210
Pyrochlore iridates, 240–243, 246

Q

Quantum Hall effect, 268, 272, 273, 279, 280
Quantum spin Hall effect, 273, 274
Quantum spin Hall insulator, 369, 389, 391, 405

R

Rashba-Edelstein effect, 314
Relaxation time scales, 165, 166

S

Scalar spin chirality, 200, 201, 203, 204
Scanning electron microscopy with polarization analysis (SEMPA), 130–132, 134, 135
Scanning transmission X-ray microscopy (STXM), 100, 104, 341
Self-organized state formation, 99
Skyrmion, 1–5, 9, 10, 12, 13, 15–17, 21, 22, 25, 28–37, 118–120, 122–126, 129, 130, 133–142, 225
Skyrmion lattice, 152–168
Slonczewski term, 314

Small-angle neutron scattering, 153, 156–158, 165–168
Soliton, 335, 336, 342, 350, 352
Space-inversion, 269
Spin accumulation, 213–215, 226–228
Spin/charge conversion, 225
Spin-dependent transverse velocity, 211
Spin-flip length, 211
Spin electromotive force, 55, 68, 69
Spin Hall damping enhancement, 220
Spin Hall effect, 178, 209, 211–215, 222, 226, 229
Spin Hall effect driven nano-oscillators, 222
Spin Hall effect tunneling spectroscopy, 225
Spin Hall magnetoresistance, 213, 214, 226
Spin Hall tunneling spectroscopy, 214, 225
Spin-mixing conductance, 218, 227
Spin-orbit coupling (SOC), 178, 211, 212, 226, 268, 272, 277, 279, 281
Spin-orbit torque, 267, 270, 281
Spin polarization, 211
Spin-polarized scanning tunneling microscopy (SP-STM), 124
Spin-polarized low-energy electron microscopy (SPLEEM), 130
Spin pumping, 217
Spin pumping experiments, 214, 218–220
Spin Seebeck effect, 230, 314
Spin torque ferromagnetic resonance, 221
Spin-torque nano-oscillator (STNO), 300
Spin- $\#A0$; torque switching, 223
Spin transfer torque, 269
Spin transfer torque driven domain walls, 224
Spin-transfer torque FMR, 222
Spin wave, 299–301, 306, 308, 310, 311, 313–316, 318, 322, 323, 325, 329
Spin-wave emitters, 80
Stray fields, 84
Strongly correlated systems, 186, 204
Super cooled process, 152, 158
Super-cooled skyrmion phase, 152
Susceptibility measurements, 158

T
Thiele equation, 51, 53–55, 58, 59, 67, 90, 104, 110
Thiele model, 89, 101, 103
Time reversal symmetry, 270, 271, 289
Topological defect, 2, 3, 5, 6, 8, 9, 12–14, 31, 38, 41–46, 63, 65, 66, 70
Topological Hall effect, 152, 155, 162, 163, 165–167
Topological insulator (TI), 270, 271
Topological invariant, 239, 240

Topological quantum computer, 362
 Topological quantum materials, 239
 Topological superconductor, 358, 362–364,
 366, 374, 375, 378, 381, 382, 385,
 387–389, 393, 397, 399, 402, 403, 405
 Topological unwinding process, 162
 Topologically non trivial phase, 178
 Transverse wall, 64, 65
 Tuning the polarization state, 103
 Tunneling magnetoresistance, 269
 Two coupled vortices, 98

V

Vortex, 3, 5, 7, 9, 13, 15–17, 75, 76, 78–80,
 82–85, 87–90, 92–94, 96–98, 100, 104,
 105, 107, 110, 111
 Vortex core, 75–77, 80, 84, 85, 87–92, 94, 95,
 98–100, 104–106
 Vortex core switching, 94
 Vortex crystal, 109

Vortex molecule, 104
 Vortex oscillator, 96, 97
 Vortex wall, 47, 64–66, 69, 78
 VRAM or AVRAM, 80

W

Weak antilocalization effect, 251, 255
 Weyl fermions, 243, 248, 255, 262
 Weyl points, 191, 193, 198
 Weyl semimetal, 239, 240, 246, 249, 250, 254,
 258, 260, 272, 273, 279, 280, 282, 283,
 285, 287

Winding number, 4, 7, 9–12, 14–17, 21–23,
 26, 27, 29, 31, 32, 37

Z

Zeeman energy, 83, 345, 346, 349
 Zero mode, 360–362, 367, 371–374, 379–385,
 387, 392, 393, 395, 396, 399, 402, 405